

Lecture Notes in Mechanical Engineering

T. S. Sudarshan · K. M. Pandey ·
R. D. Misra · P. K. Patowari ·
Swapan Bhaumik *Editors*


Recent Advancements in Mechanical Engineering

Select Proceedings of ICROME 2021

 Springer

Lecture Notes in Mechanical Engineering

Editorial Board

Francisco Cavas-Martínez , Departamento de Estructuras, Construcción y Expresión Gráfica Universidad Politécnica de Cartagena, Cartagena, Murcia, Spain

Francesca di Mare, Institute of Energy Technology, Ruhr-Universität Bochum, Bochum, Nordrhein-Westfalen, Germany


Mohamed Haddar, National School of Engineers of Sfax (ENIS), Sfax, Tunisia

Young W. Kwon, Department of Manufacturing Engineering and Aerospace Engineering, Graduate School of Engineering and Applied Science, Monterey, CA, USA

Justyna Trojanowska, Poznan University of Technology, Poznan, Poland

Series Editors

Fakher Chaari, National School of Engineers, University of Sfax, Sfax, Tunisia

Francesco Gherardini , Dipartimento di Ingegneria “Enzo Ferrari”, Università di Modena e Reggio Emilia, Modena, Italy

Vitalii Ivanov, Department of Manufacturing Engineering, Machines and Tools, Sumy State University, Sumy, Ukraine

Lecture Notes in Mechanical Engineering (LNME) publishes the latest developments in Mechanical Engineering—quickly, informally and with high quality. Original research reported in proceedings and post-proceedings represents the core of LNME. Volumes published in LNME embrace all aspects, subfields and new challenges of mechanical engineering. Topics in the series include:

- Engineering Design
- Machinery and Machine Elements
- Mechanical Structures and Stress Analysis
- Automotive Engineering
- Engine Technology
- Aerospace Technology and Astronautics
- Nanotechnology and Microengineering
- Control, Robotics, Mechatronics
- MEMS
- Theoretical and Applied Mechanics
- Dynamical Systems, Control
- Fluid Mechanics
- Engineering Thermodynamics, Heat and Mass Transfer
- Manufacturing
- Precision Engineering, Instrumentation, Measurement
- Materials Engineering
- Tribology and Surface Technology

To submit a proposal or request further information, please contact the Springer Editor of your location:

China: Ms. Ella Zhang at ella.zhang@springer.com

India: Priya Vyas at priya.vyas@springer.com

Rest of Asia, Australia, New Zealand: Swati Meherishi at swati.meherishi@springer.com

All other countries: Dr. Leontina Di Cecco at Leontina.dicecco@springer.com

To submit a proposal for a monograph, please check our Springer Tracts in Mechanical Engineering at <https://link.springer.com/bookseries/11693> or contact Leontina.dicecco@springer.com

Indexed by SCOPUS. All books published in the series are submitted for consideration in Web of Science.

T. S. Sudarshan · K. M. Pandey · R. D. Misra ·
P. K. Patowari · Swapan Bhaumik
Editors

Recent Advancements in Mechanical Engineering

Select Proceedings of ICROME 2021

 Springer

Editors

T. S. Sudarshan
Materials Modification (United States)
Fairfax, VA, USA

K. M. Pandey
National Institute of Technology Silchar
Silchar, India

R. D. Misra
National Institute of Technology Silchar
Silchar, India

P. K. Patowari
National Institute of Technology Silchar
Silchar, India

Swapan Bhaumik
Department of Mechanical Engineering
National Institute of Technology Agartala
Agartala, India

ISSN 2195-4356

ISSN 2195-4364 (electronic)

Lecture Notes in Mechanical Engineering

ISBN 978-981-19-3265-6

ISBN 978-981-19-3266-3 (eBook)

<https://doi.org/10.1007/978-981-19-3266-3>

© The Editor(s) (if applicable) and The Author(s), under exclusive license to Springer Nature Singapore Pte Ltd. 2023

This work is subject to copyright. All rights are solely and exclusively licensed by the Publisher, whether the whole or part of the material is concerned, specifically the rights of translation, reprinting, reuse of illustrations, recitation, broadcasting, reproduction on microfilms or in any other physical way, and transmission or information storage and retrieval, electronic adaptation, computer software, or by similar or dissimilar methodology now known or hereafter developed.

The use of general descriptive names, registered names, trademarks, service marks, etc. in this publication does not imply, even in the absence of a specific statement, that such names are exempt from the relevant protective laws and regulations and therefore free for general use.

The publisher, the authors, and the editors are safe to assume that the advice and information in this book are believed to be true and accurate at the date of publication. Neither the publisher nor the authors or the editors give a warranty, expressed or implied, with respect to the material contained herein or for any errors or omissions that may have been made. The publisher remains neutral with regard to jurisdictional claims in published maps and institutional affiliations.

This Springer imprint is published by the registered company Springer Nature Singapore Pte Ltd. The registered company address is: 152 Beach Road, #21-01/04 Gateway East, Singapore 189721, Singapore

Preface

This book proceedings contains the technical papers accepted and presented at the 2nd International Conference on Recent Advancements in Mechanical Engineering (ICRAME 2021), which was held during February 7–9, 2021, in Mechanical Engineering Department, National Institute of Technology Silchar, in online mode. The conference brought together experts from academic, scientific and industrial communities, who addressed new challenges and innovative ideas, presented their latest research findings and also gave perspective of the future directions in the field of mechanical engineering. A total of 50 research papers were presented at this conference by delegates from across India and also abroad. The papers accepted and presented at this conference included the following broad areas of mechanical engineering—thermal engineering, design engineering, manufacturing/production engineering, surface engineering and renewable energy. The recent developments in these areas were dealt within this conference. The papers related to the theoretical modeling works, analytical and numerical modeling including CFD, experimental investigations, and also state-of-the-art review papers in the relevant areas were considered for ICRAME 2021. This book proceedings hereby publishes all such papers of the said conference.

Fairfax, USA
Silchar, India
Silchar, India
Silchar, India
Agartala, India

T. S. Sudarshan
K. M. Pandey
R. D. Misra
P. K. Patowari
Swapan Bhaumik

Contents

Influence of Non-uniform Heating Profiles on Free Convection Entropy Generation Inside an Enclosure Filled with Nanofluid	1
Abhinav Saha, Nirmal K. Manna, and Koushik Ghosh	
Mechanical Properties, Microstructural and Surface Topography Evaluation of AISi10Mg Alloy Produced by DMLS Process	15
R. K. Shah and P. P. Dey	
Experimental Investigation of the Performance of a Low-Cost Flexible All Plastic Solar Air Heater	27
Deva Kanta Rabha, Prachurjya Goswami, Sahnawaz Ullah, Sachin Basak, and Jishu Raj Baruah	
Microbial Fuel Cell—A Review	39
Dhrupad Sarma, Parimal Bakul Barua, Ashutosh Das, Nur Mehdee Rahman, Shafiq Alom Prodhani, and Sazid Anwar	
Optimization of MRR and KW of SS 304 in Wire EDM by RSM Technique	57
Shatarupa Biswas, Yogesh Singh, and Manidipto Mukherjee	
Numerical Study on Effects of Geometrical and Operating Parameters of Bolt on Performance of Bolted Joint	69
Sandeep D. Borawake and Sachin S. Naik	
Effect of Electrode Length and AC Frequency on Mixing in a Diamond-Shaped Split-And-Recombine Electroosmotic Micromixer	83
Amrendra Kumar, Nirmal K. Manna, and Sandip Sarkar	

Parametric Optimization of Tribological Process Parameters and Their Comparative Effect on Wear Responses of TiCrN Coated Cold Work Tool Steel	93
Sunil Kumar, Saikat Ranjan Maity, Lokeswar Patnaik, and Sumit Bhowmik	
Effect of Surface Modification on the Nanomechanical and Wear Properties of AISI D3 Cold Work Tool Steel	105
Sunil Kumar, Saikat Ranjan Maity, and Lokeswar Patnaik	
Performance Analysis of Split Circular and Drop-Form Fin Geometry for Enhanced Heat Transfer Rate	115
Alok Ranjan, Sagnik Pal, and Madhujit Deb	
Effects of Thermal Aspect Ratio on MHD Thermal Convection of Cu–Water Nanofluid Saturated Porous Cavity	127
Milan K. Mondal, Nirmalendu Biswas, Aparesh Datta, Nirmal K. Manna, and Dipak Kumar Mandal	
Review the Study of Employability Concept in Technical Institutes	145
Vijay Kalbande, Nitin Mandavgade, Mahesh Kanojiya, and Riddheshwar Bilawane	
Stochastic First-Ply Failure Analysis of Laminated Composite Plate: A Moving Least Square Approach	159
Subrata Kushari, S. R. Maity, A. Chakraborty, and S. Dey	
Electric Field Modulated Drop Formation from Orifices	171
Manash P. Borthakur and Subhasis Chakravarthy	
Robotic Systems Deployed to Combat COVID-19 Pandemic: A Review	179
Deep Singh, Rutupurna Choudhury, and Yogesh Singh	
Design and Numerical Analysis of Hub Less Wheel	197
Abhishek Singh Yadav and Minesh Vohra	
Effect of Nano Alumina Reinforcements on the Tribological Behavior of Electroless Nickel-Phosphorus Coatings	211
D. Mohanty, T. K. Barman, and P. Sahoo	
Transport Phenomena in a Double Driven Cavity Involving Buoyancy, Magnetic Field and Nanofluid	223
Kanad Sen, Nirmalendu Biswas, Sandip Sarkar, and Nirmal K. Manna	
Curvature Effect of Heated Sidewall During Heat Transport of Different Prandtl Number Fluids in a Square Enclosure in the Presence of a Magnetic Field	239
Shreyasi Maitra, Nirmalendu Biswas, Nirmal K. Manna, and Dipak Kumar Mandal	

Effect of Bottom Wall Curvature on Thermal Convection of Air/Nanofluid in a Differentially Heated Cavity Subjected to a Magnetic Field 255
 Deep Chatterjee, Nirmalendu Biswas, Nirmal K. Manna, and Dipak Kumar Mandal

Climatic Parameter Analysis on Building Materials for Kolkata, Eastern Zone of India 273
 Krushna Gouda and Biplab Das

Enhanced Damping in a TLD by Slat Screens and Horizontal Baffles: A Comparative Study 287
 Tanmoy Konar and Aparna Ghosh

Additive Manufacturing: An Emerging Tool to Fabricate Bioinspired Structures 297
 Vishal Mishra, Sushant Negi, and Simanchal Kar

Taguchi Optimization of Mechanical Properties in Al-Kaoline Metal Matrix Composite Fabricated Through Powder Metallurgy Technique 313
 V. S. S. Venkatesh and Ashish B. Deoghare

Fabrication Based Analysis of Super-Hydrophobic Surface 325
 Avinash Kumar, Sushant Negi, and Simanchal Kar

Design, Analysis and Development of Virtual Working Model of Self Balancing Robot 339
 C. H. Patel, Naga Sumanth Putta, Akula S. V. S. S. Sri Manikanta, Eluri Nikhil Reddy, and Kambala Prasanna Ramesh Kumar Babu

Effect of Relative Thickness on Natural Frequency Analysis of Hybrid Hyperbolic Paraboloid Shells 351
 Vaishali and S. Dey

A Review: High Amplitude Vibration and Jump Phenomena Attenuation Methods in Different Dynamic Systems 361
 Mohd Anis Ansari, Prabina Kumar Meher, Alfa Bisoi, and Agnimitra Biswas

Investigation and Characterization of Coir Fiber Reinforced Polymer Composite Under Cyclic Loading 377
 Kshounish Brahma, Sumit Bhowmik, and Krushna Gouda

Acoustic Analysis of Effect of Louver Window Material in Noise Attenuation 389
 G. Avinash, Santosh Kumar, B. Goutham Krishna, B. Mohammed Akram, Karan Manoj, R. Eshanth, and N. S. Sriprasad

Dock Detection for an Underwater Autonomous Vehicle Using Deep Learning in a Simulated Environment	403
Swastik Jena and Saikat Ranjan Maity	
Performance Evaluation of Evacuated Tube Containing Heat Pipe Solar Collector-Based Solar Dryer	413
Adarsh Abi Mathew, R. Anandu Krishna, R. Sivakumar, and T. Venugopal	
Study and Management Aspects of Reserves, Production, Consumption and Life of Oils of the World	427
Sameer Kumar Anand and Soupayan Mitra	
Prediction of Remaining Useful Life (RUL) of Bearing Using Exponential Degradation Model	439
Keval Bhavsar and Vinay Vakharia	
Analysis of Tool Defect in Ultrasonic Machining Process Through Numerical Modelling	449
Mehdi Mehtab Mirad, Jiomani Talukdar, and Bipul Das	
An Overview: Natural Fiber Composites as Eco-Friendly Materials, Their Properties, Chemical Treatments, Applications	459
Rafid Sobhan, Afsana Mustari, Prajjayini Chakma, and N. R. Dhar	
Additive Manufacturing of Fiber Reinforced Composite: Material, Methods Challenges and Future Works	473
Kamal Kumar Ojha, Srinath Chowdarpally, and Vishal Francis	
Numerical Investigation of the Effect of Developed Thermal Stress on Ultrasonic Horn Material	485
Guddakesh Kumar Chandan and Chinmaya Kumar Sahoo	
Corrosion in Thermal Pipes: An Investigation on Problems and Causes	495
A. Hari Ganesh, R. D. Mishra, and S. Kar	
Comparative Analysis of Hybrid Renewable Energy System Using Homer: A Case Study of Silchar, India	509
Anil Kumar Singh Maisanam, Agnimitra Biswas, and Kaushal Kumar Sharma	
Impact of Wall Fuel and Air Injections Inside the Parallel Fuel Injection-Based Scramjet Combustor: A Numerical Analysis	523
Kumari Ambe Verma, Kaushal Kumar Sharma, and Krishna Murari Pandey	
Quality Tools Implementation Practice to Reduce Forging Defects in Crankshaft Manufacturing Industries: An Overview	533
Amitkumar B. Solanki, Sunilkumar S. Sonigra, and Vivek Vajpayee	

Numerical Simulation of Temperature Distribution for Low Power Laser Clad Coating of Nickel 557
 Dhiraj Raj, Saikat Ranjan Maity, and Bipul Das

Gear Profile Polishing Using Rotational Magnetorheological Abrasive Flow Finishing Process 565
 Manjesh Kumar, Abhinav Kumar, Hari Narayan Singh Yadav, and Manas Das

Particle Swarm Optimization Based Search for Optimal Operating Condition in WEDM Operation of A286 Superalloy 577
 Subhankar Saha, Saikat Ranjan Maity, and S. Dey

Parametric Analysis of Machining of Titanium Grade-2 Alloy in EDM Under Tap Water 587
 Binoy Kumar Baroi, Tapas Debnath, Jagadish, and Promod Kumar Patowari

Effect of Tool Rotation on Electrochemical Milling of Stainless Steel 316L 601
 Abhinav Kumar, Hari Narayan Singh Yadav, Manjesh Kumar, and Manas Das

Development of Finite Elemental Analysis Model for Numerical Simulation of TIG Welding of Thin Aluminium Sheet 613
 Rahul Kumar Mahato, Mohd Aslam, Lokavarapu Rama Krishna, and Chinmaya Kumar Sahoo

Experimental Analysis on the Influence of Biofuel Amalgamated Al₂O₃ Nano Particles on the Performance and Emission Attributes of a C.I. Engine 623
 Amarendra Deka, Debarup Borah, and Rahul Dev Misra

Bearing Fault Identification of Augmented Grayscale Textured Images Using K-Nearest Neighbor 637
 Jaimin Panchal and Vinay Vakharia

About the Editors

Dr. T. S. Sudarshan is the President and CEO of Materials Modification, Inc. He has a Ph.D. from Virginia Tech and has been responsible for driving the company's technological leadership in the development of next generation materials, processes and techniques for the past 34 years. He has been a passionate entrepreneur and provided employment to over 400 individuals, provided the first jobs for over 200 students, served on over 10 thesis committees for M.S. and Ph.Ds. Dr. Sudarshan has served on the National Materials Advisory Board, Ohio Third Frontier Committees, Ohio Federal Research Network, ASM International Board, Committees for the Army, NSF, NIH and DoE and Selection Committee for the R&D 100 awards. He has over 180 papers, is editor of two journals—*Materials and Manufacturing Processes* since 1988 and *Surface Engineering* since 1996, co-editor of 34 books, holder of 36 patents, winner of two R&D 100 awards, Fellow of ASM International, Fellow of IFHTSE, Fellow of IMMM, UK, and Distinguished Alumni of IITM. He has been responsible for heading the development of 18 products and has worked in difficult-to-solve problems in the area of nanotechnology and surface engineering. He has also been on the Advisory Board of ATI, South Carolina and several other companies as a consultant.

Prof. K. M. Pandey did Ph.D. in 1994 from Department of Mechanical Engineering, IIT Kanpur, India. Currently he is working as Professor (HAG) of Mechanical Engineering at National Institute of Technology Silchar, Assam, India, since September 2018 and as Professor since May 2006. He obtained B.Tech. in Mechanical Engineering from BHUIT Varanasi in 1980 now known as IITBHU and M.Tech. in Heat Power engineering in 1987 from the same institute. He has authored more than 159 research papers in SCI/SCIE/ Scopus indexed journals and conferences. His h-index is 19 in Scopus and SCI and 24 in google scholar. He has also authored 6 books and 9 book chapters. Currently he is working in the area of thermo fluids and manufacturing sciences. He has also served as seconded faculty consultant at CPSC, Manila, Philippines in 2002. He has served NIT Silchar as Dean Faculty welfare and Dean Research in the year 2011 and 2012. He has served as Head of Department for two terms of 3 years at NIT Silchar. He is taken as member of BOG, NIT Silchar twice. He

is a fellow of Institution of Engineers India and member of ASME. He is life member of Welding Society of India and life member of Fluid Mechanics and Fluid Power Society of India. Prof. K. M. Pandey had been keynote speaker and co-editor in 2nd Annual International Conference on Advanced Material Engineering [AME2016], April 15–17, 2016, Wuhan, Hubei, China; keynote speaker in International Seminar in Advances in Materials Science and Engineering, Singapore, 22–24 June 2018 and keynote speaker and General Chair 5th International Conference on Green Materials and Environmental Engineering (GMEE2019), Guangzhou, China. He is taken as member of editorial boards and reviewer in many reputed international journals. In 2020 he has been keynote speaker in 3 international conferences held in Beijing and Shanghai and he has been editor in ICMEM 2020 held in Shanghai and the proceedings is published as book by Springer in December 2020.

Dr. R. D. Misra has got his B.E. (Mechanical Engineering) from Jorhat Engineering College under Dibrugarh University in 1991. He did his M.Tech. in the specialization of Energy Studies from IIT Delhi in 1996. He has got the Ph.D. degree from IIT Roorkee in 2004. Dr. Misra has joined the Department of Mechanical Engineering of National Institute of Technology (formerly, Regional Engineering College) Silchar in 1992 as Lecturer. Presently he is serving as Professor (HAG) in the same department. He has served NIT Silchar at various administrative capacities like Dean (SW), Dean (FW), Head of Mechanical Engineering Department, Associate Dean (Administration) and Associate Dean (Research and Consultancy) and Faculty-In-Charge for a number of responsibilities. Dr. Misra has been involved in various activities under BOSs of various institutions like NIT Mizoram, NIT Arunachal Pradesh, NIT Meghalaya, etc. He is serving as Advisor (UGC Nominee) for KAUSHAL programme for Tengakhat College, Dibrugarh University. He was also involved as NBA Mentor for NBA Accreditation of UG programmes at TIT Agartala, Tripura. Dr. Misra has research experience in both experimental and computational analyses. His research focus areas are the applications of exergy and thermoeconomics in thermal systems, bio-fuel research for CI engine applications, experimental and CFD analysis of water turbines, boiling heat transfer enhancements, refrigeration and air-conditioning systems etc. Dr. Misra has guided 10 Ph.D. scholars and presently supervises 10 research scholars. He has guided about 45 M.Tech. dissertations and a number of B.Tech. projects. He has published more than 65 research articles in refereed international journals, about 60 articles in refereed national/international conferences, one book, and 3 book chapters. He has completed two research projects funded by AICTE and presently working on two high-value research projects funded by MNRE and DST, Government of India.

Dr. P. K. Patowari is a Professor in the Department of Mechanical Engineering at National Institute of Technology (NIT) Silchar, Assam. He joined NIT Silchar as faculty member in the year 1995. He served as Dean (FW) and Head of the Department. He obtained his B.Tech. degree (Mechanical Engineering) from NERIST, Itanagar, M.E. (Production Engineering) from Jadavpur University, Kolkata, and Ph.D. from the Indian Institute of Technology (IIT) Kharagpur. His major areas of

research include Advanced/Non-traditional Machining, Micro-Manufacturing and Computer Aided Manufacturing (CAM). He has published around 50 papers in international journals and around 65 papers in international and national conferences. He has published around 20 books and book chapters. He has supervised 8 Ph.D. scholars and 31 M.Tech. students. He along with his students filed 3 patents and out of which 1 patent was granted. He has 3 projects in his credit including one under DST FIST Program. Currently, he is the life member of professional bodies like Indian Society for Technical Education (ISTE), The Institution of Engineers (India) and Institute of Smart Structures and Systems (ISSS).

Dr. Swapan Bhaumik Professor and Former Head of Mechanical Engineering Department, NIT Agartala, obtained Bachelor, Master and Ph.D. degree from Tripura Engineering College under Calcutta University, Jadavpur University and IIT Roorkee in 1987, 1991 and 2003, respectively. He started his teaching profession in 1991 in Tripura Engineering College (Presently NIT Agartala). His specialization is thermo-fluid engineering and research field is boiling heat transfer. He published 65 technical papers in international and national journals and conferences, already guided 25 B.Tech., 29 M.Tech. and 3 Ph.D. Scholars and presently guiding 5 B.Tech. (Major-2 and Minor-3), 5 M.Tech. and 5 Ph.D. scholars. He is a reviewer in many international journals. He is instrumental for setting up of ISTE and IEI Student Chapters at NIT Agartala. He organized many faculty development programmes including AICTE sponsored Two Week Induction Training Programme for newly recruited faculty members and MHRD sponsored GIAN course on Sustainable Cooling Technologies. He was the First Dean (Academic) of NIT Agartala and subsequently served as Dean (Faculty Welfare). Dr. Bhaumik is the Fellow of The Institution of Engineers (India) and SEEM. He is also the Member of ISTE, ISHRAE, ISME, ASME and ISTAM. He received R&D Grants from AICTE, DST, GOI and IEI and is recipient of Chemical Weekly Award in 2006, Sir Ganga Ram Memorial Award in 2017 from IEI. He is the Founder Secretary of NIT Agartala Alumni and continued for five years. He became the first elected Council Member of IEI from North-East India and served Tripura State Centre of IEI as Past Chairman (2013–2015) and Past Honorary Secretary (2009–2011), and also has been awarded the ENGINEER OF THE YEAR-2018 by Tripura State Centre of IEI. He also became Vice-President of IEI for the session 2018–2019. Presently, Dr. Bhaumik is serving as Chairman, Committee for Advancement of Technology and Engineering (CATE) who is looking after the whole technical activities of IEI i/c publication of IEI-Springer Journals.

Influence of Non-uniform Heating Profiles on Free Convection Entropy Generation Inside an Enclosure Filled with Nanofluid



Abhinav Saha, Nirmal K. Manna, and Koushik Ghosh

Abstract The scope of the present work is to explore the influence of non-uniform heating on entropy generation during free convection in an enclosure using Cu-water nanofluid. The numerical analysis is performed using the finite volume approach. The investigation is carried out in a two-dimensional framework. The non-uniform heating is implemented on the left wall considering parabolic, linearly increasing, and linearly decreasing profiles while the total power is kept constant. The right wall is maintained isothermally cold. Other walls of the enclosure are maintained adiabatic. The numerical simulation is carried out for the fixed value of the Rayleigh number and nanoparticle volume fraction. The details of the flow and heat transfer are studied using the streamlines and isotherms. The irreversibility due to the flow and heat transfer is studied using the contours of the entropy generation rate due to the thermal conduction and viscous dissipation. The results show that for all the cases investigated, the linearly increasing heating profile is most undesirable as the rate of entropy generation is maximum. On the other hand, the parabolic profile shows a minimum entropy generation and is suggested as a better heating profile.

Keywords Free convection · Non-uniform heating · Entropy generation · Nanofluid

Nomenclature

AR Aspect ratio

A. Saha (✉) · N. K. Manna · K. Ghosh
Department of Mechanical Engineering, Jadavpur University, Kolkata, India
e-mail: saha.abhinav.2010@gmail.com

N. K. Manna
e-mail: nirmalkmannaju@gmail.com

K. Ghosh
e-mail: kghoshjdvu@gmail.com

Be	Bejan number ($= (S_{gen})_{conduction} / (S_{gen})_{total}$)
Ec	Eckert number ($= \alpha^2 k / L^3 C_p q$)
g	Acceleration due to gravity (m/s^2)
L	Dimension of a square enclosure (m)
Nu_m	Average Nusselt number ($= hL / K_f$)
Nu_m^*	Ratio of Nusselt number
P	Non-dimensional pressure
Pr	Prandtl number ($= \nu_f / \alpha_f$)
q	Heat flux
qr	Ratio of heat flux ($= q_{act} / q_{mean}$)
Ra	Rayleigh number ($= g \beta_f q L^4 / k_f \alpha_f \nu_f$)
$(S_{gen})_{av}$	Average entropy generation
T	Temperature
T_∞	Ambient temperature
T_∞^*	Non-dimensional ambient temperature
U, V	Dimensionless velocity in X and Y direct

Greek Symbols

ρ	Density (kg/m^3)
ν	Kinematic viscosity (m^2/s)
θ	Non-dimensional temperature
β	Thermal expansion coefficient
ψ	Non-dimensional stream function

Subscripts

h	Hot wall
c	Cold wall
f	Fluid
nf	Nanofluid
np	Nanoparticle

1 Introduction

Thermally induced buoyancy-driven flow commonly known as free convection finds many applications particularly in the cooling of electronic equipment. Conventionally, a fluid used in cooling applications achieves low heat transfer due to lower

thermal conductivity. The thermal conductivity is enhanced by suspension of nano-metallic particles to base fluid known as nanofluids. Putra et al. [1] investigated the free convection of nanofluid experimentally. They extensively studied the effect of solid volume fraction of nanoparticles, Rayleigh number, and aspect ratio on free convection heat transfer. Bouchoucha and Bessai'h [2] investigated nanofluid-based free convection undergoing in a cavity. This analysis is carried out considering different heater lengths. They found that the average Nusselt number increases with an increase in heater length. Free convection is usually investigated on the perspective of entropy generation as it provides an important criterion in the assessment of the quality in thermodynamic applications. The existence of temperature gradients and fluid friction in the thermodynamic system results in energy losses which give rise to entropy generation in the system. For thermal convective systems, Bejan [3] originally presented the concept of entropy generation. The effect of cavity aspect ratio (AR) on free convection entropy generation was analyzed by Ilis et al. [4]. Using differential heating configuration in a cavity and keeping the Rayleigh number the same, they found that total entropy generation at higher AR is less compared to that at lower AR. Using discrete heaters (with the heat-flux condition) placed at the bottom of a square cavity, Mukhopadhyay [5] studied the nature of entropy generation. This study was focused to determine the optimal position of heaters from the thermodynamic point of view through the analysis of entropy generation. Famouri and Hooman [6] using a partitioned cavity reported in entropy generation on free convection. The emphasis made in this study is on the location of heater position on heat transfer and entropy generation. The literature review reveals that the maximum number of works has considered either different temperature conditions or uniform heat flux conditions. The consideration of different heat-flux profiles with their comparison is missing. From the practical application point of view, non-uniform heating profiles of heat fluxes are very important. Therefore, in the present work, the attention is focused on the effect of non-uniform flux conditions on entropy generation keeping total power input constant.

2 Problem Definition

Figure 1 shows the physical domain with the heating profiles. This study considers a two-dimensional computing domain filled with a nanofluid as shown in Fig. 1a. The nanofluid consists of water (as base fluid) and nanoparticles of Cu (micron order size). Four heating profiles (as shown in Fig. 1b) are applied on the left wall of the cavity, keeping their input power the same (constant). These profiles are uniform, parabolic, and increasing and decreasing linearly as shown in Fig. 1b. The right wall is maintained cold at a uniform temperature. The top and bottom walls of an enclosure are kept adiabatic. The incompressible Newtonian flow is assumed in the enclosure. The constant physical properties of water (indicated by suffix f), Cu-nanoparticles (suffix p), and nanofluid (suffix nf) are taken during this analysis. The constant physical properties are taken during this analysis; however, the thermal effect on the

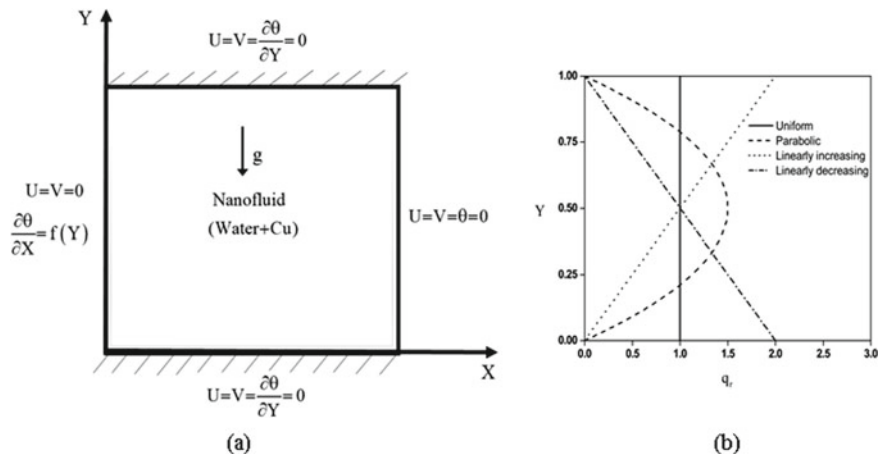


Fig. 1 a Computational domain of a square enclosure filled nanofluid b Various heating profile along the left wall

change in density is accounted for through the buoyancy term by the Boussinesq approximation.

3 Mathematical Formulation

The single-phase model is applied for this study under the steady flow condition. The flow equations are derived from the conservation principles (mass, momentum and energy). The dimensional forms of the equations under the above-mentioned assumptions can be expressed as:

$$\frac{\partial u}{\partial x} + \frac{\partial v}{\partial y} = 0 \quad (1)$$

$$\rho_{nf} \left[u \frac{\partial u}{\partial x} + v \frac{\partial u}{\partial y} \right] = -\frac{\partial p}{\partial x} + \mu_{nf} \left(\frac{\partial^2 u}{\partial x^2} + \frac{\partial^2 u}{\partial y^2} \right) \quad (2)$$

$$\rho_{nf} \left[u \frac{\partial v}{\partial x} + v \frac{\partial v}{\partial y} \right] = -\frac{\partial p}{\partial y} + \mu_{nf} \left(\frac{\partial^2 v}{\partial x^2} + \frac{\partial^2 v}{\partial y^2} \right) + (\rho\beta)_{nf} g(T - T_c) \quad (3)$$

$$u \frac{\partial T}{\partial x} + v \frac{\partial T}{\partial y} = \alpha_{nf} \left(\frac{\partial^2 T}{\partial x^2} + \frac{\partial^2 T}{\partial y^2} \right) \quad (4)$$

With the following dimensionless variables,

$$X = \frac{x}{L}, Y = \frac{y}{L}, U = \frac{uL}{\alpha_f}, V = \frac{vL}{\alpha_f}, P = \frac{\rho L^2}{\rho_{nf} \alpha_f^2}, \theta = \frac{T - T_c}{T_h - T_c} \quad (5)$$

the governing equations are non-dimensionalized as

$$\frac{\partial U}{\partial X} + \frac{\partial V}{\partial Y} = 0 \quad (6)$$

$$U \frac{\partial U}{\partial X} + V \frac{\partial U}{\partial Y} = -\frac{\partial P}{\partial X} + \frac{\mu_{nf}}{\alpha_{nf} \alpha_f} \left(\frac{\partial^2 U}{\partial X^2} + \frac{\partial^2 U}{\partial Y^2} \right) \quad (7)$$

$$U \frac{\partial V}{\partial X} + V \frac{\partial V}{\partial Y} = -\frac{\partial P}{\partial Y} + \frac{\mu_{nf}}{\alpha_{nf} \alpha_f} \left(\frac{\partial^2 V}{\partial X^2} + \frac{\partial^2 V}{\partial Y^2} \right) + \frac{(\rho\beta)_{nf}}{\rho_{nf} \beta_f} \text{Ra Pr } \theta \quad (8)$$

$$U \frac{\partial \theta}{\partial X} + V \frac{\partial \theta}{\partial Y} = \frac{\alpha_{nf}}{\alpha_f} \left(\frac{\partial^2 \theta}{\partial X^2} + \frac{\partial^2 \theta}{\partial Y^2} \right) \quad (9)$$

In the above equations, the Rayleigh (Ra) and Prandtl (Pr) numbers are defined considering the properties of the fluid as given as follows:

$$\text{Ra} = \frac{g\beta_f q L^4}{k_f \alpha_f \nu_f}; \text{Pr} = \frac{\nu_f}{\alpha_f} \quad (10)$$

Local entropy generation, S_{gen} , is obtained by the summation of the thermal (conduction) and viscous (friction) contributions of the entropy generation [5] as expressed, respectively, by the first and second terms of the following dimensional form of the equation.

$$S_{gen} = \frac{k}{T^2} \left[\left(\frac{\partial T}{\partial x} \right)^2 + \left(\frac{\partial T}{\partial y} \right)^2 \right] + \frac{\mu}{T} \left[2 \left\{ \left(\frac{\partial u}{\partial x} \right)^2 + \left(\frac{\partial u}{\partial y} \right)^2 \right\} + \left(\frac{\partial u}{\partial x} + \frac{\partial v}{\partial y} \right)^2 \right] \quad (11)$$

The above equation is transformed into the dimensionless form (NS_L) as [5]

$$NS_L = \frac{1}{(\theta + T_\infty^*)} \left[\left(\frac{\partial \theta}{\partial X} \right)^2 + \left(\frac{\partial \theta}{\partial Y} \right)^2 \right] + \frac{Ec \text{ Pr}}{(\theta + T_\infty^*)^2} \left[2 \left\{ \left(\frac{\partial U}{\partial X} \right)^2 + \left(\frac{\partial U}{\partial Y} \right)^2 \right\} + \left(\frac{\partial U}{\partial X} + \frac{\partial V}{\partial Y} \right)^2 \right] \quad (12)$$

where the Eckert number (Ec) is calculated using [5]:

$$(Ec = \alpha^2 k / L^3 C_p q) \quad (13)$$

Table 1 The properties of base fluid (H₂O) and nanoparticles (Cu)

	$\rho(\text{kg/m}^3)$	$C_p(\text{J/kg} - \text{K})$	$k(\text{w/m} - \text{K})$	$\mu(\text{kg/m} - \text{s})$	$\beta(1/\text{K})$
Water	997.5	4178	0.6129	0.0008295	0.00028
Cu- nanoparticles	8933	385	401	–	1.67E–05

The thermophysical properties of nanofluids are shown in Table 1.

The closure relations to calculate properties of nanofluid are given by Eqs. (14) to (16).

$$\rho_{nf} = (1 - \phi)\rho_f + \phi\rho_p \quad (14)$$

$$(\rho C_p)_{nf} = (1 - \phi)(\rho C_p)_f + \phi(\rho C_p)_p \quad (15)$$

$$(\rho\beta)_{nf} = (1 - \phi)(\rho\beta)_f + \phi(\rho\beta)_p \quad (16)$$

The dynamic viscosity and thermal conductivity (which are given by Brinkman and Maxwell [7, 8]) are shown in Eqs. (17) and (18).

$$\mu_{nf} = \mu_f / (1 - \phi)^{2.5} \quad (17)$$

$$K_{nf} = K_f \{ (K_p + 2K_f) - 2\phi(K_f - K_p) \} / \{ (K_p + 2K_f) + \phi(K_f - K_p) \} \quad (18)$$

The boundary conditions in the non-dimensional form are shown as follows:

$$\text{At } X = 0 : U = V = 0, \frac{\partial\theta}{\partial X} = f(Y) \quad (\text{Heat source}) \quad (19)$$

$$\text{At } X = 1 : U = V = 0, \theta = 0 \quad (\text{Cold wall}) \quad (20)$$

$$\text{At } Y = 0 : U = V = 0, \frac{\partial\theta}{\partial Y} = 0 \quad (\text{Adiabatic wall}) \quad (21)$$

$$\text{At } Y = 1 : U = V = 0, \frac{\partial\theta}{\partial Y} = 0 \quad (\text{Adiabatic wall}) \quad (22)$$

where $-f(Y) = 1, 2Y, 2(1-Y), 6(Y-Y^2)$, respectively for uniform, linearly increasing, linearly decreasing, and parabolic heating. The geometry of the cavity,

meshing, and boundary identification are carried out with the help of a pre-processor Gambit software. In a simple geometry of a 2-D square cavity in the present case, a structured grid is preferred. Also, the uniform grid in both directions is used as it facilitates the resolution of a flow equally well throughout the flow domain. In Gambit, it is achieved by using a logic option as MAP and an element type option as QUARD.

The governing Eqs. (6) to (9) are subjected to the above-mentioned boundary conditions as given in Eqs. (19) to (22). These are solved by the ANSYS FLUENT. The SIMPLE algorithm is used for decoupling of pressure and velocity. The different heating profiles are implemented by writing user-defined functions. The convergence criteria for all the governing equations are set by residuals less than 10^{-6} .

4 Results and Discussions

The free convection flow and heat transfer are carried in a square cavity. The cavity is filled with nanofluid where the base fluid is H₂O and the nanoparticle is Cu. The numerical analysis is performed for different heating profiles while keeping the Rayleigh number and solid volume fraction fixed. The non-uniform heating is carried out using different heat flux profiles such as parabolic, linearly increasing, and linearly decreasing maintaining total power constant. The Rayleigh number is fixed at 10^5 , and the solid volume fraction is kept at 0.04. The flow physics and heat transfer are studied with the help of contours of streamlines and isotherms. The irreversibility in the flow domain is studied with the help of contours of entropy generation due to conduction and viscous dissipation.

4.1 Grid Independence Study

The grid independent study is performed for free convection in a square enclosure for $Ra = 10^5$ as shown in Table 2. The left wall and right walls of an enclosure are maintained at isothermal temperature. The other two walls are kept adiabatic. The square enclosure is filled with water-based Cu nanofluid. The nanoparticle volume fraction is fixed at 0.04. The grid test is carried for three different grids, namely 50×50 , 100×100 and 150×150 , shown in Table 2. It is further observed that the results of the average Nusselt number obtained with grid counts 100×100 and 150×150 are close to each other with a deviation of 0.2%. Therefore, the

Table 2 Mesh independence test of Nu_m at $Ra = 10^5$

	Number of grid counts		
	$N_1 (50 \times 50)$	$N_2 (100 \times 100)$	$N_3 (150 \times 150)$
$Ra = 10^5$	4.987	4.938	4.927

Table 3 The comparison of Nu_m^* for differentially heated square enclosure

	Famouri and Hooman [6]	Present study	% error
$Ra = 10^3$	1.045	1.042	0.28

intermediate grid count 100×100 is used for further computations in this study as a good compromise between accuracy and computational time.

4.2 Comparison of Results

The numerical model is validated for free convection in an enclosure filled with water-based Cu nanofluid is displayed in Table 3. The numerical result of Nusselt number ratio ($Nu_m^* = Nu_m(\phi \neq 0) / Nu_m(\phi = 0)$) for $Ra = 10^5$ and the solid volume fraction of nanoparticle is 0.04. The present result shows good agreement with Famouri and Hooman [6].

The numerical model is further compared with the contours of static temperature, streamlines, entropy generation due to heat transfer, and fluid friction of Mukhopadhyay [5] which is shown in Fig. 2.

4.3 Influence of Non-uniform Heating on Heat and Fluid Flow

The details of flow physics and heat transfer are studied with the help of streamlines and isotherms. Figure 3 shows the streamlines plot for various heating profiles such as uniform, parabolic, linearly heating, and linearly decreasing. In all the cases, the flow is unicellular as the fluid gains heat from the hot wall and moves upward while it rejects heat to the cold and move downward. It is observed from levels of contours of streamlines that the maximum and minimum values of the streamfunctions are for linearly decreasing and linearly increasing heat flux, respectively. The values of streamfunctions for uniform and parabolic heat flux profiles are in between linearly increasing and linearly decreasing heat flux profile.

Figure 4 shows a temperature contour plot for different heating profiles such as uniform, parabolic, linearly heating, and linearly decreasing. In all the cases, the fluid collects the heat from the hot wall and then rejects heat to the cold wall. This results in an increase in temperature gradient near the left wall and the right wall. The glimpse of isotherm indicates that temperature gradient is maximum for linearly increasing heat flux profile and minimum for linearly decreasing heat flux.

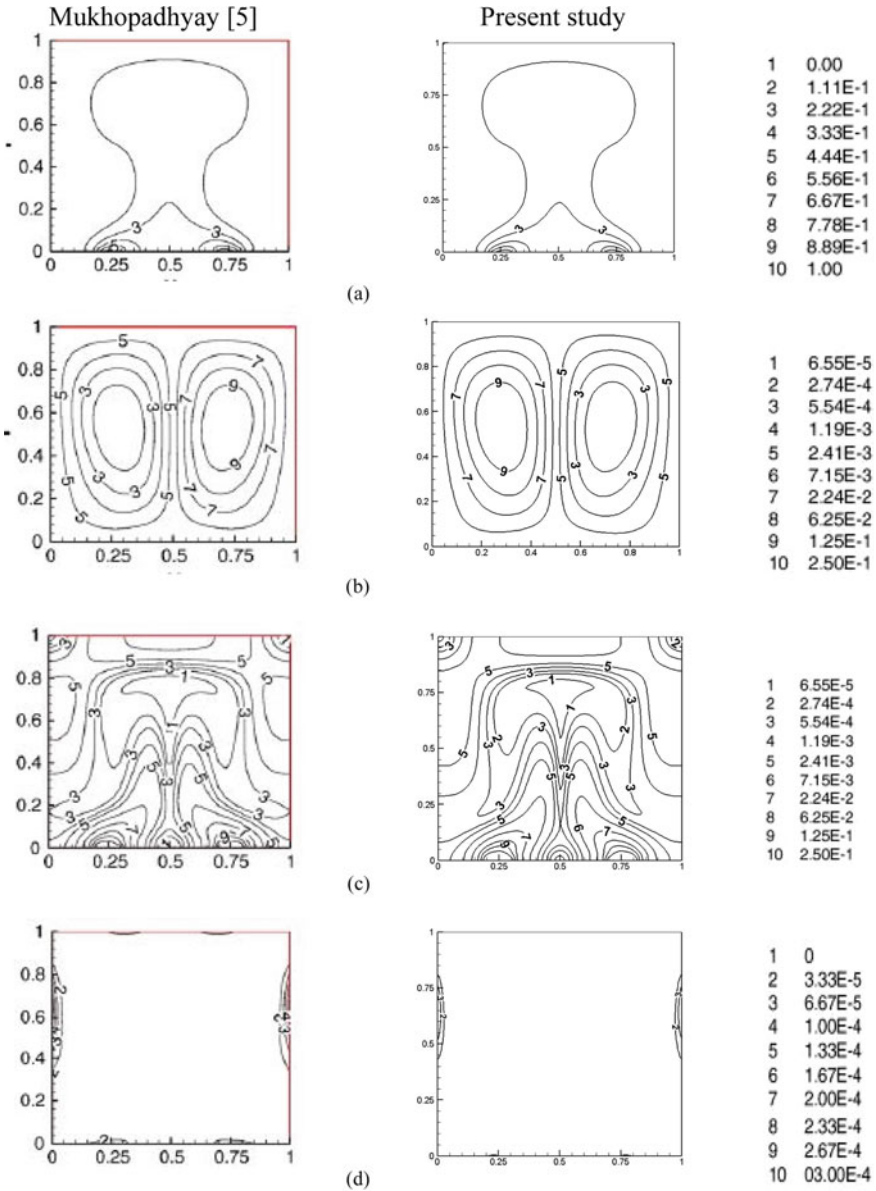


Fig. 2 Comparison of the present results with the published results [5] for $Ra = 10^6$ **a** Isotherms **b** streamlines **c** rate of entropy generation due to conduction **d** rate of entropy generation due to viscous dissipation. [Published results is reproduced with permission from the Publisher]

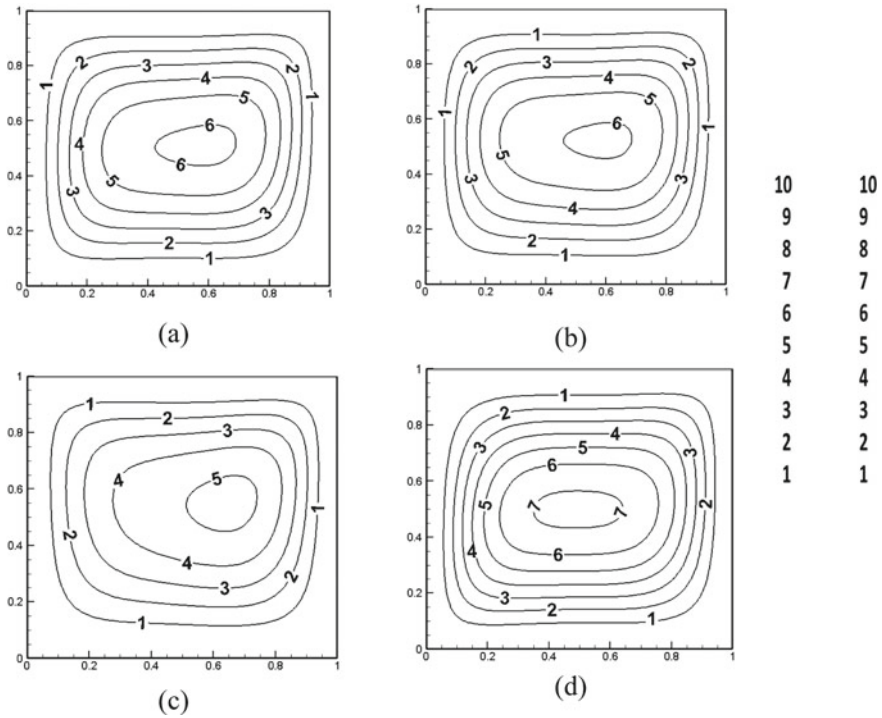


Fig. 3 Streamlines for different heating profiles **a** uniform **b** parabolic **c** linearly increasing **d** linearly decreasing

The temperature gradients of the other two cases are in between linearly heating and linearly decreasing heat flux profile.

4.4 Impact of Non-uniform Heating Profiles on Irreversibility

The irreversibility in flow and heat transfer is determined by entropy generation and the Bejan number ($Be = S_{gen}^{cond}/S_{gen}^{tot}$). In the present study, the Bejan number is close to unity. It indicates the contribution of entropy generation on account of heat transfer in total entropy generation is very high. Figure 5 shows that the contours of entropy generation due to conduction for different heating profiles such as uniform, parabolic, linearly heating, and linearly decreasing. The entropy generation by heat transfer is due to the temperature gradient. The contours of static temperature indicate that the temperature gradient is more crowded near the walls exposed to heating/cooling and very small near the wall subjected to adiabatic conditions.

For all the cases investigated, the contour levels of entropy generation due to conduction in the case of linearly heat flux are greater as compared to the other

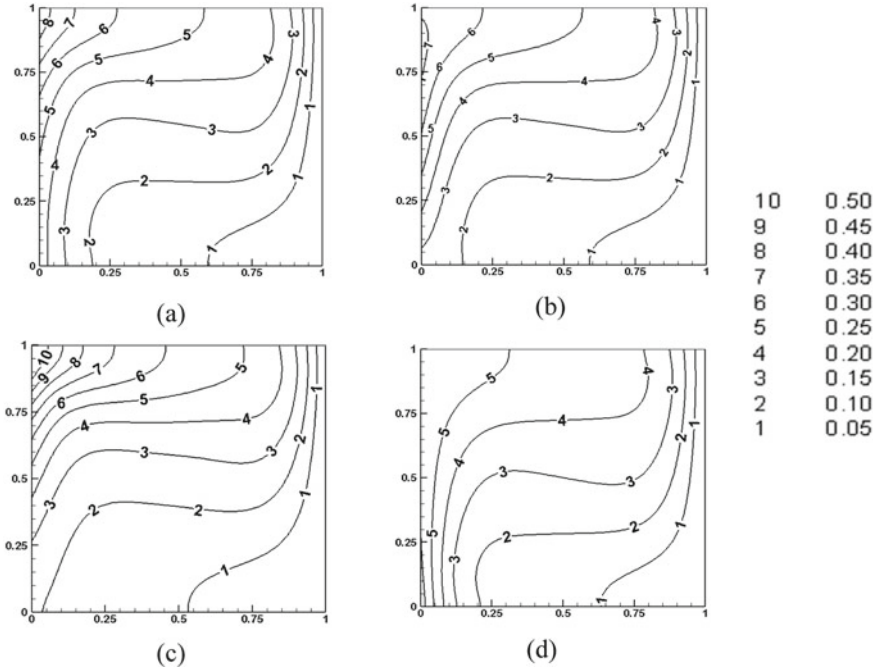


Fig. 4 Contours of isotherms for different heating profiles **a** uniform **b** parabolic **c** linearly increasing **d** linearly decreasing

cases. This is due to an increase in the density of isotherms in the case of linearly heating profiles. It is further observed that the maximum value of entropy generation occurs near the region where the value of heat flux is maximum.

The entropy generation due to viscous dissipation is shown in Fig. 6. It occurs near the walls. The comparison of levels of contours of entropy generation due to conduction and viscous dissipation, respectively, is shown in Figs. 5 and 6. It indicates that the order of magnitude of the viscous dissipation term is very less compared to the conduction term. This is similar to the results obtained by Mukhopadhyay [5] who noticed that magnitude of the viscous dissipation part of entropy generation is several orders lower than the heat conduction part of entropy generation.

Table 4 presents the entropy generation rate over the domain (domain average) in normalized value in different heating profiles. The normalized value of the rate of entropy generation is obtained by dividing the average rate of entropy generation in a particular heat flux profile by the average rate of entropy generation in the case where the value is minimum.

The results show that the rate of entropy generation of uniform and parabolic and heating profiles is nearly the same. The rate of entropy generation is maximum for linearly increasing heat flux. The percentage increase in average entropy generation for linearly increasing profile is nearly 22.5%. Therefore, the parabolic heating

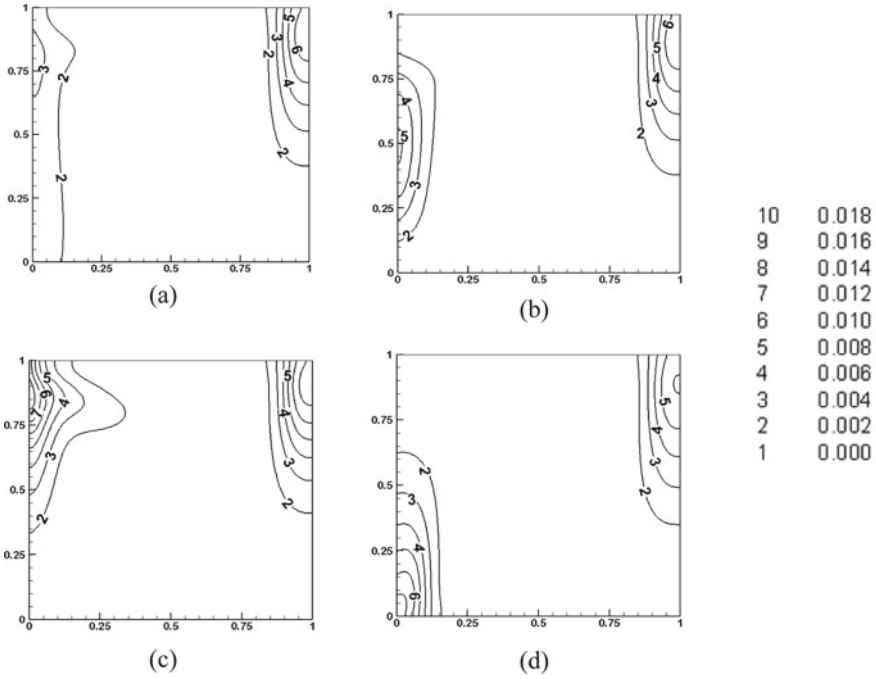


Fig. 5 Contours of the rate of entropy generation due to conduction for different heating profiles **a** uniform **b** parabolic **c** linearly increasing **d** linearly decreasing

profile is preferred as the rate of entropy generation is the minimum and the linearly increasing heating profile is undesirable as it leads to the maximum.

5 Conclusions

The salient observations are summarized as follows:

- The maximum and minimum values of the streamfunctions are found for linearly decreasing and linearly increasing heat-flux conditions, respectively.
- The contours of static temperature indicate that the temperature gradient is maximum for the linearly increasing heat flux profile and that for the linearly decreasing heat flux is minimum.
- The parabolic heating is desirable as the entropy generation is a minimum.
- The linearly increasing heating profile is undesirable as the corresponding entropy generation is found maximum.

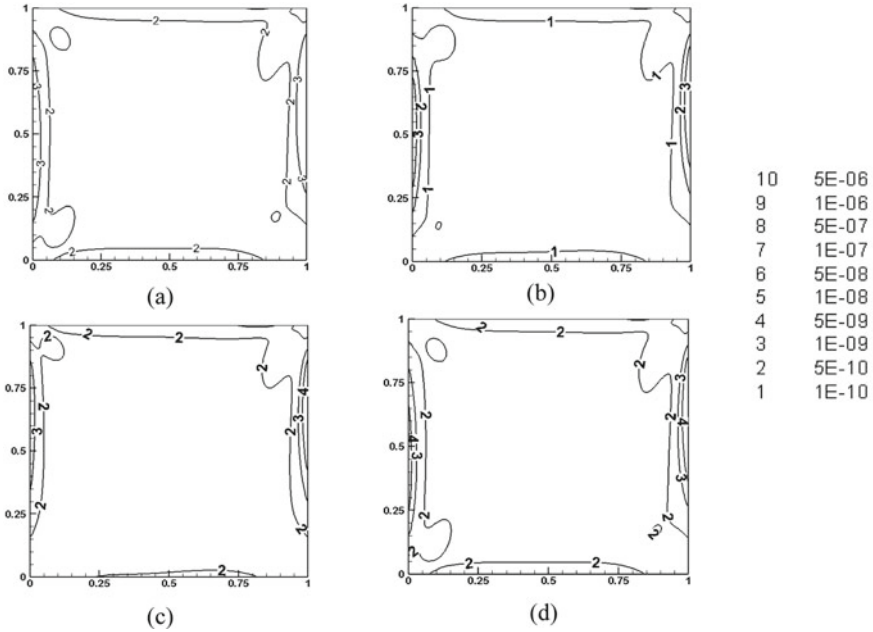


Fig. 6 Contours of the rate of entropy generation due to viscous dissipation for different heating profiles **a** uniform **b** parabolic **c** linearly increasing **d** linearly decreasing

Table 4 Average rate of entropy generation for the various heating profile in normalized form

	Uniform	Parabolic	Linearly increasing	Linearly decreasing
$(S_{gen})_{av}$	1.00774	1.00000	1.22482	1.06184

References

1. Putra N, Roetzel W, Das SK (2003) Natural convection of nanofluids. *Heat Mass Transf* 39:775–784
2. Bouchoucha AEM, Bessai’h R (2015) Natural convection in a square cavity filled with nanofluids. *FDMP* 11:279–300
3. Bejan A (1979) A study of entropy generation in fundamental convective heat transfer. *ASME* 101:719–725
4. Ilis GG, Mobedi M, Sunden B (2008) Effect of aspect ratio on entropy generation in a rectangular cavity with differentially heated vertical walls. *Int Commun Heat Mass Transf* 35:696–703
5. Mukhopadhyay A (2010) Analysis of entropy generation due to natural convection in a square enclosure with multiple discrete heat sources. *Int Commun Heat Mass Transf* 37:867–872
6. Famouri M, Hooman K (2008) Entropy generation for natural convection by heated partition in a cavity. *Int Commun Heat Mass Transf* 35:492–502
7. Brinkman HC (1952) The viscosity of concentrated suspensions and solution. *J Chem Phys* 1952(20):571–581
8. Maxwell JC (1873) *A Treatise on electricity and magnetism*. Oxford Univ Press Camb 2:54

Mechanical Properties, Microstructural and Surface Topography Evaluation of AlSi10Mg Alloy Produced by DMLS Process



R. K. Shah and P. P. Dey

Abstract In this paper, direct metal laser sintering process was used to produce AlSi10Mg components by employing different parametric combinations. Laser intensity, scan speed, and hatch distance were regarded as the autonomous parameters. A laser energy density (led) function expressed these three parameters. Fabricated component's density was evaluated by the Archimedes principle. Measured densities were demonstrated as relative density (rd) by indicating it as percentage of the actual density of the alloy (2.67 gm/cm^3). In our study, the led–rd–structure relationship is discussed. The highest led of 93.43 J/mm^3 yielded the least rd of 95.88%. Its microstructure showed numerous irregularly shaped pores; its surface topography also revealed a large amount of balling and satellite formation, whereas for the sample with the maximum rd value of 99.63%, which was fabricated by employing a led of 61.11 J/mm^3 , it showed very few pores and almost negligible balling formation. The above analysis revealed that surface topography also had an impactful role in determining the density of the component. This study also showed an interrelation between relative density and tensile strength of the alloy; the component with the best relative density showed a higher ultimate tensile strength value than the component with the least relative density value. A superior tensile strength property of the dog bone sample with the highest relative density was found when it was compared with the tensile strength properties of the A360 die-cast material.

Keywords AlSi10Mg alloy · Direct metal laser sintering · Surface topography · Relative density

R. K. Shah (✉) · P. P. Dey
Department of Mechanical Engineering, IEST, Shibpur, Howrah 71103, India
e-mail: shahronit4u@gmail.com

P. P. Dey
e-mail: ppdey2000@yahoo.com

1 Introduction

Industrial Revolution 4.0 encompasses additive manufacturing (AM). It can manufacture highly complex and intricate components that are not possible by conventional manufacturing with precise accuracy. Direct metal laser sintering (DMLS) fabricates components conforming to a 3D-CAD file with the aid of a laser beam. This 3D-CAD file is then sliced into several 2D files with pre-defined layer thickness. The laser beam then selectively sinters the desired region on the powder bed.

Although several parameters affect the quality of the DMLS components, the most crucial process parameter affecting the DMLS process are laser intensity (LI), speed of scan (SS), and hatch separation (HS). The above three parameters can be expressed by a laser energy density (led) function ψ (J/mm^3) [1–3] which is given by the equation.

$$\Psi = i/(u \times s \times t) \quad (1)$$

where i = laser intensity (W), s = speed of scan (mm/s), u = hatch separation (mm), t = thickness of layer (mm).

In our study also, this led model is used to correlate with the density and tensile strength of the component.

The Al-Si alloy has properties suitable for casting and welding. The addition of Mg to the alloy corroborates the alloy heat-treatable because of the formation of Mg_2Si precipitates which also strengthens the alloy [4]. Due to the above attractable properties combined with its low weight, this alloy has found its application in aerospace and automobile components. The inherent property of the AlSi10Mg alloy which includes low absorptivity, enhanced thermal conductivity, and negligible flowability poses a challenge in processing such alloys by the DMLS process, due to which a higher laser power is required for the sintering of such alloys. The major challenge in processing aluminum alloy parts by DMLS/SLM process is reducing its porosity. The literature is full of studies which deal with the optimization of the process parameter of the SLM or DMLS process for maximizing the density of the AlSi10Mg/Al alloy components, juxtaposition of the mechanical properties of the AlSi10Mg build specimens with the cast counterpart, and performing single scan track analysis of aluminum alloy generated by SLM [2, 4–8].

This paper focusses on the led–surface topography–density relationship of the AlSi10Mg specimens. This work emphasizes the fact that surface tension of the alloy had a profound influence on the surface topography of the components manufactured with different led. The surface tension of the components monitors the surface topography of specimens which eventually influences its rd.

2 Details of Experiment

2.1 Material

EOSGmbH Germany provided the powder, which was gas atomized, and the particle size range was from 3–40 μm as informed by the supplier. The powder's chemical composition was as per the standard DINEN-1706:2010–06, as conveyed by the supplier which is tabulated [9] (Table 1).

Table 1 Powder's chemical composition

Element	Concentration (wt %)
Si	10.7
Mg	0.43
Fe	0.17
Mn	<0.01
Cu	<0.005
Zn	<0.002
Ti	0.01
Al	Balance

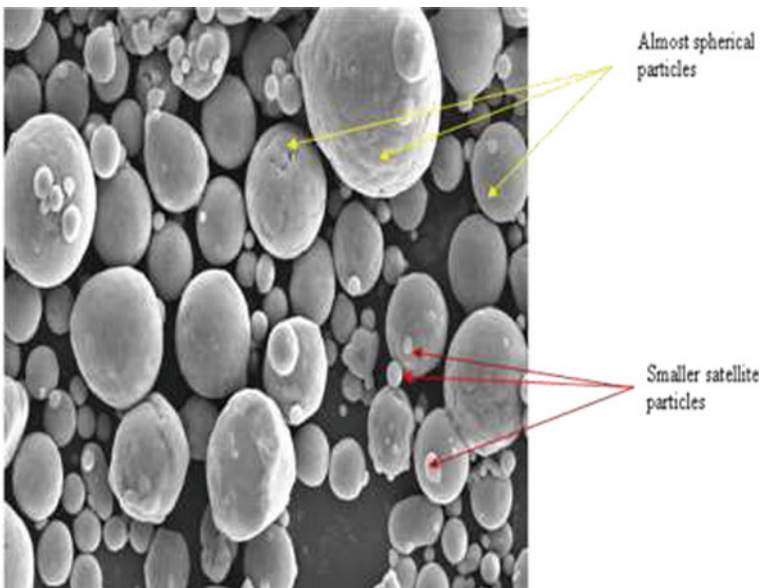


Fig. 1 Powder morphology

Powder's morphology, as shown in Fig. 1, reveals maximum spherical particles embedding miniature satellite. Powder's spherical morphology enhances the flowability and allows for uniform deposition of the powder layer; hence, it is beneficial for the DMLS process [10].

2.2 Manufacturing Strategy

The DMLS machine used to prepare the components is illustrated in Fig. 2. The maximum laser intensity that can be used in this machine is 400 W. The build plate was made up of Al and was preheated to 165 °C to relieve the internal stress which results in lowering the thermal gradient and residual stresses. The thickness of the layer was 30 μm ; the scanning strategy employed was alternating. The manufacturing chamber was maintained with an argon surrounding. The as-manufactured components were further maintained at 300 °C for 120 min to alleviate the stress further and were smoothed to obtain the eventual parts.

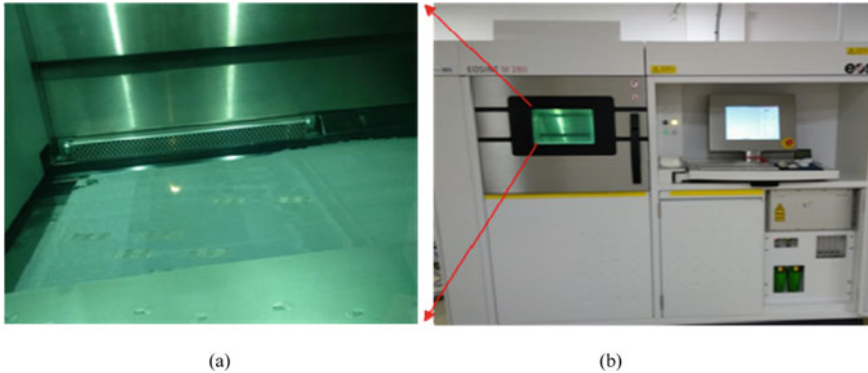


Fig. 2 a DMLS machine build chamber and b DMLS machine used

2.3 Fabrication of Specimen

For relative density (rd) analysis, cubic specimens with dimension $10 \times 10 \times 10$ mm were produced conforming to the parametric combination as given in Table 2. For tensile strength analysis, dog-bone samples (horizontally build) with 25 mm gauge length and 6 mm gauge diameter were prepared according to ASTM-E800. The horizontal as-built horizontal component is shown in Fig. 3. Cubic specimen with dimension $10 \times 10 \times 10$ mm was prepared according to the parameters of specimen 4 in Table 2 for microhardness evaluation.

Table 2 Relative density output

Sample No	LI (W)	SS (mm/s)	HD (mm)	Led (J/mm^3)	Rd (%)
1	370	1200	0.11	93.43	95.88
2	370	1300	0.15	63.25	99.25
3	370	1400	0.19	46.36	98.50
4	330	1200	0.15	61.11	99.63
5	330	1300	0.19	44.53	99.25
6	330	1400	0.11	71.42	96.25
7	290	1200	0.19	42.40	98.87
8	290	1300	0.11	67.60	97.00
9	290	1400	0.15	46.03	99.25

Fig. 3 As-built component



2.4 Examination Method

The Archimedes principle determined the density of the cubical specimen. The rd was figured out by taking the alloy's density as 2.7 gm/cm^3 and indicated as %.

Tensile testing was executed by employing 10^{-3} s^{-1} strain rate.

For Vickers microhardness analysis, the cubic specimen was polished in a double disc polishing machine so that the indentation was visible on the sample under the microscope which was operated at a magnification of 50X. The testing was carried out under 300 gf load for a dwell period of 10 s.

S-3400 N SEM was used for microstructure and surface topography evaluation and was operated at an accelerating voltage of 15 kV with varying magnification.

3 Results and Discussion

3.1 Density Analysis

The maximum LI used in our experiment was 370 W, equivalent to 92.5% of the highest LI (400 W) to maximize the led value to 93.43 J/mm^3 . In order to have a wide range of led value ($42.4\text{--}93.43 \text{ J/mm}^3$) and to examine the interrelationship, the LI was varied in the range of (290–370) W, SS was diversified in the (1200–1400) mm/s range and HD was manipulated in the span of (0.11–0.19) mm as shown in Table 2. Specimen's relative density is given in Table 2 [9].

From the table, it can be inferred that the led of 61.11 J/mm^3 gave the optimum result of rd of 99.63%, whereas a very high led of 93.43 J/mm^3 resulted in the least rd.

3.2 Microstructural Evaluation

Figure 5a and b gives the microstructural comparison between specimens 1 and 4 carried out in the XY plane, revealing the porosity. Figure 4 shows various reference planes. Figure 5a reveals large irregularly shaped pores which are caused due to the vaporization of the alloy because of the extremely high laser energy density. Vaporization includes two phenomenons: boiling and evaporation. When a led of 93.43 J/mm^3 is employed, extreme temperature is generated at the melt pool. The temperature developed exceeds the boiling point of the individual alloying element due to which bubbles of gases are formed inside the liquid melt pool and it reaches the surface and escapes into the air as gas; thus, the boiling phenomenon occurs. When an excess temperature is generated in the melt pool, the kinetic energy of the liquid molecule increases, some molecule on the melt pool surface with high kinetic energy escapes the intermolecular attractive forces of the liquid melt pool and turns into gas,

and thus, the evaporation process occurs. These two phenomena contribute to the vaporization of the alloy and increase the porosity. These pores also act as pockets in which powder particles can get trapped thereby further reducing the density, as shown in Fig. 6, further reducing the density.

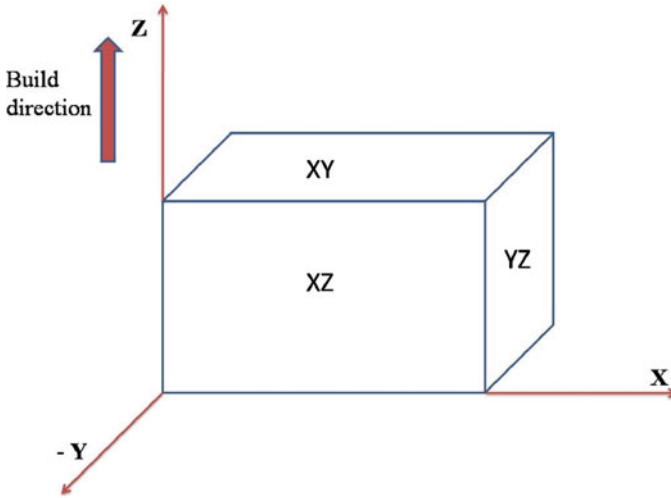


Fig. 4 Reference planes of a sample build by DMLS process

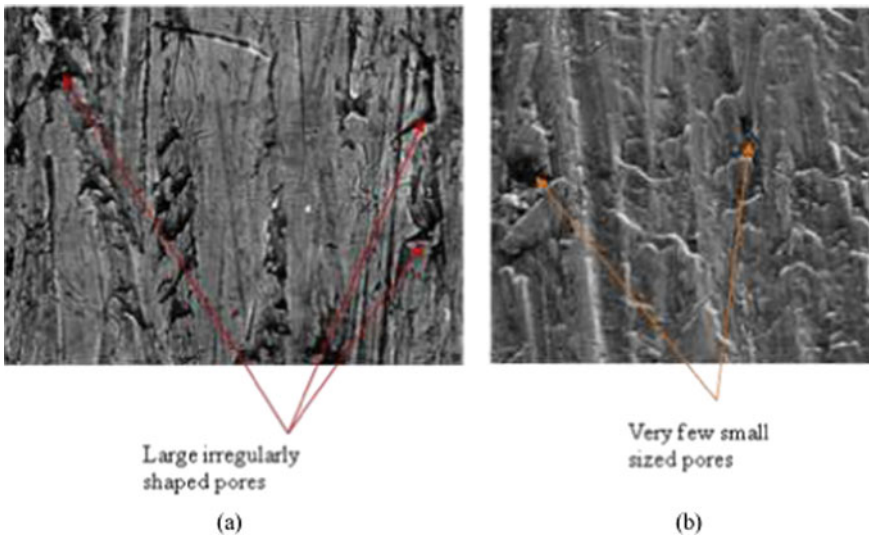


Fig. 5 Microstructural comparison between specimens 1 and 4 revealing pores

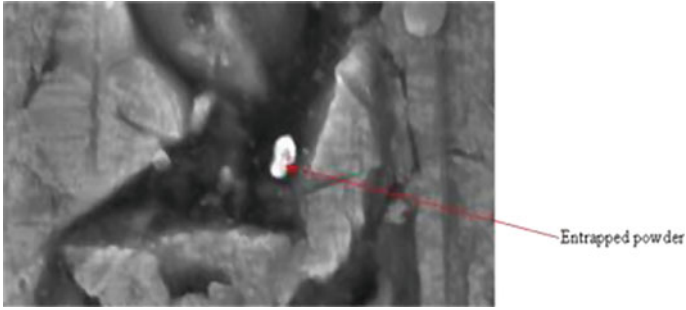


Fig. 6 Enlarged view of the pore showing entrapped powder

Figure 5b reveals few pores as compared to Fig. 5a, which accounts for its high rd, and it also shows a well-sintered specimen. The few pores observed in specimen 4 could be attributed to the use of high scan speed due to which incomplete filling of the gaps with molten metal takes place; it occurs because of rapid solidification of the molten metal.

3.3 Surface Topography

Surface topography evaluation of specimen 1 in the XY plane reveals balls and satellite and an irregular morphology as shown in Fig. 7. Balling occurs due to the molten powder solidifying in the form of a ball, and satellite formation is due to the laser spatter which happens due to the involvement between the laser and

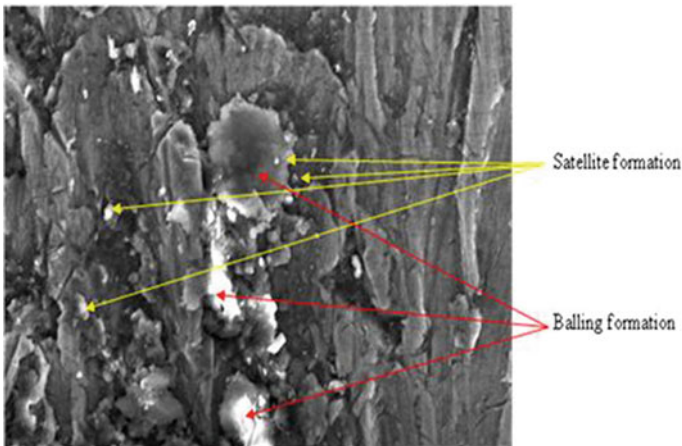


Fig. 7 Surface topography of specimen 1 in XY plane

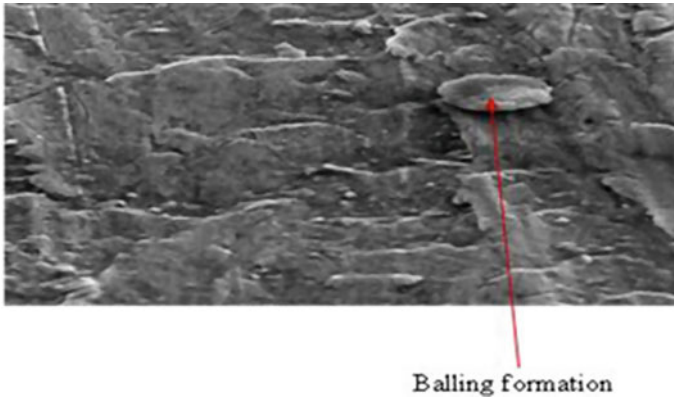


Fig. 8 Surface topography of specimen 4 in XY plane

powder material and appears as small dots sticking to the surface. The formation of satellite and balls ultimately stimulates pore development in the printed components and proliferates the surface roughness of the sintered components; thus, this surface defect not only downgrades the surface quality but also reduces the density as it restricts the uniform layer deposition and also acts a pocket for trapping the powder material. The surface defect of specimen 1 also contributes to its high porosity.

The XY plane topography of specimen 4 is illustrated in Fig. 8, which reveals an almost negligible amount of balling formation thereby reducing porosity, and it also shows a proper surface morphology as compared to specimen 1.

The possible reason between the difference in surface topography of the two samples could be a higher surface tension value when a led of 93.43 J/mm^3 is used which causes the molten alloy to solidify in the form of a ball.

The surface tension of the molten metal remains fixed; however, when solidification commences and temperature reduces, the material's surface tension enhances due to which balling occurs. When a high led of 93.43 J/mm^3 is used, the molten pool's maximum temperature is comparatively higher from the maximum temperature achieved in the molten pool when a led of 61.11 J/mm^3 is employed. The surface tension value of the AlSi10Mg alloy when it solidifies from a higher peak temperature to its solidification temperature is relatively higher when compared with the surface tension value of the alloy when it is solidifying from a comparatively lower peak temperature, due to which the specimen 1 which was built with a high led showed excessive balling formation when compared with sample 4 which employed an optimum led [11].

From the above analysis, it is clear that there is an interrelation among led, microstructure, and surface topography with the porosity of the material.

3.4 Tensile Strength Analysis

The tensile strength output for specimen 1 and 4 is shown in the table [9].

The table illustrated an interrelationship amid rd and tensile strength properties of the alloy with the best rd value sample showing better ultimate tensile strength (UTS) result than the other component with the least rd. The comparison of the best UTS result with the A360 die-cast materials is shown in the table below, which reveals a better outcome for UTS and yield strength (YS) of the horizontally build component by the DMLS process, but the ductility was lower.

3.5 Microhardness Evaluation

Vickers microhardness was carried out in the YZ plane of the cubic specimen prepared according to the parameters of specimen 4 in Table 3, microhardness (mh) was carried out at different depth starting from the top surface then with an interval of 2.5 mm up to the center, and the last reading was taken at the bottom surface. The results are shown in Fig. 9, which demonstrated that as the depth augmented the mh value

Table 3 Tensile strength output

Sample No	LI (W)	SS (mm/s)	HD (mm)	Led (J/mm ³)	Rd (%)	UTS (MPa)
1	370	1200	0.11	93.43	95.88	309
4	330	1200	0.15	61.11	99.63	335

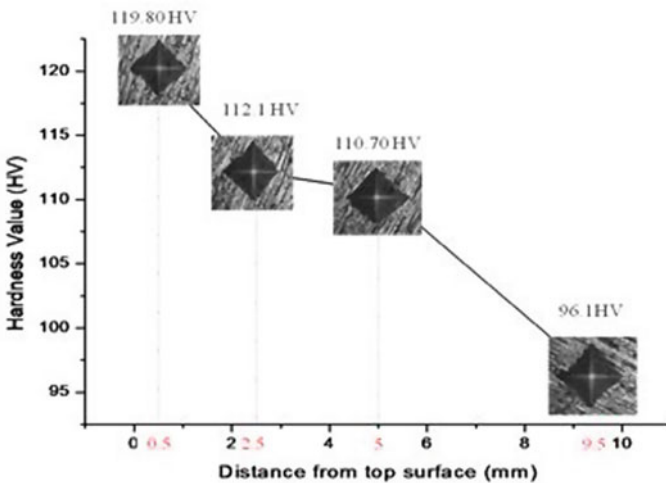


Fig. 9 Microhardness values at different depth in the YZ plane surface along the Z-axis

Table 4 Comparison of tensile strength properties

Specimen	YS (0.2% offset) (MPa)	UTS (MPa)	Elongation at failure (%)
DMLS (Horizontal)	215	335	1.7
A360 DIE CAST [2]	170	317	3.5

decreased [12]. This analysis revealed the anisotropy in the mh value in the YZ plane surface along the Z-direction. The reason behind this is that the top layers are in close association with the manufacturing chamber's atmosphere and hence cools fast; therefore, there is higher cooling rate producing finer grains and more sub-grain boundaries thus ultimately increasing the mh. On the other hand, cooling rates at the middle and bottom layers are not so high as the heat transfer rate is less as a result of which the grains gradually become coarser as the depth increases, resulting in a successive decrease in the mh value (Table 4).

4 Conclusion

AlSi10Mg components were manufactured by the DMLS process; relative density was measured; tensile strength analysis was carried out. Microstructure and surface topography analysis were also carried out. The major inferences from our work are given below.

1. Samples with relative density of almost 100% can be achieved. Interrelation among microstructure, surface topography, led with the density of the component can be seen, with the surface topography also playing a role in determining the sample's density.
2. The correlation of the tensile strength properties with the relative density and superior tensile strength properties of the DMLS sample (horizontal) with the highest relative density value when collated with the A360 die-cast material.
3. Anisotropy in the microhardness value in the YZ plane surface; as the depth increases along the Z-axis, the microhardness value decreases.

References

1. Yakout, M, Elbestawi MA, Veldhuis SC (2019). Density and mechanical properties in selective laser melting of Invar 36 and stainless steel 316L. *J Mater Process Technol* 266:403
2. Read N, Wang W, Essa K, Attallah MM (2015) Selective laser melting of AlSi10Mg alloy: process optimisation and mechanical properties development. *Mater Des* 65:417
3. Wang L-Z, Chen T, Wang S (2017) Microstructural characteristics and mechanical properties of carbon nanotube reinforced AlSi10Mg composites fabricated by selective laser melting. *Optik* 143:175

4. Kempen K, Thijs L, Yasa E, Badrossamay M, Verheecke W, Kruth J-P (2011). Process optimization and microstructural analysis for selective laser melting of AlSi10Mg. In: Solid freeform fabrication symposium. Texas, USA, Aug 2011
5. Aboulkhair NT, Everitt NM, Ashcroft I, Tuck C (2014) Reducing porosity in AlSi10Mg parts processed by selective laser melting. *Addit Manuf* 1:83
6. Krishnan M, Atzen E, Canali R, Calignano F, Manfredi D, Ambrosio EP, Luliano L (2014) On the effect of process parameters on properties of AlSi10Mg parts produced by DMLS. *Rapid Prototyping J* 20:(16)
7. Kempen K, Thijs L, Van Humbeeck J, Kruth J-P (2012) Mechanical properties of AlSi10Mg produced by selective laser melting. *Phys Procedia* 39:441
8. Aboulkhaira NT, Maskerya I, Tucka C, Ashcrofta I, Everittb NM (2016) On the formation of AlSi10Mg single tracks and layers in selective laser melting: Microstructure and nano-mechanical properties. *J Mater Process Technol* 230:92
9. Shah RK, Dey PP (2019) Process parameter optimization of dmls process to produce AlSi10Mg components. In: 2nd International conference on new frontiers in engineering, science & technology (NFEST), Kurukshetra, India, Journal of physics: conference series, 18–22 Feb 2019
10. Yang S, Evans JRG (2007) Metering and dispensing of powder; the quest for new solid freeforming techniques. *Powder Technol* 178(1):57
11. Molina JM, Voytovychb R, Louisa E, Eustathopoulos N (2007) The surface tension of liquid aluminium in high vacuum: The role of surface condition. *Int J Adhes Adhes* 27:396
12. Liu YJ, Liu Z, Jiang Y, Wang GW, Yang Y, Zhang LC (2017) Gradient in microstructure and mechanical property of selective laser melted AlSi10Mg. *J Alloys Compound* 735:11

Experimental Investigation of the Performance of a Low-Cost Flexible All Plastic Solar Air Heater



Deva Kanta Rabha, Prachurjya Goswami, Sahnawaz Ullah, Sachin Basak,
and Jishu Raj Baruah

Abstract In this study, a low-cost, single-pass, all plastic solar air heater was developed and tested. The solar air heater is merely two equal size plastic bags. One plastic bag is transparent and the other one is black. The black plastic bag is placed inside the transparent one. When the air is blown through the black plastic bag, both the bags inflate and take the shape of a concentric cylinder. The incident solar radiation on the surface of the heater transmits through the outer white transparent bag and gets absorbed on the inner black plastic bag and converted into heat. The air blown through the plastic bags gets heated up resulting in rise of the air temperature. At the solar radiation intensity of 746 W/m^2 and the air flow rate of 0.053 kg/s , the maximum outlet temperature of the heater was recorded to be $40 \text{ }^\circ\text{C}$. The average energy efficiency of the solar air heater was found to be 19.2% and the exergy efficiency was found to be only 0.35% . A sample of fenugreek leaves was dried with the hot air produced by the solar air heater in a drying chamber. The moisture content of the leaves was reduced from 86.34% to 3.95% (w.b.) in 9 h.

Keywords Flexible · Plastic sheet · Solar air heater · Energy efficiency · Exergy efficiency

1 Introduction

Space heating, drying, timber seasoning, etc., require air below $100 \text{ }^\circ\text{C}$ [1]. One of the low-cost and environmentally friendly devices for heating air is the solar air heater. A solar air heater or solar collector is one kind of thermal device that converts solar radiant energy into heat. It works on the principle of the greenhouse effect [2] and is widely used in solar dryers for producing hot air required for drying operation. Nowadays, solar dryers are widely used in drying operation as solar energy can be used efficiently. Many kinds of solar dryers with different working principles are available for drying fruits, vegetables, medicinal herbs, etc., which are classified

D. K. Rabha (✉) · P. Goswami · S. Ullah · S. Basak · J. R. Baruah
Mechanical Engineering Department, Jorhat Engineering College, Jorhat, Assam 785007, India
e-mail: devaktra@gmail.com

© The Author(s), under exclusive license to Springer Nature Singapore Pte Ltd. 2023
T. S. Sudarshan et al. (eds.), *Recent Advancements in Mechanical Engineering*,
Lecture Notes in Mechanical Engineering,
https://doi.org/10.1007/978-981-19-3266-3_3

27

as direct-type, indirect-type, and hybrid-type. In the indirect-type solar dryers, the ambient air heated by a solar air heater is supplied to a drying chamber, and the latent heat required for evaporating the moisture from the products in the drying chamber is supplied by the hot air. Therefore, the solar air heater plays a very important role in the indirect-type solar dryers.

A large number of solar air heaters of different structures have been built and tested. They are classified as simple flat-plate collectors, bare-plate collectors, single-cover and double-cover collectors, single- and double-pass collectors, finned plate and corrugated plate collectors, matrix type, and unglazed, porous solar air heaters, overlapped type, etc. [3, 4]. A simple flat-plate solar air heater consists of a transparent cover plate also known as glaze, a black colour absorber plate, and a base plate. A glass or a plastic plate is used for the cover plate and a thin metal plate painted with black colour is used as the absorber plate. The cover plate is placed above the absorber plate, and then, both the plates are fitted in an insulated rectangular box.

One of the low-cost solar heaters is the plastic solar air heater where a rigid plastic plate or a sheet is used for the transparent cover. The initial cost reduction in the construction of solar air heaters is the main objective of employing plastic materials as cover plate in the solar air heater. Usually, a toughened glass is used for the cover plate of the solar air heater. The toughened glass is costly, and increases the cost of construction of the solar air heater. Bansal et al. [5] built a solar air heater with a porous textile absorber and an UV-stabilized PVC foil cover. In this heater, the porous textile absorber was placed between two UV-stabilized PVC foils. They reported that the efficiency of the heater was mainly affected by the thickness of the insulation. At the air flow rate of 0.22 kg/s, the thermal efficiency of the heater was 71%. Esper et al. [6] tested a solar dryer with a plastic cover plate. The solar air heater had two side walls of a height 0.06 m built with bricks that supported the PVC foil. They tested the collector at different lengths (10, 20, and 30 m) and recommended that UV-stabilized foils should be used as a cover plate of the plastic solar heater. Chau et al. [7] tested a solar air heater developed with a clear plastic sheet of thickness 0.15 mm and wood. The length and width of the heater were 29.26 m and 3.66 m, respectively. A black plastic sheet was used as the absorber. They reported that the efficiency of the heater varied with the change in the flow rate of air. The efficiency of the heater was 20% at the air flow rate of $0.33 \text{ m}^3/\text{min m}^2$ and 35% at the air flow rate of $0.90 \text{ m}^3/\text{min m}^2$. Flores-Irigollen et al. [8] tested a plastic solar heater of a length of 50 m and a width of 5 m with the absorber surface of a layer of pebbles. The cover plate of the heater was a semi-transparent UV-treated polythene film of 178-micron thickness. They developed a heat transfer model of the heater and compared the theoretical results with the experimental.

Gill et al. [9] tested a single- and a double-covers plastic solar air heater and compared the performance and the cost of the heaters with a porous bed solar heater. An ultraviolet stabilized plastic sheet was used as cover plate in the heater. The authors stated that the initial cost of the single- and the double-covers heaters were 22.8% and 26.8%, respectively, of the initial cost of a porous bed heater. At the air flow rate of $0.02 \text{ m}^3/\text{s-m}^2$, the efficiencies of the single cover and the double cover were 30.29% and 45.05%, respectively, while the efficiency of the porous bed heater

was 71.68%. Abdullah and Bassiouny [10] investigated the performance of a flexible circular and elliptical sizes solar air heater. The heater had two parts; a lower part and an upper part. The lower part of the heater was built with a low-density polythene film that was used as the black absorber and the upper part of the heater was built with two layers of transparent plastic sheets. The length of the heater was 20 m. The investigators reported that the maximum temperature of the air at the outlet of the heater was found to be 80 °C at the air flow rate of 0.13 kg/s. The thermal efficiency of the heater was 50% for the elliptical shape and 60% for the circular shape. Ahmed [11] developed a solar air heater with a low-cost transparent polythene sheet. A 5-m-long heater was constructed with a plastic sheet wrapped around flexible helical metal wires. They reported that the efficiency of the heater was found to be 12.5%.

The solar air heater developed in this study is an all-plastic heater. It does not require any structure unlike the plastic solar air heaters developed by the other researchers. It can be built within a few hours.

2 The Developed Plastic Solar Air Heater

The white (transparent) and black plastic bags (Fig. 1) which are generally used as a tarpaulin for covering materials and easily available in the local markets were used for developing the solar air heater. The heater consists of one black and one white transparent plastic bags of the equal size (5 m × 0.9 m). The black plastic bag is used as the absorber, and the transparent one is used as the transparent cover or the glaze of the heater. The black plastic bag is put inside the white one. When the air is blown through the black plastic bag, both the bags inflate and take the shape of a concentric cylinder (Fig. 2). A part of the incident solar radiation on the heater transmits through the outer white transparent bag and gets absorbed on the inner black plastic bag and converted into heat. The white plastic bag traps the heat, as a result, the temperature of the black plastic bag tends to increase. The air blown through the plastic bags removes the heat and gets heated up. Thus, the temperature of the air flowing through the plastic bag rises and the inner black plastic bag is protected from overheating. The air coming out of the heater can be used in room heating or in drying applications.

Fig. 1 The plastic bags used in the air heater

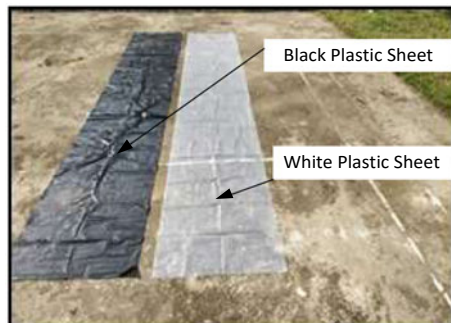
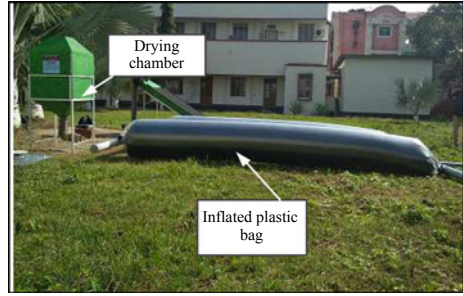


Fig. 2 The inflated plastic bags



3 Experimental Set-Up

To test the plastic heater, an experimental set-up was developed at the campus of the Jorhat Engineering College, Jorhat (26.7465° N, 94.2026° E), India. The experimental set-up has two long PVC pipes of 0.102 m in diameter, two equal size heaters of the length of 4.16 m, a drying chamber, and a blower to supply air. The schematic of the experimental set-up and its photograph are shown in Figs. 3 and 4, respectively. The PVC pipes are used as the headers, and the two heaters are placed between the headers horizontally parallel to each other. The ambient air is supplied to the header-I with the blower, and then, it is distributed to the heaters through two numbers of 0.0635 m circular PVC pipes. The air coming out of the heaters mixes in the header-II and exits from it through a 0.0635-m circular PVC pipe which is extended to the drying chamber. The air is finally used for drying a sample of a medicinal herb in the drying chamber.

The drying cabinet is a simple box type chamber made of plywood which contains a series of trays for holding the products and an outlet vent at the top through which the moisture-laden air escapes into the atmosphere. The hot air coming out of the heaters is supplied to the plenum chamber of the drying chamber.

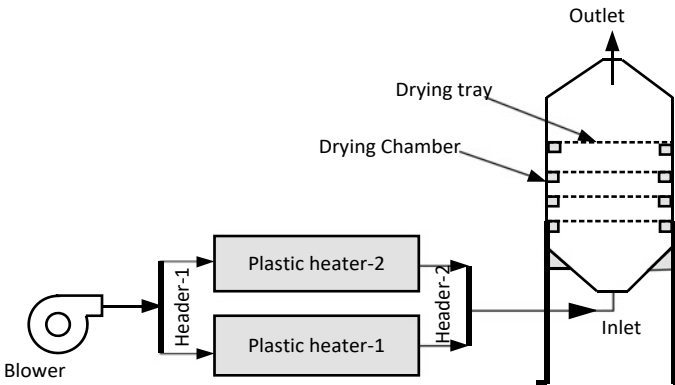


Fig. 3 The schematic of the experimental set-up

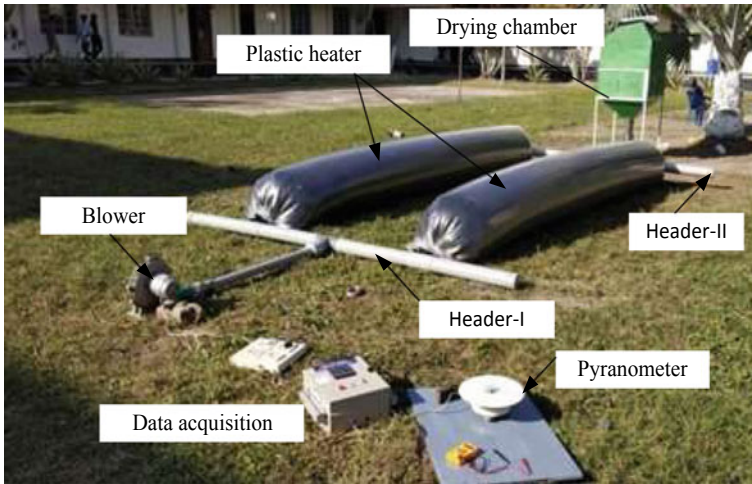


Fig. 4 Experimental set-up of the plastic solar air heater

The experimental set-up is oriented towards the South to harness the maximum solar energy. To record various operating parameters for estimating the performance of the heaters, measuring instruments like pyranometer (Make: National Instrument Laboratory, Model: M-304), thermocouple (T-type), and wind vane anemometer (Make HTA Instrumentation Pvt. Ltd, Model: Equinox EQ-618B, Accuracy $\pm 0.1\%$; Operating range 0–45 m/s) and data acquisition system were used in the experiment. The pyranometer and thermocouple were used for measuring the solar radiation intensity and the air temperatures, respectively. The wind vane anemometer was used for measuring the wind velocity and the velocity of air for estimating the mass flow rate of the air. A sample of 100 g of fenugreek leaves was dried in the drying chamber. To measure the moisture content of the product, the mass of the sample was measured at 1 h interval with an electronic balance (Make: Contech Instrument Ltd., Model: CAH/1003, Accuracy 0.001 g). The moisture contents of the product before and after drying were determined by the gravimetric method.

4 Performance Analysis

The air heater was tested initially without attaching it to the drying chamber to investigate energy and exergy efficiencies. The assumptions made in the analysis were given below.

- The flow through the heater was assumed to be steady
- The specific heat of air does not change with time
- The kinetic energy and potential energy are neglected.

The energy efficiency of the air heater was calculated by Eq. (1) [12–14]. It is defined as the ratio of the energy gained by the air passing through the heater to the total input solar radiation energy.

$$\eta_{\text{en}} = \frac{\dot{m}_a c_{\text{pa}} (T_o - T_i)}{(I \times A_p)} \quad (1)$$

where η_{en} is the thermal efficiency, I is the solar radiation intensity, m_a is the mass flow rate of air, c_{pa} denotes specific heat of the air, T_i is the temperature of the air at the inlet, and A_p is the projected area of the heater. The projected area was considered for calculating the solar energy received by the heater because the shape of the heater was cylindrical. The projected area of each air heater was 2.45 m². The exergy efficiency which is defined as the ratio of the exergy gained by the air to the exergy input to the heater was assessed by Eq. (2) [15, 16].

$$\eta_{\text{ex}} = \frac{\dot{E}x_{\text{re}}}{\dot{E}x_{\text{in}}} \quad (2)$$

The exergy received ($\dot{E}x_{\text{re}}$) by the air when it flows through the heater is estimated by Eq. (3) [17].

$$\dot{E}x_{\text{re}} = \dot{m}_a c_{\text{pa}} \left[(T_o - T_i) - T_r \ln \left(\frac{T_o}{T_i} \right) \right] - R \ln \left(\frac{P_o}{P_i} \right) \quad (3)$$

where R is the universal gas constant and T_r is the reference temperature.

The exergy input to the heater was computed as

$$\dot{E}x_{\text{in}} = \left[1 - \frac{T_r}{T_{\text{sun}}} \right] \dot{Q}_{\text{in}} \quad (4)$$

The apparent sun temperature T_{sun} was assumed to be 4500 K [15].

The solar radiation flux absorbed by the surface of the heater was estimated by the equation given below

$$\dot{Q}_{\text{in}} = I A_p \quad (5)$$

The wet basis (w.b.) moisture content of the sample was estimated by employing the following equation.

$$M = \frac{m_i - m_f}{m_i} \times 100 \quad (6)$$

where M is the moisture content (w.b.) (%), and m_i and m_f are the initial mass and the final mass (g) of the sample, respectively.

5 Experimental Results and Discussion

The solar heater was tested on 26th and 27th November 2019 every day from 8:00 h to 14:00 h at the air flow rate of 0.053 kg/s, and the intensity of solar radiation falling on the surface of the heater and the air temperatures at the inlet and outlet of the heater with respect to time are shown in Fig. 5. The temperature of the air at the inlet was in the range between 20 and 29 °C with an average of 24.5 °C and the temperature at the outlet was in the range between 31 and 40 °C with an average of 35.5 °C. The intensity of solar radiation was found to be varying between 386 and 772 W/m². The maximum temperature of the air at the outlet of the heater was recorded at 11:00 h of the day when the intensity of solar radiation was maximum.

The variations of the wind velocity and the ambient temperature are shown in Fig. 6. The average wind velocity was found to be 0.53 m/s, and the average temperature of the ambient was found to be 25.39 °C.

Figure 7 shows the energy and exergy efficiencies of the heater. The energy efficiency was found to be in the range between 15.11 and 25.25% with an average of 19.2% and the exergy efficiency of the heater was found to be in range between 0.17 and 0.59% with an average of 0.35%. A similar trend is noticed in the energy and exergy efficiencies of both the experiments. The maximum energy and exergy efficiencies were found to be at 8:00 h of the day and the lowest values were found to be at 14:00 h of the day. The lower intensity of the solar radiation and the temperature of the air at the inlet of the heater were the causes of the highest energy and exergy efficiencies at the beginning of the experiment. The rise in the temperature of the air, i.e. $(T_o - T_i)$, was almost constant from 8:00 h to 14:00 h of the day although the intensity of solar radiation increased gradually. At a fixed mass flow rate and specific heat of air, it is obvious from Eq. 1 that the energy efficiency of a solar air heater depends on the temperature of the air at the inlet and outlet of the heater and the solar radiation intensity. Therefore, for a fixed value of $(T_o - T_i)$, the energy efficiency of

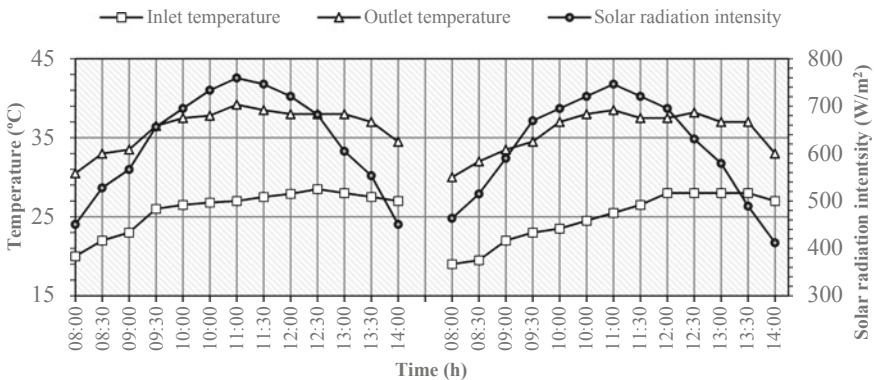


Fig. 5 Variation in the temperature of the air at the inlet and outlet of the heater and the solar radiation intensity

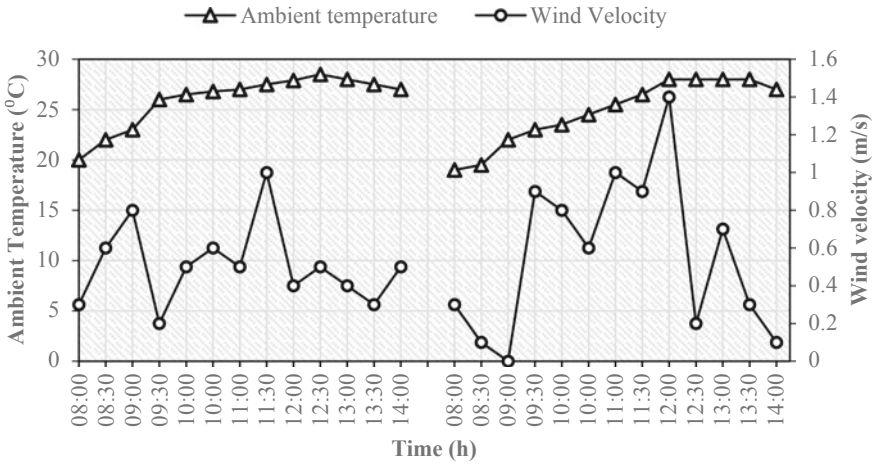


Fig. 6 Variation of wind velocity and ambient temperature

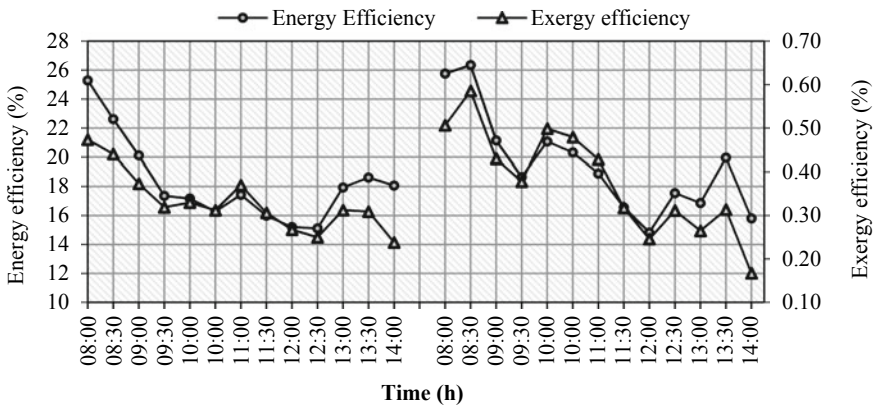


Fig. 7 Variation in the energy and exergy efficiency

a solar air heater decreases with increase in the intensity of solar radiation. The radiation and convection losses from the surface of a solar heater increase with increase in the solar radiation intensity. However, in the afternoon, the higher air temperature at the inlet of the heater may be attributed to the lower energy efficiency of the heater. In the afternoon, the temperature of the air at the inlet of the heater was recorded to be 27 °C, while in the morning, it was only 19 °C.

At the given flow rate of the air, the maximum temperature of the air at the outlet of the heater was 40 °C. For agricultural products and fruits, the maximum allowable drying temperature ranges from 45 to 75 °C [1]. Medicinal plants are generally dried at a lower temperature. The sensitive product should be dried at a lower temperature and usually between 30 and 50 °C [18]. Therefore, fenugreek leave (*Trigonella*

foenum-graecum) was selected for testing the air heater. The hot air produced in the heater was supplied to a drying chamber for drying the fenugreek leaves.

The fenugreek leaves were dried from the initial moisture content of 86.34% (w.b.) to the final moisture content of 3.95% (w.b.) in 9 h. The variation in the moisture content of the sample w.r.t. the drying time is shown in Fig. 8. The leaves were dried in temperature range between 34 and 45 °C. The photographs of the fresh and dried leaves are shown in Fig. 9a and b, respectively. Sunil et al. [19] reported that the fenugreek leaves dried at a temperature of 45.99–70 °C in an indirect-type natural convection dryer took 5–6 h to dry the leaves from the moisture content of 87 to 6.82% (w.b.). Shrivastava and Kumar [20] compared the drying process of fenugreek leaves dried in an indirect-type forced convection solar dryer and under the sun. They reported that fenugreek leaves on the first tray of the dryer dried in 9 h.

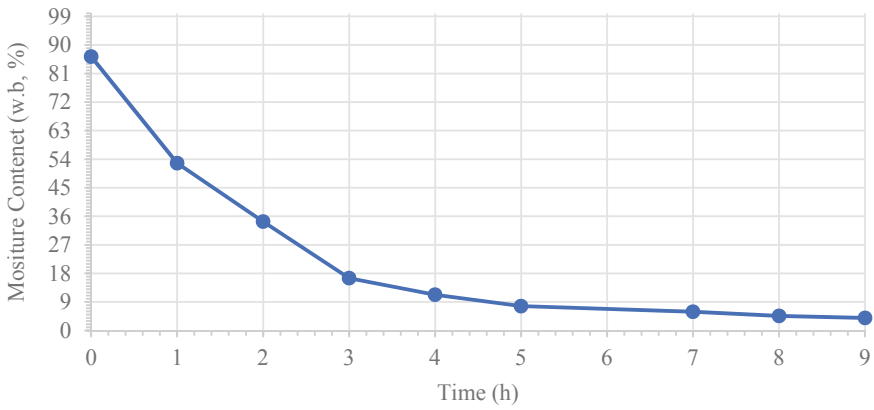


Fig. 8 Moisture content vs drying time curve of the leaves

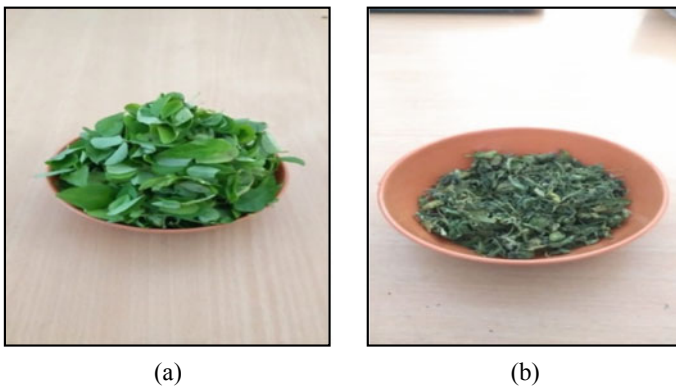


Fig. 9 (a) Fresh fenugreek leaves (b) Dried fenugreek leaves

From this study, it can be concluded that the solar air heater developed with the easily available plastic bags can be used for harnessing solar energy by producing hot air required for the low-temperature applications but it has some limitations. The longevity of the plastic material is a major problem, and also the plastic bag may easily get damaged by any kind of a pointed rod. The transmissivity of plastic also degrades with the elapse of time. Air at a high temperature cannot be produced in this kind of heater as there is a possibility of melting of the black plastic sheet at a higher temperature. Solar degradation of polymers may affect it in the longer term. It may be useful in the lower-temperature temporary applications. However, if a high-temperature resistance, durable and flexible transparent material can be developed, then the above-mentioned limitations can be overcome.

6 Conclusion

A low-cost all-plastic solar air heater built with easily available material was tested and its performance was evaluated.

- The average energy efficiency and exergy efficiency of the heater were found to be 19.2% and 0.35%, respectively, at an air flow rate of 0.053 kg/s.
- The maximum temperature at the outlet of the heater was found to be 40 °C.
- The temperature of the air at the outlet of the heater was found to be low and the heater may not suitable for the use in those applications requiring air at a higher temperature.
- The developed dryer may be useful for space heating and drying of medicinal plants and herbs at very low cost.

References

1. Fudholi A, Sopian K, Ruslan MH, Alghoul MA, Sulaiman MY (2010) Review of solar dryers for agricultural and marine products. *Renew Sustain Energy Rev* 14:1–30
2. Saxena A, Varun AA, El-Sebaei A (2015) Thermodynamic review of solar air heaters. *Renew Sustain Energy Rev* 43:863–890
3. Garg HP, Prakash J (2014) *Solar energy fundamentals and application*, 1st revised ed., McGraw Hill Education (India) Pvt. Ltd., pp 84–85
4. Oztop HF, Bayrak F, Hepbasli A (2013) Energetic and exergetic aspects of solar air heating (solar collector) systems. *Renew Sustain Energy Rev* 21:59–83
5. Bansal NK, Boeltchert A, Uhlemann R (1983) Performance of plastic solar air heating collectors with a porous absorber. *Energy Res* 7:375–384
6. Esper A, Lutz K, Mfjhlbauer W (1989) Development and testing of plastic film solar air heaters. *Sol Wind Technol* 6:189–195
7. Chau KV, Baird CD, Bagnall LO (1980) Performance of a plastic suspended screen solar air heater. *J Agric Eng Res* 25:231–238
8. Flores-Irigollen A, Fernandez JL, Rubio-Cerda FT, Poujol E (2004) Heat transfer dynamics in an inflatable-tunnel solar air heater. *Renew Energy* 29:1367–1382

9. Gill RS, Singh S, Singh PP (2012) Low cost solar air heater. *Energy Convers Manage* 57:131–142
10. Abdullah AS, Bassiouny MK (2014) Performance of cylindrical plastic solar collectors for air heating. *Energy Convers Manage* 88:88–95
11. Ahmad NT (2001) Agricultural solar air collector made from low-cost plastic packing film. *Renew Energy* 23:663–671
12. Benli H (2013) Experimentally derived efficiency and exergy analysis of a new solar air heater having different surface shapes. *Renew Energy* 50:58–67
13. Omojaro AP, Aldabbagh LBY (2010) Experimental performance of single and double pass solar air heater with fins and steel wire mesh as absorber. *Appl Energy* 87:3759–3765
14. Bahrehmand D, Ameri M (2015) Energy and exergy analysis of different solar air collector systems with natural convection. *Renew Energy* 74:357–368
15. Jafarkazemi F, Ahmadifard E (2013) Energetic and exergetic evaluation of flat plate solar collectors. *Renew Energy* 56:55–63
16. Park SR, Pandey AK, Tyagi VV, Tyagi SK (2014) Energy and exergy analysis of typical renewable energy systems. *Renew Sustain Energy Rev* 30:105–123
17. Akpınar EK, Koçyigit F (2010) Energy and exergy analysis of a new flat-plate solar air heater having different obstacles on absorber plates. *Appl Energy* 87:3438–3450
18. Bogers RJ, Craker LE, Lange D (2006) *Medicinal and aromatic plants*. Springer, Berlin
19. Sunil V, Sharma N (2014) Experimental investigation of the performance of an indirect mode natural convection solar dryer for drying fenugreek leaves. *J Therm Anal Calorim* 118:523–531
20. Shrivastava V, Kumar A (2016) Experimental investigation on the comparison of fenugreek drying in an indirect solar dryer and under open sun. *Heat Mass Transf* 52:963–1972

Microbial Fuel Cell—A Review



Dhrupad Sarma, Parimal Bakul Barua, Ashutosh Das,
Nur Mehdee Rahman, Shafiu Alom Prodhani, and Sazid Anwar

Abstract Microbial fuel cell (MFC) is a newly emerged technology whose main aim is to produce green energy from organic waste materials that is healthy for the environment. It is one of the best renewable energy sources to produce electricity from waste-sewage water, municipal solid waste, industrial and agricultural waste, etc. When sewage water is directly discharged into the water bodies, it causes eutrophication and degrades the water quality. So, using wastewater as a source of energy will decrease the amount of pollutants which will be released in the water bodies. MFC is an electrochemical cell which converts the organic and inorganic waste materials into electricity with the help of microorganisms. The performance of an MFC depends on various design and operational parameters. The main objective of this paper is to review various substrates, anode and cathode electrodes, the effect of different separators on the MFC output, also to understand the MFC performance under different operational conditions. In case of dual chamber MFC, performance significantly shows variation when electrode spacing is reduced. Use of 4-layered PTFE diffusion layer in carbon cloth cathode for single-chamber MFC shows improvement in performance. Variation of temperature and pH has great impact on MFC performance. When acetate and kitchen waste is used as substrate in single chamber and dual chamber MFC, respectively, yields maximum power density. This paper is aimed

D. Sarma (✉) · P. B. Barua · A. Das · N. M. Rahman · S. A. Prodhani · S. Anwar
Mechanical Engineering Department, Jorhat Engineering College, Jorhat, India
e-mail: thinkdpd@rediffmail.com

P. B. Barua
e-mail: parimalbakul@gmail.com

A. Das
e-mail: das.ashutosh130@gmail.com

N. M. Rahman
e-mail: immehdee006@gmail.com

S. A. Prodhani
e-mail: pshafiu@gmail.com

S. Anwar
e-mail: riyankhan459@gmail.com

to give the readers a brief understanding on this emerging technology, which is being studied to a great extent in recent years.

Keywords Coulombic efficiency · Current density · Microbial fuel cell · Power density

1 Introduction

The demand for energy has tremendously increased in today's world. With the resources getting limited and rising population, the demand for energy has increased globally. The higher percentage use of non-renewable source of energy over renewable source of energy has caused a serious threat to the environment. Another major problem that needs attention globally is the waste management. Therefore, it is high time that we start looking into technologies for energy generation that are environment friendly.

Microbial fuel cell (MFC), it is a technology that uses microorganisms as catalyst to transform chemical energy of organic waste (substrate) into electricity [1]. This technology can be a promising alternative for energy generation with the productive use of organic waste. Based on design, the MFCs can be a single-chambered MFC or a double-chambered MFC.

The single-chambered MFC has a single compartment which basically contains both the anode and the cathode, and the cathode is directly exposed to air. A proton exchange membrane (PEM) separates the anode and the cathode [2]. The most widely used and inexpensive design is the double-chambered MFC. These MFCs have separate compartments for the anode and the cathode, and the chambers are separated by a PEM or a salt bridge. The anode chamber is usually kept in anaerobic condition and contains the substrate, and the cathode chamber contains the catholyte and is kept in aerobic condition [1].

In 1911, Potter first observed that electricity can be generated by using bacterial cells [3]. The organic substrates present in the anodic chamber produced free electrons and protons under anaerobic condition [4]. Presence of oxygen in the anodic chamber inhibits the generation of electricity. Hence, it is necessary to maintain the bacteria away from oxygen [5]. Electron mediators are used to allow the free electrons from the bacterial cells to move to the anode surface [6]. The efficiency and economically effective substrate depends upon the chemical composition and concentration of the substrate [7].

The electrodes are the key component for the electron transfer from the anodic half-cell to the cathodic half-cell in the MFC. The metabolic activities of the microbes produce electrons, and this creates a potential difference between the electrodes which leads to the generation of electricity [8, 9]. Various studies have been done on electrode materials to understand its effect on performance of MFC, different electrode materials include carbon nanotube graphite modified felt anode [10], polytetrafluoroethylene (PTFE) layered graphite anode [11], carbon brush anode [12],

stainless steel mesh wire [1], carbon cloth cathode [13], etc. All these electrodes show different results when used in MFC under different conditions.

In an MFC, the anode and the cathode are separated by a separator. The role of a separator is very important; it helps in transfer of protons from the anode to the cathode through it. However, studies show that single-chambered MFC without a separator produced higher power densities [14], whereas if there is an absence of a separator, there would be higher oxygen and substrate diffusion which will lower the Coulombic efficiency [15]. During recent past many advancements have been made and variety of separators have been studied for the better proton transfer and lower oxygen diffusion. Various membranes include the anion exchange membrane (AEM), bipolar membrane (BPM), ultrafiltration membrane (UFM), cation exchange membrane (CEM), and salt bridge [15]. All these membranes have their own advantages and disadvantages; however the most simple and inexpensive separator that is commonly used is the salt bridge.

The main objective of this paper is to review various substrates, anode and cathode electrodes, the effect of different separators on the MFC output, and also to understand the MFC performance under different operational conditions.

2 Types of Microbial Fuel Cell

There are basically two types of microbial fuel cell based on number of chambers: Single-chambered MFC and Double-chambered MFC.

2.1 *Single-Chambered MFC*

In a single-chamber MFC, the cathode electrode remains exposed directly to the air [7, 16]. It consists of only anode chamber where the organic materials are fed in and the electrode is an air cathode. It has a very simple design and low operating cost in comparison with a double-chambered MFC [17]. Figure 1 shows a typical single-chambered MFC.

2.2 *Double-Chambered MFC*

It is the most common MFC design in a two-chambered setup, an ion-selective membrane separates the anode and cathode compartments [16], and it prevents oxygen from entering the anode chamber and at the same time helps proton transfer to the cathode from the anode. The organic wastewater is fed to the anode chamber which is in anaerobic condition and the cathode chamber is in aerobic condition

Fig. 1 Single-chamber MFC [2]

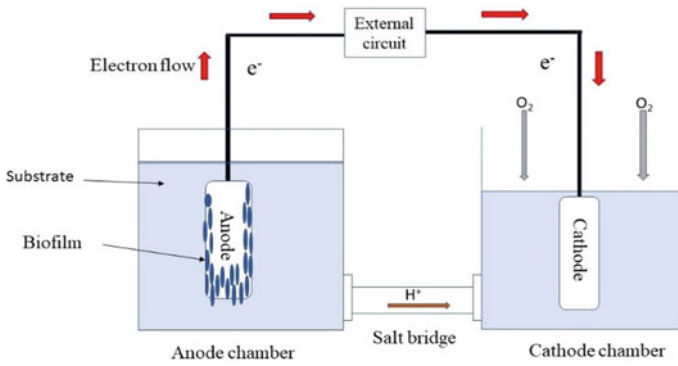
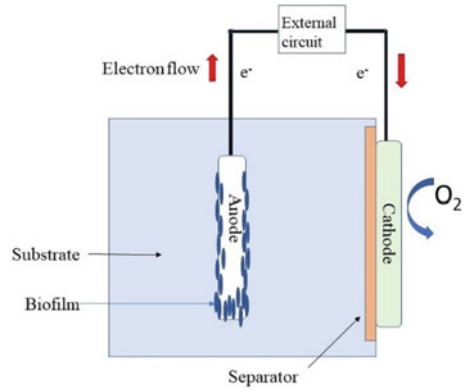


Fig. 2 Double-chambered MFC [1]

[7]. A salt bridge or membrane is used between the half cells to maintain electrical neutrality. Figure 2 shows a typical double-chambered MFC.

However, MFC can also be classified based on presence and absence of mediators.

2.3 Mediated MFC

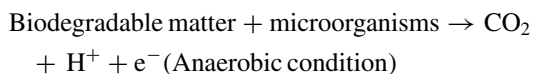
In this type of fuel cells, artificial electron mediators are added for the continuous production of ions like protons and electrons. The mediators play an active role in the electron transfer from the microorganisms that are unable to handover the electrons to the anode. Some of the microbes which require external mediator for the electron transfer are: *E. coli*, *Pseudomonas fluorescens*, *Actinobacillus succinogenes*, *Desulfovibrio desulfuricans*, etc. [18].

2.4 Mediator-Less MFC

In this type of fuel cells, there is no requirement of any artificial electron mediators for the continuous production of ions. The microorganisms develop a biofilm over the anode surface which helps in the electron transfer process. Some of the mediator-free bacterial species includes *Geobacter sulfurreducens* and *Rhodospirillum rubrum* [14, 18].

3 Substrates Used in MFC

Microbial fuel cell technology uses microorganisms like bacteria as catalysts to oxidize these organic wastes and produce electricity. The microorganisms present in the anaerobic condition break the organic waste materials into glucose, acetate, carbon dioxide and electrons as shown in the reaction given below. Electrons from the wastes are transferred to the anode; the electrons flow from anode to cathode through an external circuit producing electricity [19]. The free electrons from the bacterial cell move to the anode with the help of a mediator. Ferricyanide is an effective artificial mediator [20–22]. The addition of ferricyanide improves the overall performance of the MFC as compared to platinum [23, 24]. The maximum power output by using ferricyanide found so far is 258 W/m³ [25]. Although its performance is excellent, it is not preferred because it requires regular replacement after consumption [26, 19].



MFC is a very efficient waste management technology that produces green energy from the organic and inorganic waste materials with the help of microbes. It also reduces the chemical oxygen demand (COD) concentration from the waste materials and thus reduces the oxygen need to decompose the waste material [27].

In MFC, the anodic chamber must maintain at an anaerobic condition where all the organic wastes are kept, and the cathode chamber is filled up with catholyte. In case the cathode is exposed to air, then the setup will be called as Air Cathode MFC [1]. Oxygen is mostly used as the electron acceptor for large-scale operation. Other compounds such as ferricyanide and permanganate can also be used because of their high coulombic efficiency [28].

Sudarsan et al. [16] have conducted an experiment using different three substrates (dairy waste, sugar waste and hostel sewage) and found that hostel sewage is more effective as compared to other substrates and found a maximum current of 0.64 mA. Another experiment was performed by Jayashree et al. [29] by using three different types of wastewater and found that dairy wastewater can produce more amount of electricity as shown in Table 1.

Table 1 Experimental values of different parameters using three different types of wastewater [29]

Sr. No	Types of substrate	Current (mA)	pH	COD removal efficiency (%)
1	Dairy wastewater	5.2	7	94
2	Municipal wastewater	2.61	7	90
3	Cassava wastewater	1.93	8	61

Cow dung can also be an alternative substrate for small-scale operation. It is found that it produced a maximum current of $1.13 \times 10^{-2} \mu\text{A}$ and the corresponding maximum power generated is $9.223 \times 10^{-3} \mu\text{W}$ [30].

Vegetable slurry is also an effective substrate which is able to produce a sufficient amount of current and voltage. The maximum output parameters found out to be: mean output current (I_m) = 4.75 mA, average output voltage (V_{avg}) = 22.325 mV, average output power (P_{avg}) = 106.044 μW , average output current density (ID_m) = 19.79 mA/m² and average output power density (PD_{avg}) = 441.85 $\mu\text{W}/\text{m}^2$ [1].

Urine has been found to be an effective feed stock for MFCs due to the additional benefits of nitrogen, phosphate, and potassium. Artificial Urine Medium (AUM) was used as feedstock at the flow rate of 0.36 mL/min for both the MFCs. The MFC-S showed maximum power density of 0.053 W/m³ and MFC-L showed 0.580 W/m³. Also, the current densities produced were 7.3 and 49.1 mA/m², respectively, at the maximum power output [13].

Table 2 shows various substrates used in single chamber MFC and maximum current produced corresponding to the substrate and Table 3 shows maximum power density corresponding to different types of substrates and mediators for dual chamber MFC:

Table 2 Maximum power density corresponding to different types of substrates and mediators for single-chamber MFC [12, 31, 32]

Type of MFC	Types of substrate	Types of mediator	Maximum electrode power density mW/m ²
Single-chambered MFC	Acetate (28.16 mM ^a)	No mediator	2400 [12]
	Ethanol (10 mM)	No mediator	488 ± 12 [31]
	Galactitol (34 mM)	No mediator	84.58 [32]
	Glucose (6.7 mM)	No mediator	803.71 [32]
	Ribitol(34 mM)	No mediator	924.79 [32]
	Xylitol (34 mM)	No mediator	340.45 [32]
	Xylose (6.7 mM)	No mediator	192.14 [32]

^a mM = millimolar

Table 3 Maximum power density corresponding to different types of substrates and mediators for dual-chamber MFC [31, 33–35]

Type of MFC	Types of substrate	Types of mediator	Maximum electrode power density mW/m ²
Dual-chambered MFC	Ethanol	No mediator	40 ± 2 [31]
	Domestic wastewater	No mediator	17.9 [33]
		Methylene blue (0.3 mM)	36 [33]
		Neutral red (0.2 mM)	31 [33]
		2-Hydroxy-1,4-naphthoquinone (0.05 mM)	18.7 [33]
	Glucose with <i>Escherichia coli</i> as bacteria	Methylene blue (25 mM)	46.14 ± 3.92 [34]
	Glucose with <i>Shewanella</i> as bacteria	Methylene blue	26.91 ± 1.71 [34]
	Glucose with mixture of <i>Escherichia coli</i> and <i>Shewanella</i> as bacteria	Methylene blue (10 mM)	24.88 ± 3.63 [34]
	Kitchen waste (carbohydrate, crude protein, crude fat, ash content etc.)	No mediator	84.58 [35]
		Ethylene diamine tetra acid	803.71 [35]
		Potassium ferricyanide	924.79 [35]
		Methylene blue	340.45 [35]
		Potassium permanganate	192.14 [35]

4 Electrodes

The electrodes are the important components for the transfer of the electrons from the anodic chamber to the cathodic chamber. The performance of the MFC primarily depends on the various factors such as length of the electrodes, surface area and also the materials used in the electrodes. The basic requirement for the selection of the electrode material is cost-effectiveness and easy availability [36].

4.1 Anode Electrode

The anode electrode is a very crucial component as it is the main electron acceptor in the MFC system. Also, its performance depends on the electrode material, electrode design, MFC design and microbial electron transfer. The properties of ideal anode electrodes are: (i) chemically stable in the substrate solution; (ii) high electrical

Table 4 Anode electrode, type of the MFC, size and output power [10–12]

Sr. No	Material of anode electrode	Type of MFC	Electrode size/Surface area	Electrode power density mWm^{-2}
1	PTFE layered graphite	Single chamber	3 cm length and 1.8 cm diameter (cylindrical electrode)	760 [11]
2	Graphite felt with CNTs	Single chamber	2.6 cm^2	200 [10]
3	Carbon brush	Single chamber	0.22 m^2	2400 [12]
4	Stainless steel	Double chamber	1200 cm^2	0.441 [1]

conductivity with low resistance; (iii) non-toxic; (iv) large surface area; and (v) non-corrosive. Some of the commonly used anode electrodes are carbon cloth, carbon felt, carbon paper, graphite fiber brush, etc. [13, 37].

Hamamoto et al. [10] in their experiment on the vegetable oil observed that the use of carbon nanotube-graphite modified felt anode over the non-modified graphite felt anode showed wonderful results. The external resistance reached to a value of 100Ω from an initial value of $10,000 \Omega$ through 1000Ω , and the current density increased to a value of $500 \mu\text{Acm}^{-2}$. In another study done by Zhang et al. [11] found that 30% PTFE (polytetrafluoroethylene) layered graphite anode electrode with *Escherichia coli* as biocatalysts showed good result with power density of 760 mWm^{-2} . A comparative experiment was conducted using carbon brush anodes and carbon paper anodes; the anodes were ammonia treated and placed in bottle-MFC (B-MFC). Results show that the MFC using brush anodes produced power up to 1430 mW/m^2 , whereas the carbon paper anodes produced 600 mW/m^2 . However, using brush anodes in cube-MFC (C-MFC) produced up to 2400 mW/m^2 , which is significantly large [12]. Table 4 shows variation of output power density over different anode electrode type in single-chambered MFC.

4.2 Cathode Electrode

The cathode electrode is also a very important part of an MFC. The electrons generated from the anode chamber pass through the cathode electrode to the cathode chamber. Using cathode electrode with a suitable catalyst enhances the performance of the MFC. The most used cathode electrode materials are: Cu, carbon fiber, carbon felt, carbon paper, reticulated vitreous carbon, etc. [37].

Chouler et al. [13] in their experiment with the use of biomass obtained Oxygen Reduction Reaction (ORR) catalysts in the plain carbon cloth cathode, the internal resistance reduced to $15 \text{ k}\Omega$ and volumetric power density 1.95 Wm^{-3} . In another experiment performed by Zhang et al. [38] for the up-flow air cathode membrane-free MFC observed that the use of flexible carbon-cloth cathode electrode has shown a maximum volumetric power density of 12.8 Wm^{-3} . In case of single-chamber air

Table 5 Cathode electrode, type, size, catalyst, and power output [1, 13, 38 and 39]

Sr. No	Material of cathode electrode	Type of MFC	Electrode size/Surface area	Catalyst used	Volumetric power density Wm^{-3}	Electrode power density mWm^{-2}
1	Carbon cloth	Single-chambered air cathode	16 mm^2	Nitrogen doped carbon aerogel	1.95 [13]	–
2	Flexible carbon cloth	Single-chambered air cathode	118 cm^2	Pt powder	12.8 [38]	–
3	Carbon cloth with PTFE DL	Single-chambered air cathode	7 cm^2	Pt catalyst (0.5 mg cm^{-2})	–	766 [39]
4	Stainless steel	Double chambered	1200 cm^2	–	–	0.441 [1]

cathode MFC, water loss through the cathode is a serious issue, reducing the water loss can increase the Coulombic efficiency as well as power density of the MFC, Cheng et al., [39] suggested using diffusion layers (DL) in the air-facing side of the cathode. In the experiment conducted, various layers of polytetrafluoroethylene (PTFE) were added to test the performance of the cathode in the MFC. The initial layer contained 30% wt. PTFE solution on air facing side, and additional layers were added by applying 60% wt. PTFE solution by brushing on it. Comparing the results with MFC having no DL, it was found that using 4 DL, maximum power density of 766 mW/m^2 was obtained which was 42% greater than without DL. Also, Coulombic Efficiency (CE) significantly showed improvement with the use of DL, moreover, decrease in oxygen mass transfer coefficient was also achieved, and the water loss was almost negligible using 4 DL compared to 20% water loss without DL. Table 5 shows variation of output power density over different type of cathode electrode in single-chambered air cathode MFC.

5 Proton Exchange System

Proton exchange system is very important part in an MFC. Protons produced in the anode, drift to the cathode through the proton exchange medium [1, 15]; also it inhibits the flow of other ions as well as substrates and oxygen across the anodic and cathodic chamber [37] Also, this proton exchange medium physically separates the anodic and cathodic chambers.

5.1 PEM in Dual-Chamber MFC

Various proton exchange membranes (PEM) are used in an MFC. In case of dual-chamber MFC, performance is affected by diffusion of oxygen into anode chamber and substrate into cathode chamber through the PEM. Nafion is the most used PEM in MFC due to its high proton permeability [18]. However, in neutral pH MFCs using Nafion membranes allows cation (e.g., Na^+ , K^+ , Ca^{2+}) with concentration 10^5 times higher than H^+ to flow through them, thus reducing the flow of H^+ ions [15, 18, 37, 40]. Due to this reduction in flow of protons, accumulation of H^+ ions takes place in the anode chamber resulting in pH splitting [15]. A comparative study on Anion Exchange Membrane (AEM), Nafion and Ultrafiltration Membranes (UF-0.5 K, UF-1 K, UF-3 K) using two different setups, C-MFC with 4 cm electrode spacing and B-MFC with 12 cm electrode spacing shows that maximum power density of 610mW/m^2 and 72% CE is achievable using AEM in C-MFC, whereas not much difference in power density was observed for the membranes in B-MFC. It is concluded that electrode spacing is responsible for high internal resistance in MFC; thus it is evident that to observe the variation in performance using different membranes the electrode spacing should be lowered [40]. Kim et al. [40] also suggested that all the membranes could be used in MFC, except UF-0.5 K, as it shows high internal resistance, also UF-0.5 K produced very low power density compared to others.

5.2 Salt Bridge

Although the membrane-based separators are widely used, the disadvantage is that these membranes undergo fouling, reducing MFC lifetime [41]. A cost-effective alternative to these membranes for proton transfer is the salt bridge. It is made of agar and salts; however, its performance varies with dimensional variations and salt concentrations. Several studies compared sodium chloride and potassium chloride salts used in salt bridge with 10% agarose; results showed not much difference in current generation [42, 43]. Experiment conducted using sodium chloride 1 to 9 M showed that 1 M sodium chloride gives the optimum results [22]. Another study compared different concentrations of sodium chloride (1 to 10%) with 10% agarose; it was found that at 5% salt concentration maximum current was generated [44]. Different agarose concentration was analyzed from 7 to 12%; however maximum voltage of 0.67 mV and maximum current of 0.0642 mA was achieved using 10% agarose concentration [43]. Based on dimensional parameters of salt bridge, Sarma, et al. [1] suggested that resistance to anion flow can be reduced by decreasing the length of the salt bridge, the optimum length found was 260 mm, also with the increase in cross-sectional area of the salt bridge, resistance to anion flow can be reduced, but this leads to catholyte diffusion to the anode chamber decreasing the current

production, hence optimum current generation was achieved by lowering the cross sectional area, and the optimum cross-sectional area was found to be 506.7 mm².

5.3 Separators in Single-Chamber MFC

Though studies showed that use of separator is important for MFC performance optimization, however, in case of a single-chamber MFC, experiments conducted by Liu and Logan suggested that the maximum power density of 492 mW/m² was obtained without the use of PEM compared to the 262 mW/m² which was achieved using a PEM. This increase in power without the use of PEM is a cost-effective approach to obtain higher power output [14]. However, removing PEM resulted in lower CE. The lowering of the CE is due to the oxygen diffusion, which leads to the consumption of the substrate [14]. Fan et al. [45] suggested that using J-cloth between the electrodes could reduce the oxygen diffusion rate and hence increase the CE. At a current density of 0.6 mA cm⁻², CE of 71% was obtained with 2 layers of J cloth compared to 35% without J cloth. However, J cloth is biodegradable, with long duration use of the MFC the cloth is completely degraded [46]. Therefore, Zhang et al. [46] suggested the use of glass fiber separators which are non-biodegradable. The use of glass fiber separator of thickness 1 mm (GF1) produced a CE of 81%, whereas without separators maximum CE achieved was 34% and using J cloth the maximum CE was 40%. It is also found that GF1 used in single separator electrode assembly (SSEA) and double separator electrode assembly (DSEA) configuration gave a CE 150% higher than the MFC without separator at same current density. Table 6 shows variation of output power densities over various types of PEMs used in single- and double-chamber MFC.

6 Operational Conditions of Microbial Fuel Cell

In microbial fuel cell technology, the production of energy in a cell is highly dependent on operational conditions (temperature, humidity, pH value, electrolyte etc.). The amount of energy varies at different values of this factors. Amr et al. [47] in their research found that electricity production for the samples collected during summer was better than the samples collected during winter due to the high microbial load during the hot season. Also, at pH value of 8.6 and 7.9 the highest current values of 0.28 and 0.2 mA were obtained respectively. However, Li et al. [48] developed tubular MFC that allowed pH control for both anode and cathode compartments, the CE showed great improvement with high anodic pH. They operated MFC with high anodic pH (10.0) and low cathodic pH (2.0); results showed a maximum volumetric power density and voltage of 29.9 W/m³ and 1.04 V, respectively, which were higher than those at neutral pH MFCs. The environmental temperature also has an effect on the performance of MFC. Liling et al. [49] conducted an experiment to analyze

Table 6 PEMs, MFC type and power density [1, 40, 46]

Sr. No	Proton exchange membranes	MFC type	Power density mWm ⁻²
1	Nafion	Dual-chamber B-MFC	38 ± 1 [40]
		Dual-chamber C-MFC	514 [40]
		Single-chamber MFC	262 ± 10 [40]
2	AEM	Dual-chamber B-MFC	35 ± 3 [40]
		Dual-chamber C-MFC	610 [40]
3	CEM	Dual-chamber B-MFC	33 ± 2 [40]
		Dual-chamber C-MFC	480 [40]
4	Salt bridge (with 1 M NaCl and 10% Agarose)	Dual-chamber MFC	0.441 [1]
5	J-Cloth (2 layers)	Single-chamber MFC	896 ± 49 [46]
6	Glass fibre (GF1) 1 mm thickness	Single-chamber MFC with SSEA	1195 ± 30 [46]
		Single-chamber MFC with DSEA	963 ± 39 [46]

the performance of the MFC under five different temperatures (15, 20, 25, 35 and 40 °C); they concluded that both too high and too low temperatures were not good for the growth and reproduction of microorganisms. The MFC operated at 35 °C showed greater power generation for a long duration of time. In another research conducted by Yapping et al. [50] observed the performance of MFC in day–night temperature to understand the effect of real climate change. The MFCs performance was observed with varying and steady temperatures. MFCs with varying temperatures 6/18 °C were operated at temperatures 6 °C for 12 h and 18 °C for 12 h, similarly for 18/30 °C. Also, MFCs with steady temperatures were operated at 6 °C, 18 °C and 30 °C. Results showed that the MFC with varying temperature 18/30 °C, at 30 °C showed highest power density of 2169 ± 82 mW/m², whereas MFC operated at steady temperature of 30 °C showed lower power density. However, in case of MFC with varying temperature 6/18 °C, at 18 °C produced only 71% of the power compared to the power produced by MFC operating with steady temperature of 18 °C. It can be concluded that in the varying temperature MFCs the higher temperatures have a key role in power production. Observations were made that with change in temperatures the cathode and anode potentials also showed difference. Also, the CE and COD removal calculations for the various temperatures showed that the CE is highest for the MFC operating at varying temperatures (6/18 °C), which is 94.6 ± 5.2% [50] (Table 7).

Table 7 Experimental values of power densities corresponding to different operating conditions [47–50]

MFC type	Temperature °C	Anodic pH	Cathodic pH	Electrode power density (mW/m ²)	Volumetric power density (W/m ³)	
Single-chamber	6	–	–	0 [50]	–	
	18			1378 ± 17 [50]		
	30			1952 ± 102 [50]		
	6/18 (Alternating)			6		759 ± 25 [50]
				18		980 ± 102 [50]
	18/30 (Alternating)			18		1341 ± 20 [50]
				30		2169 ± 82 [50]
Dual-chamber	37 (Summer sample)	8.6	–	202 [47]	–	
	25 (Winter sample)	7.9		117 [47]		
	40	–	–	–	204.30 [49]	
	35				164.03 [49]	
	30 ± 1	10	2	–	29.9 [48]	
		7	2		17.9 [48]	
		10	7		15.8 [48]	
		7	7		7.9 [48]	

7 Discussions

Based on the literatures reviewed, it is observed that the performance of MFC significantly depends on parameters like the type of substrates used, use of mediators, anode and cathode materials, PEMs. Also, it depends on operational conditions like temperature and pH of the chambers. From the literature review, it is found that using acetate as substrate in single-chamber MFC without mediator showed maximum power density of 2400 mW/m² [12]. However, in case of double-chamber MFC kitchen waste as substrate with potassium ferricyanide mediator showed maximum power density of 924.79 mW/m² [35].

In single-chamber MFC, the use of carbon brush as anode showed an optimum power density of 2400 mW/m² [12], whereas carbon cloth with 4-layer PTFE diffusion layer as cathode showed power density of 766 mW/m² [39]. In case of double-chamber MFC, wire mesh of stainless-steel grade SS304 (mesh size 0.92 mm and wire diameter 0.355 mm) as anode and cathode gave optimum results [1]. Also, for a double-chambered MFC potassium ferricyanide can be used in cathode chamber as cathodic electron acceptor. Potassium ferricyanide (50 mmol/L) in potassium phosphate buffer (100 mmol/L) enhances the current production [47].

For PEM in single-chamber MFC, glass fiber (GF1) with 1 mm thickness in SSEA setup produced maximum power density of 1195 ± 30 mWm⁻² [46], whereas in case

of double-chamber MFC Nafion gives good results when used in C-MFC with 4 cm electrode spacing [40].

For single-chamber MFC operated at alternating temperature of 18/30 °C, the best results were obtained at 30 °C [49]. However, in case of dual-chamber MFC optimum temperature was found to be 35 °C [49]. Also, the MFC operated with anodic pH (10.0) and cathodic pH (2.0) resulted in higher volumetric power density [48].

8 Conclusion and Future Scope

The study of the various studies showed that microbial fuel cell is an effective and efficient technology for production of electricity from biodegradable wastes like vegetable waste, food waste, wastewater, etc. Moreover, this technology is very much in demand because it is eco-friendly. This technology provides solution to the waste disposal problems and in addition to that allows generation of electricity from the huge amount of organic waste disposed every day. Over the years, studies have been done on various parameters of the MFC to improve and optimize its performance. The results of these studies can be concluded in the following manner:

- In single-chamber MFC use of acetate substrate without mediators showed significantly higher power density, whereas in dual-chamber MFC it is observed that performance of MFC improved with the use of mediators when domestic wastewater and kitchen waste were used as substrate.
- Carbon brush used in single-chamber MFC showed better results compared to other anode materials. Use of 4-layer PTFE diffusion layered carbon cloth as cathode resulted in significant improvement in performance of single-chamber MFC by reducing water loss through the cathode as well as improving the CE.
- It has been observed in case of dual-chamber MFC that reducing electrode spacing resulted in better performance of the MFC when Nafion, AEM and CEM are used as proton exchange membrane. However, AEM showed highest power density.

Although various studies are being done in the field of MFC, still its development is in early stages. The power generated by MFCs is still very low for widespread daily use. However, there are many areas that can be explored in future studies; few of them are stated as.

- i. In-depth study of the bacterial cell-membrane may bring to light much information regarding the assistance of cellular structure and proteins on the electron transport mechanism of the MFC.
- ii. Position and shape of salt bridge in dual-chamber MFC may have significant effect on performance of dual-chamber MFC; the proton transfer ability of MFC may vary with the position of salt bridge. Studies in this area are limited and can be explored more in the future.

References

1. Sarma D, Barua PB, Dey N, Nath S, Thakuria M, Mallick S (2019) Investigation and Taguchi optimization of microbial fuel cell salt bridge dimensional parameters. *J Inst Eng India Ser C*, 100:103–112
2. Kumar R, Singh L, Zularisam AW (2017) *Microbial fuel cells: Types and applications*, Springer Link, 2017. [Online] Available from: https://link.springer.com/chapter/https://doi.org/10.1007/978-3-319-49595-8_16#citeas [Accessed 15 Sept 2020]
3. Potter MC (1911) Electrical effects accompanying the decomposition of organic compounds 84:260–276
4. Antonopoulou G, Stamatelatu K, Bebelis S, Lyberatos G (2010) Electricity generation from synthetic substrates and cheese whey using a two-chamber microbial fuel cell. *Biochem Eng J* 50:10–15
5. Rabaey K, Verstraete W (2005) Microbial fuel cell cells: novel biotechnology for energy generation. *Trends Biotechnol* 23(6):291–298
6. Bartlett PN, Tebbutt P, Whitaker RG (1991) Kinematic aspects of the use of modified electrodes and mediators in bioelectrochemistry 16
7. Pant D, Bogaert GV, Diels L, Vanbroekhoven K (2009) A review of the substrates used in MFCs for sustainable energy production. *Bioresour Technol* 101(6):1533–1543
8. Hisham NSN, Zain SM, Jusoh S, Anuar N, Suja F, Ismail A, Basri NEA (2013) Microbial fuel cells using different types of wastewater for electricity generation and simultaneously removed pollutant. *J Eng Sci Technol* 8(3):316–325
9. Kalathil S, Patil SA, Pant D (2017) Microbial fuel cells: Electrode materials. *Encycl Interfacial Chem Surf Sci Electrochem* 309–318
10. Hamamoto K, Miyahara M, Kouzuma A, Matsumoto A, Yoda M, Ishiguro T, Watanabe K (2016) Evaluation of microbial fuel cells for electricity generation from oil-contaminated wastewater. *J Biosci Bioeng* 122(5):589–593
11. Zhang T, Zeng Y, Chen S, Ai X, Yang H (2007) Improved performances of *E. coli*-catalysed microbial fuel cells with composite graphite/PTFE anodes. *Electrochem Commun* 9:349–353
12. Logan BE, Cheng S, Watson V, Estadt G (2007) Graphite fiber brush anodes for increased power production in air-cathode microbial fuel cells. *Environ Sci Technol* 41:3341–3346
13. Chouler J, Padgett GA, Cameron PJ, Preuss K, Titirici MM, IoannisIeropoulos, Lorenzo MD (2016) Towards effective small-scale microbial fuel cells for energy generation from urine. *Electrochim Acta* 192:89–98
14. Liu H, Logan BE (2004) Electricity generation using an air-cathode single chamber microbial fuel cell in the presence and absence of a proton exchange membrane. *Environ Sci Technol* 38:4040–4046
15. Li W-W, Sheng G-P, Liu X-W, Han-Qing Y (2011) Recent advances in the separators for microbial fuel cells. *Biores Technol* 102:244–252
16. Sudarsan JS, Prasana K, Nithiyantham S, Renganathan K (2015) Comparative study of electricity production and treatment of different wastewater using microbial fuel cell (MFC). *Environ Earth Sci* 73:2409
17. Kakarla R, Kim JR, Jeon B-H, Min B (2015) Enhanced performance of an air-cathode microbial fuel cell with oxygen supply from an externally connected algal bioreactor. *Bioresour Technol* 195:210–216
18. Du Z, Li H, Gu T (2007) A state of the art review on microbial fuel cells: A promising technology for wastewater treatment and bioenergy. *Biotechnol Adv* 25:464–482
19. Logan BE, Hamelers B, Rozendal R, Schroder U, Keller J, Freguia S, Aelterman P, Verstraete W, Rabaey K (2006) Microbial fuel cells: Methodology and technology. *Environ Sci Technol* 40(17):5181–5192
20. Rabaey K, Lissens G, Siciliano SD, Verstraete W (2003) A microbial fuel cell capable of converting glucose to electricity at high rate and efficiency 1531–1535
21. He Z, Minteer SD, Angenent LT (2005) Electricity generation from artificial wastewater using an upflow microbial fuel cell. *Environ Sci Technol* 39(14):5262–5267

22. He Z, Wagner N, Minteer SD, Angenent LT (2006) An upflow microbial fuel cell with an interior cathode: assessment of the internal resistance by impedance spectroscopy. *Environ Sci Technol* 40:5212–5217
23. Oh S, Min B, Logan BE (2004) Cathode performance as a factor in electricity generation in microbial fuel cells. *Environ Sci Technol* 38:4900–4904
24. Pham HT, Jang JK, Chang IS, Kim BH (2003) Improvement of cathode reaction of a mediatorless microbial fuel cell. *J Microbiol Biotechnol* 14(2):324–329
25. Aelterman P, Rabaey K, Pham HT, Boon N, Verstraete W (2006) Continuous electricity generation at high voltages and currents using stacked microbial fuel cells. *Environmen Sci Technol* 40:3388–3394
26. He Z, Angenent LT (2006) Application of bacterial biocathodes in microbial fuel cell. *Electroanalysis* 18(19–20):2009–2015
27. Scott K, Yu EH, Ghangrekar MM, Erable B, Duteanu NM (2020) Biological and microbial fuel cells. *Compr Renew Energy* 4. [Online]. Available from: https://oatao.univ-toulouse.fr/7890/1/Erable_7890.pdf [Accessed 2 Sept 2020]
28. Logan BE, Regan JM (2006) Electricity producing bacterial communities in microbial fuel cell. *Trends Microbiol* 14(12):512–518
29. Jayashree S, Ramesh ST, Lavanya A, Gandhimathi R, Nidheesh PV (2019) Wastewater treatment by microbial fuel cell coupled with peroxicoagulation process. *Clean Technol Environ Policy*, Springer Professional, 10. [Online]. Available from: <https://www.springerprofessional.de/en/wastewater-treatment-by-microbial-fuel-cell-coupled-with-peroxic/17224750>. [Accessed 2 Sept 2020]
30. Parkash A (2016) Characterization of generated voltage, current, power and power density from cow dung using double chambered microbial fuel cell. *J Phys Chem Biophysics, Res Gate* 6(2). [Online]. Available from: https://www.researchgate.net/publication/304226829_Characterization_of_Generated_Voltage_Current_Power_and_Power_Density_from_Cow_Dung_Using_Double_Chambered_Microbial_Fuel_Cell. [Accessed 8 Sept 2020]
31. Kim JR, Jung SH, Regan JM, Logan BE (2007) Electricity generation and microbial community analysis of alcohol powered microbial fuel cells. *Biores Technol* 98:2568–2577
32. Catal T, Xu S, Li K, Bermek H, Liu H (2008) Electricity production from polyalcohols in single-chamber microbial fuel cells. *Biosens Bioelectron* 24:849–854
33. Taskan E, Özkaya B, Hasar H (2014) Effect of different mediator concentrations on power generation in MFC using Ti-TiO₂ electrode. *Int J Energy Sci* 4(1):9–11
34. Miroliaei MR, Samimi A, Mohebbi-Kalhari D, Khorram M (2014) Kinetics investigation of diversity cultures of *E. coli* and *Shewanella* sp., and their combined effect with mediator on MFC performance. *J Ind Eng Chem*. [Online] Available from: <https://www.sciencedirect.com/science/article/abs/pii/S1226086X14005000> [Accessed 6 Jan 2021].
35. Adebule AP, Aderiye BI, Adebayo AA (2018) Improving bioelectricity generation of microbial fuel cell (MFC) With mediators using kitchen waste as substrate. *Ann Appl Microbiol Biotechnol J*. [Online] Available from: https://www.researchgate.net/publication/337297373_Improving_Bioelectricity_Generation_of_Microbial_Fuel_Cell_MFC_With_Mediators_Using_Kitchen_Waste_as_Substrate. [Accessed 6 Jan 2021]
36. Arun GM (2015) Review on carbon electrodes in microbial fuel cell. *Int Res J Eng Technol (IRJET)* 2(8):424–427
37. Rahimnejad M, Adhami A, Darvari S, Zirepour A, Oh SE (2015) Microbial fuel cell as new technology for bioelectricity generation: A review. *Alexandria Eng J* 54:745–756
38. Zhang JN, Zhao QL, You SJ, Jiang JQ, Ren NQ (2008) Continuous electricity production from leachate in a novel upflow air-cathode membrane-free microbial fuel cell. *Water Sci Technol—WST*, 57(7):1017–1021
39. Cheng S, Lui H, Logan BE (2006) Increased performance of single-chamber microbial fuel cells using an improved cathode structure. *Electrochem Commun* 8:489–494
40. Kim JR, Cheng S, Oh S-E, Logan BE (2007) Power generation using different cation, anion, and ultrafiltration membranes in microbial fuel cells. *Environ Sci Technol* 41:1004–1009

41. Parkash A, Aziz S, Soomro SA (2005) Impact of salt concentrations on electricity generation using hostel sludge based dual chambered microbial fuel cell. *J Bioprocess Biotech* 5(8):1–6
42. Muralidharan A, Babu OKA, Nirmalraman K, Ramya M (2011) Impact of salt concentration on electricity production in microbial hydrogen based salt bridge fuel cells. *Indian Journal of Fundamental and Applied Life Sciences* 1(2):178–184
43. Jatoi AS, Mahar H, Aziz S, Siddiq M, Furqan, Malik AA, Hussain S, Kakar E (2016) To investigate the optimized conditions of salt bridge for bioelectricity generation from distillery waste water using microbial fuel cell. *NUST J Eng Sci* 9(2):29–34
44. Sevda S, Sreekrishnan TR (2012) Effect of salt concentration and mediators in salt bridge microbial fuel cell for electricity generation from synthetic wastewater. *J Environ Sci Health Part A* 47:878–886
45. Fan Y, Hu H, Liu H (2007) Enhanced coulombic efficiency, and power density of air-cathode microbial fuel cells with an improved cell configuration. *J Power Sources* 171:348–354
46. Zhang X, Cheng S, Wang X, Huang X, Logan BE (2009) Separator characteristics for increasing performance of microbial fuel cell. *Environ Sci Technol* 43(21):8456–8461
47. Ali AE, Gomaa OM, Fathey R, Kareem HA, Zaid MA (2015) Optimization of double chamber microbial fuel cell for domestic wastewater treatment and electricity production. *J Fuel Chem Technol* 43(9):1092–1099
48. Zhunag L, Zhou S, Li Y, Yuan Y (2010) Enhanced performance of air-cathode two-chamber microbial fuel cells with high-pH anode and low-pH cathode. *Bioresour Technol* 101:3514–3519
49. Wei L, Han H, Shen J (2013) Effects of temperature and ferrous sulfate concentrations on the performance of microbial fuel cell. *Int J Hydrogen Energy* 38:11110–11116
50. Zhang Y, Sun J, Hu Y, Wang Z, Li S (2014) Effects of periodically alternating temperatures on performance of single-chamber microbial fuel cells. *Int J Hydrogen Energy* 39:8048–8054

Optimization of MRR and KW of SS 304 in Wire EDM by RSM Technique



Shatarupa Biswas, Yogesh Singh, and Manidipto Mukherjee

Abstract Current study reports the experimental analysis of SS 304 and the effect of process parameters (such as pulse-on time, pulse-off time, arc on time, arc off time, wire feed and servo voltage) on the responses (such as material removal rate and surface roughness) in Wire EDM. L27 orthogonal array offers to minimize the experimental run number and to analyze the effects of significant process parameters on the performance characteristics, the RSM (Response Surface Methodology) technique is called for. ANOVA (Analysis of Variance) analysis is carried out to resolve the outcome of process parameters and to establish a correlation among the parameters. To evaluate the responses, the second-order quadratic mathematical model has been developed. The analysis exposes that servo voltage and pulse on time (higher terms) are the most important among the process parameters for finding the MRR (Material Removal Rate) and KW (Kerf Width), respectively.

Keywords SS 304 · Wire EDM · MRR · KW · RSM

1 Introduction

Current necessities of manufacturing sectors revolve solely upon focusing on the purity of the product, better surface finish and control over costs [1]. Wire EDM is a broadly used (such as aerospace industries, automotive industries, mold and dies industries) manufacturing process that is known for giving better surface finish having a burr free surface texture, and its ability to machine small parts makes it unique [2]. This process is used for cutting hard materials with compound profiles [3]. In Wire EDM, the material gets removed by virtue of continuous sparks that occur between wire and work piece. The gap between the wire and the work piece is

S. Biswas (✉) · M. Mukherjee
Department of Mechanical Engineering, National Institute of Technology, Silchar, India
e-mail: supriticu@gmail.com

Y. Singh
CAMM, CSIR-Central Mechanical Engineering Research Institute, Durgapur, India

© The Author(s), under exclusive license to Springer Nature Singapore Pte Ltd. 2023
T. S. Sudarshan et al. (eds.), *Recent Advancements in Mechanical Engineering*,
Lecture Notes in Mechanical Engineering,
https://doi.org/10.1007/978-981-19-3266-3_5

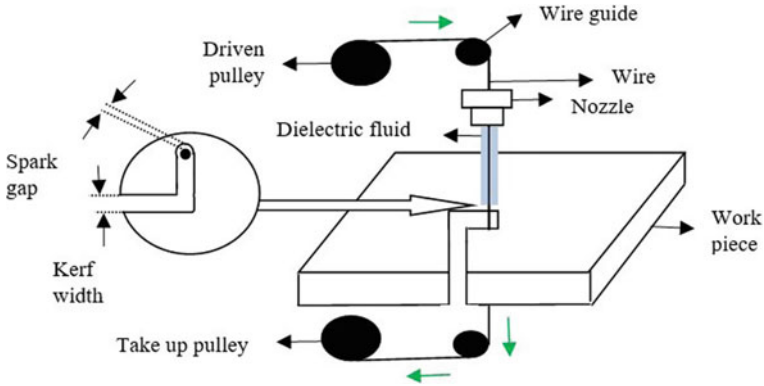


Fig. 1 Machining operation of wire EDM

submerged within the dielectric fluid. Generally, the gap range between the wire and work piece is 0.025 and 0.05 mm [1] which is kept by the CNC (Computer Numerical Control) locating system [4]. Generally, the wire is made from brass or copper. But now coated wire is broadly used, mainly zinc coated over the brass wire [5]. The machining operation of Wire EDM is shown in Fig. 1.

To develop a mathematical model and for determining the most efficient parameter among the process parameters, RSM is used [6]. Many authors previously used the RSM method [7], for developing a mathematical model to correlate the several process parameters of SS 304 in Wire EDM. Lingadurai et al. [8] observed that the gap voltage is the most effective process parameter for finding maximum MRR (0.0511 g/min) and for finding minimum SR (1.5 μm) and minimum KW (0.333 mm), wire feed and pulse on time are the important parameters. Bharathi et al. [9] found that servo voltage, pulse on time, pulse off time, and wire feed are the effective process parameters for finding maximum MRR (0.0511 g/min), minimum SR (1.5 μm) and KW (0.333 mm). Babu and Subbaratnam [10] invented that pulse on time, pulse off time, current and wire feed are the most important process parameters for finding maximum MRR (25.23 mm^3/min).

Therefore, this experimental study attempts to investigate the process parameters which mostly influence the response parameters of SS 304 machining by Wire EDM. To develop a quantitative mathematical model and to establish a relation between the parameters (process and responses) L_{27} orthogonal array and RSM is used. L_{27} orthogonal array is a technique which selects to achieve optimum progress parameters like high MRR and low KW with less number of experiments.

2 Experimental Work

The chemical composition of SS 304 is shown in Table 1 and the physical and mechanical properties of SS 304 is shown in Table 2. The work piece (SS 304) was machined on a WEDM (Model: JOEMARS WT 355, Taiwan) which is shown in Fig. 2a. The selected sample size is 50 mm × 50 mm × 5 mm for the overall experiment. Figure 2b shows the work piece and dialing of work piece. Table 3 shows the input variables with their experimental levels. These process parameters were selected through the trial experiment. Two input variables such as wire tension and water pressure were kept constant during the experiment. Deionized water was

Table 1 Chemical composition of SS 304(according to Lenntch)

Element	Cr	Ni	Mn	S	Si	N	C	P
Weight%	18.00	8.00	2.00	0.03	0.75	0.10	0.08	0.05

Table 2 Physical (according to AK Steel) and mechanical properties (according to JSL.) of SS 304

Physical properties			Mechanical properties			
Density	Modulus of elasticity	Melting point temp	Ultimate tensile strength	Yield strength	Poisson's ratio	Hardness Rockwell
8.00 g/cm ³	195 Gpa	1399–1454 °C	515 Mpa	205 Mpa	0.29	B92

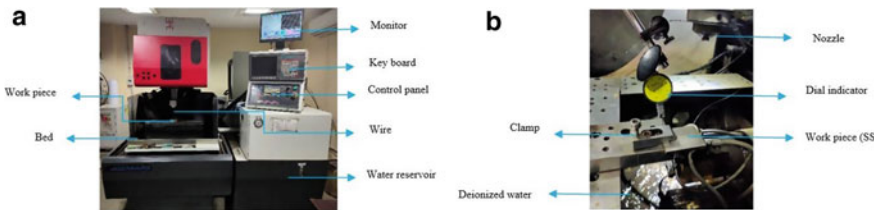


Fig. 2 a Joemars wire EDM. b Dialing of work piece (SS304)

Table 3 Experimental input variables with their levels

Sl. No	Input variable	Unit	Level 1	Level 2	Level 3
1	Pulse on time (T_{on})	μs	5	7	9
2	Pulse off time (T_{off})	μs	8	10	12
3	Arc on time (A_{on})	μs	6	8	10
4	Arc off time (A_{off})	μs	9	11	13
5	Wire feed (WF)	mm/sec	67	100	133
6	Servo voltage (SV)	v	40	50	60

used as a dielectric fluid. The brass wire (diameter is 0.25 mm) with zinc coated (Make: Maki BISI EDM, China) is used as a cutting tool in the experiment; KW and MRR are the main measured responses. KW was measured by using Profile Projector (Optomech, PP 600 V). Table 4 represents the design of L_{27} orthogonal array, which was designed using Minitab 19.

3 RSM Analysis

In the year of 1951 response surface methodology (RSM) was introduced by Box and Draper as an arithmetical technique to generate correlation models between responses and process parameters using the second degree polynomial equation. The following higher degree of polynomial equation is generally used in the RSM technique. This Eq. (1) is also used for the optimization of process variables.

$$Y = \beta_0 + \sum_{i=1}^k \beta_i X_i + \sum_{i=1}^k \beta_{ii} X_i^2 + \sum_{i,j=1}^k \beta_{ij} X_i X_j + \xi \quad (1)$$

where, Y is the response. X_i is the linear input factors, X_i^2 and $X_i X_j$ are the quadrilateral and associative terms. The second-order coefficients are β_0 , β_i , β_j and β_{ii} .

4 Result and Discussion

RSM is used to calculate the effect of distinct parameter and to establish their relations.

4.1 Modeling of MRR

The influence of process parameters (such as T_{on} , T_{off} , A_{on} , A_{off} , WF and SV) on MRR is observed using the surface plots as shown in Fig. 3. Figure 3a shows that MRR increases with increasing T_{on} and T_{off} . Further Fig. 3b shows that MRR increases with increasing A_{on} and A_{off} and vice versa. Similarly, Fig. 3c shows the effect of SV and WF on the response parameter where MRR increases with increasing SV and where MRR increases with decreasing WF. It is also understood that the correlations between variables and response is nonlinear, and thus, quadratic polynomial regression model is developed to understand the effect of parametric interactions on the response. The RSM is used to develop the following quadratic polynomial Eq. (2).

Table 4 Design of L₂₇ orthogonal array, experimental outcomes

Run No	T _{on} (μs)	T _{off} (μs)	A _{on} (μs)	A _{off} (μs)	WF (mm/sec)	SV (v)	MRR (mm ³ /min)	KW (mm)
1	5	8	6	9	67	40	4.414	0.318
2	5	8	6	9	100	50	2.859	0.299
3	5	8	6	9	133	60	2.228	0.312
4	5	10	8	11	67	40	3.986	0.291
5	5	10	8	11	100	50	3.395	0.308
6	5	10	8	11	133	60	2.570	0.309
7	5	12	10	13	67	40	4.052	0.307
8	5	12	10	13	100	50	3.512	0.311
9	5	12	10	13	133	60	2.716	0.313
10	7	8	8	13	67	50	5.015	0.319
11	7	8	8	13	100	60	4.396	0.363
12	7	8	8	13	137	40	6.134	0.359
13	7	10	10	9	67	50	5.524	0.364
14	7	10	10	9	100	60	4.506	0.359
15	7	10	10	9	133	40	5.188	0.368
16	7	12	6	11	67	50	3.581	0.341
17	7	12	6	11	100	60	2.796	0.353
18	7	12	6	11	133	40	4.574	0.342
19	9	8	10	11	67	60	5.946	0.346
20	9	8	10	11	100	40	6.886	0.359
21	9	8	10	11	133	50	5.799	0.319

(continued)

Table 4 (continued)

Run No	T_{on} (μ s)	T_{off} (μ s)	A_{on} (μ s)	A_{off} (μ s)	WF (mm/sec)	SV (v)	MRR (mm^3/min)	KW (mm)
22	9	10	6	13	67	60	4.203	0.357
23	9	10	6	13	100	40	6.899	0.356
24	9	10	6	13	133	50	5.057	0.332
25	9	12	8	9	67	60	4.829	0.340
26	9	12	8	9	100	40	7.816	0.387
27	9	12	8	9	133	50	6.791	0.353

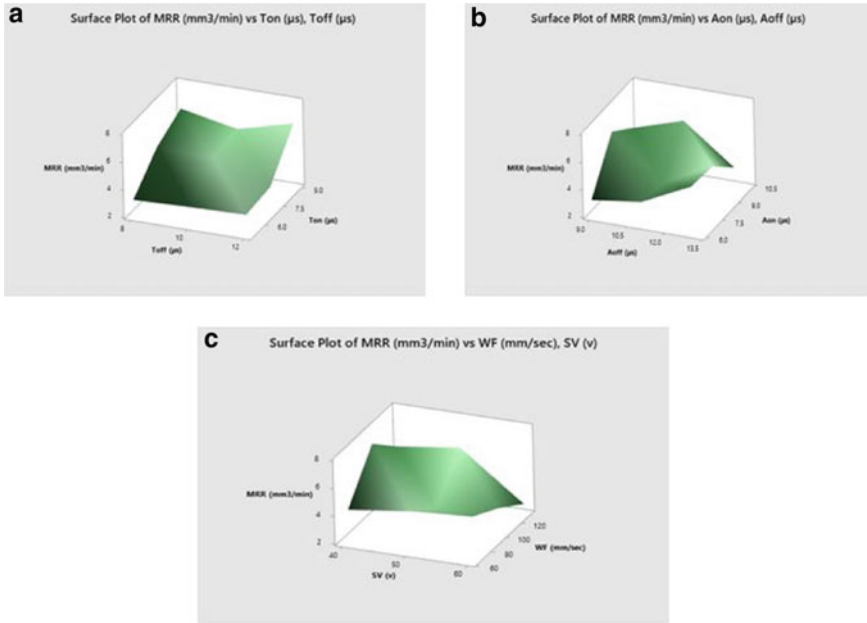


Fig. 3 a Exhibits the response surface of MRR. b Exhibits the response surface of MRR. for SS 304. c Exhibits the response surface of MRR for SS 304

$$\begin{aligned}
 \text{MRR} = & 13.8 + 1.103T_{\text{on}} - 0.58T_{\text{off}} + 1.748A_{\text{on}} \\
 & - 0.177SV - 0.1267 \times A_{\text{on}}^2 + 0.0982 \times A_{\text{off}}^2 \\
 & - 0.0144 \times T_{\text{on}} \times SV + 0.0127 \times A_{\text{on}} \times SV
 \end{aligned} \tag{2}$$

An ANOVA is performed for the developed Eq. (2), and the results of analysis are shown in Table 5. The significance of the model was determined from high *F*-value of 15.44 and low *P*-value of 0.001. The *R*² and *R*² (adj.) values of the predictive model for MRR is 97.67%, and 91.34%, respectively, which also determined the significance of the developed model with higher predictive accuracy of more than 95%. The analysis also showed that two linear terms (*A*_{off} and *WF*), four higher order terms (*T*_{on}², *T*_{off}², *WF*² and *SV*²) and five interaction terms (*T*_{on} × *WF*, *T*_{off} × *WF*, *T*_{off} × *SV*, *A*_{on} × *WF* and *A*_{off} × *WF*) in the model does not have significant impact on the response parameter and thus these terms are neglected in the development of Eq. (2). The Pareto chart with an error coefficient of 0.05 showed standard factor of 2.365 with respect to the model terms (Fig. 4a). The normal probability and residual fit plots indicated a normal distribution of the misfit data across a straight line (Fig. 4b and c).

Table 5 ANOVA table for MRR

Source	DF	Adj SS	Adj MS	F-value	P-value	Significance
Model	19	55.6602	2.92948	15.44	0.001	
Linear	6	8.5321	1.42201	7.49	0.009	
T_{on}	1	0.5328	0.53276	2.81	0.138	
T_{off}	1	0.1943	0.19431	1.02	0.345	
A_{on}	1	0.4017	0.40172	2.12	0.189	
A_{off}	1	0.0075	0.00746	0.04	0.848	Not significant
WF	1	0.0019	0.00186	0.01	0.924	Not significant
SV	1	5.9235	5.92352	31.22	0.001	
Square	6	2.6158	0.43596	2.30	0.150	
$T_{on} \times T_{on}$	1	0.0052	0.00522	0.03	0.873	Not significant
$T_{off} \times T_{off}$	1	0.0527	0.05265	0.28	0.615	Not significant
$A_{on} \times A_{on}$	1	1.5419	1.54194	8.13	0.025	
$A_{off} \times A_{off}$	1	0.9265	0.92655	4.88	0.063	
WF \times WF	1	0.0119	0.01193	0.06	0.809	Not significant
SV \times SV	1	0.0689	0.06891	0.36	0.566	Not significant
2-Way Interaction	7	1.8352	0.26217	1.38	0.340	
$T_{on} \times WF$	1	0.0742	0.07419	0.39	0.552	Not significant
$T_{on} \times SV$	1	0.3738	0.37379	1.97	0.203	
$T_{off} \times WF$	1	0.0864	0.08644	0.46	0.521	Not significant
$T_{off} \times SV$	1	0.0142	0.01419	0.07	0.792	Not significant
$A_{on} \times WF$	1	0.0655	0.06549	0.35	0.575	Not significant
$A_{on} \times SV$	1	0.2882	0.28818	1.52	0.258	
$A_{off} \times WF$	1	0.0000	0.00001	0.00	0.995	Not significant
Error	7	1.3282	0.18975			
Total	26	56.9884				

4.2 Modeling of KW

The influence of process parameters (such as T_{on} , T_{off} , A_{on} , A_{off} , WF and SV) on KW is observed using the surface plots as shown in Fig. 5. Figure 5a shows that KW decreases with decreasing T_{on} and T_{off} has negligible impact on the response. Further Fig. 5b shows that KW decreases with decreasing A_{on} and A_{off} . Similarly, Fig. 5c shows the effect of SV and WF on the response parameter where KW increases with increasing SV and increasing WF then decreasing. It is also understood that the correlations between variables and response is nonlinear, and thus, quadratic polynomial regression model is developed to understand the effect of parametric interactions on the response. The RSM is used to develop the following quadratic polynomial Eq. (3).

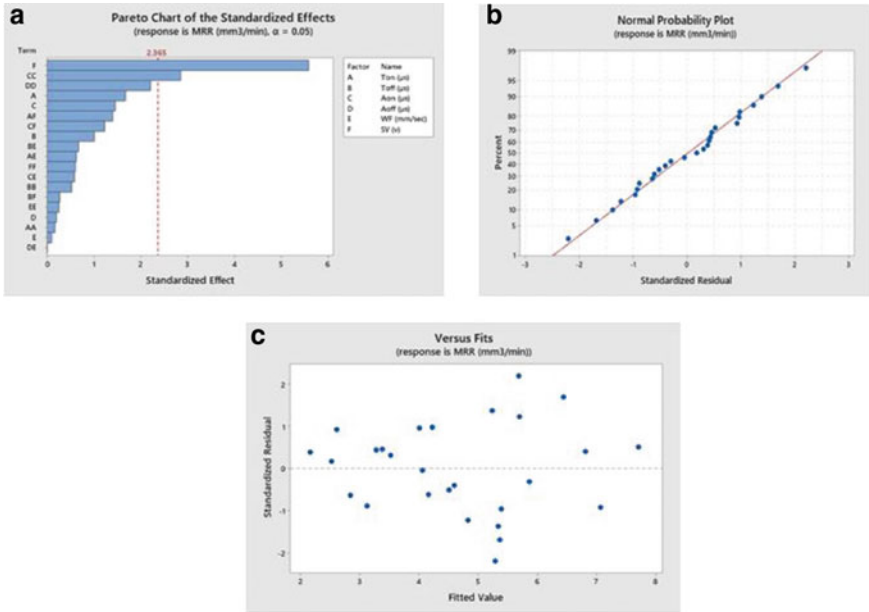


Fig. 4 a Pareto chart for MRR. b Normal Probability Plot for MRR. c Residual Plot for MRR

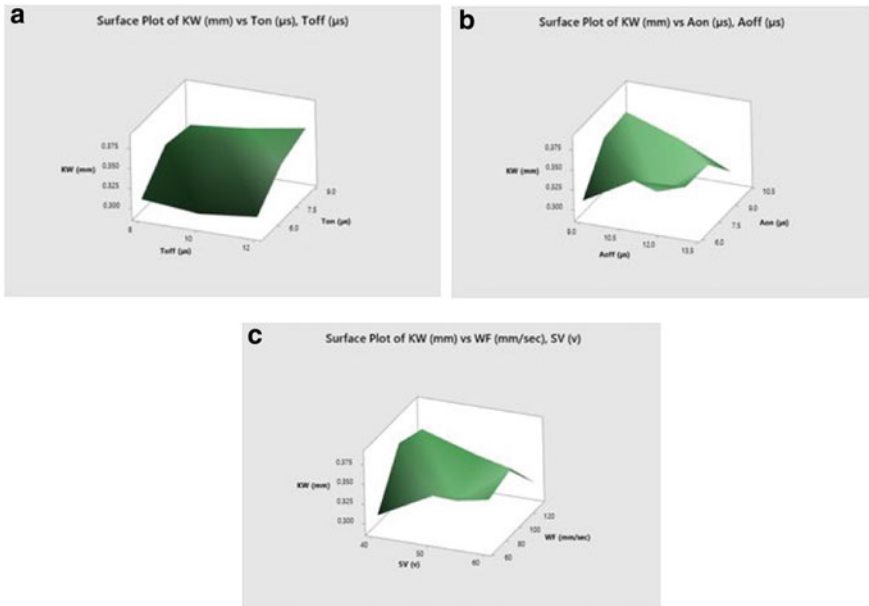


Fig. 5 a Exhibits the response surface of KW for SS 304. b Exhibits the response surface. c Exhibits the response surface graph of KW for SS 304

$$\begin{aligned}
 KW = & 0.261 + 0.1066 \times T_{on} + 0.0289 \times T_{off} \\
 & + 0.0184 \times A_{on} - 0.0745 \times A_{off} - 0.00133 \times WF \\
 & - 0.00224 \times SV - 0.00582 \times T_{on}^2 + 0.00254 \times A_{off}^2 \\
 & - 0.000009 \times WF^2 + 0.000119 \times SV^2 + 0.000095 \times T_{off} \\
 & \times WF - 0.000471 \times T_{off} \times SV + 0.000091 \times A_{on} \times WF \\
 & - 0.000515 \times A_{on} \times SV + 0.000164 \times A_{off} \times WF \tag{3}
 \end{aligned}$$

An ANOVA is performed for the developed Eq. (3), and the results of analysis are shown in Table 6. The significance of the model was determined from low *P*-value of 0.025. The *R*² and *R*² (adj.) values of the predictive model for KW is 92.42%, and 71.83%, respectively, which also determined the significance of the developed model

Table 6 ANOVA table for KW

Source	DF	Adj SS	Adj MS	F-Value	P-Value	Significance
Model	19	0.015396	0.000810	4.49	0.025	
Linear	6	0.001402	0.000234	1.29	0.368	
<i>T</i> _{on}	1	0.000566	0.000566	3.13	0.120	
<i>T</i> _{off}	1	0.000189	0.000189	1.05	0.340	
<i>A</i> _{on}	1	0.000196	0.000196	1.08	0.332	
<i>A</i> _{off}	1	0.000598	0.000598	3.31	0.111	
WF	1	0.000359	0.000359	1.99	0.201	
SV	1	0.000141	0.000141	0.78	0.407	
Square	6	0.005093	0.000849	4.70	0.031	
<i>T</i> _{on} × <i>T</i> _{on}	1	0.003249	0.003249	18.00	0.004	
<i>T</i> _{off} × <i>T</i> _{off}	1	0.000043	0.000043	0.24	0.639	Not significant
<i>A</i> _{on} × <i>A</i> _{on}	1	0.000000	0.000000	0.00	0.970	Not significant
<i>A</i> _{off} × <i>A</i> _{off}	1	0.000618	0.000618	3.42	0.107	
WF × WF	1	0.000403	0.000403	2.23	0.179	
SV × SV	1	0.000635	0.000635	3.52	0.103	
2-Way Interaction	7	0.000882	0.000126	0.70	0.676	
<i>T</i> _{on} × WF	1	0.000071	0.000071	0.40	0.550	Not significant
<i>T</i> _{on} × SV	1	0.000053	0.000053	0.30	0.603	Not significant
<i>T</i> _{off} × WF	1	0.000283	0.000283	1.57	0.250	
<i>T</i> _{off} × SV	1	0.000400	0.000400	2.21	0.180	
<i>A</i> _{on} × WF	1	0.000262	0.000262	1.45	0.267	
<i>A</i> _{on} × SV	1	0.000477	0.000477	2.64	0.148	
<i>A</i> _{off} × WF	1	0.000466	0.000466	2.58	0.152	
Error	7	0.001264	0.000181			
Total	26	0.016659				

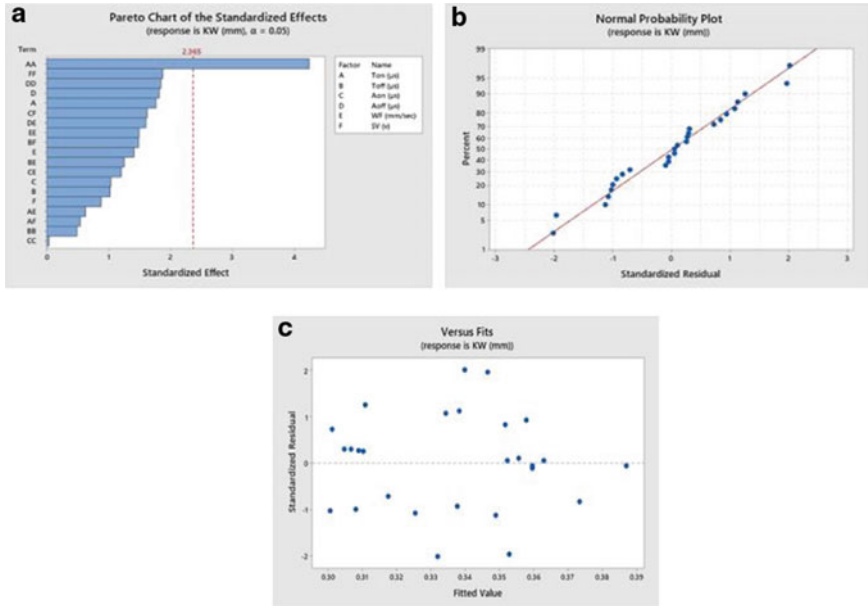


Fig. 6 a Pareto chart for KW b Normal probability plot for KW. c Residual plot for KW

with higher predictive accuracy of more than 90%. The analysis also showed that two higher order terms (T_{off}^2 and A_{off}^2) and two interaction term ($T_{on} \times WF$ and $T_{on} \times SV$) in the model does not have significant impact on the response parameter and thus these terms are neglected in the development of Eq. (2). The Pareto chart with an error coefficient of 0.05 showed standart factor of 2.365 with respect to the model terms (Fig. 6a). The normal probability and residual fit plots indicated a normal distribution of the misfit data across a straight line (Fig. 6a and b).

5 Conclusions

In this experiment of SS 304, the effects of process parameters on MRR and SR were examined. The following assumptions were made-

- The MRR increases with increasing T_{on} and T_{off} has negligible impact on the response.
- The MRR increases with increasing A_{on} and A_{off} . Similarly, MRR increases with increasing SV and decreasing WF.
- The KW decreases with decreasing T_{on} and T_{off} . Similarly, KW decreases with decreasing A_{on} and A_{off} .
- Similarly, the effect of SV and WF on the response parameter where KW decreases with decreasing SV and WF.

- The quadratic polynomial regression models are generated using RSM for MRR and KW. The models are tested using ANOVA and they are able to predict the responses with more than 95% and 90% accuracy, respectively.

References

1. Chaudhary T, Siddiquee AN, Chanda AK (2019) Effect of wire tension on different output responses during wire electric discharge machining on AISI 304 stainless steel. *Defence Technol* 15:541–544
2. Geetha M, Sreenivasulu B, Gowd GH (2013) Modeling & analysis of performance characteristics of Wire EDM of SS304. *Int J Innov Technol Explor Eng* 3:122–125
3. Bharathi P, Gouri T, Priyanka L, Rao GS, Rao BN (2016) Optimum WEDM process parameters of SS304 using taguchi method. *Int J Ind Manuf Syst Eng* 1:69–72
4. Garg RK, Singh KK, Sachdeva A, Sharma VS, Ojha K, Singh S (2010) Review of research work in sinking EDM and WEDM on metal matrix composite materials. *Int J Adv Manuf Technol* 50:611–624
5. Thomas D, Kumar R, Singh GK, Sinha P, Mishra S (2015) Modelling of process parameters in coated wire electric discharge machining through response surface methodology. *Mater Today Proceedings* 2:1642–1648
6. Thomas D, Kumar R, Singh GK, Sinha P, Mishra S (2015) Modelling of surface roughness in coated wire electric discharge machining through response surface methodology. *Mater Today Proc* 2:3520–3526
7. Kapoor J, Singh S, Khamba JS (2010) Recent developments in wire electrodes for high performance WEDM. *Proc World Congr Eng* 2
8. Lingadurai K, Nagasivamuni B, Muthu Kamatchi M, Palavesam J (2012) Selection of wire electrical discharge machining process parameters on stainless steel AISI grade-304 using design of experiments approach. *J Inst Eng Ser C* 93:163–170
9. Bharathi P, Gouri T, Priyanka L, Rao GS, Rao BN (2016) Optimum WEDM process parameters of SS304 using Taguchi method. *Int J Ind Manuf Syst Eng* 1:69–72
10. Babu TV, Subbaratnam B (2018) Experimental investigation of wire electrical discharge machining (WEDM) process parameters on SS304 using Taguchi method. *Int J Curr Eng Technol* 8:1–3

Numerical Study on Effects of Geometrical and Operating Parameters of Bolt on Performance of Bolted Joint



Sandeep D. Borawake and Sachin S. Naik

Abstract Bolted joint are extensively used in the assembly of the machine or structure. Bolted joints can become loose due to loss of preload in the bolt when subjected to vibrations of structure or machine. This vibrational loosening sometimes can cause serious problems leading to fatal failure of bolted structure, if remain undetected. In this study, a numerical investigation on loosening of bolted joint when subjected to dynamic transverse load is carried out for various values and combinations of parameters. Finite element simulation of bolted joints is carried out for ten loading cycles to investigate various causes of loosening of the joint. Preload of specific magnitude is applied using bolt pretension tool available in ANSYS software. Contact of a specific type at different locations in the bolted joints is specified as per their functional requirements while carrying out the FEA. Reduction in the preload and nut turning angle are closely observed for each cycle.

Keywords Bolted joint · Bolt preload · Dynamic load · FEA · Loosening of bolt

1 Introduction

Bolted joint is used in the assembly because they provide clamping force to machine parts during assembly and can be easily loosened for maintenance purpose. However, if such a loosening occurs due to machine operating conditions, it can cause failure of assembly. Various anti-loosening mechanisms are available in the market [1]; however, loosening in bolted joints cannot be eliminated fully. So, it is essential to study the various root causes of loosening in the bolted joint to maintain its effectiveness.

S. D. Borawake · S. S. Naik (✉)

Department of Mechanical Engineering, Veermata Jijabai Technological Institute, Mumbai, India
e-mail: ssnaik@me.vjti.ac.in

2 Literature Survey

When no relative movement occurs between the internal and external threads but preload loss occurs, it is non-rotational loosening. Various causes of non-rotational loosening are embedding loss, differential thermal expansion, localized plastic deformation, thermal creep and creep from surface coating etc. On the other hand, rotational loosening occurs when the fastener rotates under the action of external loading [2]. Liu et al. [3] investigated experimentally the loosening behavior of bolted joint under the action of dynamic axial load. They found that the preload is decreasing due to plastic deformation at initial stage of an experiment and in the later stage of the test due to fretting wear and delamination between the thread. Junker [4] experimentally investigated the loosening behavior of bolted joint subjected to dynamic axial and transverse load, it was found that dynamic transverse loads generate a far more severe condition for self-loosening than dynamic axial loads because radial movement under axial loading is significantly smaller than that which is sustained under transverse loading. Pai and Hess [5, 6] found that the loosening in the bolted joint will occur even when transverse load acting at the bolt is not sufficient to cause complete slip at bolt head contact. They studied four different loosening processes based on the status of the contact at bolt head and thread by finite element analysis and found that the loosening is also affected by localised slip at contacts. Dinger et al. [7] numerically studied the effect of different methods of preload generation on the development of residual torque. Also, they studied the performance of bolted joint subjected to dynamic transverse load based on local and global key figures which are based on the status of the contact. Zadoks and Yu [8] studied the loosening in bolted joint by considering analytical model having two degrees of freedom. They formulated a loosening estimation by considering contact stiffness using Hertz contact stress theory. It was found that the transverse impact is essential for initiation of self-loosening of bolted joint. Izumi et al. [9] numerically studied the relationship between applied torque and preload. They found that the load distribution in threads is not uniform. First thread in contact will take maximum load whereas the last thread in contact will take very less load. Also they found that the loosening will be initiated when complete slip at threaded contact will occur prior to bolt head slip. Gong et al. [10] constructed FE model of bolted joint with and without helix angle to study loosening in bolted joint under transverse vibration. They found that initially the loosening will also occur due to some plastic deformation at threaded contact. Sanclemente et al. [11] studied experimentally the effect of basic parameters such as preload, material, lubrication, size, pitch and fit on loosening of bolted joint. They found out the optimum condition to avoid self-loosening of the fastener which have high preload, low modulus of elasticity, large diameter, lubrication, tight fit and fine threads. Chetham et al. [1] experimentally studied the effect of secondary locking feature and adhesive locking on loosening of bolted joint. They found that the adhesive locking shows a good loosening resistance as compared to secondary locking feature and standard bolt. Even though secondary locking features show good resistant to loosening, the loosening still occurred in bolted joint with varying degree.

This paper presents, finite element simulations of a bolted joint carried out in order to understand the performance of a bolted joint under the influence of various geometric and material parameters when subjected to transverse cyclic load.

3 Finite Element Analysis

The finite element analysis is carried out to investigate loosening behavior of bolted joint subjected to dynamic transverse load. Due to presence of the contact, it requires non-linear solution. The FE analysis is carried out for various values of pitch of thread, preload applied to bolt and various combinations of the coefficient of friction to investigate loosening behavior of bolted joint during ten loading cycles.

3.1 Step by Step Procedure to Carryout FEA

The bolted joint is modelled according to the DIN standard. A standard bolt of size M10 is considered in this study. The hex flange bolt is modelled according to DIN 6921 having material grade 10.9 and pitch (P) 1.5 mm. The equivalent grade nut (Grade 10) is also modelled. The clamp length of the joint is 30 mm. The Young's modulus and Poison's ratio is taken as 205 GPa and 0.3, respectively. The helical thread is modelled according to ISO 965.

The Junker vibration test setup [4] is considered while modelling a bolted joint. A small region of a clamped plate having hole of 12 mm diameter around the bolt is modeled. The base plate is fixed and it does not take any part in loosening of the bolted joint. Therefore, there is no need to model it for the FEA. Fig. 1 shows the solid model of the bolted joint created in PTC CREO-3.0. *Bottom up* assembly technique is used for generating the bolted joint assembly. The assembly is imported in *ANSYS Workbench 19* using *IGES* file exchange format. The material properties for the bolt, nut and clamped plate are defined in *Engineering Data* page available in *Project Management* window of the *ANSYS* software.

Fig. 1 Simplified CAD model of bolted joint

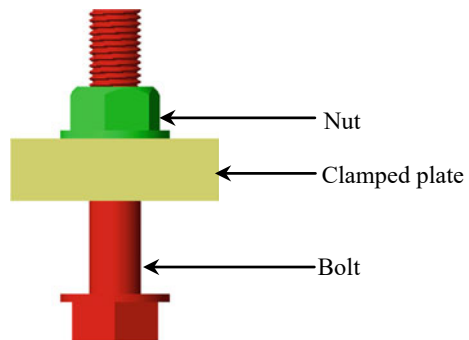
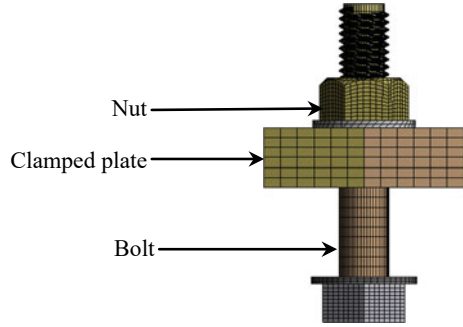


Fig. 2 FE model of joint

In order to control the mesh, the geometry is simplified to have hexahedral meshing as shown in Fig. 2. Due to the presence of thread geometry it is difficult to make hexahedral mesh on bolt and nut. So, it is necessary to model bolt shank and bolt thread separately. Entire solid model is meshed with linear hexahedral element *SOLID185* with 8 nodes and linear tetrahedral element *SOLID285* with 4 nodes. The frictional contact is defined at threaded contact (μ_T) and nut bearing contact (μ_N) with coefficient of friction 0.2 and 0.15, respectively. The normal stiffness factor is set to one for better convergence and avoids penetration of contact bodies in the target body. Bonded contacts are defined between bolt thread and bolt shank, nut and nut thread. The total assembly is meshed with 31,795 elements having 43,582 nodes.

In the finite element analysis, effect of inertia of masses and self-weight is neglected. The loading condition for dynamic analysis is shown in Fig. 3. To carry out finite element analysis, the bolt head is fixed. The clamped plate is subjected to ten displacement loading cycles of amplitude 1 mm from its mean position with frequency of 0.5 Hz. The transverse displacement applied in the direction perpendicular to the bolt axis (*X*-direction) as shown in Fig. 3. Thus the modelled joint is given transverse displacement to simulate a frequently encountered dynamic condition. The clamped plate is constrained to move only in *X*-direction. The bolt preload (F_P) of specific magnitude is applied to bolt shank using *bolt pretension tool* available within the *ANSYS* software which uses the element *PRETS 179*.

Above FE model is solved by iterative solver in order to post-process the result.

(a) **Thread surface reaction moment**

The thread surface reaction moment in axial direction on nut is the root cause of loosening in bolted joint. The thread surface reaction moment along the axis of nut is acting in loosening direction. Initially, this reaction moment at thread, due to applied preload, is in equilibrium with the frictional torque offered by the contact surfaces. When transverse load is applied on the clamped plate, the transverse force is also acting at the thread contact which will affect the magnitude and direction of contact forces along the normal and along the tangential direction of helix. When resultant tangential force exceeds the frictional force, slip will occur at the contact. Due to helical nature of the thread, contact force distribution along the helix of thread is not uniform. Hence, the slip may occur at certain locations of the contact, called as

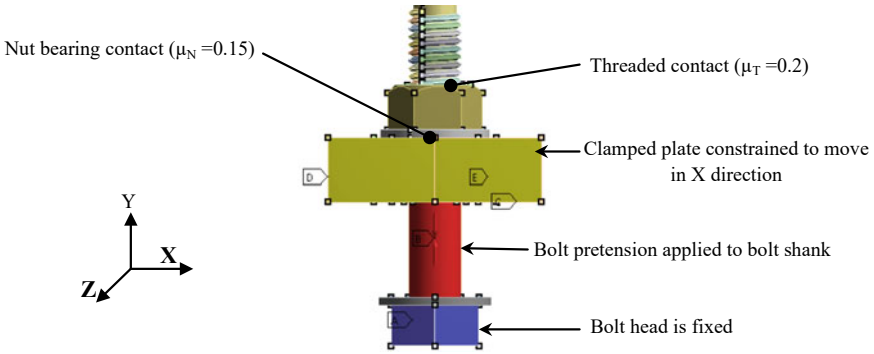


Fig. 3 Loading conditions to simulate loosening in bolted joints

localized slip. When transverse force acting at the contact is enough to overcome frictional force, complete slip at the contact will occur. When complete slip at the threaded contact and nut bearing contact occur, the nut will turn suddenly because of the thread surface reaction moment acting in loosening direction. Variation in Thread surface reaction moment with time for the 10 simulated cycles is shown in Fig. 4.

(b) **Transverse force vs transverse displacement characteristic curve**

The transverse force on clamped plate with respect to its displacement during the ten loading cycles is shown in Fig. 5a. When clamped plate is moving from mean position to right, the bolt offers resistance to its movement because of friction present between

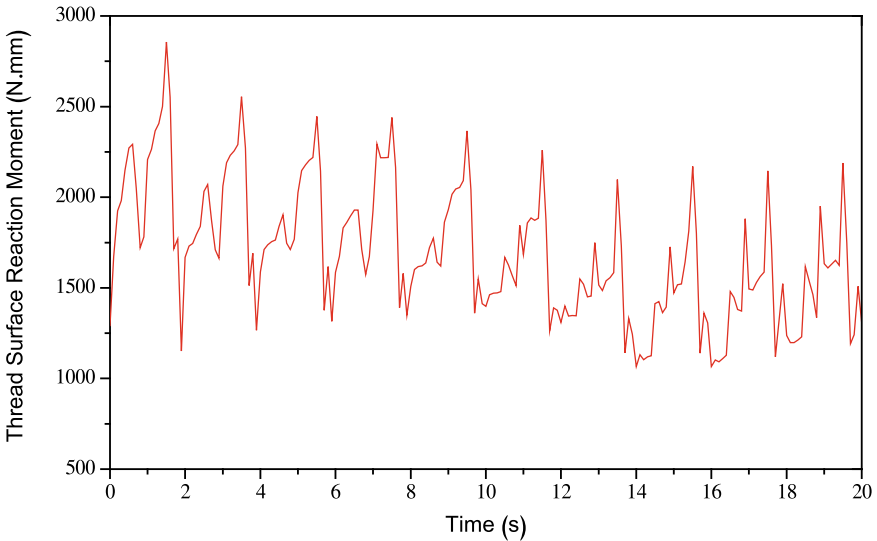


Fig. 4 Thread surface reaction moment in axial direction during ten loading cycles

clamped plate and nut, so the bolt bends elastically in the direction of movement of clamped plate. The Transverse force vs transverse displacement of bolt is shown in Fig. 5b. When the bending resistance of bolt exceeds frictional resistance, complete slip between clamped plate and nut bearing contact will occur (corresponding to position b) till clamped plate reaches to its extreme position (position c), it will occur because of radial clearance between bolt and clamped plate. The bolt tries to attain its mean position as clamped plate changes the direction of movement (from point c) as shown in Fig. 5b. Further clamped plate continues its movement towards left extreme, the bolt bends elastically until the bending resistance does not exceed the limiting frictional resistance between nut and clamped plate (from point d to e). When bending resistance exceeds the limiting frictional resistance, complete slip at the contact between clamped plate and nut will occur (from point e to f). Then, the direction of movement of the clamped plate reverses to begin the remaining half cycle. Since complete slip is occurring at the contacts during a cycle, nut is subjected to rotation in the loosening direction which will reduce the preload in the bolt. Hence, preload will decrease in each and every cycle. The transverse force acting on the bolt is directly proportional to the preload in the bolt, hence the transverse force acting on the bolt also decreases in each cycle as shown in Fig. 5.

(c) Preload decay curve and nut turning angle

Variation in preload during the loading cycles is shown in Fig. 6. It is observed that there is continued decrease in the preload with the cyclic transverse displacement applied to the plate. The increase in the preload is observed due to bending of the bolt during a cycle. Variation in nut turn angle, measured at nut bearing contact, is shown in Fig. 7. Sudden increase in the nut turn angle, as seen in the figure, is due to complete slip occurring between thread and nut bearing contacts.

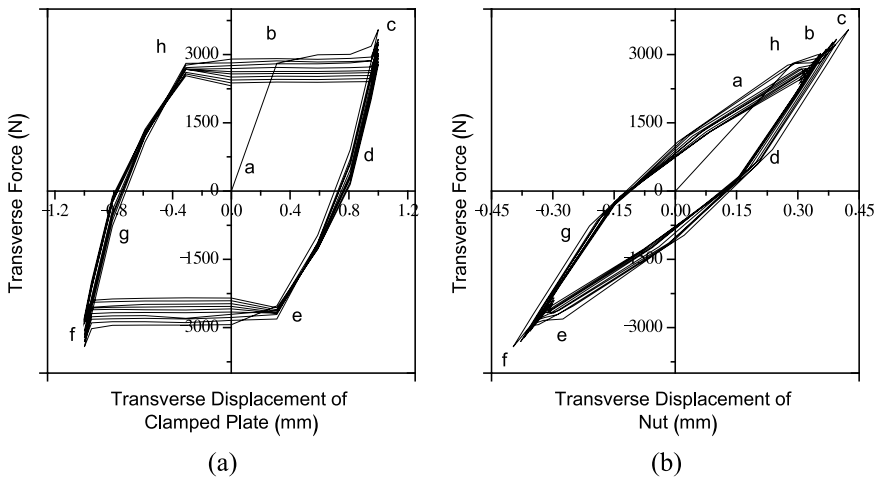


Fig. 5 Transverse force vs transverse displacement characteristic curve during ten loading cycles

Fig. 6 Preload decay curve during ten loading cycles

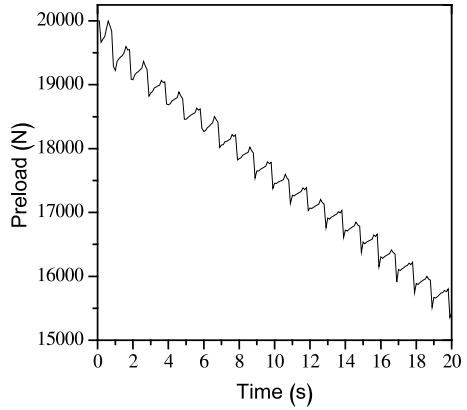
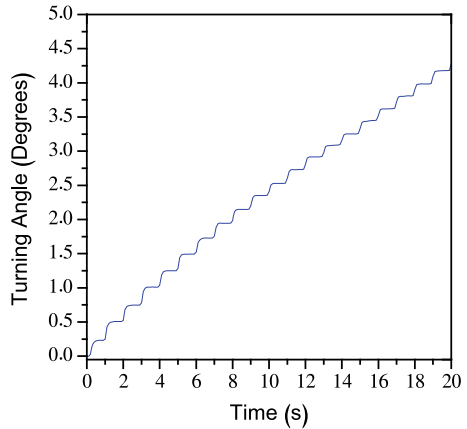


Fig. 7 Nut turn angle during ten loading cycles



4 Result and Discussion

Finite element analysis is carried out by changing some of the operating, and geometrical parameters, and for different values of preload, pitch of thread and coefficient of friction at threaded contact and nut bearing contact. The preload from 5 to 25 kN in the step of 5 kN is used for the simulations. Pitch of the thread considered is 1 mm (fine pitch), 1.25 mm (medium pitch) and 1.5 mm (course). Further, coefficient of friction values ranging from 0 to 0.2 are taken for threaded contact and from 0 to 0.15 for nut bearing contact.

(a) Effect of applied preload

Finite element analyses are carried out to investigate the effect of transverse displacement on applied preload and loosening of bolted joint. The thread surface reaction moment in axial direction will be more when applied preload is more. It will affect the loosening of bolted joint when subjected to dynamic transverse load. The preload

decay curve during ten loading cycles is shown in Fig. 8. The loss of preload per cycle is more when applied preload is more and it goes on decreasing as preload decreases. Variation in the preload during loading cycle is observed to be more when applied preload is higher because of larger value of thread surface reaction moment associated with higher preload. The decrease in preload is smaller for smaller applied preload. Increase in the nut turn angle is shown in Fig. 9. The nut turn angle goes on increasing as number of loading cycles goes on increasing. For higher preload, it is observed that the nut turn angle is larger. As preload decreases, the nut turn angle also decreases.

(b) **Effect of pitch**

Pitch values of 1 mm (fine), 1.25 mm (medium) and 1.5 mm (course) are considered for this study. When preload is applied on the bolted joint, helix angle will affect

Fig. 8 Preload decay curve during ten loading cycles at different values of applied preload ($P = 1.5$ mm, $\mu_T = 0.2$, $\mu_N = 0.15$)

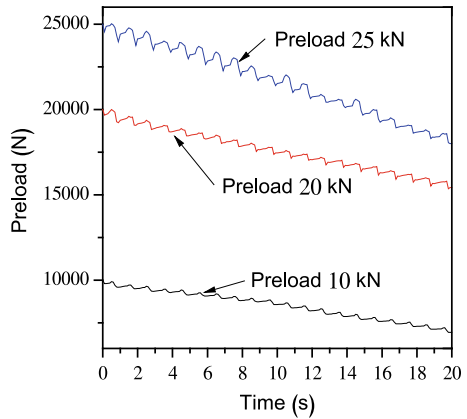
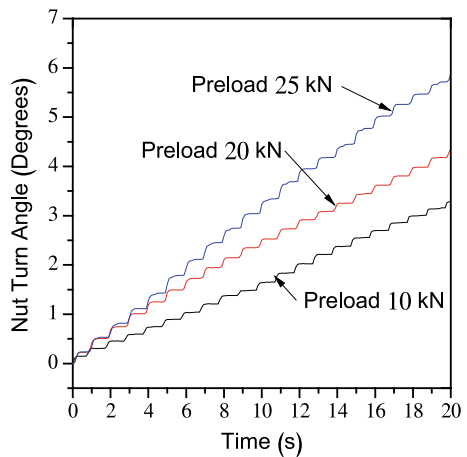


Fig. 9 Nut turn angle during ten loading cycles at different values of applied preload ($P = 1.5$ mm, $\mu_T = 0.2$, $\mu_N = 0.15$)



the normal and tangential force distribution along the helix of the threads which in turn will affect the reaction moment in axial direction at the nut thread. Thread surface reaction moment at the nut thread is more when course pitch is used. In the similar manner, for fine pitch, the thread surface reaction moment is lower at the nut thread. Variation in the thread surface reaction moment with time is shown in Fig. 10. The thread surface reaction moment at nut thread decreases as the preload goes on decreasing. The rate of loss of moment is more for course pitch thread and less for fine pitch thread.

Figure 11 shows the preload decay curve for various values of pitch during the loading. It is observed that the loss of preload is affected considerably by the pitch. The loss of preload per cycle is more for course pitch and less of finer values of pitch. It is observed that (refer Fig. 12) the residual preload at the end of the loading cycles is more for fine pitch thread and less for course pitch thread. Nut turn angle for various values of pitch is shown in Fig. 13. Threaded joints with coarse pitch fasteners show more tendency to loosen due to higher helix angle as compared to the threaded joints with medium and fine pitch as shown in Fig. 14.

(c) Effect of coefficient of friction

Effect of coefficient of friction, at threaded contact and nut bearing contact, on loosening of bolted joint subjected to dynamic transverse load for the preload of 20 kN and pitch of thread of 1.5 mm is studied. Simulations are carried out with different values of coefficient of friction at threaded contact (μ_T) and nut bearing contact (μ_N).

Resistance offered by the nut bearing contact for movement of the plate is small when coefficient of friction at nut bearing contact $\mu_N = 0.005$ (for $\mu_T = 0.2$). It

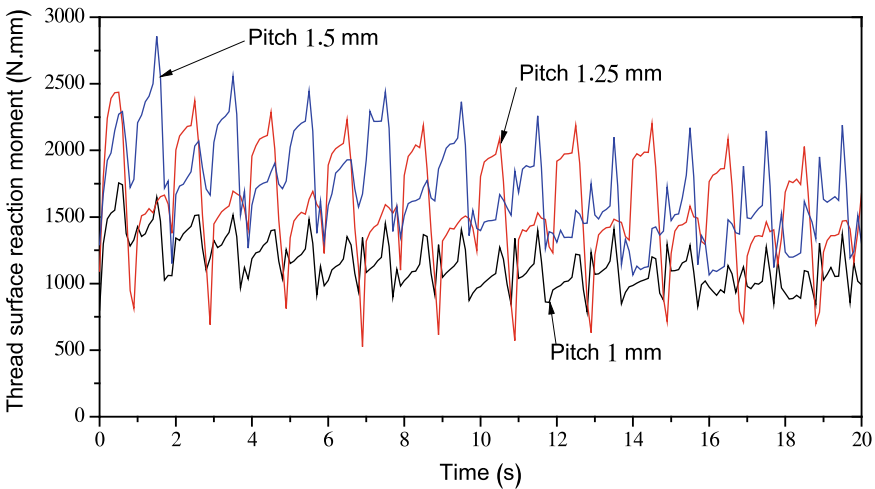


Fig. 10 Thread surface reaction moment in axil direction during ten loading cycles for different values of pitch ($F_P = 20$ kN, $\mu_T = 0.2$, $\mu_N = 0.15$)

Fig. 11 Preload decay curve during ten loading cycles at different values of pitch ($F_P = 20$ kN, $\mu_T = 0.2$, $\mu_N = 0.15$)

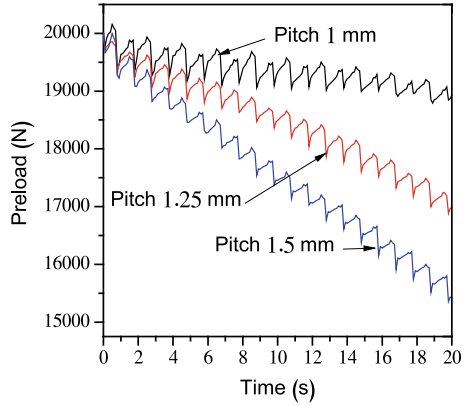


Fig. 12 Residual preload at the end of ten loading cycles for different values of applied preload for different values of pitch ($\mu_T = 0.2$, $\mu_N = 0.15$)

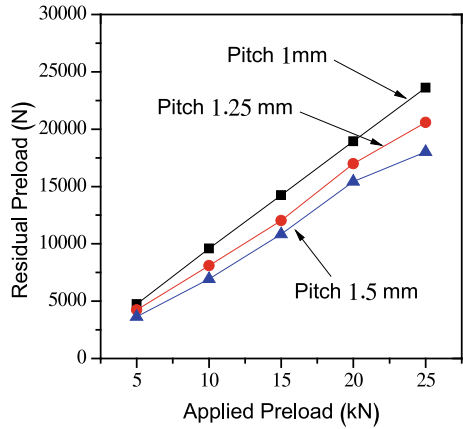


Fig. 13 Nut turn angle at the end of ten loading cycles for different values of pitch ($F_P = 20$ kN, $\mu_T = 0.2$, $\mu_N = 0.15$)

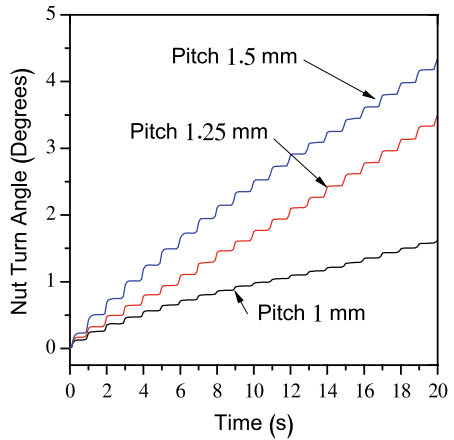
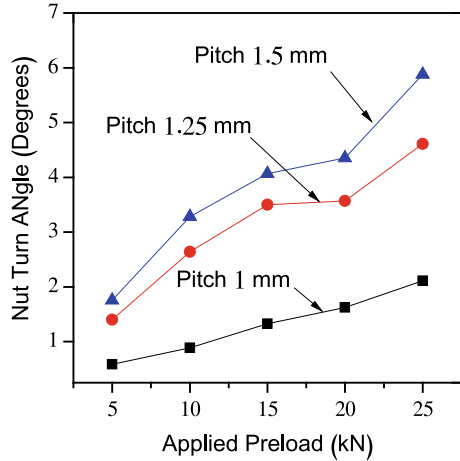


Fig. 14 Nut turn angle at the end of ten loading cycles for different values of applied preload for different values of pitch ($\mu_T = 0.2, \mu_N = 0.15$)



causes the clamped plate to move from mean position to its extreme position thereby applying negligibly small transverse force on nut which is not enough to cause slip at the threaded contact. The thread surface reaction moment is in equilibrium with the frictional torque offered by the threaded contact, hence the slip at the threaded contacts will not be observed. Hence, loss observed of the preload and increase in the nut turn angle at the end of the loading cycles is very small. It is observed that the loss of preload is more when coefficient of friction at the nut bearing contact (μ_N) is more, as shown in Fig. 15a. As expected, it causes the nut turn angle to be more in this situation as shown in Fig. 15b.

When coefficient of friction at threaded contact is $\mu_T = 0.005$ (for $\mu_N = 0.15$), the thread surface reaction moment is not in equilibrium with the frictional torque

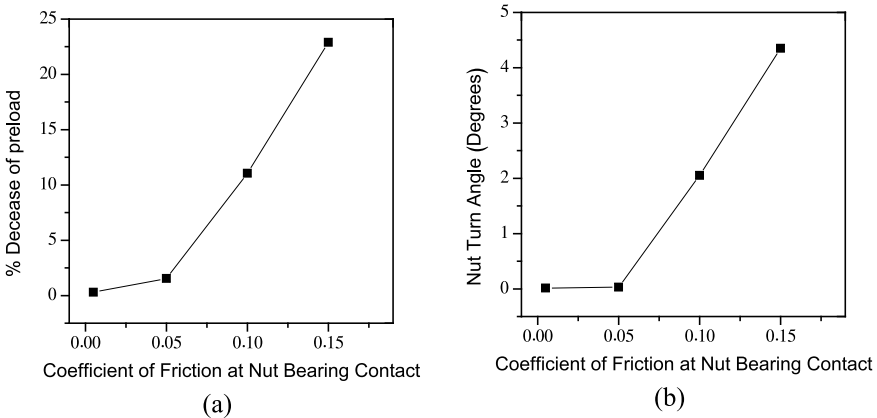


Fig. 15 % decrease of preload and nut turn angle for different values of coefficient of friction at nut bearing contact (μ_N) at the end of ten loading cycles ($F_P = 20$ kN, $P = 1.5$ mm, $\mu_T = 0.2$)

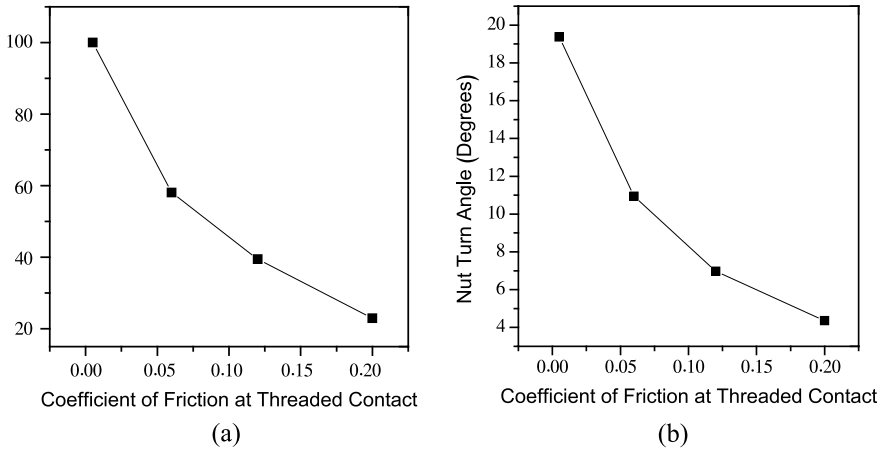


Fig. 16 % decrease of preload and nut turn angle, for different values of coefficient of friction at threaded contact (μ_T), at the end of ten loading cycles ($F_p = 20$ kN, $P = 1.5$ mm, $\mu_N = 0.15$)

offered by the threaded contact, and hence the threaded contact is always tending to slip. In such a case, the thread surface reaction moment is in equilibrium with the frictional torque offered by the nut bearing contact. Further, transverse load is applied to the plate will provide enough transverse force to cause complete slip at nut bearing contact which leads to complete slip at both the contacts. Thus, the nut will loosen until direction of loading reverses. It is observed that the loss of preload is more when coefficient of friction at threaded contact (μ_T) is small as shown in Fig. 16a. Variation of the nut turn angle with coefficient of friction at thread bearing contact is shown in Fig. 16b for the same value of μ_N .

5 Conclusions

The FE model is used to simulate the loosening behavior in bolted joint. The following conclusions are drawn from the study presented.

- (1) Rate of loss of preload per cycle is more at higher preload and it goes on reducing as preload decreases. Sudden increase in the turning angle is observed when both the contacts are undergoing complete slip. The bolted joint shows more resistance to movement of clamped plate at higher preload and it decreases as preload goes on decreasing.
- (2) Helix angle of the thread also affects loosening behavior of the bolted joint. Bolts with threads of fine pitch shows good resistance to loosening as compared to the joints with medium and course pitch.
- (3) Coefficient of friction at the nut bearing contact and thread contact also affects the loosening of bolted joint subjected to dynamic transverse load. The loosening

will be more when the coefficient of friction at threaded contact is low. Loosening tendency of the joint can be reduced by increasing coefficient of friction at threaded contact and decreasing the coefficient of friction at nut bearing contact.

References

1. Chetham C, Acosta F, Hess D (2009) Test and analysis of secondary locking features in threaded inserts. *Eng Fail Anal* 16(1):39–57
2. John H (1995) Bickford, an introduction to design and behaviour of bolted joint, 3rd edn. Marcel Dekker, New York
3. Liu J, Peng Q, Zeng C, Zhou P, Ma L, Zhu M (2016) Experimental and numerical studies of bolted joints subjected to axial excitation. *Wear* 346–347:66–77
4. Junker G (1972) Criteria for self-loosening of fasteners under vibration. *Aircr Eng Aerosp Technol* 44(10):14–16
5. Pai N, Hess D (2002) Experimental study of loosening of threaded fasteners due to dynamic shear loads. *J Sound Vib* 253(3):585–602
6. Pai N, Hess D (2002) Three-dimensional finite element analysis of threaded fastener loosening due to dynamic shear load. *Eng Fail Anal* 9(4):383–402
7. Dinger G, Friedrich C (2011) Avoiding self-loosening failure of bolted joint with numerical assessment of local contact state. *Eng Fail Anal* 18(8):2188–2200
8. Zadoks R, Yu X (1997) An investigation of the self-loosening behavior of bolts under transverse vibration. *J Sound Vib* 2:189–209
9. Izumi S, Yokoyama Y, Iwasaki A, Sakai S (2005) Three-dimensional finite element analysis of tightening and loosening mechanism of threaded fastener. *Eng Fail Anal* 12(4):604–615
10. Gong H, Liu J, Ding X (2019) Study on the mechanism of preload decrease of bolted joints subjected to transverse vibration loading. *J Eng Manuf* 233(12):2320–2329
11. Sanclemente J, Hess D (2005) Parametric study of threaded fastener loosening due to cyclic transverse load. *Eng Fail Anal* 14(1):239–249

Effect of Electrode Length and AC Frequency on Mixing in a Diamond-Shaped Split-And-Recombine Electroosmotic Micromixer



Amrendra Kumar, Nirmal K. Manna, and Sandip Sarkar

Abstract Lab-on-a-chip (LOC) and microfluidic devices have gained more and more importance in biological and chemical fields. A homogeneous mix of multiple reagents and chemicals is often essential to assist the chemical and biological reactions. Electroosmotic flow is an attractive approach for enhancing the homogeneous mix of species in a micro-scale mixer. In this work, a two-dimensional microfluidic mixture with a diamond-shaped split-and-recombine structure, using commercial software package COMSOL Multiphysics is analyzed. The choice of suitable electrode length is made by performing a series of simulations. The influence of AC (alternating current) frequency on the mixing of two fluids is also studied. The mixing efficiency of the micromixer initially increases with an increase in AC frequency and after reaching a maximum value, it starts decreasing. The best suited AC potential frequency for different electrode lengths is different. It is found from the results that the increase in electrode length does not always increase the mixing efficiency of the micromixer. The electrode length of such mixers critically affects the mixing efficiency and the suitable electrode length results in improved mixing of fluids.

Keywords Micromixer · Electroosmosis · Mixing efficiency · Electrode length

1 Introduction

With the advances in lab-on-a-chip (LOC) and microfluidic devices, microfluidics has gained more and more importance in biological and chemical fields. Mixing and pumping of several reagents and chemicals are often crucial and necessary to assist

A. Kumar · N. K. Manna · S. Sarkar (✉)

Department of Mechanical Engineering, Jadavpur University, Kolkata 700032, India

e-mail: thesandipsarkar3@gmail.com; sandipsarkar.mech@jadavpuruniversity.in

A. Kumar

e-mail: amrendraju@gmail.com

N. K. Manna

e-mail: nirmalkmannaju@gmail.com

chemical and biological reactions [1, 2]. Usually, the turbulent mixing of fluids is not possible, due to the small dimensions of the microfluidic devices [3]. Mixing of liquids in a micro-scale takes place primarily due to diffusional mixing. The mixing efficiency of such small-scale devices is not up to the mark as per production and testing levels.

The method of engendering vortices in micro-scale channels has been reported by many scholars and generally, it is divided into two groups, namely active group and passive group [4, 5]. The passive group mainly incorporates special geometries [6, 7] of microchannels and various types of obstacle shapes [8–11] or grooves [12–14] accommodated in micro-scale channels to generate vortices in the laminar flow field. This group of micromixers does not require any external source of energy, but these channels are heavily dependent on complex designs with special structures, thus increasing the fabrication difficulty. By contrast, external energy such as magnetic energy [4, 15], acoustic energy [16], and electrical energy [17, 18] is applied in an active group of micromixers to generate vortices.

The electrically actuated active (electroosmotic) method is an attractive approach for enhancing mixing. Electroosmotic mixers have a simple design, convenient working procedures, and enhanced efficiency. By applying low potential alternating currents (AC) using microelectrodes along the channel walls, the laminar flow field can be distorted and a chaotic state of the flow field is generated in the microchannel mixer. This enhances the number of interactions at the molecular level by stretching and squeezing the fluid flow, thereby increasing the mixing efficiency. These advantages have made electroosmotic technology popular among scientists and engineers studying microfluidic technology and analysis system. Huang et al. [19] developed an innovative electroosmotic micromixer with various electrode arrangements on the base surface of the Y-mixing channel, which employed micro-vortex patterns to enhance the mixing in a lab-on-a-chip device. Zhang et al. [20] numerically studied the controlling the fluid flow rate in the micro-mixer by using induced electro-osmosis in the mixer channel to generate a flow field with vortices in the fluid solution, and designed an electrokinetic microchannel mixer network that can increase the microchannel mixing efficiency with significantly small mixing length. Zhao et al. [21] studied the flow behavior of power-law fluid in a slit microchannel under the influence of the electroosmotic flow phenomenon. Nayak et al. [22] implemented the model of sequencing heterogeneous potentials on the micro-channel surface and concluded that the mixing of a Newtonian fluid in micro-channels can be improved by the pressure gradient and vortices generated by the electric field. Sasaki et al. [23] designed an AC electroosmotic Y-microchannel mixer. The bottom surface of the mixer is having a coplanar pair of sinusoidal electrodes. AC electric potential is applied to the sinusoidal electrodes and AC frequency (1–5 kHz) is varied to study its effects on mixer performance. The maximum mixer mixing efficiency of nearly 92% is reported at 20 V potential and 1 kHz frequency.

In this paper, based on mixing efficiency, a primary parameter of micro-channel mixers, the effect of electrode length for the microfluidic mixture with a diamond split-and-combine structure is analyzed. Furthermore, the influence of AC (alternating current) frequency on the mixing of fluids is also studied.

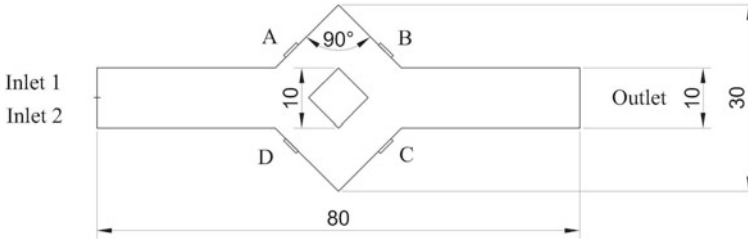


Fig. 1 Schematic of the rhombus-shaped annular micromixer

2 Numerical Model

2.1 Microfluidic Problem Model and Formulation

The schematic of the rhombus-shaped annular active micromixer is presented in Fig. 1. The channel depth to width ratio is considered sufficiently large to justify the 2D geometry assumption for the microfluidic mixer. Two fluids enter into the straight inlet channel through inlet 1 and 2, respectively. The width of the inlets (1 and 2 both) is $5 \mu\text{m}$, resulting in a combined width of the main channel as $10 \mu\text{m}$, the total length of the main channel is $80 \mu\text{m}$. The two liquids initially pass through this main channel and then enter the rhombus-shaped annular micro-mixing chamber with an outer rhombus diagonal of $d_0 = 30 \mu\text{m}$ and inner rhombus diagonal of $d_i = 10 \mu\text{m}$. Four microelectrodes (namely A, B, C, and D) are mounted on the wall of the outer rhombus of the annular mixing chamber with an angular displacement of 45° with axial direction and thus making an angle of 90° with each other. The electrode length is varied from 2 to $7 \mu\text{m}$. The initial concentration (c_0) of the liquid entering inlets 1 and 2 is considered as 1 mol/m^3 and 0 mol/m^3 , respectively. A constant value of the zeta potential is assumed on the mixer wall. The micro-electrodes are actuated with time-varying sinusoidal AC with alternating polarity, but the same potential amplitude and AC frequency. This leads to vortices generation within the annular chamber, leading to the mixed liquid flowing out of the main channel outlet.

2.2 Governing Equations and Scheme

The liquid solution is assumed as a viscous-incompressible, Newtonian and the flow is considered as laminar. Thus, the flow field is governed by the following equations of continuity and momentum:

$$\nabla \cdot \mathbf{u} = 0 \quad (1)$$

$$\rho \cdot \left(\frac{\partial u}{\partial t} + (u \cdot \nabla)u \right) = -\nabla p + \mu \nabla^2 u \quad (2)$$

The convection–diffusion equation is implemented to describe the concentration distribution of solute in fluids:

$$\frac{\partial c}{\partial t} + \nabla \cdot (-D \nabla c) = -u \cdot \nabla c \quad (3)$$

In the above equations, u represents the velocity vector (0.1 mm/s at the inlet), ρ (1000 kg/m³) is the fluid density, p is the pressure (Pa), t refers to the time (s) and μ is the dynamic viscosity coefficient of the fluid (10³ Pa s), $\mu \nabla^2 u$ is the viscous force experienced by the fluid, D (0.6 × 10⁻¹¹ m²/s) is the diffusion coefficient. It may be noted that the properties of the fluid are assumed to be similar to that of the liquid water.

The Helmholtz–Smoluchowski (HS) relation between the slip velocity and the applied AC field is chosen over the thin EDL (electric double layer) force. Thus, at the microchannel wall, an electroosmotic slip velocity condition is applied instead of the thin EDL with the HS relation as follows:

$$u = \frac{\varepsilon_0 \varepsilon_r \xi_0}{\eta} \nabla_t V \quad \text{Here, } \nabla_t V = E_t = E - (n \cdot E)n \quad (4)$$

where, $\varepsilon_0 = 8.854 \times 10^{-12}$ C/Vm is the permittivity of vacuum, $\varepsilon_r = 80.2$ is the relative permittivity of the water, ξ_0 is the zeta potential (−0.1 V), V is the applied potential (0.1 V), E refers to the bulk electrical field.

The current balance within the mixer is as follows:

$$\nabla \cdot (\sigma \nabla V) = 0 \quad (5)$$

where σ is the fluid solution conductivity and $\sigma \nabla V$ is the current density. The electric insulation condition is considered on all the boundaries except electrodes.

At the electrodes AC potential is imposed as follows:

$$V = \pm V_0 \sin(\omega t) \quad \text{Here, } \omega = 2\pi f \quad (6)$$

where V_0 is the applied voltage amplitude, ω is the angular frequency, and f represents the AC frequency.

The performance analysis parameter, mixing efficiency ($\eta\%$) is introduced to analyze the fluid mixing is as follows:

$$\eta(\%) = \left(1 - \frac{\int_{y_1}^{y_2} |c - c_\infty| dy}{\int_{y_1}^{y_2} |c_0 - c_\infty| dy} \right) \times 100\% \quad (7)$$

Table 1 Grid independence study at $t = 0.5$ s for $u = 0.1$ mm/s, $V_0 = 0.1$ V, $L_e = 5$ μ m and $f = 12$ Hz

Sr. No	Mesh	Number of elements	Mixing efficiency (%)
1	G1	3059	84.96
2	G2	3739	81.60
3	G3	4358	80.15
4	G4	7488	79.22
5	G5	8559	79.31

where c_0 represents the totally unmixed solution concentration and c_∞ represents the totally mixed solution concentration. Also, y_1 represents the upper sectional limit and y_2 represents the lower sectional limit at a particular cross section of the microchannel. The magnitude of η varies from 0 to 100%, representing the mixing performance of the micromixer.

2.3 Grid Independence Study and Model Validation

In the present study, FEM (finite element method) package COMSOL Multiphysics is used for solving all of the mathematical equations. First, a two-dimensional structure is built and the physical properties and appropriate boundary conditions are set. Then, four different mesh sizes with unstructured triangular shapes, namely G1, G2, G3, G4, and G5 consisting of 3059, 3739, 4358, 7488, and 8559 number of elements, respectively, are chosen to discover the optimum mesh element size. The mixing efficiency percentage at $t = 0.5$ s for $u = 0.1$ mm/s, $V_0 = 0.1$ V, $L_e = 5$ μ m and $f = 12$ Hz at the outlet of the micromixer for all the grid sizes is shown in Table 1. As the deviation of the mixing efficiency between G4 and G5 is negligible, thus G4 mesh size with 7458 elements is considered for further simulation.

To verify the accuracy of the present numerical scheme, the results obtained with the electrokinetic micromixer demonstrated by Wu and Li [17] are simulated. Normalized concentration at different heights of cross section (at $x = 500$ μ m) is obtained from the experimental work of Wu and Li [17] and current numerical scheme is shown in Table 2. The good agreement of results obtained from the current numerical scheme with the reported work ascertains the accuracy of the numerical model.

3 Results and Discussion

In the absence of AC electrical potential in the micromixer, the laminar flow field leads to only molecular diffusional mixing. This can be observed in Fig. 2. By applying AC potential, vortices are generated and the laminar flow field is distorted.

Table 2 Model Validation with experimental results of Wu and Li for $E = 50 \text{ V/cm}$ at $x = 500 \text{ }\mu\text{m}$ downstream from the hurdles

Sr. No	Cross-sectional height (y in μm)	Normalized concentration	
		Experimental result of Wu and Li [17]	Numerical result of present study
1	50.103	0.4162	0.4341
2	101.733	0.4753	0.4764
3	147.217	0.4993	0.5067
4	201.068	0.5502	0.5468
5	250.148	0.5931	0.5849

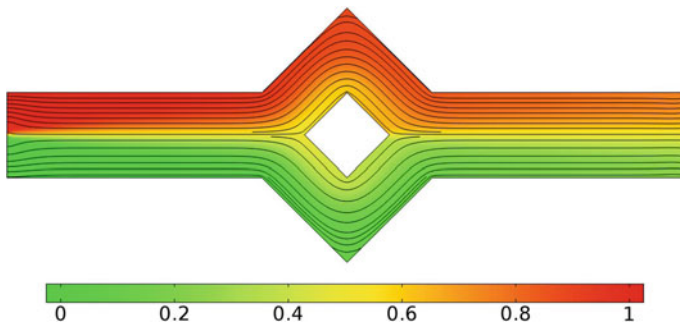


Fig. 2 Concentration and streamline plot without AC electric potential

This increases the number of interactions by stretching and overlapping of fluids at the molecular level and mixing is increased (Fig. 3).

Figure 4 shows the continuous change in mixing efficiency throughout the simulation time for electrode length $L_e = 5 \text{ }\mu\text{m}$, keeping the other parameters fixed apart from frequency. The frequency is varied from 2 to 24 Hz. It can be observed from the

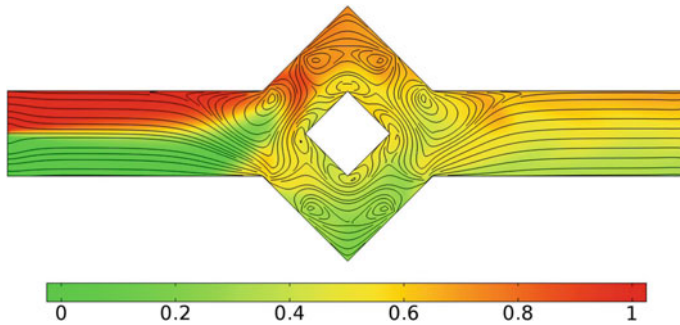


Fig. 3 Concentration and streamline plot with AC electric potential

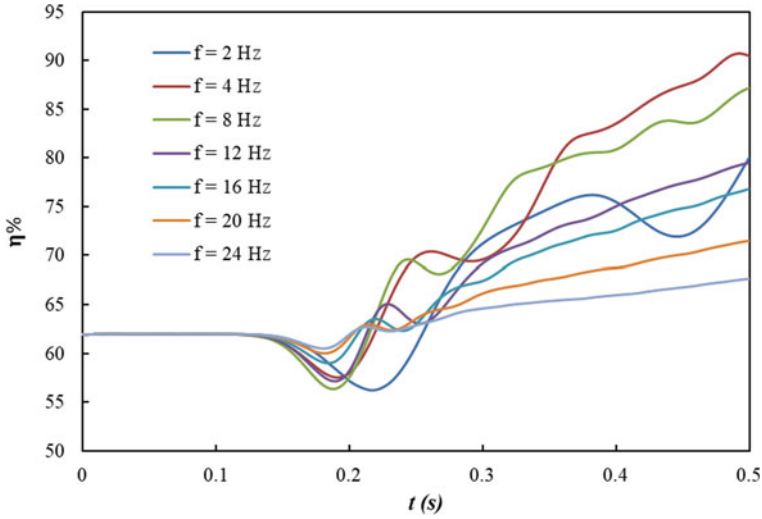


Fig. 4 Mixing efficiency variation with time for electrode length $L_c = 5 \mu\text{m}$ for $f = 2$ to 24 Hz

figure that with a change in the frequency the mixing efficiency changes dramatically. And for a particular frequency of 4 Hz, the maximum efficiency of approximately 90% at the end of simulation time is obtained.

In order to affirm that if this frequency of 4 Hz is the best frequency of operation, another electrode length of $7 \mu\text{m}$ is studied keeping the other parameters constant. Figure 5 shows the continuous change in mixing efficiency throughout the simula-

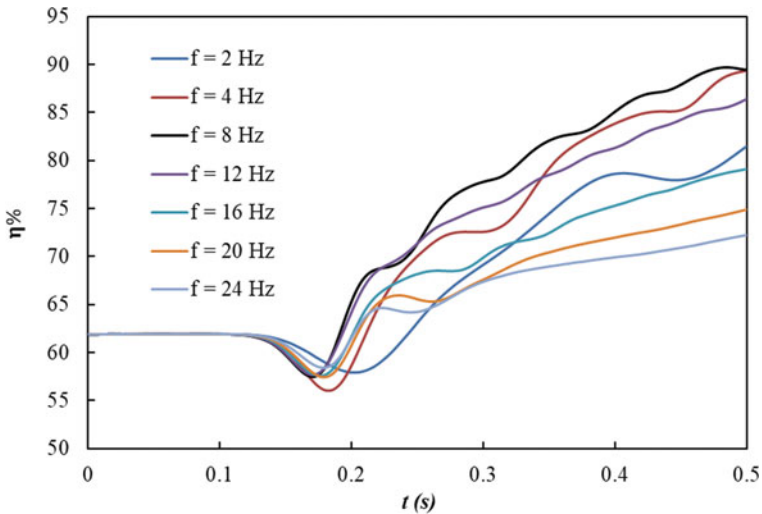


Fig. 5 Mixing efficiency variation with time for electrode length $L_c = 7 \mu\text{m}$ for $f = 2$ to 24 Hz

tion time for electrode length $L_e = 7 \mu\text{m}$. It can be observed from the figure that the frequency of 8 Hz is the best suited for the operation of the micromixer with an electrode length of $L_e = 7 \mu\text{m}$. These observations suggest that the change in electrode length of the micromixer affects the mixing efficiency, the best-suited frequency for the operation, and detailed analysis of the electrode length is needed.

In order to understand the relation between the electrode length and frequency the detailed analysis is done and electrode length is varied from $L_e = 2$ to $7 \mu\text{m}$ for frequency variation of $f = 2$ to 24 Hz . Figures 6 and 7 together show the effect of electrode length change and frequency change on mixing efficiency at time $t = 0.5 \text{ s}$. From Fig. 6, it can be observed that there is no specific trend observed for a specific frequency of operation on change in electrode length. At the two largest values of frequencies of 20 and 24 Hz, an approximately linear increase in mixing efficiency can be observed with an increase in electrode length. Though the linear trend is not observed for the frequencies of 8, 12, 16 Hz but the maximum efficiency is observed at the maximum electrode length of $L_e = 7 \mu\text{m}$. For $f = 2 \text{ Hz}$ the maximum efficiency is observed at electrode length of $L_e = 6 \mu\text{m}$, whereas for 4 Hz frequency of operation the maximum mixing efficiency of 92.82% is observed at an electrode length of $L_e = 4 \mu\text{m}$. Figure 6 indicates that initially with an increase in frequency the mixing efficiency increases for all the electrode lengths and then starts decreasing with a further increase in the frequency. Also, it is found that the best suited AC frequency in the cogent range of study is $f = 4 \text{ Hz}$.

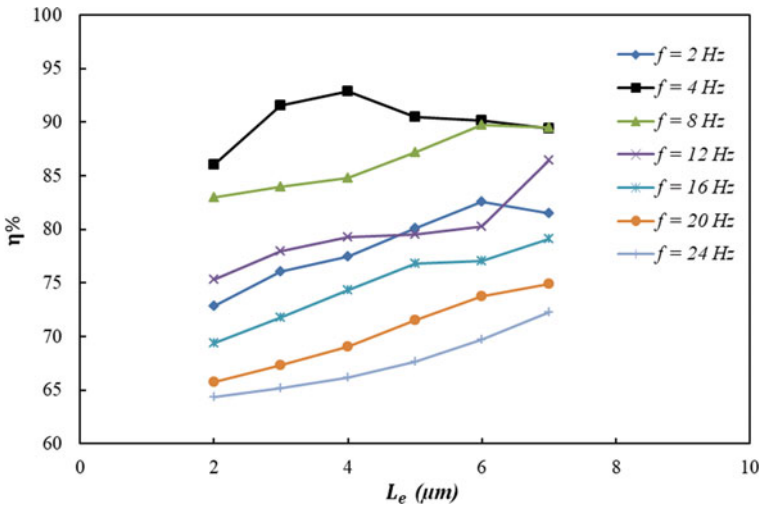


Fig. 6 Mixing efficiency variation with electrode length for $f = 2$ to 24 Hz at time $t = 0.5 \text{ s}$

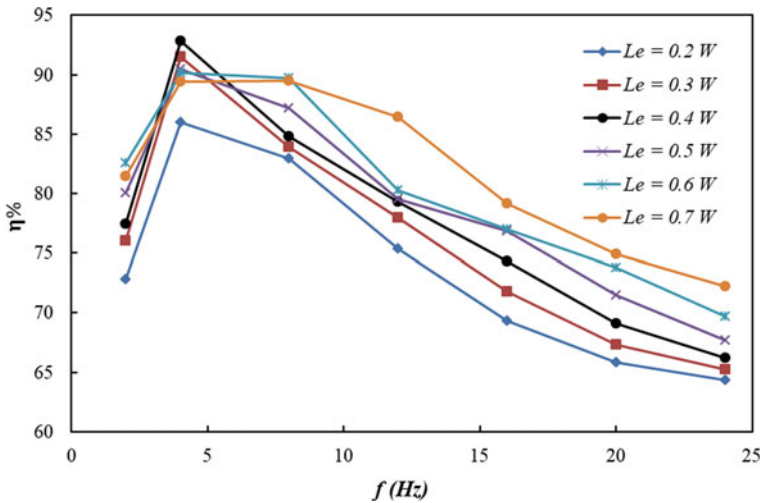


Fig. 7 Mixing efficiency variation with frequency for $L_e = 2$ to $7 \mu\text{m}$ at time $t = 0.5 \text{ s}$

4 Conclusion

In the present work, a two-dimensional rhombus-shaped annular AC micromixer equipped with four micro-electrodes is investigated numerically. A detailed analysis of the influence of electrode length and AC electrical frequency on the mixing characteristics of the microfluidic mixture is performed. Based on the studied model and suitable assumptions, the important outcomes can be summarized as follows:

- The application of AC potential distorts the flow field and the mixing efficiency of the electroosmotic mixer is greatly enhanced.
- The electrode length of the electroosmotic mixer critically affects the mixing efficiency. An increase in electrode length may increase or decrease the mixing efficiency of the micromixer. At high frequency, an increase in electrode length increases the mixing efficiency.
- The mixing efficiency of the micromixer initially increases with an increase in frequency and after reaching a maximum value, it starts decreasing.
- The best suited AC potential frequency for different electrode lengths is different. And the premier mixing efficiency is observed for the electrode length $L_e = 4 \mu\text{m}$ and frequency $f = 4 \text{ Hz}$.

References

1. Kim BJ, Yoon SY, Lee KH, Sung HJ (2009) Development of a microfluidic device for simultaneous mixing and pumping. *Exp Fluids* 46:85–95

2. Chakraborty S, Ray S (2008) Mass flow-rate control through time-periodic electro-osmotic flows in circular microchannels. *Phys Fluids* 20:083602
3. Heo HS, Suh YK (2005) Enhancement of stirring in a straight channel at low reynolds-numbers with various block-arrangement. *J Mech Sci Technol* 19:199–208
4. Chen Y, Kim CN (2018) Numerical analysis of the mixing of two electrolyte solutions in an electromagnetic rectangular micromixer. *J Ind Eng Chem* 60:377–389
5. Mondal B, Mehta SK, Patowari PK, Pati S (2019) Numerical study of mixing in wavy micromixers: comparison between raccoon and serpentine mixer. *Chem Eng Process* 136:44–61
6. Li J, Xia G, Li Y (2013) Numerical and experimental analyses of planar asymmetric split-and-recombine micromixer with dislocation sub-channels. *J Chem Technol Biotechnol* 88:1757–1765
7. Zhou T, Xu Y, Liu Z, Joo SW (2015) An enhanced one-layer passive microfluidic mixer with an optimized lateral structure with the dean effect. *J Fluids Eng* 137(9):091102
8. Miranda JM, Oliveira H, Teixeira JA, Vicente AA, Correia JH, Minas G (2010) Numerical study of micromixing combining alternate flow and obstacles. *Int Commun Heat Mass Transfer* 37(6):581–586
9. Cheri MS, Latifi H, Moghaddam MS, Shahraki H (2013) Simulation and experimental investigation of planar micromixers with short-mixing-length. *Chem Eng J* 234:247–255
10. Mondal B, Pati S, Patowari PK (2019) Analysis of mixing performances in microchannel with obstacles of different aspect ratios. *Proc Inst Mech Eng Part E: J Process Mech Eng* 233(5):1045–1051
11. Borgohain P, Arumughan J, Dalal A, Natarajan G (2018) Design and performance of a three-dimensional micromixer with curved ribs. *Chem Eng Res Des* 136:761–775
12. Hossain S, Husain A, Kim KY (2011) Optimization of micromixer with staggered herringbone grooves on top and bottom walls. *Eng Appl Comput Fluid Mech* 5(4):506–516
13. Jung SY, Park JE, Kang TG, Ahn KH (2019) Design optimization for a microfluidic crossflow filtration system incorporating a micromixer. *Micromachines* 10(12):836
14. Yoshimura M, Shimoyama K, Misaka T, Obayashi S (2019) Optimization of passive grooved micromixers based on genetic algorithm and graph theory. *Microfluid Nanofluid* 23(30):30
15. Dallakehnejad M, Mirbozorgi SA, Niazmand H (2019) A numerical investigation of magnetic mixing in electroosmotic flows. *J Electrostat* 100:103354
16. Rasoulia MR, Tabrizian M (2019) An ultra-rapid acoustic micromixer for synthesis of organic nanoparticles. *Lab on a Chip* 19(19):3316–3325
17. Wu Z, Li D (2008) Micromixing using induced-charge electrokinetic flow. *Electrochim Acta* 53:5827–5835
18. Seo HS, Han B, Kim YJ (2012) Numerical study on the mixing performance of a ring-type electroosmotic micromixer with different obstacle configurations. *J Nanosci Nanotechnol* 12:4523–4530
19. Huang SH, Wang SK, Khoo HS, Tseng FG (2007) AC electroosmotic generated in-plane microvortices for stationary or continuous fluid mixing. *Sens Actuators, B Chem* 125:326–336
20. Zhang F, Daghighi Y, Li D (2011) Control of flow rate and concentration in microchannel branches by induced charge electrokinetic flow. *J Colloid Interface Sci* 364:588–593
21. Zhao C, Zholkovskij E, Masliyah JH, Yang C (2008) Analysis of electroosmotic flow of power-law fluids in a slit microchannel. *J Colloid Interface Sci* 326:503–510
22. Nayak AK (2014) Analysis of mixing for electroosmotic flow in micro/nano channels with heterogeneous surface potential. *Int J Heat Mass Transf* 75:135–144
23. Sasaki N, Kitamori T, Kim HB (2010) Experimental and theoretical characterization of an AC electroosmotic micromixer. *Anal Sci* 26:815–819

Parametric Optimization of Tribological Process Parameters and Their Comparative Effect on Wear Responses of TiCrN Coated Cold Work Tool Steel



Sunil Kumar, Saikat Ranjan Maity, Lokeswar Patnaik, and Sumit Bhowmik

Abstract In the present study, multi-objective parametric optimization of wear parameters during dry sliding of TiCrN coated YXR-7 tool steel against WC–Co counterbody is carried out. L_{16} orthogonal array is used to design the experimental run and Grey-relational analysis has been conducted to obtain the best suitable combination of tribological parameter. Further, mean response and analysis of variance has been performed to investigate the most influential parameter. Further, linear and nonlinear mathematical model is developed and compared on the basis of R^2 value. The study shows nonlinear model shows good fitted model and better correlation between experimental and predicted values.

Keywords YXR-7 tool steel · Tribology · Taguchi · Grey relational analysis · Ranking · Specific wear rate

1 Introduction

Among all the ceramic hard coating, single-layered TiN coating has been extensively used to enhance and modify the surface of die, moulds and cutting tools due to its excellent wear and mechanical properties. However, it is observed that single layer was not suitable for high load operations due to which doping in the coatings came into picture. This type of coating draws attention of many researchers where they adopted the doping of different ions to improve various properties [1–4]. TiCrN

S. Kumar (✉) · S. R. Maity · S. Bhowmik
Mechanical Engineering Department, National Institute of Technology Silchar, Silchar, India
e-mail: sunilnits18@gmail.com

L. Patnaik
School of Mechanical Engineering, Sathyabama Institute of Science and Technology (Deemed to be University), Chennai 600 119, India
e-mail: lokeswar.nits@gmail.com

S. Kumar
Department of Mechanical Engineering, Amrita School of Engineering, Amrita Vishwa Vidyapeetham, Chennai, India

coatings are known for its outstanding mechanical, wear and oxidation properties. This coating can be deposited by using many methods such as electron beam evaporation, ion beam-assisted deposition and magnetron sputtering. Many researchers have studied the mechanical and structural properties of this coating and reported flow rate of nitrogen to be an influential parameter during deposition [5–7]. Amari et al. [8] have conducted adhesion test for different ceramic film and observed Ti element increases the adhesion of coating on the substrate. Prabakaran et al. [9] reported improved corrosion resistance of TiCrN coating. Valletti et al. [10] studied the erosion resistance of TiCrN coating and observed thicker layer of this coating have excellent erosion resistance during the loading application.

In the present study TiCrN is deposited over YXR-7 cold work tool steel and tribological experiment has been conducted against WC–Co counterbody under dry sliding condition. Further, a best suitable combination of tribological process parameters has been obtained using Grey relational analysis with Taguchi design of experiment.

2 Materials and Methods

2.1 Sample Preparation

YXR-7 tool steel was heat treated using vacuum hardening followed by plasma nitriding to enhance the mechanical and surface properties of the tool steel. The enhancement of these properties depends upon the chemical composition of the steel. This steel contains 0.8% carbon, 4.7% chromium, 5.5% molybdenum, 1.3% tungsten and 1.3% vanadium. The samples were tempered to reduce the brittleness and improve the toughness. Further, nitriding was done in vacuum chamber in presence of NH_3 gas at $\sim 500^\circ\text{C}$ temperature and ~ 900 Pa of chamber pressure. Active plasma was generated and deposited on to the substrate maintaining a suitable potential difference.

Before the deposition of TiCrN coating, substrate was cleaned by manual grinding and polishing. During the deposition of coating, current and voltage maintained for Cr and Ti targets was 70A/25 V of I/V and 60A/20 V, respectively. Substrate was rotated on the table for 45 min under the deposition pressure of 0.7 Pa and 241 sccm of N_2 gas flow rate to obtain 3.5 μm thick TiCrN film.

2.2 Experimental Plan

Tribological process parameters and their levels were selected using pilot experiments (see Table 1). L16 orthogonal array using Taguchi was designed for the experimental run. Taguchi uses different parametric design for quality characteristic

Table 1 Tribological parameter and its levels

Sr. No	Controllable parameters	Unit	Levels and its value			
			L-1	L-2	L-3	L-4
1	Applied load	N	10	15	20	25
2	Sliding velocity	m/s	0.2	0.4	0.6	0.8
3	Sliding distance	m/s	500	1000	1500	2000

[11]. The S/N ratio of Taguchi determines the best attainable alternatives for the parameters [12]. The best attainable parameter and their relative effect on measured responses was obtained using ANOVA and S/N ratio [13].

Based on the Taguchi experimental design (see Table 2), tribology experiments were conducted according to ASTM G:99 standard, each experiment was repeated for three time to get an average value. The Pin-on-disc experiments were performed on DUCOM TR20LE tribo-machine against WC–Co counterbody, friction coefficient (COF) was obtained using load cell and specific wear rate of each experiment were calculated using Eq. (1).

$$SWR = \frac{V}{P \times L} \tag{1}$$

Here, specific wear rate (SWR) is in m^2N^{-1} , V express the wear volume is in m^3 , applied load is given by P (in N) and total sliding distance is L (in m).

2.3 Grey Relational Analysis (GRA)

Taguchi along with GRA is the best solution for the combined responses [14]. Normally three steps were used to compute the GRA for ranking of the alternatives. For both the responses (COF and SWR) ‘smaller is better’ quality characteristic is applicable. Following steps are used to obtain the best combination of process parameter:

Step 1: Normalization of measured responses value.

The experimental value of the measured responses is needed to be normalized to minimize the variability and avoid the unit difference. The acceptable value is computed from the original experimental value to formulate the array which lies between 0 and 1 [15]. Normalization of the data was performed using (2).

$$Y_i^*(k) = \frac{\max Y_i(k) - Y_i(k)}{\max Y_i(k) - \min Y_i(k)} \tag{2}$$

Table 2 L16 orthogonal array and average experimental value of responses

Exp. run order	Applied load (N)	Sliding velocity (m/s)	Sliding distance (m)	Friction coefficient (μ)	Specific wear rate (m^2N^{-1}) $\times 10^{-17}$
1	10	0.2	500	0.59	5.41
2	10	0.4	1000	0.61	5.39
3	10	0.6	1500	0.67	5.89
4	10	0.8	2000	0.71	5.91
5	15	0.2	1000	0.59	6.04
6	15	0.4	500	0.52	5.83
7	15	0.6	2000	0.69	6.24
8	15	0.8	1500	0.62	6.31
9	20	0.2	1500	0.49	7.79
10	20	0.4	2000	0.53	7.83
11	20	0.6	500	0.42	7.27
12	20	0.8	1000	0.47	7.34
13	25	0.2	2000	0.36	8.73
14	25	0.4	1500	0.37	8.78
15	25	0.6	1000	0.34	8.81
16	25	0.8	500	0.29	8.34

Here, i is 1, 2, 3, 4,, n , k is 1, 2, 3,, m , $Y_i(k)$ is the sequence of original data, $Y_i^*(k)$ is the processed data, $\max Y_i(k)$ expresses the higher value of $Y_i(k)$, $\min Y_i(k)$ is the lower value of $Y_i(k)$ and Y is the selected value [16].

Step 2: Calculation of grey relational coefficient (GRC_i) and deviation in sequences (γ_{oi}) using (3) and (4) respectively.

$$\text{GRC}_i(k) = \frac{\gamma_{\min} + \theta\gamma_{\max}}{\gamma_{oi} + \theta\gamma_{\max}} \tag{3}$$

$$\gamma_{oi} = \|\gamma_o(k) - \gamma_i(k)\| \tag{4}$$

Here, γ_{oi} represents sequence deviation of reference $\gamma_o(k)$ and comparability $\gamma_i(k)$ sequence. γ_{\max} and γ_{\min} represents the maximum and minimum value of absolute deviation for all alternatives, respectively. θ expresses the identification coefficient and it lies between 0 and 1 (for this study 0.5 is taken).

Step 3: Calculation of Grey Relational Grade (GRG) using (5).

$$\text{GRG}_i = \frac{1}{n} \sum_{k=1}^n \theta_i(k) \tag{5}$$

Here, n represents number of measured responses. Interrelation between reference and comparability sequence is represented by GRG for overall quality characteristic and thus multi-objective problem has been converted into single objective optimization through GRA along with Taguchi design.

Step 4: Determination of main effect on mean GRG. In this regard, the optimum level of parameter is obtained using higher GRG that denotes the better-quality characteristic. Average value of grade for each levels of the parameter is to be calculated. The higher of average grade is taken as optimum combination of parameter for multi-objective.

2.4 ANOVA and Confirmation Experiment

As the effect of parameters on multi-response cannot be obtained using Taguchi design, ANOVA was performed to obtain the percentage contribution of parameter on to the responses at 95% of confidence interval. ANOVA separates the total variability of measured responses into contribution of individual parameter and error. As the confidence interval is at 95%, the p-value should be less than 0.05 for each parameter, then only it can be considered as significant parameter [17].

To justify the Taguchi optimum parameter, similar test was performed and the predicted value of GRG was calculated using (6).

$$\hat{\delta} = \delta_{\max} + \sum_{i=1}^p (\bar{\delta}_i - \delta_m) \quad (6)$$

Here, δ_{\max} represents total mean of GRG, $\bar{\delta}_i$ represents mean of GRG for individual parameter at optimum level, p is the number of tribological parameter [18].

3 Results and Discussion

3.1 Effect of Tribological Parameter on the Responses

Effect of tribological parameter on SWR of TiCrN coated YXR-7 tool steel is shown in Fig. 1. It indicates that SWR increases with increase in load in accordance with the Archard's law [19]. But as the velocity decreases, frictional coefficient starts to increase between the sliding pairs resulting in the increase of SWR. With increase in sliding distance, interface temperature increases causing deformation which leads to delamination thus increasing the SWR.

Surface roughness of the disc plays an important role during tribological experiment under dry sliding condition which is a major factor which determines the wear mechanism. The value of surface roughness directly influences the effect of load and sliding velocity. Initial value of friction coefficient was high due to initial roughness

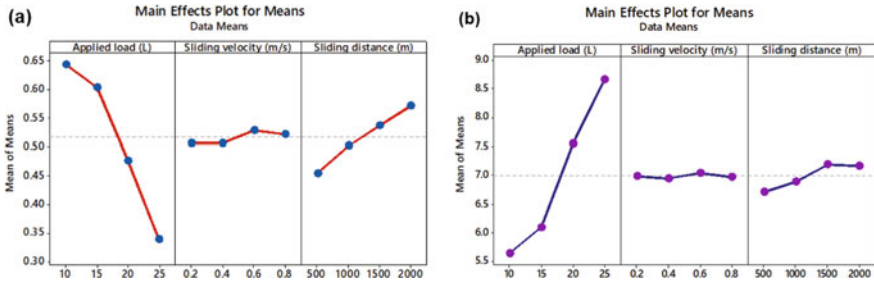


Fig. 1 Main effect of tribological parameter on a frictional coefficient and b specific wear rate

but as the load and velocity increases, frictional coefficient value starts to decrease due to adhesion wear mechanism [20–22].

3.2 Grey Relational Analysis (GRA)

The value of tribological responses is tabulated in Table 2. The values are normalized using (2) for both the responses. The quality characteristics of these responses are ‘smaller the better’.

Grey relation coefficient (GRC) was computed using (3) with the help of normalized data from Table 3. The different coefficient value for weightage of individual response was taken as 0.5 as mentioned in previous section (see Sect. 2.4). Before calculating the GRC value, deviation sequence for the responses was calculated using (4). Both the value of deviation sequence and GRC are tabulated in Table 3. Furthermore, Grey Relational Grade was computed using (5) for both the responses and based on the GRG value ranking, the alternatives are assigned (see Table 3). Higher value of GRG represents best suitable alternative (the first rank) for tribological process parameter of TiCrN coated YXR-7 tool steel.

Based on the GRG value, experiment number 1 obtained higher GRG value, which means relation between sequences is stronger which reflects better performance and optimum combination of parameters. Hence, the optimum combination of tribological parameter was $L = 10\text{ N}$, $SV = 0.2\text{ m/s}$ and $SD = 500\text{ m}$ for multi-objective response represented as $L_1\text{-}SV_1\text{-}SD_1$. The higher value of mean GRG (Table 4) indicates minimum value of COF and SWR. The individual difference of maximum and minimum value of tribological parameter at different levels was 0.14, 0.029 and 0.132 for load, sliding velocity and sliding distance, respectively (see Table 4). This value indicates applied load (L) and sliding distance (SD) are the most influential parameters compare to sliding velocity (SV).

Table 3 Value of GRC and GRG with ranking of alternatives

Exp. run order	Deviation sequence		Gray relational coefficient (GRC)		Gray relation grade (GRG)	Rank
	COF	SWR	COF	SWR		
1	0.714	0.006	0.412	0.988	0.700	1
2	0.762	0.000	0.396	1.000	0.698	2
3	0.905	0.146	0.356	0.774	0.565	7
4	1.000	0.152	0.333	0.767	0.550	8
5	0.714	0.190	0.412	0.725	0.568	6
6	0.548	0.129	0.477	0.795	0.636	4
7	0.952	0.249	0.344	0.668	0.506	13
8	0.786	0.269	0.389	0.650	0.520	12
9	0.476	0.702	0.512	0.416	0.464	15
10	0.571	0.713	0.467	0.412	0.439	16
11	0.310	0.550	0.618	0.476	0.547	9
12	0.429	0.570	0.538	0.467	0.503	14
13	0.167	0.977	0.750	0.339	0.544	10
14	0.190	0.991	0.724	0.335	0.530	11
15	0.119	1.000	0.808	0.333	0.571	5
16	0.000	0.863	1.000	0.367	0.683	3

Table 4 Response table for mean GRG

Parameters	Mean GRG of levels				Max–Min	Rank
	1	2	3	4		
Applied load	0.628	0.558	0.488	0.582	0.140	1
Sliding velocity	0.569	0.576	0.547	0.564	0.029	3
Sliding distance	0.642	0.585	0.520	0.510	0.132	2

3.3 Anova

Analysis of variance was obtained for the value of GRG and the result is tabulated in Table 5. ANOVA suggests the significance of tribological parameter on multi-objectives. In this study, it reveals that load and sliding distance was the most influential tribological parameter as its *P* value is less than 0.05, whereas *P* value for sliding velocity is greater than 0.05. Hence, it can be said that sliding velocity did not have any significant effect on the responses.

Table 5 ANOVA results for GRG

Source	DoF	Seq SS	Adj MS	F	P
Applied load (N)	3	9.8647	3.28824	23.97	0.001
Sliding velocity (m/s)	3	0.2316	0.07721	0.56	0.659
Sliding distance (m)	3	10.3117	3.43722	25.06	0.001
Residual Error	6	0.8230	0.13716		
Total	15	21.2310			

Table 6 Confirmation result for GRG

	Initial parameter	Optimum parameter	
		Predicted	Experimental
Level	L ₂ -SV ₃ -SD ₄	L ₁ -SV ₁ -SD ₁	L ₁ -SV ₁ -SD ₁
COF	0.69		0.59
SWR	6.24 × 10 ⁻¹⁷		5.41 × 10 ⁻¹⁷
GRG	0.506	0.711	0.700
Enhancement in GRG value		0.194	

3.4 Confirmation Experiment

Confirmation experiments were performed to recognize the enhancement in the GRG value at initial and optimum setting of parameters. Predicted value for GRG was calculated using (6) and the values are 0.506, 0.711 and 0.700 for initial setting, predicted and optimum setting for experiment, respectively (see Table 6). Table 6 indicates that the value of tribological response was enhanced by 0.194 on optimum setting of parameter. It also depicts that experimental GRG value and predicted GRG value are very close. Thus, it is justified that experiment number 1 is the best suitable alternative for tribology of TiCrN coated YXR-7 tool steel.

3.5 Regression Model

Regression model was formulated for both the responses with 95% of confidence interval using Minitab 18.0 software tool. The determination coefficient (R^2) value was also obtained which justify the adequacy of the model. Higher value of the R^2 indicates more significance of the model. Based on the experimental results, linear and nonlinear regression model was formulated for both the responses and it is presented in (7), (8), (9) and (10), respectively, with corresponding R^2 values.

Linear model

$$COF = 0.7680 - 0.02085 * L + 0.0337 * SV + 0.000077 * SD \quad (R^2 = 94.72\%) \quad (7)$$

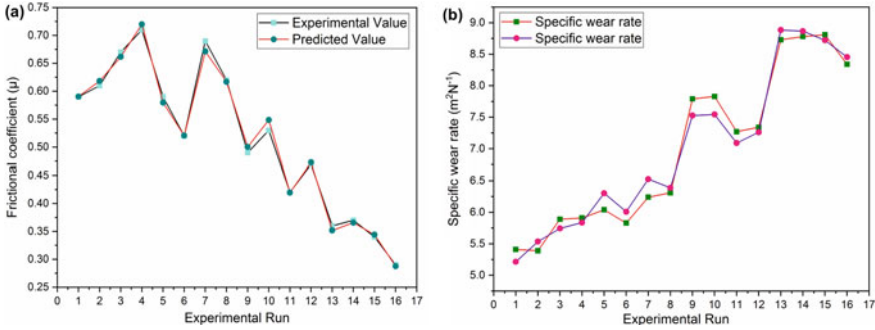


Fig. 2 Experimental value vs predicted value for **a** frictional coefficient and **b** specific wear rate

$$WR = 2.886 + 0.2100 * L + 0.021 * SV + 0.000338 * SD \quad (R^2 = 95.74\%) \quad (8)$$

Nonlinear model

$$\begin{aligned} COF = & 0.5391 + 0.01361 * L - 0.297 * SV + 0.000114 * SD \\ & - 0.000975 * L^2 - 0.0469 * (SV)^2 + 0.01080 * L * SV \\ & - 0.000003 * L * SD + 0.000126 * SV * SD \quad (R^2 = 99.51\%) \quad (9) \end{aligned}$$

$$\begin{aligned} WR = & 4.02 + 0.011 * L + 0.23 * SV + 0.00113 * SD \\ & + 0.00652 * L^2 - 0.27 * (SV)^2 - 0.0103 * L * SV \\ & - 0.000019 * L * SD + 0.000026 * SV * SD \quad (R^2 = 97.8\%) \quad (10) \end{aligned}$$

Equation (7) shows less R^2 value (94.72%), whereas (9) shows comparatively higher R^2 value (99.51%) for COF. It means nonlinear model (9) is the best fitted model and it can be said that model is statistically adequate and significant for COF. Similarly, for SWR nonlinear model has higher R^2 value (97.8%) with Eq. 10, thus it indicates model (10) is statistically adequate and significant.

Comparison of both the value (experimental and predicted) from nonlinear model is presented in Fig. 2a and b for COF and SWR, respectively. Figure shows that both the value is very close to each other for both the responses. It means nonlinear model has good relation between both the results. Thus, developed nonlinear model is significant and adequate for tribology of TiCrN coated YXR-7 tool steel.

4 Conclusion

In the present study, Grey relational analysis multi-objective multi-criteria optimization technique was used to optimize the tribological parameter for TiCrN coated

YXR-7 tool steel. The experimental run was designed by Taguchi L16 orthogonal array and the experiments were performed under dry sliding condition. Linear and nonlinear mathematical model was developed using Minitab 18.0 software tool and later compared. Based on these experimental and analytical analysis, following conclusion are drawn:

- (a) According to the GEA ranking, experiment number 1 obtained first rank which is the optimum combination of tribological process parameter with $L = 10\text{ N}$, $SV = 0.2\text{ m/s}$, $SD = 500\text{ m}$ expressed as $L_1\text{-}SV_1\text{-}SD_1$.
- (b) From the mean response and ANOVA of GRG analysis, load and sliding distance are the most significant parameter compared to Sliding velocity determining wear in TiCrN coated YXR-7 tool steel.
- (c) Improvement in GRG value was recorded at optimum setting of parameter (0.7) compared to initial parameter setting (0.506).
- (d) Nonlinear mathematical model for both the responses showed higher value of R^2 which indicates best fitted of the model which is also in good correlation between experimental and predicted data.

References

1. Yan P, Deng JX, Lian YS, Zhao J, Chen Z, Ai X (2012) Effect of depositing parameters on microstructures and properties of multi arc ion plating ZrTiN films. *Surf Eng* 28(1):17–23. <https://doi.org/10.1179/1743294411Y.0000000029>
2. Yang B, Tian CX, Wan Q, Yan SJ, Liu HD, Wang RY, Li ZG, Chen YM, Fu DJ (2014) Synthesis and characterization of AlTiSiN/CrSiN multilayer coatings by cathodic arc ion-plating. *Appl Surf Sci* 314:581–585. <https://doi.org/10.1016/j.apsusc.2014.05.166>
3. Patnaik L, Maity SR, Kumar S (2020) Status of nickel free stainless steel in biomedical field: A review of last 10 years and what else can be done. *Mater Today Proc* 26(2):638–643. <https://doi.org/10.1016/j.matpr.2019.12.205>
4. Kumar S, Maity SR, Patnaik L (2020) Effect of heat treatment and TiN coating on AISI O1 cold work tool steel. *Mater Today Proc* 26(2):685–688. <https://doi.org/10.1016/j.matpr.2019.12.367>
5. Lee KH, Park CH, Yoon YS, Jehn HA, Lee JJ (2001) Wear and corrosion properties of (Ti–xCr)N coatings produced by the ion-plating method. *Surf Coat Technol* 142:971–977. [https://doi.org/10.1016/S0257-8972\(01\)01248-8](https://doi.org/10.1016/S0257-8972(01)01248-8)
6. Nainaparampil JJ, Zabinski JS, Korenyi-Both A (1998) Formation and characterization of multiphase film properties of (Ti–Cr)N formed by cathodic arc deposition. *Thin Solid Films* 333(1–2):88–94. [https://doi.org/10.1016/S0040-6090\(98\)00840-2](https://doi.org/10.1016/S0040-6090(98)00840-2)
7. Huang M, Chen Z, Wang M, Li Y, Wang Y (2016) Microstructure and properties of TiCrN coatings by arc ion plating. *Surf Eng* 32(4):284–288. <https://doi.org/10.1179/1743294415Y.0000000039>
8. Amari D, Khireddine H, Khelfaoui Y, Saoula N (2019) Adhesion and corrosion of Ti, TiN and TiCrN films deposits on AISI 316L in SBF solution. In: Defect and diffusion forum, vol. 397, pp 39–50. <https://doi.org/10.4028/www.scientific.net/DDF.397.39>
9. Prabakaran V, Chandrasekaran K (2016) Characterisation and corrosion resistance of TiCrN composite coating on steel by physical vapour deposition method. *J Bio- Tribo- Corro* 2(4):25. <https://doi.org/10.1007/s40735-016-0055-y>

10. Valleti K, Joshi SV (2016) Studies on cathodic arc PVD grown TiCrN based erosion resistant thin films. *J Vacuum Sci Technol A: Vac Surf Films* 34(4):041512. <https://doi.org/10.1116/1.4953466>
11. Phadke MS (1995) *Quality engineering using robust design*. Prentice Hall PTR
12. Kar S, Chakraborty S, Dey V, Ghosh SK (2017) Optimization of surface roughness parameters of Al-6351 alloy in EDC process: a taguchi coupled fuzzy logic approach. *J Inst Eng (India): Ser C* 98(5):607–618. <https://doi.org/10.1007/s40032-016-0297-y>
13. Chakraborty S, Kar S, Dey V, Ghosh SK (2017) Optimization and surface modification of al-6351 alloy using SiC–cu green compact electrode by electro discharge coating process. *Surf Rev Lett* 24(01):1750007. <https://doi.org/10.1142/S0218625X1750007X>
14. Radhika N, Chandran GK, Shivaram P, Karthik KT (2015) Multi-objective optimization of EDM parameters using grey relation analysis. *J Eng Sci Technol* 10(1):1–11. <https://doi.org/10.1016/j.matpr.2019.05.190>
15. Haq AN, Marimuthu P, Jeyapaul R (2008) Multi response optimization of machining parameters of drilling Al/SiC metal matrix composite using grey relational analysis in the Taguchi method. *Int J Adv Manuf Technol* 37(3–4):250–255. <https://doi.org/10.1007/s00170-007-0981-4>
16. Tosun N, Pihitili H (2010) Gray relational analysis of performance characteristics in MQL milling of 7075 Al alloy. *Int J Adv Manuf Technol* 46(5–8):509–515. <https://doi.org/10.1007/s00170-009-2118-4>
17. Datta S, Bandyopadhyay A, Pal PK (2008) Slag recycling in submerged arc welding and its influence on weld quality leading to parametric optimization. *Int J Adv Manuf Technol* 39(3–4):229–238. <https://doi.org/10.1007/s00170-007-1224-4>
18. Sahoo AK, Sahoo B (2013) Performance studies of multilayer hard surface coatings (TiN/TiCN/Al₂O₃/TiN) of indexable carbide inserts in hard machining: Part-II (RSM, grey relational and techno economical approach). *Measurement* 46(8):2868–2884. <https://doi.org/10.1016/j.measurement.2012.09.023>
19. Zmitrowicz A (2006) Wear patterns and laws of wear—a review. *J Theor Appl Mech* 44(2):219–253. <http://www.ptmts.org.pl/jtam/index.php/jtam/article/view/v44n2p219>
20. Patnaik L, Maity SR, Kumar S (2020) Comprehensive structural, nanomechanical and tribological evaluation of silver doped DLC thin film coating with chromium interlayer (Ag-DLC/Cr) for biomedical application. *Ceram Int* 46(14):22805–22818. <https://doi.org/10.1016/j.ceramint.2020.06.048>
21. Kumar S, Maity SR, Patnaik L (2020) Friction and tribological behavior of bare nitrided, TiAlN and AlCrN coated MDC-K hot work tool steel. *Ceram Int* 46(11):17280–17294. <https://doi.org/10.1016/j.ceramint.2020.04.015>
22. Patnaik L, Maity SR, Kumar S (2020) Mechanical and tribological assessment of composite AlCrN or aC: Ag-based thin films for implant application. *Ceram Int* (2020). <https://doi.org/10.1016/j.ceramint.2020.11.016>

Effect of Surface Modification on the Nanomechanical and Wear Properties of AISI D3 Cold Work Tool Steel



Sunil Kumar, Saikat Ranjan Maity, and Lokeswar Patnaik

Abstract This work focuses on performing surface modification of cold work AISI D3 tool steel and investigating its nanomechanical and wear properties. Structural property of the coated sample was obtained using XRD analysis, whereas surface characterization was performed using optical microscope, FE-SEM. Further, the mechanical properties were investigated using nanoindentation and nanoscratch test. Results show that hardening (heat treatment) of the tool steel improves the mechanical properties by reducing the primary carbides and increasing the secondary carbides which are smaller in size and hard in nature. Mechanical properties such as hardness and elastic modulus of the surface was further enhanced by plasma nitriding followed by TiCrN coating deposition. The hardness and elastic modulus of nitrided tool steel got improved by 2.24 times and 1.36 times respectively whereas specific wear rate got reduced by four orders of magnitude after deposition of TiCrN coating.

Keywords AISI D3 tool steel · Plasma nitriding · Nanoindentation · Nanoscratch

1 Introduction

AISI D3 cold work tool steel is popularly used in manufacturing of punch and die for sheet metal cutting and forming processes. It is typically a high carbon (2–2.5%) and high chromium (11–13%) steel. Chromium carbides are present in martensitic matrix instead of ferrite in wrought D3 tool steel, whereas cast D3 tool steel having

S. Kumar (✉) · S. R. Maity

Mechanical Engineering Department, National Institute of Technology Silchar, Silchar 788 010, India

e-mail: sunilnits18@gmail.com

L. Patnaik

School of Mechanical Engineering, Sathyabama Institute of Science and Technology (Deemed to be University), Chennai 600 119, India

S. Kumar

Department of Mechanical Engineering, Amrita School of Engineering, Amrita Vishwa Vidyapeetham, Chennai, India

© The Author(s), under exclusive license to Springer Nature Singapore Pte Ltd. 2023

105

T. S. Sudarshan et al. (eds.), *Recent Advancements in Mechanical Engineering*,

Lecture Notes in Mechanical Engineering,

https://doi.org/10.1007/978-981-19-3266-3_9

eutectic chromium carbides in austenitic form at the end of solidification. Finally, chromium and carbon are segregated which reduces the mechanical properties viz. impact energy, bending strength and toughness. Hiraoka et al. [1] investigated the wear mechanism of high chromium tool steel and found that at low sliding speed (0.1 m/s and 0.3 m/s), abrasion wear is dominant whereas at medium sliding speed (0.3 m/s and 1.5 m/s), wear started to decrease due to oxide formation. However, at higher sliding speed (1.5 m/s and 4.3 m/s), interface temperature increases to melting phase of the material. Previous researchers [2, 3] have reported that high hardness reduces plowing on the surface and toughness prevents spalling and crack formation during wear. However, carbides size and their spacing in the steel microstructure effect the wear rate during the tribological test.

Nevertheless, above-mentioned properties of tool steel are not sufficient for the longer life of punch and dies under heavy load and different application in tooling industries. Ceramic hard coatings are a better option for enhancing the surface properties like wear and oxidation. Many researchers [4–8] have reported that ceramic coatings (TiN, TiCN, TiCrN, AlCrN, TiAlN, DLC etc.) have better wear, oxidation and corrosion resistance properties for application in manufacturing and biomedical industries. Among these coatings, TiCrN coating has good surface hardness along with better wear resistance. Zhang et al. [9] have investigated the effect of TiCrN coating on nitrided 5083 Al alloy and reported that coating improves the wear properties of cutting tools, molds, forging die and sheet metal dies. Huang et al. [10] have also reported improvement in mechanical properties with TiCrN coating.

In this paper, untreated AISI D3 tool steel was heat-treated, nitrided over which TiCrN film was deposited. Surface characterization of the samples was investigated using optical microscope (OM), field emission scanning electron microscopy (FE-SEM) and XRD. Further, nanoindentation and nanoscratch test were performed on each sample to investigate the nanomechanical properties and wear properties, respectively.

2 Methodology

2.1 Sample Preparation and Its Characterization

AISI D3 cold work tool steel was used as the substrate material. Initially, the commercially available untreated tool steel has a hardness of 20–22 HRC (2.5 GPa). The substrate was machined to maintain a disc dimension of $\varnothing 20$ mm and 5 mm thickness. The machined sample was divided into four groups (Group-I for untreated AISI D3, Group-II for hardened AISI D3, Group-III for nitrided AISI D3 and Group-IV for TiCrN coated AISI D3). The substrate was heated up to ~ 900 °C and quenched into the oil till temperature reduces to 30 °C, this steel was again heated to a temperature of ~ 400 °C to perform the tempering.

Further, plasma nitriding process was carried out to enhance the surface properties of the heat-treated substrate. The nitriding process was conducted in the ammonia (NH_3) environment. In this process, the substrate was heated up to $\sim 500^\circ\text{C}$ under the pressure of $\sim 900\text{ Pa}$ and a potential difference was maintained between the substrate and machine chamber. Due to this potential difference, ammonia breaks to form the plasma of nitrogen and gets deposited over the heated surface of the substrate.

Before TiCrN deposition, the samples were polished and cleaned using different grit of sandpaper and alcohol, respectively. During the deposition, negative substrate bias was maintained (1000 V) under a vacuum pressure of $3 \times 10^{-13}\text{ Pa}$. Ti and Cr targets were maintained at 60 A/20 V and 70 A/25 V of I/V, respectively, whereas nitrogen gas was supplied at 241 sccm under a deposition pressure of 0.7 Pa.

Microstructural characterization of the substrates was performed using optical microscope (De winter optical, Inc.) and XRD (Analytical B. V.) with Cu-K α radiation at 40 kV accelerated potential and 30 mA current. Scanning speed was maintained at $0.08^\circ/\text{min}$ for a diffraction angle range of $20^\circ\text{--}80^\circ$.

2.2 Analysis of Nanomechanical Properties

Nanomechanical properties were investigated using nanoindentation test on each group of the substrate. The tests were performed on Hysitron Tribometer (Ti950) by applying a load of $6000\ \mu\text{N}$ at a loading and unloading rate of $600\ \mu\text{N/s}$. Fifteen number of indentations were performed to get an average value of the responses. The hardness (H) was obtained using expression $H = P_{\text{max}}/A d_c$ in GPa, where P_{max} is the maximum applied load (in N), A is the contact area (in mm^2) and d_c is the contact depth (in mm) [5]. The elastic modulus (E) of the substrates was evaluated using $E = (1-\nu^2)/[(1/E_r) - \{(1-\nu_i^2)/E_i\}]$ where ν is the poisson's ratio of substrate and ν_i is the poisson's ratio of the indenter ($\nu_i = 0.07$) and ν , whereas E_r is the reduced modulus of elasticity (in GPa) and E_i is the modulus of elasticity of the indenter (in GPa) [5].

The wear properties of the substrate were determined by performing the nano-scratch test at a fixed load ($6000\ \mu\text{N}$) with a scratch length of $10\ \mu\text{m}$. The width and depth of the scratch track were determined using a three-dimensional profilometer made by EP Technologies (model: 500 LS). Wear properties such as scratch hardness (H_s) was calculated by expression $H_s = 2.31 (P_N/w^2)$, where maximum applied force is P_N (in N), the width of scratch is w in nm. Specific wear rate (SWR) was obtained using expression $\text{SWR} = \{V/(P \times L)\}$, where the volume of scratch is V (in m^3), normal load is P (in N) and sliding distance of indenter is L (in m).

3 Results and Discussion

3.1 Analysis of Microstructure

The microstructure of untreated AISI D3 tool steel exhibits white region with large elongated and non-uniformly distributed primary carbides and secondary carbides which are smaller compare to primary carbides (see Fig. 1a). Similar observation was reported by Naravade et al. [11]; however, upon heat treatment, the distribution of these carbides became uniform and their size also gets reduced as observed using optical microscopy (see Fig. 1b). This phenomenon improves the mechanical properties of the tool steel. Further, improvement in the mechanical properties plasma nitriding tool steel was also observed. During nitriding process, iron nitride was formed at ~ 550 °C with a low potential difference, as AISI D3 tool steel was nitrided above the critical potential of nitriding say ~ 1.88 for approximately 10 h γ -Fe₄N and ϵ -Fe₂₋₃N with small amounts of α -(Fe, N) were formed. With an increase in critical potential along with nitriding duration, the wear resistance got improved drastically as suggested in literature researchers [9, 12].

Peaks of un-tempered martensite were observed in the XRD pattern (see Fig. 2) of both the untreated and heat-treated AISI D3 tool steel. XRD pattern of heat-treated

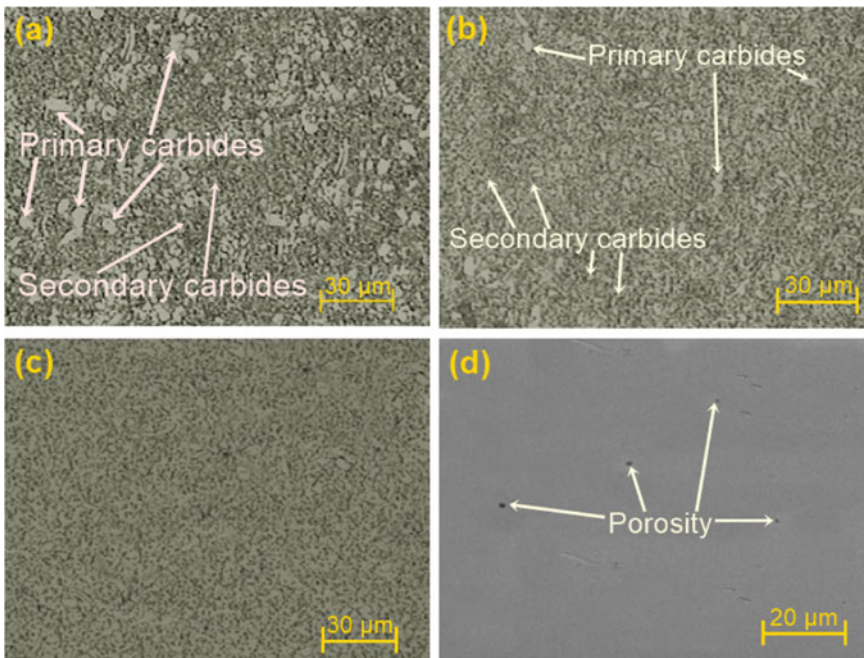
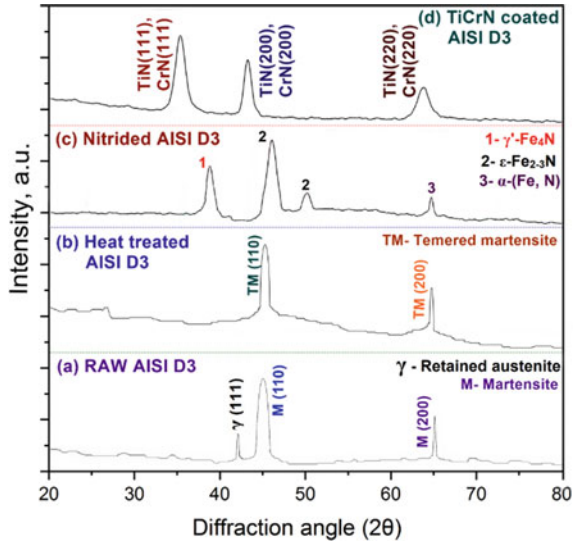


Fig. 1 OM image of **a** untreated, **b** heat-treated, **c** nitrided AISI D3 and FE-SEM image of **d** TiCrN coated AISI D3 tool steel

Fig. 2 XRD pattern of **a** untreated, **b** heat-treated, **c** nitrided and **d** TiCrN coated AISI D3 tool steel



AISI D3 tool steel exhibited tempered martensite at 45° and 65° (see Fig. 2b), similar peaks are reported in the previous study as well [13, 14]. For the nitriding sample, peaks of γ' -Fe₄N, ϵ -Fe₂₋₃N and α -(Fe, N) are visible at 42° , 45° and 65° respectively (see Fig. 2c), similar peaks were observed elsewhere [9, 12]. However, the XRD pattern of TiCrN coating exhibited two phases viz. TiN and CrN at 37° , 43° and 65° , respectively (see Fig. 2d). Xia et al. [15] have also observed similar peaks for TiCrN film.

3.2 Analysis of Nanomechanical Properties

Nanomechanical properties of the substrates were determined using nanoindentation test. Effect of normal applied load on the residual depth (h_r) was shown in Fig. 3, which depicts that untreated AISI D3 tool steel has higher residual depth compared to heat-treated, nitrided and TiCrN coated sample. Among these samples, TiCrN coated AISI D3 tool steel has the lowest residual depth which means hardness (H) of TiCrN coated tool steel is higher than the untreated, heat-treated and nitrided tool steel comparatively. The value of hardness and elastic modulus (E) was calculated using the expressions as mentioned in Sect. 2.2, respectively, and based on these values wear resistance (H/E) and plastic deformation resistance (H^3/E^2) were obtained. From Table 1, it can be said that hardness of AISI D3 tool steel increased in ascending order of 7.49 ± 2.81 , 10.16 ± 1.29 , 22.79 ± 3.18 after heat treatment, nitriding and TiCrN coating, respectively. Elastic modulus was also increased in the ascending order of 227.57 ± 8.69 , 240.73 ± 6.78 and 327.81 ± 7.63 after heat treatment, nitriding and TiCrN coating, respectively.

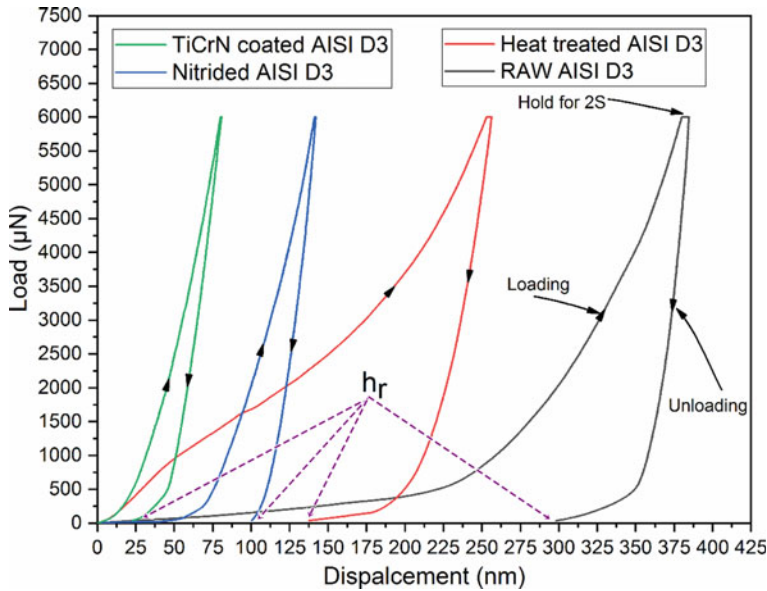


Fig. 3 Effect of load on displacement of indenter into the surface of the substrate

Table 1 Nanomechanical properties of untreated and surface treated AISI D3 tool steel

Substrate	Response of nanoindentation				
	Residual depth (h_r) in nm	Hardness (H) in GPa	Modulus of elasticity (E) in GPa	Wear resistance (H/E)	Plastic deformation resistance (H^3/E^2) in GPa
TiCrN coated AISI D3	23	22.79 ± 3.18	327.81 ± 7.63	0.0201	0.0015
Nitrided AISI D3	100	10.16 ± 1.29	240.73 ± 6.78	0.0329	0.0081
Heat treated AISI D3	143	7.49 ± 2.81	227.57 ± 8.69	0.0422	0.0181
Untreated AISI D3	300	3.81 ± 0.97	189.37 ± 5.71	0.0695	0.1102

3.3 Analysis of Wear Properties

Wear properties of the samples were investigated by conducting nanoscratch test. Under this analysis, specific wear rate, friction coefficient and scratch hardness were obtained. The value of these properties is tabulated in Table 2. From the results, it can be said that the scratch hardness of TiCrN coated tool steel is higher than the

Table 2 Nanoscratch properties of untreated and surface treated AISI D3 tool steel

Substrates	Nanoscratch properties		
	Friction coefficient (μ)	Scratch hardness (H_s) in GPa	Specific wear rate, (SWR) in m^2N^{-1}
TiCrN coated AISI D3	0.24	34.19	2.41×10^{-16}
Nitrided AISI D3	0.42	15.24	4.37×10^{-12}
Heat treated AISI D3	0.53	11.24	15.18×10^{-12}
Untreated AISI D3	0.67	5.72	8.97×10^{-8}

untreated, heat-treated and nitrided AISI D3 tool steel whereas friction coefficient and specific wear rate is comparatively lower. Scratch hardness of all the samples was higher than the nanoindentation hardness due to frictional force that exists at the interface of indenter and substrate during scratching. Untreated AISI D3 tool steel is ductile in nature with low hardness due to which it exhibits severe plastic deformation during scratching resulting in plowing (see Fig. 4a). However, heat treatment, nitriding and TiCrN deposition, increases the brittleness of the surface which might be due to the presence of residual stress in the surface material. SPM images of each sample are shown in Fig. 4. It can be seen that the width and depth scratch track for TiCrN coating is lower compare to other surfaces which is indicative of higher specific wear rate in untreated AISI D3.

4 Conclusion

AISI D3 tool steel substrate was heat-treated using conventional heat-treatment process. Further, hardened tool steel was nitrided by plasma nitriding followed by depositing TiCrN film to improve the mechanical properties of the surface. Surface characteristics were evaluated using optical microscopy, FE-SEM and XRD. And finally, nanoindentation and nanoscratch were performed to obtain the mechanical and wear properties of the surface. Based on the obtained results, following conclusions can be drawn:

- I. Upon heat treatment of AISI D3 tool steel, the primary carbides got converted into secondary carbides which are smaller in size and harder in nature. In addition, nitriding resulted in the formation of diffusion layer with different types of iron nitrides which enhances the surface properties the substrate.
- II. TiCrN film deposition resulted in the improvement in hardness of the substrate by 5.98 times upon compared heat-treated (1.97 times) and nitriding surfaces (2.67 times). A significant improvement in resistance to wear ($H/E = 0.0201$) and plastic deformation ($H^3/E^2 = 0.0015$) was also observed with TiCrN film deposition.
- III. Due to high hardness ($H = 22.79 \pm 3.18$) improved H/E ratio, TiCrN coated surface registered a narrow scratch wear track with low depth compared to

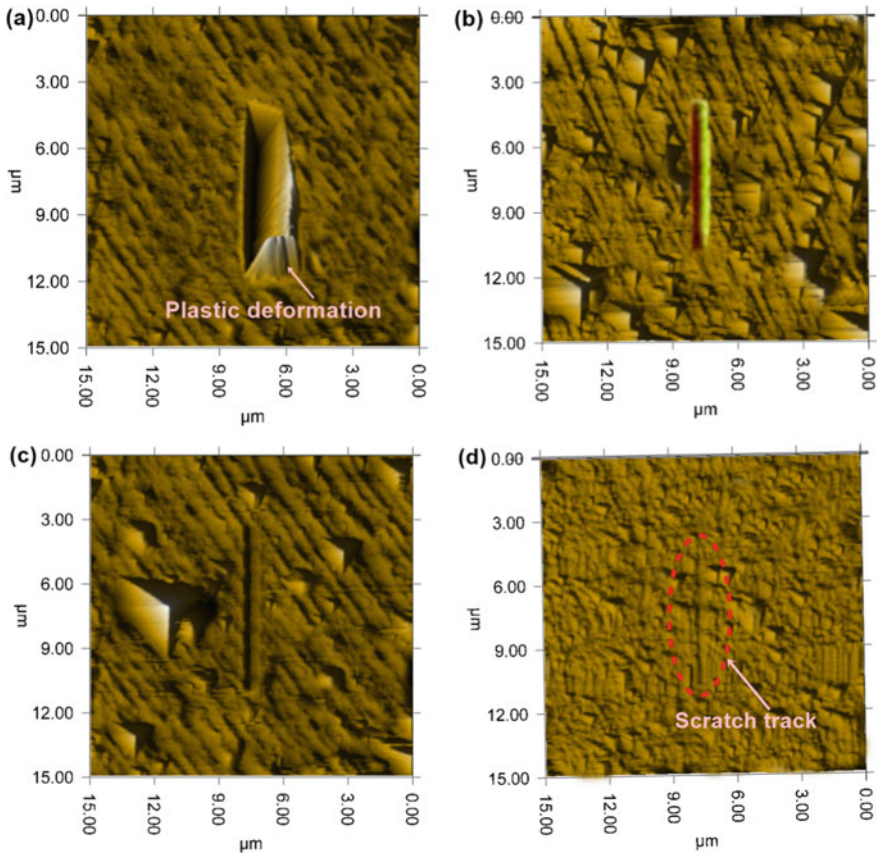


Fig. 4 SPM image of **a** untreated, **b** heat-treated, **c** nitrided and **d** TiCrN coated AISI D3 tool steel

untreated, heat-treated and nitrided AISI D3 tool steel. Moreover, specific wear rate ($2.41 \times 10^{-16} \text{ m}^2\text{N}^{-1}$) of TiCrN coated surface is much lower than the nitride ($4.37 \times 10^{-12} \text{ m}^2\text{N}^{-1}$) and heat-treated ($15.18 \times 10^{-12} \text{ m}^2\text{N}^{-1}$) AISI D3 tool steel.

References

1. Hiraoka H, Kataoka Y, Yuda K, Taniguchi K, Sasada M, Hishinuma I (1992) Application of a high chromium steel to roughing work rolls for hot strip mills. *ISIJ Int* 32(11):1177–1183. <https://doi.org/10.2355/isijinternational.32.1177>
2. Momeni M, Kheirandish S, Saghafian H, Hedjazi J, Momeni M (2014) Effects of heat treatment on mechanical properties of modified cast AISI D3 tool steel. *Mater Des* 54:742–747. <https://doi.org/10.1016/j.matdes.2013.09.002>

3. Cheng LC, Wu TB, Hu CT (1988) The role of microstructural features in abrasive wear of a D-2 tool steel. *J Mater Sci* 23(5):1610–1614. <https://doi.org/10.1007/BF01115699>
4. Patnaik L, Maity SR, Kumar S (2020) Comprehensive structural, nanomechanical and tribological evaluation of silver doped DLC thin film coating with chromium interlayer (Ag-DLC/Cr) for biomedical application. *Ceram Int* 46(14):22805–22818. <https://doi.org/10.1016/j.ceramint.2020.06.048>
5. Kumar S, Maity SR, Patnaik L (2020) Friction and tribological behavior of bare nitrided, TiAlN and AlCrN coated MDC-K hot work tool steel. *Ceram Int* 46(11):17280–17294. <https://doi.org/10.1016/j.ceramint.2020.04.015>
6. Patnaik L, Maity SR, Kumar S (2020) Mechanical and tribological assessment of composite AlCrN or a-C: Ag-based thin films for implant application. *Ceram Int*. <https://doi.org/10.1016/j.ceramint.2020.11.016>
7. Patnaik L, Maity SR, Kumar S (2020) Status of nickel free stainless steel in biomedical field: a review of last 10 years and what else can be done. *Mater Today Proc*. <https://doi.org/10.1016/j.matpr.2019.12.205>
8. Patnaik L, Maity SR, Kumar S (2021) DLC/CrN or AlCrN/CrN composite films: the better candidate in terms of anti-wear performance and lesser ion release in hip implant. *Mater Today Proc*. <https://doi.org/10.1016/j.matpr.2020.11.242>
9. Zhang F, Yan S, Yin F, He J (2018) Microstructures and mechanical properties of TiCrN/AlTiCr based coatings prepared by plasma nitriding 5083 Al alloys co-deposited with TiCr films. *Vacuum* 157:115–123. <https://doi.org/10.1016/j.vacuum.2018.08.039>
10. Huang M, Chen Z, Wang M, Li Y, Wang Y (2016) Microstructure and properties of TiCrN coatings by arc ion plating. *Surf Eng* 32(4):284–288. <https://doi.org/10.1179/1743294415Y.0000000039>
11. Naravade RH, Belkar SB, Kharde RR (2013) Effects of cryogenic treatment, hardening and multiple tempering on wear behavior of D6 tool steel. *J Eng Sci* 2–5
12. Bangari RS, Sahu S, Yadav PC (2018) Comparative evaluation of hot corrosion resistance of nanostructured AlCrN and TiAlN coatings on cobalt-based superalloys. *J Mater Res* 33(8):1023–1031. <https://doi.org/10.1557/jmr.2018.53>
13. Kumar S, Maity SR, Patnaik L (2020) Effect of heat treatment and TiN coating on AISI O1 cold work tool steel. *Mater Today Proc* 26(2):685–688. <https://doi.org/10.1016/j.matpr.2019.12.367>
14. Amini K, Akhbarizadeh A, Javadpour S (2012) Investigating the effect of holding duration on the microstructure of 1.2080 tool steel during the deep cryogenic heat treatment. *Vacuum* 86(10):1534–1540. <https://doi.org/10.1016/j.vacuum.2012.02.013>
15. Xia FF, Liu C, Wang F, Wu MH, Wang JD, Fu HL, Wang JX (2010) Preparation and characterization of Nano Ni–TiN coatings deposited by ultrasonic electro deposition. *J Alloy Compd* 490(1–2):431–435. <https://doi.org/10.1016/j.jallcom.2009.10.026>

Performance Analysis of Split Circular and Drop-Form Fin Geometry for Enhanced Heat Transfer Rate



Alok Ranjan, Sagnik Pal, and Madhujit Deb

Abstract Thermal management of any devices has always been a challenge in order to get higher performance. Extended surfaces have shown its influential use in dissipating the heat from the heated region into the immediate surroundings. The wide range of fins application has established the research in this area. In this paper, computational work is forayed toward the thermal and flow analysis of the extended surfaces viz. circular and drop-form mounted over a base plate in staggered arrangement. Initially, the numerical work gets validated using empirical result available in the existing literature. The performance parameters for assessing the heat transfer phenomenon are h , Nu , C_f , η , C_p . The flow in the computational domain varies in the laminar regime, hence the laminar flow model has been considered. The value of the convective heat transfer coefficient is found to be 30% higher than the circular fin. Further, the transverse offset of $D/8$, $D/6$, $D/4$ and $D/2$ width has been made in both the circular and drop-form fin shape. Results shows, that the thermal enhancement factor is 13% higher for drop-form split at $TÓ = D/8$ width in comparison with circular fin geometry within the considerable amount of frictional loss. The circulation phenomenon at the wake region of the fin geometry is responsible for the higher rate of heat transfer. The modelling and simulation has been performed using ANSYS 19.2.

Keywords Extended surfaces · Finite volume method · Heat transfer co-efficient · Nusselt number

Nomenclature

A_X Cross section area of duct
 A_T Total surface area of fin
 C_f Coefficient of friction

A. Ranjan (✉) · S. Pal · M. Deb
Department of Mechanical Engineering, National Institute of Technology, Agartala, India
e-mail: aranjan359@gmail.com

© The Author(s), under exclusive license to Springer Nature Singapore Pte Ltd. 2023
T. S. Sudarshan et al. (eds.), *Recent Advancements in Mechanical Engineering*,
Lecture Notes in Mechanical Engineering,
https://doi.org/10.1007/978-981-19-3266-3_10

C_p	Coefficient of pressure
c_p	Specific heat (J/kg·K)
D	Diameter of cylindrical fin (mm)
h	Film coefficient (W/m ² ·K)
h	Height of fin (mm)
K	Thermal conductivity (W/m K)
L_c	Characteristic dimension (mm)
L	Length of base plate (mm)
Nu	Nusselt number
P	Outlet pressure (Pa)
Pr	Prandtl number
Q	Heat flux (W/m ²)
Re	Reynolds number
S_l	Longitudinal pitch (mm)
S_t	Transverse pitch (mm)
T	Thickness of base plate (mm)
T_1	Isothermal inlet temperature (K)
T_2	Outlet temperature (K)
T_3	Average fin temperature (K)
U_∞	Free stream velocity of air in (m/s)

Abbreviation

T_O Transverse offset (mm)

Greek symbols

α	Thermal diffusivity (m ² /s)
μ	Dynamic viscosity (Pa·s)
ν	Kinematic viscosity (m ² /s)
ρ	Density (kg/m ³)
η	Thermal enhancement factor

1 Introduction

Thermal management of devices like CPU, vehicle battery, aero plane refrigeration system, engines, nuclear reactors, etc., are very important in order to get higher performance during its functionality. So in that way, we have seen that extended surfaces

which play a vital role in dissipating the heat in its local surrounding. Extended surfaces are nothing but an extra surface attached to the heat generating part of the device. Through the extra surface, heat can easily get conducted and simultaneously dissipated via convection into the immediate surroundings. Although, numerous shapes of fins viz. cylindrical, elliptical, drop, rectangular, square, triangular, reverted triangular, diamond etc., have been designed and studied both numerically and experimentally. Out of mentioned shapes the cylindrical, elliptical and drop fins are streamlined in nature, which in turn provides an ease to flow of fluid over it and also gives better heat transfer performance. Wang and Tao [1] have done study over the inclination of plate fin angle to the upcoming air flow and found that, an increase in the oblique angle along with the length of plate fin its heat transfer rate gets increased. Laor and Kalman [2] have presented the numerical correlation upon analytic study of cylindrical, conical and parabolic spines along with the longitudinal and annular fins for knowing its thermal behavior. Yang and Peng [3] have done numerical analysis of plate and circular-plate fins and found that the circular-plate fins are more beneficial in terms of thermal performance. Yang and Peng [4] have examined the effect of fin height of the heat sink on the thermal performance and done numerical simulation on un-uniform fin height and found that, the junction temperature can be reduced by increasing the fin height near the center of the heat sink. Islam et al. [5] have experimentally analyzed the effect of channel height on heat transfer and found that, due to the flow separation from fin edge and the formation of the vortex, there are increments in frictional losses along with heat transfer rate. Sara et al. [6] have worked for heat transfer and frictional characteristics analysis for array of a square cross section pin-fin for reducing the entropy generation by varying the clearance ratio and the inter fin distance. Yakut et al. [7] have done optimization using Taguchi method in order to analyze the thermal resistance and pressure drop characteristics for the hexagonal fins. Ndao et al. [8] worked experimentally for smooth and micro fins and found that, due to proper fluid mixing and boundary interruptions, the heat transfer rate has increased. Sajedi and Osanloo [9] have given the application of splitter plate on circular and square fin, and found that the splitter plates help in reducing the pressure drop along with the thermal resistance. Khan et al. [10] have proposed the empirical relations (h and Nu) based upon the laminar flow over pin-fin with longitudinal and transverse pitches.

In this paper, work is focused toward the thermal and flow analysis of the circular and drop-form shapes of fin. Initially, the validations of the work have been done for the circular fin with Khan et al. [10] and the results were promising. Further the drop-form shapes have been constructed by fixing the volume and height of the fin. Later on, the longitudinal offsets have been made to analyze the flow resistance and the thermal behavior of the proposed splitted drop-form shaped fin. The numerical analyses have been performed using ANSYS 19.2.

2 Geometry and Formulations

Numerical analysis has been performed in the given work by considering the circular shape fin of diameter $\text{\textit{D}}$, height h (17 in numbers) mounted over the base-plate of $118 \times 118 \text{ mm}^2$ with thickness t in staggered orient with S_L and S_T as longitudinal and transverse pitches, shown in Fig. 1. The cross-sectional view of circular, drop-form and split (both circular and drop-form) fin have shown in Fig. 2.

Now for this numerical approach, under the forced convection environment and at the steady state condition the circular fin has been analyzed. For that, a non-dimensional number known to be Nu , helps in decoding the comparative strength of the convection rate to the conduction rate need to be taken into account and is given by Eq. 2 (Eq. 1 helps in obtaining the convective heat transfer coefficient upon balancing the energy i.e., energy transferred to the fluid be equal to the input power to the fin assembly is given below).

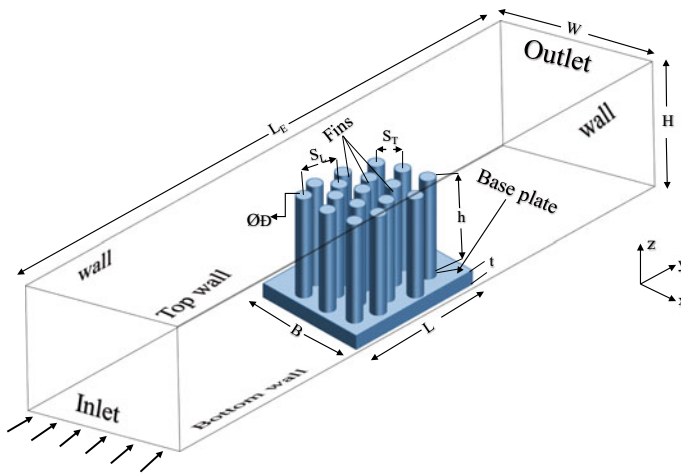


Fig. 1 Illustrative diagram of computational diagram

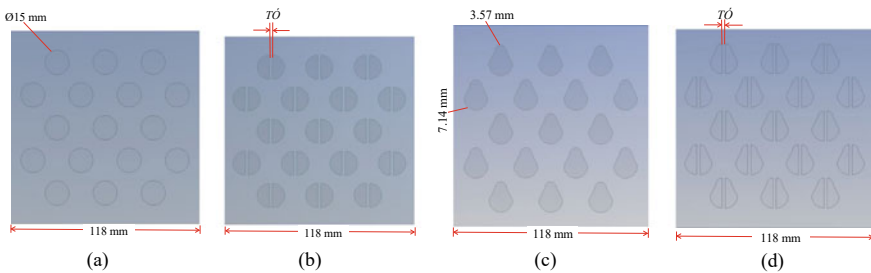


Fig. 2 Illustrative diagram of geometries of **a** circular **b** split circular **c** drop-form fins **d** split drop-form

$$h = \frac{\rho A_X V c_p (T_2 - T_1)}{A_T (T_3 - T_1)} \quad (1)$$

$$\text{Nu} = \frac{h \cdot L_c}{k} \quad (2)$$

Now, the hydraulic dimension L_C of the given shapes may influence the driving physics. In the present work, geometry of the fin is constructed by utilizing conduction–convection physics. Now for the simplification, the radiation mode of heat transfer has been neglected for the current work. The velocity field should be evaluated in order to get the solutions of mass (shown in Eq. 3) and momentum conservation equation (shown in Eq. 4). Along with that, the energy equation at steady state situation need to formalized, as shown in Eq. 5.

$$\nabla \cdot \vec{V} = 0 \quad (3)$$

$$\vec{V} \cdot \nabla \vec{V} = \frac{1}{\rho} \nabla p + \nu (\nabla^2 V) \quad (4)$$

$$\vec{V} \cdot \nabla T = k \cdot \nabla^2 T \quad (5)$$

The validation of work opens the door of performing new forms of research. The work done by Khan et al. [10] has been taken as a reference for validation of the circular shape geometry for enhancing the thermal performance. On considering the laminar model the Nu number is shown in Eq. 6,

$$\text{Nu} = \frac{h \cdot L_C}{k_f} = C_1 \text{Re}^{1/2} \text{Pr}^{1/3} \quad (6)$$

whereas, $\text{Re} = \frac{\rho U_{\max} L_C}{\mu}$. The $\text{Pr} = \frac{\nu}{\alpha}$ is a dimensionless number with fixed value of 0.71. With S_T , S_L and $S_D = \sqrt{(S_L^2 + (S_T/2)^2)}$ as the transverse, the longitudinal and the diagonal pitch, respectively, the co-efficient C_1 and the maximum velocity in the flow domain can be calculated using the following relations (mentioned in the reference Khan et al. [10]), as shown in Eqs. 7 and 8.

$$C_1 = \frac{0.61 S_T^{0.091} S_L^{0.053}}{[1 - 2 \exp(-1.09 S_L)]} \quad (7)$$

$$U_{\max} = \left\{ \max \frac{S_T}{S_T - 1} U_{\infty}, \frac{S_T}{2(S_D - 1)} U_{\infty} \right\} \quad (8)$$

For the present numerical work, the value of coefficient of skin friction has been evaluated in order to gauge the frictional drag. The coefficient of skin friction is defined as the ratio of the wall shear stress to the dynamic pressure on the fin geometry. The formula for assessing the drag is given by Eq. 9.

$$C_f = \frac{2\tau_s}{\rho U_\infty^2} \quad (9)$$

The thermal enhancement factor is the crucial term in order to gauge the heat transfer w.r.t., to the base fin. The thermal enhancement factor is expressed as the proportion of the comparative heat transfer to comparative frictional losses. The formula for thermal enhancement factor is given by Eq. 10.

$$\eta = \frac{\text{Nu}/\text{Nu}_o}{(C_f/C_{fo})^{1/3}} \quad (10)$$

Pressure drop is an important term that encompasses flow over a pin–fin. A higher pressure drop will have higher value of pumping power required to maintain a particular rate of flow. On the other hand, skin friction coefficient demonstrates the relative amount of wall shear stress per unit dynamic pressure. Presence of vortex motion in the downstream of flow over the fins leads to pressure drop at the outlet of the computational domain. Higher will be the strength of the vortex, a higher-pressure drop will be observed. So, in order to know about the pressure drop in well manner, we have pressure coefficient (C_p) which is the ratio of pressure drop at inlet and outlet to the dynamic pressure, as shown in Eq. 11.

$$C_p = \frac{\Delta P}{\frac{1}{2}\rho U_\infty^2} \quad (11)$$

where, ΔP static pressure difference at inlet and outlet of computational domain, ρ is fluid density, and U_∞ is free stream velocity.

3 Results and Discussions

The performance analysis of split drop-form shape has been presented in this present work. At first, 17 numbers of fins mounted over the base plate of dimension $118 \times 118 \times 5 \text{ mm}^3$ is placed inside the computational domain shown in Fig. 1 is analyzed. The numerical simulation has been performed for different air flow inlet velocity and upon considering flow to be laminar, steady and fully developed. The results obtained for h and Nu were compared with the empirical relations given by Khan et al. [10] as shown in Fig. 3. On validation, it was seen that, as the value of inlet flow velocity gets increase, the value of h and Nu also gets increases. For the maximum velocity of flow ($= 2.25 \text{ m/s}$), the value of Nu is highest, which reveals the fact that, the local Re number reaches the transition zone as the flow velocity increases. The current results obtained using Ansys 19.2 diverges from the empirical one with maximum and minimum of 6.8% and 0.3% at flow inlet velocity of 1 and 2.25 m/s, shown in Table 1. The grid independent test were executed with tetrahedral grid and found

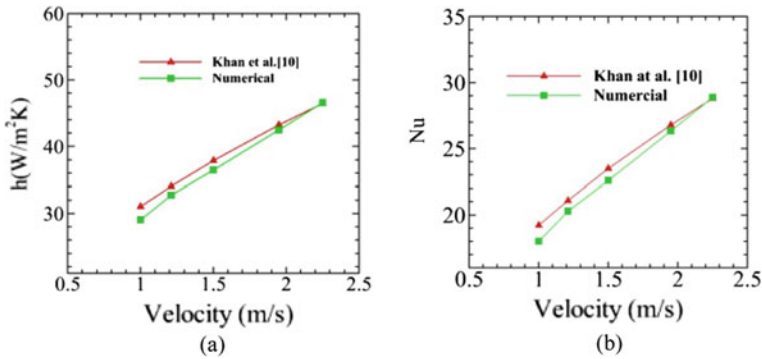


Fig. 3 Comparison of h and Nu with empirical results at different inlet flow velocity

Table 1 Validation results of Nu and h

V (m/s)	Nu		h (W/m ² K)		% error	
	Numerical result	Khan et al. [10]	Numerical result	Khan et al. [10]	Nu	h
1.0	18.00	19.23	29.04	31.02	6.8	6.8
1.21	20.29	21.10	32.73	34.05	4.0	4.0
1.5	22.60	23.50	36.47	37.91	3.9	3.9
1.95	26.32	26.79	42.46	43.22	1.8	1.8
2.25	28.88	28.78	46.59	46.43	0.3	0.3

that approx. 2.0×10^6 numbers of elements are involved in solving the governing physics.

3.1 $T\acute{O}$ Variation in Circular and Drop-Form Split

After the validation of circular shape of fin with khan et al. [10], analysis is directed toward making $T\acute{O}$'s with the $\mathcal{D}/8$, $\mathcal{D}/6$, $\mathcal{D}/4$, and $\mathcal{D}/2$ width in the circular as well as drop-from fins. For that the inlet flow velocity is taken as 1.5 m/s with considering the laminar flow model. The value of the h for drop-form fin is obtained to be 46.66 W/m²K, which is approximately 30% higher than circular fin shown in Fig. 4. Now the comparison has been made for the circular splits with its regular form and it is found that at $T\acute{O} = \mathcal{D}/8$, $\mathcal{D}/6$, and $\mathcal{D}/4$, the value of h is found to be increased by 62, 47 and 23%. For $T\acute{O} = \mathcal{D}/2$ the value of h recedes by 16%, shown in Fig. 4. Similarly splits ($T\acute{O}$'s) of width $\mathcal{D}/8$, $\mathcal{D}/6$, $\mathcal{D}/4$, and $\mathcal{D}/2$ have been made for drop-form fin, and for that the value of h is increased by 88%, 84%, 74% and 0.5% in comparison with its regular shape, shown in Fig. 4. For $T\acute{O} = \mathcal{D}/8$ in circular and drop-form fins shape, the value of h is found to be highest in comparison with its regular form; it is because

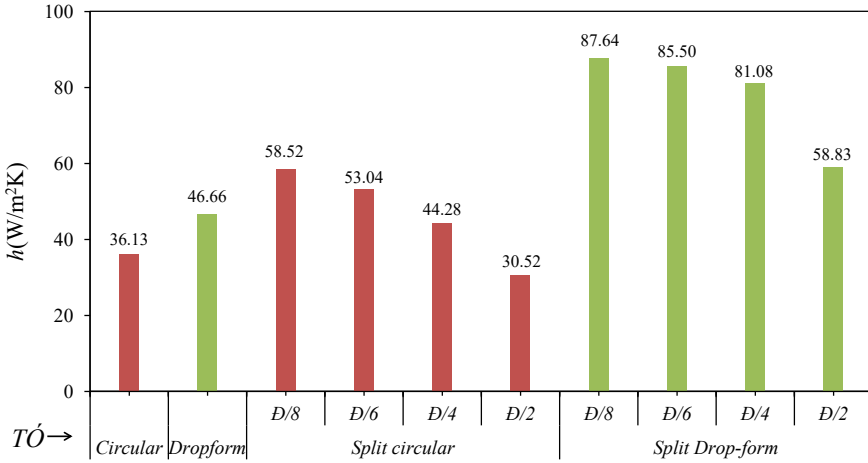


Fig. 4 Comparing h for circular, drop-form and its split shape fins at varying $T\acute{O}$ (*zero L\acute{O}*)

of the larger extent of circulation zone forming at fins trailing edge or at its wake region, shown in Fig. 5. The non-dimensional number Nu is directly proportional to the h , and its variation for both the splitted and un-splitted fins shape has been shown in Fig. 6.

The thorough study of C_f is very necessary for accounting the frictional losses in the system. The analysis of C_f may reveals about the heat transfer phenomenon

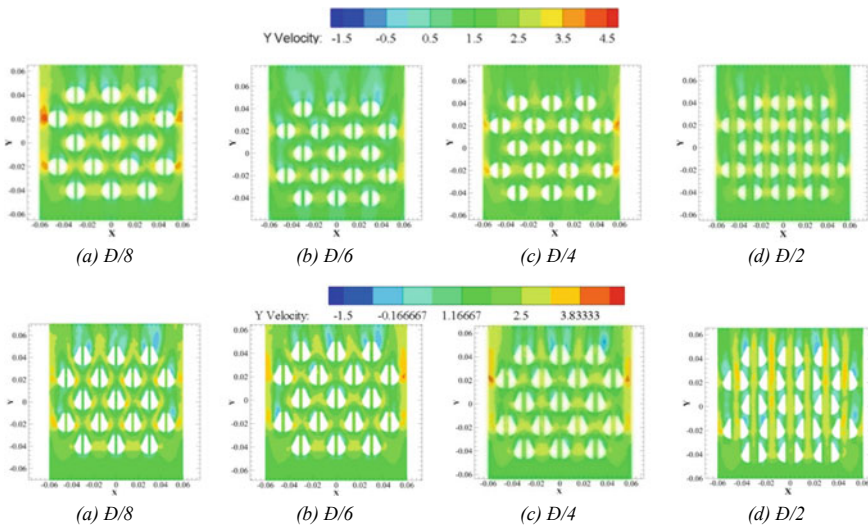


Fig. 5 Planner distribution of velocity in the flow domain for split fins of various shapes with $T\acute{O}$ of a, e, $D/8$ b, f, $D/6$ c, g, $D/4$ d, h, $D/2$ at $z = 56$ mm

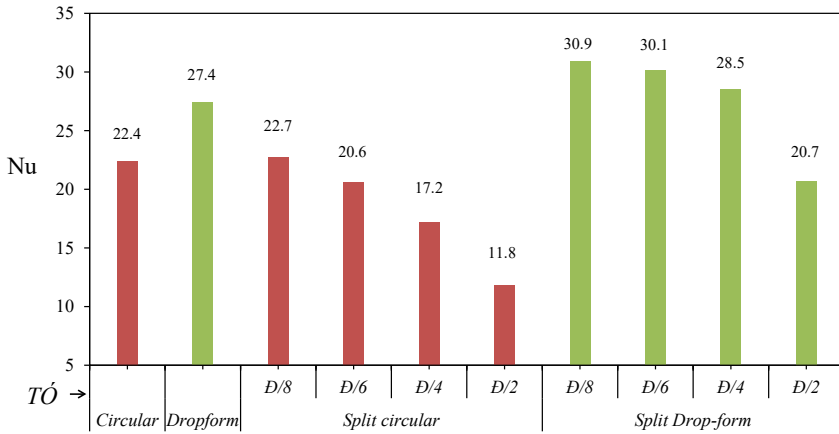


Fig. 6 Comparing Nu for circular, drop-form and its split shape fins at varying $T\acute{O}$ (zero $L\acute{O}$)

occurring in the computational domain. The C_f is defined as the ratio of the wall shear stress to dynamic pressure. For our work, at $T\acute{O} = D/8$ in both the circular and drop-form fins, the value of C_f is found to be improved by 16% and 28% in comparison with its respective regular shape, as shown in Fig. 7. The ease in fluid flow will be difficult at the lesser width of $T\acute{O}$, which in turns provides more amount of circulation zone and thus the value of C_f is highest for respective width.

The thermal enhancement factor plays a great role in order to determine the fin of higher performance in comparison with the base fin. The thermal enhancement factor is defined as the ratio of relative Nu to the relative frictional losses. Here, the circular fin is considered as the base fin, and the comparison has been shown in Fig. 8. At

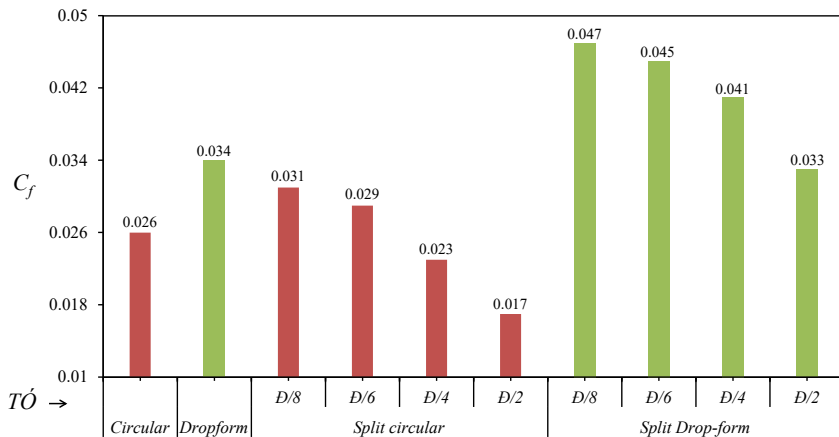


Fig. 7 Comparing C_f for circular, drop-form and its split shape fins at varying $T\acute{O}$ (zero $L\acute{O}$)

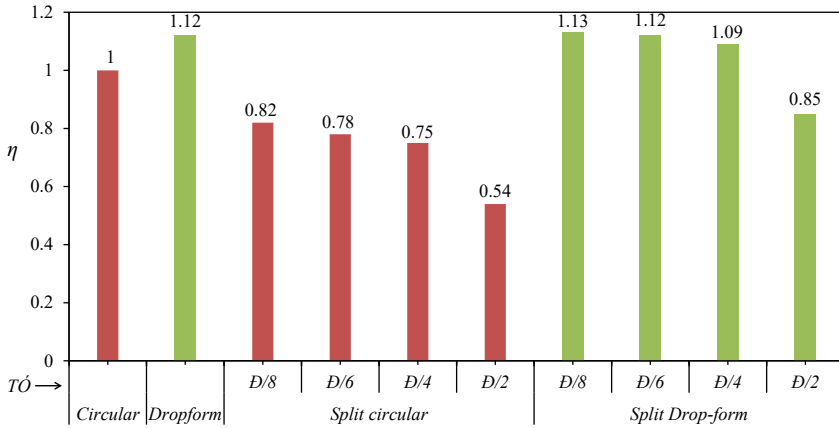


Fig. 8 Comparing η for circular, drop-form and its split shape fins at varying $T\acute{O}$ (zero $L\acute{O}$)

$T\acute{O} = D/8$, the value thermal enhancement factor is found to be 1.13, which is 13% higher than the base circular fin, shown in Fig. 8.

The coefficient of pressure term is very important in order to decode the pressure drop (in between the inlet and outlet), for the better functioning of the any system. Here the pressure drop has been accounted for the circular, split circular, drop-form, and split drop-form fins geometry in the square duct. The highest value (= 4.83) of coefficient of pressure has been shown by split circular fin geometry of $T\acute{O} = D/8$. For the drop-form fin shape, the value of C_p is found to be 4.30. Over splitting the drop-form fin geometry from $T\acute{O} = D/8$ to $D/4$, the value of C_p gets approximately increased by 38%, 36.53% and 13.46% as compared to circular fin geometry, shown in Fig. 9. Similarly for the split circular fin geometry ($T\acute{O} = D/8$ to $D/6$), the value

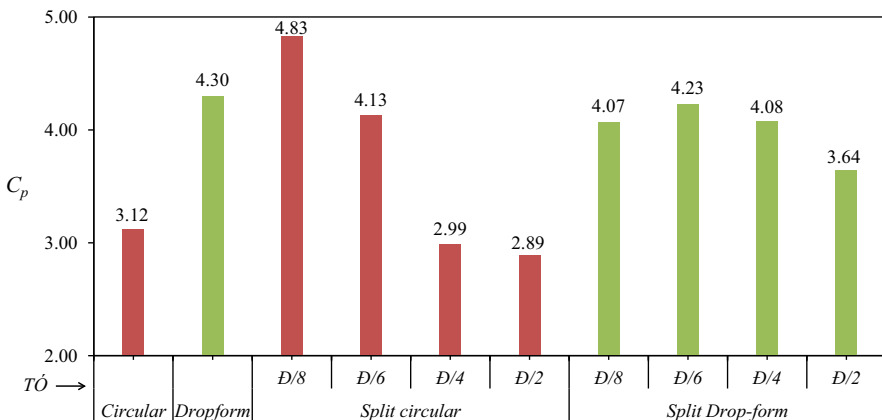


Fig. 9 Comparing C_p for circular, drop-form and its split shape fins at varying $T\acute{O}$ (zero $L\acute{O}$)

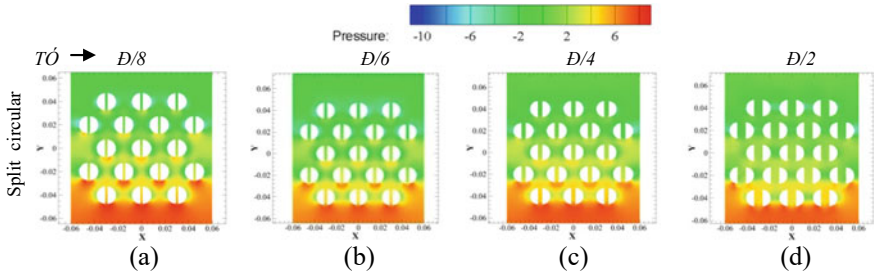


Fig. 10 Pressure drop plot for circular and its split shape fins at varying $T\acute{O}$ (zero $L\acute{O}$)

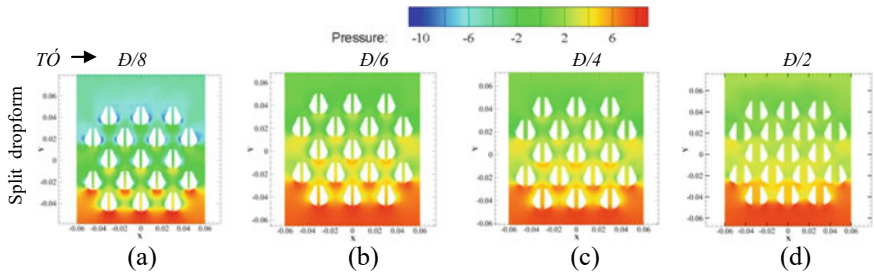


Fig. 11 Pressure drop plot drop-form and its split shape fins at varying $T\acute{O}$ (zero $L\acute{O}$)

of C_p gets increased by 54.80% and 32.37%, while for $T\acute{O} = D/4$, the value gets recedes by 4.34%, shown in Fig. 9. More pressure drop reveals the role of the friction in dissipating heat into the surrounding along with the pumping power. More will be the pressure drop; high will be the cost of pumping power. For the split circular fin of $T\acute{O} = D/8$, the value of C_p found to be highest. Figures 10 and 11 show the variation of pressure across the fin geometry.

4 Conclusions

Thermal and fluid flow behavior has been scrutinized for the circular fin, drop-form fin and its splits ($L\acute{O}$ & $T\acute{O}$) shapes using numerical simulation in ANSYS 19.2. For the validation of the numerical results, Khan et al. [10] has been used. The maximum (6.8%) and minimum (0.3%) error have accounted for the air flow velocities of 1 m/s and 2.25 m/s.

Conclusions drawn from the analysis are mentioned below:

- The value of h for drop-form fin is obtained to be 46.66 W/m²K, which is approximately 30% higher than circular fin. This is because of the lesser windward blockage of the flow at the wake region of the drop-form fin.

- On making splits, the effective surface area of the fin geometry gets increased, which allow the fluid to excesses more contact area.
- As the width of the $T\acute{O}$ gets varies from $D/8$ to $D/2$, the value of performance parameters also gets recedes, it is because of the ease in flow of fluid in between the width gap.
- In comparison of circular splits, the thermal enhancement factor is obtained to be highest for drop-form split fin with $T\acute{O} = D/8$ by 13%.
- The highest value of C_p ($= 4.83$) has been shown by circular split fin geometry (at $T\acute{O} = D/8$).

Acknowledgements Department of Chemical Engineering, NIT Agartala PIN-799046, India.

References

1. Wang LB, Tao WQ (1995) Heat transfer and fluid flow characteristics of plate-array aligned at angles to the flow direction. *Int J Heat Mass Transf* 38(16):3053–3063
2. Laor K, Kalman H (1996) Performance and optimum dimensions of different cooling fins with a temperature—dependent heat transfer coefficient. *Int J Heat Mass Transf* 39–9:1993–2003
3. Yang YT, Peng HS (2009) Investigation of planted pin fins for heat transfer enhancement in plate fin heat sink. *Microelectron Reliab* 49:163–169
4. Yang YT, Peng HS (2009) Numerical study of the heat sink with un-uniform fin width designs. *Int J Heat Mass Tran* 52:3473–3480
5. Islam MD, Oyakawa K, Yaga M, Kubo I (2009) The influence of channel height on heat transfer enhancement of a co-angular type rectangular finned surface in narrow channel. *Int J Therm Sci* 48:1639–1648
6. Şara ON, Yapıcı S, Yılmaz M (2001) Second law analysis of a rectangular channels with square pin-fin. *Int Commun Heat Mass* 28:617–630
7. Yakut K, Alemdaroglu N, Kotcioglu I, Celik C (2006) Experimental investigation of thermal resistance of a heat sink with hexagonal fins. *Appl Therm Eng* 26:2262–2271
8. Ndao S, Lee HJ, Peles Y, Jensen MK (2012) Heat transfer enhancement from micro pin fins subjected to an impinging jet. *Int J Heat Mass Transf* 55:413–421
9. Sajedi R, Osanloo B, Talati F, Taghilou M (2016) Splitter plate application on circular and square pin-fin heat sinks. *Microelectron Reliab* 62:91–101
10. Khan WA, Culham JR, Yovanovich MM (2008) Modeling of cylindrical pin-fin heat sinks for electronic packaging. *IEEE Trans Compon Packag Technol* 31–3:1521–3331

Effects of Thermal Aspect Ratio on MHD Thermal Convection of Cu–Water Nanofluid Saturated Porous Cavity



Milan K. Mondal, Nirmalendu Biswas, Aparesh Datta, Nirmal K. Manna, and Dipak Kumar Mandal

Abstract This work scrutinizes the thermal energy transportation under the effect of varying thermal aspect ratio through the porous substances in an enclosure packed with Cu–H₂O nanofluid subjected to an externally imposed magnetizing field. The square porous enclosed space is sinusoidally heated at the bottom based on various thermal aspect ratios (a) and cooled partially at the middle-half portion of the sidewalls. Considering the imposed condition of the thermal aspect ratios (a), the thermo-fluidic phenomena and allied thermal energy transport process altered markedly within the flow domain. The porous substance modeling is handled through Brinkman–Forchheimer–Darcy Model. The finite volume method is implemented for developing in-house computing code and the same is utilized for solving coupled transport equations. The study is conducted under the impact of various controlling variables like modified Rayleigh number (Ra_m), the permeability of the porous matrix (using Darcy number, Da), the strength of the magnetic field (using Hartmann number, Ha), nanofluid volume fraction (χ) and thermal aspect ratios (a). The thermal behavior of these cases is analyzed systematically and illustrated using streamlines, isotherms, heatlines contour, and heat transport characteristics. It is observed that the rate heat transfer is more at higher Ra_m with the increasing value of thermal aspect

M. K. Mondal

Department of Mechanical Engineering, M S Govt Polytechnic, Midnapur, West Bengal, India

N. Biswas (✉)

Department Power Engineering, Jadavpur University, Salt Lake City, Kolkata, India

e-mail: biswas.nirmalendu@gmail.com

A. Datta

Department of Mechanical Engineering, NIT-Durgapur, Durgapur, West Bengal, India

e-mail: adatta96@gmail.com

N. K. Manna

Department Mechanical Engineering, Jadavpur University, Jadavpur, Kolkata, India

e-mail: nirmalkmannaju@gmail.com

D. K. Mandal

Department of Mechanical Engineering, College of Engineering and Management, Kolaghat, India

e-mail: dipkuma@yahoo.com

© The Author(s), under exclusive license to Springer Nature Singapore Pte Ltd. 2023

T. S. Sudarshan et al. (eds.), *Recent Advancements in Mechanical Engineering*,

Lecture Notes in Mechanical Engineering,

https://doi.org/10.1007/978-981-19-3266-3_11

ratio still in the existence of porous substance under the impact of the magnetic field. As the Da value increases, the heat transfer rate decreases significantly. The inclusion of nanoparticles in the host liquid apparently improves the heat exchange rate ~ 0.11 – 2.15% .

Keywords Heatlines · Heat transfer · Nanofluid · Porous media · Sinusoidal heating · Thermal aspect ratio

Abbreviations

a	Thermal aspect ratio
B	Magnetizing field (Tesla)
Da	Darcy number
g	Gravitational acceleration (ms^{-2})
H	Cavity height (m)
Ha	Hartmann number
k	Thermal conductivity ($\text{Wm}^{-1} \text{K}^{-1}$)
K	Porous media permeability
Nu	Nusselt number
p	Pressure (Pa)
Pr	Prandtl number
Ra	Rayleigh number
Ra_m	Darcy-Rayleigh number
T	Temperature (K)
U, V	Dimensionless velocity
X, Y	Dimensionless coordinates

Greek symbols

α	Thermal diffusivity (m^2s^{-1})
β	Thermal expansion coefficient of fluid (K^{-1})
θ	Temperature in dimensionless form
μ	Dynamic viscosity ($\text{kgm}^{-1} \text{s}^{-1}$)
ν	Kinematic viscosity (m^2s^{-1})
ρ	Mass density (kgm^{-3})
σ	Electrical conductivity (Sm^{-1})
χ	Volumetric concentration of nanoparticles
ψ	Streamfunction in dimensionless form

Subscripts

<i>c, h</i>	Cold wall, hot wall
<i>f</i>	Base fluid
<i>s</i>	Solid

1 Introduction

Thermal management including basic flow physics of natural convective heat transfer under an external magneto-hydrodynamic (MHD) field through a porous substance is the key challenge in promising engineering mechanisms in the last few decades. Such situations are reflected in diverse technological applications such as MEMs, electronic appliances cooling, solar thermal application, food processing system, heat exchangers, chemical industry, and others. Consequently, thermal convection within the porous structure and MHD effect with heat sources and heat sinks, have always been a topic of interest [1–3]. Any localized heating and cooling causes more complex thermo-fluid phenomena in the presence of other multiphysical situations. In many exercises, available working fluid like hydraulic oils, water, ethylene glycol, air polymer solutions fails to rapid response to the heat exchange process. Thus, the addition of nano-sized material (like Cu, Al, Ag, Al₂O₃, Fe₃O₄, and TiO₂) into the base fluid shows considerable improvement in heat transfer [4]. Furthermore, induced horizontal magnetic fields can alter effectually the hydrothermal performances and related heat transport in numerous industrial applications even in biomedical appliances [5]. On the above background, the present work is formulated considering MHD combined free convection of nanofluid packed porous geometry heated sinusoidally at the the bottom and partial cooling over the vertical walls.

In the available literature, several researchers have studied the thermal convection of pure fluid/nanofluid/hybrid nanofluid through porous structure with/without magnetic effect. Pordanjani et al. [6] studied the behavior of water-Al₂O₃ nanoliquid-filled porous enclosure under the effect of non-uniform or uniform heating under imposed inclined magnetic field. They observed that the sinusoidal heating profile corresponds to the highest heat transfer. In this context, Biswas et al. [7] reported the benefit of mean temperature-based heating either uniformly or non-uniformly in a porous enclosure. Later, Manna et al. [8] reported that spatial heating (following the sinusoidal heating profile) can be a way to improve heat transfer in a thermal-hydraulic system. The investigations by several researchers have shown the convective process of nanofluid/hybrid nanofluid flow in various cavities [3, 7–9]. Applying different boundary conditions, Ramakrishna et al. [10] reported the bouncy-induced convective phenomena in a porous enclosure containing different fluids. The thermo-magnetic convective process is carried out by Sheremet and Pop [11], Malik and Nayak [12], Javaherdeh and Najjarnezami [13], Vo et al. [14] through nanofluid and porous substance influenced by the sinusoidal heating condition. Cimpean et al. [15]

analyzed the thermal convection in an inclined porous cavity subjected to sinusoidal heating at the sidewalls. It is observed that sinusoidal heating significantly alters the thermal behavior of the cavity. In a recent study, the beneficial aspect of Cu–Al₂O₃–H₂O hybrid nanofluid heating effect under the influence of sinusoidal heating is carried out by Tayebi and Chamkha [16]. In other works, following the sinusoidal heating profile, buoyancy-driven convection of a nanofluid flow has been explored by Oztop et al. [17], and within a porous domain has been studied by Alsabery et al. [18]. A further detailed survey on the above could be found in refs. [3, 9].

From the immense pool of available literature, this is realized that the non-uniform spatial heating application is relevant in various thermal–hydraulic systems for enhanced heat transfer and proper management of it. Therefore, this work aims at the magneto-hydrodynamic thermal convection of Cu–H₂O filled porous enclosure heated sinusoidally. The fundamental aspect of the thermo-fluid phenomena under multiphysical scenarios considering spatial heating conditions has not been explored adequately. This motivates to carry out the present study. The sinusoidal heating profile is applied at the lower wall of the enclosure adopting the dimensionless parameter “thermal aspect ratio (a).” The heated fluid is cooled by releasing heat through the partially cold sidewalls. Therefore, this study is framed and motivated by the need to analyze the thermo-fluid performance of such a sinusoidally heated and cooled discretely under various important parameters. A list of involved parameters is modified Rayleigh number (Ra_m), the permeability of the porous matrix (using Darcy number, Da), the strength of the magnetic field (using Hartmann number, Ha), nanofluid volume fraction (χ), and thermal aspect ratios (a). The outcomes of the analysis are illustrated by local contours of isotherms, streamlines, heatlines, and global parameter Nusselt number (average). It is pertinent to mention that, the heatline is a visualization tool to illustrate thermal energy in the cavity from the hot wall to the cold wall. Implementation of thermal aspect ratio along with other multiphysical conditions is an innovative contribution in the research field.

2 Model Aspects and Simulation Approach

The diagrammatic representation of the nanofluid packed square porous enclosure with a sinusoidal bottom heat source (at T_h) and partially both side cold cavity (at T_c) in the presence of outside induced horizontal MHD field (with magnitude B) is given in Fig. 1. The computing area is a 2-D (in Cartesian coordinate) square enclosed space of height H (in length scale). The middle half section (with dimension $0.5H$) of the vertical sidewalls on either side are cooled isothermally (as $T_c < T_h$). The cavity is packed with homogeneous mixing of nanosized Cu particles in water as base fluid and filled with porous medium. The porous substance is expressed following the Brinkman-Forchheimer-Darcy model with the validity of LTE (local thermal equilibrium) involving nanoliquid and porous layers [3, 9]. The solid walls are impermeable and no-slip conditions over the walls are assumed. The fluid flow is presumed to be steady, Newtonian, incompressible, laminar and within Boussinesq

approximation. The conservation equations in the dimensionless form are derived [14, 17] as:

$$\frac{\partial U}{\partial X} + \frac{\partial V}{\partial Y} = 0 \quad (1)$$

$$\begin{aligned} \frac{1}{\varepsilon^2} \left(U \frac{\partial U}{\partial X} + V \frac{\partial U}{\partial Y} \right) &= -\frac{\rho_f}{\rho} \frac{\partial P}{\partial X} + \frac{\nu \text{Pr}}{\nu_f \varepsilon} \left(\frac{\partial^2 U}{\partial X^2} + \frac{\partial^2 U}{\partial Y^2} \right) \\ &\quad - \left(\frac{\nu \text{Pr}}{\nu_f \text{Da}} + \frac{F_c \sqrt{U^2 + V^2}}{\sqrt{\text{Da}} \varepsilon^{3/2}} \right) U \end{aligned} \quad (2)$$

$$\begin{aligned} \frac{1}{\varepsilon^2} \left(U \frac{\partial V}{\partial X} + V \frac{\partial V}{\partial Y} \right) &= -\frac{\rho_f}{\rho} \frac{\partial P}{\partial Y} + \frac{\nu \text{Pr}}{\nu_f \varepsilon} \left(\frac{\partial^2 V}{\partial X^2} + \frac{\partial^2 V}{\partial Y^2} \right) \\ &\quad - \left(\frac{\nu \text{Pr}}{\nu_f \text{Da}} + \frac{F_c \sqrt{U^2 + V^2}}{\sqrt{\text{Da}} \varepsilon^{3/2}} \right) V \\ &\quad - \frac{\rho_f}{\rho} \frac{\sigma}{\sigma_f} \text{Ha}^2 \text{Pr} V + \frac{(\rho\beta)}{\rho\beta_f} \text{Ra}_m \frac{\text{Pr}}{\text{Da}} \theta \end{aligned} \quad (3)$$

$$\left(U \frac{\partial \theta}{\partial X} + V \frac{\partial \theta}{\partial Y} \right) = \frac{\alpha}{\alpha_f} \left(\frac{\partial^2 \theta}{\partial X^2} + \frac{\partial^2 \theta}{\partial Y^2} \right) \quad (4)$$

In above Eqs. (2) and (3), Da-terms represents the resistance caused by the porous structure following the BFDM model. The dimensionless parameters of U , V , X , Y , θ and P stand for the velocity, coordinate position, temperature, and pressure, respectively, as given below

$$\begin{aligned} (U, V) &= (u, v)H/\alpha_f; \quad (X, Y) = (x, y)/H; \\ P &= (p - p_a)H^2/\rho_f\alpha_f^2; \quad \theta = (T - T_c)/(T_h - T_c); \\ \text{Pr} &= \frac{\nu_f}{\alpha_f}; \quad \text{Da} = \frac{K}{H^2}; \quad F_c = \frac{1.75}{\sqrt{150}}; \\ \text{Ra} &= \frac{g\beta_f(T_h - T_c)H^3}{\nu_f\alpha_f}; \quad \text{Ra}_m = \text{Ra} \times \text{Da}; \quad \text{Ha} = BH\sqrt{\frac{\sigma_f}{\mu_f}} \end{aligned} \quad (5)$$

where, F_c is Forchheimer coefficient. The boundary conditions for the computational domain are:

- $\theta = 0$, $V = U = 0$, cold sidewalls ($X = 1, 0$ within $0.25 \leq Y \leq 0.75$),
- $\frac{\partial \theta}{\partial Y} = 0$, $V = U = 0$, adiabatic walls ($Y = 0, 1$),
- $V = U = 0$, $\theta = a + (1 - a) \sin(\pi X)$ for the bottom heated wall (i.e. at $Y = 0$).

where a stands for the non-dimensional thermal aspect ratio [$a = (T_h - T_c)/(T_h - T_c)$] and it can vary between 0 and 1. When $a = 0$, it implies to non-uniform heating

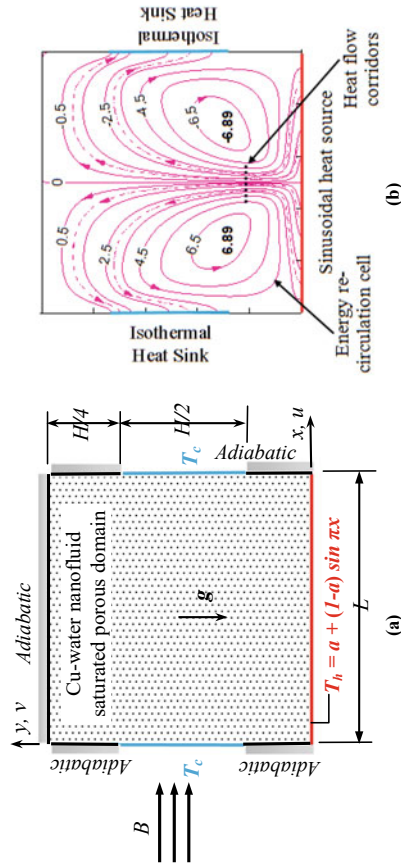


Fig. 1 **a** Physical geometry of the computational domain including boundary conditions and **b** heat energy flow structure

condition, and $a = 1$, corresponds to a heating condition as an isothermal condition. For the calculation of global heat transfer rate at the sinusoidal bottom heated split cold sidewalls, the Nusselt number Nu (average) is estimated as

$$Nu = \left(\frac{k}{k_f}\right) \int_{0.25}^{0.75} \left(-\frac{\partial\theta}{\partial X}\Big|_{X=0,1}\right) dY \tag{6}$$

The fluid flow contours are generated through the streamlines and is obtained by solving the streamfunction (ψ), which is given as

$$\frac{\partial\psi}{\partial Y} = U \text{ and } -\frac{\partial\psi}{\partial X} = V \tag{7}$$

Furthermore, the visualization of heat-energy transfer corridors is carried out through heatlines. Heat function (Π) [3, 9, 19] is used to obtain headlines contour, which is given as

$$-\frac{\partial\Pi}{\partial X} = V\theta - \frac{k}{k_f} \frac{\partial\theta}{\partial Y} \text{ and } \frac{\partial\Pi}{\partial Y} = U\theta - \frac{k}{k_f} \frac{\partial\theta}{\partial X} \tag{8}$$

The thermo-fluid properties of water, signified by the subscript “ f ” with a fixed value of $Pr = 6.93$ and nanosized Cu-particles are given in Table 1 [20]. The Cu nanoparticles are computed by the volumetric fraction of nanoparticles (χ) dissolved in the host fluid. To obtain the mass density of nanofluid, specific heat and coefficient of thermal expansion following relations are enumerated

$$\begin{aligned} \rho &= (1 - \chi)\rho_f + \chi\rho_{Cu}; \quad (\rho C_p) = (1 - \chi)(\rho C_p)_f \\ &+ \chi(\rho C_p)_{Cu}; \quad (\rho\beta) = (1 - \chi)(\rho\beta)_f + \chi(\rho\beta)_{Cu} \end{aligned}$$

The thermal conductivity (k) effective electrical conductivity (σ), thermal diffusivity α , and effective absolute viscosity of nanofluid [20, 21] are set by

$$k = k_f \left[\frac{(k_s + 2k_f) - 2\chi(k_f - k_s)}{(k_s + 2k_f) + \chi(k_f - k_s)} \right];$$

Table 1 The properties of nanoparticles and base fluid

Properties	ρ (kgm ⁻³)	μ (kgm ⁻¹ s ⁻¹)	C_p (J kg ⁻¹ K ⁻¹)	K (W m ⁻¹ K ⁻¹)	β (K ⁻¹)
Water	997.1	9.09×10^{-4}	4179	0.613	21×10^{-5}
Cu	8933	–	385	401	1.67×10^{-5}

$$\sigma = \sigma_f \left[1 + \frac{3(\sigma_s/\sigma_f - 1)\chi}{(\sigma_s/\sigma_f + 2) - (\sigma_s/\sigma_f - 1)\chi}; \quad \alpha = \frac{k}{(\rho C_p)}; \quad \mu = \frac{\mu_f}{(1 - \chi)^{2.5}} \right] \quad (9)$$

The dimensionless governing Eqs. (1)–(4) and boundary conditions are computed through a written computing code following the FVM. The governing equations are discretized and then solved iteratively using SIMPLE algorithm [22] and TDMA approach. The iterative process is allowed by considering the residuals limit for the mass-defect to $<10^{-8}$ and 10^{-10} , separately. The developed solver has been checked through several numerical verification under buoyant and mixed convection problems [3, 9, 19, 23, 24]. In the present problem geometry, 200×200 uniformly allocated grid size is selected for the present computations after mesh sensitivity checking.

3 Results and Discussion

The present study scrutinized the impact of sinusoidal heating with the various thermal aspect ratio values on the heat transport and nanofluid flow through porous enclosure under the MHD effect. The cavity is heated sinusoidally at the lower horizontal wall and cooled partly at the middle half of the vertical walls. The impacts of different pertinent parameters are investigated extensively for wide ranges of parameters, keeping porosity ($\varepsilon = 0.8$) fixed. The present study is performed for Rayleigh-Darcy number ($Ra_m = 1$ to 10^4), Darcy value ($Da = 10^{-5}$ to 10^{-1}), Hartmann number ($Ha = 0$ to 50), thermal aspect ratio ($a = 0$ to 1.0), volume fraction, $\chi = 0$ to 2% . The results are presented using flow structure, static temperature allocation, the flow of thermal energy, and overall heat transfer rate (presented by the contours of streamlines, isotherms, and heatlines, and average Nu value, respectively).

3.1 Influence of Modified-Rayleigh Number (Ra_m)

The impact of varying modified-Rayleigh numbers ($Ra_m = 10$ to 10^4) are examined in Fig. 2 maintaining supplementary parameters constant ($Da = 10^{-3}$, $Ha = 30$, $\chi = 0.1\%$, $a = 0.5$) to signify the strength of present convective problem. Here top panels illustrate the superimposed plots of streamlines and isotherms; whereas the bottom panel illustrates heatlines contours. With the effect of bottom sinusoidal heating and symmetrical partial split cooling at the sidewalls, there appears one pair of the circulating cells within the cavity. Hot nanofluid adjoining to bottom wall goes upward and after being obstructed by the top insulated wall, flow divides in portion and travels toward the sidewalls. After rejecting heat through the sidewalls, cold fluid moves downward, which causes fluid circulation. At the lower $Ra_m = 10$, the heat effect is mainly administered by the mode of conduction. Thus, isotherms lines show

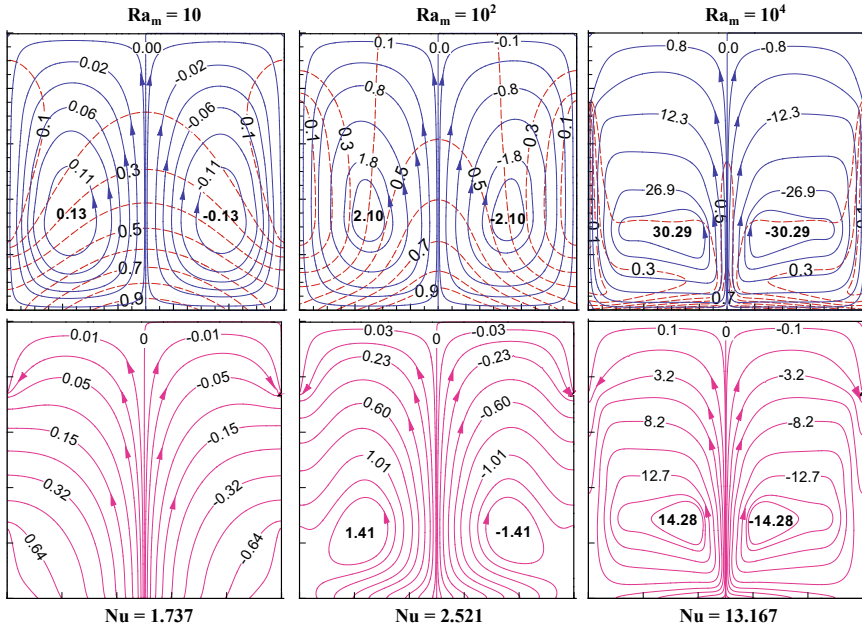


Fig. 2 Combined isotherm and streamlines (upper panel) and heatlines contour (lower panel) with varying Darcy-Rayleigh number (Ra_m) at $Da = 10^{-3}$, $Ha = 30$, and $\chi = 0.1\%$, $a = 0.5$

a peak value at the mid-point of the hot wall and then static temperature decreases gradually. The contours of heatlines clearly signify that energy flux from the bottom heat source travels toward partially cooled sidewalls on either side. The active heat flow symmetrically takes place in reference to the central vertical line.

When Ra_m value increases to 10^2 and 10^4 , the heat transfer mechanism is dictated by the convection mode. As a result, strong fluid circulation is noted from the maximum stream function value. At the higher Ra_m value,

circulating cells stretched horizontally and corresponding isotherms lines are clustered near the active lines. From the heatlines contours distribution, it is also pertinent that, with the increase in the Ra_m , corridors of heat energy-transportation decreases (with an increase in intensity) and guided by the heat-energy recirculation cells. Heat energy is directly transported through the active corridors. The temperature distributions denoted by isotherms vary curvilinearly because of the combination of temperature and imposed magnetic fields. Corresponding thermal boundary layer thickness lowers, and it shows higher heat transfer as shown by Nu values (below the heatlines contours). Mostly, the Nu value augments as Ra_m rises.

3.2 Effect of Thermal Aspect Ratio (a)

The increase in thermal aspect ratio ($a = 0, 0.5, \text{ and } 1$) in coupled isotherms-streamlines, heatline contours and value of average Nu are exemplified in Fig. 3 for the constant parameters as $Ra_m = 10^3$, $Da = 10^{-3}$, $Ha = 30$, $\phi = 0.1\%$. Thermal Aspect Ratio, $a = 0$ implies the heating effect is purely sinusoidal profile, whereas $a = 1$, denotes the bottom wall heated isothermally. It is evident that, the rise of a from 0 to 1 in the thermo-fluid porous enclosure causes to an rise in the fluid circulation intensity resulting in an augmentation in the heat exchange. This development of heat transport is due to the rise of a that leads to an growth in the effectual thermal behavior of the working medium. Therefore, development in buoyancy impact, and allied heat exchange rate enhances. Therefore, the heat transmission rate is improved when “ a ” increases compared to pure sinusoidal heating. This happens so “ a ” approaches to unity, the temperature of the bottom wall reaches to isothermal condition.

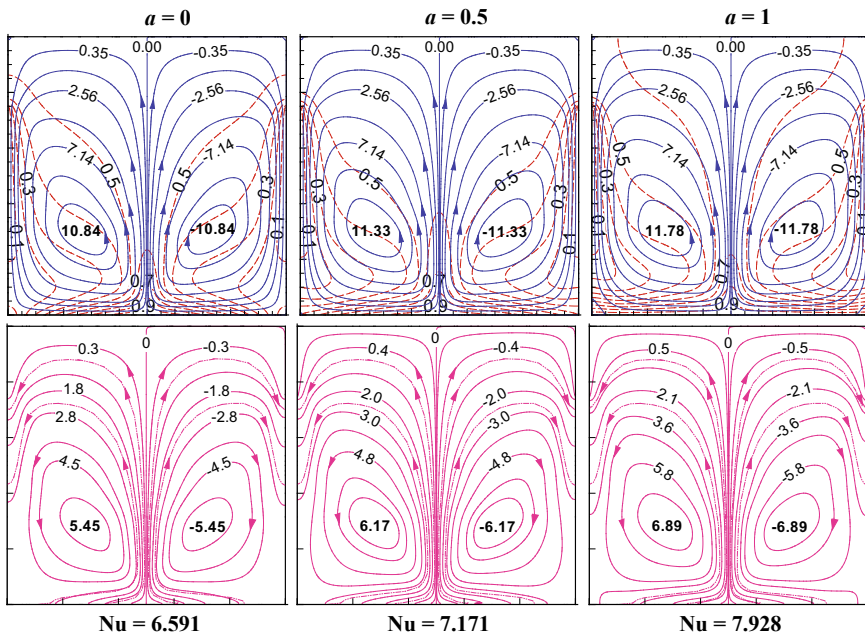


Fig. 3 Combined isotherm and streamlines (upper panel) and heatlines contour (lower panel) with varying thermal aspect ratio (a) at $Ra_m = 10^3$, $Da = 10^{-3}$, $Ha = 30$, $\phi = 0.1\%$

3.3 Impact of Permeability (Da)

Effects of permeability denoted by Darcy number under the MHD fields with constant parameters $Ra_m = 10^3$, $Ha = 30$, $\chi = 0.1\%$ and $a = 0.5$ are depicted in Fig. 4 for increasing Da ($= 10^{-4}$ to 10^{-1}). In general, a low magnitude of Da is associated with elevated resistance in the porous structure. Hence, combined energy transmission and fluid flows acquire within the confined boundaries with high resistivity, subsequently increase in Nu value. With the augmentation of Da to 10^{-1} , as anticipated with the improved permeability have a low resistance to flow. Symmetrical-circulations forms in the streamlines as well as heatlines. Analogous isotherms are symmetrical but distributed in a twisted manner from the hot wall to the cold wall. For the fixed Ra_m , an increase in Da means a reduction in the fluid-based Ra (since, $Ra_m = Ra \times Da$). Thus, fluid-based Ra indicates a lesser buoyant convection at $Da = 10^{-1}$ (as $Ra = 10^4$) in comparison with $Da = 10^{-4}$ (as $Ra = 10^7$). Thus, on the whole heat transfer reduced significantly as reproduced by the average Nu .

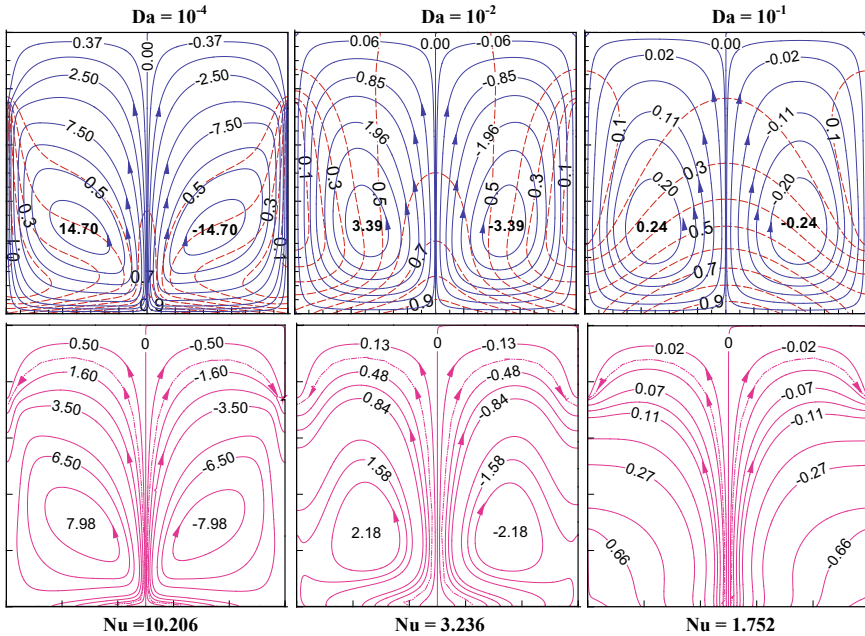


Fig. 4 Combined isotherm and streamlines (upper panel) and heatlines contour (lower panel) with varying Da at $Ra_m = 10^3$, $Ha = 30$, and $\chi = 0.1\%$, $a = 0.5$

3.4 Influence of the Strength of Magnetic Field (Ha)

The magneto-hydrodynamic (MHD) impact due to externally imposed horizontal field (denoted by Ha) in the contours of coupled isotherms-streamlines and heatlines contour are visualized in.

Figure 5 for changing value of $Ha = 0$ (indicates no magnetic field), 10, 50 maintaining other parameters constant at $Ra_m = 10^3$, $Da = 10^{-3}$, $\chi = 0.1\%$, and $a = 0.5$. For the ease of perception, no magnetic field condition ($Ha = 0$) is inspected also as illustrated in Fig. 4 (first column). The energy-fluid flow configuration explains symmetrical allocation with reference to the middle vertical plane. Now, to strengthen the induced field by rising the Ha magnitude equal to 10, 50, there is no such change is noted in the overall flow pattern with no magnetic field. Conversely, the convection-dominated circulation turns out to be weaker (as reflected by maximum stream function magnitude). This guides to poor heat exchange rate and this diminution are greatest at elevated $Ha = 50$. On the whole, the heat transfer decrement is about 0.74–14.97% compared to no magnetic field, $Ha = 0$.

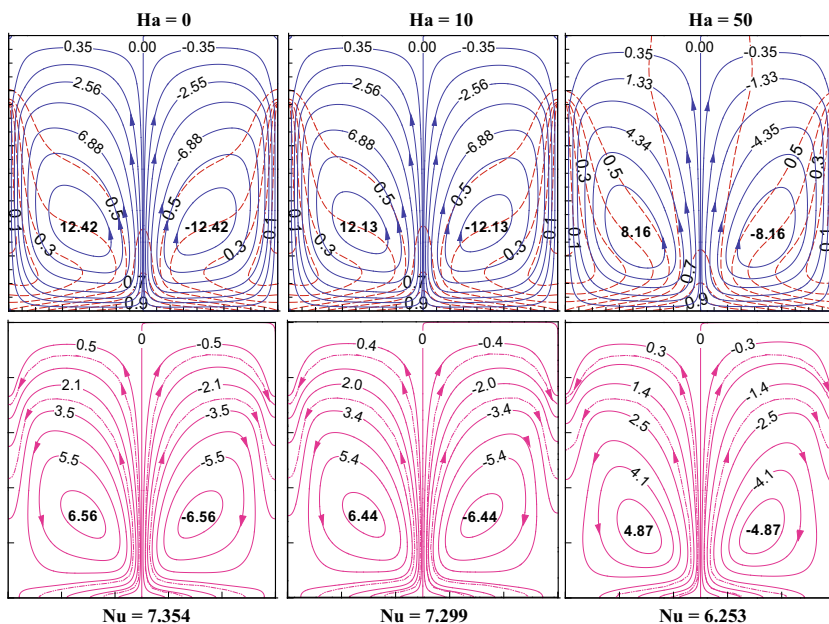


Fig. 5 Combined isotherm and streamlines (upper panel) and heatlines contour (lower panel) with varying Hartmann number (Ha) at $Ra_m = 10^3$, $Da = 10^{-3}$, and $\chi = 0.1\%$, $a = 0.5$

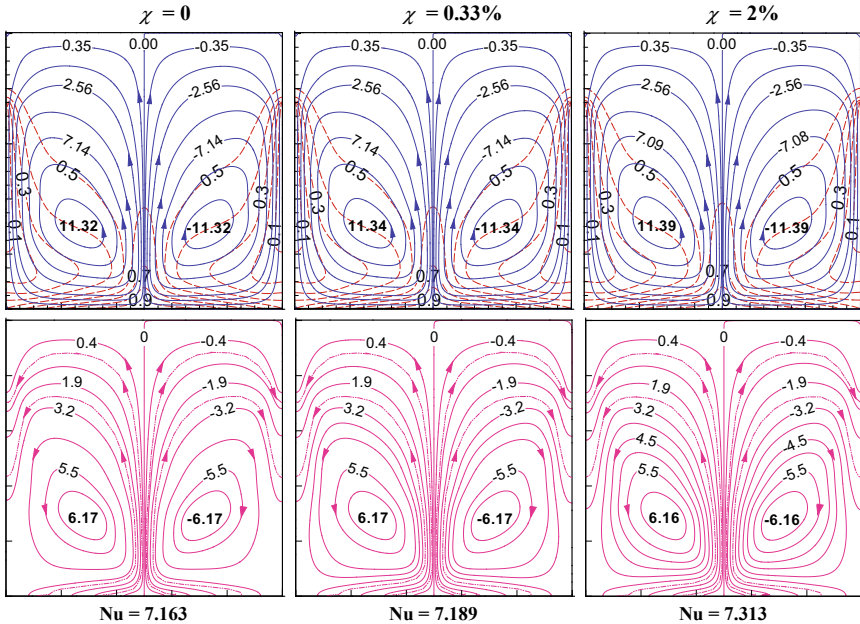


Fig. 6 Effects of nanoparticles concentration (χ) on the combined isotherm and streamlines (upper panel) and heatlines contour (lower panel) at $Ra_m = 10^3$, $Da = 10^{-3}$, $Ha = 30$, $a = 0.5$

3.5 Effect of Nanoparticles Volume Concentration (χ)

The augmentation in nano-dimension Cu particles volume concentration χ ($= 0, 0.33\%$, and 2%) on the three type contours and Nu value are exemplified in Fig. 6 at constant parameters of $Ra_m = 10^3$, $Da = 10^{-3}$, $Ha = 30$, $a = 0.5$.

This is significantly noted down that, blending of nanoparticles in the water causes to a rise in the flow intensity, consequently boosting in the heat transfer. This augmentation is because of the increase in χ dominates that augments in effective thermal conductivity of the working fluid and thus the enhancement in the buoyant force, and heat transport. Therefore, the heat transfer augmentation is in the range of $0.35\text{--}2.09\%$ comparison to the host fluid ($\chi = 0$).

3.6 Assessment of Heat Transfer Rate

Diagrammatic allocation of mean Nu value with varying thermal aspect ratio, (a) are presented in Fig. 7a to d for the different Ra_m , Ha , Da , and χ at constant values of other pertinent parameters. The effect of Ra_m under different values of a are depicted in Fig. 7a at other fixed parameters. The figure undoubtedly reveals that,

with the augment Ra_m , Nu enhances for every a value. In the porous substance, an increase in Ra_m corresponds to the flow resistance increase (as $Da = 10^{-3}$, fixed), and also the blending of nano-sized particles rises the effectual thermal conductivity of nanofluid medium; it shows the way to increase the flow strength. As a consequence, more energy flux is transported from sinusoidal heated sources to partial sidewall sinks. So, heat transfer is enhanced by changing the Darcy-Rayleigh number ($Ra_m = 10-10^4$).

Figure 7b, shows Nu curves have a consistently declining tendency with the rising Da with other parameter fixed. The trend is almost alike for all a values, with the exception of $Da = 10^{-2}$ to 10^{-1} (as Nu values show almost the same decreasing trend). The cause behind this information may be recognized by scrutinizing the flow contour pattern at higher Da (refer to Fig. 3). In addition, the choice of the Da value influences the thermo-fluid flow heating and cooling process. In general, the decrement rate of heat transport with varying Da ($= 10^{-4}-10^{-1}$) is noted.

Figure 7c shows Nu curves have a constantly declining trend with the getting higher Ha (for $\chi = 0.1\%$). This can be explained in the governing Eq. (3) for the existence of the “-ve” source term by Ha , which counteracts the buoyancy impact. The declining tendency is just about alike for all “ a ” apart from $Ha = 50$ (with Nu

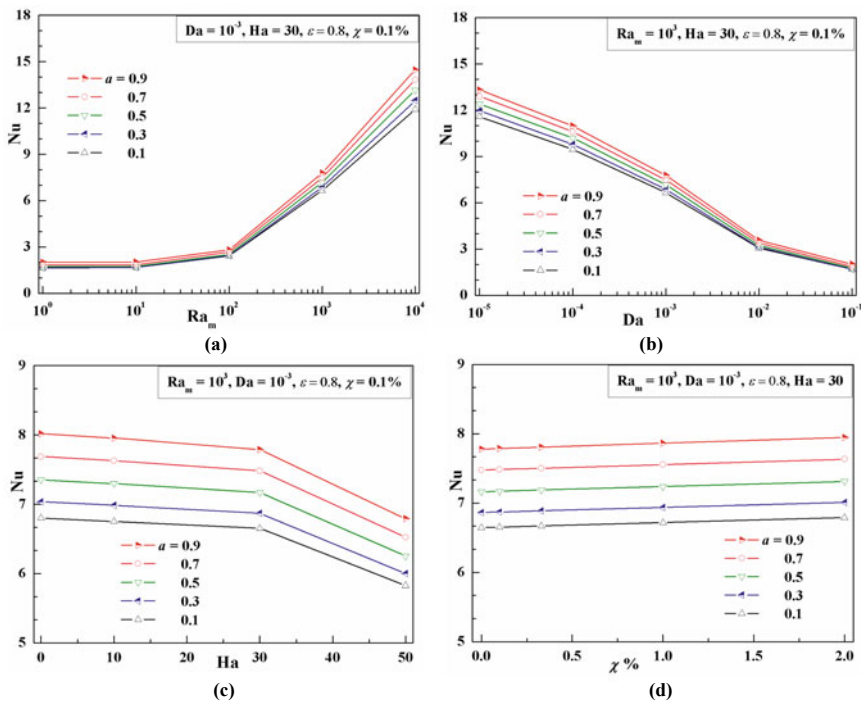


Fig. 7 Overall heat transfer rate (average Nu value) with changing **a** Ra_m , **b** Da , **c** Ha , and **d** χ for different a

curve shows a sharp decreasing trend). The basis behind this phenomenon may be accepted by scrutinizing the flow contour pattern at higher Ha (as reflected in Fig. 5). The buoyancy strength is counteracted by the magnetic field. Consequently, heat transport progression is altered rigorously. Therefore, choosing a value critically influences the thermal management of the flow domain. However, the heat transfer decrement varying $Ha = 10\text{--}50$ is about 0.69–14.30% (for $a = 0.1$), 0.74–14.97% (for $a = 0.5$), 0.78–15.27% (for $a = 0.9$) in comparison with no magnetic field.

The impact of change in volumetric concentration of nano Cu-particles in water with varying the magnitude of a is revealed in Fig. 7d at various constant parameters. Figure undoubtedly reveals that, with the augment in χ , Nu values increases for all values of a . Inclusion of nano-sized spherical particles shows the way to boost effectual thermal conductivity characteristics of the nanofluid that in turn improves the flow velocity. Therefore higher amount of heat is transported from the heated surface to the sink. Generally, heat exchange augmentation rate with varying volume fraction ($\chi = 0.1\text{--}2\%$) of Cu nanopowders is about 0.11–2.17% (for $a = 0.1$), 0.11–2.09% (for $a = 0.5$), 0.11–2.15% (for $a = 0.9$) in comparison with the host fluid ($\chi = 0$).

4 Conclusions

A novel investigation of thermal aspect ratio-based sinusoidal heating and isothermal partial cooling effect on the transport of heat and flow features of fluid through porous square enclosure filled with nanosize Cu-particles suspended in host fluid water with the effect of applied MHD is numerically analyzed. The thermal energy transmission and fluid flow information are investigated in the influences of various parameters like Ra_m , Da , Ha , and χ . The important conclusions are:

- In the convective heat transfer process, the selection of Ra_m is the key variables. The heat transport features increases appreciably for $Ra_m > 10^2$ and is superior at $Ra_m = 10^4$.
- With an increase in Darcy numebr, the buoyancy impact is opposed by resistance to flow considering the permeability of porous media. Consequently, the heat transfer is decreases. This reduction is more at elevated $Da > 10^{-2}$.
- An increase in Ha , the magnetizing force counteracts the buoyant force. Consequently, the heat transfer reduces with the augmentation of Ha . Such reduction rate is more at elevated $Ha = 50$.
- Enhance in the nanosized Cu-particles volume fraction in range of $\chi = 0.1\text{--}2\%$, the heat transfer rate enhances $\sim 0.11\text{--}2.15\%$ (for $a = 0.9$) compared to base fluid ($\chi = 0$).

The outcome of this study will be helpfull for designing sophisticated devices, where small control of transport phenomena is needed. Based on specific needs, the proper adjustment in the length, positions, and number of active cooling wall lengths could be searched for. The exhaustive study on the above considering various

fluids, and multi-physical conditions can be the potential future scope of research experimentally or numerically.

References

1. Bejan A, Dincer I, Lorente S, Miguel AF, Reis AH (2004) Porous and complex flow structures in modern technologies. Springer, New York
2. Yan S-R, Pordanjani AH, Aghakhani S, Goldanlou AS, Afrand M (2020) Effect of nano powder shapes on natural convection of nanofluids inside a square enclosure in presence of Fins with different shapes and magnetic field effect. *Adv Powder Technol* 31(7):2759–2777
3. Biswas N, Manna NK, Chamkha AJ (2021) Effects of half-sinusoidal nonuniform heating during MHD thermal convection in Cu–Al₂O₃/water hybrid nanofluid saturated with porous media. *J Therm Anal Calorim* 143:1665–1688
4. Kasaeeian A, Daneshazarian R, Mahian O, Kolsi L, Chamkha AJ, Wongwises S, Pop I (2017) Nanofluid flow and heat transfer in porous media: a review of the latest developments. *Int J Heat Mass Transf* 107:778–791
5. Sheikholeslami M, Rokni HB (2017) Simulation of nanofluid heat transfer in presence of magnetic field: a review. *Int J Heat Mass Transf* 115:1203–1233
6. Pordanjani AH, Aghakhani S, Alnaqi AA, Afrand M (2019) Effect of alumina nano-powder on the convection and the entropy generation of water inside an inclined square cavity subjected to a magnetic field: uniform and non-uniform temperature boundary conditions. *Int J Mech Sci* 152:99–117
7. Biswas N, Mahapatra PS, Manna NK (2016) Merit of non-uniform over uniform heating in a porous cavity. *Int J Heat Mass Transf* 78:135–144
8. Manna NK, Biswas N, Mahapatra PS (2019) Convective heat transfer enhancement: effect of multi-frequency heating. *Int J Numer Meth Heat Fluid Flow* 29(10):3822–3856
9. Biswas N, Sarkar UK, Chamkha AJ, Manna NK (2021) Magneto-hydrodynamic thermal convection of Cu–Al₂O₃/water hybrid nanofluid saturated with porous media subjected to half-sinusoidal nonuniform heating. *J Therm Anal Calorim* 143:1727–1753
10. Ramakrishna D, Basak T, Roy S, Pop I (2013) Analysis of heatlines during natural convection within porous square enclosures: effects of thermal aspect ratio and thermal boundary conditions. *Int J Heat Mass Transf* 59:206–218
11. Sheremet MA, Pop I (2014) Natural convection in a square porous cavity with sinusoidal temperature distributions on both side walls filled with a nanofluid: Buongiorno's mathematical model. *Transp Porous Media* 105:411–429
12. Malik S, Nayak AK (2017) MHD convection and entropy generation of nanofluid in a porous enclosure with sinusoidal heating. *Int J Heat Mass Transf* 111:329–345
13. Javaherdeh K, Najjarnezami A (2018) Lattice Boltzmann simulation of MHD natural convection in a cavity with porous media and sinusoidal temperature distribution. *Appl Math Mech Engl Ed* 39(8):1187–1200
14. Vo DD, Shah Z, Sheikholeslami M, Shafee A, Nguyen TK (2019) Numerical investigation of MHD nanomaterial convective migration and heat transfer within a sinusoidal porous cavity. *Phys Scr* 94:115225
15. Cimpean DS, Revnic C, Pop I (2019) Natural convection in a square inclined cavity filled with a porous medium with sinusoidal temperature distribution on both side walls. *Transp Porous Media* 130:391–404
16. Tayebi T, Chamkha AJ (2017) Buoyancy-driven heat transfer enhancement in a sinusoidally heated enclosure utilizing hybrid nanofluid. *Comput Therm Sci* 9(5):405–421
17. Oztop HF, Abu-Nada E, Varol Y, Al-Salem K (2011) Computational analysis of nonisothermal temperature distribution on natural convection in nanofluid filled enclosures. *Super Micro* 49:453–467

18. Alsabery AI, Chamkha AJ, Saleh H, Hashim I, Chanane B (2017) Effects of finite wall thickness and sinusoidal heating on convection in nanofluid saturated local thermal non-equilibrium porous cavity. *Phys A* 470:20–38
19. Mondal MK, Biswas N, Manna NK (2019) MHD convection in a partially driven cavity with corner heating. *SN Appl Sci* 1, Article no 1689
20. Biswas N, Manna NK, Datta P, Mahapatra PS (2018) Analysis of heat transfer and pumping power for bottom-heated porous cavity saturated with Cu-water nanofluid. *Powder Technol* 326:356–369
21. Mallick H, Mondal H, Biswas N, Manna NK (2021) Buoyancy driven flow in a parallelogrammic enclosure with an obstructive block and magnetic field. *Mater Today Proc* 44(2):3164–3171
22. Patankar SV (1980) *Numerical heat transfer and fluid flow*. New York NY Hemisphere
23. Biswas N, Manna NK (2017) Enhanced convective heat transfer in lid-driven porous cavity with aspiration. *Int J Heat Mass Transf* 114:430–452
24. Biswas N, Manna NK (2018) Magneto-hydrodynamic marangoni flow in bottom-heated lid-driven cavity. *J Mol Liq* 251:249–266

Review the Study of Employability Concept in Technical Institutes



Vijay Kalbande, Nitin Mandavgade, Mahesh Kanojiya,
and Riddheshwar Bilawane

Abstract In Today's scenario, a skill sets along with educational qualification is necessary for engineering students to get an employment. This set of skills differs from sector to sector, country to country, state to state. Education system plays a very important role in developing employability potential in the under graduate technical students. Promotional activities of an institutes/university mostly focus on employment offered in campus placement activities and training methodology adopted by the institute. Dedicated/experienced faculty is needed in the institute to implement the best practices like internships, live projects, placement opportunities and personality development training module, skill based training, etc. This paper helps to have clarity on employability concept in engineering institutes.

Keywords Employability · Campus placement · Engineering graduate · Employability skills

1 Introduction

The demand for the technocrats is increasing in India due to the globalization and substantial growth. The second shift in same campus and new technical institutes has been approved by All India Council of Technical Education (AICTE), New Delhi to fulfil this requirement of the technocrats. The making of Technical Institutes in India has been expanded from multiple points of view to meet the necessities of future technocrats. The norms of specialized instruction and the employability of designing graduates have been straight forwardly influenced by this unprecedented quantitative development of specialized establishments. The issue of designing employability is not just an issue for specialized foundations, yet in addition for enterprises and the public authority on the loose. Association between the establishment and the industry is currently generally perceived as a significant essential for the preparation and creation of the correct kind of specialized staff needed for the development [1].

V. Kalbande (✉) · N. Mandavgade · M. Kanojiya · R. Bilawane
Nagpur Institute of Technology, Nagpur, India
e-mail: drvijaykalbande@gmail.com

© The Author(s), under exclusive license to Springer Nature Singapore Pte Ltd. 2023
T. S. Sudarshan et al. (eds.), *Recent Advancements in Mechanical Engineering*,
Lecture Notes in Mechanical Engineering,
https://doi.org/10.1007/978-981-19-3266-3_12

145

Schooling work and preparing assessment concentrate by Aspiring Minds found that about 62% of designing students expect preparing to make them employable for IT administrations occupations [2]. It is noticed that in IT administrations organizations, employability is most noteworthy in the North, trailed by East, West and afterward south. It is discovered that states with greater government universities are more employable contrasted with private colleges. Six lakhs of designing alumni pass out every year and only 18.43% of them are employable for the function of computer programming IT administrations, while just 3.95% are adequately able to be conveyed straight forwardly on ventures. Simply 7.49% are employable for center work in mechanical, electronic/electrical and common positions [3].

Dr. Abdul Kalam accurately asserted that India doesn't have a joblessness issue, but has an employability issue. The industry has progressed quickly and innovation has likewise improved; however, the instructive organizations and educational program have not changed so rapidly. As per Mr. Karnik, President of NASSCOM (National Association of Software and Services Company), just 25% of specialized alumni are reasonable for occupations in the rethinking ventures because of the absence of English talking and composing limit. Indian and global industries grumble that solitary 25% of recruited specialized alumni are discovered employable after finishing of trial instructional classes by means of grounds exercises [4].

As per research directed by PurpleLeap, when all elements like specialized abilities, logical aptitudes and relational abilities are considered, just 7% of designing undergraduates are viewed as employable. Shockingly, over 80% of graduates do not meet the critical thinking and scientific abilities standards. It was discovered that it was uniquely through developing critical thinking and scientific capacities that employability could be improved more than twice, for example 7 to 16% [5]. As indicated by a review led by the Federation of Indian Chambers of Commerce, Industry (FICCI) and the World Bank, 64% of industries are not content with the norm of designing alumni students' skills [6]. The Merit Track research overview shows that 10% of all scholastic ability produced today is employable [7].

Most of graduates who select Maharashtra State designing and innovation courses come from non-English-talking backgrounds [8]. In view of their helpless relational abilities and absence of confidence, many designing alumni in India are discovered to be jobless. It has been distinguished that students actually need trust in the way toward selecting worldwide organizations into their foundations on campus [9].

By 2020, India intends to turn into a worldwide super force. The current circumstance is stressing and eventual fate of thousands of graduate students in designing is in question. In understanding this fantasy, any little advance the right way by corporate/specialists to sustain and make a skilled and employable labor force will assume a huge job. As of now, in spite of the fact that the occupation situation does not need possibilities, there is a critical absence of employable ability.

Utilizing Statistical Quality Control, Complete Quality Control, Six Sigma, Industry-Institute cooperation, and so on, the greater part of the creators/analysts did deal with updating the nature of the specialized foundation. AICTE, New Delhi is stepping up to the plate and redesigning the Technical Institute by conceding plans, for example, IIPC Cell, ED Cell, MODROB, and so forth Ventures are likewise stepping

up and connecting the Industry-Institute hole by leading diverse grounds interface programs in specialized foundations. Both of these recommend that the establishment needs to change its regular accentuation furthermore, put forth uncommon attempts to assist its students with improving aptitudes that better energize employability.

2 Purpose of the Study

In today's scenario, engineering graduate student's placement in industries through on campus placement recruitment plays a crucial role. Campus recruitment/placement has become an important criteria used by leading ranking agencies around the world. Parents favor universities and organizations that help their wards by attempted grounds situation exercises to give arrangement openings. Every school/establishment is endeavoring to advance its situation proportion. The open doors for graduates in various areas have expanded colossally over the previous decade, particularly in the designing area. By pooling undergraduates from various colleges, establishments organize nearby and off-grounds position camps and occupation fairs. Organizations in data innovation utilize these students in huge numbers. There are a few new alumni, then again, who cannot get past the enlistment cycle nearby.

A requesting climate for graduates has been created by ongoing specialized and monetary movements. More abilities from late designing alumni at the section level are needed to fulfill the needs of worldwide organizations. Globalization has increased the weight on organizations to effectively deal with their representatives and their clients too. Colleges and universities are feeling the squeeze to plan graduates for a quickly developing, profoundly serious work market. Associations depend on colleges to deliver graduate students who can think fundamentally, inventively, adapt autonomously and interface successfully.

The obvious clarification behind the enlistment by data innovation organizations of new designing alumni, paying little heed to the designing division, is the assumed thought that specialists will be better at tackling industry issues by goodness of good scientific, correspondence and mechanical aptitudes than different alumni. Then again, selection representatives from the center designing field take better thought of the person's expert aptitudes and just enroll engineers from the connected designing branch. The explanation is to guarantee that through their scientific capacities, engineers in the center designing field can apply essential designing abilities in their individual regions to take care of business issues.

India's global partnerships are searching for employable individuals who are knowledgeable. Bosses need graduates with substantially more remarkable qualities than scholarly accomplishment. In any event, they anticipate cooperation aptitudes, relational connections and solid insightful abilities. For any individual to convey well and to succeed, these delicate aptitudes are significant today. In any case, most alumni are acceptable at scholastic outcomes, yet not effective at relational abilities, and that puts an obstruction to their profession openings. Developing the stock of

graduates and lessening the interest for industries to expand their alumni norms. The absence of information on the changing work market is a specific test for graduates, especially the individuals who have not taken on specific positions during their examinations. Such enhancements greatly affect graduates at the section stage. Ventures need enlisted people to be knowledgeable in current fields and have the option to apply ability to them. They ought to likewise have capacities that are specialized and delicate. To accomplish occupations, understudy certifications, for example, degrees regulars should be adjusted by adaptable aptitudes or social abilities [13]. This demand focuses on common competencies like Aptitude skills, Communication skills and Personality skills apart from proficiency in their subjects.

The campus recruitments may not be a new phenomenon but the true potential is being realized due to tough competition. The right assessment of their own qualities and profession objectives is a huge determinant of the accomplishment of alumni in finding and catching vocation openings, as just these will add to a decent individual occupation fit. This is a climate where the situation division of colleges/schools should assume a key function as; it is intended to be a beginning stage for information, administrations, projects and open positions. Most of the placement departments require qualified staff and career counselors who approach information on businesses recruiting graduates, vocation openings and nearby boss administrations, just as extending employment opportunity looking for aptitudes and profession way support [10].

NAAC (National Assessment and Accreditation Council) & NBA (National Board of Accreditation) a self-governing body established by the University Grants Commission and AICTE lays down the setting-up of a 'Placement Cell' in institutes to increase Industry-Institute interaction. The prime responsibility of cell is to work as one point of contact to conduct Industry activities i.e. Industrial Training, Campus Placement drives and interaction of company expert in the institutes. Due to high expectations from graduate students by multinational companies, basic activities run by cell are not sufficient to get offers. The institutes need to train their students during four year engineering course to raise employability skills.

3 Employability: Definitions and Concepts

Inside various ways, the possibility of employability will in general be applied both to those at work and to those looking for work. Hence, while it is adequately simple to designate a straightforward word reference importance to employability, for example, the character or standard of being employable, it is a considerably more nuanced cycle to show up at a working definition. Maybe naturally, industries consider employability to be chiefly an individual characteristic. Employability is portrayed by the Confederation of British Industry (CBI) as: "Employability is a person's ownership of the characteristics and abilities expected to meet the developing necessities of managers and clients and along these lines to help understand their occupation goals and potential" [11].

Essentially, the UK government has shown up at a definition that while proposing employability-creation is an administration need, again puts the aptitudes of people at the center of the idea of employability infers the advancement of abilities and versatile representatives where each one of those ready to work are urged to build up the abilities, experience, innovation and flexibility to empower them to create [12].

A more deliberate methodology has been proposed by different endeavors to characterize the term, focusing because of both human qualities and work market factors, for example both interest for work and supply factors. THE CONCEPT OF EMPLOYABILITY 1999 The Development Board of the Canadian Government gave the accompanying definition: "Employability is a person's general capacity to accomplish important work, given the connection between close to home conditions and the work market" [13].

The Northern Irish methodology appears to follow approaches, for example, those recommended by Hillage and Pollard, who set up a wide portrayal of the term, considering employability to be the capacity of an individual to accomplish introductory business, hold work, switch between positions inside a similar association, and if important, get new industry and (preferably) secure sufficient and satisfactory work. This additionally incorporates both jobless people looking for business and working people looking for elective positions or advancements. Employability accordingly requires the capacity to go through the work market independently to acknowledge limit through practical positions. Employability relies upon the person's experience, skill and mentality, how they utilize those resources and present them to bosses and the foundation they have (for example individual conditions and work market climate) inside which they look for the work [14].

The appreciation of aptitudes and individual attributes that make graduates bound to get industry and dominate in their picked professions that help themselves, the labor force, the network and the economy. Employability is not equivalent to having a work, but instead implies something about the alumni's capacity to work in the working environment and have the option to switch between occupations, getting employable for the duration of their lives [15].

The researcher McQuaid suggested that Employability stays an argumentative idea regarding its application in both way of thinking and strategy, and has been utilized as both a fundamentally work supply and work request idea all through the previous century. They keep on arguing that, anyway the idea is valuable both. They state that the activity approach's smaller stockpile side accentuation is valuable in making a set or set of abilities and advancing public and institutional strategies and practices that can prompt its development, improving individual employability. All in all, the distinctions in perspectives appear to be on a very basic level rotate around whether the accentuation is on the attributes and "readiness" of the person for work, or on the elements impacting an individual finding into a line of work (or job "match" in job search theory), changing positions or improving their work [16].

The meaning of employability in this examination work is viewed as the capacity to get industry (offer letter) in global organizations through grounds situation exercises acted in specialized establishments.

4 Campus Placement Activity in Technical Institutes

Campus placement activities in private technical institutions are very important for Industries, Institutes and Students. Campus recruitment or placement success has become an important criterion used by leading ranking agencies around the world. Parents incline toward foundations that help their workers in contribution choices for position. Any school and association endeavors to streamline its arrangement proportion. By embraced grounds arrangement drive at rumored establishments, global partnerships accomplish their 60–70% new designing alumni prerequisite. Ventures decide the organizations to be visited for grounds enrollment drive to utilize new architects dependent on the arrangement record of the earlier year. NBA and NAAC, a self-governing body established by the University Grants Commission and AICTE, give more emphasis on employability enhancement activities run by institutes and actual offer received in campus placement activities.

When all is said in done, designing students need to have occupations in great worldwide IT organizations. Graduates begin making arrangements for the cycle of grounds selecting in view of the point of the organizations. It is noticed that most respectable IT organizations need to have every school's first space in the grounds determination methodology and decay to visit after the fifth opening. Among the initial five worldwide organizations, a foundation expects to accomplish ideal situation. Due to high expectations from graduate students by multinational companies, basic activities run by T & P cell are not sufficient to get offers. The cell conducts various activities during the four year academic tenure to raise employability of their students and get maximum students placed in first 5 opportunities. Initially the cell targets bulk recruiters to visit their institute for campus placement activity. Hence the researcher decided to consider placement of engineering students in first 5 multinational IT Sector companies. The remaining students who participated but did not receive offer are considered to be unplaced students.

4.1 *College Perception Regarding Campus Placement Activity*

The four year college and university teaching market enjoy the highest priority among graduate students. Yet, this market is a tough one to break into these days, and failure here is the single biggest cause of demoralization, loss of self-esteem as well as new opportunities.

The role of placement cell in the institute is not only to organize campus placement activity but also to prepare students during four year to grab the opportunities. Generally speaking, the professional job market follows the academic year. T & P officer needs to guide the students from time to time about market condition and skill set required by them as freshers at entry level at the same time provide necessary

hospitality and infrastructure for smooth conduction of campus placement recruitment process. Official notification to come only after the job has been finally offered and accepted and applicants have been eliminated from competition.

4.2 Industry Perception Regarding Campus Placement Activity

It is important to understand what recruiting company thinks and exercises before visiting the colleges for campus recruitment procedure.

Selecting institute to visit:

It is conceivable to utilize various rules to choose which foundations to focus on employing new designing alumni. One of the fundamental standards is the result of a year ago's determination of worldwide partnerships. Spot can be a limitation too. The understudy body's size might be of concern. To accomplish the necessary number of enlisted people, the industry visits in early slot. Notwithstanding, almost certainly, more associations are visiting the bigger organizations, bringing about more rivalry. The company tries to make the recruitment process cost efficient. Hence it tries to reduce the number of visits to the institutes, thus controlling the budget and gaining maximum. The companies try to visit in early slot with intention to get more no of good students.

It is extraordinary to have the best graduates at the highest point of the organization. In any case, rivalry is wild for those students. Well-quality representatives who have the most obvious opportunity with regards to being effective in their association are what the organization needs. The association starts to assess the accomplishment of previous recruits in their associations. By seeing who has been fruitful before and who has not been effective previously, they will perceive a gathering of associations that have created great workers.

Preparing for the visit timing:

The industry should choose when the grounds visit should be arranged. Enrollment specialists are ordinarily inside a generally limited time range nearby. In spite of the fact that they include some adaptability inside that time, on the off chance that they visit early, their prosperity would be more noteworthy. You risk getting the effective students effectively out of the opposition in the event that you meet later than the conventional scout. It is hence essential to choose the typical enlistment cycle and afterward consider understudy situated issues for example, test times and occasions, just as your own favored timetable.

Method to measure employability skills in campus placement:

The multinational IT Sector companies' measures employability skills by conducting systematic selection process that includes written test, group discussion (GD) and personnel interview (PI). With the help of written test or online test, the companies measure skill like Aptitude, Communication and Technical skills. The personality traits and oral communication skills are measured by conducting group discussion and personal interviews.

4.3 Students Perception Regarding Campus Placement Activity

Parents select technical professional course based on history of campus placement activities conducted by multinational companies. Campus recruitment or placement success has become an important criterion used by leading ranking agencies around the world. The entire campus recruitment process is made available on social sites for reference. Before taking admission, the students check the ranking of the institutes, the accreditations, the infrastructure and the remarks given by pass-out students on social sites. Due to less competition in campus placement activities as compared to off campus placement activities, getting offer through campus placement activities is much easier. Owing to sudden changes in technology and tough competition, the companies demand quality students to contribute more in their industry. The students need to understand industry requirements and accordingly start preparing early to raise their skill sets to enhance employability in campus placement.

5 Employability Scenario

The employability scenario of engineering graduate students varies country-wise, state-wise and sector-wise.

5.1 Country-Wise Employability Scenario

The Global Employability University Survey 2014 was carried out by Chris Parr to identify the position of various universities based on employability. Nonetheless, the rundown is overwhelmed by US establishments, who hold six of the main ten spaces. The discoveries, gathered by the German surveying and examination establishment Emerging Associates, a French HR counseling firm, depend on studies of 2500 unfamiliar selection representatives in 20 nations. The high level players, the worldwide brands, all of which will in general be American and British, keep on driving, while other Anglo-Saxon colleges, for the most part territorial players, will in general do less well, with other Anglo-Saxon colleges a normal of five spots lost in correlation with a year ago. In view of employability, INDIA has arrived at 22nd spot. From one perspective, however an enormous number of Indian graduates travel to another country to concentrate in worldwide advanced education foundations, there is few approaching unfamiliar students, contrasted and 190,055 students concentrating abroad in advanced education organizations in 2012, just 31,000 unfamiliar students came to India [17].

New Delhi asserted at the 2014 FICCI Higher Education Summit that Indian alumni's low employability is roused by components that include the outdated educational programs, absence of value educators, high understudy instructor proportions, absence of institutional and industry connections, and absence of self-sufficiency to actualize new and creative courses. In many associations, an examination accentuation and culture are missing. It additionally noticed that the accentuation on industry on grounds is insignificant, reflected in the way that there are not many foundations that offer business venture developers and have dynamic brooding/industry cells. In spite of the fact that India's number of patents documented expanded by a CAGR of 12% somewhere in the range of 2008 and 2012, these figures are little contrasted with those recorded by the USA and China. In 2012, 18,173 patents were recorded by India, contrasted with 561,377 by China, 488,744 by Japan and USA documented 268,782 patents in 2012 [18].

5.2 *State-Wise Employability Scenario*

India is a different country, and the variety stretches out through countries to designing alumni. The Employability Study of the States tends to the area savvy employability of graduates from each state. In the course of the most recent decade, India's specialized schooling has extended to incorporate 1000 s of designing universities spread the country over length and expansiveness, producing over a large portion of 1,000,000 designing alumni yearly.

The examination of Aspiring Minds is centered around the aftereffects of AMCAT-biggest India's employability trial of more than 120,000 designers the nation over. As the key employability metric, AMCAT can dependably foresee the employability of designers in various specialized positions, including IT administrations, IT merchandise, KPOs, BPOs, specialized help, and so on The investigation shows the diminishing in the level of employability of designers for different areas across various countries. Maharashtra reached to 11th position in India based on employability of engineering graduate students [19]. Figure 1 shows the position of different states based on Employability of Engineering graduate students.

Concerning Fig. 1, in IT administrations firms, employability is most noteworthy in the North, trailed by the East, at that point the West and afterward the South. Delhi and Bihar-Jharkhand have arisen as states with the most noteworthy employability rate. With its chose schools, Delhi has arisen as a center point for training with high instructive principles and drawing in the best personalities from across the world.

In India, various designing universities are amassed in a couple of states. The investigation took a gander at the positioning of states known as "designing centers" in the IT Services area by employability. It is noticed that states with greater government schools are more employable comparative with private universities. With an expansion in the quantity of designing universities in a given express, the level of employability diminishes, unmistakably demonstrating that initial additionally designing schools doesn't take care of the issue of value. Because of numerous

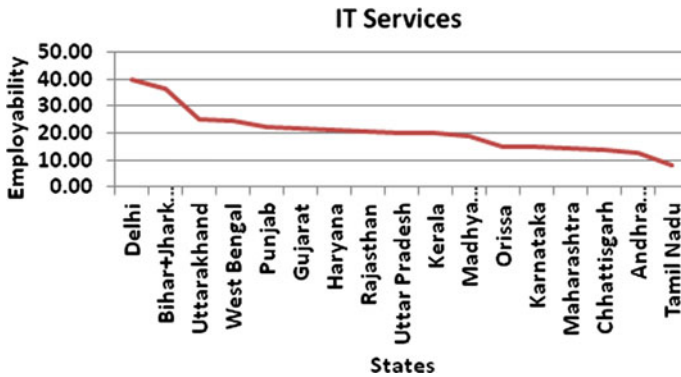


Fig. 1 Position of Maharashtra based on employability (Aspiring Mind Report 2011)

financial and formative factors, employability for a state is a powerful interaction. A more noteworthy accentuation on upgrading the norm of designing training is the thing that is required.

As indicated by the Ministry of Human Resource Development, India has 6214 designing and innovation organizations, with 2.9 million students selected. Specialists accept that an economy with an enormous extent of jobless yet qualified candidates is a recipe for social turmoil, not simply wasteful. Furthermore, the extraordinary confound in the desire of graduating engineers and their ability to work is prolific ground for dissatisfaction and bafflement for a huge scope.

5.3 Sector-Wise Employability Scenario in Maharashtra

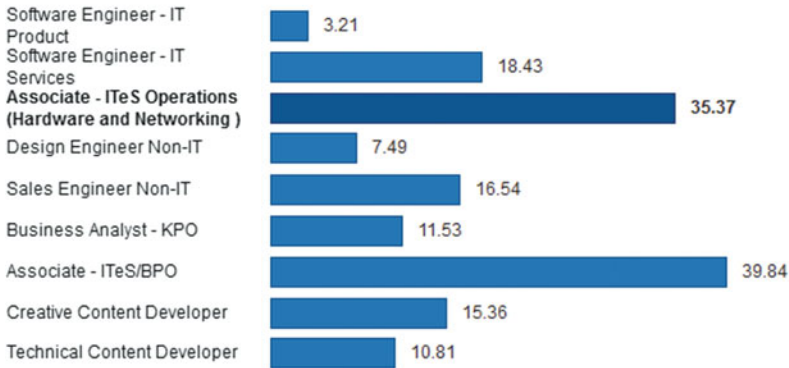
Hopeful Minds investigated engineers are principally occupied with equipment and systems administration. While 90% of designing alumni need occupations in mechanical, hardware/electrical what is more, considerate designing, just 7.49% are employable in these positions. Programming was the favored area for 53% of specialists in meetings directed for the report, while 44% favored center designing work.

With reference to Fig. 2, for programming work, under 20% of architects are employable. Simply 18.43% of the 600,000 designers graduating yearly are employable for the situation of programmer IT benefits; close to 3.95% can be straightforwardly conveyed on activities. In this way, most of specialists are keen on equipment and systems administration. Their work essentially incorporates specialized backing and support of organizations. Among non-IT positions, deals engineers who offer programming backing to organizations have high employability.

In non-tech positions, most specialists secure positions prevalently in tele-calling and backend handling in the industry cycle reevaluating (BPO) field. Simply 11.5%

Information Technology Engineers: How many are employable?

Figures are in %



Created with [Datawrapper](#)

Source: [National Employability](#). [Get the data](#)

Fig. 2 Sector-wise employability scenario in Maharashtra

of specialists likewise fit the bill for the situation of industry experts in the more rewarding field of data handling activities (KPO), an area of high incomes. An absence of English correspondence and poor insightful and quantitative abilities are the vital explanations behind low employability.

The critical purpose behind such helpless employment possibilities, in accordance with the report, is “deficient readiness inside the area space, the ability to utilize essential standards of state, pc designing or innovation, to true issues. These thoughts and standards in school information, however there is a spot in instructing and learning instructional method being continued in greater part of schools. Employability changes marvelously across resources. For instance, 18.26% of bundle engineers are work arranged in level 1 urban communities, similar to Mumbai, metropolitan focus and Hyderabad, while 14.17% ar employable from resources in level 2 urban areas, as Pune, Nagpur and Surat. This variety is reflected across states [20].

The IT administrations exchange is not developing at steady movement as in the past and accordingly the development of section level positions is diminishing. Organizations ar as of now attempting to discover employing up-and-comers United Nations office have just got tight involvement with programming. Also, IT administrations companies nowadays notice that inside 2 years of the obligation, the up-and-comer can have to speak with worldwide clients. As these patterns make up for lost time across exchange, the employability for IT administrations area, that will be that the biggest supervisor in designing, can lessen more. To remain serious inside the employment market, schools and colleges should have a contemporary concentration toward programming and English (both composed and spoken) [21].

5.4 Government Initiatives to Enhance Employability

UGC and the Ministry of Human Resource Development (MHRD) have made arrangements to dispatch bunch courses and expertise-based courses to support the status of graduates. UGC plans to place in more aptitude-based courses and guarantees that all designing colleges ace the abilities prior to moving out of schools and being employable, Science, Electronics and Automotive divisions. The UGC, which, following a Supreme Court request, assumed control over all the specialized foundations in the nation from the All India Technical Education Council (AICTE), will execute the National Skill Qualification System (NSQF) and the National Vocational Educational Qualification Framework (NVEQF) to give colleges mobility.

Rashtriya Uchatar Shiksha Abhiyan (RUSA) or Higher Education Mission on an expense of Rs. 50,000 crores will likewise be started by the UGC and the MHRD. The MHRD would disperse the equilibrium to self-financing designing universities, which had essential standards and met the exhibition-based markers, though the UGC had been designated Rs. 25,000 crores. Since the designing schools needed quality human resources, the UGC proposed making 5000 posts and 1000 MHRD posts and starting a designing school and Inter-University Center for preparing the staff.

All India Technical Education Council (AICTE) to pioneer another essential way to deal with industry interest activities zeroed in on the exceptional methodology of creating abilities and employability through the updating of aptitudes offered by industry pioneers. AICTE picked BSNL to oversee the “Preparation Program for Employability Enhancement” (EETP). The Employability Enhancement Training Program (EETP) around innovative encouraging models and incorporated ranges of abilities and offers a structure for address and satisfy the necessities of the Industry. Students can learn skills through intensive hands-on practical training on state-of-the-art telecommunications equipment available at BSNL training locations through this program.

In the wake of including industry agents in their educational program advancement exercises, AICTE created model educational plans for different specialized instruction programs as a component of abilities activities in various areas that upgrade employability. In their particular specializations/areas, the AICTE has set up 16 areas and 79 specializations and furthermore built up the essential educational plan for the different degrees of aptitudes.

In Lok Sabha, the Union Minister of Human Resource Development, Honorable Mrs. Smriti Irani, said the plan was additionally informed under the National Employability Enhancement Mission (NEEM) to give commonsense preparing at work and embraced the National Skill Qualification System (NSQF) to expand the employability of youthful alumni. The Government has set up a target to increase the Gross Enrolment Ratio (GER) in Higher Education to 30% by the end of year 2020.

AICTE is also giving grant to engineering institute under Industry Institute Partnership Cell (IIPC), Entrepreneurship Development cell, MODROB, etc., to increase employability of students during course. AICTE keep more marks on steps taken by institutes to increase skill sets of the students during various accreditations like NBA,

NAAC, ISO, etc. It is mandatory for institute to have separate cell name as “Training and Placement Cell” to run skill set improvement base activities for students.

5.5 Companies Initiatives to Enhance Employability

Most of the IT sector bulk recruiter companies are taking initiative to connect with engineering students through program like Mission 10X by Wipro firm, Campus connects by Infosys and TCS Ignite by TCS. Based on reputation of the institute, they have tied up with few institutes to run program which will cover skill sets required in multinational companies under Corporate Social Responsibility (CSR). Due to large number of technical institutes (367) and passing out 1.5 lakh engineer in Maharashtra state every year, the companies are able to cover only 5–10% top institutes.

6 Conclusions

This study shows that Employability scenario is very low in India. It is necessary to carry out detail study by the researchers to find out the best practices to raise the Employability skills in the engineering graduates. Technical institutes need to approach for NBA accreditation to achieve graduates attributes. Institutes need to be more focus on industry connected activities like internships, live projects, placement opportunities, personality development training and skill development training module. The study helps to get more clarity on employability concept in technical institutes. All of these suggest that the institutions should make rigorous attempts to improve skill sets and make them qualified and employable.

References

1. Sreeram M, Naresh K (2012) Status of technical education in India—emerging issues and challenges. Uman_Resource_16_Feb_2012, subscribe digital library, pp 67–72
2. Amit B (2010) CEO aspiring minds, 62% of engineering graduates needs training to be employable, BS Reporter/Mumbai, 17 August 2010
3. Aspiring minds report on national employability study IT/ITeS sector (2014)
4. NASSCOM (2005) The IT industry in India: strategic review. NASSCOM, New Delhi
5. PurpleLeap study on low employability skills among engineering students, in Andhra Pradesh, published in Reachout’s News Bureau (2009)
6. Federation of Indian Chambers of Commerce and Industry (FICCI) and World Bank survey on employability of fresh engineering during training period (2009)
7. MeritTrack study on Experiment in Employability Enhancement—a pioneering industry-Academia Initiative (2001)

8. Clement A et al (2015) English for employability: a case study of the English language training need analysis for engineering students in India. *Can Cent Sci Educ* 8(2):116–125
9. Albert P et al (2008) Developing engineering student's communication skills by reducing their communication apprehension. *Engl Specif Purp World* 7(4):101–106
10. Gokuldas VK et al (2011) Predictors of employability of engineering graduates in campus drives of Indian software services companies. *Int J Sel Assess* 19(3):313–319
11. Confederation of British Industry (CBI) (1999) Making employability work: an agenda for action. CBI, London
12. Treasury HM (1997) Treasury press release 122/97, 13th October: Gordon brown unveils UK employment action plan. HM Treasury, London
13. Canadian Labour Force Development Board (1994) Putting the pieces together: towards a coherent transition system for Canada's labour force. Ottawa
14. Hillage, Pollard (1998) *Employability: developing a framework for policy analysis*: London
15. Knight, Yorke (2006) Encouraging the development of employability. ESECT, York, pp 3–16
16. Mcquaid RW et al (2005) Are new deal employment initiatives on target? Evidence from job search success in local labour markets. *Int J Manpow* 22:392–410
17. Parr C (2014) Global Employability University Ranking results
18. Saraswathy M (2014) Employability of graduates big concern, says FICCI-EY report. New Delhi
19. Employability of engineers state-wise: aspiring mind national employability report 2011
20. Saiyadain MS (2009) *Human resources management*. McGraw Hill, New Delhi
21. Gowsalya G, Ashokkumar M (2015) Employability skill: a literature review. *Int J Adv Res Comput Sci Manage Stud* 3(3):353–360

Stochastic First-Ply Failure Analysis of Laminated Composite Plate: A Moving Least Square Approach



Subrata Kushari, S. R. Maity, A. Chakraborty, and S. Dey

Abstract Stochastic first-ply failure analysis of a carbon-epoxy-based laminated composite plate is conducted based on Monte Carlo simulation (MCS) and moving least squares (MLS)-based surrogate model. A five-noded finite element (FE) model is developed to determine the deterministic first-ply failure load. The inherited randomness in the geometrical properties like Young's modulus, shear modulus, Poisson's ratio, density, ply orientation, stacking sequence, etc., are predominant. A stochastic analysis provides a valid design method to analyse such critical subjects. Five failure criteria, viz. maximum strain, maximum stress, Tsai–Hill, Tsai–Wu and Hoffman theories, are employed to analyse the first-ply failure of the laminated plate. At first, a probabilistic model is developed based on the MCS approach with stochasticity in input material properties. To reduce the computational time, MLS is utilized as the surrogate model. It is further validated with MCS. Probability density function (PDF) and scatter plot are utilized to depict the validation of the MLS model with MCS. The results further verify that the computationally efficient MLS model can be utilized in place of MCS for further analysis.

Keywords Monte Carlo simulation (MCS) · Moving least squares (MLS) · First-ply failure and surrogate model

S. Kushari (✉) · S. R. Maity · S. Dey
Department of Mechanical Engineering, National Institute of Technology Silchar, Silchar, India
e-mail: subrata734@gmail.com

S. R. Maity
e-mail: sрмаity@mech.nits.ac.in

S. Dey
e-mail: sudip@mech.nits.ac.in

A. Chakraborty
Department of Civil Engineering, Indian Institute of Technology Guwahati, Guwahati, India
e-mail: arunasis@iitg.ernet.in

1 Introduction

The development of laminated composites in the production process is always subjected to vast unpredictability due to manufacturing imperfection, environmental erosion and various operational factors. Due to its characteristic anisotropy and complexity, manufacturing of laminated structures accurately according to exact design standards is a huge task, resulting in unavoidable uncertainties in its output behaviour especially when it is subjected to failure. It involves many sources of uncertainty associated with manufacturing, material properties at different scale levels, environmental and operational conditions. Hence, it becomes fully exposed to risk while dealing with failure load. Thus, the structural reliability can be insured by quantifying the uncertain failure zone. The early methods to develop failure theories were mostly confined to the deterministic approach. Failure theories for laminates were formulated on homogenous solids considering anisotropy induced by fibre orientations. However, in practical laminated composites contain defects on account of a specific manufacturing process. These flaws are induced due to failure in the weak regions (between connecting regions of the interfaces) [1]. Azzi and Tsai [2] developed a theory based on laminated and unidirectional composites employing simple material properties and considering only unidirectional specimens for anisotropic materials. Reliability and performance behaviour are analysed for carbon fibre-reinforced composite in the stochastic regime [3]. The results show high accuracy for the computational framework. A stochastic constitutive model is developed by Mansour et al. [4]. Random mechanical response of arbitrary size is predicted for isotropic thin fibre networks. Uniyal et al. [5] formulated a finite element method using Halpin and Tsai equations and rule of mixtures in micro-scale. Laminate properties considering strength for the off-axis failure for dissimilar volume fractions are determined. For failure of the fibre, a five-cylindrical axis-symmetric finite element model is developed to conduct stress analysis [6]. A multi-scale failure theory is developed based on multiple off-axis tension tests for 3-D mechanism-based damage scrutiny criterion [7]. The stochastic approach proves to be rather efficient than the deterministic approach as observed by Zhou et al. [8]. A stochastic multi-scale approach is developed for the reliability analysis of composite where the uncertainties were considered for both micro- and macro-scale. The model is validated with Monte Carlo simulation. It is concluded that rather than the tiresome process this approach is quite efficient in terms of computational time. Multi-scale progressive failure analysis is predicted using Schapery theory based on thermodynamics for laminated composites by Pineda et al. [9]. A stochastic model based on the reduced-order stochastic multi-scale computational model is developed by Bogdanor et al. [10]. The progressive damage development, as well as failure in the composite, is predicted. The proposed model is formulated to analyse the ultimate tensile strength for open-hole composite at several loading points under quasi-isotropic conditions. A multi-scale finite element modelling approach by Gotsis et al. [11] with a bottom-up strategy is employed to study the failure of the model. The first-ply failure and fracture in composites, glass fibres and graphite fibres are considered for the laminates and epoxy matrices, respectively.

The novelty of the current paper is to explore the stochastic first-ply failure analyses of laminated composite plate utilizing Monte Carlo approach and moving least square (MLS)-based approach. Both the analyses provide the stochastic results of first-ply failure analyses. The MLS-based approach is utilized to improve the computational efficiency.

2 Mathematical Formulation

The governing equation for a multi-layered laminated composite as depicted in Fig. 1 is mainly derived from the minimum total potential energy theorem. It further allows us to form the basis of finite element modelling of the laminated structure.

The total potential energy of a body is defined by the sum of total energy due to strain and total work potential of the body due to external forces. The equation is given as follows:

$$\Pi = U + V \tag{1}$$

where the total strain energy is defined by the volume integral of the total volume and defined as

$$U = \frac{1}{2} \int_{\phi} \{u\}^T \{\sigma\} d\phi \tag{2}$$

The total amount of work done due to the externally applied load can be defined as an integral of the total area

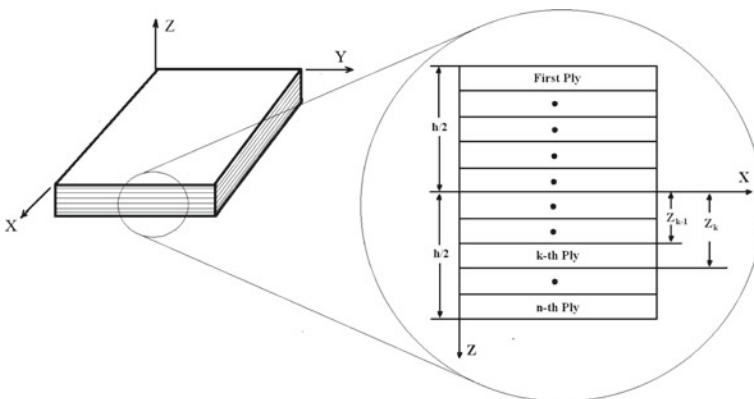


Fig. 1 Isometric and layer thickness representation of a laminated composite

$$W = \iint_A [u]^T [q] dA \text{ where } \{q\} = \{0 \ 0 \ q_z \ 0 \ 0\}^T \quad (3)$$

The load intensity of laminate is denoted as q_z . The final equation for the laminate can be stated as,

$$[F] = [\varepsilon][D] \quad (4)$$

where F = final stress vector, ε = strain vector and D = elastic matrix of the laminate.

Due to the presence of nonlinearities and complexity in the model, it is required to develop a FE-based model to evaluate the first-ply failure of the laminated plate. First-order shear deformation theory (FSDT) is implemented to solve the equations in the model where each element is eight-noded and every single node has five degrees of freedom (three translational and two rotational).

2.1 Failure Criteria for Laminated Composite

In the present work, an eight-layered laminated plate is considered to study the failure analysis. The orientation of the laminate is $[45^\circ, -45^\circ, 45^\circ, -45^\circ]_s$. The five failure criteria are utilized to investigate the first-ply failure load of the laminated plate.

Maximum stress theory This theory involves two forms of stress (normal stress and shear stress) theories. It specifies that when a material exceeds its maximum stress enduring capacity in any of its axes, it fails [12]. It can be expressed as,

$$(\sigma_1^c)_u < (\sigma_1) < (\sigma_1^T)_u \quad (5)$$

$$(\sigma_2^c)_u < (\sigma_2) < (\sigma_2^T)_u \quad (6)$$

$$(\tau_{12})_u < (\tau_{12}) < (\tau_{12})_u \quad (7)$$

where σ_1 σ_2 and represent the normal stresses in x -axis and y -axis, respectively. While τ_{12} represents the shear stress, σ^c and σ^T represent the compressive stress and tensile stress, respectively, through the laminate. Here the suffix 'u' is used to signify the ultimate stress point.

Maximum strain theory This theory is based on the maximum normal strain theory for isotropic materials as predicted by Sokolnikoff [13]. According to this theory when the shear and principal strain exceeds the ultimate strain, the material tends to rupture or fail. The mathematical deduction for the same can be expressed as

$$(\varepsilon_1^c)_u < (\varepsilon_1) < (\varepsilon_1^T)_u \tag{8}$$

$$(\varepsilon_2^c)_u < (\varepsilon_2) < (\varepsilon_2^T)_u \tag{9}$$

$$\gamma_{12} < \Gamma_{12} \tag{10}$$

where ε_1 and ε_2 represent the normal strains in the x -axis and y -axis while γ_{12} represents the shear strain. ε^c and ε^T represent the compressive strain and tensile strain, respectively, through the laminate, and Γ_{12} represents the ultimate shear strain.

Tsai–Hill (energy-based criterion) theory Tsai–Hill theory [14] for the failure of laminate is a combination of distortion energy (which is responsible for change of the shape) and dilation energy (which causes volumetric changes in the material). The failure in the material is depicted as follows.

$$f(\sigma_{ij}) = F(\sigma_2 - \sigma_3)^2 + G(\sigma_3 - \sigma_1)^2 + H(\sigma_1 - \sigma_2)^2 + 2L\sigma_4^2 + 2M\sigma_5^2 + 2N\sigma_6^2 = 1 \tag{11}$$

where F, G, H, L, M and N signify strength parameters of the material. σ_4, σ_5 and σ_6 are the shear stress components.

Tsai–Wu (Interaction tensor polynomial) theory The Tsai–Wu failure criterion is a special case of the general quadratic failure criteria developed by Gol’denblat and Kopnov. It is depicted as [15]

$$F_i\sigma_i + F_{ij}\sigma_i\sigma_j \geq 1 \tag{12}$$

where F_i and F_{ij} are the first-order and fourth-order strength tensors of the material. Here σ_i denotes the difference between compressive- and tensile-induced stress. The term $\sigma_i\sigma_j$ defines an ellipsoid along with the stress space.

Tsai–Hill’s Hoffman failure criteria The Tsai–Hill’s Hoffman criterion is a special condition of Tsai–Hill failure criteria. In Hoffman’s failure criteria, the difference between the strength of tension and compression is considered which is ignored in the case of Tsai–Hill failure criteria which is significant if brittle materials are considered. The modified criteria are established by adding the odd functions of the principal stress components (σ_1, σ_2 and σ_3) in the actual expression of Tsai–Hill criteria [16]. Thus,

$$C_1(\sigma_2 - \sigma_3)^2 + C_2(\sigma_3 - \sigma_1)^2 + C_3(\sigma_1 - \sigma_2)^2 + C_4\sigma_1 + C_5\sigma_2 + C_6\sigma_3 + C_7\sigma_4^2 + C_8\sigma_5^2 + C_9\sigma_6^2 = 1 \tag{13}$$

Here C_1 to C_9 denote the material parameters.

2.2 Development of Stochastic Model

The stochastic effect is provided on the current model based on combined variation of the material properties. Equation (14) defines the stochastic effect of ply-orientation angle for the current eight layered model. The combined variation of the current model for the material properties can be defined as Eq. (15).

$$\theta(\varpi) = \{\theta_1, \theta_2, \theta_3, \theta_4, \theta_5, \theta_6, \theta_7, \theta_8\} \quad (14)$$

$$\begin{aligned} &g\{\theta(\varpi), E_1(\varpi), E_2(\varpi), G_{12}(\varpi), G_{13}(\varpi), G_{23}(\varpi), \rho(\varpi), \mu(\varpi)\} \\ &= \{\lambda_1(\theta_1 \dots \theta_8), \lambda_2(E_{1_1} \dots E_{1_8}), \lambda_3(E_{2_1} \dots E_{2_8}), \lambda_4(G_{12_1} \dots G_{12_8}), \\ &\lambda_5(G_{13_1} \dots G_{13_8}), \lambda_6(G_{23_1} \dots G_{23_8}), \lambda_7(\rho_1 \dots \rho_8), \lambda_8(\mu_1 \dots \mu_8)\} \end{aligned} \quad (15)$$

where $\theta(\varpi), E_1(\varpi), E_2(\varpi), G_{12}(\varpi), G_{13}(\varpi), G_{23}(\varpi), \rho(\varpi), \mu(\varpi)$ signify stochastic ply-orientation angle, longitudinal and transverse young's modulus of elasticity, shear modulus along the longitudinal and transverse direction, mass density and Poisson's ratio. In Eqs. (14) and (15), " ϖ " defines the stochastic character of the material properties. Stochastic model is designed based on $\pm 10\%$ deviation (as per industrial standards) for the material properties. Figure 2 represents the stochastic modelling of the first-ply failure analyses. Monte Carlo simulation-based approach is employed along with FE-based model for first-ply failure analysis of composite laminate plates.

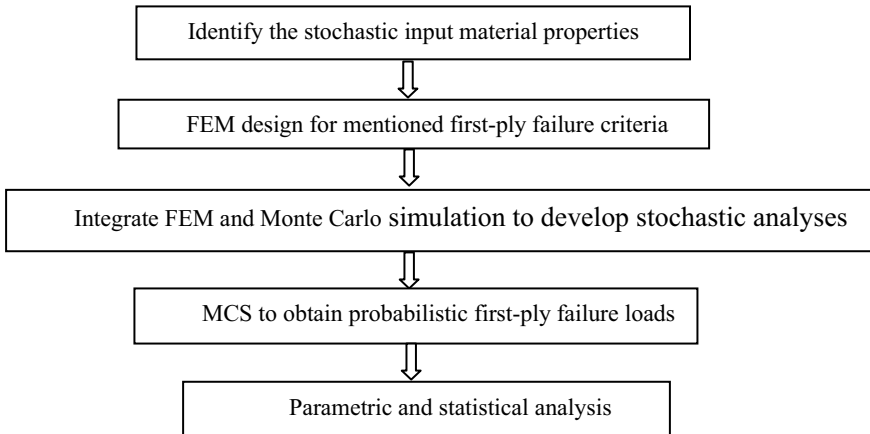


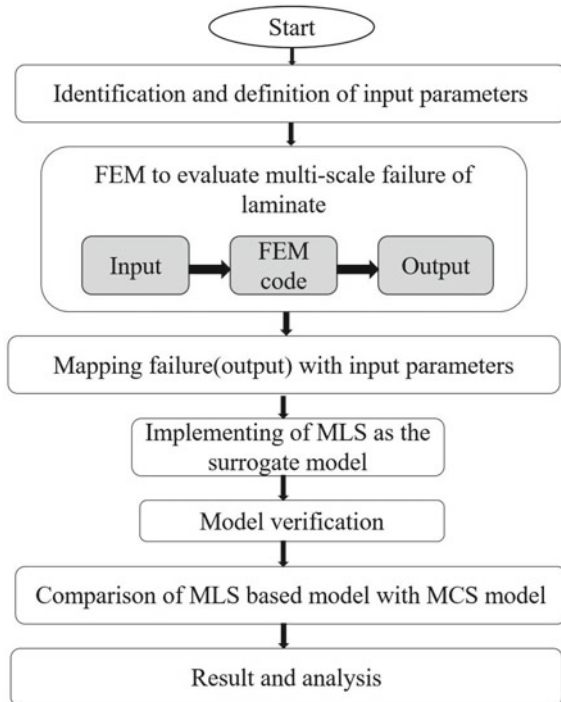
Fig. 2 Flow chart for the development of MCS-based stochastic model for first-ply failure analyses

2.3 Moving Least Square (MLS)-Based Surrogate Model

MLS-based surrogate model is developed to reduce the computational time by considering the best suited experimental points from a given polynomial function. The flow chart for the employed surrogate model is depicted in Fig. 3. To represent the nonlinear limit surface, a limit state function (LSF) or a weighted interpolation function is developed. This method is an advanced version of the least square method. In a probabilistic analysis, the uncertainties can be depicted as, $\kappa = [\kappa_1, \kappa_2, \dots \kappa_n]$. A normal distribution is deployed to plot the probability density function. Response surface method (RSM) is utilized to mitigate the error due to dimensionality for the randomized input variables. The experimental points are selected by axial sampling method. The selected points are fitted considering second-order polynomial expansion and neglecting the cross terms. The approximated response surface function (RSF) is expressed as

$$z(\kappa) = \alpha_0 + \sum_{i=1}^l \alpha_i \kappa_i + \sum_{i=1}^l \alpha_{ii} \kappa_i^2 \tag{16}$$

Fig. 3 Flow chart for MLS-based surrogate model to analyse the first-ply failure of the laminate plate



where α_0 , α_i and α_{ii} represent the unknown coefficient terms of the polynomial function. The approximated response surface function $D(\kappa)$ is predicted as

$$D(\kappa) = p(\kappa)^T q(\kappa) \quad (17)$$

where $p(\kappa)$ is the basis function and $q(\kappa)$ is the coefficient vector. The local MLS function [17] at k is denoted as

$$D(\kappa, \kappa_i) = q(\kappa) p(\kappa_i)^T \quad (18)$$

The basis function $p(\kappa)$ is depicted as

$$p(\kappa) = [1 \kappa_1 \dots \kappa_n \kappa^2 \dots \kappa_n^2]^T \quad (19)$$

The unknown coefficient vector term, $q(\kappa)$, is evaluated by reducing the error for the approximated and experimental values of the LSF. The error can be defined as

$$\begin{aligned} E(\kappa) &= \sum_{i=1}^n w(\kappa - \kappa_i) [D(\kappa, \kappa_i) - D(\kappa_i)]^2 \\ &= (Pa - D)^T w(\kappa) (Pa - D) \end{aligned} \quad (20)$$

where

$$\begin{aligned} D &= [L(\kappa_1), L(\kappa_1), \dots, L(\kappa_n)]^T \\ P &= [p(\kappa_1), p(\kappa_1), \dots, p(\kappa_n)]^T \\ W(\kappa) &= \text{diag. } [w_1(\kappa_1 - \kappa), w(\kappa_2 - \kappa), \dots, w_m(\kappa_n - \kappa)] \end{aligned} \quad (21)$$

n = number of experimental points

The transformed coefficient vector $q(\kappa)$ can be defined as

$$q(\kappa) = [P^T W(\kappa) P]^{-1} P^T W(\kappa) D \quad (22)$$

The estimated RSF is obtained from (16), (19) and (20) as

$$D(\kappa) = q(\kappa)^T (P^T W(\kappa) P)^{-1} P^T W(\kappa) D \quad (23)$$

3 Result and Discussion

The present analysis is considered for an eight-layered graphite-epoxy-based laminated composite plate. The dimension of laminated composite plate is taken as length (l) = 1 m, breadth (b) = 1 m and thickness (t) = 0.005 m. The stacking sequence of plies is considered as [45, -45, 45, -45, -45, 45, -45, 45] (Table 1).

Deterministic results are obtained for first-ply failure loads for the mentioned five failure criteria. The results obtained are validated with earlier literature [19]. The dimension of the plate considered is 1 m length, 1 m breadth and 5 mm thick, respectively. The finite element model is designed considering (8 × 8) mesh plane. Thus, a total number of 64 elements are formed. The current mesh configuration (8 × 8) is chosen as it is found that it displays significant reduction in error as compared to other mesh configuration when compared with the past literature. In nodal region, each node possesses five degrees of freedom (DOF) (three translational and two rotational). The deterministic results are validated with previous literature. The validation for a three-layered T300/5208 graphite-epoxy laminate with [45°, -45°, 45°] ply orientation angle is presented in Table 2.

The stochastic analysis is formulated first by modelling the probabilistic MCS model for ten thousand samples. The MLS-based surrogate model is developed further to reduce computational time. It is found that at sample size (N) = 2048 the MLS-based surrogate model merges with the MCS. The three-dimensional probability density function graph is plotted for five failure theories and stochastic first ply-failure load (Fig. 4).

Based on the MLS model with sample size (N) = 2048, a scatter plot is portrayed in Fig. 5. It is observed that the surrogate model and the MCS model converge at sample size (N) = 2048. It can be predicted that the computationally time-consuming MCS model can be replaced with the efficient MLS-based model which takes a fraction of time as compared to MCS-based model.

Table 1 Material properties of T300/5208 graphite-epoxy laminated plate [18]

E_1 (GPa)	E_2 (GPa)	G_{12} (GPa)	G_{13} (GPa)	G_{23} (GPa)	μ	ρ (kg/m ³)
132.37	10.7	5.65	5.65	3.37	0.3	1600

Table 2 Validation of the present FE model with previous literature [19]

Failure theories	First-ply failure loads (N)	
	Reddy et al. [19]	Present deterministic model
Maximum stress	1908.16	1962.50
Maximum strain	1940.48	1994.75
Tsai-Hill	1530.40	1563.70
Tsai-Wu	1917.76	1957.32
Hoffman	1905.76	1962.10

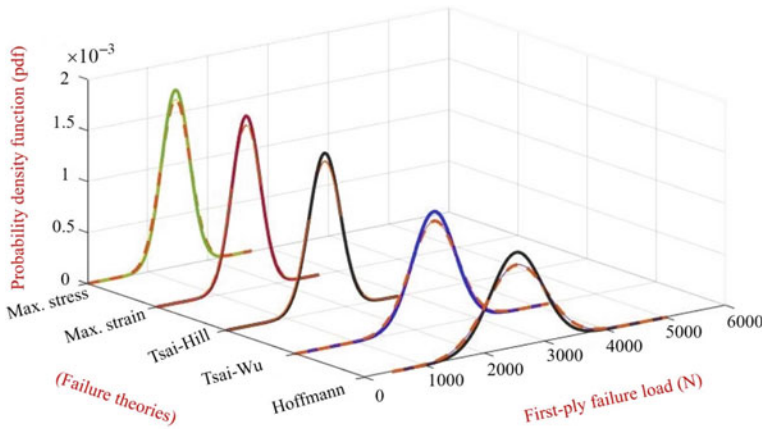


Fig. 4 Probability density function plot for different failure theories

4 Conclusion

A novel stochastic-based approach is utilized to quantify the uncertainty in the first-ply failure load analysis. The present work is restricted to develop a computationally efficient surrogate model which can be implemented to analyse the failure in place of time-consuming MCS-based approach. MLS-based surrogate model is highly efficient in analysing the present failure model. The MLS-based model converges with the MCS-based model at sample size (N) = 2048. The PDF plot in Fig. 4 depicts the conclusiveness of the surrogate-based MLS model. It can be quantified that MLS-based model can be further utilized to quantify complex probabilistic-based model in future.

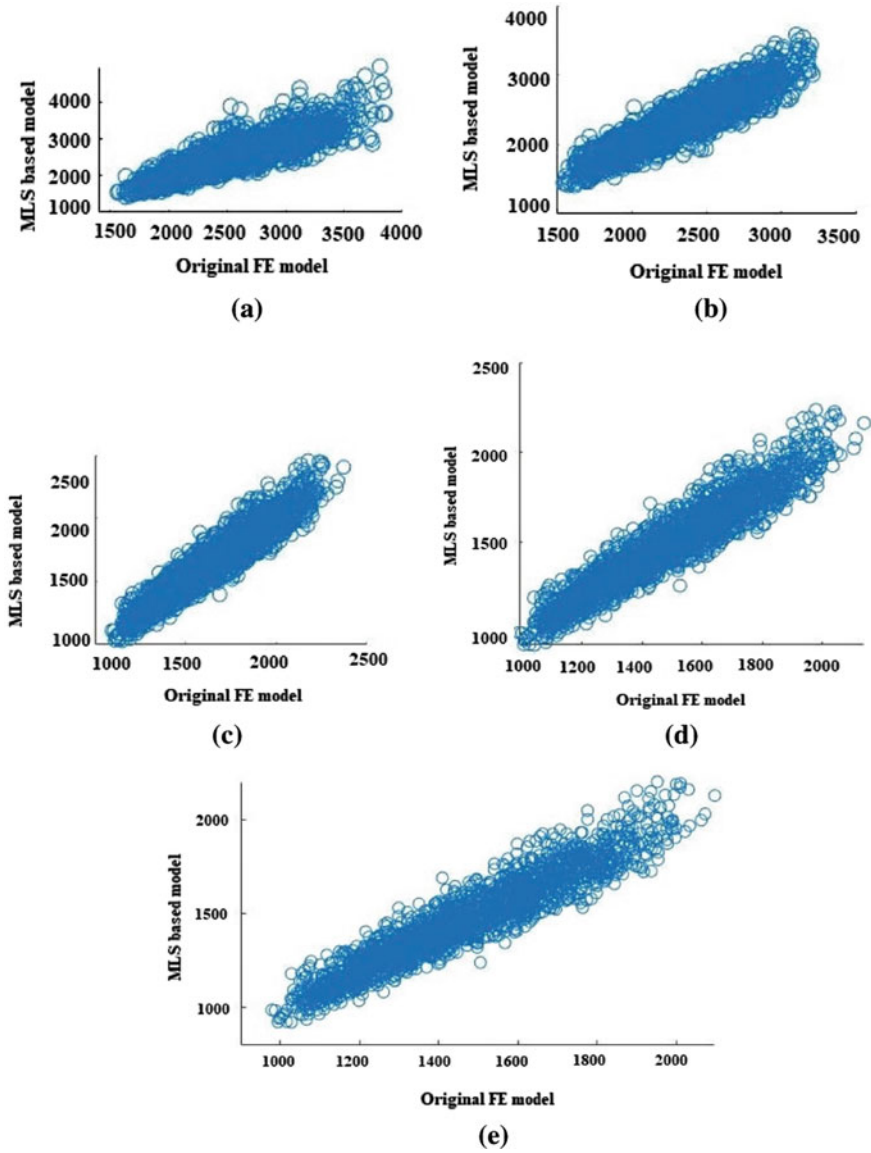


Fig. 5 Scatter plot of 2048 samples-sized MLS model with the original finite element model for **a** Maximum stress theory, **b** maximum strain theory, **c** Tsai–Hill theory, **d** Tsai–Wu theory and **e** Hoffman failure theory

Acknowledgements The authors would like to acknowledge the Aeronautics Research and Development Board (AR&DB), Government of India (Project Sanction no.: ARDB/01/105885/M/I), for the financial support for the present research work.

References

1. Talreja R (2014) Assessment of the fundamentals of failure theories for composite materials. *Compos Sci Technol* 105:190–201
2. Azzi VD, Tsai SW (1965) Anisotropic strength of composites. *Exp Mech* 5(9):283–288
3. Thapa M, Mulani SB, Walters RW (2019) Stochastic multi-scale modeling of carbon fiber reinforced composites with polynomial chaos. *Compos Struct* 213:82–97
4. Mansour R, Kulachenko A, Chen W, Olsson M (2019) Stochastic constitutive model of isotropic thin fiber networks based on stochastic volume elements. *Materials* 12(3):538–566
5. Uniyal P, Gunwant D, Misra A (2016) Multi scale modeling and failure analysis of laminated composites. *J Appl Mech Eng* 5:229
6. Talreja R (2016) Multiscale modeling of failure in composite materials. *Proc Indian Natl Sci Acad* 82(2)
7. Li X, Guan Z, Li Z, Liu L (2014) A new stress-based multi-scale failure criterion of composites and its validation in open hole tension tests. *Chin J Aeronaut* 27(6):1430–1441
8. Zhou XY, Gosling PD, Ullah Z, Kaczmarczyk L, Pearce CJ (2017) Stochastic multi-scale finite element based reliability analysis for laminated composite structures. *Appl Math Model* 45:457–473
9. Pineda E, Waas A, Bednarczyk B, Collier C, Yarrington P (2008) A novel multiscale physics based progressive failure methodology for laminated composite structures. In: 49th AIAA/ASME/ASCE/AHS/ASC structures, structural dynamics, and materials conference, 16th AIAA/ASME/AHS adaptive structures conference, 10th AIAA non-deterministic approaches conference, 9th AIAA gossamer spacecraft forum, 4th AIAA multidisciplinary design optimization specialists conference, p 1929
10. Bogdanor MJ, Oskay C, Clay SB (2015) Multiscale modeling of failure in composites under model parameter uncertainty. *Comput Mech* 56(3):389–404
11. Gotsis PK, Chamis CC, Minnetyan L (1998) Prediction of composite laminate fracture: micromechanics and progressive fracture. *Compos Sci Technol* 58(7):1137–1149
12. Tresca HE (1864) *Sur l'écoulement des corps solides soumis a de fortes pressions*. Imprimerie de Gauthier-Villars, successeur de Mallet-Bachelier, rue de Seine-Saint-Germain, 10, près l'Institut
13. Sokolnikoff IS, Specht RD (1956) *Mathematical theory of elasticity*, vol 83. McGraw-Hill, New York
14. Mises RV (1913) *Mechanik der festen Körper im plastisch-deformablen Zustand*. Nachrichten von der Gesellschaft der Wissenschaften zu Göttingen, Mathematisch-Physikalische Klasse 1913:582–592
15. Tsai SW, Wu EM (1971) A general theory of strength for anisotropic materials. *J Compos Mater* 5(1):58–80
16. Hoffman O (1967) The brittle strength of orthotropic materials. *J Compos Mater* 1(2):200–206
17. Lancaster P, Salkauskas K (1981) Surfaces generated by moving least squares methods. *Math Comput* 37(155):141–158
18. Köhler L, Spatz HC (2002) Micromechanics of plant tissues beyond the linear-elastic range. *Planta* 215(1):466
19. Reddy JN, Pandey AK (1987) A first-ply failure analysis of composite laminates. *Comput Struct* 25(3):371–393

Electric Field Modulated Drop Formation from Orifices



Manash P. Borthakur and Subhasis Chakravarthy

Abstract We investigate the effect of an electric field on the formation and breakup of droplets by employing axisymmetric numerical simulations. The volume-of-fluid approach is used for capturing the interface motion, and the fluids are assumed as leaky dielectric. The simulations reveal that the droplets formed can be either oblate or prolate in shape, which is determined by the relative dissimilarity of fluid properties across the interface. The Coulombic forces are found to be the dominant electrical forces that influence the droplet morphology. Additionally, the nature of circulatory flow occurring inside the drop can be significantly different, depending on the relative combination of the electrical properties of the drop and surrounding fluids.

Keywords Drop formation · Electro-hydrodynamics · Volume of fluid

1 Introduction

The phenomenon of drop formation and breakup is commonly encountered in a wide range of industrial as well as daily life processes [1]. The morphology of the fluid–fluid interface can be effectively tuned by applying electric forces at the interface. In recent years, electric field-modulated processes have gained widespread popularity in a host of commercial applications, such as electro-hydrodynamic (EHD) printing, electro-wetting and emulsification, to name a few [2].

Starting from the pioneering work of Taylor on drops placed in electric field [3], a plethora of analytical, experimental and computational studies have been performed to explore the influence of electric field on the morphology and response of droplets [4–6]. One of the earliest studies on formation of drops in electric field was conducted

M. P. Borthakur (✉)

Institute for Complex Systems, National Research Council, Rome, Italy

e-mail: manash.pborthakur@gmail.com

S. Chakravarthy

Department of Mechanical Engineering, NIT Silchar, Silchar, India

e-mail: subhasischakravarthy88@gmail.com

© The Author(s), under exclusive license to Springer Nature Singapore Pte Ltd. 2023

T. S. Sudarshan et al. (eds.), *Recent Advancements in Mechanical Engineering*,

Lecture Notes in Mechanical Engineering,

https://doi.org/10.1007/978-981-19-3266-3_14

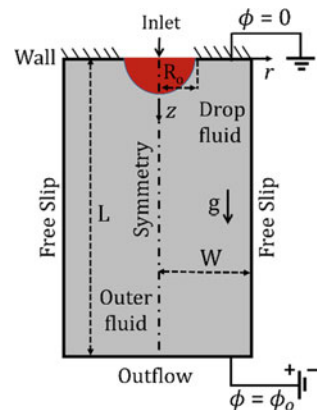
by Basaran and Scriven [7], wherein the drops remained pendant to a surface. In a later study, both conducting and non-conducting fluids were used as the drop medium and the consequence of exerting an electric field was explored [8]. However, the majority of the prior studies considered the outer medium to be an insulating gaseous substance, like air. It was demonstrated by He et al. [9] that in the presence of an electric field, droplet volumes can be significantly altered, when the surrounding medium is taken as a viscous oil. The effect of an alternating electric field on droplets of liquid hydrocarbons formed in water was investigated by Sato [10]. However, the detailed interplay of the electro-hydrodynamic forces and their impact on the droplet morphology as well as flow structure are heretofore absent in the literature.

In the above context, the current study explores the dynamics of electric field-modulated drop formation from an orifice into a quiescent liquid medium. We invoke the idealization of leaky dielectric fluids to characterize the electrical nature of both the drop and outer fluids. By performing extensive numerical computations, we uncover the fascinating coupling of hydrodynamic and electric stresses, which ultimately decides the response of the droplets.

2 Problem Description

We present a representative snapshot of the domain employed in our simulations in Fig. 1. The upper wall consists of a small orifice through which drop fluid is injected into a quiescent outer medium. The radius of the orifice is denoted by R_o . Both the fluids exhibit Newtonian rheology and remain mutually immiscible. Considering the dynamics to be axi-symmetric, we employ a cylindrical coordinate system (r, z) . The center of the orifice is taken as the origin. The width and length of the domain are considered as $16R_o$ and $48R_o$, respectively. The size of the computational domain has been chosen after careful analysis to ensure that the results are independent of the domain size. The lower wall is considered to be a positive electrode, maintained at a potential of ϕ_o , and the upper boundary is grounded to generate an electric field across the domain.

Fig. 1 Setup of the computational domain (not to scale) and the applied boundary conditions in an axisymmetric cylindrical coordinate system. The drop liquid is injected through the orifice into a quiescent immiscible medium. The direction of gravity is along the positive $+z$ axis. The lower and upper boundaries act as electrodes to create an external electric field



The differential equations which govern the physical problem are given as

$$\nabla \cdot \mathbf{U} = 0, \quad (1)$$

$$\rho \left[\frac{\partial \mathbf{U}}{\partial t} + (\mathbf{U} \cdot \nabla) \mathbf{U} \right] = -\nabla p + \rho \mathbf{g} + \nabla \cdot [\mu(\nabla \mathbf{U} + \nabla \mathbf{U}^T)] + \mathbf{F}_{st} + \mathbf{F}_e. \quad (2)$$

Here, the velocity field is denoted by $\mathbf{U} = (u, v)$, pressure is represented by p , the gravitational acceleration by $\mathbf{g} = (0, g)$ and the density and viscosity are denoted by ρ and μ , respectively. Using the continuum surface force (CSF) model of Brackbill et al. [11], the surface tension force acting at the interface is given by $\mathbf{F}_{st} = \gamma \kappa \mathbf{n} \delta$, wherein γ represents the surface tension, κ denotes the curvature and n represents the interface normal. The δ represents a Dirac delta function, having a nonzero value only at the interfacial cells.

The interface is captured by adding an equation for volume fraction α , given as,

$$\frac{\partial \alpha}{\partial t} + \nabla \cdot (\mathbf{U} \alpha) = 0 \quad (3)$$

The volume fraction α is considered as 1 inside the drop and zero everywhere else.

From electrodynamics, the Gauss law can be written as, $\nabla \cdot (\epsilon \mathbf{E}) = q$. Here, the symbols E , ϵ and q denote the electric field intensity, the permittivity and volumetric charge density, respectively. Additionally, the electric field is considered as irrotational, i.e., $\nabla \times \mathbf{E} = 0$. As such, the electric potential can be defined as $\mathbf{E} = -\nabla \phi$. The equation for charge can be written as

$$\frac{\partial q}{\partial t} + \nabla \cdot (q \mathbf{U}) = -\nabla \cdot (\sigma \mathbf{E}), \quad (4)$$

where σ denotes the electrical conductivity of the fluids. The Maxwell stress tensor is given as $\mathbf{M} = \epsilon[\mathbf{E} \otimes \mathbf{E} - \frac{1}{2}(\mathbf{E} \cdot \mathbf{E})\mathbf{I}]$. Thus, the electrostatic force is given as

$$\mathbf{F}_e = \nabla \cdot \mathbf{M} = -\frac{1}{2} \mathbf{E} \cdot \mathbf{E} \nabla \epsilon + q \mathbf{E} \quad (5)$$

The governing equations are solved in conjunction with the following initial and boundary conditions. Initially, a hemispherical drop is taken pendant at the orifice and both fluids remain quiescent. A fully developed velocity profile is applied at the orifice, while the rest of the wall is considered as a no-slip and no penetration surface. Outflow conditions are applied at the bottom boundary, whereas free slip condition is applied at the lateral boundary. In addition, the lower surface is maintained at given potential ($\phi = \phi_o$), while the top surface is electrically grounded ($\phi = 0$). Since we employ a single fluid formalism for solving the interfacial flow configuration, no explicit boundary conditions need to be specified at the interface.

The non-dimensional parameters pertinent to the problem are given as:

$$\begin{aligned} \text{Re} &= \frac{\rho_d U_{\text{avg}} R_o}{\mu_d}, \quad \text{We} = \frac{\rho_d U_{\text{avg}}^2 R_o}{\gamma}, \quad \text{Bo} = \frac{\rho_d g R_o^2}{\gamma}, \quad \text{Re}_E = \frac{\epsilon_d U_{\text{avg}}}{\sigma_d R_o}, \\ \eta &= \frac{\rho_s}{\rho_d}, \quad \lambda = \frac{\mu_s}{\mu_d}, \quad S = \frac{\epsilon_s}{\epsilon_d}, \quad R = \frac{\sigma_s}{\sigma_d}, \end{aligned} \quad (6)$$

where the subscripts s and d denote the surrounding and drop fluids, respectively. Here, the Reynolds number (Re) signifies the importance of inertia over viscous forces, Weber number (We) shows dominance of inertia over surface tension forces and Bond number (Bo) depicts the significance of gravity over surface tension forces. The electric Reynolds number (Re_E) compares charge relaxation time scale to the flow time scale. The density, viscosity, permittivity and conductivity ratios are given by η , λ , S and R , respectively. In addition, the dimensionless electric field intensity is given by $E^* = \frac{E}{u_{\text{avg}} \sqrt{\frac{\epsilon_d}{\rho_d}}}$. For the discussions below, we designate E^* by E and consider the values of Re, We, Bo, η and λ fixed at 30.0, 0.4, 0.2, 0.8 and 7.5, respectively. The physical properties are chosen corresponding to a tetrachloroethylene drop suspended in glycerin-water solution. The electrical properties are taken as representative values, in order to highlight the differing dynamics of drops, depending on the relative strength of permittivity and conductivity of the fluids.

The open-source solver '*Basilisk*' is used for performing the computations. The spatial discretization is done using the finite volume approach, and a height function-based method is employed to calculate the interfacial curvature. The pressure Poisson equation is solved using a multigrid solver with a convergence tolerance of 1×10^{-4} . Due to the explicit treatment of the convective and surface tension terms, the maximum allowable timestep is restricted by the standard CFL and capillary constraints. The solver is equipped with a parallelized framework to accelerate the computations. Additionally, the EHD toolbox is employed to simulate the effect of the electric field.

3 Results and Discussion

We first validate the numerical framework with experimental observations. In Fig. 2a and b, we compare our computed results with the experimental measurements of Subramani et al.[12]. It can be clearly observed that the computed drop profile at pinch-off shows good agreement with the experimental result, thereby demonstrating the accuracy of our numerical framework. Additionally, we demonstrate grid convergence by performing a grid resolution test. The minimum grid sizes corresponding to the three different resolutions are 0.12, 0.06 and 0.03. It can be discerned that the difference in the interfacial profile is negligible when the grid is progressively

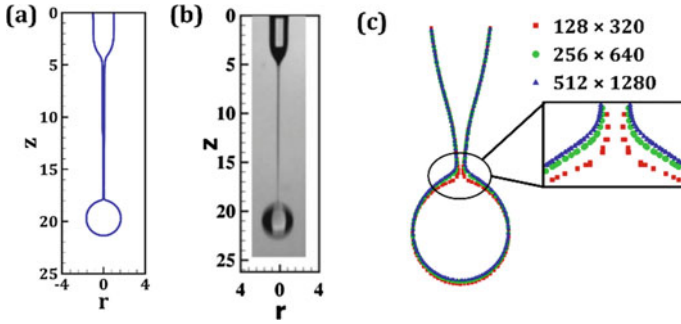


Fig. 2 Comparison of drop formation between **a** results from our computations and **b** experimental observations of Subramani et al. [12]. **c** Grid independence test showing the interfacial profiles for different grid resolutions

refined. For our study, we have employed the resolution of 256×768 for optimal computational performance.

We now discuss the impact of the electric field on formation of the droplets. As mentioned earlier, the fluids are assumed as leaky dielectrics. Such fluids allow a small amount of free charges, thereby resulting in both tangential and normal electric stresses acting at the interface. However, the time scale of relaxation of charges (t_E) is much lower than the flow time scale (t_F). Thus, the bulk fluid remains free of any charge carriers. As such, the magnitude of electric Reynolds number ($Re_E = t_E/t_F$) remains lesser than unity. In our study, we have fixed this value to be 0.1. Furthermore, the analysis is performed by considering two different configurations—Systems A and B. These systems are defined by the relative magnitude of R and S . System A considers the value of (R, S) as $(2.0, 0.5)$, whereas System B considers the value of (R, S) as $(0.5, 2.0)$. In a physical sense, for System A, the drop fluid is less conducting than the outer medium and possesses a higher permittivity than the outer medium. In contrast, for System B, the fluid of the drop is more conducting, but possesses a smaller permittivity than outer medium.

Figures 3 and 4 illustrate the contrasting impact of electric field on the drops for the two systems being investigated. In case of System A, the electric field leads to lateral deformation of the drop, thereby producing an oblate shape. In contrast, the electric field ushers axial deformation of the drop, for System B, leading to a prolate shape. The drop deformation can be augmented by increasing the intensity of electric field. However, it should be highlighted here that the overall deformation of the droplets is significantly higher for System B, in comparison with System A. Furthermore, for System B, the drop formation transitions from a dripping regime to a jetting regime, beyond a critical value of E .

The differing behavior of droplet deformation for both the systems can be explained by observing the nature of electric forces. The total force at the interface consists of two components—polarization component influencing the dipoles and Coulombic component acting on the free charge carriers. Figure 5 depicts the variation in forces for the two different configurations. It can be observed that the

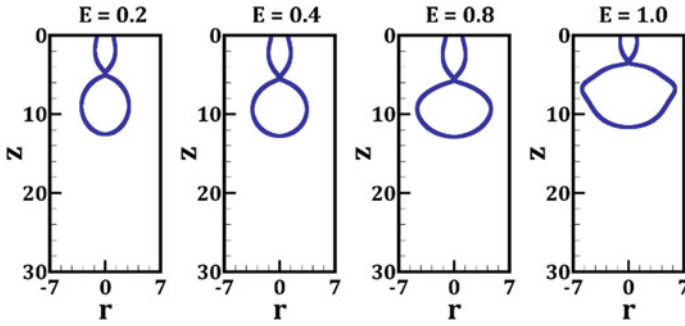


Fig. 3 Variation in droplet profiles at the moment of pinch-off with electric field intensity for System A configuration

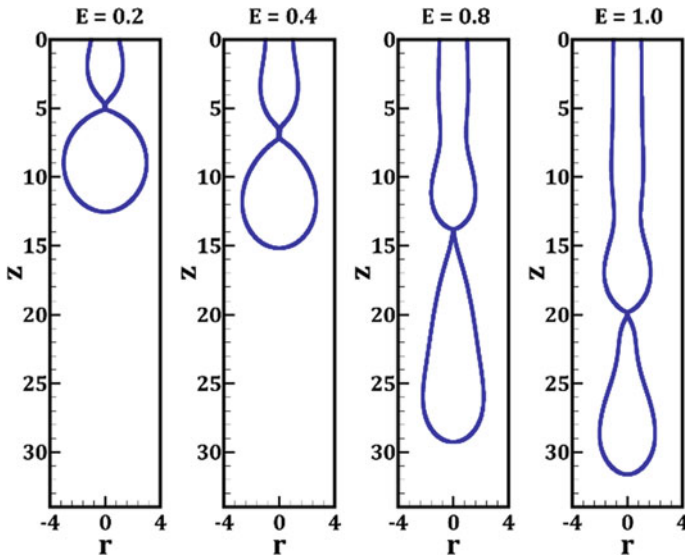
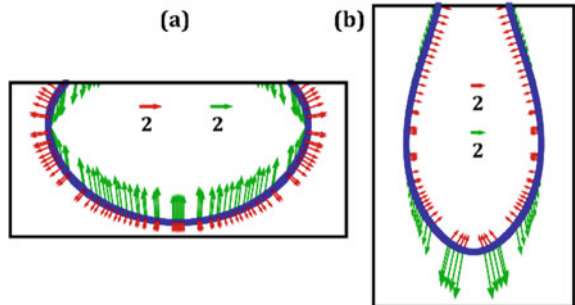


Fig. 4 Variation in droplet profiles at the moment of pinch-off with electric field intensity for System B configuration

Fig. 5 Illustration of electric forces at the interface of the drops for **a** System A and **b** System B. The polarization forces are shown in red color, whereas the Columbic forces are represented in green color



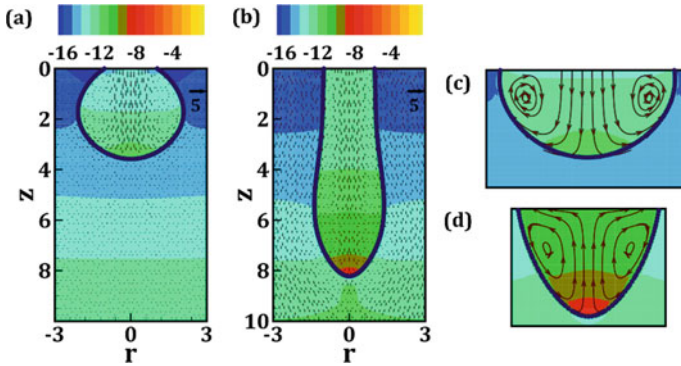


Fig. 6 Visualization of the flow field (in the droplet reference frame) for **a** System A and **b** System B. **c** and **d** present magnified view of the flow near the droplet tip for Systems A and B, respectively. The colored contours represent the variation in pressure over the domain

magnitude of polarization forces is far smaller than the Columbic forces for both the configurations. Hence, the dynamics is completely decided by the nature as well as magnitude of Columbic forces. For System A, the forces near the tip of the drop are compressive, which results in lateral deformation leading to an oblate shape. In contrast, the Columbic forces are tensile near the tip in System B, which promotes axial elongation, thereby creating a prolate shape. Additionally, the strength of the electric forces is augmented in System B. Consequently, the droplets of System B are significantly more deformed than System A.

Finally, we examine the flow field inside the droplet for both the systems in Fig. 6. The drop fluid flows from the drop tip toward the equatorial region for the case of System A. This observation also supports the oblate deformation of the droplet, under such a configuration. In contrast, the drop fluid flows from the equator to the tip for System B, thereby leading to creation of prolate shaped drops.

4 Conclusions

We present a computational investigation of the influence of an imposed electric field on the formation of droplets in a quiescent ambient medium. The interface is resolved by a volume-of-fluid approach, and the leaky-dielectric model is considered for characterizing the electrical behavior of the fluids. Two different configurations, namely Systems A and B, are considered, which differ in the relative magnitudes of electrical conductivity and permittivity. The simulations demonstrate that due to electro-hydrodynamic effects, the two systems present a contrasting behavior of droplet deformation. The droplets of System A deform into oblate shape, whereas prolate drops are formed in case of System B. The deformation is significantly higher

for the case of System B. A closer inspection of the interfacial electric forces indicates that compressive Columbic forces are developed for System A, while tensile Columbic forces are developed in System B. The polarization force is negligible for both the systems under consideration. The drop fluid flows from the tip to the equator, under the condition of System A. In contrast, flow from equator to the tip is observed for droplets of System B. The fundamentally opposing nature of electric forces as well as flow structure promotes the radically different deformation patterns for the two systems under consideration.

References

1. Borthakur MP, Biswas G, Bandyopadhyay D (2017) Formation of liquid drops at an orifice and dynamics of pinch-off in liquid jets. *Phys Rev E* 96(1):013115
2. Basaran OA (2002) Small-scale free surface flows with breakup: drop formation and emerging applications. *Am Inst Chem Eng (AIChEJ)* 48(9):1842
3. Taylor GI (1966) Studies in electrohydrodynamics. I. The circulation produced in a drop by an electric field. In: *Proc R Soc London Ser A Math Phys Sci* 291(1425):159–166
4. Zhang X, Basaran OA (1996) Dynamics of drop formation from a capillary in the presence of an electric field. *J Fluid Mech* 326:239–263
5. Mandal S, Bandyopadhyay A, Chakraborty S (2016) The effect of uniform electric field on the cross-stream migration of a drop in plane Poiseuille flow. *J Fluid Mech* 809:726–774
6. Timung S, Chaudhuri J, Borthakur MP, Mandal TK, Biswas G, Bandyopadhyay D (2017) Electric field mediated spraying of miniaturized droplets inside microchannel. *Electrophoresis* 38(11):1450–1457
7. Basaran OA, Scriven LE (1989) Axisymmetric shapes and stability of charged drops in an external electric field. *Phys Fluids A Fluid Dyn* 1(5):799–809
8. Harris MT, Basaran OA (1993) Capillary electrohydrostatics of conducting drops hanging from a nozzle in an electric field. *J Colloid Interface Sci* 161(2):389–413
9. He W, Baird MHI, Chang JS (1991) The effect of electric field on droplet formation and motion in a viscous liquid. *Can J Chem Eng* 69(5):1174–1183
10. Masayuki S (1984) The production of essentially uniform-sized liquid droplets in gaseous or immiscible liquid media under applied AC potential. *J Electrostat* 15(2):237–247
11. Brackbill JU, Kothe DB, Zemach C (1992) A continuum method for modeling surface tension. *J Comput Phys* 100(2):335–354
12. Subramani HJ, Yeoh HK, Suryo R, Xu Q, Ambravaneswaran B, Basaran OA (2006) Simplicity and complexity in a dripping faucet. *Phys Fluids* 18(3):032106

Robotic Systems Deployed to Combat COVID-19 Pandemic: A Review



Deep Singh, Rutupurna Choudhury, and Yogesh Singh

Abstract The COVID-19 epidemic has been deemed a pandemic by the World Health Organization. It is triggered due to the severe acute respiratory syndrome coronavirus 2 (SARS-CoV-2). It originated and spread from Wuhan, China, in December 2019. At present, the entire world is struggling from this virus due to large confirmed positive and death cases of COVID-19. People of every nation have been isolated, and lockdowns are instituted. Despite the introduction of several precautionary measures, the spread of the virus is still increasing at an alarming pace. Although promising development has been made for the development of vaccines for SARS-CoV-2, no vaccines have been reported to cure the infection. Different antiviral therapies have also been attempted but do not seem to be successful for every patient. To deter the dissemination and control the spread of virus, the frontline healthcare staff and police officers deployed numerous autonomous systems for an increased line of protection. Robots are deployed to conduct different operations including decontamination, package delivery, etc. It also acts as a mediator for two-way communication between the doctors and patients. Recent advancement in robotics for its application in healthcare facilities has been found very effective for the healthcare officials to communicate with the virus affected patients, and this literature has addressed it.

Keywords COVID-19 · Coronavirus · Robotic systems · Pandemic

1 Introduction

The outbreak of the novel coronavirus 2019 (Covid-19) started in December 2019 and has created havoc for the humans globally. The outbreak of COVID-19 disease originated from Wuhan city, China, in January 2020 as per the ICTV (International Committee on Taxonomy of Viruses) [1]. It was first identified in Wuhan, China, and confirmed to the Country Office of the WHO (World Health Organisation) in

D. Singh · R. Choudhury · Y. Singh (✉)

Department of Mechanical Engineering, National Institute of Technology Silchar, Silchar, Assam 788010, India

e-mail: yogeshsingh15@gmail.com

China on 31 December 2019 [2]. Initially, 40 cases were found admitted in the hospitals of Wuhan city infected by “Viral Pneumonia of Unknown Etiology” [3]. Bats and Snakes might be the potential reservoir of COVID-19 [4]. The disease has been established as a new virus and named Novel Corona Virus or 2019-nCoV or COVID-19 by the WHO [3].

The first death was reported on 11 January 2020 of a 61-year-old man exposed to the seafood market. The disease spread to the other parts of the world rapidly and infected many within a few weeks. Hence, on 30 January 2020, WHO declared it as a Public Health Emergency of International Concern. On 2 February, the first death outside China was reported in the Philippines of a Chinese citizen from Wuhan. On 11 March, 2020, the Covid-19 was declared a pandemic by WHO. Till then, about 114 countries already proclaimed a total of 118,000 confirmed cases of COVID-19 in their region [3].

This virus is a threat to the health of the public and humankind and its outbreak has led to Public Health Emergency internationally. As on 12 July 2020 at 1:35 P.M. (CEST), the Covid-19 dashboard of WHO dictates that most countries are affected by the pandemic [5]. WHO reports 12,486,484 confirmed cases globally, which includes 560,814 deaths, as depicted in Fig. 1. Out of the confirmed cases, almost 4.491% death has been reported and it threatens the humankind. Also, as per The World Bank, the global population in the year 2019 shows a total of 7.594 billion, which indicates that till date over 0.164% population of the world has been affected by this deadly virus. There is no decline in the daily confirmed cases and deaths worldwide. Figure 2 represents the COVID-19 daily confirmed and death cases globally as declared by WHO. Figure 3 represents the cumulative confirmed and death cases globally. Figures 2 and 3 indicates no decline in confirmed and death cases [5].

The coronaviruses are named based on their shape. The outer fringe of envelope proteins is a family of enveloped RNA viruses and resembles a crown (in Latin ‘corona’) [3, 4]. It is pathogenic to mammals and birds. In humans, it can cause mild infection in the upper airway. It can spread human-to-human through respiratory fomites similar to Severe Acute Respiratory Syndrome Coronavirus (SARS-CoV)

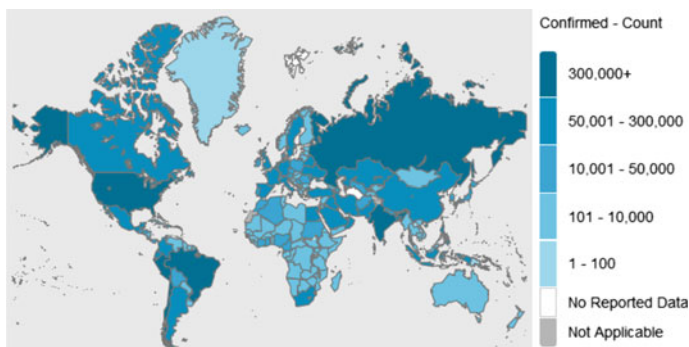


Fig. 1 Overview of the global COVID-19 pandemic effect on 12 July 2020 (1:35 P.M. CEST)

Fig. 2 Daily confirmed and death cases globally [5]

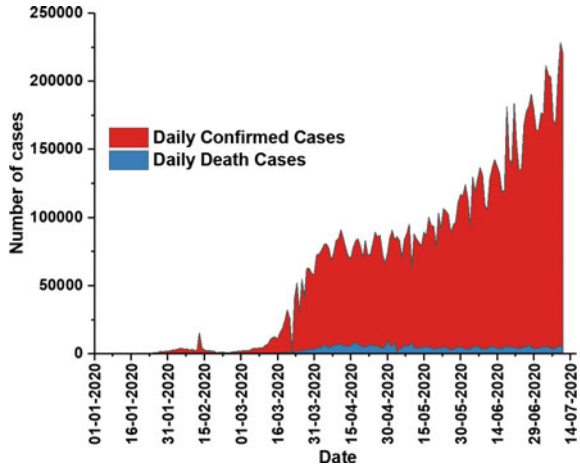
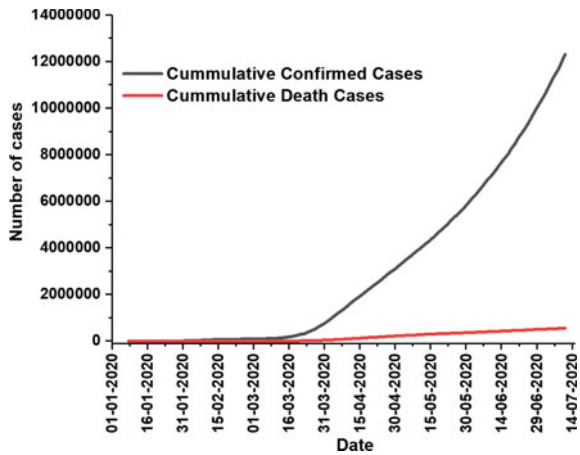


Fig. 3 Cumulative confirmed and death cases globally [5]



and Middle East Respiratory Syndrome Coronavirus (MERS-CoV). These two beta coronaviruses, SARS-CoV and MERS-CoV outbreak, took place in the year 2003 and 2015, respectively [2, 3, 6], and has resulted in more than 10,000 cumulative cases with mortality rates of 10% and 37%, respectively [7].

The COVID-19 is also caused by Severe Acute Respiratory Syndrome Coronavirus-2 (SARS-CoV-2). Research indicates that nCoV-19 is transmitted from human-to-human during the asymptomatic incubation period, while respiratory viruses are more infectious when patients become symptomatic. It is estimated that the asymptomatic incubating duration is 2–10 days. COVID-19 has an average incubation period of 5.2 days, with a confidence level of 95% [6].

2 COVID-19 Symptoms

The symptoms of the first four patients admitted at the local hospital of Huanan in Southern China include fever, low lymphocyte count, low or normal white cell count, radiographic evidence of pneumonia. The symptoms of COVID-19 include systematic disorders such as fever, cough, fatigue, headache, sputum production, hypoxemia, diarrhoea, acute cardiac injury, dyspnoea, lymphopenia, haemoptysis and respiratory disorders such as rhinorrhoea, ground-glass opacities, sore throat, sneezing, pneumonia, acute respiratory distress syndrome and RNAemia [8]. Older patients with co-morbidities (heart disease, diabetes) are at higher risk for adverse outcomes [9].

3 Prevention of COVID-19 Spread

COVID-19 pandemic, being a core priority of global public health management, appropriate control measures should be adopted to prevent the outbreak. A person is suspected to be positive for COVID-19 if he has travelled to Wuhan or had any direct contact with patients with symptoms, such as fever or respiratory problems within 14 days of illness onset, from Wuhan [6]. Patients with mild COVID-19 symptoms have a higher tendency to spread the virus and hence should seek medical assistance at the earliest [9]. To prevent COVID-19 exposure, spread and infection, one should be alert and adopt a few of the healthy habits such as:

- Wash hand with soap and water for a minimum of 20 s.
- Use alcohol-based sanitizer during the unavailability of soap and water.
- Do not brush unwashed hands on eyes, nose and mouth.
- Use tissue while coughing and sneezing and discard it in a closed bin.
- Frequently handled surfaces and objects must be cleaned and disinfected.
- Seek immediate medical assistance when it seems to have COVID-19 symptoms.

4 Development of Vaccine for COVID-19

The vaccine is the key to COVID-19 prevention and boycott. Vaccines increase immune levels to prevent the spread of COVID-19. New advances in COVID-19 testing enable research towards vaccine development across the globe. Depending on the research and development, vaccines are classified into various groups; namely, inactivated vaccines, live attenuated vaccines, vectored vaccines, nucleic acid-based vaccines and recombinant subunit vaccines [10, 11]. Although more than 50 vaccine candidates are in trials, the vaccines Sputnik, Covaxin and Covishield are being primarily used to suppress virus transmission and mortality [12].

Sputnik, the first vaccine developed in Russia, observed efficacy of about 91.4% [13]. Bharat Biotech in collaboration with ICMR—National Institute of Virology, India, has developed COVAXIN, India's indigenous inactivated vaccine. It qualifies all the clinical tests and gets approval by DCGI for commercial use [14]. The vaccine Covishield developed by the Serum Institute of India has been approved for emergency use in Britain and Argentina [15].

5 Impacts of COVID-19

The outbreak of COVID-19 has become a huge risk to everyone. Frontline healthcare staff worldwide are more susceptible and vulnerable to emerging and highly transmissible pathogens—COVID-19 [16]. Antiviral therapy and vaccine are being tested and established across the globe. Staffs in health services are at considerable risk of negative health consequences due to long hours of work and high risk of infection, shortage of personal protective equipment (PPE), loneliness, physical fatigue and family separation [17]. As reported by WHO on 14 February 2020, there were 1716 healthcare staff infected with the virus [16]. COVID-19 has affected one's daily life, businesses and also disrupted world trade and movements. The global economy is slowing down due to the exponential rise in COVID-19 cases in every region of the world [18]. Most industrial sectors have been affected by the closure or with slowing down product production and providing services, including the pharmaceuticals industry, information and electronics industry, tourism, solar power sector, etc. [18–20]. The ICU community must be prepared for the excessive patient influx. They must be able to diagnose and isolate rapidly, monitor clinically and avoid infection.

As research for COVID-19 progresses, many facts tend to evolve and keep changing, and many misconceptions about prevention and infection control still prevail among the common public. These misconceptions have been circulated exponentially with the aid of social media, particularly fake news. Hence, numerous sites like the WHO offer credible knowledge and myth-buster [3].

Major prevention and control measures have been adopted globally. The prevention measure also includes travel screenings to prevent virus transmission [21]. As of 5 March 2020, local COVID-19 transmissions in Hong Kong, Singapore and Japan have been sustained. The strategy to control and avoid the smaller chain of virus infection from amplifying through a large population seemed effective [22].

The COVID-19 scenario in India is far better than in other nations, as precautionary measures were adopted very early in contrast with others. To prevent community spread, the Union Government has implemented essential steps, but the understanding of the situation to the general public is ineffective [1].

After the onset of the COVID-19 pandemic, a rapid increase in consumers of masks [3] and sanitizers has culminated in the depletion of the goods in the market [3]. The shortage of PPE is a major concern for medical professionals worldwide, including India. India, being a heavily populated country, effective preventive steps should be taken to restrict the spread of the virus, particularly in areas such as Dharavi,

Mumbai. As of 30 March 2020, Government of India has declared a total of 1250 confirmed COVID-19 cases, including 101 cured and 32 death cases [3]. The governments, the media, celebrities, physicians, police, academics and other members of society have been encouraging people to stop public events, family functions, sports, meetings, religious ceremonies, school courses. An appeal to the public to avoid public gatherings, sports, family functions, religious ceremonies, meetings, classes in schools has been made by governments, media, doctors, researchers, celebrities, police and other stakeholders of the society [3, 23].

Although the Indian Government has introduced ambitious public safety initiatives, including Lockdown 1.0–Lockdown 4.0 (from 25 March to 31 May 2020), treating COVID-19 patients has been a challenging task. Healthcare workers require adequate training to handle the virus affected patients. The available PPE and life-saving equipment (including ventilators) do not seem sufficient for the future. Also, in the UK and US, the government is unable to supply adequate amount of PPE [22, 24].

The physicians, doctors and health systems are rapidly seeking virtual healthcare strategy to prevent direct contact with patients and other healthcare professionals. Various robotic systems are now being commonly deployed to reduce the dissemination of COVID-19. It is done to restrict physical interaction with the COVID-19 patients and even with the general public.

While the new Industry 4.0 revolution is booming and its effect is growing at a faster rate, COVID-19 has served as a trigger for it and has further enhanced its pace of research, its use for testing and emergencies. Emergency health, safety and security workers were introduced to several robotic systems after the global lockdown to continue their most dangerous roles while enforcing physical distance and other strict government protocols to minimize virus transmission. A hospital was developed in Wuhan, China, which is primarily run by robots to execute all the protocols, as discussed in Sect. 6, which is a significant accomplishment towards Industry 4.0. Various other robotic devices, in regards to medical emergencies, have also been developed which are discussed in subsequent sections.

6 Role of Robotics in Combating COVID-19

In the present scenario of exponential COVID-19 growth, the best and most efficient tool considered is robotics. Robotics is renowned for its wide-ranging applications, including medical facilities. As a vaccine has not been developed yet, it is unwise to expose ourselves to virus by actively visiting COVID-19 affected patients unless urgent. Robotic devices are resistant to COVID-19 and other viruses. Robotic devices can work non-stop round the clock. Robots are highly efficient and accurate and can execute tasks across a broad variety of applications. Being resistant to virus, robots can play a very critical role during pandemic.

The sports centre in Wuhan, China, has been converted to a new hospital ward for patients (needing basic medical care) exhibiting early COVID-19 symptoms.

Robotics operate the hospital entirely to shield medical personnel from the virus. On 7 March 2020, about 200 patients with early COVID-19 symptoms were admitted to this hospital. The robot at this hospital delivers essentials to the patients and also keeps the ward clean. This trial was undertaken in collaboration with CloudMinds, a Beijing based robotic firm, and China Mobile, a mobile operator, along with Wuhan Wuchang Hospital. If the health condition of the patient becomes acute, the patient is transferred to the hospital run by humans or if the patient recovers, they are sent home under quarantine. The patients in the robot-based hospital wore sensors integrated bracelet. The sensors are used to monitor temperature and heart rates. It helped medical personnel to keep patient’s health track and assign tasks to the robots. Any abnormality can be interpreted and immediate action could be taken [25].

6.1 Worldwide Use of Ground and Aerial Robotics for COVID-19

During pandemic, robotic devices are being adapted to perform a wide array of applications with a motive to monitor and prevent COVID-19 from spreading. Many robotic devices have been reported to be functioning globally. The application of robotic devices fighting for COVID-19 is summarized in Table 1 [26].

Table 1 Applications of robotic devices to fight COVID-19 [26]

Public safety, public works, non-clinical public health	Clinical care	Work, critical infrastructure, quality of life	Laboratory and supply chain automation	Non-hospital care
(16 countries)	(8 countries)	(7 countries)	(5 countries)	(4 countries)
Quarantine enforcement	Disinfecting healthcare wards	Delivery	Delivery	Quarantine or nursing home socializing
Disinfecting public places	Telepresence	Socializing	Infectious material handling	Delivery to quarantined
Infected person identification	Package dispensing	Tele-commerce	Laboratory automation	Off-site testing
Announcement at public places	Patient intake and visitors	Robot assistants	PPE manufacturing	Testing and care in nursing homes
Traffic monitoring	Socializing	Critical infrastructure protection		

6.2 Robotics for Disinfecting Point of Care and Public Places

During the COVID-19 pandemic, robotic devices integrated with non-contact ultraviolet (UV) lights are deployed to carry out the surface disinfection in the hospital wards, hotels, airports, streets and other public places. It can decontaminate frequently touched surfaces and objects effectively. The decontamination performed by robotic device is very fast and efficient as compared to the manual disinfection process. These robots eliminate the need for cleaning personnel and reduce the risk of exposure to the virus [27].

A Danish company called UVD Robots built robots to disinfect point of care facilities. The robot is used to disinfect operating theatres, ICU, rooms of patients, etc. [28]. Similar disinfecting robots such as Youibot [29], Bolb [28], DJI drones [30], LightStrike [31] and also the robots built by CloudMinds [29], Shanghai enterprise [32] are being used against COVID-19.

On 23 March 2020, the Tamil Nadu government sent drones, developed by the start-up Garuda aerospace, to disinfect the area near Rajiv Gandhi Government General Hospital [33]. Several self-driving robots were deployed at the Hong Kong International Airport for disinfection of public places. Whiz and Intelligent Sterilization Robot (ISR) are being used to sanitize public places, including toilets. Its service improves efficiency, and human cleaners can be reallocated to perform critical cleaning and disinfection tasks [34].

6.3 Robotics to Handle Contaminated Materials or Samples

Manual handling of contaminated objects or test samples is highly dangerous and should be avoided. Ground robots can carry out this task in hospitals and aerial robots to transport the contaminated materials and samples from one place to another in a much faster and efficient way.

Antwork launched its first urban air transportation system on 6 February 2020 by flying a medical supply drone from the People's Hospital of Xinchang County to the Xinchang County, Disease Control Center. Compared to ordinary road transport, the air transportation channel required 50% lesser time for transportation. The transportation is also pollution-free [35].

6.4 Robotics to Decontaminate PPE

The PPE shortfall has threatened the life of frontline healthcare staff worldwide. To address this issue, robotic devices integrated with UV lights can be implemented to decontaminate PPE enabling numerous usages.

Nebraska Medicine (Omaha) has built a robot equipped with ultraviolet light for the safe disinfection process of N-95 masks [36]. Tru-D (Total Room Ultraviolet Disinfectant), a 5 ft. 6 in. robotic device equipped with ultraviolet germicidal irradiation, disinfects porous and non-porous surfaces, including N-95 masks [37].

6.5 Robotics for Foods and Prescription Dispensing

It is quite unsafe for humans to visit the virus affected patients for delivering medical and food supplies. Being higher chances of cross-infection, automated robotic devices can be very beneficial to deliver the essentials. Automated robotics devices can work non-stop efficiently and are not prone to fatigue.

Qianxi Robotic Catering, a Chinese real estate affiliate of giant Country Garden, developed unmanned food stations and donated to the frontline medics in Wuhan, fighting COVID-19. A pink robot catering station setup outside Hannan Red Cross Hospital serves traditional brown rice clay-pot casserole dishes free of charge. It has the capacity to cook 144 meals/h and runs 24 h [38]. Shenzhen-based Pudu Technology has also installed similar robots for catering services in over 40 hospitals around the country for the medics [39].

Sense Time, an AI firm, develops contactless temperature sensing software and could be installed for monitoring community centres, schools and underground stations in Shanghai, Beijing and Shenzhen [39].

6.6 Robotics to Deliver Packages and Other Necessities

Apart from robots being used at hospitals for delivery, robotic devices can also be implemented to deliver packages in the form of UAV and unmanned ground vehicles. This will also play a major role in preventing the virus from spreading. It can also be implemented for delivering essentials from shops to home.

Robotemi, an Israeli start-up, developed an AI driven Temi robot assistant, as depicted in Fig. 4. A 10-in. tablet stands at three feet tall and could roll on four wheels continuously for eight hours on battery. It could be connected with Bluetooth, LTE and Wi-Fi. It has an integrated sound system with the technology of Amazon's Alexa. An autonomous mode of navigation helps it to roam by itself by avoiding obstacles. It is also integrated with a thermal camera, thermometer and a sink attached to wash hands to combat COVID-19 [40].

JD.com has developed an in-house level 4 (L4) autonomous delivery robot (Fig. 5). When the robot arrives at the destination, it sends a message with a collection code to the recipient's phone. The collection code when entered, the robot releases the package [41]. White Rhino, an unmanned vehicle, was used to transport medical supplies, meals to patients and doctors and also to perform various emergency services in hospitals [42].

Fig. 4 AI-powered Temi robot assistant [40]



Fig. 5 JD.com's autonomous delivery robot [41]



6.7 Robotics for Telepresence of Healthcare Workers

“Robots are tireless assistants that can’t get infected, that can’t get sick,” said by Francesco Dentali, Director of Circolo Hospital’s ICU [43]. The application of telepresence robots reduces the risk of healthcare staff from being exposed to the virus. When integrated with the necessary devices, the robot can autonomously navigate to the patient room and assist in two-way communication. It also helps monitor various health parameters of the patient remotely [44]. The application of robots is not limited to perform human duties. It can also help communicate with dear ones via video calls.

Considering a single PPE kit per patient, a doctor needs a larger number of PPE kits if he visits the patients physically. These PPE kits are discarded after every use. Hence, the healthcare workers discard huge sets of PPE kits in a single day. Although healthcare staff are equipped with PPE, there are chances to be exposed to the virus. Hence, telepresence robots play a vital role in fighting against viruses. Monitoring patients remotely avoid any exposure to the virus and numerous PPE kits are saved from being used for acute cases [44].

As coronavirus can spread human-to-human, doctors have taken an extra caution in the form of using robots. Telehealth robotic systems enable doctors to conduct

basic diagnostic tasks and communicate remotely with patients, thus reducing close interaction and minimizing the risk of the virus [45].

The first COVID-19 patient is diagnosed with a few medical staff and a robot. The robot has a stethoscope that lets doctors, via a widescreen, to monitor the critical conditions. Additional staff is needed to drive the robot [46]. Various robots such as Vici (InTouch Health) [45], Ginger (CloudMinds') [47], Ninja robots [48], Tommy [49], LionsBot [44] and Zorabots [50] have been developed for the purpose of telepresence.

Human Augmented Robot Intelligence with eXtreme Reality (HARIX), an AI platform, is a combination of intelligent bracelets and patient-wearing rings and offers remote monitoring of patients' vital signs, including blood oxygen level, heart rate and temperature [47].

China has developed an intelligent robot jointly by the Guangzhou Institute of Respiratory Health and the Shenyang Institute of Automation under the Chinese Academy of Sciences. The robotic device takes throat swab samples precisely with the help of a snake-shaped mechanical arm. It also consists of a binocular endoscope to provide real-time high definition 3D anatomical scenes. The test result showed high-quality sampling with a single success rate of over 95%. The robot ensures cross-infection prevention as being operated remotely [51].

6.8 Robotics to Socialize and Conduct Events Virtually

During the pandemic, robotic devices are being utilized for multiple applications and in a very innovative way. Wheel-based robotic devices are also being used for delivering diplomas to the graduates during virtual convocation. Business Breakthrough University in Tokyo used mobile robots from Newmeto to award diplomas to the graduates on 28 March 2020 [52]. Similar robots can be used to host various ceremonies and functions, including graduation ceremonies, online events and conferences. A group of eight elementary school students also conducted a virtual graduation ceremony in the game Minecraft [52].

6.9 Robotics to Automate Laboratories

Opentrons' have built a COVID-19 testing system to automate the testing process, thereby increasing efficiency of test results along with rapid testing of about 2400 samples a day [53]. Two new automated assay ready workstations, MagExSTARlet and PCR Prep STARlet, have been developed by Microlab® STARlet for rapid diagnostic and testing of COVID-19 [54].

6.10 Robotics to Help Police Officials Monitor the Region and Crowd Dispersal

While government and health authorities urge to maintain the lockdown, several people are roaming around as nothing has happened. To hold people indoors, officials in various regions are making announcements using drones and advise people to remain safe at home to prevent the exponential spread of the virus [55].

MicroMultiCopter (MMC), a Chinese drone company, has developed drones to spray disinfectant in public places [56]. These are also used for various applications such as aerial broadcasting, disinfectant spraying, aerial thermal monitoring and traffic control. It is also used to evacuate worksites and to identify persons with COVID-19 symptoms via thermal imaging cameras [56]. Similar drones are also being used by the authorities of UK [57], Spain [55], California [58], Madrid [59], Oahu [60], Dubai [61] and Kuwait [62]. Police officers in China are flying drones with a large QR code for the people to scan and register their health information online with the government [63]. In French Riveria city [64] and Daytona beach [65], police warn people with drones to remain at home during the lockdown.

Police in most of the India's southern states like Kerala is performing drone-based surveillance to identify lockdown violators. Some drones are even equipped with flashing lights, police sirens and a recorded warning message to deter people from entering public areas for no good cause [66]. Six drones developed by Alpha Drone Technology, a start-up in Bengaluru, India, are being used by the Bengaluru authorities to spray disinfectant in the streets of the city during lockdown [65]. A drone company in Gujarat, India, is utilizing drones for the surveillance of gatherings in public places with the support of the state government. Karnataka and Andhra Pradesh are also using drones to spray disinfectants in public places [65]. Hyderabad authorities often use drone technologies developed by Cyient to monitor critical regions and ensure people stay safe at home, to control public places and avoid gatherings. Cyient-developed drones could also be operated even at night in the absence of light. It provides a live feed to the police authorities and helps them to make efficient decisions [67].

Drone integrated with an air atomizer system has been developed by The Quint to spray disinfectants effectively by breaking the liquids into droplets [65].

A pilot tracking system has also been developed and released in Hangzhou. Individuals need to fill out an online form including travel history, ID card number, etc. The form consists of questionnaires related to COVID-19 symptoms. Based on the uploaded data, the individuals are given a colour code—red, yellow or green. A red code indicates a 14-day quarantine is required for the person with regular health updates on an application developed by Alibaba. A yellow code indicates one-week quarantine and a green code suggests that the person is free to wander about [68].

6.11 Robotics for Public Information

A five-foot-tall robot with a friendly face, Promobot, is equipped with a touch screen on its chest. A start-up developed it in Philadelphia. With the aid of a touch screen, anyone can fill a short questionnaire. Based on filled data, the robot informs the person whether he might be affected by the virus or not. This robot can even communicate with humans [69].

6.12 Robotics for the Security of Critical Infrastructures

Amidst lockdown, various Indian Railway assets such as coaches and PRS counters are out of sight. Also, access to signaling infrastructure, stations, relay rooms, goods sheds and wagon stock, open widespread of railway tracks might not be possible in the pandemic. Thus, during the national lockdown, the East Coast Railway (ECoR) has deployed drones to keep a watchful eye on its properties, installations and critical facilities to deter the spread of COVID-19 [70].

6.13 Robotics for Telecommerce Applications

Patrol cars built by UBTECH Robotics have been deployed in China to help police officials monitor whether any person individuals are equipped with masks or not. At the toll gates, this robot monitors the temperature using infrared thermometers and allows the police to interact efficiently with the help of a speaker [71].

Robotics has also been implemented for online home touring to attract potential customers amidst the COVID-19 pandemic. Zenplace, a real estate start-up, offers virtual home tours with the aid of robots. The real estate agent can also communicate in a video call with a buyer with the help of the robot and can lead around the house [72].

6.14 An Overview of Robotic Devices Being Implemented Globally to Fight the Pandemic

Public space disinfection can be performed by robotics such as UAVs, as humans are extremely susceptible to the virus. It also provides an additional line of defence [73]. Various drones have already been addressed in the earlier sections, which perform multiple operations, thereby delivering assistance to frontline healthcare staff, police officers and other authorities fighting against the pandemic. The drones are used for a broad variety of applications in multiple countries across the globe, including

disinfectant spraying, contactless package delivery and surveillance of public places to prevent gathering [74]. Other ground-based robots, as discussed, also facilitate various operations and assist. Various ground-based robots have been implemented to monitor the health of COVID-19 patients, package delivery, encouraging the patients, providing telepresence features, contactless communication between patients and healthcare workers, sample collection, etc.

7 Conclusion

The COVID-19 pandemic has revolutionized, and most activities have been made virtually possible. Robotics is being adapted to perform multiple activities to avoid virus exposure. Rapid research and development of robotic devices and its application during the pandemic catalyse a revolutionary future with autonomous operations and virtual interaction. Ground and aerial robotic devices serve as an additional line of defence between the patients and healthcare staff. Disinfection activity is being carried out at healthcare facilities, public places, hotels, airports, offices, etc. using robotic devices. Packages, groceries and contaminated objects are also being delivered by the robots. Public places are being monitored with drones and ground-based robots to maintain lockdown and alert violators. Also, the robots are able to recognize individuals having high fever and also individuals without masks. Robots are also developed to collect samples and transport to the testing facilities. Robotic devices play a very important role in minimizing virus dissemination.

Online classes and interactions have been embraced virtually by each nation. To avoid gatherings, international exhibitions, conferences, press meets, etc. are being conducted online through various platforms such as Google Meet, Zoom and Cisco Webex Meet. Governments around the globe also discuss and take crucial and critical decisions through electronic video calling platforms.

Although the pandemic prompted the start of such a revolution, even after the pandemic, the research and development in robotics, its applications and transformation to virtual interaction should progress at the same pace towards a better future.

References

1. Krishnakumar B, Rana S (2020) COVID 19 in INDIA: strategies to combat from combination threat of life and livelihood. *J Microbiol Immunol Infect*
2. Centers for Disease Control and Prevention (2020) Coronavirus disease. Centers for Disease Control and Prevention. [Online]. Available from: <https://tinyurl.com/w27huwm>. Accessed 12 July 2020
3. Roy D, Tripathy S, Kar SK, Sharma N, Verma SK, Kaushal V (2020) Study of knowledge, attitude, anxiety & perceived mental healthcare need in Indian population during COVID-19 pandemic. *Asian J Psychiatr* 51:102083

4. Burrell CJ, Howard CR, Murphy FA (2017) Coronaviruses. In: Burrell CJ, Howard CR, Murphy FA (eds) Fenner and White's medical virology, 5th edn. Academic Press, London, pp 437–446
5. WHO (2020) WHO coronavirus disease (COVID-19) dashboard, 12 July 2020. [Online]. Available from: <https://covid19.who.int/>. Accessed 12 July 2020
6. Li Q et al (2020) Early transmission dynamics in Wuhan, China, of novel coronavirus–infected pneumonia. *N Engl J Med*
7. Huang C, Wang Y, Li X, Ren L, Zhao J et al (2020) Clinical features of patients infected with 2019 novel coronavirus in Wuhan, China. *Lancet* 39:497–506
8. Rothan HA, Byrareddy SN (2020) The epidemiology and pathogenesis of coronavirus disease (COVID-19) outbreak. *J Autoimmun*
9. Carlos WG, Dela C, Cao B, Parnick S (2020) Novel Wuhan (2019-nCoV) coronavirus. *Am J Respir Crit Care Med* 201(4):7–8
10. Shi Y, Wang G, Cai XP et al (2020) An overview of COVID-19. *J Zhejiang Univ Sci B* 21(5):343–360
11. Gao S, Song SQ, Zhang LL (2019) Recent progress in vaccine development against chikungunya virus. *Front Microbiol* 28–81
12. ICMR (2021) Worldwide covid-19 candidate vaccines, 12 Jan 2021. [Online]. Available from: <https://vaccine.icmr.org.in/covid-19-vaccine>. Accessed 12 July 2020
13. Sputnik vaccine, 12 Jan 2021. [Online]. Available from: <https://sputnikvaccine.com/about-vaccine/>. Accessed 14 Jan 2021
14. Bharatbiotech (2021) India's first indigenous COVID-19 vaccine, 12 Jan 2021. [Online]. Available from: <https://www.bharatbiotech.com/covaxin.html>. Accessed 14 Jan 2021
15. Ray A (2021) COVID-19 vaccine Covishield by Serum Institute: how effective is it? How much will it cost, 14 Jan 2021. [Online]. Available from: <https://tinyurl.com/y58wcy37>. Accessed 14 Jan 2021
16. Petersen E et al (2020) Li Wenliang, a face to the frontline healthcare worker, the first doctor to notify the emergence of the SARS-CoV-2 (COVID-19) outbreak. *Int J Infect Dis* 93:205–207
17. Rajkumar RP (2020) COVID-19 and mental health: a review of the existing literature. *Asian J Psychiatry*
18. Haleem A, Javaid M, Vaishya R (2020) Effects of COVID 19 pandemic in daily life. *Curr Med Res Pract*
19. Jin YH, Cai L, Cheng ZS, Cheng H, Deng T et al (2020) A rapid advice guideline for the diagnosis and treatment of 2019 novel coronavirus (2019-nCoV) infected pneumonia (standard version). *Mil Med Res* 7(1):4
20. Campbell D, Busby M (2020) 'Not fit for purpose'. UK medics condemn Covid-19 protection. *The Guardian*, 16 Mar 2020. [Online]. Available from: <https://tinyurl.com/rk14p3q>. Accessed 17 Mar 2020
21. Rothan HA, Byrareddy SN (2020) The epidemiology and pathogenesis of coronavirus disease (COVID-19) outbreak. *J Autoimmun* 109:102–433
22. Legido-Quigley H, Asgari N, Teo YY, Leung GM, Oshitani H et al (2020) Are high-performing health systems resilient against the COVID-19 epidemic? *Lancet* 395(10227):848–850
23. McCloskey B, Zumla A, Ippolito G, Blumberg L, Arbon P et al (2020) Mass gathering events and reducing further global spread of COVID-19: a political and public health dilemma. *Lancet*
24. Misra A (2020) Doctors and healthcare workers at frontline of COVID 19 epidemic: admiration, a pat on the back, and need for extreme caution. *Diabetes Metab Syndr* 14(3):255–256
25. NS Medical Staff Writer (2020) Baptist health among first hospital systems to use robots to disinfect N95 masks during COVID-19. *NS Medical Devices*, 1 Apr 2020. [Online]. Available from: <https://tinyurl.com/yxwwgxeq>. Accessed 12 July 2020
26. Ackerman E (2020) New consortium mobilizes roboticists to help with COVID-19 and future crises. *IEEE Spectrum*, 22 Apr 2020. [Online]. Available from: <https://tinyurl.com/yyovz2by>. Accessed 12 July 2020
27. Yang GZ (2020) Combating COVID-19—the role of robotics in managing public health and infectious diseases. *Sci Robot* 5

28. Electro Optics (2020) UV light solutions deployed in fight against Covid-19. Electro Optics, 20 Mar 2020. [Online]. Available from: <https://tinyurl.com/yxf2ddcy>. Accessed 12 July 2020
29. Marr B (2020) Robots and drones are now used to fight COVID-19. The Forbes, 18 Mar 2020. [Online]. Available from: <https://tinyurl.com/yyx7xxuz>. Accessed 12 July 2020
30. Synced (2020) Volunteer drone teams organize for COVID-19 disinfection. The Synced, 22 Feb 2020. [Online]. Available from: <https://tinyurl.com/y5qwmt24>. Accessed 12 July 2020
31. Murray A (2020) Coronavirus: robots use light beams to zap hospital viruses. BBC News, 20 Mar 2020. [Online]. Available from: <https://tinyurl.com/t892x95>. 12 July 2020
32. Xinhua (2020) Disinfection robots deployed on frontlines to combat coronavirus. Chinadaily.com.cn, 7 Feb 2020. [Online]. Available from: <https://tinyurl.com/y2d68pgz>. Accessed 12 July 2020
33. Anand N (2020) Chennai-based start-up Garuda Aerospace, disinfests hospitals, institutions, with drones. The Hindu, 9 Apr 2020. [Online]. Available from: <https://tinyurl.com/yy5o4o4q>. Accessed 12 July 2020
34. Asaf S (2020) Hong Kong Airport is using virus-killing robots to disinfect public areas. Business Traveller, 5 Apr 2020. [Online]. Available from: <https://tinyurl.com/woqyhqw>. Accessed 12 July 2020
35. Terra News (2020) Terra Drone business partner Antwork helps fight coronavirus in China with medical delivery drones. Terra Drone, 7 Feb 2020. [Online]. Available from: <https://tinyurl.com/y35k4zkz>. Accessed 12 July 2020
36. York General Hospital (2020) York General to use ultraviolet light robot to sanitize N95 masks during COVID 19 pandemic. KRVN, 6 Apr 2020. [Online]. Available from: <https://tinyurl.com/yxv2ulnd>. Accessed 12 July 2020
37. Tyree E (2020) Robot allows UVA health to reuse thousands of masks in COVID-19 fight. abc 13NEWS, 14 Apr 2020. [Online]. Available from: <https://tinyurl.com/yya8bz35>. Accessed 12 July 2020
38. King L (2020) Robots make 36 meals every 15 minutes for doctors treating coronavirus victims. Mirror, 19 Feb 2020. [Online]. Available from: <https://tinyurl.com/uez24oz>. Accessed 12 July 2020
39. Jakhar P (2020) Coronavirus: China's tech fights back. BBC News, 3 Mar 2020. [Online]. Available from: <https://tinyurl.com/r4grq8z>. Accessed 12 July 2020
40. Shemer S (2020) Israeli robot assistant deployed in Asia to help minimize coronavirus spread. Nocamels, 1 Mar 2020. [Online]. Available from: <https://tinyurl.com/sdsuzlk>. Accessed 12 July 2020
41. Jingli S (2020) JD.com uses L4 autonomous driving solutions to deliver goods in locked-down Wuhan. KrASIA, 7 Feb 2020. [Online]. Available from: <https://tinyurl.com/yxf5nr5d>. Accessed 12 July 2020
42. Arthus C, Shuhui R (2020) In China, robot delivery vehicles deployed to help with COVID-19 emergency. United Nations Industrial Development Organization, 1 Apr 2020. [Online]. Available from: <https://tinyurl.com/y4gryz4z>. Accessed 12 July 2020
43. Trigg L (2020) Union Hospital deploys 'robots' in fight against COVID-19. Tribune-Star, 2 Apr 2020. [Online]. Available from: <https://tinyurl.com/seofbdl>. Accessed 12 July 2020
44. Meah N (2020) Robot to deliver meals, medication to Covid-19 patients at Alexandra Hospital to reduce exposure of healthcare workers. Today, 5 Mar 2020. [Online]. Available from: <https://tinyurl.com/ycjtmfcn>. Accessed 12 July 2020
45. Matyus A (2020) Meet the robot helping doctors treat coronavirus patients. Digitaltrends, 28 Jan 2020. [Online]. Available from: <https://tinyurl.com/y4u2nojz>. Accessed 12 July 2020
46. Chavez N, Kounang N (2020) A man diagnosed with Wuhan coronavirus near Seattle is being treated largely by a robot. CNN Health, 24 Jan 2020. <https://tinyurl.com/wddmkjn>. Accessed 12 July 2020
47. Clifford C (2020) Look inside the hospital in China where coronavirus patients were treated by robots. CNBC make it, 23 Mar 2020. [Online]. Available from: <https://tinyurl.com/y4fmxta8>. Accessed 12 July 2020

48. Meisenzahl M (2020) Thailand has ‘ninja robots’ monitoring COVID-19 patients—take a look. Business Insider India, 24 Mar 2020. <https://tinyurl.com/yy4qschx>. Accessed 12 July 2020
49. Qi W (2020) China develops intelligent robots for throat swab sampling of coronavirus tests. Global Times, 10 Mar 2020. [Online]. Available from: <https://www.globaltimes.cn/content/1182175.shtml>. Accessed 12 July 2020
50. TRT World (2020) Italy’s doctors look for help from sleek new robots. TRT World, 4 Apr 2020. [Online]. Available from: <https://tinyurl.com/yxozkpggh>. Accessed 12 July 2020
51. APP (2020) Coronavirus: China develops robot for throat swab sampling. Tech, 10 Mar 2020. [Online]. Available from: <https://tinyurl.com/y2p659tc>. Accessed 12 July 2020
52. Meisenzahl M (2020) A Japanese University used remote-controlled robots to hold a virtual graduation. Business Insider India, 5 Apr 2020. [Online]. Available from: <https://tinyurl.com/y6r2t77a>. Accessed 12 July 2020
53. Canine W (2020) Testing for COVID-19 with Opentrons. Opentrons, 9 Mar 2020. [Online]. Available from: <https://tinyurl.com/y525aep2>. Accessed 12 July 2020
54. Hamilton (2020) Hamilton announces automated coronavirus (COVID-19) testing workstations and priority fast tracking for any orders related to combatting the viral pandemic. Hamilton, 17 Mar 2020. [Online]. Available from: <https://tinyurl.com/y5xnhcq5>. Accessed 12 July 2020
55. Linder C (2020) Police are using drones to yell at people for being outside. Linder, 17 Mar 2020. <https://tinyurl.com/yxhw3v32>. Accessed 12 July 2020
56. Doughlas A (2020) MMC drones spraying disinfectant to fight coronavirus. Commercial Drone Professional, 10 Feb 2020. [Online]. Available from: <https://tinyurl.com/y3hqxyer>. Accessed 12 July 2020
57. Claburn T (2020) Drones intone ‘you must stay home,’ eliciting moans from those in the zone: flying gizmos corral Brits amid coronavirus lockdown. The Register, 28 Mar 2020. [Online]. Available from: <https://tinyurl.com/yxh2v222>. Accessed 12 July 2020
58. PYMNTS (2020) California cops enlist drones for lockdown. PYMNTS.com, 20 Mar 2020. [Online]. Available from: <https://tinyurl.com/y4utmmdw>. Accessed 12 July 2020
59. Doffman Z (2020) Coronavirus spy drones hit Europe: this is how they’re now used. The Forbes, 16 Mar 2020. <https://tinyurl.com/y3pvmcp2>. Accessed 12 July 2020
60. Wu N (2020) Honolulu to use drones to enforce ‘stay-at-home’ order at local beaches. Star Advertiser, 10 Apr 2020. [Online]. Available from: <https://tinyurl.com/ug3hns9>. Accessed 12 July 2020
61. Deccan Chronicle (2020) Drones urge people to stay home and away from coronavirus in Madrid and Dubai. Deccan Chronicle, 16 Mar 2020. [Online]. Available from: <https://tinyurl.com/vggerf7>. Accessed 12 July 2020
62. Gibbon G (2020) Dubai police using drones to keep public spaces ban enforced. Arabian Business/Industries, 24 Mar 2020. [Online]. Available from: <https://tinyurl.com/yy5aclat>. Accessed 12 July 2020
63. Novak M (2020) China using drones in increasingly Dystopian ways to combat coronavirus outbreak. Gizmodo, 14 Feb 2020. [Online]. Available from: <https://tinyurl.com/rgd2qxq>. Accessed 12 July 2020
64. Reuters Staff (2020) On French Riviera, overhead police drone gives coronavirus orders. Reuters, 20 Mar 2020. [Online]. Available from: <https://tinyurl.com/vsyy5hb>. Accessed 12 July 2020
65. Sircar S, Dev A (2020) With humans under lockdown, how drones are helping fight COVID-19. The Quint, 10 Apr 2020. [Online]. Available from: <https://tinyurl.com/uu3jppq>. Accessed 12 July 2020
66. Nandy S (2020) Lockdown violators in Kerala spot police drones, run like “tracer bullets”. NDTV, 8 Apr 2020. [Online]. Available from: <https://tinyurl.com/yxmfrbdw>. Accessed 12 July 2020
67. Choudhary M (2020) Hyderabad is using drones for implementing COVID-19 lockdown. Geospatial World, 4 Apr 2020. [Online]. Available from: <https://tinyurl.com/yxbehuwg>. Accessed 12 July 2020

68. Giovannini M (2020) China leverages technology in its fight against COVID-19. CGTN, 20 Feb 2020. [Online]. Available from: <https://tinyurl.com/y3n2q6o4>. Accessed 12 July 2020
69. Reuters (2020) Robot with coronavirus advice hits Times Square. CNBC, 11 Feb 2020. [Online]. Available from: <https://tinyurl.com/uo86j6h>. Accessed 12 July 2020
70. Odishatv Bureau (2020) COVID-19 lockdown: ECoR deploys drones to keep vigil of assets, infrastructure. Odishatv.in, 7 Apr 2020. [Online]. Available from: <https://tinyurl.com/yyo xwjqz>. Accessed 12 July 2020
71. Vardhan H (2020) Autonomous robots aid in patrolling and disinfecting COVID-19 hit China. Geospatial World, 3 June 2020. [Online]. Available from: <https://tinyurl.com/y2p4xsef>. Accessed 12 July 2020
72. Olick D (2020) Virtual, robot and solo home touring soar as social distancing hits the housing market amid coronavirus fear. CNBC, 30 Mar 2020. [Online]. Available from: <https://tinyurl.com/rspewez>. Accessed 12 July 2020
73. NDTV (2020) COVID-19: Chennai based start-up using drones to disinfect hospitals. NDTV, 31 Mar 2020. [Online]. Available from: <https://tinyurl.com/yxwou5q3>. Accessed 12 July 2020
74. Sagar M (2020) How drones are assisting government in China fight COVID-19. Opengov, 11 Mar 2020. [Online]. Available from: <https://tinyurl.com/y5n8o9jw>. Accessed 12 July 2020

Design and Numerical Analysis of Hub Less Wheel



Abhishek Singh Yadav and Minesh Vohra

Abstract Centered on the two main factors, i.e., demand for two-wheelers and safety aspects connected with the use of automobile components in India, this work has been intensified with the theme of proposing an inexpensive hub less wheel design in the two wheelers, as most injuries occur in the traditional wheel model of Spokes form due to legs or clothes being entangled. The two-wheelers are in high demand, so it would help to minimize repair costs and reduce total cost if this wheel arrives on the market. In this work, the proposed model for the hub less wheel has been presented and the computational analysis has been performed with the key elements of the wheel i.e., Rim, under static load condition for which the maximum load is restricted up to 780 N with the ratio of the ultimate strength of material to the actual working stress which is considered as one and based on the simulated outcome on ANSYS, then evaluation of Total deformation, Equivalent Stress Equivalent Strain has been investigated.

Keywords Hub less wheel · Equivalent stress · Deformation · Analysis

1 Introduction

Keeping into mind of day-to-day use of a vehicle and its main purpose either travelling or transportation, the key role which plays the most important part in making the vehicle movable is no other than “Wheel”. In Normal or Conventional wheel, the rim often constitutes of spoke or alloy which are responsible for suspension and steering components of any conventional vehicle. In Indian Automotive industry, hub less wheel models are still not being simulated and manufactured due to lack of equipment for testing, but few companies are still working on this hub less segments wheel for their operational aspects on the Indian Road. Coming to the referenced used for the design and Evaluation of the hub less wheel, the survey has been performed. Algat discussed on the development of hub less wheel bicycle with gear train drive

A. S. Yadav · M. Vohra (✉)
School of Mechanical Engineering, Lovely Professional University, Phagwara, India
e-mail: minesh.15783@lpu.co.in

© The Author(s), under exclusive license to Springer Nature Singapore Pte Ltd. 2023
T. S. Sudarshan et al. (eds.), *Recent Advancements in Mechanical Engineering*,
Lecture Notes in Mechanical Engineering,
https://doi.org/10.1007/978-981-19-3266-3_16

197

mechanism is designed to transform effort into mechanical output through paddling and results shows that the product has potential to minimize fatigue of rider with improvement in the efficiency of power transmission followed by maximum bicycle speed limit [1]. Ross in his study proposed the innovative mechanism that involves a frame with a seat framework and a handle bar, a rear bracket with rear bearings within which a rear wheel is rotatable and a drive train that drives the rear wheel [2]. Sbarro had previously addressed that the latest invention that results in the transfer of steering forces at a point as close as possible to the interface region between tire and the road [3]. Mallya has proposed the hub less wheel in this configuration and defined on the use of MC-901 nylon gears that are much lighter than their metal counter sections [4]. Mothafar in his US Patent on a hub less wheel, proposed an idea of a lightweight hub less wheel with the method of construction process to be followed for the same [5]. Hung in his study, suggested an electric bicycle model followed by a simulation analysis of the operating characteristics of an electric bike [6]. Pinto in his research covers an optimization of the frame content of the wheels and simulation analysis built in this project on the hub less wheel was referred [7]. Fuji, FEM carried out CATIA program for kinematic simulation in his research work followed by simulation findings in accordance with the static and dynamic analysis results[8]. Many investigators which have been working on the design of a wheel, addressing the safety of the passenger by eliminating the hub and the spokes in a bicycle but the limited work has been done in the simulation area of the wheel. The wheel which is proposed in this work is a wheel without hub which would play as one of the most important components of the vehicle with fixed rim connected to the outer rammer where in between bearing, that helps in transmitting rotary motion to the outer rim and thus the freely movement of the vehicle would be possible and hence makes this design as a unique one in comparison to the conventional models already proposed. In this work the Numerical analysis under the static condition of the proposed hub less design has been executed using ANSYS and the feasibility of this product in real life has been investigated based on the idea to bring these models in two wheelers at least. So, the main objective of this work is as follows:

- To design a hub less wheel for light vehicle like bicycle, bike, and car.
- To numerically investigate the deformation aspects based on the load condition.

2 Design and Modelling of Hub Less Wheel

With a proper description of the modules that were part of this design portion, the entire design process is illustrated step by step below.

2.1 Model Components

- **Inner Part of Rim:** Fig. 4 represents the isometric representation of inner portion of the hub less wheel followed by consecutive dimension represented from Figs. 1, 2 and 3, that is used to stabilize the bearing and to help drive the bearing in the clockwise and anti-clockwise direction simultaneously with the chassis. Dimensions two consecutive rings are taken out:
 - (i) Diameter of the ring is 360 mm
 - (ii) Width of the ring is 60 mm
 - (iii) Width of groove in ring is 40 mm.

Fig. 1 Front view of inner rim

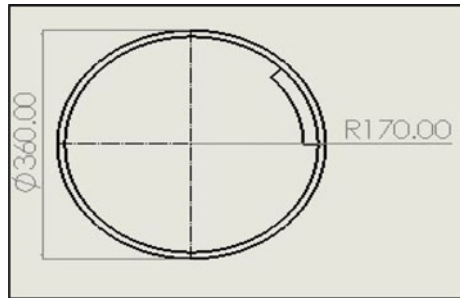


Fig. 2 Top view of inner rim

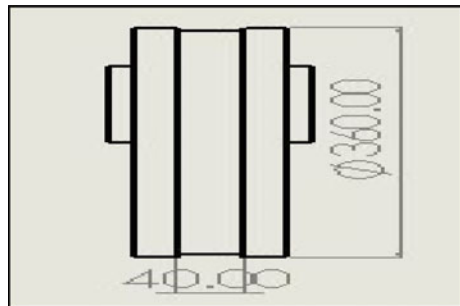
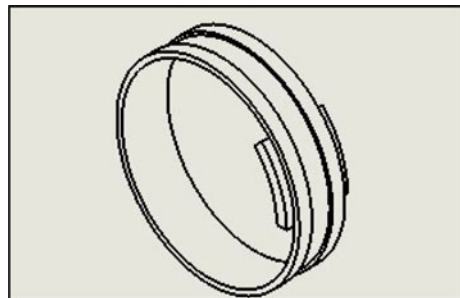


Fig. 3 Inner part of rim



- **Outer Part of Rim:** Fig. 8 represents the isometric representation of outer portion of the Rim used in hub less wheel followed by consecutive dimension represented from Figs. 5, 6 and 7. Outer rim is used to mount tire and set into rotation with the help of bearing. Dimensions two consecutive rings are taken out:

Fig. 4 Isometric view

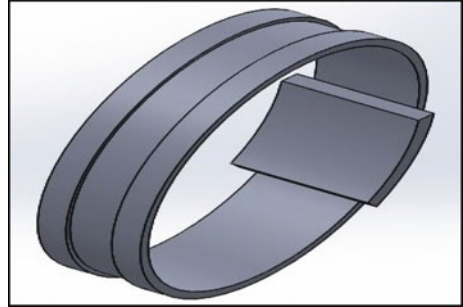


Fig. 5 Top view of outer rim

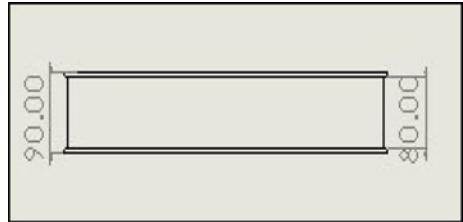


Fig. 6 Isometric view of outer rim

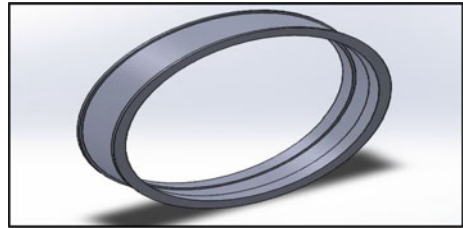


Fig. 7 Front view of outer rim

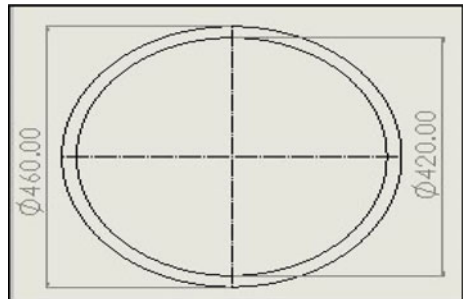
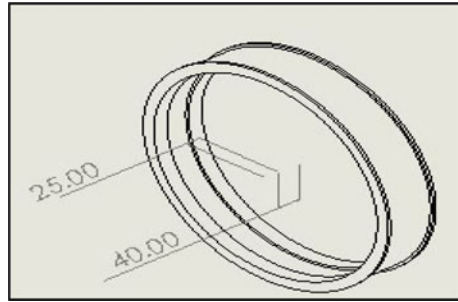


Fig. 8 Top view of outer rim



- (i) Diameter of the ring is 460 mm
- (ii) Width of the ring is 60 mm
- (iii) Width of inside groove in ring is 40 mm.

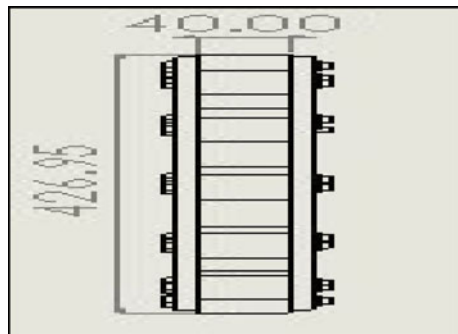
• **Dummy Bearing:** Fig. 11 represents the isometric view of Dummy Bearing followed by consecutive dimensions represented in Figs. 10 and 11. Dummy Bearing is used in between inner and the outer rim in order to maintain the speed as well as to provide support while in operation. Another most important feature of bearing is to continue provide frictionless movement of the parts. Dimensions of bearing are taken out:

- (i) Diameter of the bearing is 418 mm
- (ii) Width of the bearing is 40 mm
- (iii) Width of inside groove in ring is 40 mm (Fig. 9).

Components of Dummy Bearing consists of:

- Ring
- Ball
- Nut
- Strut (Figs. 12, 13 and 14).

Fig. 9 Top view of bearing



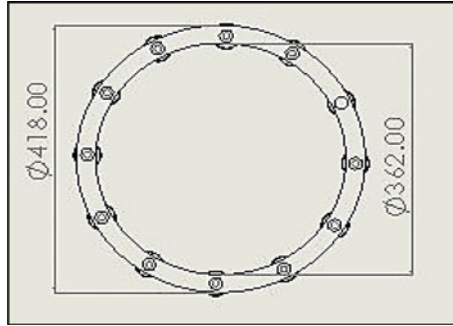


Fig. 10 Side view of bearing

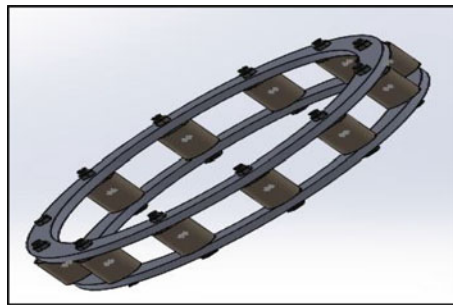


Fig. 11 Isometric view of bearing

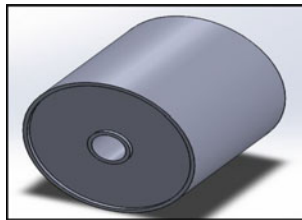


Fig. 12 Ball

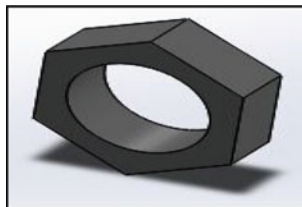
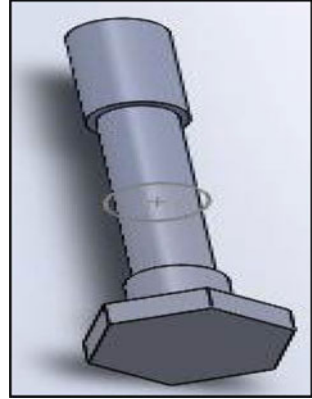
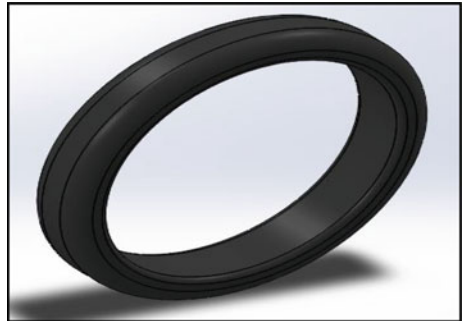


Fig. 13 Nut

Fig. 14 Strut**Fig. 15** Tire

- **Tire:** Tires are the most critical factor that makes the vehicle travel, bringing it in contact with the proper friction offered by the road. Figure 15 indicates the tire that will be mounted over the outer rim of the hub less wheel and the rpm associated as acquired by Dummy Bearings dependent on the friction over the road.

2.2 Complete Assembly

This zone represents the various components of hub wheel shown in Figs. 16 and 17 and its assembly where the assembly components are listed below:

1. Inner Rim
2. Dummy Bearing
3. Outer Rim
4. Tire.

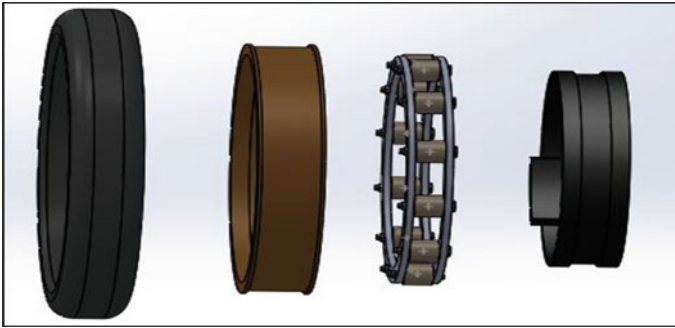


Fig. 16 Assembly of components

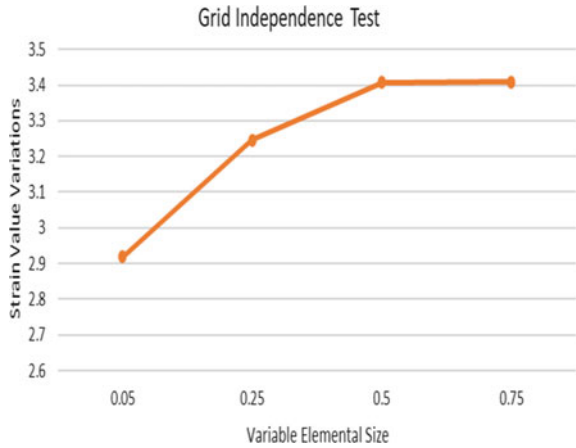


Fig. 17 Assembled hub less wheel

2.3 Working of the Hub Less Wheel

The hub less wheel is mounted on the front wheeler’s axle. The inner portion of the hub less wheel’s rim is connected to the axle through nut and bolt arrangement over which the load is equally spread. And the same load is evenly spread on the Outer Rim with the aid of dummy bearing and to the tyre also. The bearing sets the rotation in the outer rim while the vehicle is accelerated at particular speed keeping the inner Rim fixed along the axis of rotation.

Fig. 18 Grid independence result



2.4 Grid Independence Test

In the hub less wheel we have to choose a mesh which would not be get distorted with the boundary conditions applied and have to decide the optimized number of elemental sizes that can be considered for the further static analysis on the hub less wheel. For the same the grid independence study has been performed as demonstrated in Fig. 18. Based on the elemental size and the variation in strain value over the hub less wheel, from the graph it has been concluded that the best suited elemental size for is 0.5 with 34,000 elements (approx.) as the variation of strain on the wheel with respect to elemental size of 0.75 shows almost the same behavior and the percentage variation is minimum in two of the cases where the elemental size is 0.5 and 0.75.

2.5 Meshing and Material Specifications

So, the final mesh has been considered as mentioned in Fig. 19, for the numerical approach with meshed properties as mentioned in Table 1 and different element sizing in Ansys where the load of 750–1000 N on the upper part of rim has been applied considering the average masses of the passenger over the two-wheeler to be 80 kg including the mass of the two-wheeler.

For the analysis, the ratio of the ultimate strength of a member or piece of material to the actual working stress is considered as one and the analysis type is changed to Static Loading Condition.

The material has been considered as structural steel with the properties as mentioned in Table 2 as used in Computational analysis.

Fig. 19 Meshed model

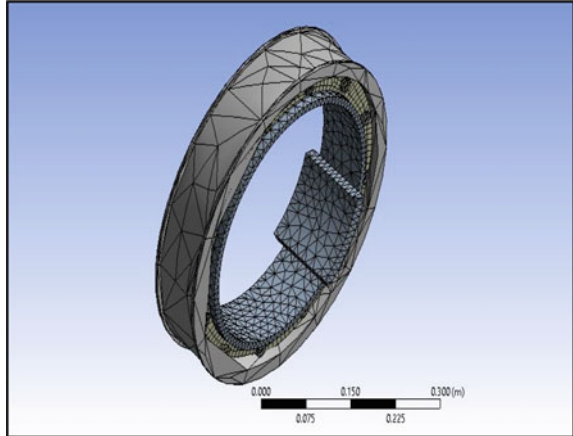


Table 1 Mesh details of rim

Sr. No.	Parameters	Values
1	Size functions	Adaptive
2	Relevance center	Fine
3	Smoothing	Medium
4	Transition	Fast
5	Elements	34,329
6	Nodes	77,348
7	Element size	0.5 m
8	Behavior	Hard

Table 2 Material properties of rim

Sr. No.	Material properties	Values
1	Density	7.84 g/cc
2	Load	780 N
3	Yield strength	362 MPa
4	Poisson ratio	0.3
5	Thermal conductivity	W/m K

3 Result and Discussion

The three major factors have been investigated considering load conditions of 780 N and factor of safety as 1 in order to find out the following:

1. Total deformation,
2. Equivalent Stress,
3. Equivalent Strain.

Table 3 Analysis output for rim

Sr. No.	Results	Values
1	Maximum total deformation (μm)	2.597×10^{-2}
2	Maximum equivalent stress (N/m^2)	3.406×10^5
3	Maximum equivalent elastic strain	1.744×10^{-6}

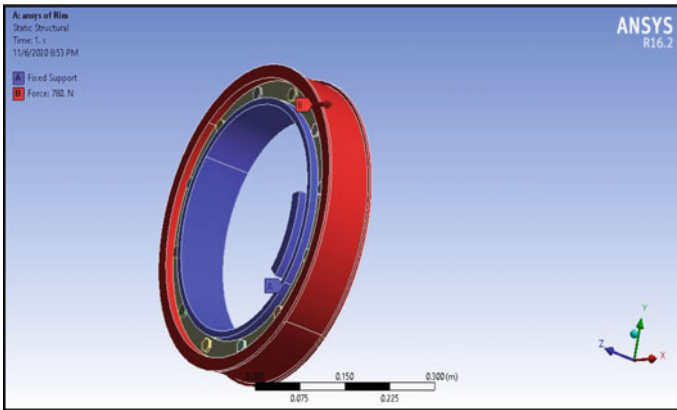


Fig. 20 Load condition on rim

The hub less wheel used in this study as designed, can bear load up to 780 N, which it may fail and factor of safety may vary upon the material of the wheel which is used while manufacturing.

Static Analysis:

The static analysis of the components is carries out using Ansys.

Outer Rim: For the material is Structural Steel. The force applied was 780 N in radial outwards direction (Figs. 20, 21, 22 and 23).

Based on the analysis for the two-wheeler where the hub less wheel is mounter on the front axle under static conditions the behavior of the wheel is demonstrated in Table 3 that shows the maximum total deformation, equivalent stress generated followed by elastic strain of the material proposed for the rim.

4 Conclusion

The hub less wheel which have been designed and worked upon in this project bring light upon on various altercations which could have been done earlier or could be done now-onwards considering the fact it is one most important factor to be considered while purchasing a vehicle and we all better know that safety is above all parameters

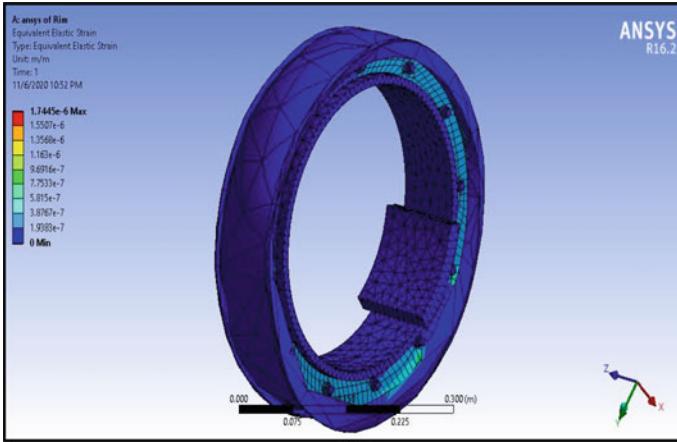


Fig. 21 Equivalent strain of rim

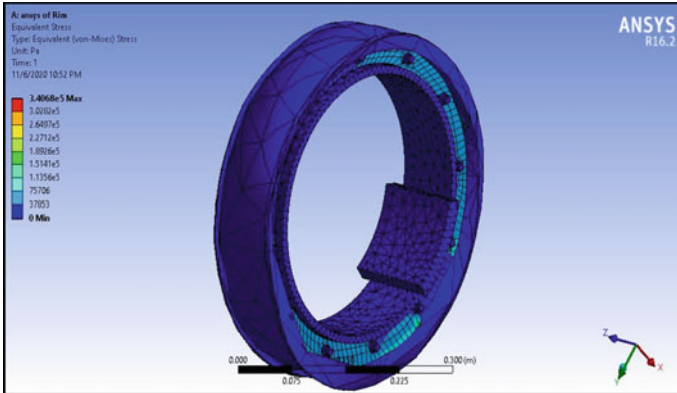


Fig. 22 Equivalent stress of rim

to be considered before buying any product for our use where our very own life is at risk.

This particular design can be used in two wheelers, four wheelers, trolley wheel after some modifications in design and by weight distribution. Along with weight reduction this hub less design of wheel would also help in coping up with problems dealing with suspension system of vehicles which may be installed by altering the design required for two wheelers, four wheelers, etc. The wheel design and manufacturing in this project is only the prototype. There are many modifications possible such as provision of shock absorbers, proper braking system, mountings to connect in vehicle. Furthermore, the work can also be carried out in the proportions listed below:

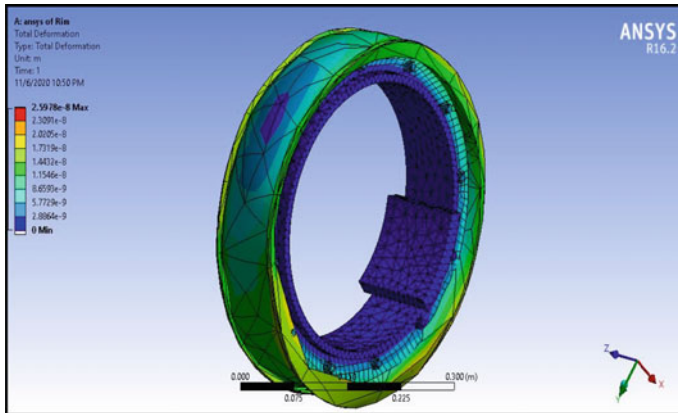


Fig. 23 Total deformation of rim

1. Optimization of Cost.
2. To Reduce the Weight of the Wheel as much as possible by removing of Centre Hub.
3. To Increase the ability to handle the vehicle with more efficient brakes.

References

1. Algat VV, Bhalerao RS, Autade KN, Shimpi GB, Godake AP (2015) Hubless wheel bicycle with gear train drive mechanism. IJRET 3(2)
2. Ross B (1999) Spoke-less bicycle system. US patents. [Online]. Available from: <https://patents.google.com/patent/US6224080B1/en>
3. Sbarro F (1992) Hubless cycle for engine driven vehicle. US patents. [Online]. Available from: <https://patents.google.com/patent/US5248019A/en>
4. Mallya MR, Prasad U (2016) Design of hubless wheel for an automobile. Int J Emerg Technol Adv Eng 6(2)
5. Mothafar A (2016) Hubless wheel system for motor vehicles. US patents. Available from: <https://patents.google.com/patent/US9440488B1/en>
6. Hung NB, Sung J (2017) A simulation and experimental study of operating characteristics of an electric bicycle. Science Direct 232–245
7. Pinto S, Raj Kumar E (2014) Design and analysis of hubless personal vehicle. In: International conference in advances in design and manufacturing, NIT Tiruchirappalli, Tiruchirappalli, 5 Dec 2014
8. Fuji S (2003) Crash analysis of motorcycle tire. Procedia Eng 147:471–475

Effect of Nano Alumina Reinforcements on the Tribological Behavior of Electroless Nickel-Phosphorus Coatings



D. Mohanty, T. K. Barman, and P. Sahoo

Abstract Nickel-Phosphorus electroless coatings are of versatile nature. In the present research, an effort has been made to study the tribological behavior of the Nickel-Phosphorus coatings reinforced with nano alumina powders. The study includes the incorporation of 1 g/l of nano alumina powder into the Nickel-Phosphorus coatings. Prior to the introduction of the alumina powder into the coating bath, it was ultrasonicated in a wet media (deionized water). After preparing a sound reinforced as-deposited coating of Nickel-Phosphorus-Alumina (nano), it was compared to a binary Nickel-Phosphorus coating and an uncoated mild steel specimen. These were subjected to a sliding wear test on a pin-on-disk setup and the wear rate was evaluated from the difference in weight (before and after the test). The reinforced (Nickel-Phosphorus-Alumina) coating was found to be the most resistant to wear amongst the three. Besides this, the present research also compares the coating with respect to their scratch hardness and micro-Vicker hardness. This research also includes a characterization study of the as-deposited reinforced coating surface via X-ray diffractometry and Scanning electron microscopy (SEM).

Keywords Electroless coating · Nano-particles · Nickel-Phosphorus · Scratch hardness · Wear behavior

1 Introduction

Coatings are surface modification methods used to impart specific properties to the material while leaving the bulk property of the material intact. Electroless nickel coating is one such surface modification method which provides enhanced mechanical as well as corrosion protection to the substrate materials. These coatings have operational simplicity, need low investment and form very thin coating [1]. Besides, electroless coatings have an added advantage as they can be deposited on non-metallic substrates. Such a property paves the path for the use of these coatings in the computer

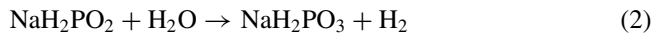
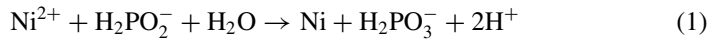
D. Mohanty (✉) · T. K. Barman · P. Sahoo
Department of Mechanical Engineering, Jadavpur University, Kolkata, WB 700032, India
e-mail: deviprasannamohanty.me@gmail.com

© The Author(s), under exclusive license to Springer Nature Singapore Pte Ltd. 2023
T. S. Sudarshan et al. (eds.), *Recent Advancements in Mechanical Engineering*,
Lecture Notes in Mechanical Engineering,
https://doi.org/10.1007/978-981-19-3266-3_17

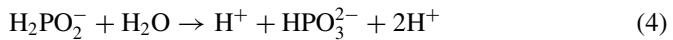
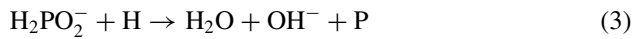
211

industry. Nickel coatings are used for storage devices like compact disks. A number of oxides, carbides and ceramics are being used as second phase material. These secondary phases help in improving the mechanical properties of these coatings [2–4]. Corrosion behavior, hardness and microstructure of these coatings is dependent on the particle size as well as the distribution of these particles in the coatings [5]. Yu et al. [6] discussed the effect of nano-dispersed SiO_2 , CeO_2 in Nickel phosphorus electroless coatings on the wear behavior and electrochemical corrosion resistance of the coatings. Similar reports for the co-deposition of ZnSiO_3 , ZnSnO_3 , and $\text{Zn}_3(\text{PO}_4)_2$ [7] particles are also available in the literature. The mechanism of co-deposition of nano diamond particles in Nickel-Phosphorus coatings is well studied by Xiang et al. [8].

There are a number of mechanisms that have been proposed to explain the process of autocatalytic deposition method. “Atomic hydrogen mechanism” [9], identified two core equations to be the basis for this plating process.



These reactions showed that the coating was made up of pure nickel (without any phosphorus), which was later on disproved experimentally. A solution to this ambiguity was proposed by Gutzeit [10], he suggested that the presence of elemental phosphorus may be explained by the following reaction.



From Eq. (3) it is observed that an excess of OH^- ion is produced this in turn increases the pH of the solution. Due to this increase in pH the reaction in Eq. (2) speeds up thus resulting in more H^+ ions. This cyclic process generates a layered deposition of EN coatings on the substrates. However, this mechanism is unable to provide a proper explanation about the simultaneous reduction of the both nickel and hydrogen during the EN plating process. Other mechanisms include the “Hydride transfer mechanism” [11, 12].

In the present study, nano alumina particles are added in assistance with ultrasonication. The coating deposition is characterised by SEM imaging and X-Ray diffraction. The Nickel-Phosphorus coated, Nickel-Phosphorus-nano alumina coated and uncoated (MS substrate) samples were compared on the basis of scratch hardness and wear.

2 Experimental Details

2.1 Sample Preparation

The deposition was done on mild steel samples. Flat ground samples of dimension 15 mm × 15 mm × 2 mm were used for scratch testing and coating characterisations. Cylindrical ground samples of length 30 mm and diameter 6 mm were used for the tribo testing. The samples were polished with different grades of emery papers and finally cloth polished with 1 μm sized Alumina particles to maintain the surface finish. These samples were then cleaned in an ultrasonic bath. The samples were next subjected to acid pickling (HCl, 30 wt %) to remove any foreign materials from the surface. Finally the samples were dipped in a Pd⁺⁺ activator for 15 s before being introduced into the coating bath.

2.2 Bath Preparation and Coating Deposition

The bath solution was prepared in a clean and rinsed beaker. Using a stirrer the coating bath elements were mixed with deionized water as the solvent. The Nickel ions (Ni⁺⁺) were sourced from a combination of Nickel sulphate hexahydrate and Nickel chloride hexahydrate. Sodium succinate acted as the complexing agent while Sodium hypophosphite was used as a reducer in the bath. Table 1 lists the composition of all the bath components. The deposition of Nickel-Phosphorus and Nickel-Phosphorus nano alumina was carried out for two hours to get an optimum coating thickness, while maintaining the coating bath temperature at 85 °C.

Simultaneously, a suspension of nano alumina in deionized water was prepared separately. The suspension was sonicated for one hour at 60 kHz. In order to keep the particles suspended and allow for uniform distribution of the nano particles during the deposition, a surfactant (Sodium Dodecyl Sulphate) was used. This suspension

Table 1 Composition of the coating bath

Chemicals	Amount in the bath (g/l)	Use
Nickel chloride (II) hexahydrate	20	Source of Ni
Nickel (II) sulphate hexahydrate	20	Source of Ni
Sodium succinate	12	Complexing agent
Sodium hypophosphite	12	Reducing agent
Nano alumina	1	Reinforcement

of nano alumina in water suspension was introduced into the coating bath at the beginning of the coating.

2.3 Hardness Measurement

The coatings and substrate materials were tested for their Vicker's microhardness (UHL VHMT, Germany) using a pyramid type indenter. The indentations were obtained at a dwell time of 15 s, load of 100 gf and penetration rate of 25 $\mu\text{m/s}$. An average microhardness of 10 indentations is reported for each of the samples.

2.4 Scanning Electron Microscopy and X-Ray Diffractometry

The SEM micrographs were measured using FESEM (Jeol JSM 7610F, Germany). Secondary electron images were taken at an Extra High Tension (EHT) potential of 20 kV and a working distance of 9.5 mm. XRD (X-ray diffraction) instrument (Bruker D8 advance, USA) was used to identify phases in the coatings. A copper (Cu-K α , $\lambda_{\text{Cu}} = 1.54 \text{ \AA}$) target was used during XRD scanning. In order to get the X-Ray pattern, the 2θ angle was varied from 0° to 100° .

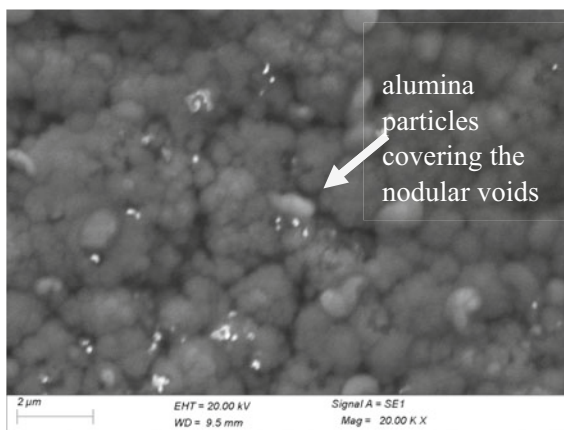
2.5 Scratch Test

The scratch hardness and scratch width is obtained using a scratch tester (Ducom TR-101-IAS, India). The scratch hardness is evaluated under a constant load of 20 N. The scratch tester employs a Rockwell C type diamond indenter with a radius of 200 μm and a flank angle of 120° . Stroke length and indentation speed, were selected as 10 mm, 0.1 mm/s, respectively. The images were taken using 'Scarview' imaging software. Each reported value of hardness is an average hardness of 5 scratches taken on the sample.

2.6 Wear Test

Wear tests of the substrate and the coatings were conducted using a pin on disk type tribometer (Ducom, India). The sample acted as the pin while an EN31 (hardened steel) disc was used as the rubbing counter face. The wear tests were performed at nominal load, rpm and sliding distance of 1 kgf, 100 rpm, and 500 m, respectively. Each of the samples was tested thrice and the average specific wear rate is reported in this study.

Fig. 1 SEM micrograph of the Nickel-Phosphorus-1 g/l nano Al_2O_3



3 Result and Discussion

3.1 Micro Structure and Micro Hardness

Figure 1 shows the as deposited electroless microstructure replete with typical cauliflower like nodular structures. The cross-section revealed the columnar structure of the Nickel-Phosphorus coatings. The deposition kinetics of the coatings highly depends on the temperature of the bath as well as the duration of the coating. The presence of alumina particles is observed in Fig. 1 and the agglomerated particles can be observed to be embedded in the porosities and voids. These particles being hard tend to improve the wear resistance and average hardness of the material of the coating. As has been reported elsewhere, in the case of Ni-B- Al_2O_3 finer nodules were formed on addition of alumina nano particles [13]. This also contributed in the improved hardness. Figure 2 shows the Vicker's micro hardness values for the specimen under study. Hardness increased by approximately 18% on addition of the nano particles. This could be attributed to the high hardness of the alumina particles which is effective in restricting the dislocation flow.

3.2 XRD Pattern

Figure 3 shows the XRD (X-Ray diffraction) pattern of the Nickel-Phosphorus-nano Al_2O_3 coatings. 60 kV and 60 mA were operating voltage and current, respectively. X'Pert Highscore plus software was used to analyze the diffraction data and to identify the phases corresponding to the peaks obtained, on the basis of JCPDS data. The as-deposited nickel peak shows an amorphous nature. It is observed that by adding nano alumina particles to the coating the nature of the coating does not

Fig. 2 Vickers's micro hardness for MS (mild steel), as deposited Nickel-Phosphorus and as deposited Nickel-Phosphorus-1 g/l nano Al_2O_3

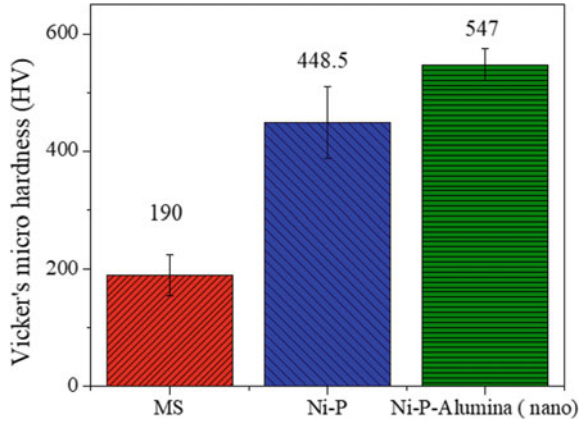
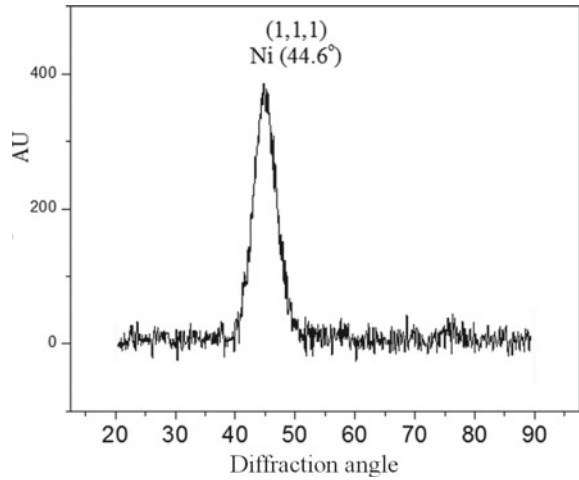


Fig. 3 XRD of as deposited Nickel-Phosphorus-1 g/l nano Al_2O_3

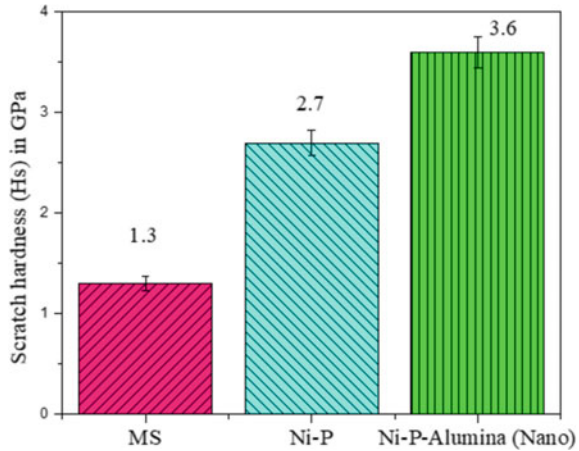


change, i.e.: no transition from amorphous to crystalline is seen in XRD pattern. The nodules changed from coarser to finer structure, same was reported for Ni-B electroless coatings reinforced with nano alumina particles [13]. At a diffraction angle (2θ) of 44.6° Nickel peak was identified.

3.3 Scratch Hardness

The scratch hardness values of the specimen are shown in Fig. 4. The scratch hardness of the alumina reinforced coating is the highest amongst the three. This can be a result of the hard alumina nano particles embedded in the coatings. These particles tend

Fig. 4 Scratch hardness for MS (mild steel), as deposited Nickel-Phosphorus and as deposited Nickel-Phosphorus-1 g/l nano Al_2O_3



to provide resistance to penetration as well as the travel of the diamond indenter resulting in high scratch hardness.

Figure 5 shows the scratches taken on mild steel, as deposited Nickel-Phosphorus and as deposited Nickel-Phosphorus-1 (g/l) Al_2O_3 (nano). It is observed that for the Nickel-Phosphorus coating there is coating peel off around the scratch. The same is not observed for mild steel sample or the Nickel-Phosphorus-1 (g/l) Al_2O_3 sample. The coating peel off may be attributed to the brittleness of these coatings. In case of the Nickel-Phosphorus-1 (g/l) Al_2O_3 coating, the addition of alumina seems to have made the coating more ductile. The average scratch width was found to be 206 μm , 135.4 μm and 117.4 μm for the mild steel, as deposited Nickel-Phosphorus and as deposited Nickel-Phosphorus-1 (g/l) Al_2O_3 (nano) specimen, respectively. The alumina reinforced coating shows the least width which can be attributed to its high hardness. The scratch hardness is calculated from the equation [14]

$$H_s = \frac{8 F_N}{\pi w^2} \quad (5)$$

where, H_s is the scratch hardness, F_N is the normal force applied and w is the scratch width.

It should be noted here that the semi-circular curves obtained at the edges are due to the shape of the scratch indenter. During the measurement of the width, these semicircular portions are not considered. The average scratch width is a measure of only the linear portion of the scratch.

3.4 Wear Performance

Figure 6 shows the specific wear rate of as deposited Nickel-Phosphorus, MS and as deposited Nickel-Phosphorus-1 (g/l) Al_2O_3 (nano) is shown in Fig. 6.

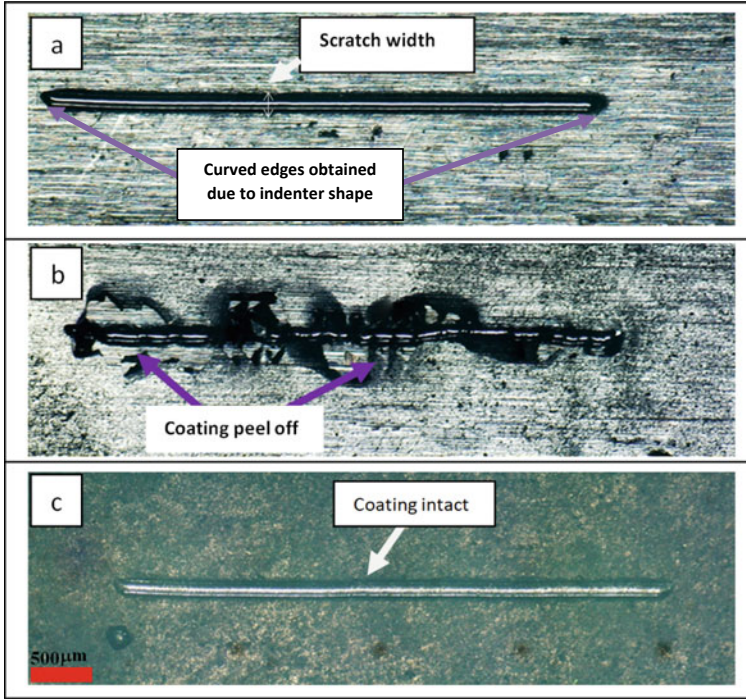


Fig. 5 Scratch profile for **a** MS (mild steel), **b** as deposited Nickel-Phosphorus and **c** as deposited Nickel-Phosphorus-1 g/l nano Al_2O_3

Fig. 6 Specific wear rate of MS (mild steel) of as deposited Nickel-Phosphorus and as deposited Nickel-Phosphorus-1 g/l nano Al_2O_3

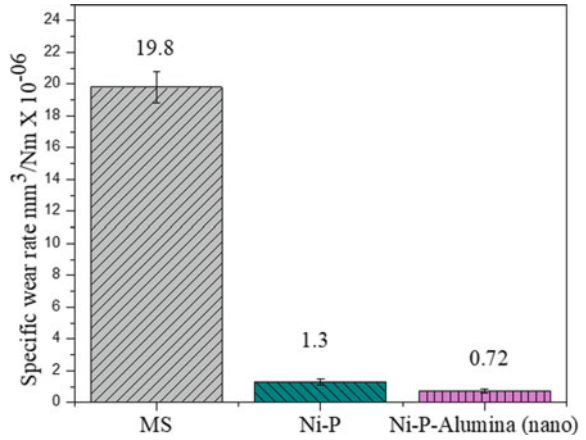
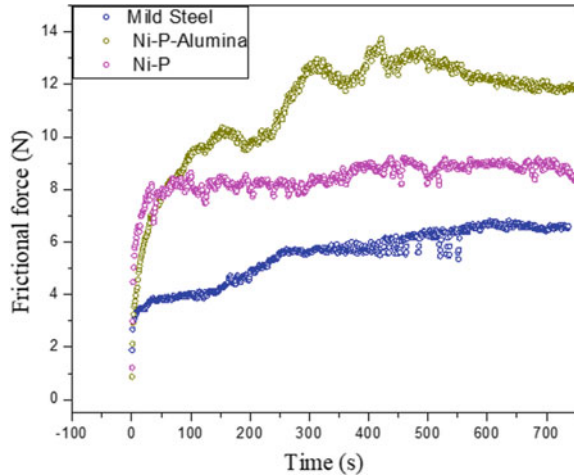


Fig. 7 Frictional force plot of MS (mild steel), as deposited Nickel-Phosphorus and as deposited Nickel-Phosphorus—nano Al_2O_3 (1 g/l)



As expected the wear rate of the reinforced coating is the lowest amongst the three. The specific wear rate of Nickel-Phosphorus-1 (g/l) Al_2O_3 (nano) is nearly 26 times less than that of the substrate material (MS). Such an observation is expected as the hardness of the reinforced coating is nearly 1.8 times that of the uncoated MS (mild steel).

Figure 7 shows the frictional forces exerted on the specimen during the sliding wear test. The average frictional force obtained for mild steel, as deposited Nickel-Phosphorus and as deposited Nickel-Phosphorus-Alumina are 6.1 N, 8.3 N and 12.5 N, respectively. The increased frictional force is an indicator of the higher resistance of the as deposited Nickel-Phosphorus-Alumina to the sliding motion during the wear test. This can be attributed to the addition of nano particles which being hard result in improved resistance to the sliding movement. This increased resistance results in an increase in frictional force. The frictional force is a measure of the materials ability that provides resistance to any sliding motion; hence, these coatings can be used in applications where the material is subjected to wear due rubbing against a counterpart.

4 Conclusion

Nickel-Phosphorus and Nickel-Phosphorus-Alumina (nano) coatings were deposited for the present research. The co-deposition of 1 g/l alumina was achieved by ultrasonically dispersing the alumina in deionized water (prior to being introduced into the bath) in presence of sodium dodecyl sulphate. The coatings were characterized by XRD method and were also observed under a SEM (scanning electron microscope). The coatings and the base material (mild steel) were weighed up on the basis of their micro hardness, wear behavior and scratch hardness.

On the basis of the present research following conclusions may be presented:

- Refinement of nodules was achieved with addition of nano particles.
- 18% increase in microhardness was observed for composite Nickel-phosphorus-alumina coating as compared as deposited Nickel-phosphorus coating.
- The Nickel-Phosphorus-Alumina coatings display an improved scratch-hardness and a low scratch width.
- The Nickel-Phosphorus-Alumina showed an increase of wear resistance by 1.8 times as compared to the binary as deposited Nickel-Phosphorus coatings.

Acknowledgements The authors would like to acknowledge COE (Center of Excellence) in Phase Transformation and Product Characterisation, TEQIP-III for their support and funding in making this research possible.

References

1. Kazimierczak H, Wierzbicka-Miernik A, Kwiecien I, Szczerba MJ, Korneva A, Mosialek M, Miernik K, Wojewoda-Budka J (2019) Electroless deposition of Ni-P and Ni-P-Re alloys from acidic hypophosphite baths. *Electrochim Acta* 303:157–166
2. Hou KH, Han-Taowang H, Sheu HH, Ger MD (2014) Preparation and wear resistance of electrodeposited Ni-W/diamond composite coatings. *Appl Surf Sci* 308:372–379
3. Chen W, Gao W, He Y (2010) A novel electroless plating of Ni-P-TiO₂ nano-composite coatings. *Surf Coat Technol* 204(15):2493–2498
4. Dong D, Chen XH, Xiao WT, Yang GB, Zhang PY (2009) Preparation and properties of electroless Ni-P-SiO₂ composite coatings. *Appl Surf Sci* 255(15):7051–7055
5. Balaraju JN, Kalavati, Rajam KS (2006) Influence of particle size on the microstructure, hardness and corrosion resistance of electroless Ni-P-Al₂O₃ composite coatings. *Surf Coat Technol* 200(12–13):3933–3941
6. Yu X, Wang H, Yang Z, Yin P, Xin X (2000) XPS and AES investigation of two electroless composite coatings. *Appl Surf Sci* 158(3):335–339
7. Tao P, Mei-Hua M, Fei-Bo X, Xin-Quan X (2001) XPS and AES investigation of nanometer composite coatings of Ni-P-ZnX on steel surface (ZnX = ZnSnO₃, Zn₃(PO₄)₂, ZnSiO₃). *Appl Surf Sci* 181(3–4):191–195
8. Xiang Y, Zhang J, Jin C (2001) Study of electroless NI-P nanometer diamond composite coatings. *Plat Surf Finish* 88(2):64–67
9. Brenner A, Riddell GE (1946) Nickel plating on steel by chemical reduction. *J Res Natl Bur Stand* 37(1):31
10. Gutzeit G (1959) Catalytic nickel deposition from aqueous solution. *Plat Surf Finish* 46:1158–1164, 1275–1278, 1377–1378
11. Gutzeit G (1955) Industrial nickel coating by chemical catalytic reduction. *Trans IMF* 33(1):383–423

12. Genutiene I, Lenkaitiene J, Jusys Z, Luneckas A (1996) Simultaneous reduction of perrhenate and nickel ions by hypophosphite. *J Appl Electrochem* 26(1):118–120
13. Mohanty D, Barman TK, Sahoo P (2019) Characterisation and corrosion study of electroless nickel-boron coating reinforced with alumina nanoparticles. *Mater Today Proc* 19:317–321
14. Sundararajan G, Roy M (2001) Hardness testing. In: *Encyclopedia of materials: science and technology*. Elsevier, pp 3728–3736

Transport Phenomena in a Double Driven Cavity Involving Buoyancy, Magnetic Field and Nanofluid



Kanad Sen, Nirmalendu Biswas, Sandip Sarkar, and Nirmal K. Manna

Abstract In this work, an attempt has been taken to characterize numerically the transport phenomena in a double-driven cavity. Two identical square cavities with the differential heating at the outer sidewalls are placed at a 40% overlapped position aligning their diagonals. The horizontal walls are adiabatic and translate in reverse directions. Such a flow situation has practical relevance in the material processing industry. For this reason, we embrace this study using common fluids (such as air and water) and a special fluid of CuO-water nanofluid considering some effects thermal gradients and magnetic fields in the laminar zone with appropriate validation. The transports of thermo-fluid flow in the cavity are analyzed using pertinent dimensionless parameters, the Prandtl number, Reynolds number, Rayleigh number, and Hartmann number. The variation in nanofluid concentration (<5%) is utilized for the study of the special fluid. It revealed that the speed of the translating wall and imposed thermal gradient markedly alters the thermal behavior within the cavity. The outcome of this work will enrich many insights to the system designers by providing some in-depth insights into the physical process control aspect.

Keywords Double driven cavity · Magnetohydrodynamics (MHD) · CuO-water nanofluid · Mixed convection · Thermal mixing · Heat transfer

K. Sen · S. Sarkar · N. K. Manna
Department of Mechanical Engineering, Jadavpur University, Kolkata, India
e-mail: kanadsen01@gmail.com

S. Sarkar
e-mail: sandipsarkar.mech@jadavpuruniversity.in

N. K. Manna
e-mail: nirmalkmannaju@gmail.com

N. Biswas (✉)
Department of Power Engineering, Jadavpur University, Kolkata, India
e-mail: biswas.nirmalendu@gmail.com

Nomenclature

B_0	Magnetic field, Tesla
g	Gravitational acceleration (ms^{-2})
H	Height of the cavity, length scale (m)
Ha	Hartmann number
k	Thermal conductivity ($\text{Wm}^{-1} \text{K}^{-1}$)
K	Porous medium permeability
L	Length of each side of the cavity (m)
Nu	Average Nusselt number
p	Pressure (Pa)
Pr	Prandtl number
Ra	Rayleigh number
Re	Reynolds number
T	Temperature (K)
U, V	Dimensionless velocity components
X, Y	Dimensionless coordinates

Greek Symbols

α	Thermal diffusivity (m^2s^{-1})
β	Thermal expansion coefficient of fluid (K^{-1})
θ	Dimensionless temperature
μ	Dynamic viscosity ($\text{kgm}^{-1} \text{s}^{-1}$)
ν	Kinematic viscosity (m^2s^{-1})
ρ	Density (kgm^{-3})
σ	Electrical conductivity (Sm^{-1})
ϕ	Nanoparticle volume fraction
ψ	Stream function

Subscripts

c, h	Cold wall, hot wall
f	Base fluid
s	Solid

1 Introduction

Problems involving simple lid-driven enclosures have been one of the earliest problems that have existed since the beginning of cavity flow problems and it has been studied extensively with various complex geometry. It has been one of the most popular problems. The reason for its popularity is the simplicity of its setup. It can be solved for large ranges of the Reynolds number (Re). The practical industrial importance of studying lid-driven cavity can be found from the different models such as the fluid flow through the slots of the gate in a water-reservoir [1], transport processes in lakes can be studied by the heating sidewall of the cavity [2] and development of industrial applications [3, 4].

The lid-driven cavity problems allow us to use a blend of forced and natural convection, which is termed mixed convection. The mixed convection arises from two mechanisms—shearing force and buoyancy force. The shearing action due to the moving lid is controlled by Re , whereas, the buoyancy is controlled by the Rayleigh number (Ra). In the problem, the magnetic field is applied, which is controlled by the Hartmann number (Ha). This combination involving the effects of magnetizing field and mixed convective phenomena is also termed as Magnetohydrodynamics (MHD) and is very useful for controlling different devices pertaining to a thermal gradient. In fact, thermo-fluid flow behavior in any thermal system could be modulated markedly by controlling the magnetic field intensity.

In our problem, a special geometry of lid-driven cavity is formed by overlapping two squares, which is referred to as a double-driven cavity. A benchmark work on the same geometry was published by Zhou et al. [5] with fluid flow phenomena over a wide range of Reynolds numbers ($Re = 50-3200$). In fact, Nithiarasu and Liu [6] have also examined the lid-driven double cavity. It was observed that at a lower Reynolds number ($Re \leq 1000$), the solution is steady-state; whereas at a higher Re the solution is unsteady. In another work, Tekić et al. [7] studied both parallel and anti-parallel translating staggered lid-driven enclosure for $Re = 50-3200$.

Most of the conventional methods have been utilized to their maximum potential especially by the last two methods. Therefore, a search for a more efficient cooling liquid began which allowed maximum heat transfer removal rate. Usually most of the common working fluids used for any thermal system (like water, ethylene glycol, oil, and others), transport less amount of heat due to its inherent lower thermal conductivity in comparison to solids materials. This criterion substantially limits the compactness, weightiness, and efficacy aspects of the heat exchanging device. It is therefore becoming very much necessary to improve the thermal transport capability of these common working fluids. The scientist and engineers, therefore, have been trying to resolve the issue by blending ultra-fine solid particles (maintaining correct proportion) in the host fluid. In 1993, Masuda et al. [8] examined the thermal behavior of fluid with the suspension of nanopowders. Later, in 1995, Choi [9] have introduced the terminology “nanofluid” and since then, the smart working fluid gained a reputation in the heat transfer domain. Due to the higher thermal energy transport capability of the nanofluids in comparison to normal or conventional fluids, the nanofluids are

anticipated as the preferred fluid for real-life applications also. A comprehensive review of the above has been reported by Kabeel et al. [10].

As we have discussed previously, the magnetic field reduces the magnitude of convective circulating flows due to its effect on electrically conductive fluids. Thus, adding nanoparticles with low conductivity which can increase heat transfer can be useful in highly sensitive devices which require cooling under the influence of the magnetizing field. In this regard, Ghasemi et al. [11] investigated the impact of a horizontally imposed magnetizing field in a square cavity occupying Al_2O_3 nanofluid. They have observed a significant improvement in heat transfer characteristics with an increase in the nanoparticles concentrations even in the presence of flow dampening magnetic field. The thermal behavior of any system involving nanofluid as well as magnetic field becomes more complex when one or more bounding walls are translating. Considering the above boundary conditions, many researchers have studied investigated different complex problem geometries. There are many recent works [12–16] on lid-driven cavities.

In most cases, the lid-driven cavity is used in heat transfer applications. Furthermore, the geometry studied is mostly square in shape. Complex geometry involving overlapping of two enclosures has not been examined adequately. Thus, the aim of this study is to explore the transport phenomena in a double-driven cavity. Two identical square cavities with the differential heating at the outer sidewalls are placed at a 40% overlapped position aligning their diagonals. We have used both air and water as working fluids. Furthermore, CuO-water nanofluid has also been considered as a recent development of special fluids for various engineering applications. The comparison has been specifically done to identify the optimal fluid, which will enhance heat transfer under all conditions.

2 Problem Descriptions and Mathematical Modelling

In the framework of two-dimensional analysis, the problem geometry including boundary conditions of the present problem addressing a double-driven cavity has been shown in Fig. 1. Two identical square cavities (of length and height H) with isothermal heating and cooling at the outermost sidewalls (AB and EF) are placed at a 40% overlapped position aligning their diagonals. As such, there is a 60% clear zone as indicated by S ($= 0.6$) on the figure. The remaining parts of the walls (designated with AH, GH, GF, DE, CD, BC) are adiabatic. The horizontal walls (DE and EH) are translating moving in reverse directions. Thus, shear-induced flow is generated within the geometry at various velocities (controlled with Reynolds number). The numerical experiments are conducted using common working fluids, air and water, and nanofluid. Recent advances in many engineering applications suggest as a working fluid the use of engineered nanofluids. As such, the present study is extended using CuO-water nanofluid. The nanofluid study assumes uniform CuO nanopowders (having 29 nm dia) suspended homogeneously in water without any sedimentation or agglomeration. No-slip condition is considered on the bounding

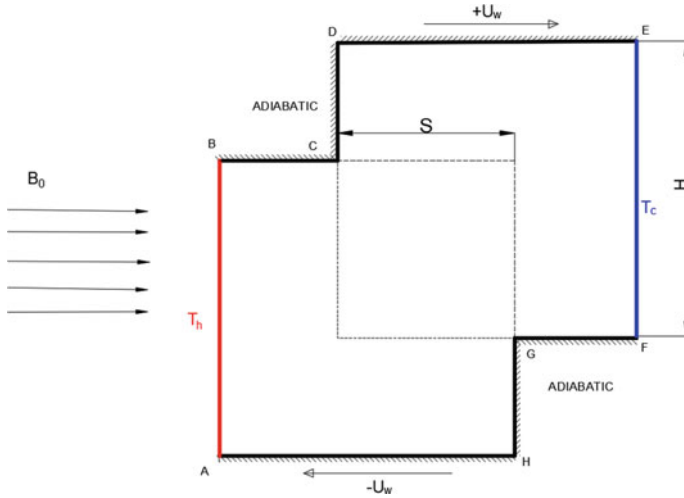


Fig. 1 Physical domain with boundary conditions of the double-driven cavity

walls. The overlapped region parameter R is chosen as 0.4 (for this page limited study) following an existing benchmark paper used here for the validation of the present numerical work. A uniformly distributed magnetic field (of strengths B_0) is applied horizontally.

Further to the above-mentioned conditions and assumptions, a few other points are assumed as given below.

1. The heat generation due to viscous dissipation evolved from the fluid friction is very small and neglected.
2. Flow is two-dimensional, laminar, incompressible, and Newtonian.
3. No chemical reaction has been considered between the carrier fluid and nanoparticles.
4. The radiative heat transfer within the computational domain is ignored.
5. Local thermal equilibrium situation occurs between the suspended solids and host fluid.
6. The enclosure walls are electrically non-conducting and have no effect on the magnetic field.
7. The magnetic induction for the CuO-water nanofluid is mainly governed by the electrical conductivity of the water.
8. Due to the weak electrically conducting behavior of water as well as air, the Hartmann number can safely be considered up to 100 neglecting the secondary effects like Joule heating and Hall effects. Only the flow dampening Lorentz force is taken into account in the governing equations.
9. The highly diluted (<5% by volume) mixture of the CuO nanoparticles in water is considered as a single-phase fluid.

Following the above-mentioned assumptions, the transport governing equations are derived for the steady-state flow situation. The governing continuity, Navier–Stokes, and energy equations in the Cartesian coordinate system in dimensional form are written as

$$\frac{\partial u}{\partial x} + \frac{\partial v}{\partial y} = 0 \quad (1)$$

$$u \frac{\partial u}{\partial x} + v \frac{\partial u}{\partial y} = \frac{1}{\rho_{\text{wf}}} \left[-\frac{\partial p}{\partial x} + \mu_{\text{wf}} \left(\frac{\partial^2 u}{\partial x^2} + \frac{\partial^2 u}{\partial y^2} \right) \right] \quad (2)$$

$$u \frac{\partial v}{\partial x} + v \frac{\partial v}{\partial y} = \frac{1}{\rho_{\text{wf}}} \left[-\frac{\partial p}{\partial y} + \mu_{\text{wf}} \left(\frac{\partial^2 v}{\partial x^2} + \frac{\partial^2 v}{\partial y^2} \right) + (\rho\beta)_{\text{wf}} g (T - T_c) - \sigma_{\text{wf}} B_0^2 v \right] \quad (3)$$

$$u \frac{\partial T}{\partial x} + v \frac{\partial T}{\partial y} = \alpha_{\text{wf}} \left(\frac{\partial^2 T}{\partial x^2} + \frac{\partial^2 T}{\partial y^2} \right) \quad (4)$$

Here, the buoyancy force is included in the y -momentum equation succeeding the Boussinesq approximation. Furthermore, the Lorentz force (due to the imposed horizontal magnetic field) is also included in the y -momentum equation. Thus, the dimensionless transport equations are obtained as

$$\frac{\partial U}{\partial X} + \frac{\partial V}{\partial Y} = 0 \quad (5)$$

$$\left(U \frac{\partial U}{\partial X} + V \frac{\partial U}{\partial Y} \right) = -\frac{\rho_{\text{bf}}}{\rho_{\text{wf}}} \frac{\partial P}{\partial X} + \frac{\nu_{\text{wf}}}{\nu_{\text{bf}}} \frac{1}{\text{Re}} \left(\frac{\partial^2 U}{\partial X^2} + \frac{\partial^2 U}{\partial Y^2} \right) \quad (6)$$

$$\begin{aligned} \left(U \frac{\partial V}{\partial X} + V \frac{\partial V}{\partial Y} \right) &= -\frac{\rho_{\text{bf}}}{\rho_{\text{wf}}} \frac{\partial P}{\partial Y} + \frac{\nu_{\text{wf}}}{\nu_{\text{bf}}} \frac{1}{\text{Re}} \left(\frac{\partial^2 V}{\partial X^2} + \frac{\partial^2 V}{\partial Y^2} \right) \\ &+ \frac{\rho_{\text{bf}}}{\rho_{\text{wf}}} \frac{\sigma_{\text{wf}}}{\sigma_{\text{bf}}} \frac{\text{Ha}^2}{\text{Re}} V + \frac{(\rho\beta)_{\text{wf}}}{\rho\beta_{\text{bf}}} \frac{\text{Ra}}{\text{Re}^2 \text{Pr}} \theta \end{aligned} \quad (7)$$

$$\left(U \frac{\partial \theta}{\partial X} + V \frac{\partial \theta}{\partial Y} \right) = \frac{\alpha_{\text{wf}}}{\alpha_{\text{bf}}} \frac{1}{\text{Re Pr}} \left(\frac{\partial^2 \theta}{\partial X^2} + \frac{\partial^2 \theta}{\partial Y^2} \right) \quad (8)$$

utilizing the following scaling variables

$$\begin{aligned} X &= \frac{x}{H}, \quad Y = \frac{y}{H}, \quad U = \frac{uH}{\alpha_{\text{bf}}}, \quad V = \frac{vH}{\alpha_{\text{bf}}} \\ \theta &= \frac{T - T_h}{T_h - T_c}, \quad \text{Ra} = \frac{g\beta H^3 (T_h - T_c)}{\nu_{\text{bf}} \alpha_{\text{bf}}}, \quad \text{Re} = U_w H / \nu_{\text{bf}} \end{aligned}$$

$$\text{Pr} = \frac{\nu_{\text{bf}}}{\alpha_{\text{bf}}}, \quad \text{Ha} = B_0 H \sqrt{\frac{\sigma_{\text{wf}}}{\rho_{\text{wf}} \nu_{\text{wf}}}}$$

For the study of common fluids (air/water), the base fluid (subscript bf) and the working fluid (subscript wf) are the same. For the CuO-water nanofluid, the effective fluid properties are adopted from the well-known relations of properties as given in Refs. [17–21]. The thermo-physical parameters (specific heat, thermal conductivity, volumetric expansion coefficient, density, and electrical conductivity) of CuO nanoparticles are taken as: 540.0 J/kgK, 18.0 W/mK, 0.85×10^{-5} 1/K, 6500 kg/m³, and 2.7×10^{-8} T, respectively.

3 Computational Aspects

The conservation equations are solved through a numerical approach following Galerkin's finite element technique. The domain of computation is split into numbers of elements and then the conservation equations are transformed into integral equations, which are further converted into a set of algebraic equations succeeding Gauss's quadrature approach. The algebraic equations are computed iteratively setting the convergence limit in between successive iterations as $<10^{-8}$. The data obtained from the simulations are then processed to visualize the flow and temperature distribution [22].

3.1 Validation Study

The present solver has already been utilized for validation study [23] as well as other work [22, 24]. This exercise clearly depicts the efficacy of the present solver for the computations. Further to the above, another set of validation studies on forced convective phenomena is reported here by modeling the benchmark problem of Zhou et al. [5]. The results are illustrated in Fig. 2 using the contours of streamlines and vorticity at $\text{Re} = 50$, and 400 by setting buoyancy and MHD terms as zero (Ra and Ha are zero). The comparison shows a closer prediction of the contours using the present computations. This exercise signifies the accuracy of the present solver and also the selection of appropriate mesh structure.

4 Results and Discussion

In this work, an attempt has been taken to characterize numerically the transport phenomena in a double-driven cavity. Two identical square cavities with the differential heating at the outer sidewalls are placed at a 40% overlapped position aligning

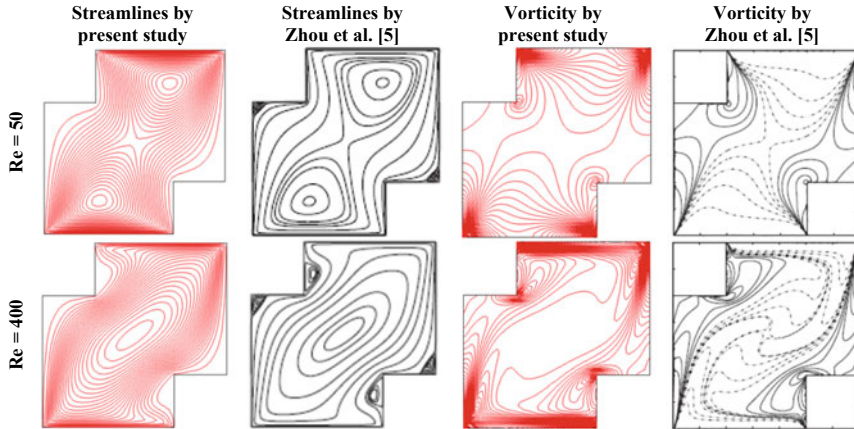


Fig. 2 Comparison of the present study with the published work of Zhou et al. [5] through the contours of streamlines and vorticity at $Re = 50$, and 400 . Reproduced with permission from the publisher

their diagonals. All the horizontal walls are adiabatic and translated in reverse directions. The analysis is carried out for a wide range parameters like: Rayleigh number ($Ra = 10^3 - 10^5$), Reynolds number ($Re = 10 - 1000$), nanoparticle concentration ($\phi = 0.01 - 0.05$), Hartmann number ($Ha = 0 - 100$). In fact, the chosen geometry has practical relevance in the alloying/material processing industry. For this reason, we embrace this study using common fluids (such as air and water) and a special fluid of CuO-water nanofluid considering some effects thermal gradients.

4.1 Comparison of Flow Characteristics of Air and Water at $Ra = 10^3$

The influence of Re on thermofluid flow behaviors is studied in Fig. 3 using different values of Re . It sets different speeds of moving upper and lower lids that are adiabatic. For the same geometry, using different fluids (air and water) and Re values of 10, 100, 200, and 1000, the comparison is shown in terms of streamlines and isotherms. Other parameters, Ra and Ha , have been kept constant at 10^3 and 0, respectively. At low Re of 50 and 100, two distinct vortices are seen. It could be the result of Ra dominated effect on the flow structures. The vortices show a tendency of flattening in the case of air more prominently than in the case of water.

As Re increases, the vortices merge together and form a continuous circulation. The velocity of the fluid at the center of the circulation is small and it increases towards the periphery. At lower Re , there is a significant difference between the streamlines of air and water. In the case of water at $Re = 10$, two distinct vortices appear; whereas, for the case of air it shows a sign of merging. However, at higher

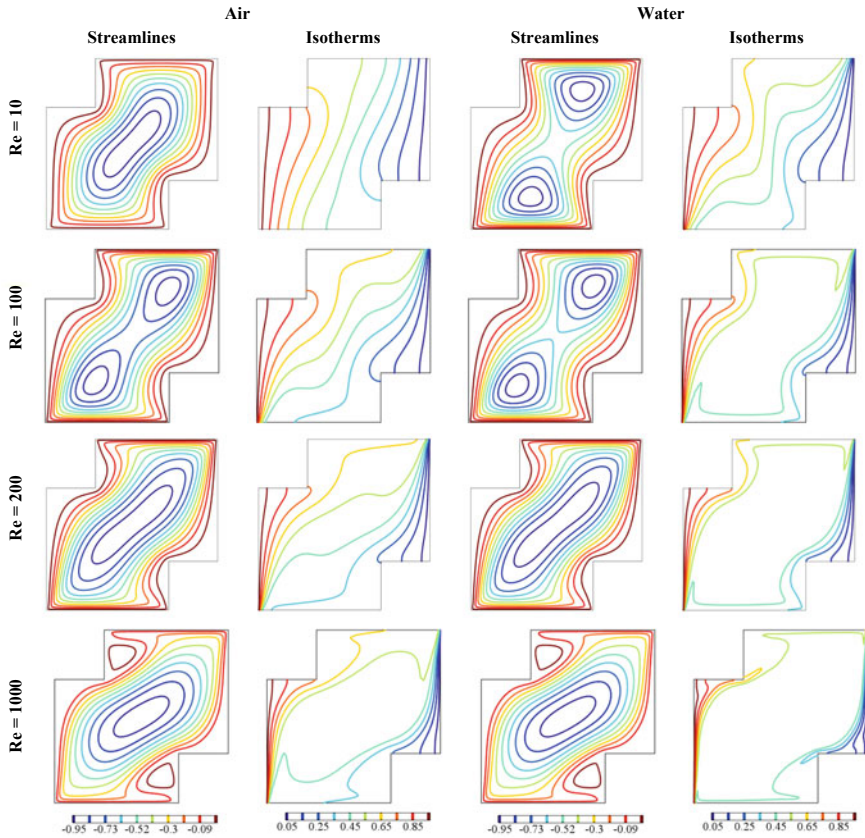


Fig. 3 Impact of Reynolds number on flow structures (streamlines and isotherms) of the respective fluids (air and water)

Re, we find relatively little difference except in the magnitude of the value of ψ_{\max} which is greater for air. At a higher Re of 1000, the streamline pattern does not change much for the geometry irrespective of the fluid as the flow is driven by forced convection. For air at $Re = 10$ and $Re = 100$, nearly distortion-free isotherms are obtained indicating that heat transfer mainly depends on Ra and the effect of Re is less. This also shows that heat transfer is more predominant due to conduction dominance. In the case of water, thickly packed isotherms have been observed near the walls and the consequence of forced convection is more significant. So, heat transfer through convection is more in the case of water than that of air. Even at higher Re, the isotherms are densely packed in case of water than in case of air. The isotherms follow the fluid flow direction.

4.2 Influence of Hartmann Number on Flow Characteristics of Air and Water at $Ra = 10^3$

For the current work, the effect of a uniform horizontal magnetic field which has been shown in Fig. 1 is studied using Hartmann number (Ha). From the governing Eq. (3) it is clear that Ha severely impacts the vertical component of velocity. As a coupling effect of three forces (magnetic, buoyancy, and shear) it is found that Ha has a very significant impact on flow characteristics. For this, the streamlines as a means of comparison are depicted in Fig. 4 for different Ha values with two different combinations of Re and Ra . At low $Re = 20$ and $Ha = 20$, the buoyant flow dominates over shear-induced flow, and uniform circulating cells throughout the cavity are observed which increases on increasing the value of Ra . As Ha increases, it causes complete disruption of convection currents and as water has a higher magnetic susceptibility than air, so with an increase in Ha , the effects are more prominent in water than in air. On increasing the values of Ha , a significant reduction in energy of convection currents is observed irrespective of the increase in Re . With an increase in Re , the localization of convection currents in two vortices is observed in the upper and lower regions of the cavity, which severely dampens the heat transfer process.

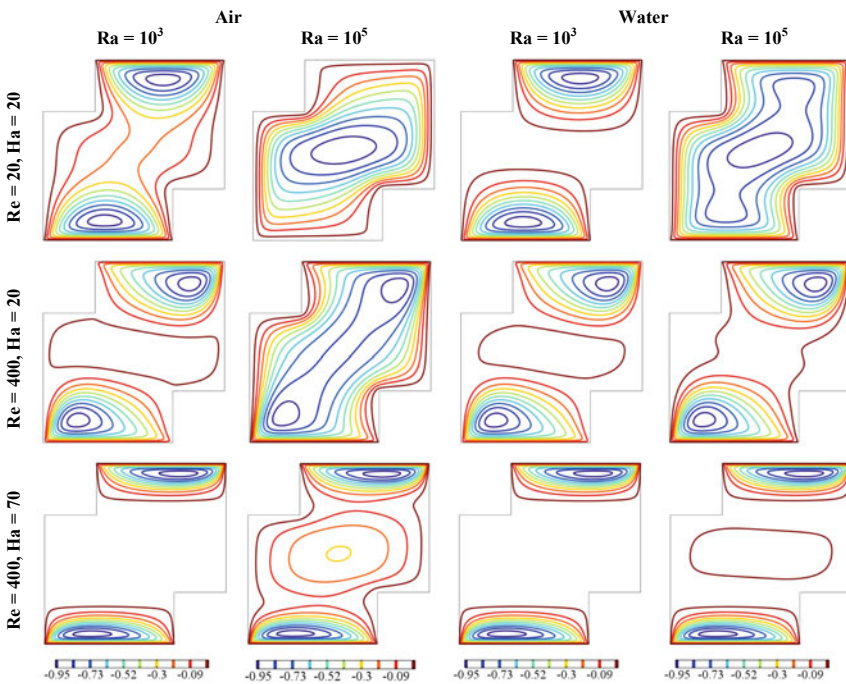


Fig. 4 Effect of Hartmann number on flow characteristics at $Re = (20, 400)$ and $Ra = (10^3, 10^5)$

From the streamlines, it is found that in the case of the magnetic field is applied at upper Ra is preferred as high Ra aids in the formation of a convection current.

4.3 Effect of ϕ on Thermo-Fluid Flow Structure

The consequence of various values of Ha with nanoparticle volume fraction $\phi = 0.01$ and 0.03 is shown in Fig. 5 for $Re = 100$ and $Ra = 10^3$. Negligible change is found in the streamline patterns with a change in ϕ for a particular value of Ha. In the case of $Ha = 0$, for both ϕ values, the value of ψ_{max} remains the same. With increasing values of Ha, it is found that the value of ψ_{max} decreases which shows that Ha decreases the flow in the cavity. The increase in Ha decreases the vertical component velocity. It can be clearly noted from Fig. 5 that a rise in Ha completely divides the cavity into two zones, which clearly affects fluid mixing necessary for thermal energy transport. The heat transfer from the hotter wall to the colder wall declines as the convection currents becomes reduced due to a decrease in vertical velocity. This can be seen in the difference in the absence of vortices and the streamlines in the overlapping region for higher values of Ha as compared to $Ha = 0$. However, with increasing values of ϕ , the value of ψ_{max} increases. Also, as ϕ increases the difference in ψ_{max} decreases. At higher values Ha, we find there is nearly a constant difference between the values of ψ_{max} for $\phi = (0.01, 0.02, 0.03, 0.04, 0.05)$.

Figure 6 compares the effect of $Ra = 10^5$ and 10^3 for $\phi = 0.02$ and 0.05 using the streamlines and isotherms. In this case, a constant value of $Re = 400$ and $Ha = 50$ is taken for comparison. For both values of Ra, there is no change in the streamline pattern or the number and pattern of vortices with an increasing value of ϕ . For Ra =

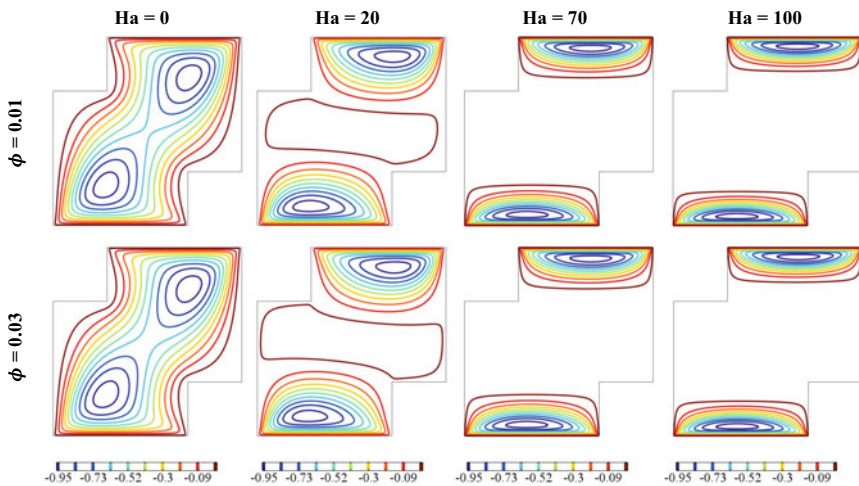


Fig. 5 Effect of Ha on the streamlines at $Re = 100$ and $Ra = 10^3$ for $\phi = 0.01$ and 0.03

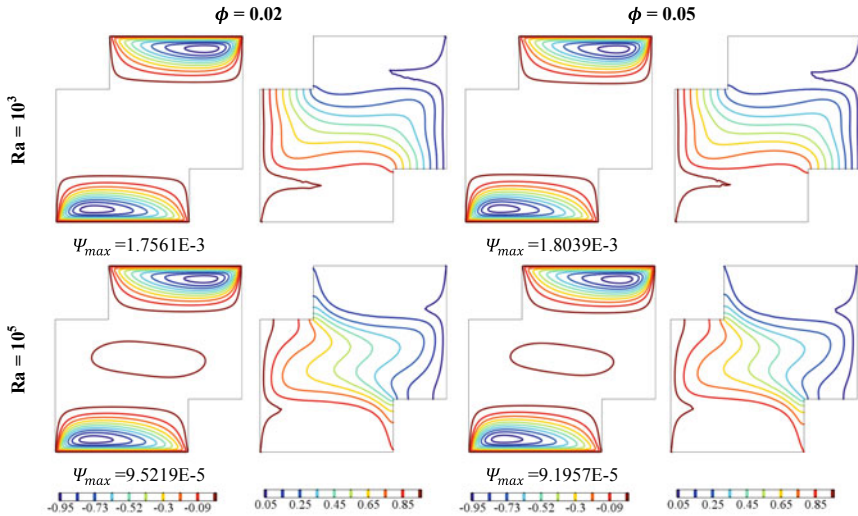


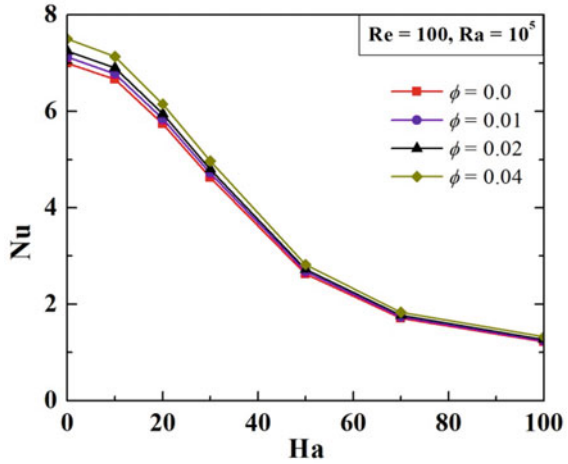
Fig. 6 Effect of Ra on flow characteristics (streamlines and isotherms) of nanofluid at Re = 400, Ha = 50, and $\phi = 0.02$ and 0.05

10^3 on the increasing value of ϕ the value of ψ_{max} increase. However, for the same ϕ as Ra increases from 10^3 to 10^5 , it can be seen that the ψ_{max} values decreases. The ψ_{max} value also decreases for increase in ϕ for Ra = 10^5 , Re = 400 and Ha = 50 but on comparing it in the case of Ra = 10^5 , Re = 200 and Ha = 50 the value of ψ_{max} increases with the increase in ϕ values. This anomaly is similarly noted in case Re = 200 and Ha = 70 for Ra = 10^5 . However, in general, for an increase in ϕ , the value of ψ_{max} increases. This can be understood from the fact that as Ha increases the vertical velocity is much more affected than horizontal velocity and so the effect of buoyancy-driven flow gets reduced. Since increased Ra means increased vertical velocity which is impeded by Ha so the value of ψ_{max} decreases with an increase in Ra for a particular Ha.

4.4 Heat Transfer Analysis

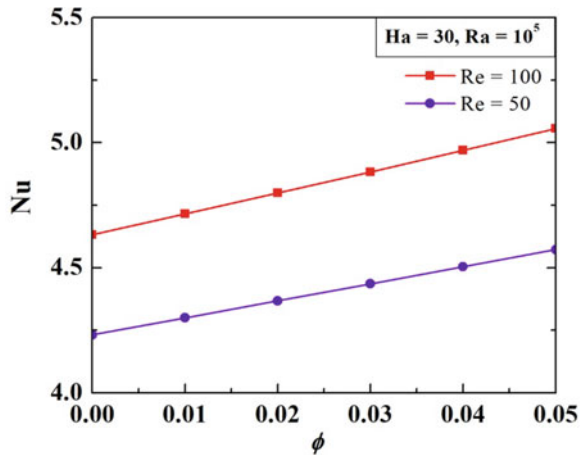
Figure 7 compares the bearing of Hartmann number (Ha) on the global heat transfer rate (Nu) for different nanopowders volume fractions ($\phi = 0, 0.01, 0.02, 0.04$). For flow conditions, we have applied Re = 100 and Ra = 10^5 . It can be seen from the figure that as Ha increases Nu decreases for all values of ϕ . This can again be attributed to the effect of Ha on reducing the velocity of the flow. For Ha = 0 we find a 1.808% increase in Nu for $\phi = 0.01$ from $\phi = 0$ and a 3.489% increase in Nu for $\phi = 0.04$ from $\phi = 0.02$. However, for Ha = 70, it is seen that an increase of 1.719% increase in Nu for $\phi = 0.01$ from $\phi = 0$ and a 3.481% increase in Nu for $\phi = 0.04$

Fig. 7 Influence of Ha on Nu at different ϕ for Re = 100 and Ra = 10^5



from $\phi = 0.02$. Also, it can be seen that for a particular value of Ha as ϕ increases Nu increases. So, it can be said for high values of Ha higher values of ϕ is preferred and at upper values of Ha, the increase in Nu with an increase in ϕ remains constant. Figure 8 gives us the values of the average Nu for Re = 50 and 100 for Ha = 30 at altered values of ϕ . As Re increases the Nu value increases and the increase is more with increasing values of ϕ .

Fig. 8 Influence of Re on Nu at different ϕ for Ha = 30 and Ra = 10^5



5 Concluding Remarks

The present study explores the thermo-fluidic transport behavior in a double-driven enclosure considering thermal convection and magnetic fields. In this study, both common fluids (air and water) and a nanofluid (CuO-water) are considered as a working medium (separately). The outcomes of this study are concisely presented below.

- (a) The difference is significant in the streamline pattern at low Re between air and water. However, it becomes negligible at higher Re. In a double-driven cavity, we find two distinct vortices at low Re at $Ha = 0$ and $Ra = 10^3$ for both air and water. Also, from the isothermal patterns for all conditions of $Ha = 0$, it can be concluded that water is a better fluid for heat transfer than air.
- (b) The impact of the Hartmann number on the water is more than that of air. Since Ha affects the vertical component of velocity we find two localized vortices near the upper and lower lids for water for $Re = 400$, $Ha = 70$ for both $Ra = 10^3$ and $Ra = 10^5$. However, for air as Ra increases there is a substantial improvement in heat transfer through convection even at high Ha . So, air can be a better heat transfer medium at high Ha .
- (c) For a particular Ha with a change in ϕ , no change is observed in the streamline pattern. At $Ha = 0$, the value of $|\psi|_{\max}$ remains the same for all values of ϕ . For a particular Ra , the value of $|\psi|_{\max}$ declines as Ha rises. For a given Ha value, when ϕ increases, the value of $|\psi|_{\max}$ increases. The pattern of vortices is also the same for a particular value of Ha as that of water.
- (d) Lower values of Ra are preferred for the optimum heat-transfer performance of nanofluid in the existence of magnetizing field as seen from the isotherms and streamlines where they perform poorly at high values of Ha .
- (e) For all the values of ϕ , the Nu value decreases with increasing Ha . For a particular Ha value, Nu rises with increasing values of ϕ . For higher Ha values, upper values of ϕ are preferred and at higher values of Ha , the rate of increase in Nu with an increase in ϕ remains constant.
- (f) As Re increases, the value of Nu increases and the growth is more with increasing values of ϕ . There is a maximum enhancement of heat transfer for lower values of Ha with increasing values of Re. However, at high values of Ha , it is found that for higher $Re = 200$, the average Nu is less than the values for that of lower Re for certain values of Ha .

References

1. Vischer D, Hager W (1998) Dam hydraulics. In: Wiley series in water resources engineering. Wiley
2. Stefanovic DL, Stefan HG (2000) Simulation of transient cavity flows driven by buoyancy and shear. *J Hydraul Res* 38:181–195

3. Triantafillopoulos NG, Aidun CK (1990) Relationship between flow instability in short-dwell ponds and cross-directional coat weight nonuniformities. *TAPPI J* 73(6):127–136
4. Zumbrennen DA, Miles KC, Liu YH (1996) Auto-processing of very finescale composite materials by chaotic mixing of melts. *Appl Sci Manuf* 27:37–47
5. Zhou YC, Patnaik BSV, Wan DC, Wei GW (2003) DSC solution for flow in a staggered double lid driven cavity. *Int J Numer Meth Eng* 57:211–234
6. Nithiarasu P, Liu CB (2005) Steady and unsteady incompressible flow in a double driven cavity using the artificial compressibility (AC)-based characteristic-based split (CBS) scheme. *Int J Numer Meth Eng* 63:380–397
7. Tekić PM, Radenović JB, Lukić NL, Popović SS (2010) Lattice Boltzmann simulation of two-sided lid-driven flow in a staggered cavity. *Int J Comput Fluid Dyn* 24(9):383–390
8. Masuda H, Ebata A, Teramae K, Hishinuma N (1993) Alteration of thermal conductivity and viscosity of liquid by dispersing ultra-fine particles (dispersion of Al_2O_3 , SiO_2 and TiO_2 ultra-fine particles). *Netsu Bussei* 7(4):227–233
9. Choi SUS (1995) Enhancing thermal conductivity of fluids with nanoparticles. In: *Proceedings of the 1995 ASME international mechanical engineering congress and exposition*, New York, 99–105
10. Kabeel AE, El-Said EMS, Dafea SA (2015) A review of magnetic field effects on flow and heat transfer in liquids: present status and future potential for studies and applications. *Renew Sustain Energy Rev* 45:830–837
11. Ghasemi B, Aminossadati SM, Raisi A (2011) Magnetic effect of natural convection in a nano-filled square enclosure. *Int J Therm Sci* 50:1748–1756
12. Biswas N, Manna NK (2017) Enhanced convective heat transfer in lid-driven porous cavity with aspiration. *Int J Heat Mass Transf* 114:430–452
13. Biswas N, Manna NK (2018) Magneto-hydrodynamic Marangoni flow in bottom-heated lid-driven cavity. *J Mol Liq* 251:249–266
14. Mondal MK, Biswas N, Manna NK (2019) MHD convection in a partially driven cavity with corner heating. *SN Appl Sci* 1–1689
15. Biswas N, Mahapatra PS, Manna NK (2017) Enhanced convective heat transfer in lid-driven porous cavity with aspiration. *Int J Heat Mass Transf* 114:430–452
16. Biswas N, Mahapatra PS, Manna NK (2016) Enhanced thermal energy transport using adiabatic block inside lid-driven cavity. *Int J Heat Mass Transf* 100:407–427
17. Biswas N, Manna NK, Datta P, Mahapatra PS (2018) Analysis of heat transfer and pumping power for bottom-heated porous cavity saturated with Cu-water nanofluid. *Powder Technol* 326:356–369
18. Biswas N, Manna NK, Chamkha AJ (2021) Effects of half-sinusoidal nonuniform heating during MHD thermal convection in Cu– Al_2O_3 /water hybrid nanofluid saturated with porous media. *J Therm Anal Calorim* 143:1665–1688
19. Biswas N, Sarkar UK, Chamkha AJ, Manna NK (2021) Magneto-hydrodynamic thermal convection of Cu– Al_2O_3 /water hybrid nanofluid saturated with porous media subjected to half-sinusoidal nonuniform heating. *J Therm Anal Calorim* 143:1727–1753
20. Mondal MK, Biswas N, Dattam A, Sarkar BK, Manna NK (2021) Positional impacts of partial wall translations on hybrid nanofluid flow in porous media: real coded genetic algorithm (RCGA). *Int J Mech Sci* 107030
21. Mandal DK, Mondal MK, Biswas N, Manna NK, Gorla RSR, Chamkha AJ (2022) Nanofluidic thermal-fluid transport in a split-driven porous system working under a magnetic environment. *Int J Numer Meth Heat Fluid Flow* 32(7):2543–2569
22. Mallick H, Mondal H, Biswas N, Manna NK (2021) Buoyancy driven flow in a parallel-grammic enclosure with an obstructive block and magnetic field. *Mater Today Proc* 44(2):3164–3171
23. Sen K, Biswas N, Manna NK (2022) Thermo-fluidic transport process in a double-driven cavity with triangular adiabatic obstacles. *Mater Today Proc* 52(3):524–531
24. Chatterjee D, Manna NK, Biswas N (2022) Thermo-magnetic convection of nanofluid in a triangular cavity with a heated inverted triangular object. *Mater Today Proc* 52(3):427–433

Curvature Effect of Heated Sidewall During Heat Transport of Different Prandtl Number Fluids in a Square Enclosure in the Presence of a Magnetic Field



Shreyasi Maitra, Nirmalendu Biswas, Nirmal K. Manna,
and Dipak Kumar Mandal

Abstract The present work numerically investigates the characteristics of heat transfer in the presence of a sidewall curvature in a square enclosure. The left heated wall includes three cases consisting of vertical and assumes the sinusoidal shape of the form $\cos(2\pi Nx)$, and the other adjoining walls remain completely straight. The working fluids are taken as air ($Pr = 0.71$) and Al_2O_3 -water nanofluid ($Pr = 5.83$) with the nanoparticle concentration $\varphi = 0.01$. A constant magnetic field is imposed externally to influence the transport processes in the enclosure. The corresponding magnetic field is simulated using various values of the Hartmann number ($Ha = 0-50$). The analysis is carried out using different Rayleigh numbers (Ra) ranging from 10^3 to 10^6 . The streamlines, isotherms and Nusselt numbers are used for studying the heat transfer characteristics. The fluid flow and heat transfer characteristics are analyzed considering a two-dimensional laminar flow. The conservation equations of mass, momentum and energy are utilized within the validity of the Boussinesq approximation. The study is conducted numerically using Galerkin finite element methodology. The result reveals that the heat transfer is most effective with increasing Ra for the convex-walled curvature compared to straight wall and concave wall. Strength of the applied magnetic field reduces the heat transfer rate significantly depending on the wall curvature.

Keywords Curved wall · Nanofluid · Magnetohydrodynamic (MHD) flow · Heat transfer

S. Maitra · N. Biswas (✉)

Department of Power Engineering, Jadavpur University, Salt Lake, Kolkata 700106, India
e-mail: biswas.nirmalendu@gmail.com

N. K. Manna

Department of Mechanical Engineering, Jadavpur University, Kolkata 700032, India
e-mail: nirmalkmannaju@gmail.com

D. K. Mandal

Department of Mechanical Engineering, College of Engineering and Management, Kolaghat 721171, India
e-mail: dipkuma@yahoo.com

Nomenclature

B_0	Magnetic field, Tesla
g	Acceleration due to gravity (ms^{-2})
H	Height of the cavity, length scale (m)
Ha	Hartmann number
k	Thermal conductivity ($\text{Wm}^{-1} \text{K}^{-1}$)
L	Length of each side of the cavity (m)
Nu	Average Nusselt number
p	Pressure (Pa)
Pr	Prandtl number
Ra	Rayleigh number
T	Temperature (K)
U, V	Dimensionless velocity components
X, Y	Dimensionless coordinates

Greek Symbols

α	Thermal diffusivity (m^2s^{-1})
β	Thermal expansion coefficient of fluid (K^{-1})
θ	Dimensionless temperature
μ	Dynamic viscosity ($\text{kgm}^{-1} \text{s}^{-1}$)
ν	Kinematic viscosity (m^2s^{-1})
ρ	Density (kgm^{-3})
σ	Electrical conductivity (Sm^{-1})
φ	Nanoparticle volume fraction
ψ	Dimensionless streamfunction

Subscripts

c, h	Cold wall, hot wall
f	Base fluid
s	Solid

1 Introduction

The study related to magnetohydrodynamics (MHD) flow along with natural convection has several areas of application in science and engineering. This is a vital area of interest for the researchers because of its wide range of application involving MEMS devices, nuclear reactors, cooling devices, solar energy collectors, room ventilators, MHD power systems, geothermal energy extractions, biomedical engineering and so on [1–4]. Due to the technological advancement, above applications demand more sophistication from its control point of view. Even, in the presence of the thermal gradient such control becomes more complex. Several researchers are continually paying their attention for the development of the devices/systems undergoing magneto-thermal systems [5–7]. Recent development in the nanofluid and later hybrid nanofluid (suspension of nano-sized solid particles in the host fluid) helps the designer for the enhanced heat transfer of the magneto-thermal devices/systems [8–10]. Detailed reviews on the preparation and application of nanofluid/hybrid nanofluid are available in the open literature [11].

In the area of MHD convective flow, the shape of an enclosure, surface undulation or curving surface significantly alters convective phenomena. The near-wall phenomena have substantial impact on the transport process. The fundamental aspects of the transport process along with heat transfer in the presence of wavy surfaces are documented in book [12]. There exist a number of research works on the buoyancy-driven convective heat transfer from different types of surface waviness like: irregular, corrugated, curved, sinusoidal or other wavy surfaces involving various other coupled multiphysics [13, 14]. The surface waviness of a confined space significantly alters thermal-fluid phenomena and associated heat transfer characteristics. Of course, with the surface waviness the interfacial surface area between the surface and the adjacent fluid layer enlarges. This boosts heat transfer mechanism. Alsabery et al. [15] examined the influence of cold, corrugated sidewalls on the buoyancy-driven thermal convection of nanofluid filled porous cavity heated discretely from the bottom. They found that the number of undulation could effectively control the heat transfer. Sheremet et al. [16] investigated the buoyancy-induced convection of nanofluid filled porous cavity with wavy cold left sidewall (with three peaks) and partially heated right wall. Magnetohydrodynamic natural convective heat transfer of nanofluid filled heat generating porous cavity with the heated wavy wall (varying number and height of undulations) has been investigated by Ahmed and Rashed [17]. The study revealed that the rate of heat transfer is an increasing function of the number and height of the undulations. Adopting complex wavy walls, the thermal convection in a cavity has been studied with and without nanofluid, which are documented in Refs. [13–17].

The extensive literature survey shows that the effect of wall curvature either convex or concave on the heat transfer characteristics has been explored adequately. However, a limited number of work on the effect of wall curvature on the heat transfer rate in the presence of magnetic field were observed. Thus, the present study is focused on the curvature effect of heated sidewall during heat transfer in

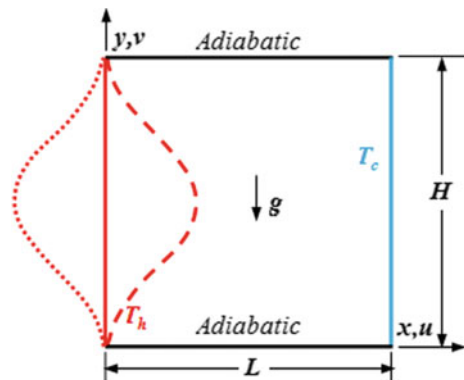
a square enclosure in the presence of a magnetic field with fluids having different Prandtl number. The numerical analysis is carried out by studying the isotherms, entropy generation contours and streamlines of the defined problem. Therefore, the new study promises to be useful and fulfilling in various areas of engineering and medical aspects. The analysis is carried out using different Rayleigh numbers (Ra) ranging from 10^3 to 10^6 . The streamlines, isotherms and Nusselt numbers are used for studying the heat transfer characteristics. The conservation equations of mass, momentum and energy are utilized within the validity of the Boussinesq approximation. The study is conducted numerically using Galerkin finite element methodology.

2 Problem Formulation

The geometry of the problem considers a two-dimensional, laminar, incompressible natural convective flow in a square enclosure ($L \times H$) with constant magnetic field of amplitude B . Three different cases are studied keeping the left wall vertical (shown in firm line) as the base case and two other case where it assumes the sinusoidal shape either convex (in short dashed line) or concave (in long dashed line) in the form $\cos(2\pi Nx)$, and its adjacent walls perfectly straight. The left wall is heated isothermally (at temperature T_h) and the right wall is kept at a lower temperature (at temperature T_c , where $T_h > T_c$) as illustrated in Fig. 1.

The top and bottom walls are isothermally insulated. The applied magnetic field is in the x -direction and the electric field is kept perpendicular to the x - y plane. Two types of working fluid are considered for the study either air ($Pr = 0.71$) and Al_2O_3 -water nanofluid (with $Pr = 5.83$) with the nanoparticle concentration $\varphi = 0.01$. The fluid flow and heat transfer characteristics are analyzed considering a two-dimensional laminar flow. The conservation equations of mass, momentum and energy are utilized within the validity of the Boussinesq approximation. The study is conducted numerically using Galerkin finite element methodology. The dimensional

Fig. 1 Schematic diagram of the problem geometry along with coordinate system and boundary conditions



transport equations are converted into non-dimensional equations by defining the following non-dimensional parameters.

$$(X, Y) = (x, y)/H; (U, V) = (u, v)H/\alpha; \theta = (T - T_c)/(T_h - T_c);$$

$$P = ((p + \rho gy) - p_a)H^2/\rho\alpha^2$$

where (u, v) are dimensional velocity components, and (U, V) are dimensionless velocities. The dimensional and non-dimensional axes are (x, y) and (X, Y) , respectively. The non-dimensional pressure P constitutes of ambient pressure and pressure change along the vertical (ρgy) , respectively. The non-dimensional governing equations in the Cartesian coordinate system are mentioned below:

$$U \frac{\partial U}{\partial X} + V \frac{\partial V}{\partial Y} = 0 \tag{1}$$

$$U \frac{\partial U}{\partial X} + V \frac{\partial U}{\partial Y} = -\frac{\partial P}{\partial X} + \text{Pr} \left(\frac{\partial^2 U}{\partial X^2} + \frac{\partial^2 U}{\partial Y^2} \right) \tag{2a}$$

$$U \frac{\partial V}{\partial X} + V \frac{\partial V}{\partial Y} = -\frac{\partial P}{\partial Y} + \text{Pr} \left(\frac{\partial^2 V}{\partial X^2} + \frac{\partial^2 V}{\partial Y^2} \right) - \sigma \text{Ha}^2 V + \text{Ra Pr } \theta \tag{3a}$$

$$U \frac{\partial \theta}{\partial X} + V \frac{\partial \theta}{\partial Y} = \left(\frac{\partial^2 \theta}{\partial X^2} + \frac{\partial^2 \theta}{\partial Y^2} \right) \tag{4a}$$

The above equations are valid for common working fluid (air and water). However, in case of nanofluid the momentum and energy equations are to be

$$U \frac{\partial U}{\partial X} + V \frac{\partial U}{\partial Y} = -\frac{\rho_f}{\rho_{nf}} \frac{\partial P}{\partial X} + \frac{\nu_{nf}}{\nu_f} \text{Pr} \left(\frac{\partial^2 U}{\partial X^2} + \frac{\partial^2 U}{\partial Y^2} \right) \tag{2b}$$

$$U \frac{\partial V}{\partial X} + V \frac{\partial V}{\partial Y} = -\frac{\rho_f}{\rho_{nf}} \frac{\partial P}{\partial Y} + \frac{\nu_{nf}}{\nu_f} \text{Pr} \left(\frac{\partial^2 V}{\partial X^2} + \frac{\partial^2 V}{\partial Y^2} \right)$$

$$- \frac{\rho_f}{\rho_{nf}} \frac{\sigma_{nf}}{\sigma_f} \text{Ha}^2 V + \frac{(\rho\beta)_{nf}}{\rho_{nf}\beta_f} \text{Ra Pr } \theta \tag{3b}$$

$$U \frac{\partial \theta}{\partial X} + V \frac{\partial \theta}{\partial Y} = \frac{\alpha_{nf}}{\alpha_f} \left(\frac{\partial^2 \theta}{\partial X^2} + \frac{\partial^2 \theta}{\partial Y^2} \right) \tag{4b}$$

where the dimensionless numbers Pr, Ra and Ha are Rayleigh number (Ra), Prandtl number (Pr) and Hartmann number (Ha), which are defined as

$$\text{Pr} = \frac{\nu_f}{\alpha_f}; \text{Ra} = \frac{g\beta_f(T_h - T_c)H^3}{\nu_f\alpha_f}; \text{Ha} = \frac{BH}{\sqrt{\nu_f\rho_f/\sigma_f}} \tag{5}$$

The fluid properties (such as thermal diffusivity α , kinematic viscosity ν and volumetric expansion coefficient) are assumed to be constant except density (ρ) variation, which is taken care by the Boussinesq approximation.

The thermal condition of the top and bottom wall is adiabatic ($\partial\theta/\partial Y = 0$), right sidewall is isothermally cold ($\theta = 0$), and the left sidewall is isothermally heated ($\theta = 1$). All the walls are set at zero velocity ($U = V = 0$).

In the dimensionless governing Eqs. (2b)–(4b), the thermophysical properties of Al_2O_3 nanoparticles volumetric concentration (φ) in the based fluid (water) are observed. The effective density ρ_{nf} , specific heat capacity $(c_p)_{nf}$ and thermal expansion coefficient β_{nf} of the hybrid nanofluid are modified appropriately adopting the property relations as reported in the standard literature [9, 10, 18]. Here, the subscript ‘*nf*’ corresponds to the Al_2O_3 –water nanofluid.

The dimensionless governing Eqs. (1)–(4) including the boundary conditions are solved numerically following the Galerkin weighted finite element methodology (FEM) using the SIMPLE algorithm. The solutions is carried out in an iterative process, with successive minimization of residuals of the mass, momentum and temperature equations to a set value $<10^{-8}$. In order to select correct grid size for the present chosen problem, a mesh sensitivity test is carried out. Finally, 160×160 grids distributed non-uniformly are selected for the study. Furthermore, using the present solver an extensive validation study has been carried out by simulating the different problems available in the open literature [18, 19]. The validation study shows reasonably good agreement in-between present simulated results and results published in the literature. This verification ensures about the accuracy of the finite element solver for the present study. However, for brevity the validation study is not presented here.

The equations of streamfunction have been evaluated and availed to present the flow field pattern in terms of streamlines. The stream function (ψ) is expressed as

$$-\frac{\partial\psi}{\partial X} = V; \quad \frac{\partial\psi}{\partial Y} = U \quad (6)$$

In order to analyze the heat transfer characteristics for the bottom heated inclined square enclosure, the average Nusselt number is calculated on the hot wall as

$$\text{Nu} = \frac{k_{nf}}{k_f} \int_0^1 \left(-\frac{\partial\theta}{\partial X} \Big|_{X=0,1} \right) dY \quad (7)$$

3 Results and Discussion

In the present study, buoyancy-induced thermal convection in the presence of a sidewall curvature in a square enclosure is investigated numerically. The left heated

wall includes three cases consisting of vertical and assumes the sinusoidal shape of the form $\cos(2\pi N\chi)$. In this study, amplitude of the curvature is taken as 0.2. Two different working fluids are taken as air ($Pr = 0.71$) and Al_2O_3 -water nanofluid ($Pr = 5.83$) with the nanoparticle concentration $\varphi = 0.01$. A constant magnetic field is imposed externally to influence the transport processes in the enclosure. The analysis is carried out for a wide range of influencing parameters like Rayleigh number ($Ra = 10^3, 10^4, 10^5, 10^6$) and Hartmann number ($Ha = 0, 10, 30, 50, 70, 100$). The results of the study are illustrated by the visualization of streamlines, isotherms, contours and average Nusselt number (Nu).

3.1 Effect of Rayleigh Number (Ra)

The effect of Ra on the flow structure of air as a working fluid is illustrated using streamlines, isotherms and average Nu for $Ra = 10^3, 10^4, 10^6$ and keeping $Ha = 30$ fixed as shown in Figs. 2 and 3, respectively. First column illustrates the straight-walled cavity, second column shows the concave-walled cavity, and last column presents convex-walled cavity. For the different magnitudes of evolved parameters,

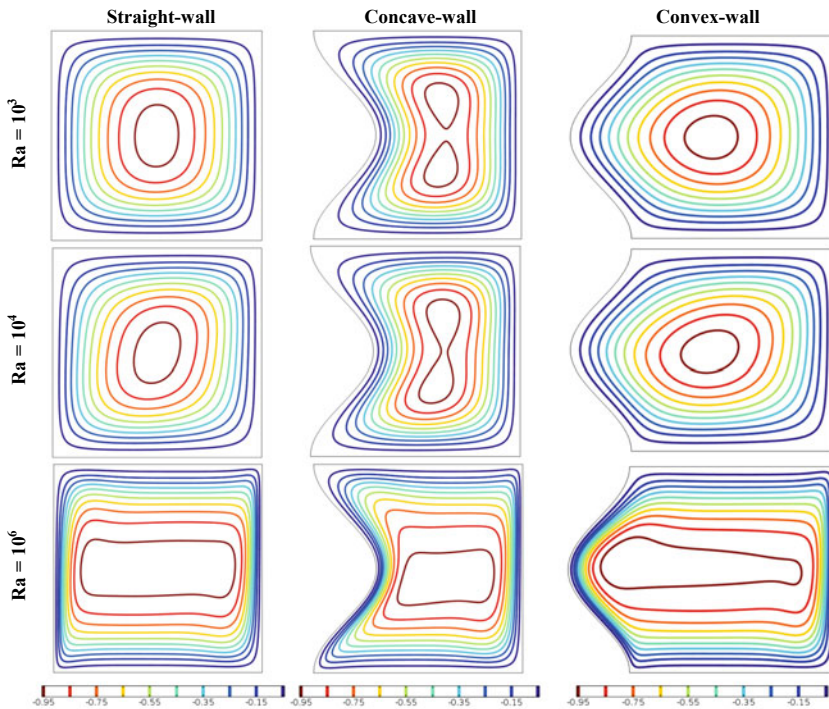


Fig. 2 Effect of Ra and wall curvature on the streamlines for $Ha = 30$ with working fluid as air

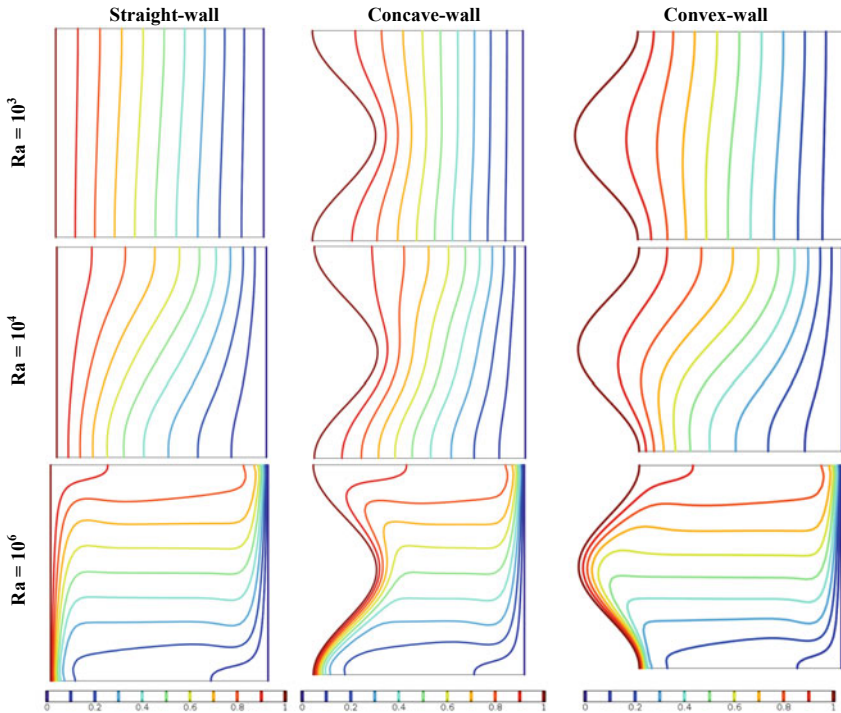


Fig. 3 Effect of Ra and wall curvature on the isotherms for $Ha = 30$ with working fluid as air

one convective circulation cell is formed inside the enclosure clockwise (CW). The circulation cell is formed due to the differential heating at the left side and cooling at the right sidewall.

As a result, heated fluid traverses and spreads evenly inside the entire enclosure and it is obstructed by the top and bottom adiabatic wall. At lower $Ra (= 10^3)$, conduction is responsible for the heat transfer, and hence, the fluid circulation is less. As Ra increases from 10^3 to 10^4 and 10^6 , convection mode heat transfer starts to dominate and becomes maximum at $Ra = 10^6$.

The buoyancy effect dominates the Lorentz force at higher Ra . With the concave curvature of the side wall, it is observed that the fluid flow becomes symmetrical along the mid-horizontal plane and there appears two circulating cells. But the symmetry gradually decreases as the Ra value rises. There is a significant concentration of the streamlines near the convex curvature as the Ra value gradually increases. At higher $Ra = 10^6$, the flow structure stretched horizontally. Of course, with the concave-walled curvature effective fluid volume is less and with convex-walled curvature, fluid volume is higher within the cavity compared to the square cavity. As a result, the flow structure is compressed with concave-walled cavity, whereas it is elongated with convex-walled cavity. The contours of isotherms get distorted at higher values of Ra , due to the convection mode of heat transfer, whereas at lower $Ra (= 10^3)$

isotherm lines are almost vertical and parallel to the active side walls. The isotherm concentration is greater near the heated left side wall. The value of the Nusselt number is lower for the convex curvature as compared to the concave one, indicating that the concavity of the left side wall enhances the heat transfer mechanism for lower values of Ra but as soon as higher Ra ($= 10^6$) the convex curvature has a sudden rise in the Nusselt number followed by better heat flow. Also, heat transfer increases as the Ra value rises.

The contours of streamline and isotherms for different Ra ($= 10^3, 10^4, 10^6$) of Al_2O_3 -water nanofluid with $\varphi = 0.01$ as a working fluid are analyzed keeping the $Ha = 30$ fixed as shown in Figs. 4 and 5. The fluid flows evenly inside the cavity. However, the flow structure as well as static temperature distribution alters significantly compared to the patterns with air as working fluid. At higher Ra, circulating cell stretched little bit diagonally. With the nanofluid as working medium, thermal conductivity of the working fluid improves compared to the air, resulting higher fluid velocity within the cavity and more heat transfer.

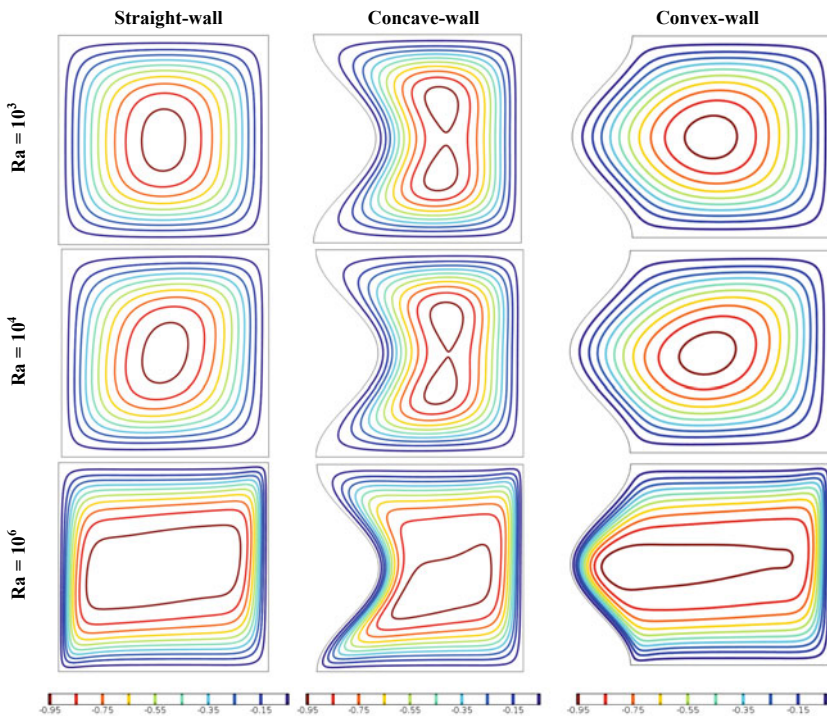


Fig. 4 Effect of Ra and wall curvature on the streamlines for $Ha = 30$ with working fluid as nanofluid

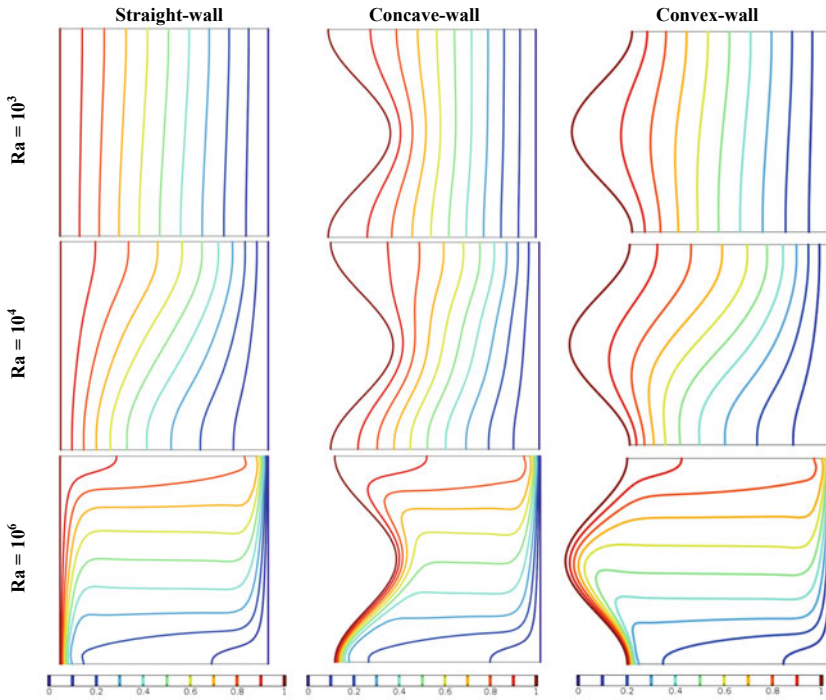


Fig. 5 Effect of Ra and wall curvature on the isotherms for $Ha = 30$ with working fluid as nanofluid

3.2 Effect of Hartmann Number (Ha)

The impact of imposed magnetic field along with change in the wall curvature at $Ha = 0, 50, 70$ and $Ra = 10^5$ shown in Figs. 6 and 7, respectively, considers air as a working medium. To analyze the MHD effect, the contours of isotherms and streamlines are carefully observed. The case of no-magnetic field ($Ha = 0$) is introduced first (in the first row). Gradually, the magnetic field strength is increased by increasing the value of $Ha = 50$ and 70 . A single cell rotating in clockwise direction occupies the entire cavity. Interestingly at $Ha = 0$, there are two smaller circulating cells inside the large circulating cell for the straight-walled cavity and the slow structure stretched diagonally from left-top corner toward right-bottom corner. In case of concave-walled cavity, inner two circulation cells merged and formed a single circulating cell. Finally, with the convex-walled cavity two smaller circulating cells form. However, the shape of the flow structure changes with the change in the left wall curvature, but pattern-wise the flow structure remains similar. When the magnetic field is imposed with $Ha = 50$ (second row) and 70 (last row), the flow structure modifies markedly. In case of straight-walled cavity and convex-walled, there appears single CW circulating cell, whereas with concave-walled cavity there are two smaller circulating cells inside the large one. Furthermore, in all the cases of wall curvature the flow structure is

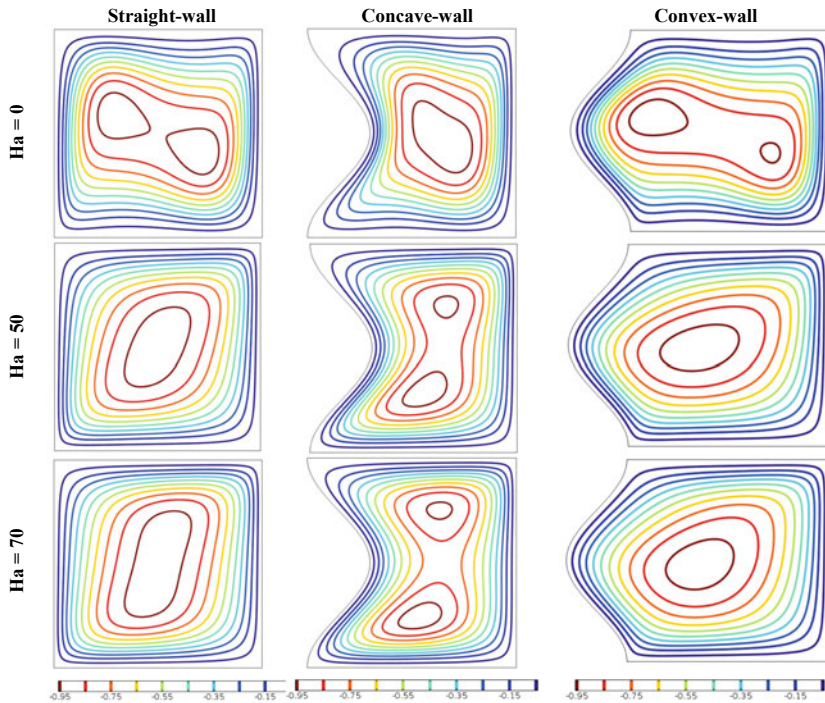


Fig. 6 Effect of Ha and wall curvature on the streamlines for $Ra = 10^5$ with working fluid as air

stretched diagonally from left-bottom corner toward right-top corner. This shows an opposite pattern compared to no-magnetic field case ($Ha = 0$). This happens so, due to the presence of negative magnetic force term in the Y -momentum equation and it counteracts the buoyancy force. At the higher magnetic field strength $Ha = 70$, stretching effect of the fluid flow is more with reduced flow strength. This causes reduction heat transfer. This fact can easily be realized from the isotherm contours. For the no-magnetic field ($Ha = 0$) case (first row in Fig. 7), isotherm contours are stretched almost horizontally except near the active sidewalls. However, with the increase in the Ha value to 50 and 70, isotherm lines are stretched diagonally from left-bottom corner to right-top corner of the cavity. This shows a decrement in the temperature gradient and thus heat transfer decreases gradually as Ha value increases. Further to this, the heat transfer rate increases when the curvature of the left hot wall becomes concave and falls as it becomes convex. This implies that heat transfer enhances if the left wall bulges inwards (convex) and significantly decreases when the same wall becomes concave. On controlling the magnetic field strength and the curvature of the heated wall, thermal convection can be controlled substantially.

The effect of different magnetic field strength on the thermal convection of nanofluid flow for the varying Ha ($= 0, 50, 70$) and fixed $Ra = 10^5$ is and different curvature of the heated wall is analyzed and presented in Figs. 8 and 9, respectively.

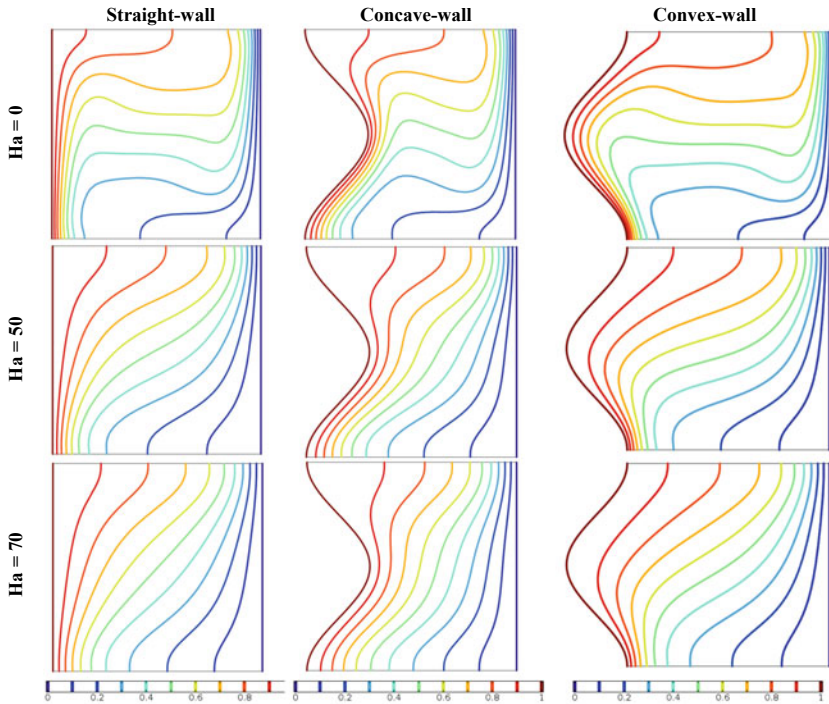


Fig. 7 Effect of Ha and wall curvature on the isotherms for $Ra = 10^5$ with working fluid as air

The right circular clockwise single cell flow inhabits the whole cavity. When $Ha = 0$, the fluid flow stretched almost horizontally. In the concave curvature cavity, circulating cell compressed markedly, whereas it stretched significantly for the convex-walled cavity. In all the cases, flow structure remains symmetrical about the mid-horizontal plane. The streamlines in the convex curvature cavity are focused near the curvature when $Ha = 0$. However, as Ha increases to 50 and 70, circulating cells stretched diagonally as in the case of air as a working medium. Isotherm contours almost horizontally when $Ha = 0$, and stretched diagonally with the increase in Ha .

3.3 Heat Transfer Characteristics

The global thermal performance of the cavity with different curvature is evaluated using the average Nu and plotted in Fig. 10a, b, respectively, with the variation of Ra and two different working fluids (air and nanofluid) for $Ha = 30$. From the figure, it is clearly observed that there is no change in average Nu up to $Ra \leq 10^4$ and beyond that heat transfer increases markedly as Ra increases. This happens as the heat transfer process is mainly due to the conduction mode for $Ra \leq 10^4$ and after

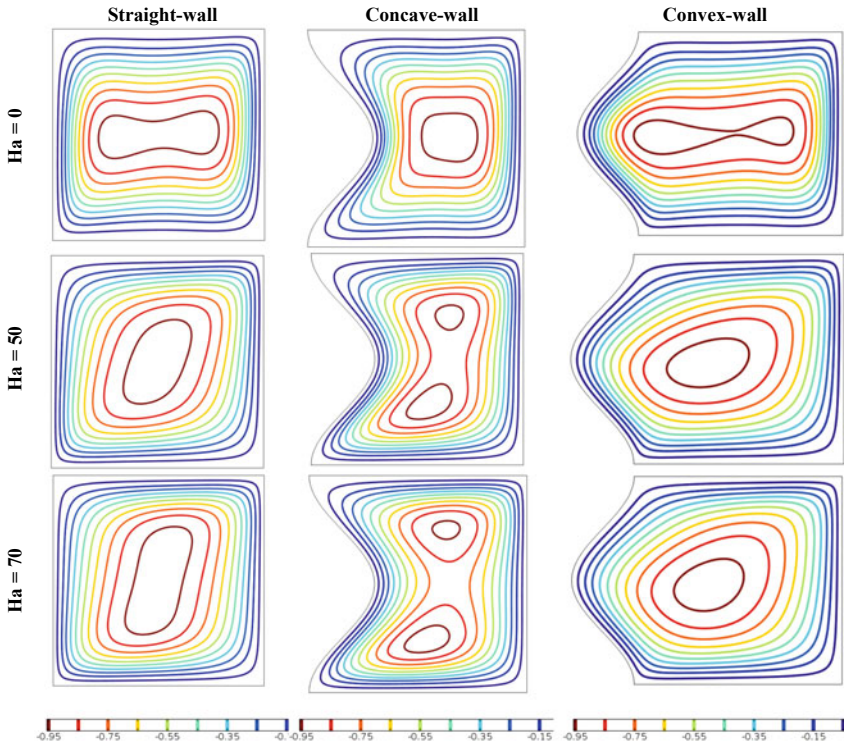


Fig. 8 Effect of Ha and wall curvature on the streamlines for $Ra = 10^5$ with working fluid as nanofluid

that convection mechanism increases significantly and it leads to the increment in average Nu . Furthermore, it is observed that convex-walled cavity shows superior heat transfer compared to the straight-walled cavity and heat transfer enhancement is in the range of 6% (for convex-walled cavity) and 4% (for concave-walled cavity). The trend is similar for both air and nanofluid as working medium.

4 Conclusion

The present study numerically investigates the characteristics of heat transfer in the presence of a sidewall curvature in a square enclosure under the impact of external magnetic field. The right-side wall is kept isothermally cold with top and bottom wall adiabatic. The thermomagnetic convection is explored under various parameters like Ra and Ha . The thermo-fluid flow is analyzed thoroughly using streamlines, isotherms and average Nusselt number. Some of the major observations:

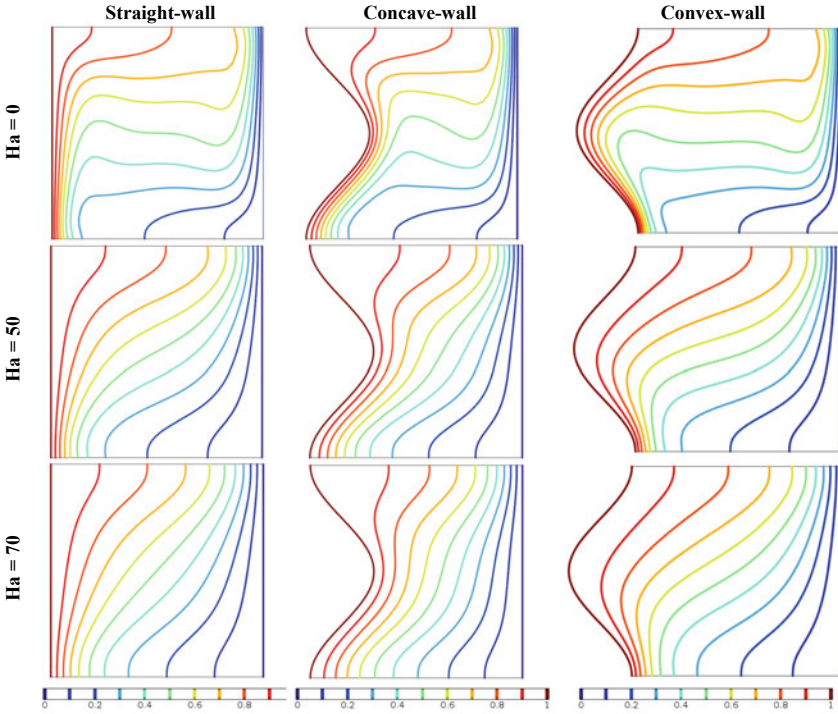


Fig. 9 Effect of Ha and wall curvature on the isotherms for $Ra = 10^5$ with working fluid as nanofluid

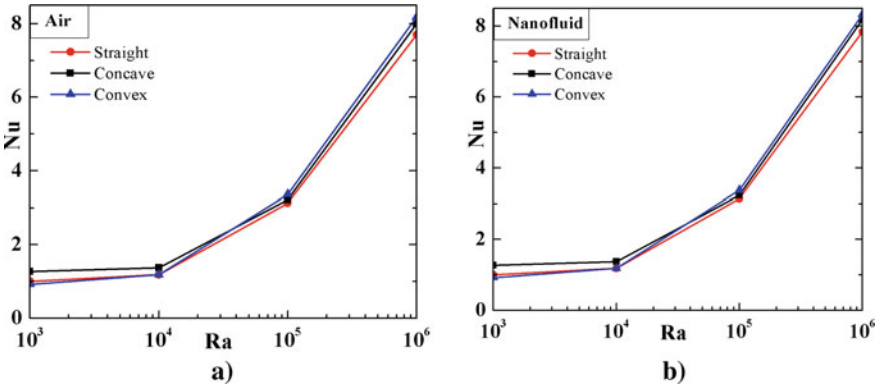


Fig. 10 Heat transfer characteristics for varying Ra. a Air, and b Al_2O_3 nanofluid

- (a) With the increase in Ra, heat transfer is most effective for the convex-walled curvature and decreases as the curvature becomes straight and then concave eventually.
- (b) As the strength of the applied magnetic field increases, it reduces the convection process within the enclosure. As a result, heat transfer decreases significantly. Heat transfer enhancement is in the range of 6% (for convex-walled cavity) and 4% (for concave-walled cavity).

References

1. Davidson PA (2001) An introduction to magnetohydrodynamics. In: Cambridge texts in applied mathematics. Cambridge University Press, Cambridge
2. Ozoe H (2005) Magnetic convection. Imperial College Press, Singapore
3. Shercliff JA (1965) A textbook of magnetohydrodynamics. Pergamon Press, Oxford
4. Mondal MK, Biswas N, Manna NK (2019) MHD convection in a partially driven cavity with corner heating. *SN Appl Sci* 1–1689
5. Ganguly R, Sen S, Puri IK (2004) Thermomagnetic convection in a square enclosure using a line dipole. *Phys Fluids* 16(7):2228–2236
6. Szabo PSB, Früh W-G (2018) The transition from natural convection to thermomagnetic convection of a magnetic fluid in a non-uniform magnetic field. *J Magn Magn Mater* 447:116–123
7. Biswas N, Manna NK, Datta A, Mandal DK, Benim AC (2020) Role of aspiration to enhance MHD convection in protruded heater cavity. *Prog Comput Fluid Dyn* 20(6):363–378
8. Biswas N, Manna NK, Datta P, Mahapatra PS (2018) Analysis of heat transfer and pumping power for bottom-heated porous cavity saturated with Cu-water nanofluid. *Powder Technol* 326:356–369
9. Biswas N, Manna NK, Chamkha AJ (2021) Effects of half-sinusoidal nonuniform heating during MHD thermal convection in Cu–Al₂O₃/water hybrid nanofluid saturated with porous media. *J Therm Anal Calorim.* 143:1665–1688
10. Biswas N, Sarkar UK, Chamkha AJ, Manna NK (2021) Magneto-hydrodynamic thermal convection of Cu–Al₂O₃/water hybrid nanofluid saturated with porous media subjected to half-sinusoidal nonuniform heating. *J Therm Anal Calorim.* 143:1727–1753
11. Sarkar J, Ghosh P, Adil A (2015) A review on hybrid nanofluids: recent research, development and applications. *Renew Sustain Energy Rev* 43:164–177
12. Shenoy A, Sheremet M, Pop I (2016) Convective flow and heat transfer from wavy surfaces: viscous fluids, porous media and nanofluids. CRC Press, Taylor & Francis Group, New York
13. Dalal A, Das MK (2006) Natural convection in a cavity with a wavy wall heated from below and uniformly cooled from the top and both sides. *Int J Heat Mass Transf* 128:717–725
14. Lin Y-T, Cho C-C (2019) Analysis of energy flux vector on natural convection heat transfer in porous wavy-wall square cavity with partially-heated surface. *Energies* 12:4456
15. Alsabery AI, Tayebi T, Chamkha AJ, Hashim I (2020) Natural convection of Al₂O₃-water nanofluid in a non-Darcian wavy porous cavity under the local thermal non-equilibrium condition. *Sci Rep* 10:18048
16. Sheremet MA, Cimpean DS, Pop I (2017) Free convection in a partially heated wavy porous cavity filled with a nanofluid under the effects of Brownian diffusion and thermophoresis. *Appl Therm Eng* 113:413–418
17. Ahmed SE, Rashed ZZ (2019) MHD natural convection in a heat generating porous medium-filled wavy enclosures using Buongiorno's nanofluid model. *Case Stud Therm Eng* 14:100430

18. Ghasemi B, Aminossadati SM, Raisi A (2011) Magnetic field effect on natural convection in a nanofluid-filled square enclosure. *Int J Therm Sci* 50(9):1748–1756
19. Davies GDV (1983) Natural convection of air in a square cavity a bench mark numerical solution. *Int J Numer Meth Fluids* 3:249–264

Effect of Bottom Wall Curvature on Thermal Convection of Air/Nanofluid in a Differentially Heated Cavity Subjected to a Magnetic Field



Deep Chatterjee, Nirmalendu Biswas, Nirmal K. Manna,
and Dipak Kumar Mandal

Abstract Phenomena involving natural convection in a bottom heated and partially side cold cavity have been a subject of extensive study due to the various practical applications. This paper proposes and demonstrates a modification of the classical bottom heated and partially side cold cavity introducing a bottom wall curvature as a convex or concave shape. The attempt is made to find out how the heat transfer rate is affected by the heated bottom wall curvature. Only the bottom wall curvature is varied keeping other walls straight. The results are derived considering two separate working fluids: air and nanofluid (Al_2O_3 -water). A uniform field of magnetism is applied to influence the flow physics of the modified differentially heated cavity. The investigation is performed for the different Hartmann numbers ($\text{Ha} = 0-100$) and Rayleigh numbers ($\text{Ra} = 10^3-10^6$). The effect of the curvature is analyzed using the plots of streamlines, isotherms and the average Nusselt number (Nu) for both the cases of air and Al_2O_3 -water nanofluid. Some positive outcomes if obtained due to the change of bottom wall curvature, it would be very helpful for different practical applications by implementing a simple cost-effective modification.

Keywords Magnetohydrodynamics (MHD) · Curved wall · Nanofluid · Natural convection · Heat transfer

D. Chatterjee · N. K. Manna

Department of Mechanical Engineering, Jadavpur University, Kolkata 700032, India
e-mail: nirmalkmannaju@gmail.com

N. Biswas (✉)

Department of Power Engineering, Jadavpur University, Kolkata 700106, India
e-mail: biswas.nirmalendu@gmail.com

D. K. Mandal

Department of Mechanical Engineering, College of Engineering and Management, Kolaghat
721171, India
e-mail: dipkuma@yahoo.com

Nomenclature

B_0	Magnetic field, Tesla
g	Acceleration due to gravity (ms^{-2})
H	Height of the cavity, length scale (m)
Ha	Hartmann number
k	Thermal conductivity ($\text{Wm}^{-1} \text{K}^{-1}$)
L	Length of each side of the cavity (m)
Nu	Average Nusselt number
p	Pressure (Pa)
Pr	Prandtl number
Ra	Rayleigh number
T	Temperature (K)
U, V	Dimensionless velocity components
X, Y	Dimensionless coordinates

Greek Symbols

α	Thermal diffusivity (m^2s^{-1})
β	Thermal expansion coefficient of fluid (K^{-1})
θ	Dimensionless temperature
μ	Dynamic viscosity ($\text{kgm}^{-1} \text{s}^{-1}$)
ν	Kinematic viscosity (m^2s^{-1})
ρ	Density (kgm^{-3})
σ	Electrical conductivity (Sm^{-1})
χ	Nanoparticle volume fraction
ψ	Dimensionless streamfunction

Subscripts

c, h	Cold wall, hot wall
f	Base fluid

1 Introduction

Proper control of transport process under the buoyancy-driven convection is a major challenge to the manufacture/technology developer. Such buoyancy-driven

convection convective phenomena can be found in diverse fields of emerging engineering, electronic cooling and biomedical devices involving various coupled multiphysical scenarios. The transport process becomes more complex in the presence of magnetic fields. Convective flow under the impact of magnetic field is also known as magneto-hydrodynamics (MHD). Now a day, many applications involving thermal-magneto systems operate under different multiphysical situations like nanofluid/hybrid nanofluid, different thermal conditions, porous substances, etc. Application of MHD convective transport is growing at a faster rate in diverse field engineering as well as medical sciences [1–6].

By adjusting the strength and orientation of the magnetic fields, the convective transport process can be altered substantially during buoyancy-driven convection in a confined space. The control of any thermal-magneto system in the presence of the thermal gradient is rather complex phenomena. Researchers are devoting their attention for the development of the devices/systems maintaining its sophistication and miniaturization [7, 8]. However, such sophistication faces tremendous challenge for efficient cooling the thermal-magneto devices for ensuring safe operation temperature. In this context, recent development in the suspension of nano-sized solid particles in the host fluid (nanofluid and later hybrid nanofluid) shows a promising technique for enhanced heat transfer of any magneto-thermal devices/systems. Number of works on the usage of nanofluid/hybrid nanofluid can be found in the open literature [9–11]. Sarkar et al. [12] have conducted a detailed review on the nanofluid/hybrid nanofluid.

Apart from the usage of nanofluid/hybrid nanofluid, in the area of MHD convective flow several authors have taken initiative for enhancing the heat transfer characteristic. Thus, proposed several modifications to the geometry or part of the geometry of the cavity. Such modifications significantly alter the convective transport phenomena due to the change in near-wall phenomena. As the surface curvature changes, the interfacial surface area between the surface and the adjacent fluid layer modifies, which alters the heat transfer process. In this context, effects of surfaces waviness and its fundamental aspects on the heat transport process are well documented in book [13]. Considering different types of surface waviness like: curved, irregular, corrugated, sinusoidal, or other wavy surfaces along with other multiphysical scenario, a number of research work can be found in open literature [14, 15]. A discrete heating at the bottom and cooled through corrugated sidewalls of a porous cavity filled with nanofluid has been investigated by Alsabery et al. [16]. In this study, it is observed that the heat transfer rate is significantly alters by the number of undulation. Sheremet et al. [17] studied the natural convection of nanofluid flow through porous domain packed in a cavity with cold wavy wall at the left side and partial heating at the right sidewall. Ahmed and Rashed [18] investigated the MHD convective heat transfer of nanofluid flow through heat generating porous substances in a cavity with heated, wavy wall. They have analyzed the number and height of undulations and found an increasing trend of heat transfer as the number and height of the undulations increases.

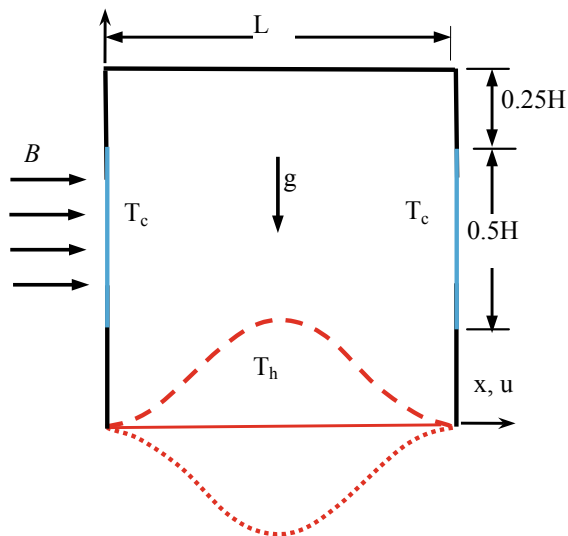
From the vast pool of available literature, it is found that the effect of heated curved-wall either convex or concave in the presence of externally applied magnetic

field on the heat transfer characteristics has not investigated adequately. The aim of present study is to propose and demonstrate a modification of the classical bottom heated and partially side cold cavity introducing a wall curvature as a convex or concave shape. The attempt is made to find out how the heat transfer rate is affected by the heated bottom wall curvature. The results are derived considering two separate working fluids: air and nanofluid (Al_2O_3 -water). A uniform field of magnetism is applied to influence the flow physics of the modified differentially heated cavity. The investigation is performed for the different Hartmann numbers ($\text{Ha} = 0\text{--}100$) and Rayleigh numbers ($\text{Ra} = 10^3\text{--}10^6$). The effect of the curvature is analyzed using the plots of streamlines, isotherms and the average Nusselt number (Nu) for both the cases of air and Al_2O_3 -water nanofluid. The study is conducted numerically using Galerkin finite element methodology.

2 Problem Formulation

A two-dimensional bottom heated square cavity ($L \times H$) under the effect of a uniformly applied magnetic field has been taken, as shown in Fig. 1. The cavity is kept horizontal at all times; the effect of change in base curvature for three cases: flat surface, concave and convex surface in the form $\cos(2\pi Nx)$ has been taken. The bottom wall isothermally heated (at temperature T_h). Two symmetrically placed isothermally cold sidewalls act as heat sink (at temperature T_c , where $T_h > T_c$) length of cold sidewalls is half the height of the cavity and placed at the middle. The upper wall and the remaining portions of the left and right sidewalls are insulated. A uniform field of magnetism (of intensity B) is applied to influence the flow physics of

Fig. 1 Schematic of the problem geometry along with coordinate system and boundary conditions



the modified differentially heated cavity. Two separate working fluids: air ($Pr = 0.71$) and nanofluid (Al_2O_3 -water) (with $Pr = 6.93$) with the nanoparticle concentration $\varphi = 0.01$. For the analysis, the fluid flow assumed to be laminar, incompressible, Newtonian. While formulating the governing equations, density variations have been considered only in the buoyancy term through the use of Boussinesq approximation. Also, effects like Joule’s heating and displacement current have been ignored. The non-dimensional governing equations in the Cartesian coordinate system are mentioned below:

For air:

$$\frac{\partial U}{\partial X} + \frac{\partial V}{\partial Y} = 0 \tag{1}$$

$$U \frac{\partial U}{\partial X} + V \frac{\partial U}{\partial Y} = -\frac{\partial P}{\partial X} + Pr \left(\frac{\partial^2 U}{\partial X^2} + \frac{\partial^2 U}{\partial Y^2} \right) \tag{2}$$

$$U \frac{\partial V}{\partial X} + V \frac{\partial V}{\partial Y} = -\frac{\partial P}{\partial Y} + Pr \left(\frac{\partial^2 V}{\partial X^2} + \frac{\partial^2 V}{\partial Y^2} \right) - \sigma Ha^2 V + Ra Pr \theta \tag{3}$$

$$U \frac{\partial \theta}{\partial X} + V \frac{\partial \theta}{\partial Y} = \left(\frac{\partial^2 \theta}{\partial X^2} + \frac{\partial^2 \theta}{\partial Y^2} \right) \tag{4}$$

The non-dimensional governing equations have been constructed from the following scale factors: $(X, Y) = (x, y)/H$; $(U, V) = (u, v)H/\alpha$; $\theta = (T - T_c)/(T_h - T_c)$; $P = (p - p_a)H^2/\rho\alpha^2$.

For Cu-water nanofluid:

$$\frac{\partial U}{\partial X} + \frac{\partial V}{\partial Y} = 0 \tag{5}$$

$$U \frac{\partial U}{\partial X} + V \frac{\partial U}{\partial Y} = -\frac{\rho_f}{\rho_{nf}} \frac{\partial P}{\partial X} + \frac{\nu_{nf}}{\nu_f} Pr \left(\frac{\partial^2 U}{\partial X^2} + \frac{\partial^2 U}{\partial Y^2} \right) \tag{6}$$

$$U \frac{\partial V}{\partial X} + V \frac{\partial V}{\partial Y} = -\frac{\rho_f}{\rho_{nf}} \frac{\partial P}{\partial Y} + \frac{\nu_{nf}}{\nu_f} Pr \left(\frac{\partial^2 V}{\partial X^2} + \frac{\partial^2 V}{\partial Y^2} \right) - \frac{\rho_f}{\rho_{nf}} \frac{\sigma_{nf}}{\sigma_f} Ha^2 V + \frac{(\rho\beta)_{nf}}{\rho_{nf}\beta_f} Ra Pr \theta \tag{7}$$

$$U \frac{\partial \theta}{\partial X} + V \frac{\partial \theta}{\partial Y} = \frac{\alpha_{nf}}{\alpha_f} \left(\frac{\partial^2 \theta}{\partial X^2} + \frac{\partial^2 \theta}{\partial Y^2} \right) \tag{8}$$

The non-dimensional governing equations have been constructed from the following scale factors: $(X, Y) = (x, y)/H$; $(U, V) = (u, v)H/\alpha_f$; $\theta = (T - T_c)/(T_h - T_c)$; $P = (p - p_a)H^2/\rho_{nf}\alpha_f^2$ where (U, V) are dimensionless

velocities, (X, Y) are non-dimensional coordinates, P is the non-dimensional pressure P , respectively. However, dimensionless numbers Pr, Ra and Ha are Rayleigh number (Ra), Prandtl number (Pr), and Hartmann number (Ha), which are defined as

$$\text{Pr} = \frac{\nu_f}{\alpha_f}; \text{Ra} = \frac{g\beta_f(T_h - T_c)H^3}{\nu_f\alpha_f}; \text{Ha} = \frac{BH}{\sqrt{\nu_f\rho_f/\sigma_f}} \quad (9)$$

The fluid properties (α , ν , and β) are assumed to be constant except density (ρ) variation, which is taken care by the Boussinesq approximation. The bottom wall of the cavity is heated isothermally ($\theta = 1$), left sidewall having length $0.5H$ is cooled isothermally ($\theta = 0$). All the walls are set at zero velocity ($U = V = 0$). Top wall and part of the sidewalls are taken as adiabatic ($\partial\theta/\partial X = \partial\theta/\partial Y = 0$). The thermophysical properties of Al_2O_3 nanoparticles (effective density ρ_{nf} , specific heat capacity $(c_p)_{\text{nf}}$, thermal expansion coefficient β_{nf}) are taken by adopting the property relations from the standard literature [9–11]. The volumetric concentration of nanoparticles is taken as φ .

The dimensionless governing Eqs. (1)–(8) are solved numerically applying appropriate boundary conditions following the Galerkin weighted finite element methodology (FEM). The solutions are carried out in an iterative process, with successive minimization of residuals of the mass, momentum, and temperature equations to a set value $<10^{-8}$. For the present study, 160×160 grids distributed non-uniformly are chosen. This grid has been selected after conducting grid independence study. Before conducting the extensive simulation of the present study, validation study has been carried out using the present solver by simulating the different problems available in the open literature [19, 20]. All the validation study shows good agreement between the present simulated results and published results.

In order to analyze the heat transfer characteristics for the bottom heated inclined square enclosure, the average Nusselt number is calculated on the hot wall as

$$\text{Nu} = \frac{k_{\text{nf}}}{k_f} \int_0^1 \left(-\frac{\partial\theta}{\partial Y} \Big|_{Y=0} \right) dX \quad (10)$$

3 Results and Discussion

This present work proposes and demonstrates a modification of the classical bottom heated and partially side cold cavity introducing a bottom wall curvature as a convex or concave shape. The bottom wall curvature is varied keeping other walls straight. The results are derived considering two separate working fluids: air and nanofluid (Al_2O_3 –water). A uniform field of magnetism is applied to influence the flow physics of the modified differentially heated cavity. The investigation is performed for the

different Hartmann numbers ($Ha = 0-100$) and Rayleigh numbers ($Ra = 10^3-10^6$). The effect of the curvature is analyzed using the plots of streamlines, isotherms and the average Nusselt number (Nu) for both the cases of air and Al_2O_3 -water nanofluid.

3.1 Effect of Rayleigh Number (Ra)

In this section, the effects of varying $Ra (= 10^3, 10^4 \text{ and } 10^5)$ on the local distribution of streamlines and isotherms are illustrated in Figs. 2, 3, 4 and 5 keeping $Ha = 20$ fixed for Air and Al_2O_3 -water nanofluid, respectively. Due to the heating from the bottom and partial cooling at the side walls, two symmetrical flow circulations are observed, with opposite circulations (can be inferred from the positive and negative values of the stream function for the two zones). With an increase in Rayleigh number or the

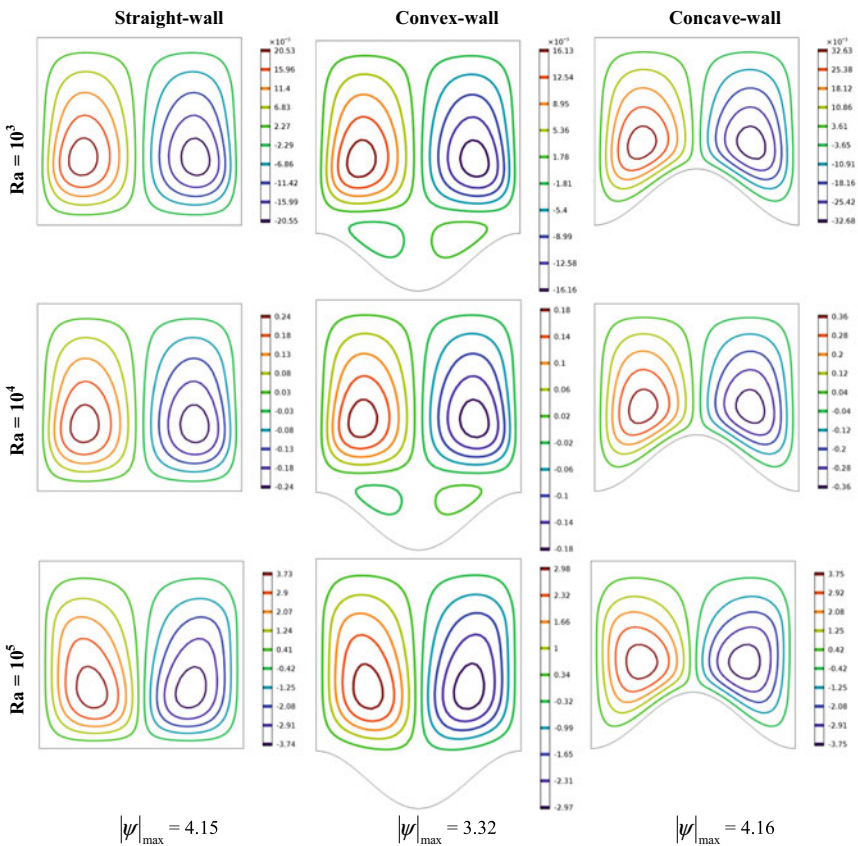


Fig. 2 Impact of wall curvature on the streamlines varying Ra and fixed $Ha = 30$ with working fluid as air

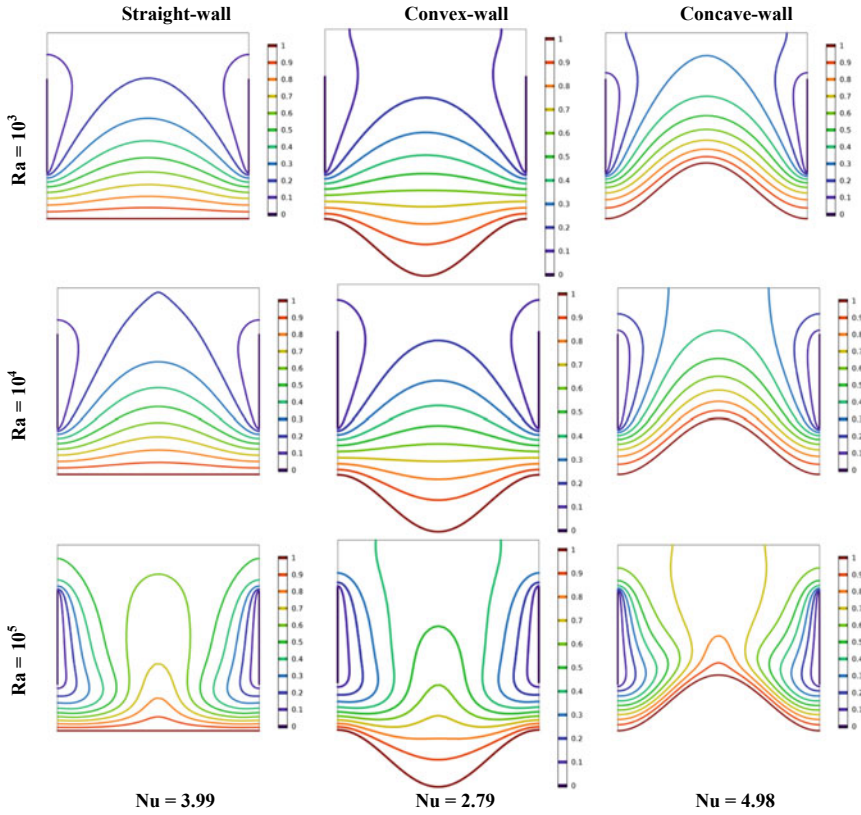


Fig. 3 Effect of Ra and wall curvature on the streamlines for $Ha = 30$ with working fluid as air

buoyant forces, the core of the two circulation cells are seen to orient themselves away from each other-towards the cold walls, although the spacing between streamlines remains the same (the change is more apparent from $Ra = 10^4$ to 10^5). For the convex cavity, as the Rayleigh number increases from 10^4 to 10^5 , the vortices near the bottom wall disappear. The flow separation which led to the formation of eddies is thus not present as the strength of flow increases when the Rayleigh number reaches an appreciable value. Also, comparing the maximum values of stream function, the concave cavity shows the highest value; the magnitude being the least when the cavity is convex. The convex cavity, having maximum fluid volume and the concave cavity where the fluid volume is least: both these cases have the same heating length. Hence, a stronger flow is observed when the cavity is concave. The straight-walled cavity has the least heating length and an intermediate fluid volume and thus presents an intermediate value of maximum stream function accordingly.

The isotherm contours as depicted in Fig. 3 show that the fluid flow at high temperature is confined near the bottom hot wall for low values of Rayleigh number. With increasing value of Rayleigh number, the isotherm lines shift in a way that the

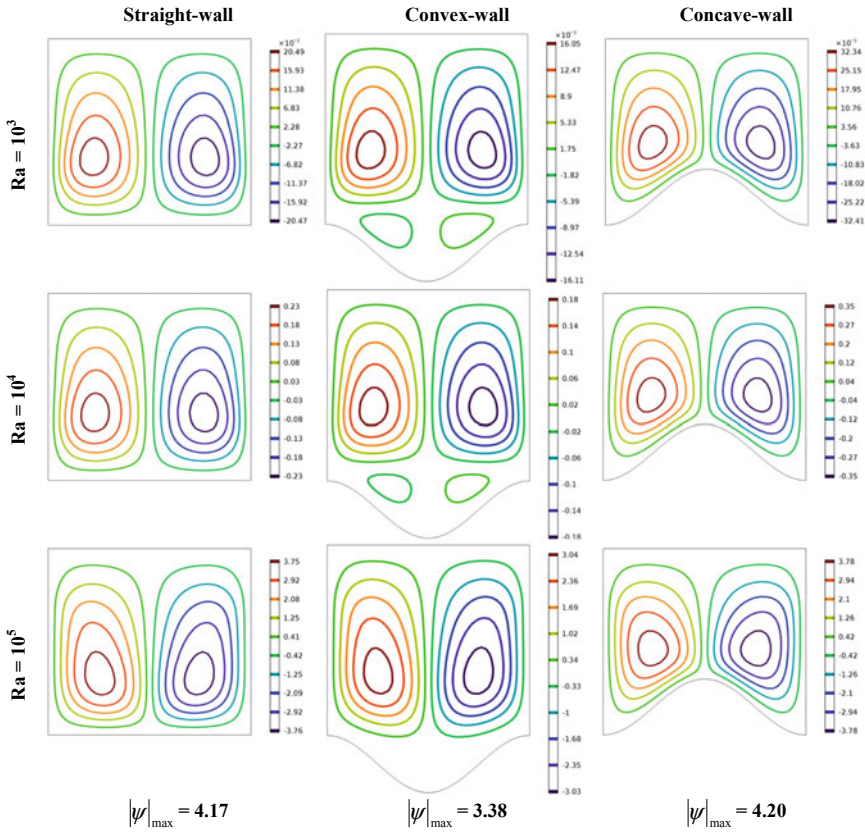


Fig. 4 Effect of Ra and wall curvature on the streamlines for $Ha = 30$ with working fluid as nanofluid

lines of constant temperature near the bottom hot wall starts spreading out towards the cold top wall near the middle of the cavity, which indicates a higher degree of mixing of the hot and cold fluid zones. Also, the isotherm lines become increasingly separated into two symmetrical zones near the sidewalls—this effect is especially prominent from $Ra = 10^4$ to 10^5 . At 10^5 , it is observed that the cold fluid near the cold sidewalls is completely surrounded by warmer fluid as the buoyant forces become predominant. The average Nusselt number increases with increasing Ra values—due to higher buoyant forces and hence a higher degree of mixing—as discussed before. Again, the concave cavity shows the highest value of average Nusselt number, and hence a higher heat transfer rate through convection; while the convex cavity shows the least values.

As shown, in Fig. 4, the streamline contours for the nanofluid show a similar pattern to air. With increasing values of Rayleigh number, the two principal streamline patterns orient away from one another. Also, the concave bottomed cavity shows the maximum velocity and thus strongest fluid flow—similar to what was found in case

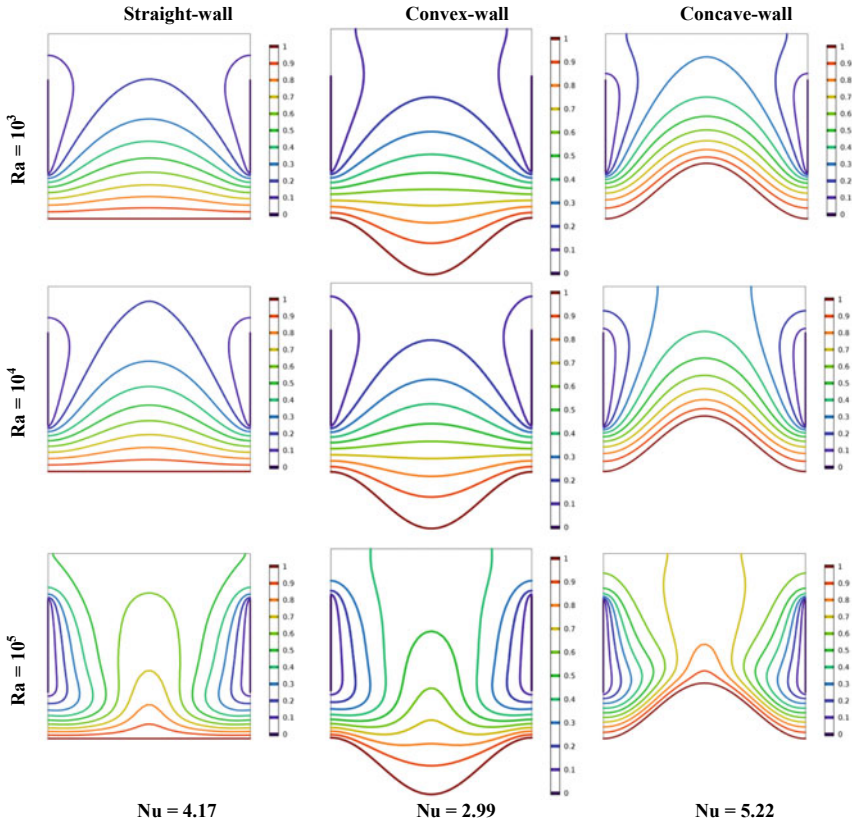


Fig. 5 Effect of Ra and wall curvature on the isotherms for $Ha = 30$ with working fluid as nanofluid

of air. The stream function values for the nanofluid, however, are slightly greater than when air was used as the fluid medium at $Ha = 30$ (observed for the case of $Ra = 10^5$), even though the opposing Lorentz forces are higher for the nanofluid. This is due to a higher coefficient of thermal expansion for the nanofluid than air which leads to a greater flow strength.

The isotherm plots shown in Fig. 5 depict an increased value of Nusselt number and hence convective heat transfer at higher values of Rayleigh number. Also, for a fixed value for Rayleigh number, the concave cavity has the highest value of average Nu number. The isotherm plots also show that as the Rayleigh number increases for a given cavity shape, the temperature distribution throughout the cavity improves, while the isotherm lines become more separated into two symmetrical domains and concentrated near the two sidewalls. The Nu values obtained are slightly higher than the corresponding values for air as the fluid material—which again, can be explained by a higher coefficient of thermal expansion for the nanofluid.

3.2 Effect of Hartmann Number (Ha)

Figures 6, 7, 8 and 9 illustrate the effects of varying Ha ($= 0, 50$ and 70) on the local distribution of streamlines and isotherms keeping $Ra = 10^5$ fixed for Air and Al_2O_3 -water nanofluid, respectively. The variation of streamline profiles with increasing values of Ha at a fixed value of Ra shows that the streamline patterns flowing in the clockwise and counter-clockwise directions diverge gradually and the spacing between streamlines increases in regions away from the heated wall. Correspondingly, the maximum value of stream function decreases as the Ha value increases which is expected due to increased values of opposing Lorentz forces. Also, for the case of convex cavity, the additional secondary vortices generated near the heated bottom wall become more prominent as the circulation decreases with increasing Ha values. The values of maximum stream function are generally highest for the concave cavity (where the fluid volume is least), except when $Ha = 0$ (no external magnetic

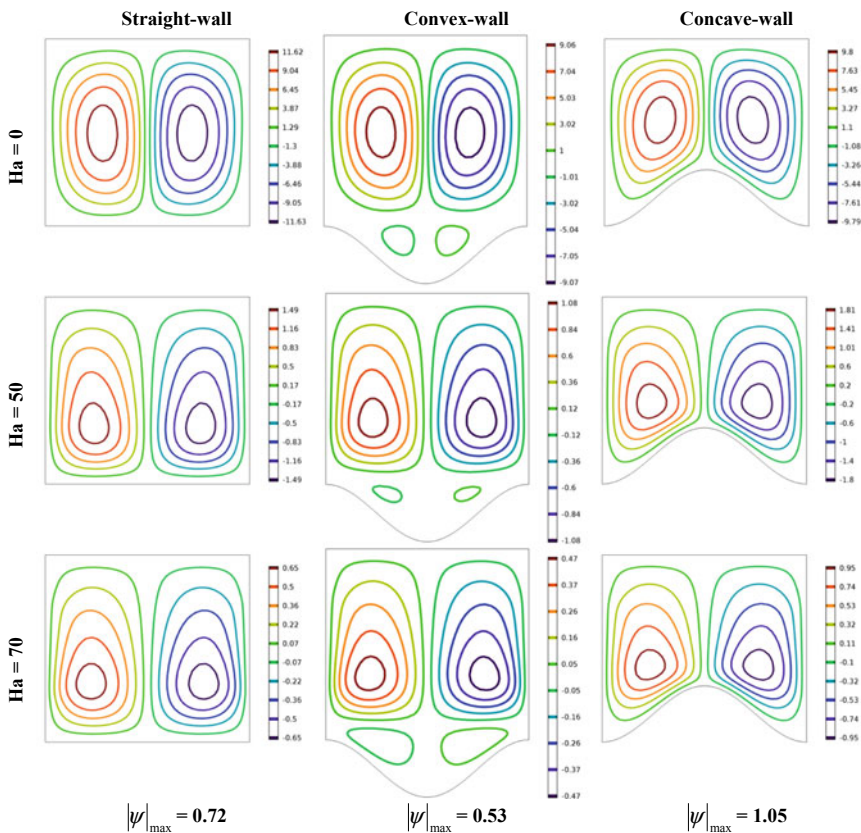


Fig. 6 Effect of Ha and wall curvature on the streamlines for $Ra = 10^5$ with working fluid as air

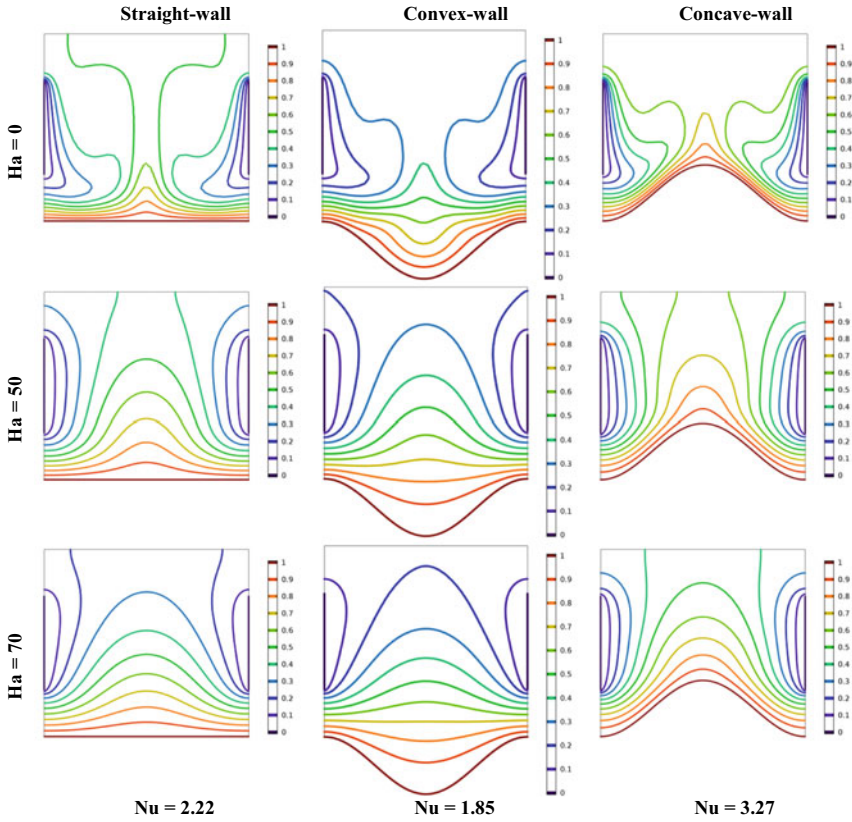


Fig. 7 Effect of Ha and wall curvature on the isotherms for $Ra = 10^5$ with working fluid as air

field) for which the square cavity exhibits the highest value of average velocity in departure with the general trend.

The isotherm profiles in Fig. 7 reveal that as the Hartmann number increases keeping the value of Rayleigh number fixed ($Ra = 10^5$), the isotherm lines which initially indicated an appreciable temperature distribution and a prominent separation of heat transfer regime into two symmetrically placed zones (at $Ha = 0$) gradually becomes more concentrated near the bottom wall of the cavity and less dense near the two cold sidewall regions indicating that the temperature distribution grows weaker and thus the heat transfer rate via convection decreases. This is also reflected in the decreasing values of Nu with increasing Ha values. The streamline profile of Fig. 6 showed that the average flow velocity for the concave profile is less than that for the square cavity when $Ha = 0$. The Nu values however indicate that the concave cavity enjoys the maximum value of Nu for all value of Ha at $Ra = 10^5$.

The streamline profiles in Fig. 8 show Al_2O_3 -water as the working fluid. When compared to air, the maximum stream function values are lower, due to the higher density of the nanofluid and also due to the higher values of opposing Lorentz forces

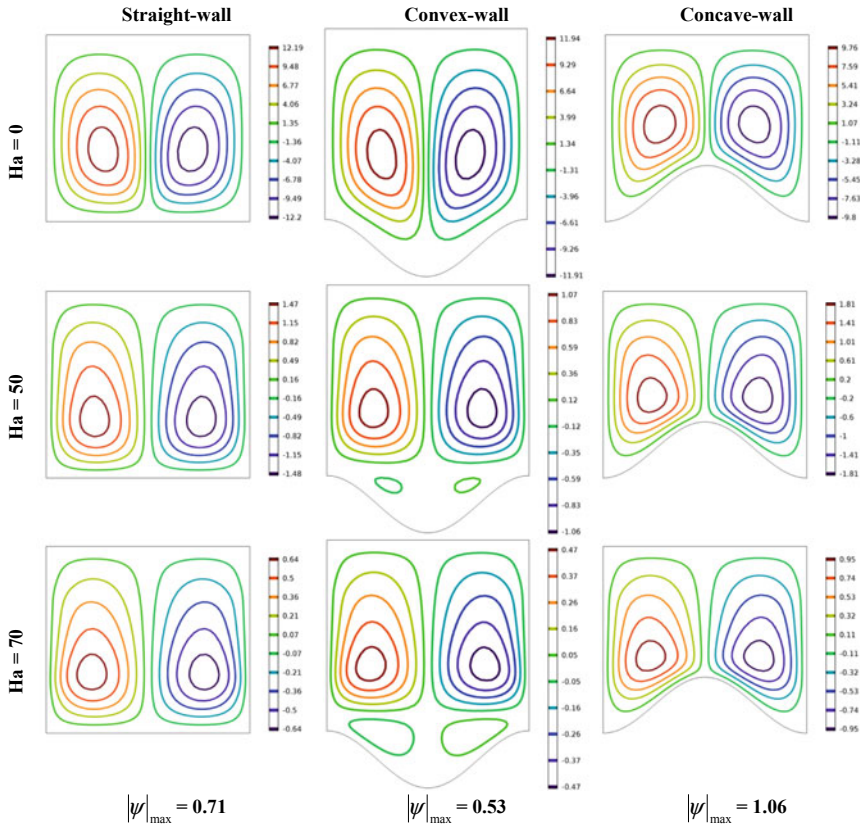


Fig. 8 Effect of Ha and wall curvature on the streamlines for $Ra = 10^5$ with working fluid as nanofluid

acting on it (for nonzero Ha). As was for air, here also, the two opposing flows seem to diverge near the middle of the cavity, accompanied by a reduced overall flow strength (indicated by the decreasing values of stream function), as the Ha value increases.

From Fig. 9, we find that the Nu values are higher for Al_2O_3 -water nanofluid compared to air (Fig. 7). It is due to the higher thermal conductivity of the nanofluid over air that even though the average flow velocity is lower than air, the modeling shows an improved heat transfer rate by convection.

3.3 Heat Transfer Characteristics

Figure 10a, b shows a comparative plot of average Nu values versus Ra number as the Hartmann number is kept fixed ($Ha = 20$). In the initial smaller ranges of Ra

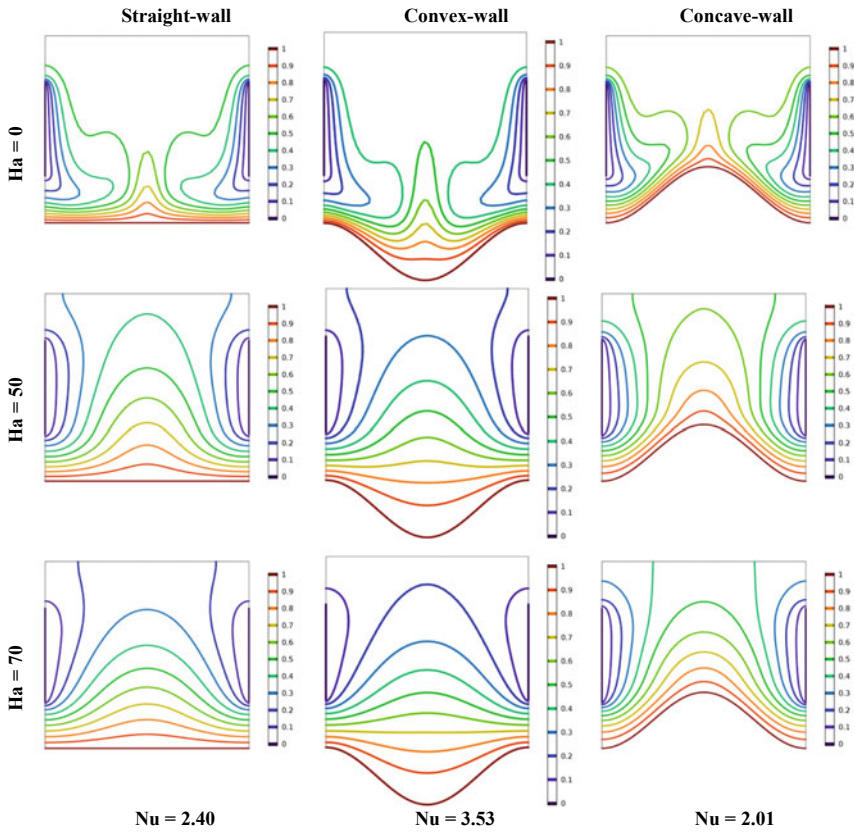


Fig. 9 Effect of Ha and wall curvature on the isotherms for $Ra = 10^5$ with working fluid as nanofluid

value ($\sim 10^3$), the Nu values show little increase, but an appreciable increases in Nu value are observed as the Rayleigh number further increases.

The plots (Fig. 10c, d) show variation of average Nusselt number versus Hartmann number for air and Al_2O_3 -water nanofluid at $Ra = 10^4$. The Nusselt number value, a measure of convective heat transfer decreases as the Ha increases and reaches a nearly stable value when the Ha value increases beyond 30. Further increase in Hartmann number (i.e., externally applied magnetic field) produces little change in the Nu values.

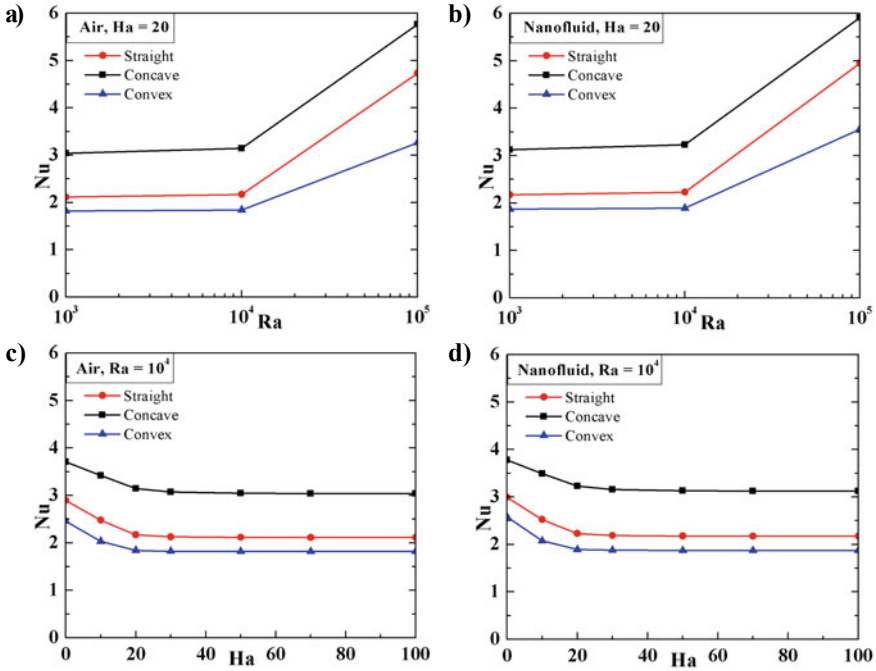


Fig. 10 Heat transfer characteristics for varying Ra considering working fluid as: **a** Air, and **b** Al₂O₃ nanofluid, for varying Ha considering working fluid as: **c** Air, and **d** Al₂O₃ nanofluid

4 Conclusion

The present investigation proposes and demonstrates a modification of the classical differentially heated cavity introducing a bottom wall curvature as a convex or concave shape. The bottom wall curvature is varied keeping other walls straight. The results are derived considering two separate working fluids: air and nanofluid (Al₂O₃–water). A uniform field of magnetism is applied to influence the flow physics of the modified differentially heated cavity. The effect of the curvature is analyzed using the plots of streamlines, isotherms and the average Nusselt number (Nu) for both the cases of air and Al₂O₃–water nanofluid.

From the effect of variation of Rayleigh number at a fixed Ha value, it was observed that as the Rayleigh number increases, so does the corresponding heat transfer rate and flow velocity. In this regard, the concave cavity was found to present the maximum value of Nu and hence the highest heat transfer rate through convection. The convex shape of the bottom wall was found to be least effective for the same as it holds more fluid but has a heating length equal to the concave cavity. Further, for this study, the buoyant forces were found to be particularly predominant at Ra = 10⁵, where a significant change in flow pattern and improvement in Nusselt number was

observed. The Al_2O_3 –water nanofluid was found to have an improved heat transfer rate via convection than air, even though the fluid velocity was lower for the nanofluid.

The study of the effect of Hartmann number for $\text{Ra} = 10^5$ depicted that the opposing Lorentz forces gradually increase and correspondingly the heat transfer rate deteriorates as the Ha was raised. The concave cavity was again found to be most effective for heat transfer; and a comparison between air and the nanofluid also depicted the increased heat transfer rates in the nanofluid for similar conditions.

The plots drawn to compare Nusselt number versus Rayleigh number showed a linear increase; with the rate of increases of Nu value significantly improving at higher ranges of Rayleigh number (Ha was kept fixed at 20). The plot depicting variation of Nu with Ha for $\text{Ra} = 10^4$ showed an initial decrease in Nu followed by a stable value of Nu after a certain value of Ha was reached. In both these plots, it was further observed that the concave cavity shows the greatest value of Nu , followed by the square cavity and the heat transfer rate is lowest for the convex bottomed cavity—which is in keeping with the results obtained in the previous sections.

References

1. Shercliff JA (1965) A textbook of magnetohydrodynamics. Pergamon Press, Oxford
2. Davidson PA (2001) An introduction to magnetohydrodynamics. In: Cambridge texts in applied mathematics. Cambridge University Press, Cambridge
3. Ozoe H (2005) Magnetic convection. Imperial College Press, Singapore
4. Puri IK, Ganguly R (2014) Particle transport in therapeutic magnetic fields. *Annu Rev Fluid Mech* 46:407–440
5. Mondal MK, Biswas N, Manna NK (2019) MHD convection in a partially driven cavity with corner heating. *SN Appl Sci* 1–1689
6. Ganguly R, Sen S, Puri IK (2004) Thermomagnetic convection in a square enclosure using a line dipole. *Phys Fluids* 16(7):2228–2236
7. Biswas N, Manna NK, Datta A, Mandal DK, Benim AC (2020) Role of aspiration to enhance MHD convection in protruded heater cavity. *Prog Comput Fluid Dyn* 20(6):363–378
8. Szabo PSB, Früh W-G (2018) The transition from natural convection to thermomagnetic convection of a magnetic fluid in a non-uniform magnetic field. *J Magn Magn Mater* 447:116–123
9. Biswas N, Manna NK, Datta P, Mahapatra PS (2018) Analysis of heat transfer and pumping power for bottom-heated porous cavity saturated with Cu-water nanofluid. *Powder Technol* 326:356–369
10. Biswas N, Manna NK, Chamkha AJ (2021) Effects of half-sinusoidal nonuniform heating during MHD thermal convection in Cu– Al_2O_3 /water hybrid nanofluid saturated with porous media. *J Therm Anal Calorim.* 143:1665–1688
11. Biswas N, Sarkar UK, Chamkha AJ, Manna NK (2020) Magneto-hydrodynamic thermal convection of Cu– Al_2O_3 /water hybrid nanofluid saturated with porous media subjected to half-sinusoidal nonuniform heating. *J Therm Anal Calorim.* 143:1727–1753
12. Sarkar J, Ghosh P, Adil A (2015) A review on hybrid nanofluids: recent research, development and applications. *Renew Sustain Energy Rev* 43:164–177
13. Shenoy A, Sheremet M, Pop I (2016) Convective flow and heat transfer from wavy surfaces: viscous fluids, porous media and nanofluids. CRC Press, Taylor & Francis Group, New York
14. Dalal A, Das MK (2006) Natural convection in a cavity with a wavy wall heated from below and uniformly cooled from the top and both sides. *Int J Heat Mass Transf* 128:717–725

15. Lin Y-T, Cho C-C (2019) Analysis of energy flux vector on natural convection heat transfer in porous wavy-wall square cavity with partially-heated surface. *Energies* 12:4456
16. Alsabery AI, Tayebi T, Chamkha AJ, Hashim I (2020) Natural convection of Al_2O_3 -water nanofluid in a non-Darcian wavy porous cavity under the local thermal non-equilibrium condition. *Sci Rep* 10:18048
17. Sheremet MA, Cimpean DS, Pop I (2017) Free convection in a partially heated wavy porous cavity filled with a nanofluid under the effects of Brownian diffusion and thermophoresis. *Appl Therm Eng* 113:413–418
18. Ahmed SE, Rashed ZZ (2019) MHD natural convection in a heat generating porous medium-filled wavy enclosures using Buongiorno's nanofluid model. *Case Stud Therm Eng* 14:100430
19. Davies GDV (1983) Natural convection of air in a square cavity a bench mark numerical solution. *Int J Numer Meth Fluids* 3:249–264
20. Ghasemi B, Aminossadati SM, Raisi A (2011) Magnetic field effect on natural convection in a nanofluid-filled square enclosure. *Int J Therm Sci* 50(9):1748–1756

Climatic Parameter Analysis on Building Materials for Kolkata, Eastern Zone of India



Krushna Gouda and Biplab Das

Abstract Advanced building materials have significant contribution for developing better construction and retrofitting of present buildings, and this can be possible by understanding the various building performance parameters through proper planning and design. However, today's unpredicted climatic variation has a major role for the selection of building materials for construction of house and buildings all over the world. Keeping these on mind, the current investigation is focused on the influence of climatic condition on the existing and advanced buildings materials. The climatic zone of Kolkata as a major city from eastern zone of Indian subcontinent is selected. The overall year's performance on different building materials, considering these materials for wall as well as roof of a building. The objectives will focus on the influence of the conventional materials, advanced alternative building materials and bio-based insulating materials. This will be helpful in developing thermal comfort building and an energy-efficient occupation. Apart from these, the role of overall heat transfer coefficient will definitely be helpful for the designers to develop a building. The effect of various wall and roof configurations on thermal load is studied according to all-weather conditions. The investigation exhibited that addition of bio-based insulation increased the time lag value up to 10.97 h and thermal transmittance value around 0.665 W/m² K.

Keywords Building materials · Climate comfort · Weather conditions · Bio-based insulating materials

K. Gouda (✉) · B. Das

School of Aeronautical Sciences, Hindustan Institute of Science and Technology, Chennai,
Tamil Nadu, India
e-mail: krushna.gouda1991@gmail.com

B. Das

Mechanical Engineering Department, NIT Silchar, Silchar, Assam, India
e-mail: bpd@mech.nits.ac.in

1 Introduction

In today's scenario, the purpose of a building is not only for the purpose of shelter, security but also to provide thermal comfort for a healthy living environment. The building is composed of different materials as a boundary that separates from the outer environment for a suitable comfort zone. The building boundary is mainly responsible for maintain the thermal comfort according to the external climate. The proper balance of thermal comfort in a building becomes a major demand that is increasing day by day due to varied environmental temperature. The building boundary materials have taken as a solution to regulate according to the external thermal behavior [1].

The increasing demand of the thermal comfort requirement is directly linked to the energy consumption rate in a building. So, building boundary construction plays a substantial role to control the energy depletion in a modern building. The building construction materials selection according to the climatic zone is concentrated for regulating the inner thermal comfort. The standard construction materials usually have sufficient necessary structural and durability performance. So, addition of insulation or phase change material in-between the standard building materials will be favorable option to regulate the indoor thermal environment of a building. Thermal insulation is a material property which help to minimize heat transfer in it. Insulation material addition to a building acts as significant construction layer to obtain thermal comfort for the occupants at different climatic conditions. Country like India has composite climate consisting of cold winter and hot summer. Attaching insulation with conventional wall or roof will help to minimize heat loss and gain through it. This will partially contribute in the energy saving and reduce the energy consumption in the cooling and heating devices. A suitable thermal insulation for the wall or roof will not only save the air conditioning or room heater system size but also significantly it will save the overall life span of the building energy consumption. In addition, this also helps to support in maintaining the comfort of the room without depending upon any additional device, especially during the inter-seasonal climate periods [2].

In-depth understanding of building material with suitable insulating and phase change material will support in saving energy consumption, resulting in reducing the electrical and gas bills. Also, the CO₂ emission rate from various energy generation sources will be minimized and leading to protect the environment pollution. There exist various types of thermal insulation materials for providing as an additional layer on the roof or walls, and this is also possible to retrofitting the existing building structures. From the previous study, this is revealed that sixty percentage of heat transfer in building happens through the roof [3]. Hence, insulating the roof is much important than the walls of a building to prevent temperature in-out during the day and night. The overall heat transfer coefficient (*U*-factor) for non-insulating roof varies in the range of 7.76–18.18 W/m² K, 7.76 W/m² K as the roof thickness from 25 to 10 cm for the concrete building material [4].

The heat transfer rate with a non-insulated building is higher than an insulated building. So, in order to cut the energy consumption rate retrofitting in the existing buildings is a suitable option. To improve the thermal management, proper understanding of the climatic behavior effect on the building material is essential. Also, the insulation material and its thickness can be decided based on the composite climate of Kolkata. To a certain extent the phase change materials and volume of phase change material will support to be incorporated in the development of thermal management in a building. The hybrid building material management system is much beneficial to regulate the thermal management of a system. However, the amount energy saving will depend upon various factors such as types of building, external weather condition, place of building location, wall or roof thickness of the building, and construction materials used in the building. For the building materials, amount of heat transfer that takes place in it will determine the thermal management and its response according to various weather conditions.

In general, building materials depend upon various properties such as density, porosity, thermal conductivity, and moisture content. Keeping a focus on the insulating materials for a building, different insulating materials that are used mostly to reduce heat loss. Materials like natural fibers, vermiculite, rock wool, glass fiber, polystyrene, urethane foam. Based on the temperature, these are classified as low-temperature insulating material and high-temperature insulating material. Insulating materials such as expanded polystyrene (EPS), polyurethane foam (PUF), glass wool and expanded polyethylene come under low-temperature insulating materials. Similarly, insulating materials like silica cloth, vermiculite fiber glass, ceramic wool, Teflon sheet, rock wool and perlite concrete are categorized under high-temperature insulating materials. Insulation materials that are selected for building insulation should have low thermal conductivity and have an ability to prevent heat transfer through the building wall and roof. As per the thermal response, the optimal building environment comfort for number of occupants in a building is determined for attaching suitable heating and cooling device [5].

The effectiveness of an insulating materials is generally determined by its resistance value (R -value). However, this value needs to be taken into consideration as this value varies according to the quality of building construction and local environment parameters. As the R -value for the insulation material increases, this helps to reduce a good amount energy depletion for the space heating and cooling in building in all-weather conditions. The effect on insulation material is high during the extreme cold and hot weather condition to prevent temperature flow from in-out or vice versa [6]. The time lag (T) and decrement factors (DF) are the thermo-physical properties to evaluate the heat-storing capacity of a material. The time lag or phase lag of a material helps to determine the time taken by a material to propagate heat waves from external surface to internal surface or in reverse. The process of diminishing ratio of its amplitude during this process is called as decrement factor. The characteristics of the thermo-physical properties, overall heat transfer coefficient (U -value), material thickness for different phase lags and DF can be achieved. So, evaluating these parameters computationally for different hybrid composite materials will be beneficial for developing a suitable thermal comfort building [7, 8].

The literature study makes a clear understanding about the thermal comfort of building factors that are influenced by time lag (T), DF, which regulate the heat transfer rate of building enclose. However, apart from this, there are various other factors that influence the heat transfer among the external and internal environment of building and thermal mass location [9]. The thermal enclose of the building regulate the heat absorption and heat transfer, high thermal mass material have more potential to store heat energy. When open to external climate condition, heat source also discharges the stored heat continuously when the heat supply is detached [10]. Balaji et al. examined the thermal response of building walls made from conventional and alternative materials. Evaluated the effect of time lag, DF, inner and outer thermal load, effect of thermal conductivity on material thickness [11]. Mohammad and Shea investigated the thermal performance in a modern building in semi-arid continental climate Tehran. The significance of building enclose for energy saving potential because of energy-efficient building materials [12].

Barrios et al. evaluated the thermal properties to understand the thermal behavior of building wall and roofs without air condition. Computational stimulation over a periodic heat transfer at five different configurations was performed. The result exhibited that heat energy transferred through the walls and roofs during day time, DF, discomfort duration, hot and cold thermal performance index [13]. Shaik and Setty determined the influence of material behavior and thickness of building material on different thermal parameters.

Analysis was performed to examine the optimum building thickness, thermal conductivity effect on wall decrement factor, surface factors of homogeneous and composite walls [14]. Ng et al. determined experimentally the thermal inertia, transient thermal performance and wall temperature of aerated building materials. The internal and external surface temperature, T , DF are calculated from the wall temperature, and finite difference method was used to determine the results. The average surface temperature difference between the experimentation and computational results is 1.4–2.4% [15].

Ozel evaluated the thermal response of building walls and optimized the insulation thickness of different building materials. The investigation exhibited that optimum thickness changes from 2 to 8.2 cm as per the climatic condition of Elazig, Turkey [16]. Keeping all things in mind in the present work cement stabilized soil blocks (CSSB), insulation materials for a building, computational analysis of hybrid composite materials R -value, U -value, T , DF, thickness of material are evaluated over a span of complete year for Kolkata, India. Objectives of the present study are to determine the thermal behavior of the conventional and alternative building enclose materials, by using the experimentally calculated thermo-physical properties of different building materials. Also, to evaluate and compare the conventional, cement stabilized soil blocks (CSSB), developed bio-based insulation materials for a building wall, by using computational analysis of hybrid composite materials R -value, U -value, time lag, decrement factor for various building materials that are sustainable at different weather conditions of Kolkata, India.

2 Building Materials and Methods

The thermal properties of the different insulating materials are experimentally determined density, thermal conductivity and specific heat capacity from the previous works of Gouda et al. [17]. An thermal insulating polymer developed from 12.5 wt.% of natural bamboo filler and thermoset epoxy matrix. To achieve better bonding between the natural filler and epoxy thermosetting polymer chemical treatment of natural filler was carried out [18]. The developed neat epoxy polymer GB12.5 as an insulating polymer material for surface coating of the building enclose, which have a good potential to prevent from the corrosion resistance in the moisture weather condition. Various other alternative materials such as CSSB, fly ash brick, auto-claved aerated concrete block (AACB), table molded brick (TMB). The conventional building materials such as Jaipur brick, Bangalore brick, Challakere brick, cellular concrete brick, dense concrete plaster and cement plaster are experimentally determined and conventional materials as per Indian standards (IS 3792-1978) for validation propose used in the present study [19, 20].

The insulating, conventional and alternative buildings materials are studied for understanding its response toward the weather condition of Kolkata, India. The thermal behavior of the building and roof walls and composite insulated walls is investigated for examining the study and dynamic response to the weather conditions. There are various methods available to evaluate the steady and dynamic thermal behavior of the building enclose. The current study is focused on evaluating the material properties using Java code-based software, and the results are compared with numerical and analytical method. These methods are constrained to simplified problems and approximate problems. Obtaining precise numerical solutions in a limited time interval is difficult. The present study is adopted to in overcome the limitations of numerical and analytical methods. In the analytical methods parameters that are collected from the harmonic interpretation adopted to unsteady heat equations. Thermal parameters such as DF, material surface factor and corresponding time lag values are evaluated as per CIBSE and UNI EN ISO 13786:2007 and surface heat loss and heat gain [21].

These thermal parameters values directly depend upon the material properties thickness, density, specific heat and thermal conductivity. Apart from this, the building material enclose position and its exposer to the weather condition play a significant role in maintaining the thermal environment of the building [22]. The numerical approaches include mathematical expressions of thermal response of building enclose, for evaluating the static and dynamic response. These numerical methods are mostly used for evaluating the temperature distribution of the surface, heat inflow and outflow and weather-dependent thermal responses. In general, finite difference numerical (FDN) scheme is adopted for getting approximate solution. This helps to obtain the effect of building wall configuration on time delay, decrement factor, interior and exterior surface temperature response according to weather conditions. Java code-based open learning software is used for evaluating building

thermal response parameters for very quickly and to make a clear understanding about types of material used for developing the building encloses.

Figure 1a–c represents the homogeneous, composite wall with cement plaster and composite wall made with both cement plaster and bio-insulation in the inner surface of building wall. Where T_3 , T_2 and T_1 represent the 200 mm homogeneous wall, cement plaster wall of 30 mm provided both inside and outside of the homogeneous wall and bio-based polymer of 20 mm inside the room surface is designed and prediction thermal response for all-weather condition of Kolkata.

This helps to evaluate the building parameters at different weather conditions; for this purpose, the weather condition data file is collected. The climate data can be easily available from weather stations. The data file is easily incorporated into the software for all-weather conditions to obtain results at difference surface position

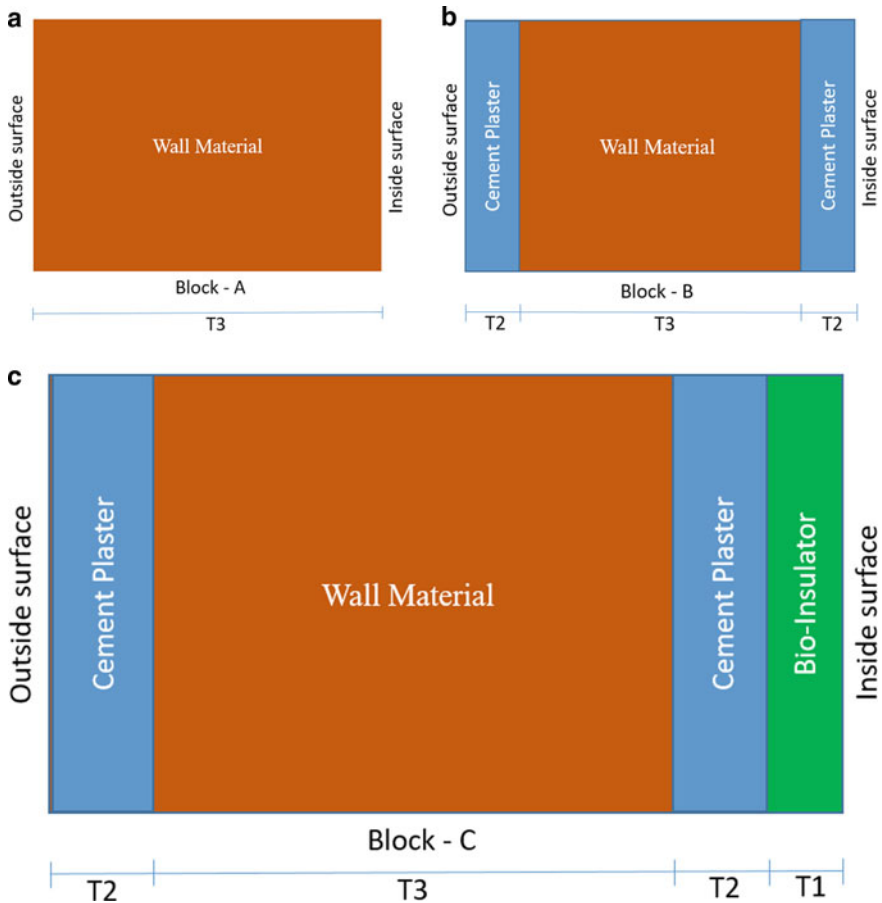


Fig. 1 a Homogeneous wall. b Composite cement plaster wall. c Composite wall made with both cement plaster and bio-insulation

that by varying tilt positions. A clear visual understanding about the temperature variation of wall and roof of a building over each months is easily predicted. The variation in the U value, time lag, decrement factor as per different wall and roof thicknesses is evaluated. Along with this, heat gain and heat loss from the building surfaces are predicted. To get into in-depth analyses, the direct normal radiation, total surface radiation, altitude and bearing angle values are predicted. This pre-predicted information will help the people of Kolkata, West Bengal, while building any infrastructure for maintaining proper thermal and energy management. However, this is not only limited Kolkata but can be implemented any part of the world with standard weather condition report to evaluate the material response at different climates. The detailed thermal properties of the conventional and alternative material properties are shown in Table 1.

Table 1 Thermal properties of different building materials

Alternative and conventional building materials	Thermal conductivity value (W/m K)	Density (kg/m ³)	Specific thermal capacity (J/kg K)	References
GB12.5	0.352	1550	1150	[17]
CSSB 31.6	1.0651	1700	1096.4	[19]
CSSB 10.5	1.0083	1700	1016.7	
CSSB 5	0.8422	1700	1028.4	
CSSB 12	1.0764	1700	1053.1	
CSSB 16	1.0972	1700	938.3	
CSSB 1.7	1.0655	1700	1065.3	
CSSB 1.8	1.2014	1800	1065.3	
CSSB 1.9	1.3025	1900	1036.4	
FAL-G	0.856	1650	930.9	
CSSB (1:7:7)	1.184	1800	1036.4	
AAC	0.166	700	1450.5	
TMB	0.564	1775	1020.5	[20]
Jaipur-brick (JB)	0.811	1820	880	
Bangalore-brick (BB)	0.811	1000	1820	
Challakere-brick (CB)	0.850	1500	840	
Cellular concrete (CC)	0.188	704	1050	
Dense concrete (DC)	1.74	2410	880	
RCC wall	1.58	2288	880	
Cement plaster (CP)	0.721	1762	840	

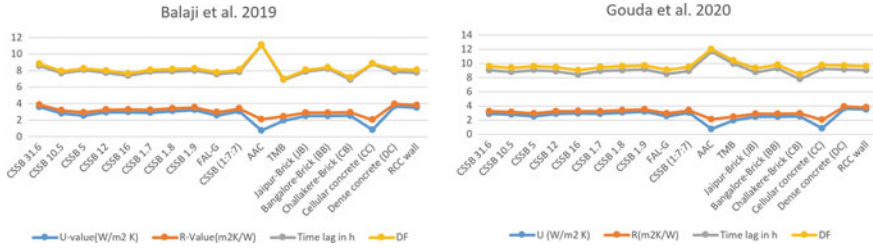


Fig. 2 Computational validation of thermal response of homogeneous building materials

3 Results and Discussion

The present aim of this study is to understand the thermal response of different building materials and their impact inside building environment. In general, the building materials are divided as per the thermal conductivity range and specific heat values.

3.1 Homogeneous, Composite Cement Plaster and Composite Cement Plaster with Bio-Based Material

To validate the computational result thermo-physical characteristics of thermal conductivity, density and specific thermal capacity of the developed materials are evaluated experimentally. For computational analysis different building materials such as conventional materials, alternative materials and bio-based insulators as building enclosure are considered here. Based on the input parameter, the output results such as thermal transmittance value (U in $W/m^2 K$), thermal resistance (R in $m^2 K/W$), time lag (TL in hours) and decrement factor (DF) are evaluated and validated shown in Fig. 2a, b [11]. After initial validation, the investigation is carried out for the composite wall with cement plaster and composite wall made with both cement plaster and bio-insulation in the inner surface of building wall. The composite material with their material configuration with thickness is presented in Table 2a, b with respective wall IDs.

3.2 Effect of Homogeneous and Composite Plaster Walls on Time Lag and DF

Thermal response of different building materials is presented in Tables 3 and 4. The influence of Kolkata weather temperature on these materials is evaluated on the homogeneous and composite wall. The heat-storing capacity and thermal resistance

Table 2 Composite walls with wall IDs representations

Alternative and conventional building materials	Wall IDs
(a)	
30 mm CP + CSSB 31.6 + 30 mm CP	(WCP1)
30 mm CP + CSSB 10.5 + 30 mm CP	(WCP2)
30 mm CP + CSSB 5 + 30 mm CP	(WCP3)
30 mm CP + CSSB 12 + 30 mm CP	(WCP4)
30 mm CP + CSSB 16 + 30 mm CP	(WCP5)
30 mm CP + CSSB 1.7 + 30 mm CP	(WCP6)
30 mm CP + CSSB 1.8 + 30 mm CP	(WCP7)
30 mm CP + CSSB 1.9 + 30 mm CP	(WCP8)
30 mm CP + FAL-G + 30 mm CP	(WCP9)
30 mm CP + CSSB (1:7:7) + 30 mm CP	(WCP10)
30 mm CP + AAC + 30 mm CP	(WCP11)
30 mm CP + TMB + 30 mm CP	(WCP12)
30 mm CP + Jaipur-brick (JB) + 30 mm CP	(WCP13)
30 mm CP + Bangalore-brick (BB) + 30 mm CP	(WCP14)
30 mm CP + Challakere-brick (CB) + 30 mm CP	(WCP15)
30 mm CP + Cellular concrete (CC) + 30 mm CP	(WCP16)
30 mm CP + Dense concrete (DC) + 30 mm CP	(WCP17)
30 mm CP + RCC wall + 30 mm	(WCP18)
(b)	
30 mm CP + CSSB 31.6 + 30 mm CP + 20 mm GB12.5	(WCPB1)
30 mm CP + CSSB 10.5 + 30 mm CP + 20 mm GB12.5	(WCPB2)
30 mm CP + CSSB 5 + 30 mm CP + 20 mm GB12.5	(WCPB3)
30 mm CP + CSSB 12 + 30 mm CP + 20 mm GB12.5	(WCPB4)
30 mm CP + CSSB 16 + 30 mm CP + 20 mm GB12.5	(WCPB5)
30 mm CP + CSSB 1.7 + 30 mm CP + 20 mm GB12.5	(WCPB6)
30 mm CP + CSSB 1.8 + 30 mm CP + 20 mm GB12.5	(WCPB7)
30 mm CP + CSSB 1.9 + 30 mm CP + 20 mm GB12.5	(WCPB8)
30 mm CP + FAL-G + 30 mm CP + 20 mm GB12.5	(WCPB9)
30 mm CP + CSSB (1:7:7) + 30 mm CP + 20 mm GB12.5	(WCPB10)
30 mm CP + AAC + 30 mm CP + 20 mm GB12.5	(WCPB11)
30 mm CP + TMB + 30 mm CP + 20 mm GB12.5	(WCPB12)
30 mm CP + Jaipur-brick (JB) + 30 mm CP + 20 mm GB12.5	(WCPB13)
30 mm CP + Bangalore-brick (BB) + 30 mm CP + 20 mm GB12.5	(WCPB14)
30 mm CP + Challakere-brick (CB) + 30 mm CP + 20 mm GB12.5	(WCPB15)
30 mm CP + Cellular concrete (CC) + 30 mm CP + 20 mm GB12.5	(WCPB16)

(continued)

Table 2 (continued)

Alternative and conventional building materials	Wall IDs
30 mm CP + Dense concrete (DC) + 30 mm CP + 20 mm GB12.5	(WCPB17)
30 mm CP + RCC wall + 30 mm CP + 20 mm GB12.5	(WCPB18)

Table 3 Composite cement plaster wall thermal response

Wall IDs	(<i>U</i>) in W/m ² K	(<i>R</i>) in m ² K/W	(<i>T</i>) in hours	(DF)
(WCP1)	2.32	0.43	7.7	0.37
(WCP2)	2.264	0.44	7.57	0.39
(WCP3)	2.081	0.48	8.08	0.37
(WCP4)	2.331	0.43	7.53	0.39
(WCP5)	2.351	0.43	7.09	0.43
(WCP6)	2.32	0.43	7.59	0.38
(WCP7)	2.441	0.41	7.5	0.38
(WCP8)	2.52	0.4	7.49	0.37
(WCP9)	2.097	0.48	7.56	0.41
(WCP10)	2.426	0.41	7.44	0.38
(WCP11)	0.691	1.45	11.83	0.25
(WCP12)	1.673	0.6	9.51	0.3
(WCP13)	2.042	0.49	7.86	0.39
(WCP14)	2.042	0.49	8.35	0.35
(WCP15)	2.09	0.48	6.88	0.48
(WCP16)	0.765	1.31	9.49	0.39
(WCP17)	2.792	0.36	7.01	0.38
(WCP18)	2.70	0.37	7.05	0.39

properties of the building materials help to control and maintain the indoor thermal comfort. The amount of accumulated by the building wall mostly depends upon the thermal mass of the building materials. More the amount of thermal mass, it can store more heat and minimizes heat transfer rate from outside to inside [23].

The enclosure configuration and the thermo-physical properties of the building material like specific heat capacity and thermal conductivity which effect the time lag and decrement factor. Building material with low *U*-value exhibits lower inside room temperature. From the result in Tables 3 and 4, this can be well predicted that when the *U*-values are low, higher in the time lag value is observed and decrease in the decrement factor. Most of the previous studies make clear that in order to reduce the temperature variation inside the room, the walls and roof surface should have more *T* and minimum DF. In order to obtain better thermal response in a building, it is desirable to develop composite wall multilayer building materials, with diverse thermo-physical properties [24].

Table 4 Bio-insulator-based composite cement plaster wall thermal response

Wall IDs	(<i>U</i>) in W/m ² K	(<i>R</i>) in m ² K/W	(<i>T</i>) in hours	(DF)
(WCPB1)	2.05	0.49	8.68	0.29
(WCPB2)	2.006	0.5	8.75	0.31
(WCPB3)	1.861	0.54	9.1	0.29
(WCPB4)	2.058	0.49	8.52	0.3
(WCPB5)	2.074	0.48	8.1	0.34
(WCPB6)	2.05	0.49	8.58	0.3
(WCPB7)	2.144	0.47	8.47	0.29
(WCPB8)	2.204	0.45	8.44	0.29
(WCPB9)	1.874	0.53	8.6	0.33
(WCPB10)	2.132	0.47	8.41	0.3
(WCPB11)	0.665	1.5	10.97	0.21
(WCPB12)	1.528	0.65	10.58	0.24
(WCPB13)	1.829	0.55	8.89	0.31
(WCPB14)	1.829	0.55	9.37	0.27
(WCPB15)	1.868	0.54	7.95	0.39
(WCPB16)	0.733	1.36	10.7	0.33
(WCPB17)	2.409	0.42	7.92	0.29
(WCPB18)	2.344	0.43	7.98	0.3

To develop a good building enclosure for any building, which able to provide higher than 8 h of *T* and DF able to control and regulate the inside building thermal response with different weather conditions. This is observed that homogeneous building enclosure with AAC exhibited time lag around 9.6 h and decrement factor 0.33 and Challakere-Brick (CB) come up with lowest time lag value 4.86 h and high decrement factor 0.67, which have low time lag and high decrement factor than other all other homogeneous building materials considered here. However, the *T* and DF for the CSSB’s and FAL-G building materials are almost consistence. But in case of other materials, the variation in the time lag and decrement values is more, and this is observed due to the different thermo-physical properties of the building materials. The composite plaster wall with their composite materials are shown in Table 3.

From Table 3, composite plaster walls with wall IDs WCP3, WCP11, WCP12, WCP14 and WCP16 have time lag values of 8.08 h, 11.83 h, 9.51 h, 8.35 h and 9.49 h, respectively. These composite plaster walls will perform better thermal as the time lag values are greater than 8 h and minimum decrement factor. Other building materials after cement plastering both the sides with 30 mm each able to increase the time lag value and reduced the decrement factor of the walls. The thermal transmittance value (*U*) and thermal resistance value (*R*) are also calculated. However, to increase further the time lag value, the developed bio-based thermal insulating material is attached

to the inside surface of the building with 20 mm thickness. For evaluating all these thermal response of the building Kolkata weather condition is adopted.

The evaluated results with addition of bio-based composite to the composite cement plaster wall are presented in Table 4. From the tabulated values, this can be wall predicated that the bio-based thermal insulator material able to improve the time lag values. Building materials with wall IDs WCPB15, WCPB17 and WCPB18 failed to the cross the minimum time lag value. The WCPB11 has highest time lag response of around 10.97 h and decrement factor of 0.21 after addition of bio-based hybrid materials. This increase in the value of time lag due to addition of the extra insulation material inside the building wall. The decrement factor value rises as with addition of 30-mm cement plaster and 20-mm bio-insulation layer addition. The materials with high thermal conductivity value, low density of the material and specific heat capacity have great influence on the building thermal response.

4 Conclusions

The evaluation of different building materials properties for conventional, alternative and bio-based insulation materials that can be used as a building enclosure for Kolkata, India. Various types of building materials have different thermal responses for all-weather condition sustainable material. This is observed that the addition of cement plaster and bio-based insulator increased the time lag of building walls.

- The investigation of the different building materials thermal response helps in the selection of suitable material. From the present investigation, this is observed that homogeneous building materials have very less potential to thermal stress.
- Among all the homogeneous material, AAC has good thermal resistance around $1.36 \text{ m}^2 \text{ K/W}$; hence, this is the only individual material have higher time lag around 9.6 h.
- Addition of the 30 mm cement plaster to the homogeneous building materials improved the thermal resistance, this method is mostly adopted in India. Composite combination 30 mm CP + TMB + 30 mm CP (WCP11) has highest time lag around 11.83 h and thermal transmittance value $2.526 \text{ W/m}^2 \text{ K}$.
- The developed bio-based material has low thermal conductivity around 0.352 W/m K . Addition of 20 mm insulator inside surface of the wall helps to enhance the thermal stability for all the CPBs materials except WCPB15, WCPB17 and WCPB18.

Acknowledgements The authors would like to acknowledge the DST, India, Sanction order no. TMD/CERI/BEE/2016/063 for providing financial support to National Institute of Technology Silchar.

References

1. Hegger M, Fuchs M, Stark T, Zeumer M (2012) *Energy manual: sustainable architecture*. Walter de Gruyter, p 10
2. Soubdhan T, Feuillard T, Bade F (2005) Experimental evaluation of insulation material in roofing system under tropical climate. *Sol Energy* 79(3):311–320
3. Suman EA, Srivastava RK, Agarwal E (2007) Experimental investigation on role of roof insulation of thermal comfort in building, pp 117–122
4. Aye L, Charters WW, Fandiño AM, Robinson JR (2005) Thermal performance of sustainable energy features. *Sol Energy* 1–10
5. Niachou A, Papakonstantinou K, Santamouris M, Tsangrassoulis A, Mihalakakou G (2001) Analysis of the green roof thermal properties and investigation of its energy performance. *Energy Build* 33(7):719–729
6. Straube J, Lstiburek J, Pettit B, Rudd A, Schumacher C, Baker P, Ueno K, Lukachko A, Smegal J, Grin A, Neuhauser K (2011) Building America special research project: high R-value enclosures for high performance residential buildings in all climate zones. Research report 1005, Feb 2011. Building Science Cooperation, Westford, MA
7. Asan H, Sancaktar YS (1998) Effects of wall's thermophysical properties on time lag and decrement factor. *Energy Build* 28(2):159–166
8. Asan H (1998) Effects of wall's insulation thickness and position on time lag and decrement factor. *Energy Build* 28(3):299–305
9. Al-Sanea SA, Zedan MF, Al-Ajlan SA, Abdul Hadi AS (2003) Heat transfer characteristics and optimum insulation thickness for cavity walls. *J Therm Envel Build Sci* 26(3):285–307
10. Gregory K, Moghtaderi B, Sugo H, Page A (2008) Effect of thermal mass on the thermal performance of various Australian residential constructions systems. *Energy Build* 40(4):459–465
11. Balaji NC, Mani M, Reddy BV (2019) Dynamic thermal performance of conventional and alternative building wall envelopes. *J Build Eng* 21:373–395
12. Mohammad S, Shea A (2013) Performance evaluation of modern building thermal envelope designs in the semi-arid continental climate of Tehran. *Buildings* 3(4):674–688
13. Barrios G, Huelsz G, Rojas J, Ochoa JM, Marincic I (2012) Envelope wall/roof thermal performance parameters for non-air-conditioned buildings. *Energy Build* 50:120–127
14. Shaik S, Setty ABTP (2013) Analytical computation of admittance, decrement factor, time lag and surface factors for different exterior wall materials of the buildings in Dakshina Kannada district. In: Proceedings of the 22th national and 11th international ISHMT-ASME heat and mass transfer conference
15. Ng SC, Low KS, Tioh NH (2011) Newspaper sandwiched aerated lightweight concrete wall panels—thermal inertia, transient thermal behavior and surface temperature prediction. *Energy Build* 43(7):1636–1645
16. Ozel M (2011) Thermal performance and optimum insulation thickness of building walls with different structure materials. *Appl Therm Eng* 31(17–18):3854–3863
17. Gouda K, Bhowmik S, Das B (2020) Synergetic effect of micro-bamboo filler and graphene nanoplatelets on thermomechanical properties of epoxy-based hybrid composite. *JOM* 23:1–11
18. Gouda K, Bhowmik S, Das B (2020) Thermomechanical behavior of graphene nanoplatelets and bamboo micro filler incorporated epoxy hybrid composites. *Mater Res Express* 7(1):015328
19. Balaji NC, Praseeda KI, Mani M, Reddy BV (2015) Influence of varying mix proportions on thermal performance of soil-cement blocks. In: Proceedings of the 2nd IBPSA Italy conference, building simulation application—2015 (BSA 2015). BU Press, Bozen-Bolzano, p 8
20. Balaji NC, Mani M, Venkatarama Reddy BV (2017) Thermal conductivity studies on cement-stabilised soil blocks. *Proc Inst Civ Eng Constr Mater* 170(1):40–54

21. The Concrete Center (2010) Dynamic thermal properties calculator. MPA—The Concrete Centre, London, p 6
22. Hafezi MR. Buildings in a hot climate with variable ventilation at night. Doctoral dissertation, University of Leeds
23. Van Straaten JF (1967) Thermal performance of buildings. Elsevier Publishing Company
24. Vijayalakshmi MM, Natarajan E, Shanmugasundaram V (2006) Thermal behaviour of building wall elements. JApSc 6(15):3128–3133

Enhanced Damping in a TLD by Slat Screens and Horizontal Baffles: A Comparative Study



Tanmoy Konar and Aparna Ghosh

Abstract The damping due to liquid viscosity and free surface contamination in the tuned liquid damper (TLD) is often insufficient to dissipate the vibrational energy that is transferred to the damper from the primary structure during their dynamic interaction. Installation of flow damping devices (FDDs) in the TLD can enhance its energy dissipation capacity manifold. FDDs are specially designed appendages that induce added damping by providing hydraulic resistance to the motion of the sloshing liquid. Among the available FDDs, slat screens and horizontal baffles are widely studied by researchers. A comparative study of the added damping provided by these two FDDs, along with their other advantages and disadvantages, is presented in this paper. Additional damping induced by the said FDDs is evaluated numerically considering a standard rectangular TLD configuration.

Keywords Flow damping devices · Horizontal baffle · Slat screen · Tuned liquid damper

1 Introduction

The term tuned liquid damper (TLD) represents the class of dynamic vibration absorber in which the secondary mass consists of liquid residing in a container and in which the damping arises due to the motion of the liquid. Based on the mode of liquid motion, TLDs are principally divided into two groups, namely (a) tuned liquid column damper [1] and its variations, such as liquid column vibration absorber [2] and tuned liquid column ball damper [3], having a U-shaped container configuration in which the liquid experiences oscillatory motion during vibration, and (b) tank damper [4] in which sloshing motion is induced in the liquid when excited.

T. Konar (✉) · A. Ghosh
Department of Civil Engineering, IIST, Shibpur, Howrah, India
e-mail: tanmoykonar@gmail.com

A. Ghosh
e-mail: aparna@civil.iiests.ac.in

Conventionally, the term TLD is taken to imply the tank damper. In TLD, sloshing liquid dissipates energy through the viscous boundary layer near the tank walls and through contamination of the free surface. However, the damping that arises from these mechanisms often proves to be inadequate. For example, as per the numerical model developed by Abramson [5], a circular TLD having a diameter and liquid depth equal to 1.0 m and 0.1 m, respectively, and water as residing liquid, has a damping ratio of only 0.22%. As a result, in many cases, a portion of the vibrational energy transferred to the TLD from the primary structure remains un-dissipated. That un-dissipated energy flows back to the primary structure to cause a beating phenomenon in the response of the primary structure [4]. To overcome this problem and to enhance the damping of TLDs in general, flow damping devices (FDDs) are incorporated within the TLD tank [6]. FDDs are appendages of specific form, shape, and size, designed to dissipate energy through hydraulic interaction with the sloshing liquid. Examples of FDDs include screens, baffles, nets, floating objects, poles, etc. It is pertinent to mention here that the concept of FDDs was originally introduced to suppress sloshing in vibrating liquid containers [7]. Subsequently, around the late 1980s, the idea to enhance the damping of the TLD by the inclusion of FDDs was adopted so as to improve its effectiveness as a dynamic vibration absorber. Figure 1a shows a schematic diagram of a structure with a conventional TLD. Figure 1b depicts a structure to which is attached a TLD in which an FDD has been incorporated.

In the simplified lumped-mass models of TLD, FDDs are represented by an additional dashpot attached to the lumped-mass (Fig. 2a, b). The effectiveness of a particular FDD is often quantified in terms of an equivalent viscous damping coefficient.

Possibly, the first study on the utilization of FDD in TLD was accomplished by Noji et al. [8]. They placed wire nets across the sloshing liquid to derive added damping. However, the difficulty of keeping it rigid and in place during vibrational motion of the TLD dents the acceptability of wire nets as FDD. In the early 1990s,

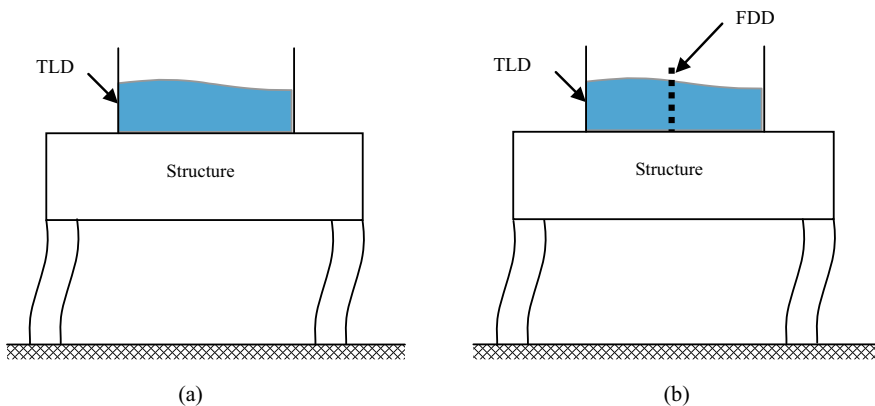


Fig. 1 a Structure with TLD and b structure with TLD-FDD system

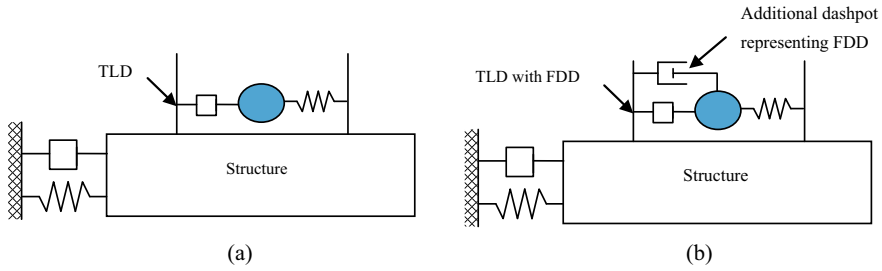


Fig. 2 **a** Lumped-mass model of structure–TLD system and **b** lumped-mass model of structure–TLD-FDD system

poles were used as FDDs in the TLDs employed for wind-induced vibration mitigation of the freestanding pylons of the Ikuchi Bridge, Japan, at the construction stage [9]. Subsequent researchers have shown limited interest in this FDD, probably due to the reason that the pole with its circular cross section produces lower drag resistance as compared to other FDDs. Floating objects comprise another type of FDD which found early application when floating hollow cylindrical polyethylene pieces were used to enhance the damping of the TLDs placed in the Tokyo International Airport Tower, Japan [10]. However, there is no general mathematical model to estimate the added damping induced by these floating objects. Among the various other FDDs, slat screens and horizontal baffles have advantages in terms of adequate added damping, ease of fixing, and availability of acceptable mathematical models. Hence, these two FDDs are receiving attention from researchers and designers. In this paper, first, the damping mechanisms of these two FDDs are discussed. This is followed by a comparative study of their performance in terms of the added damping, considering the TLD to be of rectangular shape. The advantages and disadvantages of the said FDDs are also elaborated upon.

2 Slat Screens as FDD in TLD

A slat screen consists of a plate-like appendage with alternate slats and slots (Fig. 3a, b). It is placed across the direction of sloshing. During sloshing, liquid flows through the slots and the slats to provide hydraulic resistance to the liquid motion, resulting in the dissipation of energy. The solidity ratio of the screen (S_0), given by the ratio of the solid area of the screen to its total area normal to the flow, is kept low ($S_0 < 0.5$), to avoid any significant impact of the screen on the liquid sloshing frequency [11]. To extract maximum damping, slat screens are generally placed near the middle of the tank. More than one screen can be used. However, the use of too many screens may provide resistance to the liquid motion beyond an optimum limit, leading to a reduction in damping due to the slowing down of sloshing. The use of two slat screens at $0.4L$ and $0.6L$ from the left wall of the tank is found to be effective by earlier studies

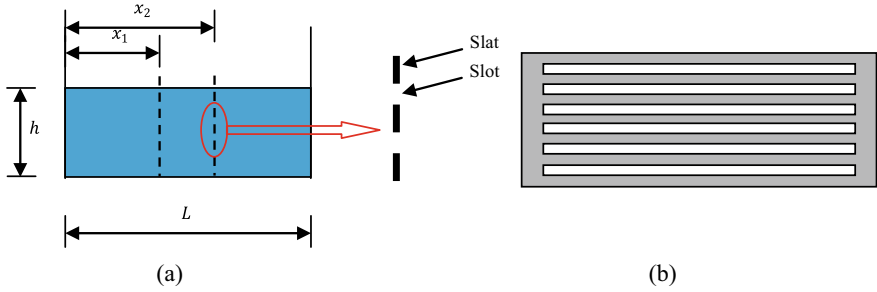


Fig. 3 **a** TLD fitted with slat screens and **b** front view of slat screen

[12], where L is the length of the TLD along the direction of propagation sloshing waves. Sometimes, TLDs with slat screens in two mutually perpendicular directions are used to control vibrations from two principal directions [12].

The energy dissipation by a slat screen system in a rectangular TLD in terms of equivalent damping ratio is estimated by the following [13],

$$\xi_{eq,s} = S_0 C_0 \sqrt{\frac{2}{\pi}} \tanh\left(\frac{\pi h}{L}\right) \Delta \frac{\sigma_\eta}{L} \sum_{i=1}^N \sin^3 \frac{\pi x_i}{L} \tag{1}$$

Here, h is the liquid depth, C_0 is the drag coefficient of the slat screen, σ_η is the root mean square (rms) response of the free liquid surface in the fundamental mode, N is the total number of screens, Δ is as given by Eq. (2).

$$\Delta = \frac{1}{3} + \frac{1}{\sinh^2\left(\frac{\pi h}{L}\right)} \tag{2}$$

Considering the sloshing waves are of the harmonic form, Eq. (1) can be modified as,

$$\xi_{eq,s} = S_0 C_0 \frac{4}{3\pi} \tanh\left(\frac{\pi h}{L}\right) \Delta \frac{\eta}{L} \sum_{i=1}^N \sin^3 \frac{\pi x_i}{L} \tag{3}$$

Here, η is the maximum amplitude of the sloshing wave.

The experimental validation of Eq. (3) is available in [13].

TLDs with slat screens have been installed in many landmark high-rise buildings around the world. One King West and L-Tower of Toronto, One Rincon Hill of San Francisco, and York Place of Hong Kong are a few examples [6].

3 Horizontal Baffles as FDD in TLD

Baffles are submerged plates of specific shape and size that project from the floor or walls of the TLD. To maximize the added damping, baffles are fixed in the region of maximum liquid motion in the TLD. Horizontal baffles projecting out of the TLD wall, close to the free liquid surface, are an effective option as FDD (Fig. 4). The size and location of horizontal baffles can influence the natural sloshing frequency of the TLD. To avoid this, the ratio of the length of the baffles (w) to the length of the TLD (L) is kept small [14]. In deep TLDs ($h/L \geq 0.5$), horizontal baffles convert standing sloshing waves into ‘apparent’ traveling waves in the zone close to the baffles [15]. This enhances the damping effectiveness significantly as standing sloshing waves have nominal energy dissipation ability in comparison to the traveling waves generated in the conventional TLD of shallow liquid depth [15].

The damping produced by a single set of horizontal baffles in a rectangular TLD can be denoted in terms of equivalent viscous damping ratio as [14],

$$\xi_{eq,b} = \frac{24}{L^2} \sqrt{w\eta} \left(\frac{\sinh \frac{\pi d}{L}}{\sinh \frac{\pi h}{L}} \right)^{2.5} \tanh \left(\frac{\pi h}{L} \right) \left[\frac{L}{12\pi} \sin \left(\frac{3\pi w}{L} \right) + \frac{3L}{4\pi} \sin \left(\frac{\pi w}{L} \right) \right] \tag{4}$$

Here, d is the distance of the baffle from the bottom of the TLD. The other parameters are as defined in Eqs. (1) and (3).

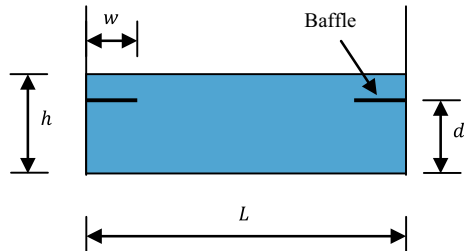
For small values of w/L , given by $w/L < 0.125$, Eq. (4) can be simplified as follows [14].

$$\xi_{eq,b} = 24 \left(\frac{w}{L} \right)^{1.5} \sqrt{\frac{\eta}{L}} \left(\frac{\sinh \frac{\pi d}{L}}{\sinh \frac{\pi h}{L}} \right)^{2.5} \tanh \left(\frac{\pi h}{L} \right) \tag{5}$$

Through extensive experimental studies, Goudarzi et al. showed that Eq. (5) can fairly predict the value of $\xi_{eq,b}$ (see Fig. 5) [14].

Though there are significant research works on the utilization of horizontal baffles as FDD in TLDs [6], there is no major real-life implementation of this FDD till now.

Fig. 4 TLD fitted with horizontal baffles



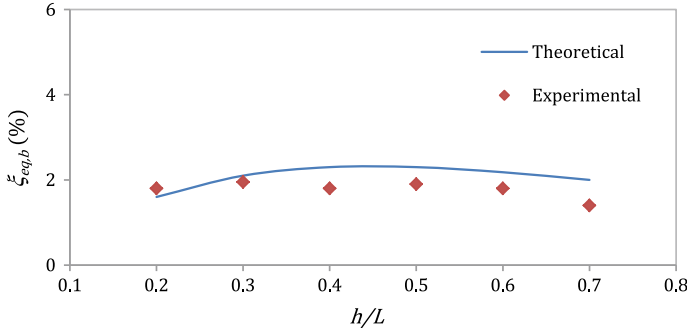


Fig. 5 Comparison of theoretically and experimentally determined values of $\xi_{eq,b}$ for different h/L when a rectangular TLD is subjected to sinusoidal excitation of amplitude 0.5 mm ($w/L = 0.083$, $d/h = 0.8$, $L = 96$ cm) [14]

The main disadvantage of the horizontal baffle is its high sensitivity to liquid level fluctuation in the TLD.

4 Comparison Between Slant Screens and Horizontal Baffles

In this section, a comparison between the performances of the slant screens and the horizontal baffles as FDDs in the TLD is presented. It is clear from Eqs. (3) and (5) that the performance of both the FDDs depends on the ratios η/L and h/L which, respectively, represent the sloshing amplitude and the liquid depth in non-dimensional terms. Higher η/L indicates higher sloshing amplitude which implies higher excitation to the TLD. For slant screens, the equivalent damping ratio is proportional to η/L , whereas, for horizontal baffles, it is proportional to $\sqrt{\eta/L}$. The h/L ratio in conventional TLDs is normally kept to the tune of 0.1 [4]. With such a low h/L ratio, the behavior of the TLD becomes highly nonlinear. When the h/L ratio is increased, the degree of nonlinearity reduces but the energy dissipation capacity of the damper falls. As the inherent damping of the TLD is much less as compared to what is induced by the FDDs, the h/L ratio of TLD with FDDs is often kept a little high, normally in the range of $0.1 < h/L < 0.5$ [16]. Here, the viscous damping ratios equivalent to the energy dissipation provided by the considered FDDs for a range of η/L ratio from 0.0 to 0.1 and for five specific h/L ratios, namely 0.1, 0.2, 0.3, 0.4, 0.5, are presented in Fig. 6a, b. In addition to η/L and h/L , the damping provided by slant screens depends upon S_0 , C_0 , number of screens, and the position of the screens. As already mentioned, the value of S_0 should be taken less than 0.5 to avoid any influence of the presence of the screen on the liquid sloshing frequency. For the present study, S_0 is taken as 0.3 [17]. For a slant screen, the value of C_0 depends chiefly upon S_0 and Keulegan–Carpenter (K–C) number [17]. From the experimental results presented by Fediw et al. [17], for a slant screen with $S_0 = 0.3$, a conservative

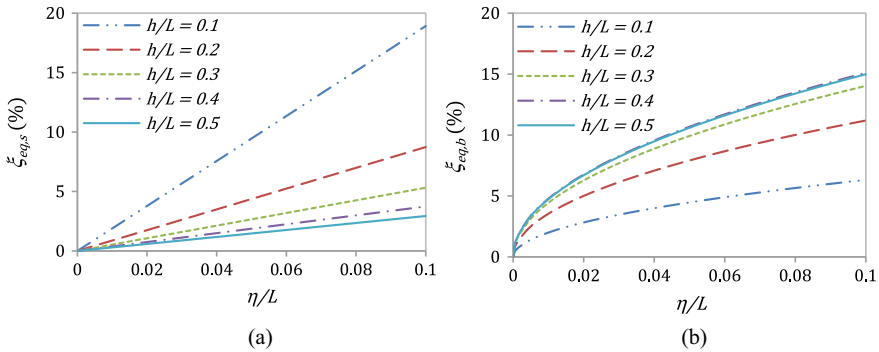


Fig. 6 Equivalent viscous damping ratio versus η/L for different h/L : **a** slat screens and **b** horizontal baffles

value of C_0 equal to 2.8 is taken. As a set of two screens at $0.4L$ and $0.6L$ from the left wall of the TLD has proven to be effective by several early works [12, 16], the same is used for the present study. In the case of horizontal baffles, the energy dissipation depends upon the ratios w/L and d/h , in addition to η/L and h/L . To avoid the effect of w/L on the sloshing frequency, a low value of w/L equal to 0.12 is considered. Again, to achieve high damping, a large value of d/h equal to 0.85 is adopted for the present study.

It is evident from Fig. 6a, b that both slat screens and horizontal baffles are highly effective in enhancing TLD damping, as for TLD without FDDs the effective damping ratio remains less than 1% [17]. As expected, with the increase in η/L , which indicates higher energy transferred to the TLD, the effectiveness of both FDDs increases. However, at low η/L , which represents low amplitude sloshing, horizontal baffles are more effective. It is also observed that slat screens perform better when h/L is low, i.e., in shallower TLDs. As h/L increases in a TLD, the impulsive liquid mass, which is the portion of liquid that does not participate in sloshing, increases and this makes the lower part of the screens ineffective. On the other hand, horizontal baffles produce higher damping in deeper TLDs. This is because horizontal baffles are placed in the upper region of the TLD. As the TLD becomes deeper, the impulsive liquid mass increases, and the sloshing liquid mass in the upper region carries most of the vibrational energy. However, as h/L increases, the rate of change in equivalent viscous damping ratio with the increase in h/L reduces. As sloshing liquid mass in a rectangular TLD becomes almost constant at $h/L > 0.5$, the effect of h/L on the effective damping ratio would become negligible for $h/L > 0.5$. In fact, for horizontal baffles, there is no variation in $\xi_{eq,b}$ observed for $h/L = 0.4$ and $h/L = 0.5$.

5 Conclusions

Installation of FDDs in TLDs is an effective technique to tackle the problem of very low inherent damping of sloshing TLDs. Slat screens and horizontal baffles are two widely studied FDDs for their ability to develop adequate added damping, due to the availability of proper mathematical models, and for ease of fixing. A comparative study of the performances of the said FDDs is presented in this paper. The energy dissipation capacities of the FDDs are calculated in terms of equivalent viscous damping within a practical range of the governing parameters. The maximum enhancement in damping achieved by both the FDDs is more than 15 times that of the conventional TLD without FDD. At higher η/L , that is for stronger excitation, both the FDDs produce higher damping. However, during low amplitude sloshing, the performance of horizontal baffles is better. As slat screens interact with liquid throughout its submerged height, with the increase in h/L , the effectiveness of the screen reduces for the increase in impulsive liquid mass which makes the lower part of the screens ineffective. On the other hand, an increase in h/L results in better performance of horizontal baffles. This is because, in deeper TLDs, the impulsive liquid mass is higher and most of the vibrational energy is carried by the limited sloshing liquid mass available in the upper region of the TLD, with which horizontal baffles interact. However, for $h/L > 0.5$, the effect of h/L on the energy dissipation capacity of both the FDDs becomes negligible as sloshing liquid mass in a rectangular TLD approaches a constant value at $h/L > 0.5$. While designing TLD systems with these FDDs, the effect of FDD parameters on the natural sloshing frequency of the damper should be reviewed. During design, S_0 for slat screen and w/L ratio for horizontal baffles are kept low (normally $S_0 < 0.5$ and $w/L < 0.125$) to avoid any significant influence of the FDDs on TLD frequency.

References

1. Soaka Y, Sakai F, Takaeda S, Tamaki T (1988) On the suppression of vibrations by tuned liquid column dampers. In: JSCE annual meeting, JSCE
2. Konar T, Ghosh A (2010) Passive control of seismically excited structures by the liquid column vibration absorber. *Struct Eng Mech* 36:561–573
3. Al-Saif KA, Aldakkan KA, Foda MA (2011) Modified liquid column damper for vibration control of structures. *Int J Mech Sci* 53:505–512
4. Fujino Y, Pacheco BM, Chaiseri P, Sun LM (1988) Parametric study on tuned liquid damper (TLD) using circular containers by free oscillation experiment. *Struct Eng Earthq Eng* 5:177–187
5. Abramson HN (1966) The dynamic behavior of liquids in moving containers. NASA SP-106
6. Konar T, Ghosh AD (2020) Flow damping devices in tuned liquid damper for structural vibration control: a review. *Arch Comput Methods Eng*. <https://doi.org/10.1007/s11831-020-09450-0>
7. Langner G (1963) A preliminary analysis for optimum design of ring and partition antislosh baffles. Technical Report No. 7, Apr 1963. Southwest Research Institute
8. Noji T, Yoshida H, Tatsumi E, Kosaka H, Hagiuda H (1988) Study on vibration control damper utilizing sloshing of water. *J Wind Eng* 37:557–566

9. Ueda T, Nakagaki R, Koshida K (1992) Suppression of wind-induced vibration by dynamic dampers in tower-like structures. *J Wind Eng Ind Aerodyn* 43:1907–1918
10. Tamura Y, Kohsaka R, Nakamura O, Miyashita KI, Modi VJ (1996) Wind-induced responses of an airport tower—efficiency of tuned liquid damper. *J Wind Eng Ind Aerodyn* 65:121–131
11. Faltinsen OM, Firoozkoobi R, Timokha AN (2011) Steady-state liquid sloshing in a rectangular tank with a slat-type screen in the middle: quasilinear modal analysis and experiments. *Phys Fluids* 23. <https://doi.org/10.1063/1.3562310>
12. Tait MJ, El Damatty AA, Isyumov N (2005) An investigation of tuned liquid dampers equipped with damping screens under 2D excitation. *Earthq Eng Struct Dyn* 34:719–735
13. Tait MJ (2008) Modelling and preliminary design of a structure-TLD system. *Eng Struct* 30:2644–2655
14. Goudarzi MA, Sabbagh-Yazdi SR, Marx W (2010) Investigation of sloshing damping in baffled rectangular tanks subjected to the dynamic excitation. *Bull Earthq Eng* 8:1055–1072
15. Anderson JG, Semercigil SE, Turan ÖF (2000) An improved standing-wave-type sloshing absorber. *J Sound Vib* 235:702–710
16. Lago A, Trabucco D, Wood A (2019) Damping technologies for tall buildings
17. Fediw AA, Isyumov N, Vickery BJ (1995) Performance of a tuned sloshing water damper. *J Wind Eng Ind Aerodyn* 57:237–247

Additive Manufacturing: An Emerging Tool to Fabricate Bioinspired Structures



Vishal Mishra, Sushant Negi, and Simanchal Kar

Abstract Smart industries require faster production of robust components developed from CAD models with better mechanical and metallurgical properties. As a result, various researchers are working to build bioinspired 3D printed models. This includes the exploration of fundamental design and structural property in correlation with nature. Consequently, the developed physical model will bear enhanced mechanical as well as material properties. In this paper, a review of the various research work is presented that has been successfully conducted by the application of additive manufacturing to produce bioinspired models/structures. The paper comprises three sections, namely, 3D printing, bioinspired structures, and specific application of 3D printed components, especially in health care, automobile, and automation industries. The paper is aimed to provide a brief insight on layered structures, namely honeycomb, cellular and intricate structures, 3D printed surface texture that are inspired from nature such as microneedles of bees, fins, and scales of fish and collapsible armor of an armadillo that are aimed for specific applications and 3D printed bionic robots mimicking the movement of the corresponding biological body part or an animal.

Keywords Additive manufacturing · 3D printing · Biomimicry · Bio-microneedle · Dental implant

V. Mishra (✉) · S. Negi · S. Kar
Department of Mechanical Engineering, NIT Silchar, Silchar, India
e-mail: vishal_rs@mech.nits.ac.in; vishalmishra2812.me@gmail.com

S. Negi
e-mail: sushant@mech.nits.ac.in; negiindia@gmail.com



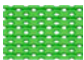


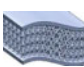

S. Kar
e-mail: simanchal@mech.nits.ac.in; simanchal.kar@gmail.com

1 Introduction

The field of biomimetics and biomaterials, representing the science of materials and engineering into biology, is actively advancing [1–3]. Bioinspired models are the models that are the biomimicry of the structure (living thing) which exists in nature. The study of biomimetics leads to the development of models that are far more superior than the models in terms of strength, lightweight, etc., which are prepared by the use of basic science. The physical and mechanical properties of the bioinspired structure are demonstrated in Table 1.

Over the past few years, additive manufacturing, more precisely rapid prototyping, has been an essential tool for the manufacturing of complex bioinspired models/structures [4]. Self-assembly, self-healing, multi-functionality, the hierarchy of structure, synthesis, the importance of hydration, Evolution environmental

Table 1 Different principal structural design elements

Sr. No.	Structure	Shape	Remarks
1	Fibrous structure		When aligned in a single direction, they show high tensile strength property, and they buckle under compression showing low compression strength property
2	Helical/ Bauligand structures		These structures are familiar to composites and are characterized by fiber rotation in a sequential manner. The enhances the toughness creating difficulty in crack propagation, and also provides stiffness and strength during in-plane isotropy
3	Gradient structures		This structure design increases the toughness of the building sample by avoiding interfacial mismatch stress
4	Layered structures		It is used for designing complex composite. This design increases the toughness of brittle materials due to the interfacial introduction. Ex. nacreous structure in shells
5	Tubular structure		It enhances the energy absorption tendency and assists in crack deflection
6	Cellular structures		It provides direct stress distribution and energy absorption to lightweight porous or foam structures
7	Suture interfaces		They are used to connect the stiffer components

constraints are the unique characteristics of biomaterials [5]. The current challenge to AM is the multi-material alliance, control of intrinsic defects, and multiscaleability [4]. Mineral and organic components are the two structural architecture of biological elements, where minerals are good in providing compressive strength and stiffness, and organic components provide tensile strength. This review extensively covers the recent advances of 3D printing for manufacturing bioinspired structures. The review not only provides the information regarding the recent researches that have been carried out in the past few years but, it also helps the reader/researcher to find research gap. This will lead to exploration of nature and the invention of new bioinspired structures which will be beneficial for the society. Energy absorption applications, armors, robotics, etc., are some applications that are discussed in the paper.

2 Additive Manufacturing (AM) Processes

The current challenge in the sector of AM is the preparation/manufacture of a bioinspired structure comprising unique mechanics and heterogeneous properties. In the previous year's AM technology has been implemented to manufacture the biomimetic structure, and as a result, it has provided a versatile platform for rapid and precise fabrication ranging from small scale to large scale [6–9]. Various additive manufacturing techniques such as fused deposition modeling, direct ink writing, selective laser sintering, stereolithography, polyjet technology, and 4D printing are widely used for manufacturing bioinspired models. Table 2 represents the use of different AM materials for various applications.

2.1 *Fused Deposition Modeling (FDM)*

In this process, a solid filament (polymer) is pushed into a heating chamber to get liquefied by a tractor wheel arrangement. The pushing develops the extrusion pressure by which layer deposition takes place. The schematic diagram of FDM is shown in Fig. 1a. The arrangement comprises of build material spool, extrusion head, drive wheel, liquefiers, and the extrusion nozzles. The movement of the extrusion head is programmed for the controlled deposition to take place. ABS plus is the most popular material which is used for sample preparation. Sometimes ABS is blended with polycarbonate to enhance the properties [10].

Table 2 AM materials

Sr. No.	Process	Material	Applications
1	FDM	ABS, polycarbonate, polylactide, acrylonitrile	Jigs and fixtures, drug delivery devices that contain an accurate dose of medicines, etc
2	DIW	Polymer nanocomposites, graphene flakes, hydrogels, alloys and pure metals, titanium dioxide inks, ethanol	Thin printed films and patterns like parallel lines at any angle, grid patterns, meandering lines, etc
3	IP	Thermoplastics such as polyester	Rapid tooling patterns, medical devices, jewelry, etc
4	SLS	Powders of polyamides, polystyrene, thermoplastic elastomers, etc	Investment casting patterns, automotive hardware, wind tunnels, jigs and fixtures, rapid tooling, etc
5	SL	ABS (Protogen 18,420), polypropylene	Investment casting patterns, rapid tooling, jigs and fixtures, molds, designer models, etc
6	PPT	Photopolymers, thermoplastics, Acrylonitrile butadiene styrene (ABS)	Replicas of the organs that need replacement, prosthetic limbs, accurate crowns, etc

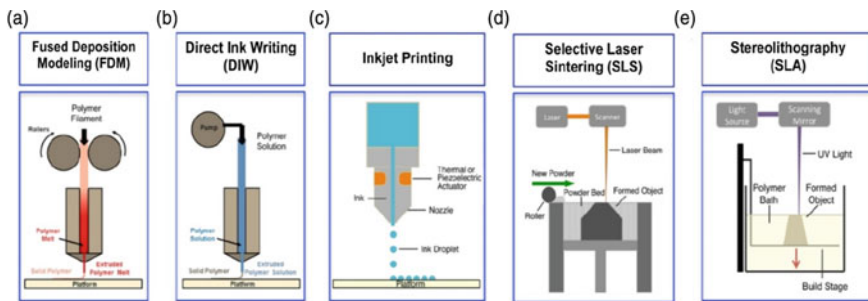


Fig. 1 a Fused deposition modeling, b direct ink writing, c inkjet printing, d selective laser sintering, e stereolithography [11]

2.2 Direct Ink Writing (DIW)

The extrusion process is the key basis of this process. This technique is successful for manufacturing material comprising a wide range of geometries, dimensions, etc. [12–14]. This technology is flexible for both hardware and software in combination with inexpensive nozzle and materials [12]. This system dispenses continuous viscoelastic filament form of material from the syringe in a controlled path and controlled flow. Figure 1b demonstrates this technique. Viscosity, mechanical yield stress under shear and compression, etc., are the rheological behavior characteristic of the ink, which tailors required application properties [15, 16]. This technique is used to manufacture

hydrogel scaffolds. The ink has to be fluid in such a manner that printing from the nozzle must be satisfied, and the desired shape under gravity is achieved [17].

2.3 Inkjet Printing (IP)

It is a widely and commercially available technique due to its flexibility and cost-effectiveness in order to construct complex structures [18]. It is an extended version of 2D printing to 3D printing by the use of binding powders. The schematic diagram of the technique is shown in Fig. 1c. Induration to the process of manufacturing, firstly, solid powder particles are made to rest on to the platform. Furthermore, on to the powder on the platform, a layer of liquid binding material of the desired structure is laid through the use of an inkjet printing head. After the solidification of the first layer of liquid binding material, unbounded powders are removed, and the second layer will be laid by the printing head, and the process continues till the design structure is made. The process is fully computer-controlled through programming. This technique offers fabrication of heterogeneous materials in well-balanced composition and properties [7, 12]. The inkjet printer is capable of printing multi-material objects, and it is not only limited to photopolymers, unlike photocurable inkjet printers. Due to material independence, inkjet generates heterogeneous 3D multi-material objects having a distribution of variable stiffness materials and in addition to enhanced strength and toughness. The basic drawback to this technique is that the additional processing can only be done when the layer gets fully solidified. The surface roughness and quality require additional improvement due to the reduction of surface roughness by 50% because of layer by layer origination of the printed part [19].

2.4 Selective Laser Sintering (SLS)

It uses powder as a raw material for 3D printing. As shown in Fig. 1d, in this technique, the part building takes place in a closed chamber that is flooded with nitrogen gas in order to lessen the oxidation and to stop the decay of the powdered material. Over the building platform, the powder bed is placed at an elevated temperature or the glass transition temperature of the powder. For maintaining the elevated temperature, infrared heaters are used, a concentrated CO₂ laser beam is made to move over the bed in such a manner that it thermally bonds the material to get the desired shape. A layer thickness of nearly 0.1 mm can be achieved by this process [10].

2.5 Stereolithography (SL)

It is the first AM method used for the fabrication of light-induced polymerization [20]. Improvement in laser performance increases the advancement level of this technique. In this technique, the UV laser tracks the configuration of a 3D sample in a 2D plane by focusing on the photo resin. The schematic diagram of this technique is shown in Fig. 1e. The polymerization takes place in the layer by layer model [21]. Manufacturing of polymer-based composite is possible through stereolithography by the addition of filler particles in liquid resin [22, 23]. It is restrictive to photopolymers only because it requires the use of ultrahigh magnetic field response within the reactive resin for the control of the direction of particles [24]. More precisely electromagnetic controller is used for better orientation of particles [25]. Based on the polymer-based given theory, bioinspired complicated composite structure can be manufactured due to controlled orientation. The stereolithography technique is able to achieve a high resolution of 50 μm (dependent on no. of photons applied) [26]. The greatest disadvantage with this technique is that for bioinspired material development, the printing of multi-material in one sequence is not possible.

2.6 Polyjet Printing (PP) Technology

Polyjet multi-material 3D printing technology is photocurable technology in which a jet of liquid polymer droplets is used for layer-by-layer deposition. After each layer deposition, ultraviolet lamps are used to cure the layers immediately. After the final process, the desired structure/object is obtained with no additional cure requirement and reduced production time. Polyjet technology is capable of depositing multiple materials comprising of distinguished mechanical properties simultaneously [27]. Bioinspired material (that are often composites) fabrication is more actively achieved by this technique with gradient material properties. Resolution of 600 dots per inch and thickness of 16–30 μm per layer is possible with polyjet technology. The supporting material provides firmness to jetted droplets that can easily be detached by hand or by water jet [4].

2.7 4D Printing

4D printing fabricated the structure with the variable arrangement, outlines (geometries), properties, and performance [28]. Under an exterior stimulus, the accepted combination, numerous smart materials act mutually to trigger the printed structure to relocate from one firm configuration to another [29, 30]. 4D printing essentially is a two-step process in which, firstly, processing of model into original shape is done, and secondly, it is intermediately temporized into another shape and finally

programmed to convert another shape in a self-folding pattern [28]. The major objective of the paper is to discuss a brief review of the different researches that had been carried on the bioinspired structural design using different additive manufacturing techniques. By the end of the paper, a reader will have good information on the research that was done earlier.

3 Applications of Additively Manufactured Bioinspired Structures

Biomimicry is a nature-inspired innovation. It involves the study of the use of the natural system (biological) in engineering applications to solve engineering problems [31]. The presented review paper will try to fill the gap between the approached area of biomimicry by the use of AM and the future scope for biomimetics in the field of AM.

3.1 Sports Sector

The biomimetics of the honeycomb (Fig. 2a), spiderweb, pinecone, and carbon atom configuration are used to fabricate the 3D core by selecting various process parameters as shown in Table 4 to design the structure of an on-water sports board such as a surfboard and kiteboard. A fused deposition modeling technique was adopted for the fabrication of a surfing board, as shown in Fig. 2b, c, using polylactic acid (PLA) material. Various experiments (analytical and numerical based) were conducted to validate the various patterns of the honeycomb structure. The mechanical property of PLA was experimentally determined. An FDM 3D printed sample of ASTM D638 standard was prepared for determining the tensile properties of Plastics. The bottom and top shells were 3D printed individually on a smaller scale using PLA filament. Furthermore, the parts are glued together strongly by adhesive [32].

The three-point bending test was performed, followed by linear analytical and nonlinear FEM simulation. Apart from a honeycomb structure, different core patterns, as shown in Fig. 3, are designed and fabricated by FDM, and analysis

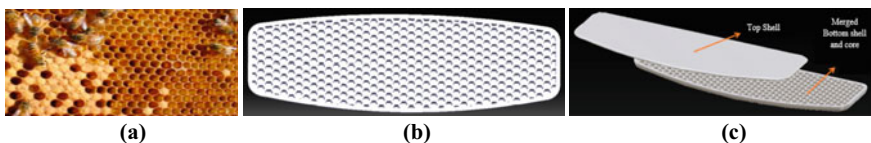


Fig. 2 a Natural honeycomb structure, b designed bioinspired honeycomb core (CATIA V5 Software), c board components: top shell and merged bottom shell and core [32]

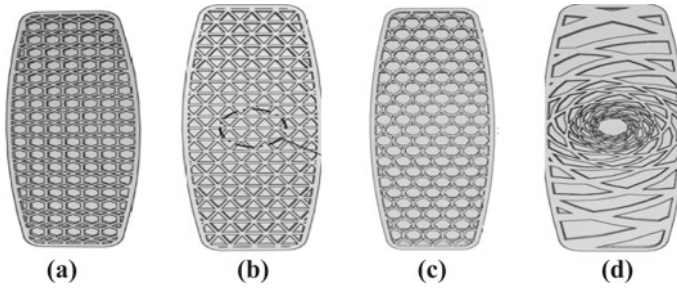


Fig. 3 Different core patterns **a** hexagonal rhombic structure, **b** triangular honeycomb structure, **c** hexagonal carbon lattice structure, **d** pinecone inspired structure [32]

was conducted. As a result, functionally graded honeycomb (FG honeycomb) structure and fully filled board are capable of tolerating the maximum and minimum forces, respectively. FG honeycomb board experiences large deflections of 4 mm at 595 N force and reduces the central deflection by 31% resulting in an enhancement of 12% in force. At a constant load of 400 N, central deflection is reduced by 97% for the FG pattern as compared to full filled core. Uniform honeycomb shows slightly better bending performance as compared to carbon atom lattice structure. In addition to playing equipment, safety is a vital part to be considered in sports, like the shell structure of armadillo (Fig. 4a, b), which provides efficient protection from predators and have high armor hardness as well as hard limbs. Based on the shell design, a bioinspired knee protector for light recreational sports was fabricated [33]. Figure 4c shows the bending pattern of the shell. The knee protectors are designed by considering the armadillo's shell, as shown in Fig. 4d, e, f. Through this bioinspired model, one can fabricate good knee protection equipment with one primary protection plate at the center and small plastic tiles provided as the secondary rings by using hard plastic with the mesh of carbon fiber. This design put presents a better free knee maneuver with upgraded comfort and air ventilation system during the sports.

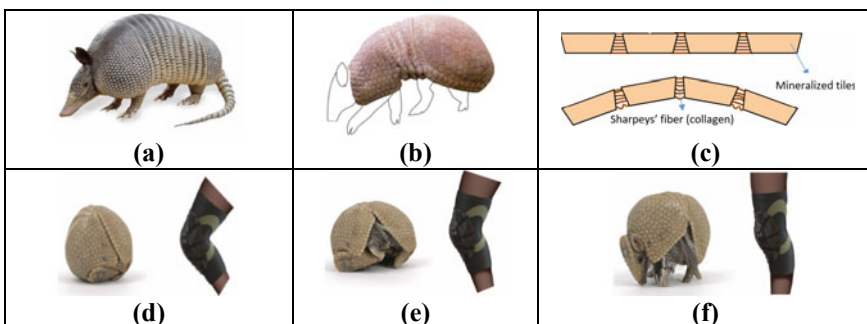


Fig. 4 **a** North American armadillo, **b** unbent and bent shell structure, **c** Armadillo carapace (hard shell), different protection position, **d** bent knee, **e** half bent knee and **f** straight knee [33]

3.2 Healthcare Sector

An artificial micro fish was developed using microscale continuous optical printing (μ COP) [34]. Incorporating polydiacetylene nanoparticles, the micro fish was demonstrated for utility in toxin neutralization. It will also be used for drug delivery in the human body. μ COP technique uses a digital micromirror array made by comprising 2 million micromirrors [35]. Each mirror individually is controlled to project the precise image onto a photopolymer monomer solution. Figure 5 demonstrates the various stages that are required for the micro fish fabrication, and it also describes the various materials to be used for fabrication in individual steps. The process of functionalization of micro fish is shown in Fig. 5.

3D printed micro fish [34] has high fidelity shape and structure and is composed of polyethylene glycol diacrylate-based hydrogels and functional nanoparticles. The thickness of fabricated micro fish is 30 μ m (approx.), and the length is 120 μ m. It is using hydrogen peroxide as a fuel source for the micro fish. The microfish achieves a speed of 780 μ m/s by consuming 15% of peroxide. The speed of fish depends on the shape/geometry of the fish. At the same Pt concentration load, common shape fish achieves an average speed of 1.5 times higher than that of fish having manta ray shape. It was concluded that to gain higher speed, and more optimization will be required. When talking about drug delivery in the human body, the stringer of a honeybee, mosquitoes, porcupine, etc., can also serve the purpose of drug delivery. Table 3 demonstrates the unique features of bio-microneedles. Honeybee has a unique type of stringer with micro barbs is that it can easily penetrate the hostile animal’s skin and gets trapped. This is done by the honeybee to inject its toxins into the prey’s body for self-defense. This stringer is painless in insertion, requires low penetration force, highly stiff, and has good biocompatibility. In inspiration with the honeybee stringer, a bioinspired microneedle was fabricated for drug delivery in the human body by

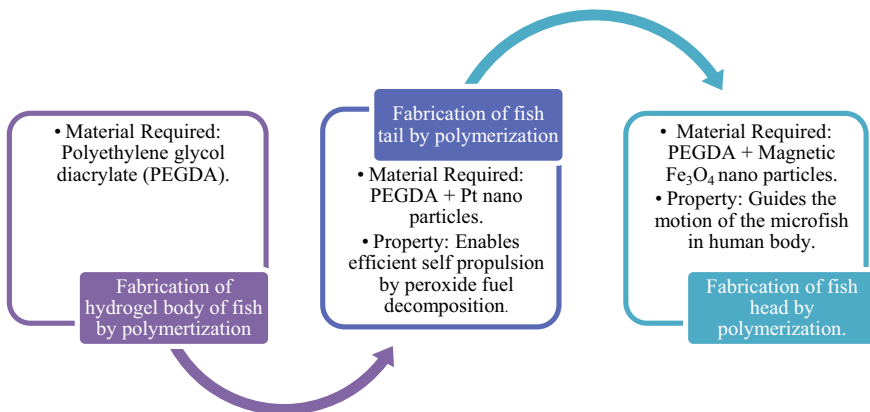

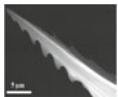

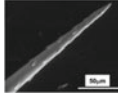

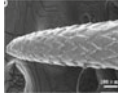

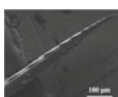


Fig. 5 Various stages of micro fish fabrication provided with the material used in each stage [34]

Table 3 Peculiar parameters of bio-microneedles [36]

Type	Bio-microneedles	SEM images	Geometry	Penetration force	Pull out force
Fascicle of aedes asbopictus mosquito			Diameter: 30 μm Length: 1.5–2.5 μm	Average: 18 μN Range: 6–38 μN	NA
The spine of paras consocia caterpillar			Diameter: 30–50 μm Length: 500–700 μm	Average: 173 μN Range: 80–265 μN	NA
Quill of North American porcupine			Diameter: 1.26 μm Length: several centimeters	Average: 0.043 N	Avg.: 0.44 N
Stringer of the worker honeybee			Diameter: 90 μm Length: 1.8 mm	Average: 5.75 mN	Avg.: 113.5 mN

employing magnetorheological drawing lithography [36, 37]. Honeybee stringer was the bionics used for the purpose.

Figure 6 explains the various stages required for microneedle fabrication. For the purpose of fabrication, a curable magnetorheological fluid (CMRF) as a raw material is used. A two-step fabrication process was followed, as mentioned below:

1. Parent microneedle fabrication.
2. Micro barbs fabrication.

In comparison to barbless microneedle, the extraction-penetration force ratio of bioinspired microneedle was found to be 1.75, whereas 0.55 for barbless microneedle. The barbs were moored in the skin during the withdrawal, which fundamentally improved the draw out power/force. Moreover, a combination of Selective Laser Sintering (SLS) and Stereolithography (SL) [38] was also used to fabricate less expensive and suitable dental implants followed by topology optimization, which will be used to overcome edentulism problem as shown in Fig. 7.

Figure 7 demonstrates the CAD model and the physically fabricated model of the dental implant. These implants do not require any initial surgery [38]. The combined fabrication process was divided into stages for precise manufacturing of the implants, as shown in Fig. 8. The combination of both the additive process increases the mechanical strength and gradient physical properties with optimized mass/volume ratio.

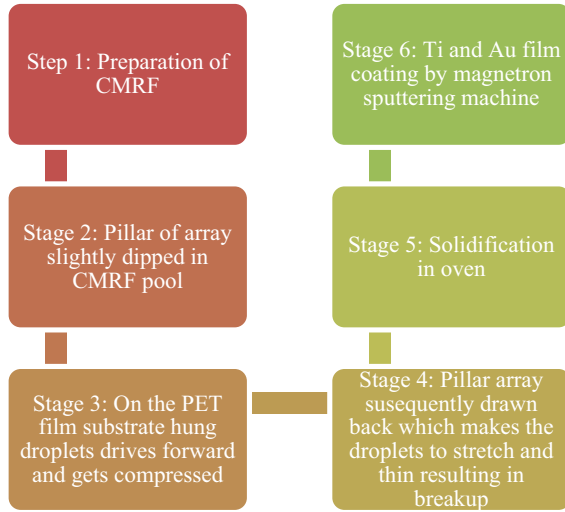


Fig. 6 Various steps for magnetorheological drawing lithography

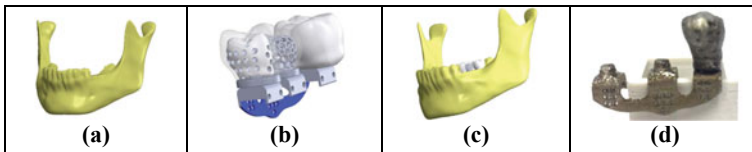


Fig. 7 3D CAD model. **a** maxilla of a patient suffering from edentulism problem, **b** generated topology optimized core geometry dental bridge, **c** assembly, **d** physical model of the dental bridge [38]



Fig. 8 Stages of sample preparation

3.3 Automobile Sector

To minimize noise pollution generated by the cooling fan blade of automobiles, a bioinspired cooling fan blade structure was fabricated. The bioinspired structure selected comprises three shark skin ribbed ridges, as shown in Fig. 9a. The ribs are

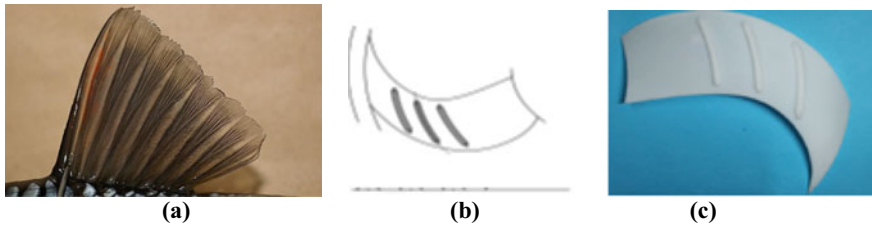


Fig. 9 a Fin configuration, b schematic diagram of bioinspired cooling fan blades, c fabricated bionic fan blade [39]

concentrically distributed to the fan hub axis for uninterrupted airflow. The schematic diagram, as shown in Fig. 9b, shows the specification of a fan. The bionic fan blades are fabricated using future 800 resin (polyamide high heat resistant resin), as shown in Fig. 9c [39].

Based on different operating conditions, blades are fabricated using the 3D printer by selecting future 8000 resin. The analysis shows that the surface texture of the bioinspired blade increases the fan rotational speed in which fan having radius 136 mm, ridge width 4 mm, ridge height 2 mm, and ridge pitch distance 15 mm was found to be most efficient with a speed range from 1500 to 2500 rpm. At 1750 rpm, all fans show reduced noise pollution. To lower the aerodynamic fan noise, there is a need to control the airflow over the fan blades through designs based on natural features leading to the concept of a bioinspired design [39].

3.4 Robotics Sector

Underwater robots are used for exploration, observation, military tasks, a better understanding of environmental issues, etc. Underwater robots fabricated was bionics of fish (tensegrity architecture) [31, 40]. Body stiffness, swimming speed, thrust force are some required characteristics of the robot. The robot comprises elastic cables and rigid elements that are inspired by bone/tissue and fish muscles. Conventional 3D printers were adopted to fabricate the robot, as shown in Fig. 10a. In Fig. 10a, section (a) demonstrates the individually fabricated parts, whereas section (b) demonstrates the underwater bioinspired robots after the assembly of individual parts with the help of elastic cables. By varying elastic cables cross section, the stiffness of the robot body can be varied [41].

The head and the rigid elements were fabricated using PLA, having a young's modulus of 15.2 MPa [42], and the cables are fabricated by thermoplastics polyurethane. Figure 10b shows the sequence of robot swimming at the driving frequency of 1.5 Hz. The proposed design is simple and easy than other tensegrity fish robots. It was concluded that there was a quite difference between the experimental data and calculated data in regard to bending stiffness and cable width. There

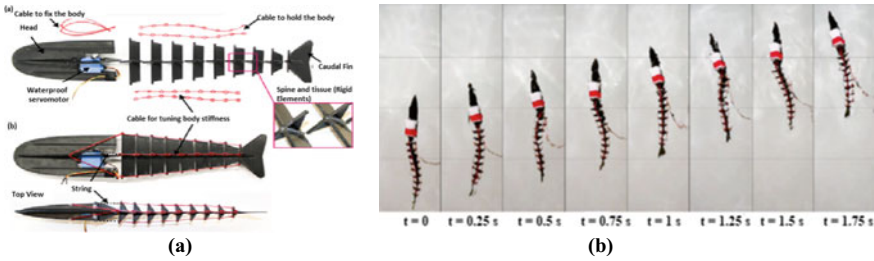


Fig. 10 **a** Dissembled robot consisting of a head part having servomotor which is waterproof and the body comprising several rigid elements and elastic cable and assembled robot with pre-stretched cables to make body under compression and in shape. **b** sequence of robot swimming at the driving frequency of 1.5 Hz [40]

were changes in the swimming speed and thrust force at different cable cross sections with the increase in driving frequency [40].

4 Recent Challenges and Future Perspectives

The remarkable properties of nature lead to the bring-up of a new revolution in the engineering field. The explosive combination of AM and nature make the fabricate product more superior than ever since. With the development of multi-material printing technology, nature-inspired composites can be well fabricated, but the major challenge is the control of particle orientation, which sometimes leads to unwanted property development and certain defects. So, this field needs to be investigated and explored. Apart from the orientation, there is a need to study the hidden mechanics of nature as nature is too vast.

5 Conclusion

It is inferred that the biomechanics behind the living organism and specially developed defense mechanisms like the shell of the armadillo, collapsible scale of the fish, and many similar superficial organs have led to the collaboration of biomimetics and AM. This conglomeration has resulted in the fabrication of complex geometries like the motion of a bionic fish, fin-shaped fan blade for improved aerodynamics, and bionic arms with touch and motion sensor fingers which mimics the arm of a human body. The AM fabrication process made it easier, quicker, and effective to produce mechanically durable component. Newer materials like honeycomb-based structures, metal matrix composites, and high entropy alloys can also be used to design mechanically and metallurgically improved components in a shorter period through process. However, this field of bio-mechanical design and fabrication is in

its nascent stage and requires further research. Many short comes like the high cost in metallic deposition, problems related to surface finish, and limited application of FDM for metallic components are yet to be explored.

References

1. Ritchie RO (2014) In pursuit of damage tolerance in engineering and biological materials. *MRS Bull* 39(10):880–890. <https://doi.org/10.1557/mrs.2014.197>
2. Meyers MA, McKittrick J, Chen PY (2013) Structural biological materials: critical mechanics-materials connections. *Science* (80) 339(6121):773–779. <https://doi.org/10.1126/science.1220854>
3. Meyers MA, Chen PY, Lopez MI, Seki Y, Lin AYM (2011) Biological materials: a materials science approach. *J Mech Behav Biomed Mater* 4(5):626–657. <https://doi.org/10.1016/j.jmbbm.2010.08.005>
4. Velasco-Hogan A, Xu J, Meyers MA (2018) Additive manufacturing as a method to design and optimize bioinspired structures. *Adv Mater* 30(52). <https://doi.org/10.1002/adma.201800940>
5. Arzt E (2006) Biological and artificial attachment devices: lessons for materials scientists from flies and geckos. *Mater Sci Eng C* 26(8):1245–1250. <https://doi.org/10.1016/j.msec.2005.08.033>
6. Wang Q, Meng Q, Wang P, Liu H, Jiang L (2015) Bio-inspired direct patterning functional nano thin micro lines: controllable liquid transfer. *ACS Nano* 9(4):4362–4370. <https://doi.org/10.1021/acs.nano.5b00861>
7. Studart AR (2016) Additive manufacturing of biologically-inspired materials. *Chem Soc Rev* 45(2):359–376. <https://doi.org/10.1039/c5cs00836k>
8. Zhang C, McAdams DA, Grunlan JC (2016) Nano/micro-manufacturing of bioinspired materials: a review of methods to mimic natural structures. *Adv Mater* 28(30):6292–6321. <https://doi.org/10.1002/adma.201505555>
9. Zadpoor AA, Malda J (2017) Additive manufacturing of biomaterials, tissues, and organs. *Ann Biomed Eng* 45(1):1–11. <https://doi.org/10.1007/s10439-016-1719-y>
10. Ramkumar J (2017) Additive manufacturing (NPTEL Lecture 5). Depart Mech Eng IIT Kanpur. <http://home.iitk.ac.in/~jrkumar/download/Lecture-5.pdf>
11. Jordan RS, Wang Y (2019) 3D printing of conjugated polymers. *J Polym Sci Part B Polym Phys* 57(23):1592–1605. <https://doi.org/10.1002/polb.24893>
12. Lewis JA (2006) Direct ink writing of 3D functional materials. *Adv Funct Mater* 16(17):2193–2204. <https://doi.org/10.1002/adfm.200600434>
13. Barry RA, Shepherd RF, Hanson JN, Nuzzo RG, Wiltzius P, Lewis JA (2009) Direct-write assembly of 3D hydrogel scaffolds for guided cell growth. *Adv Mater* 21(23):2407–2410. <https://doi.org/10.1002/adma.200803702>
14. Ginger DS, Zhang H, Mirkin CA (2004) The evolution of dip-pen nanolithography. *Angew Chemie - Int Ed* 43(1):30–45. <https://doi.org/10.1002/anie.200300608>
15. Smay JE, Cesarano J, Lewis JA (2002) Colloidal inks for directed assembly of 3-D periodic structures. *Langmuir* 18(14):5429–5437. <https://doi.org/10.1021/la0257135>
16. Gratson GM, Lewis JA (2005) Phase behavior and rheological properties of polyelectrolyte inks for direct-write assembly. *Langmuir* 21(1):457–464. <https://doi.org/10.1021/la048228d>
17. Ahn BY et al (2009) Omnidirectional printing of flexible, stretchable, and spanning silver microelectrodes. *Science* (80) 323(5921):1590–1593. <https://doi.org/10.1126/science.1168375>
18. Gu GX, Su I, Sharma S, Voros JL, Qin Z, Buehler MJ (2016) Three-dimensional-printing of bio-inspired composites. *J Biomech Eng* 138(2). <https://doi.org/10.1115/1.4032423>
19. Köpplmayr T, Mühlberger M (2016) Inkjet printing of polylactic acid on substrates prepared by fused deposition modeling and its potential for selective surface finishing. *J Appl Polym Sci* 133(23):1–8. <https://doi.org/10.1002/app.43527>

20. Melchels FPW, Feijen J, Grijpma DW (2010) A review on stereolithography and its applications in biomedical engineering. *Biomaterials* 31(24):6121–6130. <https://doi.org/10.1016/j.biomaterials.2010.04.050>
21. Martin JJ, Fiore BE, Erb RM (2015) Designing bioinspired composite reinforcement architectures via 3D magnetic printing. *Nat Commun* 6:1–7. <https://doi.org/10.1038/ncomms9641>
22. Kumar S, Hofmann M, Steinmann B, Foster EJ, Weder C (2012) Reinforcement of stereolithographic resins for rapid prototyping with cellulose nanocrystals. *ACS Appl Mater Interfaces* 4(10):5399–5407. <https://doi.org/10.1021/am301321v>
23. Sommer MR, Erb RM, Studart AR (2012) Injectable materials with magnetically controlled anisotropic porosity. *ACS Appl Mater Interfaces* 4(10):5086–5091. <https://doi.org/10.1021/am301500z>
24. Melchels FPW, Bertoldi K, Gabbriellini R, Velders AH, Feijen J, Grijpma DW (2010) Mathematically defined tissue engineering scaffold architectures prepared by stereolithography. *Biomaterials* 31(27):6909–6916. <https://doi.org/10.1016/j.biomaterials.2010.05.068>
25. Melchels FPW, Domingos MAN, Klein TJ, Malda J, Bartolo PJ, Huttmacher DW (2012) Additive manufacturing of tissues and organs. *Prog Polym Sci* 37(8):1079–1104. <https://doi.org/10.1016/j.progpolymsci.2011.11.007>
26. Dizon JRC, Espera AH, Chen Q, Advincula RC (2018) Mechanical characterization of 3D-printed polymers. *Addit Manuf* 20:44–67. <https://doi.org/10.1016/j.addma.2017.12.002.S>
27. Tappa K, Jammalamadaka U (2018) Novel biomaterials used in medical 3D printing techniques. *J Funct Biomater* 9(1). <https://doi.org/10.3390/jfb9010017>
28. Momeni F, Mehdi Hassani SMN, Liu X, Ni J (2017) A review of 4D printing. *Mater Des* 122:42–79. <https://doi.org/10.1016/j.matdes.2017.02.068>
29. Gao B, Yang Q, Zhao X, Jin G, Ma Y, Xu F (2016) 4D bioprinting for biomedical applications. *Trends Biotechnol* 34(9):746–756. <https://doi.org/10.1016/j.tibtech.2016.03.004>
30. Li YC, Zhang YS, Akpek A, Shin SR, Khademhosseini A (2017) 4D bioprinting: the next-generation technology for biofabrication enabled by stimuli-responsive materials. *Biofabrication* 9(1):1–16. <https://doi.org/10.1088/1758-5090/9/1/012001>
31. Yuh J (2000) Design and control of autonomous underwater robots: a survey. *Auton Robots* 8(1):7–24. <https://doi.org/10.1023/A:1008984701078>
32. B M, Aref Soltani RH, Noroozi R (2020) 3D Printing on-water sports boards. *Polym Artic* 12(250):1–18
33. Zdravkova A, Mircheski I, Sidorenko S (2020) Bio-inspired approach for innovative design of knee protectors for recreational sports. *FME Trans* 48(4):849–854. <https://doi.org/10.5937/fme2004849Z>
34. Zhu W et al (2015) 3D-Printed artificial microfish. *Adv Mater* 27(30):4411–4417. <https://doi.org/10.1002/adma.201501372>
35. Zhu W et al (2017) Direct 3D bioprinting of prevascularized tissue constructs with complex microarchitecture. *Biomaterials* 124:106–115. <https://doi.org/10.1016/j.biomaterials.2017.01.042>
36. Chen Z et al (2018) Additive manufacturing of honeybee-inspired microneedle for easy skin insertion and difficult removal. *ACS Appl Mater Interfaces* 10(35):29338–29346. <https://doi.org/10.1021/acsami.8b09563>
37. Ling J et al (2017) Effect of honeybee stinger and its microstructured barbs on insertion and pull force. *J Mech Behav Biomed Mater* 68(August 2016):173–179. <https://doi.org/10.1016/j.jmbbm.2017.01.040>
38. Silva M, Felismina R, Mateus A, Parreira P, Malça C (2017) Application of a hybrid additive manufacturing methodology to produce a metal/polymer customized dental implant. *Proce Manuf* 12(December 2016): 150–155. <https://doi.org/10.1016/j.promfg.2017.08.019>
39. Wang S et al (2020) Noise reduction of automobile cooling fan based on bio-inspired design. *Proc Inst Mech Eng Part D J Automob Eng*. <https://doi.org/10.1177/0954407020959892>
40. Shintake J, Zappetti D, Peter T, Ikemoto Y, Floreano D (2020) Bio-inspired tensegrity fish robot. *Proc-IEEE Int Conf Robot Autom* 2887–2892. <https://doi.org/10.1109/ICRA40945.2020.9196675>

41. Leftwich MC, Tytell ED, Cohen AH, Smits AJ (2012) Wake structures behind a swimming robotic lamprey with a passively flexible tail. *J Exp Biol* 215(3):416–425. <https://doi.org/10.1242/jeb.061440>
42. Qiu K et al (2018) 3D printed organ models with physical properties of tissue and integrated sensors. *Adv Mater Technol* 3(3):1–9. <https://doi.org/10.1002/admt.201700235>

Taguchi Optimization of Mechanical Properties in Al-Kaoline Metal Matrix Composite Fabricated Through Powder Metallurgy Technique



V. S. S. Venkatesh and Ashish B. Deoghare

Abstract Aluminium-based metal matrix composites are widely used in automobile industry to fabricate parts like pistons, connecting rods and brake disc, etc., due to the inherent properties like lighter weight, higher corrosion resistance and ease of fabrication of aluminium metal matrix composites compared to other matrix materials like Mg and Cu. In this paper Al- $x\%$ Kaoline ($x = 0, 5, 10, 15, 20, 25$) MMC fabricated through powder metallurgy technique by applying the pressure of 350, 400 and 450 MPa for each reinforcement percentage. Taguchi optimization technique was employed to identify the optimal processing parameters for fabricating Al-Kaoline MMC. Two processing parameters, i.e. % reinforcement and compaction pressure, were optimized for corresponding values of hardness, ultimate tensile strength, compression strength. Experiments were performed based on L18 orthogonal array. The response of the processing parameters was investigated using analysis of variance (ANOVA) and the results showed that % reinforcement is most influencing processing parameter for output responses. Finally, conformation test was performed based on optimal parameters to validate the results. The obtained hardness, ultimate tensile stress and compression strength at corresponding optimal process parameters were 169 VHN, 312 MPa and 309 MPa, respectively.

Keywords Kaoline reinforcement · Metal matrix composite · Taguchi approach · ANOVA

V. S. S. Venkatesh (✉) · A. B. Deoghare
Department of Mechanical Engineering, NIT Silchar, Silchar, India
e-mail: vssvenkateshnits@gmail.com

A. B. Deoghare
e-mail: ashishdeoghare@gmail.com

© The Author(s), under exclusive license to Springer Nature Singapore Pte Ltd. 2023
T. S. Sudarshan et al. (eds.), *Recent Advancements in Mechanical Engineering*,
Lecture Notes in Mechanical Engineering,
https://doi.org/10.1007/978-981-19-3266-3_24

313

1 Introduction

Now a days there is an era of using metal matrix composites due to their tailorability property and higher strength-to-weight ratio makes suitable for fabricating automobile pistons and brake discs in automobile industry [1, 2]. Different types of ceramic reinforcements like SiC, B₄C, reinforced in Al matrix improve the mechanical properties of matrix material [3, 4]. Kaoline is low-cost ceramic reinforcements which contains oxides of Al and Si such as Al₂O₃, Si₂O₃ and Fe₂O₃, which processes higher hardness and wear resistance [5]. The main requirement in processing of metal matrix composite is to obtain the higher hardness and strength which is suitable for particular application. Different combinations of input variables are available like % reinforcement and compaction pressure which should be selected properly to obtain the maximum value of mechanical properties with minimizing the experiment cost. In this present work, aluminium–Kaoline metal matrix composite fabricated through powder metallurgy technique by varying reinforcement percentage and compaction pressure. Mechanical properties like hardness, UTS and compression strength are noted at these different levels based on L18 orthogonal array and partial experiments were conducted at optimal levels in order to reduce number of experiments. Optimal process parameters were identified by using Taguchi approach and ANOVA is carried out to find the % contribution of each parameter on the output response.

2 Taguchi Technique

Taguchi optimization technique is orthogonal array-based experiment which will arrange input controlling parameters for experiments by minimizing variance. This method was used by various engineering applications to obtain the optimal performance characteristics. Taguchi approach is adopted to experiment design to:

- To minimize the variance in the targeted value.
- Design the process design or process as robust to required output.

Taguchi developed three-step approach for the optimization of product or process, viz. system design, parameter design and tolerance design [6]. System design represents the knowledge regarding the engineering design of component and parameter design involves the selection of optimal process parameters which enhances the required outcome from the developed component [7]. Tolerance design gives the optimal input process parameters for designing the engineering component. Depending on the number of input controllable parameters and experimental result an orthogonal array was developed. S/N (signal to noise) ratio determines how closely our design to minimal variance values. Depending on the output response the available stages in S/N ratio was selected which has smaller is better, larger is better and nominal is better [8, 9]. Despite from the Taguchi approach ANOVA gives the effect of different processing parameters such as % reinforcement, compaction pressure

on the hardness and UTS and compression strength of the composite such that the optimal combination of input parameters can be selected for further design of the engineering component. Optimization of Taguchi design can be performed by the following steps. (a) Design of factorials, (b) measurement of hardness, UTS and compression strength, (c) design of L18 orthogonal array, (d) finding of S/N ratio and ANOVA, (e) calculation of hardness, UTS, compression strength and (f) conformation test for the results obtained from the Taguchi approach and experimental data.

3 Fabrication of Composite and Experimental Details

3.1 Fabrication of Composite

Al-Kaoline MMC was developed by using powder metallurgy technique by varying the Kaoline reinforcement from 0 to 25% in steps of 5%. In each percentage of reinforcement composite three samples are made by the application of pressure of 350, 400 and 450 MPa during the compaction stage of powder metallurgy technique. Initially the matrix and reinforcement powders in calculated proportions are ball milled to induce the strain hardening between these powders and to disperse the reinforcements uniformly throughout the matrix aluminium [10–13]. The milled powders are placed in pre-moulded dies to compact the blended powders by the application of pressure of 350 MPa, 400 MPa and 450 MPa, respectively, to initiate the cold welding between these matrix and reinforcement powders. These compacted specimens are sintered in muffle furnace at 500 °C for 8 h to improve grain refinement and formation of closed intermetallic bond between Al particle and Kaoline powder particles.

3.2 Taguchi Based Experimental Design

Series of experiments were conducted based on L18 orthogonal array to minimize the number of experiments. L18 orthogonal array comprises of eighteen rows and two columns. The number of degrees of freedom is 17 which was obtained by subtracting one from number of rows. Mixed-level approach was chosen to formulate the orthogonal array table. One parameter with three levels and second parameter with six levels are selected for analysis. MINITAB 14 software was used to get the values for S/N ratios and response tables for hardness and UTS and compression strength values.

The S/N ratio for maximum hardness, UTS and compression strength can be expressed by selecting “Higher is better” characteristic which can be estimated as logarithmic equation as shown.

$$\eta = -10 \log \left(\frac{1}{n} \sum_{i=1}^n \frac{1}{y_i^2} \right) \tag{1}$$

4 Result and Discussion

4.1 Optimization of Process Parameters for Hardness

The hardness results according to L18 orthogonal array is shown in Table 1. Larger the better is suitable characteristic for hardness. From *S/N* ratios graph it was observed that hardness value is maximum at fifth level of reinforcement and third level of compaction pressure as shown in Fig. 1. Based on the percentage of contribution, the most significant parameter will be discriminated towards the hardness.

Table 1 Hardness values with *S/N* ratios

S. No.	% Reinforcement	Compaction pressure (MPa)	Hardness (VHN)	<i>S/N</i> ratio
1	0	350	69	36.7770
2	0	400	74	37.3846
3	0	450	79	37.9525
4	5	350	79	37.9525
5	5	400	83	38.3816
6	5	450	89	38.9878
7	10	350	96	39.6454
8	10	400	101	40.0864
9	10	450	105	40.4238
10	15	350	146	43.2871
11	15	400	152	43.6369
12	15	450	149	43.4637
13	20	350	176	44.9103
14	20	400	169	44.5577
15	20	450	179	45.0571
16	25	350	147	43.3463
17	25	400	149	43.4637
18	25	450	141	42.9844

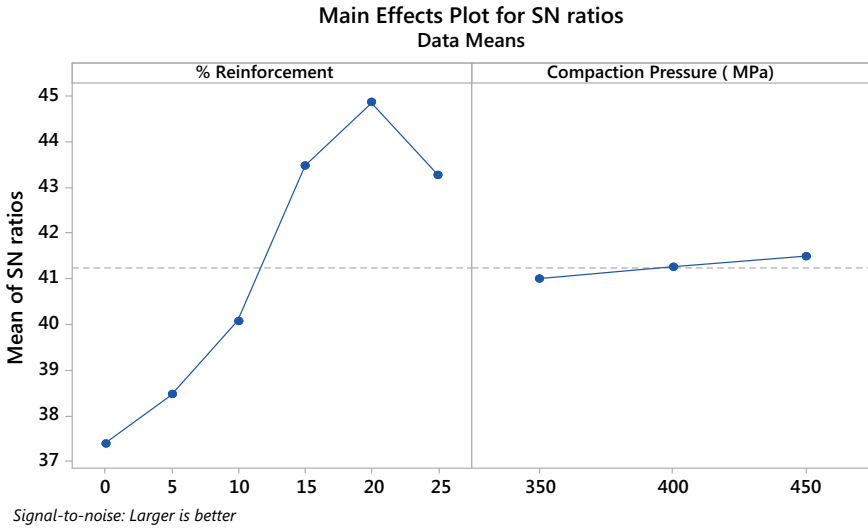


Fig. 1 Main effects plot for S/N ratio of hardness

Table 2 Analysis of variance table for hardness

Source	DF	Seq SS	Adj SS	Adj MS	% Contribution
% Reinforcement	5	138.678	138.678	27.7356	98.68
Compaction pressure (MPa)	2	0.727	0.727	0.3635	0.51
Residual error	10	1.128	1.128	0.1128	0.8026
Total	17	140.533			100

4.1.1 Analysis of Variance (ANOVA) for Hardness

Table 2 represents the ANOVA results for hardness. Last column of table represents % contribution which tells about how much that particular parameter influences the response. It was clear that % contribution has major contribution and compaction pressure has least contribution on hardness response.

4.1.2 Optimal Condition for Higher Hardness

It can be noticed that higher value of hardness is at fifth level of % reinforcement and compaction pressure is at any level say level 3, i.e. 450 MPa. The optimum process parameters for hardness are represented in Table 3.

Table 3 Optimal condition for hardness

S. No.	Parameter	% Contribution	Level description
1	% Reinforcement	98.68	(20) ₅
2	Compaction pressure (MPa)	0.51	(450) ₃

Table 4 Conformation table for hardness result

Parameter	Optimal parameter (A ₅ B ₃)		Mean parameter (A ₃ B ₂)
	experimental	predicted	
Hardness (VHN)	89.05	91.0	109
S/N ratio	44.08	45.081	40.08

% Error = 2.270

4.1.3 Conformation Test for Optimal Hardness Result

Conformation test was done to validate the experimental result with the results obtained from the Taguchi. Based on the optimal results obtained from Taguchi, Experiment Was conducted at the optimal response and the value of *S/N* ratio was found based on the formula as described in equation in 1. This value was compared with the *S/N* ratio value at optimal response. The % error was calculated based on these experimental and Taguchi values (Table 4).

4.2 Optimization of Process Parameters for Ultimate Tensile Strength (MPa) and Compression Strength

The experimental results obtained according to L18 orthogonal array are shown in Table 5. Larger is better is the suitable characteristic for ultimate tensile strength and compression strength. *S/N* ratio is maximum at fifth level of reinforcement and third level of compaction pressure for UTS and Fifth level of % reinforcement and second level of compaction pressure for compression strength (Figs. 2 and 3).

4.2.1 Analysis of Variance (ANOVA) for UTS and Compression Strength

Tables 6 and 7 represent the ANOVA results for UTS and compression strength, respectively. Last column of table represents % contribution which tells about how much that particular parameter influences the response. It was clear that % contribution has major contribution and compaction pressure has least contribution on both UTS and compression strength value response.

Table 5 UTS and compression strength with S/N ratios

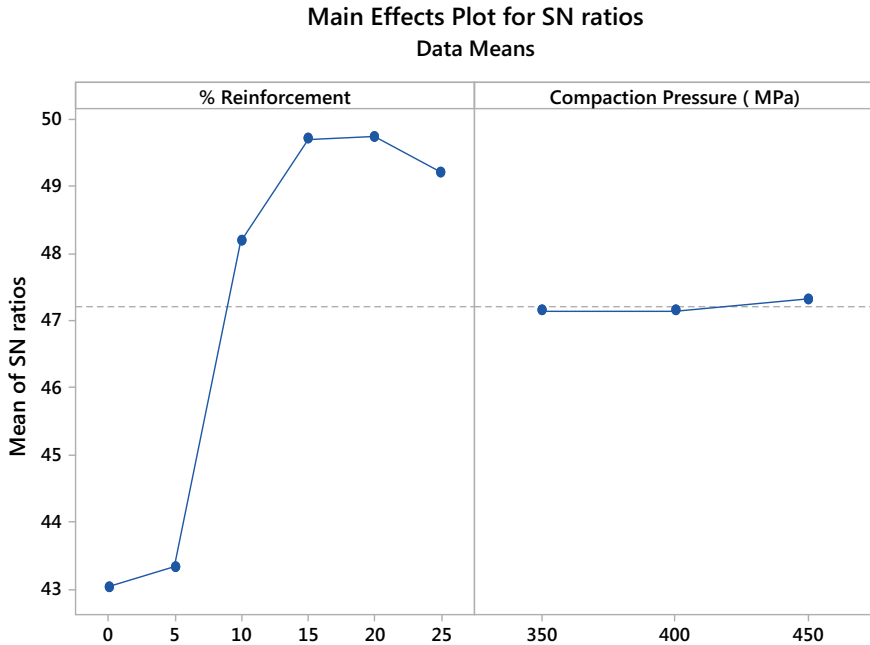
S. No.	% Reinforcement	Compaction pressure (MPa)	UTS (MPa)	Compression strength (MPa)	S/N ratio for UTS	S/N ratio for compression strength (MPa)
1	0	350	139	152	36.7770	42.8603
2	0	400	141	149	37.3846	42.9844
3	0	450	145	151	37.9525	43.2274
4	5	350	147	152	37.9525	43.3463
5	5	400	142	154	38.3816	43.0458
6	5	450	151	156	38.9878	43.5735
7	10	350	250	281	39.6454	47.9588
8	10	400	259	291	40.0864	48.2660
9	10	450	261	290	40.4238	48.3328
10	15	350	309	309	43.2871	49.7992
11	15	400	297	314	43.6369	49.4551
12	15	450	312	316	43.4637	49.8831
13	20	350	296	329	44.9103	49.4258
14	20	400	312	331	44.5577	49.8831
15	20	450	314	339	45.0571	49.9386
16	25	350	297	314	43.3463	49.4551
17	25	400	289	317	43.4637	49.2180
18	25	450	281	304	42.9844	48.9741

4.2.2 Optimal Condition for UTS and Compression Strength

It can be observed that maximum value of UTS is at fourth level of % reinforcement and compaction pressure is at any level say level 3, i.e. 450 MPa. For compression strength maximum values are fifth level of % reinforcement and second level of compaction pressure. The optimum process parameters for UTS and compression strength are represented in Tables 8 and 9, respectively.

4.2.3 Conformation Test for Optimal UTS and Compression Strength Result

See Tables 10 and 11.



Signal-to-noise: Larger is better

Fig. 2 Main effect plot for S/N ratio of UTS

5 Conclusion

This paper summarizes the Taguchi design of experiment and optimization of parameters for the mechanical processing of Al-Kaoline metal matrix composite. The below interferences are drawn from the experiment and Taguchi approach.

- The mechanical behaviour of Al-Kaoline metal matrix composite was studied by varying the % reinforcement and compaction pressure. The experimental results conclude that the improvement in the mechanical properties of the composite is compared to unreinforced Al metal.
- For all three responses, i.e. hardness, UTS and compression strength, % reinforcement is more influential parameter and the effect of compaction pressure was insignificant during the fabrication of composite.
- The % of contribution of reinforcement contribution was 98.68, 99.58 and 99.85%. Confirmation test concludes that the experimental result and predicted values are in close to each other and the % error for Hardness, UTS and compression strength are below 10%.

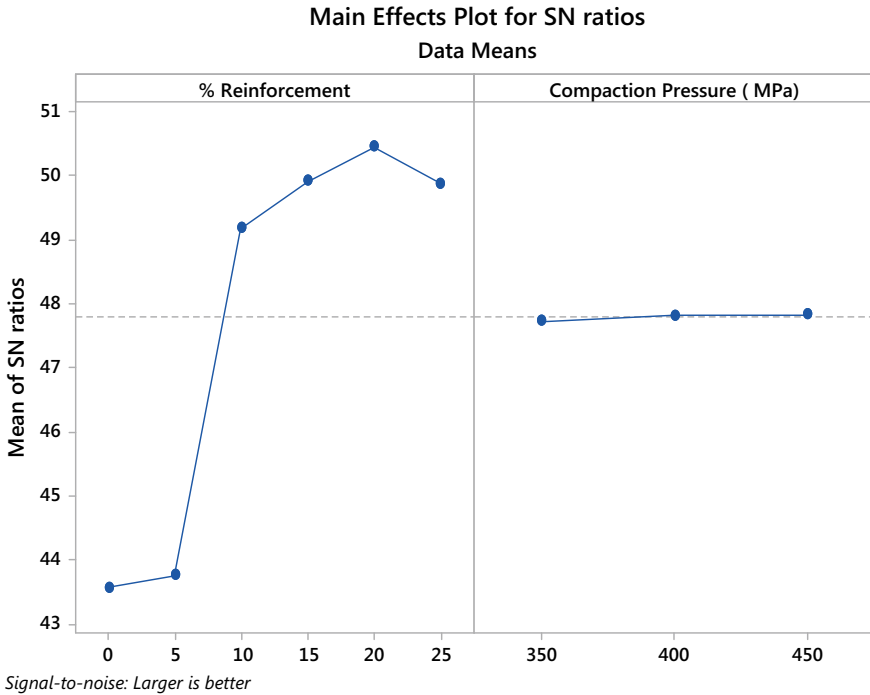


Fig. 3 Main effect plot for *S/N* ratio of compression strength

Table 6 Analysis of variance (ANOVA) for UTS (MPa)

Source	DF	Seq SS	Adj SS	Adj MS	% Contribution
% Reinforcement	5	150.927	150.927	30.1854	99.58
Compaction pressure (MPa)	2	0.131	0.131	0.0656	0.086
Residual error	10	0.538	0.538	0.0538	0.354
Total	17	151.596			

Table 7 Analysis of variance (ANOVA) for compression strength

Source	DF	Seq SS	Adj SS	Adj MS	% Contribution
% Reinforcement	5	156.025	156.025	31.2051	99.85
Compaction pressure (MPa)	2	0.037	0.037	0.0183	0.023
Residual error	10	0.191	0.191	0.0191	0.122
Total	17	156.253			

Table 8 Optimum condition for UTS

S. No.	Parameter	% Contribution	Level description
1	% Reinforcement	99.58	(15) ₄
2	Compaction pressure (MPa)	0.086	(450) ₃

Table 9 Optimum condition for compression strength

S. No.	Parameter	% Contribution	Level description
1	% Reinforcement	99.85	(20) ₅
2	Compaction pressure (MPa)	0.023	(400) ₂

Table 10 Conformation test for UTS (MPa)

Parameter	Optimal parameter (A ₄ B ₃) experimental predicted		Mean parameter (A ₃ B ₂)
UT S (MPa)	311.09	312.3	298
S/N ratio	48.08	49.8332	46

% Error = 3.64

Table 11 Conformation test for compression strength (MPa)

Parameter	Optimal parameter (A ₅ B ₂) Experimental predicted		Mean parameter (A ₃ B ₂)
Compression strength (MPa)	319.5	321.3	304
S/N ratio	49.08	50.4877	48.9

% Error = 2.86

References

1. Manohar G, Paney KM, Maity SR, Effect of compaction pressure on mechanical properties of AA7075/B4C/graphite hybrid composite fabricated by powder metallurgy techniques. Mater Today Proc. <https://doi.org/10.1016/j.matpr.2020.05.194>
2. Venkatesh VSS, Deoghare AB (2020) J Phys Conf Ser 1451:012025. IOP Publishing. <https://doi.org/10.1088/1742-6596/1451/1/012025>
3. Taha MA (2001) Practicalization of cast metal matrix composites. Mater Des 22:231–241
4. Surappa MK (2003) Aluminium matrix composites: challenges and opportunities. Sadhana 28:319–334
5. Venkatesh VSS, Deoghare AB, Fabrication and mechanical behaviour of Al-Kaoline metal matrix composite fabricated through powder metallurgy technique. Mater Today Proc. <https://doi.org/10.1016/j.matpr.2020.10.021>
6. Ghani AK, Choudhary LA, Husni (2002) The influence of machining parameters on vibration signals in multi-tool turning process. J Mater Process Technol 127:17–22

7. Ozel T, Hsu TK, Zeren E (2005) Effects of cutting edge geometry, workpiece hardness, feed rate and cutting speed on surface roughness and forces in finish turning of hardened AISI H13 steel. *Int J Adv Manufact Technol* 25:262–269
8. Oktem H, Erzurumlu T, Col M (2006) Optimization of surface roughness and material removal rate in milling of AISI 1005 carbon steel using Taguchi approach. *Int J Adv Manufact Technol* 28:694–700
9. kumar R, Kumar K, Bhowmik S (2014) Optimization of mechanical properties of epoxy based wood dust reinforced green composite using Taguchi method. *Proc Mater Sci* 5:688–698
10. Zaki MU, Hussain S, Impact of addition of manganese and boron carbide on aluminium metal matrix composites using powder metallurgy process. *Mater Today Proc.* <https://doi.org/10.1016/j.matpr.2020.10.562>
11. Raynova S, Yang F, Bolzoni L, Mechanical behaviour of induction sintered blended elemental powder metallurgy Ti alloys. *Mater Sci Eng: A.* <https://doi.org/10.1016/j.msea.2020.140157>
12. Wang HK, Wang ZH, Wang MC (2020) Using the Taguchi method for optimization of the powder metallurgy forming process for industry 3.5. *Comput Ind Eng* 148(October):106635. <https://doi.org/10.1016/j.cie.2020.106635>
13. Venkatesh VSS, Deoghare AB, Effect of controllable parameters on mechanical and Tribological behaviour of metal matrix composites: a review. *Recent Adv Mech Eng.* https://doi.org/10.1007/978-981-15-7711-6_31
14. Perez H, Rios J, Diez E, Vizan A (2008) Estimation of cutting forces in micromilling through the determination of specific cutting pressures. *J Mater Process Technol* 201:486490

Fabrication Based Analysis of Super-Hydrophobic Surface



Avinash Kumar, Sushant Negi, and Simanchal Kar

Abstract A superhydrophobic surface is a modified texture or coating that has the ability to repelling water droplets on its surface. Such coated surface inhibits chemical corrosion and applicable in various manufacturing industries where corrosion is inevitable. Currently, the superhydrophobic coating process can be fabricated typically by following different methods such as electrochemical deposition, electroless plating, sol-gel, and chemical etching methods. In this paper, superhydrophobic structures are studied and deal with a deep understanding to enhance corrosion resistance and chemically stable long-term industrial applications. The superhydrophobic surfaces concerning various wetting models such as Young's model, Wenzel model, and Cassie-Baxter model measure the suitable sliding angle and water contact angle. To get the superhydrophobic surfaces sliding angle must be less than 10° , and the water contact angle should be higher than 150° . The further various methodology models of surface preparation are presented to create superhydrophobic. Moreover, the multiple strategies for improving corrosion resistance, self-cleaning surfaces, drag reduction, chemical and mechanical stability are reviewed and discussed to modify the superhydrophobic structure.

Keywords Superhydrophobic structure · Electroless plating · Sol-gel method · Young's model · Wenzel model · Cassie-Baxter model

A. Kumar (✉) · S. Negi · S. Kar
Mechanical Engineering, National Institute of Technology Silchar, Silchar, Assam, India
e-mail: avinash_rs@mech.nits.ac.in

S. Negi
e-mail: sushant@mech.nits.ac.in

S. Kar
e-mail: simanchal@mech.nits.ac.in

1 Introduction

The superhydrophobic surface was first observed in nature where surfaces have low energy surface to resist wetting on the surface of butterfly wings, lotus leaf, peanut leaf, red rose petal, water strider legs, and fish scale, etc. [1–4]. Owing to its unique surface property, the water contact angle (WCA) is larger than 150° , and the sliding angle smaller than 10° was required, which minimizes slippery and stickiness properties of the superhydrophobic surface against water. Higher WCA values allow the droplets to maintain a spherical shape on the surface, reduce their surface area, and lower WCA spreads [5, 6]. Presently, superhydrophobic surfaces effectively deal with corrosion resistance, self-cleaning surfaces, drag reduction, anti-icing properties, and anti-properties and antibacterial properties on a solid surface [6–9]. In this paper, an exhaustive analysis of superhydrophobic based on the surface preparation process is discussed. There are primarily four popular methods of producing superhydrophobic property. Such an analytical study is limited due to the limited availability of published work based on this new technology. The paper aims to associate the different processes under a single analytical study to help the researcher compare the parameters and the outcomes more effectively. Initially, the underlying parameters that govern the superhydrophobic structure are discussed, followed by the process analysis. The superhydrophobic coating is generally influenced by the surface characteristics, as discussed below.

1.1 Wettability

Wetting is the potential of liquid to keep in contact with a solid surface. It is determined by a force balance between adhesive and cohesive force and measured contact angle of a surface. It reflects the wetting ability of the droplet on it. The contact angle is determined, which is formed when a solid and liquid surface is in touch with each other [1, 10]. The angle formed by the intersection of solid, liquid, and solid–gas interface is known as the contact angle. Larger contact angles are formed when there is a lower contact area between solid and liquid, whereas smaller contact angles are observed when the liquid is dispersed on the surface. Figure 1 shows the contact angle at the different conditions of wetting properties.

Wettability is controlled by two parameters they are free to surface energy and surface roughness, where the impact of both is more influence for controlling the wettability [12].

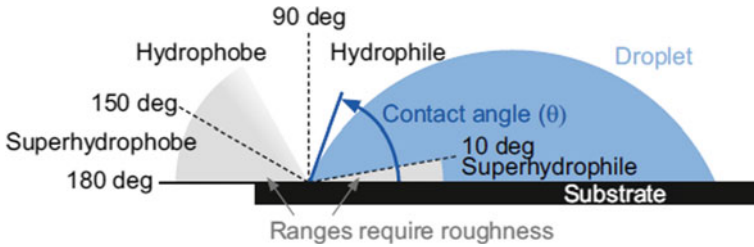


Fig. 1 Contact angles of wetting properties [11]

1.2 Surface Energy

Surface energy plays a vital role in the generation of superhydrophobic surfaces. The superhydrophobic surface can be improved by reduce in surface energy. A surface-active agent is used for lowering the surface energy. Due to the presence of CF_2 and CF_3 groups in fluoroalkyl silanes, this silane group is efficient for reducing the surface energy. Stearic acid and polymer are also used to reduce the surface energy due to their low cost and less hazardous to the environment compared to fluoroalkyl silanes [6, 12–14].

1.3 Surface Roughness

The superhydrophobic surface can be helpful due to an uneven rough surface. Such surfaces are needed because air bubbles are seized on the surface’s up and downs, which does not allow water to contact all surface points. Due to low surface energy and air, it does not allow water to penetrate the valley. Due to this reason, water slips on the surface easily, and a reduction in friction was achieved [12, 13].

Since the wetting angle plays a key purpose in defining the wettability property, it is essential to study the surface’s wetting angle. Various wetting models are discussed below to measure the mechanism of transition from hydrophobic to superhydrophobic concerning superhydrophobic surfaces such as Young’s model, Wenzel model, and Cassie–Baxter model.

2 Wetting Models

2.1 Young’s Model

The first wetting model was given by Young’s in 1805. This model does not consider the surface roughness of the solid surface, and for a drop of liquid on a flat surface, the wetting equation is given below:

$$\cos \theta = \gamma_{SG} - \gamma_{SL} / \gamma_{LG} \quad (1)$$

where θ = contact angle, γ_{SG} = surface free energy of solid/gas, γ_{SL} = surface free energy of solid/liquid, γ_{LG} = surface free energy of liquid/gas. However, this model is applicable for the ideally smooth surface only; hence, Wenzel presented a modified model [12, 15].

2.2 Wenzel Model

Some surfaces are not smooth in most cases, so the Young's model could not be determined correctly for the contact angle. Thus, the Wenzel equation was proposed [12, 13]. This model equation shows wetting of the surface occurs uniformly.

$$\cos \theta_w = r \cos \theta \quad (2)$$

where θ_w = Wenzel contact angle, θ = Young's contact angle, r = surface roughness factor. This model is only applicable to the homogenous interfacial areas, not for non-homogeneous surfaces. So, the Cassie–Baxter model was developed to incorporate the Wenzel model's limitation [12].

2.3 Cassie–Baxter Model

Cassie and Baxter give a model for heterogeneous surfaces in 1944. It mainly consists of two parts; the first one includes a surface fraction f_1 , and contact angle of θ_1 , and the other part comprises surface fraction f_2 , and contact angle θ_2 , and hence, the contact angle is defined as:

$$\cos \theta = f_1 \cos \theta_1 + f_2 \cos \theta_2 \quad (3)$$

where θ = Cassie and Baxter contact angle and f_1 is the ratio of surface area that liquid is in contact with solid and f_2 is the ratio of the area in contact with air packets confining inner side of surface cavities ($f_1 + f_2 = 1$). It was assumed that the liquid is in contact with the surface at the roughness tip, and several air pockets are trapped below the liquid. Further, the part of the surface where the air is trapped is not wetted by the liquid, and the air between the solid, liquid θ_2 will make a contact angle of 180° [12, 13, 16]. Thus, the equation is written as

$$\cos \theta_{CB} = f_s (\cos \theta_s + 1) \quad (4)$$

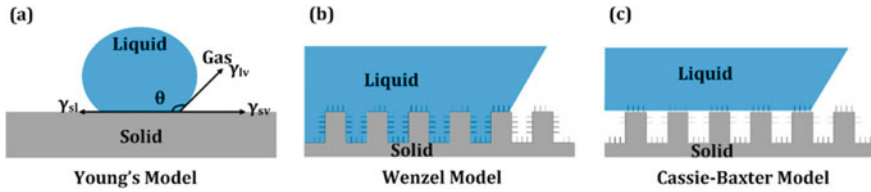


Fig. 2 Wetting models. a Young, b Wenzel, and c Cassie–Baxter wetting models [17]

where f_s is the fractional solid surface with a contact angle of θ_s . The wetting model is shown in Fig. 2.

The superhydrophobic coating is currently developed through four typical known processes, as discussed in the following section.

3 Fabrication Methods

At present, there are several methods used for the fabrication of superhydrophobic coating. Some of them are discussed below.

3.1 Electrodeposition Method

Electrodeposition is an in situ metallic coating deposition process using an electric current on a conductive material immersed in a salt solution. Various processing techniques such as anodic deposition, and deposition using galvanic cells are utilized for the formation of superhydrophobic coating or surface [18–20]. A schematic diagram of an electrodeposition process to produce a superhydrophobic coating is shown in Fig. 3.

Research work related to this process is available in abundance owing to the simplicity of the process. The significant research works are discussed in this section.

Liu et al. [19] fabricated the superhydrophobic surfaces on Mg alloy substrate via the electrodeposition method and reported the water contact angle is about $160.8 \pm 1^\circ$ and sliding angle $1.8 \pm 1^\circ$. Morphology shows cauliflower-like structures that can capture a considerable amount of air. Further, the author’s Li and Yin [22] created a similar superhydrophobic Cu–Zn coating on a steel substrate using the electrodeposition method. They obtained the highest static contact angle of 154.73° and a sliding angle of 6.5° . Sarkar et al. [23] reported aluminum stearate thin films on copper substrates for superhydrophobic coating. The results found that the water contact angle is about $161 \pm 1^\circ$ and contact angle hysteresis $2 \pm 1^\circ$. They obtained a uniform porous structure with a surface roughness of $3\mu\text{m}$ on a copper substrate, polarization resistance, an impedance value of thin films of $962\text{ k}\Omega\text{cm}^2$ and

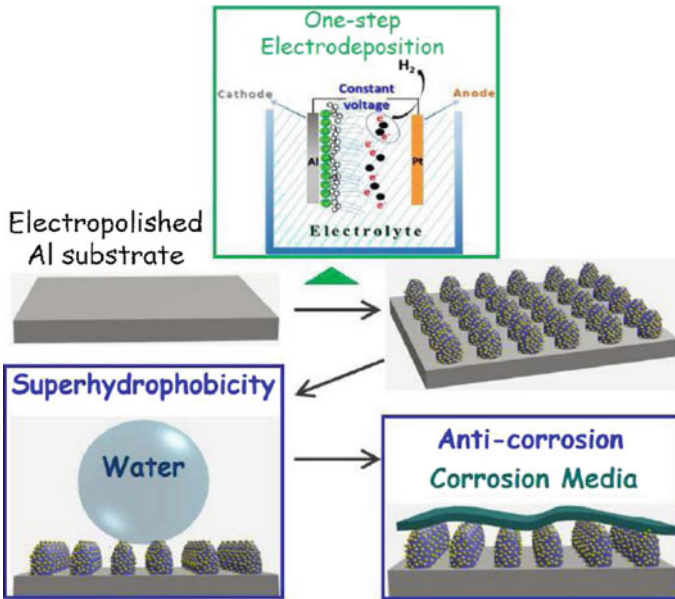


Fig. 3 Schematic diagram of an electrodeposition process to produce superhydrophobic coating [21]

10 M Ω cm², respectively. Salehi et al. [24] fabricated a superhydrophobic nanocomposite of Ni–TiO₂ on copper substrate by electrodeposition process. They obtained the highest water contact angle of 151.6° and a sliding angle of 6.2°. SEM images of surface morphology show snail-like structure indicating deposition of Ni on copper increased the surface roughness effectively. Shen et al. [25] experimented with superhydrophobic nickel coating on graphite substrate by electrodeposition process. The substrate was polished with different grit sandpapers and rinsed with DI water; the solution's temperature was 50 °C, and PH was adjusted 4.0 with ammonia. The proposed static water contact angle was observed as 155.4°, sliding angle 6.5°, and morphology shows a cauliflower-like surface. However, the process has one major disadvantage of non-uniform growth of coatings, especially at corners and thin sections. The next process has a similar significance owing to its cost-effectiveness and simpler method.

3.2 Electroless Plating

Electroless plating is a chemical reduction process that depends on the nickel ions' catalytic reduction process in an aqueous solution. It is the simplest and cost-less method of coating process without electricity [25–27]. An electroless bath set-up for surface coating is shown in Fig. 4. At present, owing to its ease of fabrication

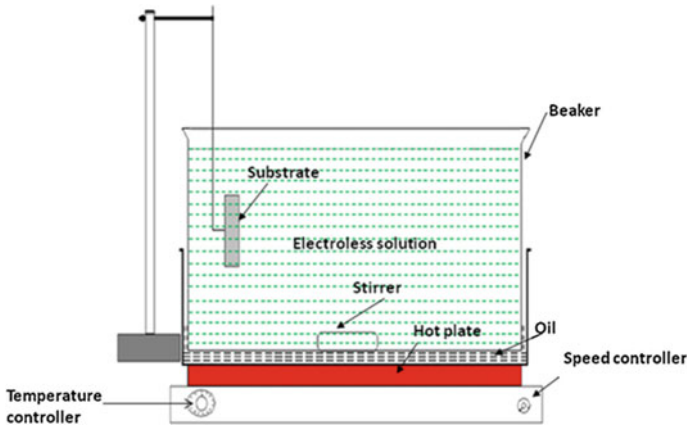


Fig. 4 Electroless bath set-up [28]

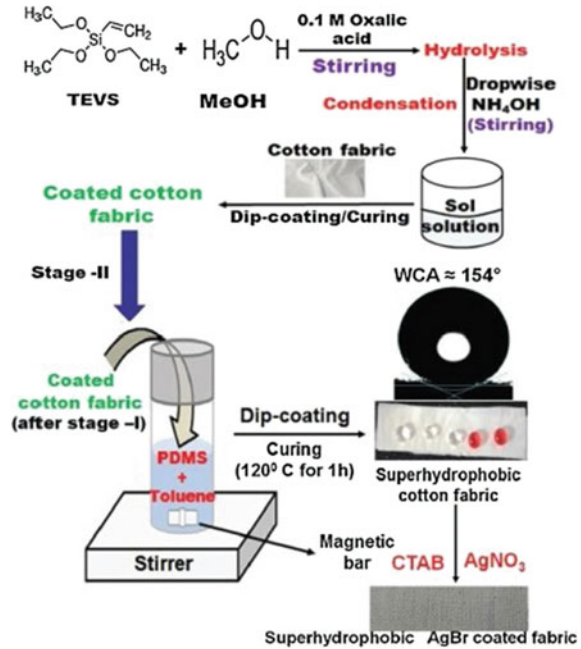
and better coating properties, electroless plating has gained a lot of interest from researchers. A few relevant articles were studied to understand the parameter effect and the wettability conditions, and results are presented as follows.

Wang et al. [29] studied super hydrophobic nickel coating deposited on Mg alloy was fabricated through electroplating and chemical modification. They obtained the highest static water contact angle of 153° and a sliding angle of 7.2° . Feng et al. [1] proposed a simple and efficient method for the fabrication of Ni coating on the copper substrate via electroless plating. Copper substrates were cleaned ultrasonically in ethanol, washed with DI water, and dried at room temperature. It was investigated that the coating exhibits a contact angle of 156.4° and a gliding angle of 4° . Song et al. [21] fabricated superhydrophobic Ag coating on a steel substrate. The steel plate is chemically treated with CuSO_4 and AgNO_3 solution followed by fluoroalkyl silane for 2 min to change the color of steel surfaces from silvery to red. They obtained the highest contact angle of $163.4^\circ \pm 1.8^\circ$ and a rolling angle of $1.5^\circ \pm 0.5^\circ$. Yuan et al. [5] fabricated the superhydrophobic surfaces on AZ61 magnesium alloy substrate via electroless plating. Mg alloy substrates are immersed in stearic acid solution. They obtained the highest contact angle of $155.6^\circ \pm 0.3^\circ$ and a sliding angle of about 2° . Another popular method of fabricating superhydrophobic coating, generally used in laboratories and industries, is the sol–gel process. It has the least effect on temperature and a wide range of coating prospects.

3.3 Sol–Gel Method

Sol–gel is a process where solid materials are obtained from small material. It is a low pressure, low temperature, and cost-less process that gives rough surfaces on various oxides. It requires prepared silica sol, which requires a long fabrication time

Fig. 5 Schematic diagram of the synthesis of superhydrophobic by sol–gel method [21]



[21, 30–32]. A typical schematic diagram for the synthesis of superhydrophobic fabrics by the sol–gel method is shown in Fig. 5. A few research articles based on the development of hydrophobic coating using this process are discussed as follows:

Raimondo et al. [33] fabricated superhydrophobic coating to improve corrosion behavior on the copper surfaces using a sol–gel method. The copper surface was washed with acetone and chemically etched to achieve micro-roughness on the surface. They obtained a static water contact angle of 170° and a sliding angle of 5° . SEM images of surface morphology show uniform flower-like structure on the copper surface. Pratiwi et al. [34] succeeded in preparing a low-cost superhydrophobic surface by depositing TiO_2 films on the glass substrate. They found coated glass shows an excellent superhydrophobic surface with a water contact angle of $158 \pm 2^\circ$ and a sliding angle of $4 \pm 1^\circ$. Vidal et al. [35] reported the preparation of superhydrophobic SiO_2 surface with tetraethoxysilane (TEOS) and methyltriethoxysilane (MTES) precursors. They obtained homogeneous silica coatings with a water contact angle of 149° . Mahadik et al. [31] fabricated a hierarchical structure of silica particles on a glass substrate using a spray deposition method. They found a static water contact angle of $167 \pm 1^\circ$, sliding angle of $2 \pm 1^\circ$ and suggested a new approach to enhancing superhydrophobicity surface for thermal stability.

However, the selective reaction and formation of oxide lead to the generation of porosity and brittleness.

3.4 Chemical Etching

Chemical etching is a method to remove material by high pressure and high temperature by chemical spray. It uses strong acid and alkali, which are harmful to the operator and environment. In this process, a superhydrophobic surface on a metal substrate is obtained easily because of simplicity and less equipment required [35, 36]. A typical schematic diagram for superhydrophobic coating by chemical etching method is shown in Fig. 6.

A review of the wettability condition obtained through this process is discussed below:

Varshney et al. [38] successfully fabricated superhydrophobic coating on Al substrate having contact angle 70° by chemical etching with HNO_3 and HCl solution. After etching by immersion in lauric acid solution, the rough surface is obtained with a water contact angle of 153° . Kumar and Gogoi [39] reported the chemical etching method for preparing superhydrophobic Al surfaces with a mixture of HNO_3 and HCl acids, followed by treatment with hexadecyltrimethoxysilane. They found a contact angle of $162^\circ \pm 4.2^\circ$ and a sliding angle of $4 \pm 0.5^\circ$. Huang et al. [40] obtained superhydrophobic Al alloy surfaces by a chemical etching process using 1 M NaOH solution followed by passivation using 0.01 M ethanolic stearic acid (SA) solution. They obtained a water contact angle of more than 150° and found a flake-like surface of aluminum stearate. Fang et al. [41] applied superhydrophobic coating on Al alloy's surface via a chemical etching method and water contact angle of $161.2 \pm 1.7^\circ$ and sliding angle smaller than 8° . The corrosion resistance of aluminum alloy improved and shows the superhydrophobic coating.

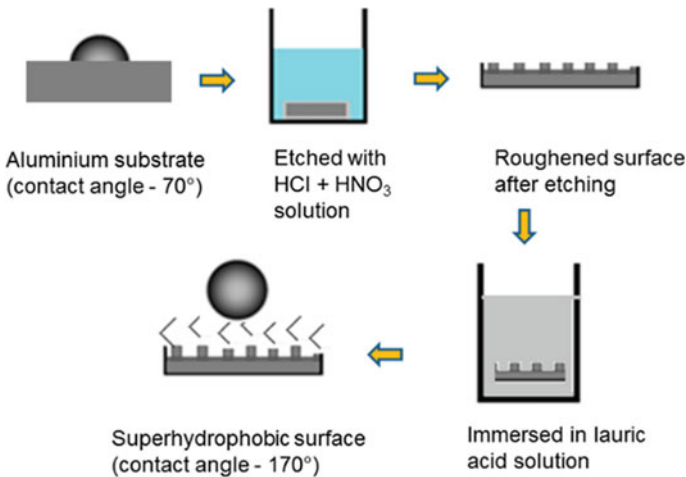


Fig. 6 Schematic diagram of coating preparation by a two-step process: chemical etching with a mixture of hydrochloric acid and nitric acids [37]

4 Application of Superhydrophobicity

The superhydrophobic surface has many potential applications in industry, especially in energy-related fields, summarized in Fig. 7, and some of the applications are discussed below briefly.

4.1 Corrosion Resistance

Corrosion is one of the serious problems in our society. Our economy has a significant impact due to surface damage of most of the components [4, 39]. It has lured more awareness of the researcher/scientist to decrease corrosion resistance. But recently developed superhydrophobic coatings are used to prevent corrosion rate by trapping a large amount of air in the valley and rough structure of superhydrophobic surface [39, 42, 43].

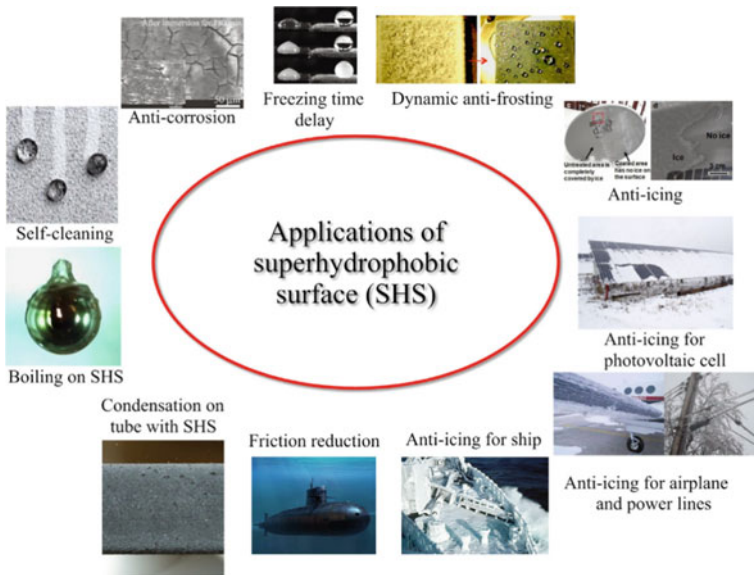


Fig. 7 The applications of superhydrophobic surfaces [41]

4.2 Self-Cleaning Surfaces

The presence of dust and contaminated particles in our surrounding environment decreases the properties of the material. It can be improved by coating a superhydrophobic surface with wax, by which water slides on the body, and improves self-cleaning properties [29, 44].

4.3 Drag Reduction

Drag force is one of the prominent issues faced by ship components, submarines, and aircraft industry moving on water surface [12]. Drag reduction phenomenon was reported in 1991. Inside this surface structure, air pockets inspired the lotus leaf plant to reduce the contact between solid and liquid surfaces [45, 46].

4.4 Anti-Icing Properties

Every year due to the emergence of ice storms and deposition of ice on the surface of the communication signal, electrical transmission equipment, highways, aircraft, etc., affect the environment. It can be reduced by superhydrophobic coatings of surfaces that cause the water droplets to slide easily from the surfaces [46, 47].

4.5 Antibacterial Properties

One of the main concerns in food packaging, the medical industry, biosensors, marine equipment, and many more is environmental pollution. Due to pollution and the growth of bio-films, it can cause infection in patients after surgery. It can be minimized by an antibacterial coating of the surface, which decreases the bacterial adhesion to the surface [48, 49].

5 Conclusion

The superhydrophobic coating can be developed using the deposition processes, as mentioned earlier. It is possible to obtain a hydrophobic surface using the techniques discussed above. However, electroless plating is recommended because of its versatility, mobility, ease of operation, cost-effectiveness, and nature. Unlike electroplating, it does not require any electricity to operate. Further, it is a highly effective

method compared to other processes like the chemical etching method that uses strong acid and alkali, which are harmful to the operator and environment. Sol–gel methods require prepared silica gel, which requires an extended processing time to fabricate.

References

1. Feng XJ, Shi YL, Wang YS, Yue GR, Yang W (2013) Preparation of superhydrophobic silver nanocoatings with feather-like structures by electroless galvanic deposition. *Chin Sci Bull* 58(16):1887–1891
2. Feng BL et al (2002) Superhydrophobic surfaces: from natural to artificial. *Adv Mater* 24:1857–1860
3. Barthlott W, Neinhuis C, Verlot H, Schott CLZ (1997) Purity of the sacred lotus, or escape from contamination in biological surfaces. *Planta* 1–8
4. Zang D, Zhu R, Zhang W, Yu X, Lin L, Guo X (2017) Corrosion-resistant superhydrophobic coatings on mg alloys surfaces inspired by lotus seedpod. *Adv Func Mater* 201605446:1–7
5. Yuan J, Wang J (2017) Fabrication and properties of a superhydrophobic film on an electroless plated magnesium alloy. *RSC Adv* 7:28909–28917
6. She Z, Li Q, Wang Z, Li L, Chen F, Zhou J (2012) Novel method for controllable fabrication of a superhydrophobic CuO surface on AZ91D magnesium alloy. *Appl Mater Interfaces* 4:4348–4356
7. Wang H et al (2016) A novel electrodeposition route for the fabrication of the superhydrophobic surface with unique self-cleaning, mechanical abrasion, and corrosion resistance properties. *Chem Eng J* 303:37–47
8. Gong A, Zheng Y, Yang Z, Guo X, Gao Y, Li X (2020) Spray fabrication of superhydrophobic coating on aluminum alloy for corrosion mitigation. *Mater Today Commun* 101828
9. Liang T et al. (2020) Surface and coatings technology corrosion inhibition effect of nano-SiO₂ for galvanized steel superhydrophobic surface. *Surf Coat Technol* 126673
10. Guo F, Guo Z (2016) Inspired smart materials with external stimuli-responsive wettability: a review. *RSC Adv* 6(43):36623–36641
11. Comanns P (2018) Correction: passive water collection with the integument: mechanisms and their biomimetic potential. *J Exp Biol* 153130
12. Barati G, Aliofkhazraei M, Khorsand S, Sokhanvar S, Kaboli A (2018) Science and engineering of superhydrophobic surfaces: review of corrosion resistance, chemical and mechanical stability. *Arab J Chem*
13. Shadmani S, Khodaei M, Chen X (2020) Superhydrophobicity through coatings prepared by chemical methods
14. Schondelmaier D, Cramm S, Klingeler R, Morenzin J, Eberhardt W (2002) Orientation and self-assembly of hydrophobic fluoroalkylsilanes. *Langmuir* 47(2):6242–6245
15. Whyman G, Bormashenko E, Stein T (2008) The rigorous derivation of young, cassie–baxter, and wenzel equations and the analysis of the contact angle hysteresis phenomenon. *Chem Phys Letter* 450:355–359
16. Nguyen HH, Tieu AK, Wan S, Zhu H, Pham ST, Johnston B (2020) Surface characteristics and wettability of superhydrophobic silanized inorganic glass coating surfaces textured with a picosecond laser. *Appl Surf Sci* 537:147808
17. Samanta A, Wang Q, Shaw SK, Ding V (2020) Roles of chemistry modification for laser textured metal alloys to achieve extreme surface wetting behaviors. *Mater Des* 192:108744
18. Qian H, Li M, Li Z, Lou Y (2017) Mussel-inspired superhydrophobic surfaces with enhanced corrosion resistance and dual-action antibacterial properties. *Mater Sci Eng C*

19. Liu Y, Yin X, Zhang J (2014) A electrodeposition process for fabrication of biomimetic superhydrophobic surface and its corrosion resistance on magnesium alloy. *Electrochim Acta* 125:395–403
20. Zheng T, Hu Y, Pan F (2019) Fabrication of corrosion-resistant superhydrophobic coating on magnesium alloy by one-step electrodeposition method. *J Alloys* 7:193–202
21. Song J, Liu X (2012) A rapid two-step electroless deposition process to fabricate superhydrophobic coatings on steel substrates. *Coat Technol* 9(5):643–650
22. Li H, Yin X (2019) Modifier-free fabrication of durable superhydrophobic electrodeposited Cu–Zn coating on steel substrate with self-cleaning, anti-corrosion, and anti-scaling properties. *Appl Surf Sci* 481:872–882
23. Xu W, Rajan K, Chen XG, Sarkar DK (2019) Facile electrodeposition of superhydrophobic aluminum stearate thin films on copper substrates for active corrosion protection. *Surf Coat Technol* 364:406–415
24. Salehi M, Mozammel M, Emarati SM (2019) Superhydrophobic and corrosion-resistant properties of electrodeposited Ni–TiO₂/TMPSi nanocomposite coating. *Colloids Surf A* 573:196–204
25. Shen L, Fan M, Qiu V, Jiang W, Wang Z (2019) Superhydrophobic nickel coating fabricated by scanning electrodeposition. *Appl Surf Sci* 483:706–712
26. Sugar J, Lian J, Sha W (2013) Electroless nickel, alloy, composite, and nano coatings—a critical review. *J Alloys Compd* 571:183–204
27. Jagatheeshwaran MS, Elayaperumal A, Arulvel S (2015) Wear characteristics of electroless NiP/bio-composite coatings on En8 steel. *J Manufact Process*
28. Correa E et al (2012) Nickel–boron plating on magnesium and AZ91D alloy by a chromium-free electroless process. *Surf Coat Technol* 206(13):3088–3093
29. Wang Y, Gu Z, Xin Y, Yuan N, Ding J (2017) Facile formation of superhydrophobic nickel coating on magnesium alloy with improved corrosion resistance. *Colloids Surfaces Physicochem Eng Asp*
30. Hooda A, Goyat MS, Kumar J, Kumar A, Gupta R (2020) A review on fundamentals, constraints and fabrication techniques of superhydrophobic coatings. *Prog Org Coat* 142:105557
31. Mahadik SA et al. (2012) Thermally stable and transparent superhydrophobic sol-gel coatings by spray method. *J Sol-Gel Sci Technol*
32. Larissa ME et al. (2020) Superhydrophobic coatings on cotton fabrics using sol-gel technique by spray. *J Sol-Gel Sci Technol*
33. Raimondo M, Veronesi F, Boveri G, Guarini G (2017) Applied surface science superhydrophobic properties induced by sol-gel routes on copper surfaces. *Appl Surf Sci* 422:1022–1029
34. Pratiwi N, Syukri Z, Admi A (2020) Self-cleaning material based on superhydrophobic coatings through an environmentally friendly sol-gel method. *J Sol-Gel Sci Technol*
35. Silica S, Vidal K, Mart A (2019) The synthesis of a superhydrophobic and thermal. *Coating*
36. Yang L, Cao X, Wu Y, Chen S, Xie X, Zhu Q (2020) Improvement of corrosion resistance and mechanism analysis for self-assembled vinyltriethoxysilane versus films on low carbon steel using a novel chemical etching method. *Corros Sci* 177:109002
37. Wei D, Wang J, Liu Y, Wang D, Li S, Wang H (2021) Controllable superhydrophobic surfaces with tunable adhesion on Mg alloys by a simple etching method and its corrosion inhibition performance. *Chem Eng J* 404:126444
38. Varshney V, Mohapatra SS, Kumar A (2016) Superhydrophobic coatings for aluminum surfaces synthesized by a chemical etching process. *Int J Smart Nano Mater* 7(4):248–264
39. Kumar A, Gogoi B (2018) Development of durable self-cleaning superhydrophobic coatings for aluminium surfaces via chemical etching method. *Tribol Int*
40. Huang Y, Sarkar DK, Chen XG (2015) Applied surface science superhydrophobic aluminum alloy surfaces prepared by chemical etching process and corrosion resistance properties. *Appl Surf Sci* 356:1012–1024
41. Yin B, Fang L, Hu J, Tang AQ, He J, Mao JH (2012) A facile method for fabrication of superhydrophobic coating on aluminum alloy, *Sur Interface Anal* 439–444

42. Song Z, Xie Z, Ding L, Zhang Y (2018) Corrosion resistance of super-hydrophobic coating on AZ31B Mg alloy. *Int J Electrochem Sci* 2018(13):6190–6200
43. Bandi P, Kausley S, Rai BB (2020) Development of superhydrophobic and corrosion-resistant coatings on mild steel a greener approach. *Mater Today Commun* 25:101625
44. Dalawai SP et al (2019) Progress in organic coatings recent advances in durability of superhydrophobic self-cleaning technology: a critical review. *Prog Org Coat* 138:105381
45. McHale G, Newton MI, Shirtcliffe NJ (2010) Immersed superhydrophobic surfaces: gas exchange, slip and drag reduction properties. *Soft Matter* 6:714–719
46. Wang N, Tang L, Cai Y, Tong W, Xiong D (2018) Scalable superhydrophobic coating with controllable wettability and investigations of its drag reduction. *Colloids Surf A* 555:290–295
47. Lein HL (2019) Coatings and surfaces with hydrophobic and anti-icing properties. Norwegian University of Science and Technology, Trondheim, Norway, pp 257–269
48. Liu C, Liu Q, Jin R, Lin Z, Qiu H, Xu Y (2020) Mechanism analysis and durability evaluation of anti-icing property of the superhydrophobic surface. *Int J Heat Mass Transf* 156:119768
49. Zhang L et al. (2015) Inhibitory effect of superhydrophobicity on silver release and antibacterial properties of superhydrophobic Ag/TiO₂ nanotubes. *Soc Biomater* 1004–1012

Design, Analysis and Development of Virtual Working Model of Self Balancing Robot



C. H. Patel, Naga Sumanth Putta, Akula S. V. S. S. Sri Manikanta, Eluri Nikhil Reddy, and Kambala Prasanna Ramesh Kumar Babu

Abstract This paper represents the main aspect of self-balancing robot which balances on two wheels by using motors, Gyro, accelerometer and microprocessor. This robot is based on the principle inverted pendulum cart, as the name defines that it should be balanced without falling. To balance the robot a closed loop controller should be used. The controller used in many papers that are reviewed by us are PID controller. By comparing LQR and PID theoretically and made a decision to use LQR controller which is more accurate and zero error. In this project we done the robot with MPU6050 which has 3-axis gyro and 3-axis accelerometer. This robot not only balance the self-weight but also extra weight by taking an example of Segway. We designed CAD model and did optimization on MATLAB which made us to estimate the requirements and simple light weight design. This robot can also make turn and balances on the camber surfaces. This robot significantly improves mobility and decreases its radius if turn to zero. Due to the presence of two wheels it can make turn instantly, whereas the four wheeled or three wheeled cannot. It is more useful for riders when riding bikes in high speed which makes the rider not to fall from bike and also can be responsible for preventing accidents.

Keywords PID (Proportional Integrative Derivative) · LQR (Linear Quadratic Regulator) · MPU6050 · MATLAB · Segway

1 Introduction

Self-adjusting robot depends on electronic gadget and installed control and being utilized as a human carrier in numerous zone. Oneself adjusting Robot depends on the Inverted Pendulum model (IP). To adjust at two-wheeled upset pendulum robot,

C. H. Patel (✉)

School of Mechanical Engineering, Lovely Professional University, Phagwara, Punjab, India
e-mail: patel.15755@lpu.co.in

N. S. Putta · A. S. V. S. S. Sri Manikanta · E. N. Reddy · K. P. R. K. Babu

Department of Automobile Engineering, Lovely Professional University, Phagwara, Punjab, India

© The Author(s), under exclusive license to Springer Nature Singapore Pte Ltd. 2023

339

T. S. Sudarshan et al. (eds.), *Recent Advancements in Mechanical Engineering*,

Lecture Notes in Mechanical Engineering,

https://doi.org/10.1007/978-981-19-3266-3_26

it is important to have precise data of the live tilt point from utilizing an estimation on it. Oneself adjusting robot is an uncommon sort of wheeled robots which structure a class of nonlinear, coupled and under-activated frameworks. Accordingly, the demonstrating, control and application issues of oneself adjusting robot have gotten expanding consideration from scientists and have been generally examined. As of late some different and proficient control plans have been proposed for oneself adjusting robot. In the displaying and control configuration were read for self-adjusting two-wheeled vehicles.

A versatile backstepping self-adjusting control was created for a two-wheeled electric bike in the use of fluffy control conspire was read for a self-adjusting two-wheeled vehicle. Versatile neural organization control was proposed for a self-adjusting two-wheeled bike. Simultaneously, some unsettling influence eyewitness based control plans have been created for different robots.

In a nonlinear DOBC configuration was given for a mechanical exoskeleton fusing fluff estimate. Nonlinear aggravation eyewitness based unique surface control was proposed for portable wheeled rearranged pendulum. A strong following control conspire was created for wheeled portable robots with sliding and slipping utilizing fluffy aggravation spectator. In any case, to improve the following exhibition, the strong following control conspire dependent on the aggravation eyewitness should have been additionally refined for oneself offsetting portable robot with obscure unsettling influences. The robot was characteristically insecure and should have been continually controlled to address itself and equilibrium.

There were two boundaries to be controlled in this situation: course and quickening. While the bearing of the movement relied on the course of pivot of the wheels, the speeding up was subject to the rakish quickening of the wheels. The tilt of the robot must be detected to give the vital input to the regulator and adequately drive the remedy components. This was accomplished by actualizing a shut circle control framework, the PID regulator.

2 Literature Survey

By perusing the portion of the examination papers we used to see the significant changes, adding the highlights in model from paper to paper.

To accomplish strength of the vehicle PID regulator is utilized to be more steady even outer limited hasty power. In this there is additionally an examination of basic PID regulator and auto-tuned PID regulator to have elite in mentality control and adjustment of robot. The auto-tuning highlight spares the trouble of perusing the dangerous and excess errand of physically tuning all the PID coefficients, however a near examination of the reactions in both basic and auto tuned. Not with standing, the auto-tuned framework shows a more modest consistent state blunder and more modest ascent time and settling time [1].

This examination characterizes plan and model of a bike that can adjust without driver by utilizing a response wheel. Segments utilized are Triple pivot accelerometer ADXL 335, Dual hub Gyroscope IDG500, microcontroller ATmega 16, 24 V DC engine, response wheel, Motor driver L293D [2].

A plan called hearty global positioning framework which depends on nonlinear unsettling influence spectator is utilized to build up the Auto settling robot with outer obscure aggravations. For development in execution of global positioning framework, a nonlinear aggravation onlooker is created which is utilized to know the obscure unsettling influence of the Auto Stabilizing robot [3].

The wheels equipped for free pivot with high limit DC engine. Whirligig and accelerometer are utilized to realize how much point inclined. 6DOFIMU (Inertial estimating unit) was prepared and separated to acquire exact qualities which were taken care of the computer chip on board [4].

Planning of a CAD (Computer Aided Design) model with all necessities and re-enacted it. The robot is controlled just a single way which depends on pitch point. As indicated by pitch point which is estimated by accelerometer and Gyroscope made robot to control in severe situation by utilizing Algorithm in Arduino [5].

By the powers (which is applied and following up on robot) and minutes determining conditions and afterwards ascertaining state space condition. By this condition, we become acquainted with the how robot is constrained by what power and minutes and how effectively the robot reaction is. By taking this model we need to take a framework that contains all the test segments with all their attributes. In the wake of examining the framework, we will get the conditions which assist with determining the state space model.

The demonstrator can get rakish information and position information, it's conceivable to encourage information for all the states that are needed for a state space controller [5]. For the improvement of programmed adjusting robot we need to infer the state space condition. At that point we going to plan a PID regulator to control the nearby circle function [6].

For adjusting the robot the primary things are accelerometer, Gyroscope and control Algorithm. Based on the previously mentioned things will balance out the robot in an erect position. Accelerometer and Gyroscope are for the most part used to distinguish the point and control the robot by quickening and powers following up on it. For Algorithm there are many control frameworks to utilize. Here PID and corresponding channel utilized for better execution moment stability [7].

The code is as discussions, online journals and instructional exercises. All through the task different adaptations of code grew, each for a particular reason, for instance the accelerometer point to see the exhibition of the Kalman Filter or code to describe the engines. A piece of the code is equivalent to it would be in a condition from, so just the non-insignificant angles are considered here and the explanations for are mentioned [8].

3 Design Methodology

Design of Self-balancing robot is done in SolidWorks software, which is user friendly software to design any product. Here design is made by making different sub parts like platform, tyres, Motors, Rods, nuts, etc. Here we mostly used the command extrude which is a basic command for creation of material. Figure 1 is assembly of different parts. So the parts are shown in Figs. 2, 3, 4, 5, 6, 7, 8, 9 and 10.

These are the part models we deigned and assembled to self-balancing robot. In assembly mate is used to place the component in exact position and locked it. Like this the product can be designed and assembled using different of type of selection like face, collinear, parallel, perpendicular, etc. The design is main thing in which assembly model or part model can be used as prototype and we can analysis with practical or experimental values in any software that which makes us to conclusion to optimize or changes in modelling.

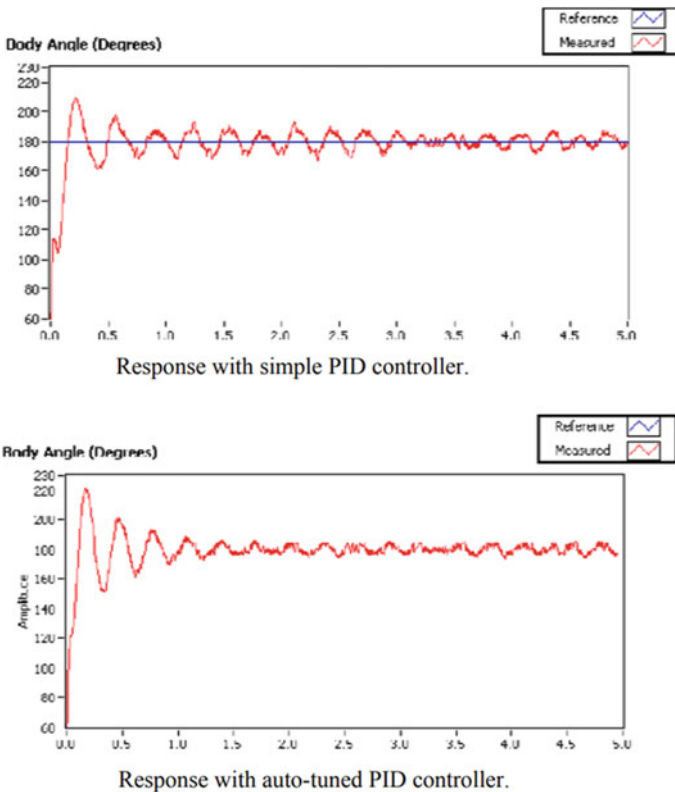


Fig. 1 Comparing manually tuned and auto-tuned response [1]

Component	Abbreviation	Value
mass of cart	M	1 K.G.
Mass of pendulum	m	1 K.G.
coefficient of friction on wheel	b	0.1 N/M/sec
length to pendulum from the hinge point	l	0.3 M
pendulum angle from vertical (down)	Φ	To be calculated
moment of inertia of the pendulum	I	0.025 K.G.*m ²
force applied to the cart	F	Will be given

Fig. 2 A table having details of requirements [6]

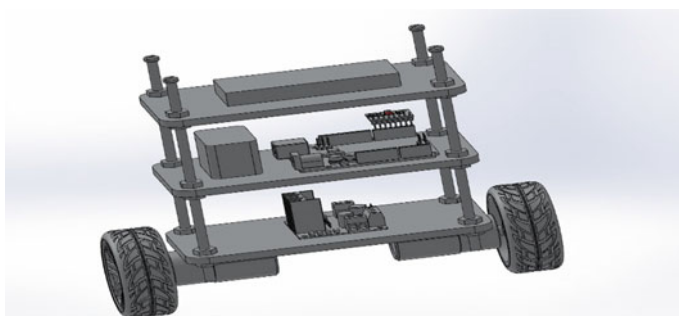


Fig. 3 Self-balancing robot assembly

Fig. 4 Chassis board

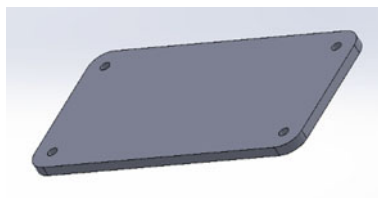




Fig. 5 Rod for support

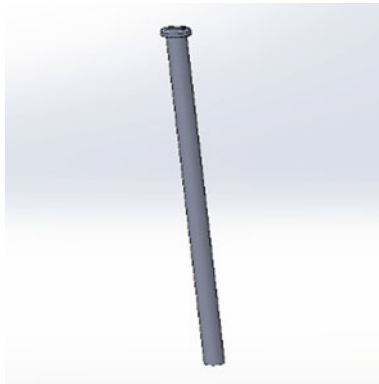


Fig. 6 Wheel with connector

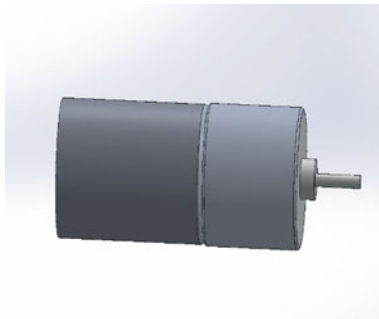


Fig. 7 DC motor with clamp

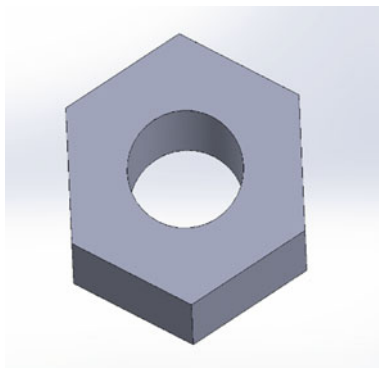


Fig. 8 Nut

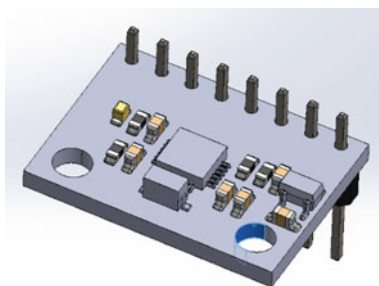


Fig. 9 MPU6050

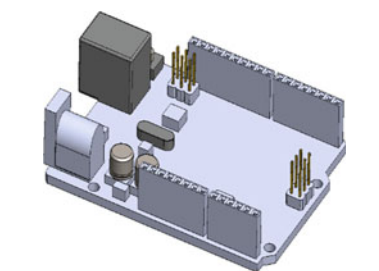


Fig. 10 Arduino Uno

4 Analysis

The state space equation obtained

$$\begin{bmatrix} \dot{x} \\ \ddot{x} \\ \dot{\theta}_b \\ \ddot{\theta}_b \end{bmatrix} = \begin{bmatrix} 0 & 1 & 0 & 0 \\ 0 & 2k_m k_e \frac{(M_b l r - I_b - M_b l^2)}{R r^2 A} & \frac{M_b^2 g l^2}{A} & 0 \\ 0 & 0 & 0 & 1 \\ 0 & \frac{2k_m k_e (r B - M_b l)}{R r^2 A} & \frac{M_b g l}{A} & 0 \end{bmatrix} \begin{bmatrix} x \\ \dot{x} \\ \theta_b \\ \dot{\theta}_b \end{bmatrix} + \begin{bmatrix} 0 \\ \frac{2k_m (I_b + M_p l^2 - M_p l r)}{R r A} \\ 0 \\ \frac{2k_m (M_b l - r B)}{R r A} \end{bmatrix} U_a$$

$$A = (I_b + 2M_b l^2 (M_w + (I_w / r^2))), \quad B = 2M_w + (2I_w / r^2) + M_b$$

Output

$$y = \begin{bmatrix} 0 & 0 & 1 & 0 \end{bmatrix} \begin{bmatrix} x \\ \dot{x} \\ \theta_b \\ \dot{\theta}_b \end{bmatrix}$$

The Linear Quadratic Regulator (LQR) is a method that can dispense the optimal control feedback gains to high performance design of systems and enable the closed-loop stable (Fig. 11).

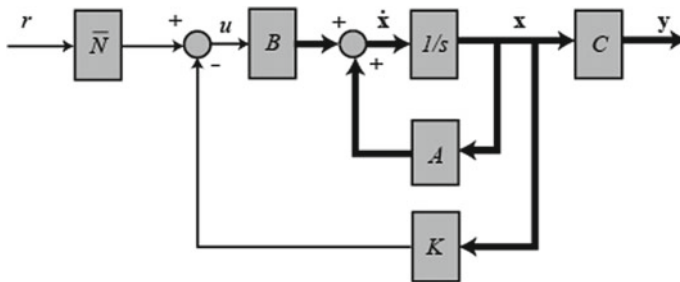


Fig. 11 Block diagram of LQR controller

Table 1 Values required for calculation

Parameters	Values
k_m	0.0135 N m/A
k_e	0.01368 V/rad/s
G	9.8 m/s ²
M_b	2 kg
M_w	0.03 kg
R	0.035 m
L	0.014 m
I_b	0.0074 kg m ²
I_w	0.0041 kg m ²

$$J = \int_0^{\infty} (X^T Q X + u^T R u) dt$$

Q and R matrices are mutually restricted to each other. The Q value is directly proportional to anti-interference ability. As R increased the energy consumption of system will be less. So for better performance, we need to find better weighted Q matrix and R matrix.

The values state feedback matrix K is only confirmation for final output performance of robot.

i.e. $K = \text{lqr}(A, B, Q, R)$. K is the optimal gain matrix which defines the LQR.

Above function is MATLAB function which is used for LQR controller (Table 1).

Equation is obtained by actual values

$$\begin{bmatrix} \dot{x} \\ \ddot{x} \\ \dot{\theta} \\ \ddot{\theta} \end{bmatrix} = \begin{bmatrix} 0 & 1 & 0 & 0 \\ 0 & -6.75 & 35.53 & 0 \\ 0 & 0 & 0 & 1 \\ 0 & -3.05 & 15.23 & 0 \end{bmatrix} \begin{bmatrix} x \\ \dot{x} \\ \theta \\ \dot{\theta} \end{bmatrix} + \begin{bmatrix} 0 \\ 5.21 \\ 0 \\ 23.87 \end{bmatrix}$$

Then the optimal solution for better Q and R matrices is

$$Q = \begin{bmatrix} 150 & 0 & 0 & 0 \\ 0 & 150 & 0 & 0 \\ 0 & 0 & 150 & 0 \\ 0 & 0 & 0 & 150 \end{bmatrix}$$

$$R = 1.2$$

5 Experimental

As we made robot with components using Arduino Uno as microprocessor, L289N as motor driver, DC motors, MPU6050 for 3-axis Gyro and accelerometer, Li ion battery and we used acrylic sheets as body structure for better stiffness.

Figure 12 shows the circuit of the self-balancing robot we used. The circuit is very simple and there is no complex in connecting components. We created Arduino code and algorithm run it on robot without weight on it, and the reaction time of the robot is about 2–3 s. When weight is added on it and again we run the code using Arduino and the reaction time of the robot is like 3–4 s. We can also make the robot more advanced by connecting Arduino with Bluetooth module and control with our smart phone or device, which will be very easier to operate the robot.

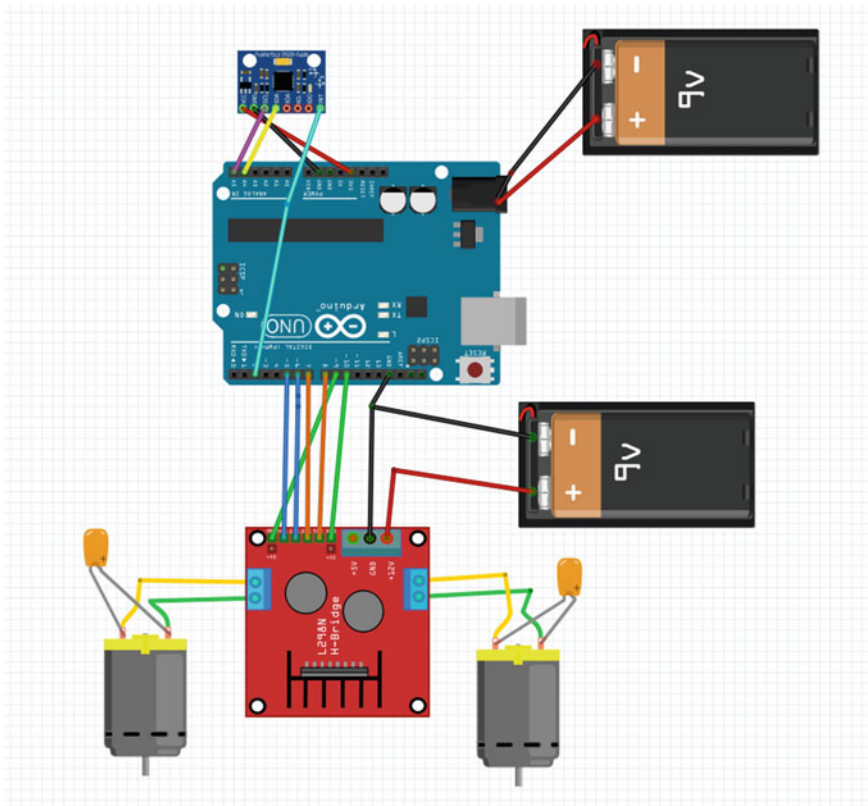


Fig. 12 Circuit for self-balancing robot

6 Results and Discussion

The state feedback value is

$$K = [-10.0; -16.23; -71.111; -53.95]$$

So the result of feedback value is above mentioned. Here K is the optimal gain matrix which defines the LQR. As any changes in Q and R matrix made a more optimized value for K . Here Q and R matrix defines the time and performance of the robot. So, both should be optimal to be considered particularly for a value which can give high performance. LQR controller is better when compared to PID controller because of that state space error for PID controller is there but very low. Although the PID controller has low steady state error, the LQR controller is like zero steady state error, which makes the robot to control its position and direction in a best way time (Fig. 13).

So the reaction of the robot relies upon the heaviness of the robot that which changes the exhibition of the robot. We considered the heaviness of the robot resembles around 2 kg and as indicated by the weight the reaction of the robot will be in around 2 s. Because of the MPU6050 which is 3-hub accelerometer and 3-hub Gyroscope compute the point, bearing, speed and direction precisely and balance the robot as quickly as time permits.

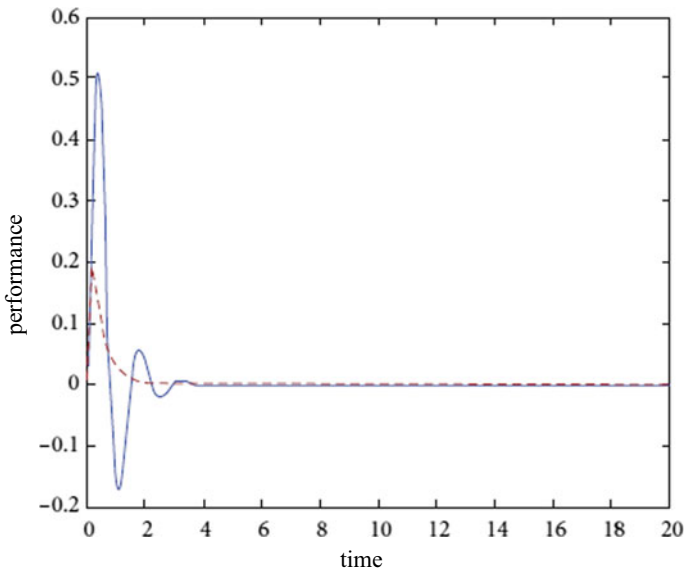


Fig. 13 Response of robot

7 Conclusion

The entire task was to be steep learning because of the wide cluster of orders required from development and configuration, to control and programming execution.

By contrasting exploratory consequences of straightforward and auto tuned PID regulator, basic one makes more reaction for given power than auto tuned. The ascent time is tentatively found by taking a gander at the time needed by the reaction to reach from 10 to 90% of its progression tallness.

Indeed, even the Automatic adjusting robots is exposed to the irregular power or an information power, the situation of the robot will be steady in no time. There are numerous regulators utilized like PID, Robust, utilization of item conveying and a few kinds of channels likewise utilized yet LQR regulator is the most exact regulator which can zero state space mistake. Coming to whirligig and accelerometer which are utilized to notice point and quickening are utilized as various parts like 2 axis spinner and 3-pivot accelerometer yet MPU6050 is mix of 3-hub gyator and accelerometer which can decrease weight and increment execution. In the adjusting of weight limit of individuals neglected to offset the robot with weight or an article carrying on it. In this way, by LQR regulator can be utilized for weight adjusting which can be utilized for outside applications.

References

1. Bhatti OS, Mehmood-ul-Hasan K, Imtiaz MA (2015) Attitude control and stabilization of a two wheeled self-balancing robot. CEAI 17(3)
2. Kumar MP, Nirwan NW (2016) Design and fabrication of automatic balancing bicycle. Int J Sci Eng Technol Res (IJSETR) 5(2)
3. Chen M (2017) Robust tracking control for self-balancing mobile robots using disturbance observer. IEEE 4(3)
4. Sondhia S, Ranjithpillai R, Hegde SS, chakole S, Vora V (2017) Development of self-balancing robot with PID control. IJRRD 7(1)
5. Das SK, Triparthy PK (2014) Design and control of two wheeled robotic walker. Masters Thesis
6. Clark W, Khodaei MJ (2013) Self-balancing robot using concept of inverted pendulum. Ethesis
7. Suhani NMHHM (2015) Development of control system for a two wheeled self-balancing transporter. TWOWSB Trans
8. Samak C, Samak T (2018) Design of a two wheeled novel state feedback for PID controller using on-board state estimation algorithm. Res Gate

Effect of Relative Thickness on Natural Frequency Analysis of Hybrid Hyperbolic Paraboloid Shells



Vaishali and S. Dey

Abstract This article reflects the effect of relative thickness of various components of hybrid structures on random natural frequencies of hyperbolic paraboloid shells. The total thickness, other geometrical parameters and the material properties are kept constant. Here, the hybrid shell structure is composed of three different components: laminated composite, functionally graded material (FGM) and the soft core. The shell structure considered is of hyperbolic paraboloid type. Here eight nodes are taken for FE formulation having an isoperimetric quadratic element. For obtaining the material properties at different layers of FG part of hybrid shell, power law is used. For analyzing the first three random natural frequencies, we have employed Monte Carlo Simulation (MCS) integrated with standard Eigen value problem. Here linear regression model (LRM) is used as a surrogate model and is integrated with traditional MCS model for increasing computational efficiency by reducing the computational time and cost. This study is carried out to enlighten the effect of relative thickness of different components of hybrids on the random modes of frequencies. The outcomes obtained here are the first known results. In future these outcomes can be employed for optimal design of structures constructed from hybrids.

Keywords Hybrid structures · Hyperbolic paraboloid shells · Monte Carlo simulations · Random natural frequency

1 Introduction

In last few decades, composite laminate, FGM and sandwich structures are exhaustively investigated individually because of their outstanding properties and superior performances in comparison to traditional monolithic structures. As we know that human need is the driving force for development, therefore need for superior and

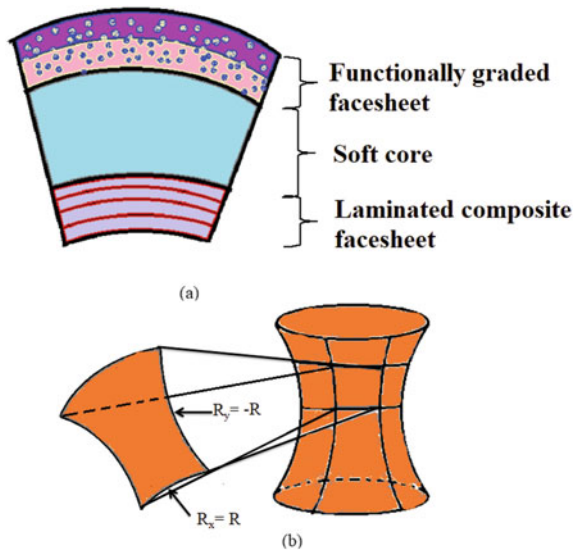
Vaishali (✉) · S. Dey

Department of Mechanical Engineering, National Institute of Technology Silchar, Silchar, Assam, India

e-mail: vaishali765@gmail.com

advanced materials lead to the development of hybrid structures. These hybrid structures have multifunctional applications; here we can obtain the advantages of its various components in one structure. But these structures frequently suffer various uncertainties like manufacturing. Even though a limited number of studies on individual structures like composites [1], sandwich [2] and FGM [3] can be found in the stochastic domain, the hybrid structural forms [1, 4, 5] have not yet received adequate attention concerning the aspect of inevitable uncertainty or variability. In this article, we firstly obtain the results using traditional MCs technique, then we implemented surrogate model with MCS to make our process more efficient. After validating the surrogate model, we further investigate the influence of relative thickness of the three constituting layers of the hybrid structural forms proposed in Fig. 1. We have considered three different components in the hybrid structures: laminated composite, FGM and the soft core (as shown in Fig. 1). The natural frequencies of the hybrid structures are influenced by the relative thickness of each of these three components, even if the total thickness, other geometrical parameters and the material properties are kept constant. In this article, we have plan to showcase the random natural frequencies (first three) of hybrid hyperbolic paraboloid shells taking into account the effect of relative thickness of various layers. Here, the article is divided into various sections such as Sect. 1: introduction, Sect. 2: showing the theoretical formulation of hybrid hyperbolic paraboloid shell, Sect. 3: shows the outcome obtained followed by deep explanation and lastly Sect. 4: showing the concluding remarks.

Fig. 1 **a** Hybrid structure considered for present study.
b Hyperbolic paraboloid shell structure



2 Theoretical Formulation

In hybrid structure, for the part composed of FGM, there power law [6] is used for getting the material properties at various depths,

$$K(\hat{s}) = K_m(\hat{s}) + [K_c(\hat{s}) - K_m(\hat{s})][w/t(\hat{s}) + 0.5]^P \tag{1}$$

where K_m shows properties of metal while K_c shows the properties of ceramic, P indicates the exponent of power law. Here, \hat{s} presents the randomness degree. Configuration of the hyperbolic paraboloid shell is presented in Fig. 1. In global form, the motion equation can be shown as [7] (for free vibration)

$$[M(\hat{s})]\{\ddot{\delta}_p\} + ([K(\hat{s})] + [K_\sigma(\hat{s})])\{\delta_p\} = 0 \tag{2}$$

where $\{\delta_p\}$ represents displacement vector, $[M(\hat{s})]$ is mass matrix while $[K(\hat{s})]$ and is elastic stiffness matrix and $[K_\sigma(\hat{s})]$ is geometric stiffness matrix. We can get the value of NF ($\omega(\hat{s})$) by considering the Eigen value problem [8],

$$[A(\hat{s})]\{\phi\} = \lambda(\hat{s})\{\phi\} \tag{3}$$

where

$$[A(\hat{s})] = ([K(\hat{s})] + [K_\sigma(\hat{s})])^{-1}[M(\hat{s})]$$

and

$$\lambda(\hat{s}) = 1/[\omega(\hat{s})]^2 \tag{4}$$

The methodology adopted for this work is represented in Fig. 2. The general equation for a multiple linear regression is represented below

$$y = B_0 + B_1x_1 + B_2x_2 + \dots + B_nx_n + E \tag{5}$$

where y represents response, x_1, x_2, \dots, x_n represents independent variable, B_0, B_1, \dots, B_n represents coefficient while E represents random error or noise. After getting LMR coefficient, we can easily obtain random response statistical moments.

For relative thickness analysis, let us assume thicknesses of the top and bottom layers of a three-layer hybrid structure are t_1 and t_3 , while that of the middle layer (i.e., core) is t_2 . Therefore, the total thickness t can be represented as

$$t = t_1 + t_2 + t_3 \tag{6}$$

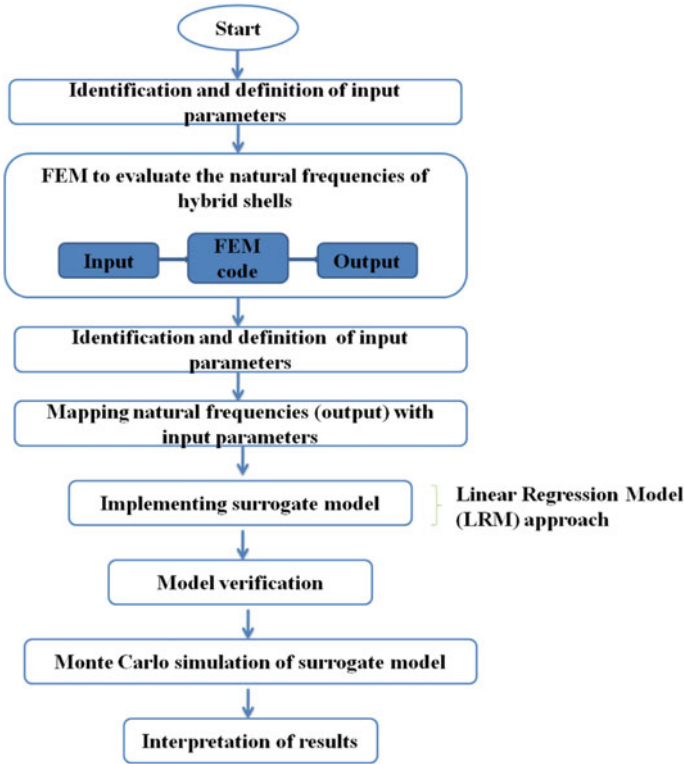


Fig. 2 Flowchart representing the complete procedure of present study

Subsequently we can define the parameters α and β as

$$\alpha = \frac{t_1}{t} \tag{7}$$

$$\beta = \frac{t_3}{t}$$

Another parameter γ can be obtained as

$$\gamma = \frac{t_2}{t} = 1 - (\alpha + \beta) \tag{8}$$

Here we will present the numerical results as a function of α and β so that the corresponding value of γ can be obtained readily. Note that it is possible to obtain the actual thickness of the respective layers by multiplying this parameter with the total thickness t . The range of α and β are considered in a way so that the two outer

layers are present in all the hybrid structural configurations, while the middle layer (i.e., core) may or may not be present depending on the value of α and β .

3 Results and Discussion

In this article, MCS technique is employed for the analysis of random natural frequency of hybrid hyperbolic paraboloid shells. For hyperbolic paraboloid shell geometry, the radius of curvature have $R_x = R, R_y = -R$. Here, uncertain input parameters considered are the various material properties. Simply supported boundary condition has been considered. Here, for FE formulation, we have considered an isoperimetric quadratic element having eight nodes. The isoperimetric formulation allows elements to be created that are nonrectangular and have curved sides and as we are considering hyperbolic paraboloid shell geometry, so we have considered isoperimetric formulation. The compositions of the materials considered for this work are furnished in Table 1. The results obtained is compared with the results of the past literatures [9] and is shown in Table 2 where (for plate, $R_x = R_y = \infty$). As a surrogate, linear regression model (LRM) is employed. Firstly the results obtained from traditional MCS technique is validated with the results obtained from LRM surrogate mode. For this purpose, different sample size is considered; here we have considered sample sizes as 64, 128 and 256. The results obtained from different sample sizes using LRM is compared with that of MCS results. This is done with the help of PDF plots and scatter plots. From the PDF plot (refer to Fig. 3) it is observed that as the sample size is increasing the deviation of results from the original results (i.e., MCS results obtained from 10,000 sample size) is decreasing. For sample size 256 we can observe that the results are overlapping with that of MCS, showing the least deviation which is desired. So, for later analysis sample size 256 is taken into consideration. Furthermore on considering the scatter diagram (refer to Fig. 4) for 64, 128 and 256 sample size (I), it is seen that for $I = 256$, there is a minimum deviation

Table 1 The various constituents of hybrid shell along with its material properties

		E (GPa)	ν	ρ (kg/m ³)
FG facesheet	Ceramic	151	0.3	3000
	Metal	70	0.25	2707
Core		0.85	0.42	1000
Lower facesheet	Laminated composite	19.3	0.25	2600

Table 2 The first natural frequency of symmetric FG square plate

Power law exponent value	Baferani et al. [9]	Present study
1	0.0891	0.0883
2	0.0819	0.0797

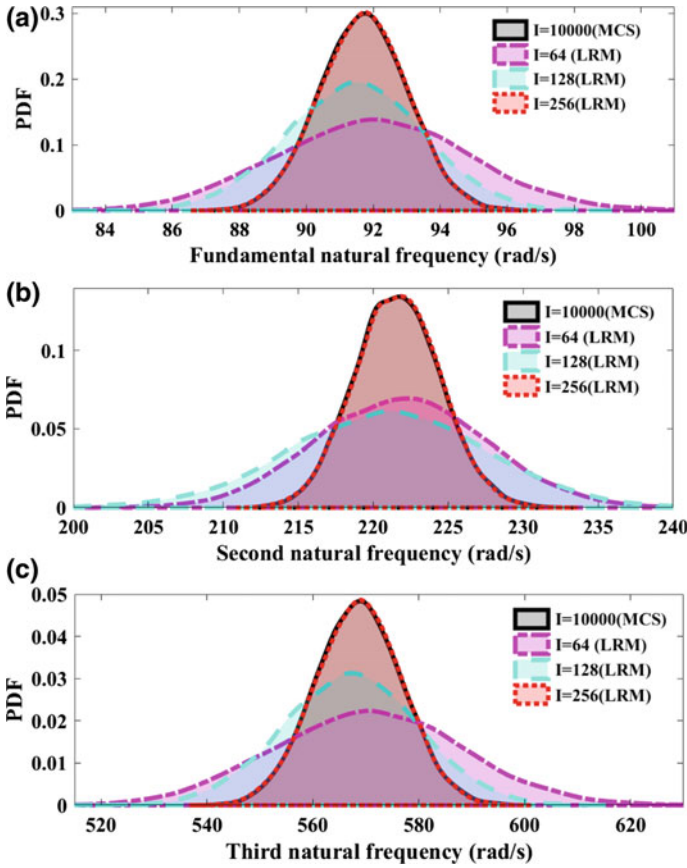


Fig. 3 PDF for the natural frequencies considering LMR surrogate for sample size of 64, 128 and 256

between the results obtained from LRM and the results obtained from MCS. So it further confirms that for sample size 256 the output obtained are in acceptable limit, so we will extend our study considering sample size as 256. For relative thickness analysis, let us assume thicknesses of the top and bottom layers of a three-layer hybrid structure are t_1 and t_3 , while that of the middle layer (i.e., core) is t_2 . To show the individual and interaction effects of α and β (refer to Eq. 7) on the natural frequencies of these hybrid structures having hyperbolic paraboloid shell geometry (refer to Fig. 1) contour plot has been presented in Fig. 5. Here, α = upper facesheet thickness/total thickness and β = lower facesheet thickness/total thickness. Figure 5 presents the contour plot, where it can be seen that greater values of the natural frequencies are obtained as the relative thickness of the facesheets becomes lesser. The parametric analysis presented here in terms of the contour plots will help the designers to have a comprehensive idea regarding the variation of natural frequencies in the entire design space of layer-wise thickness.

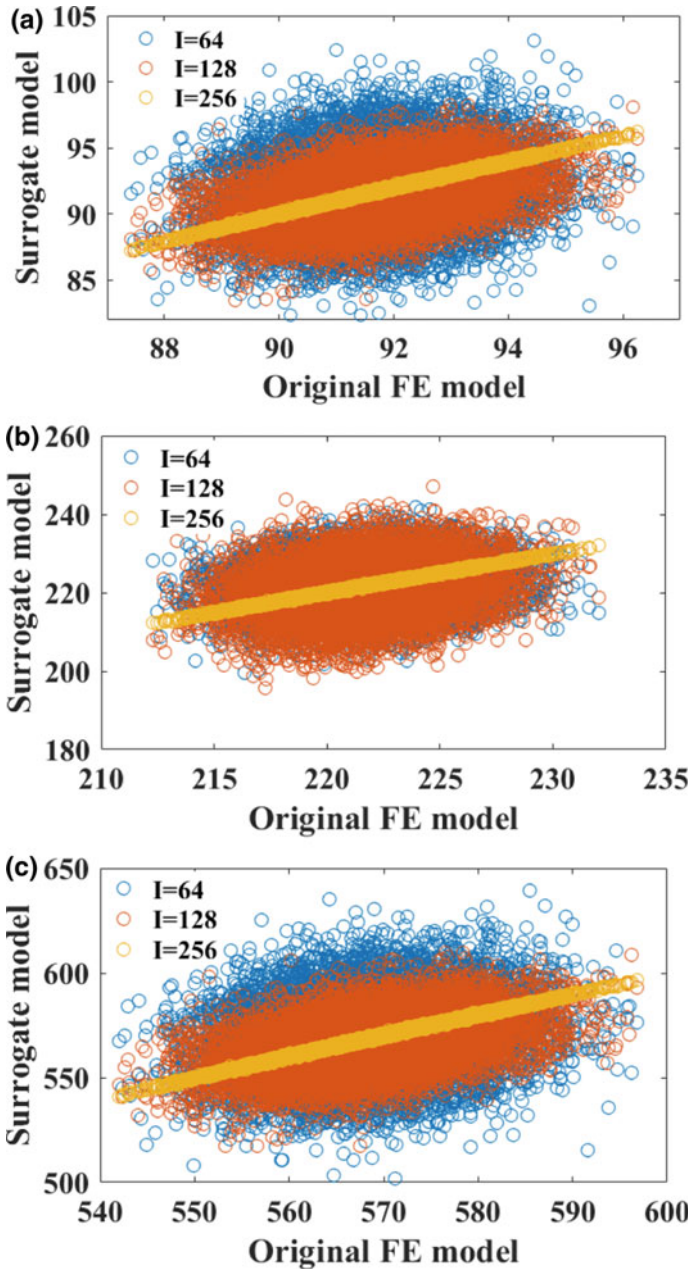


Fig. 4 Scatter diagram for the natural frequencies (rad/s) considering LMR surrogate for sample size of 64, 128 and 256

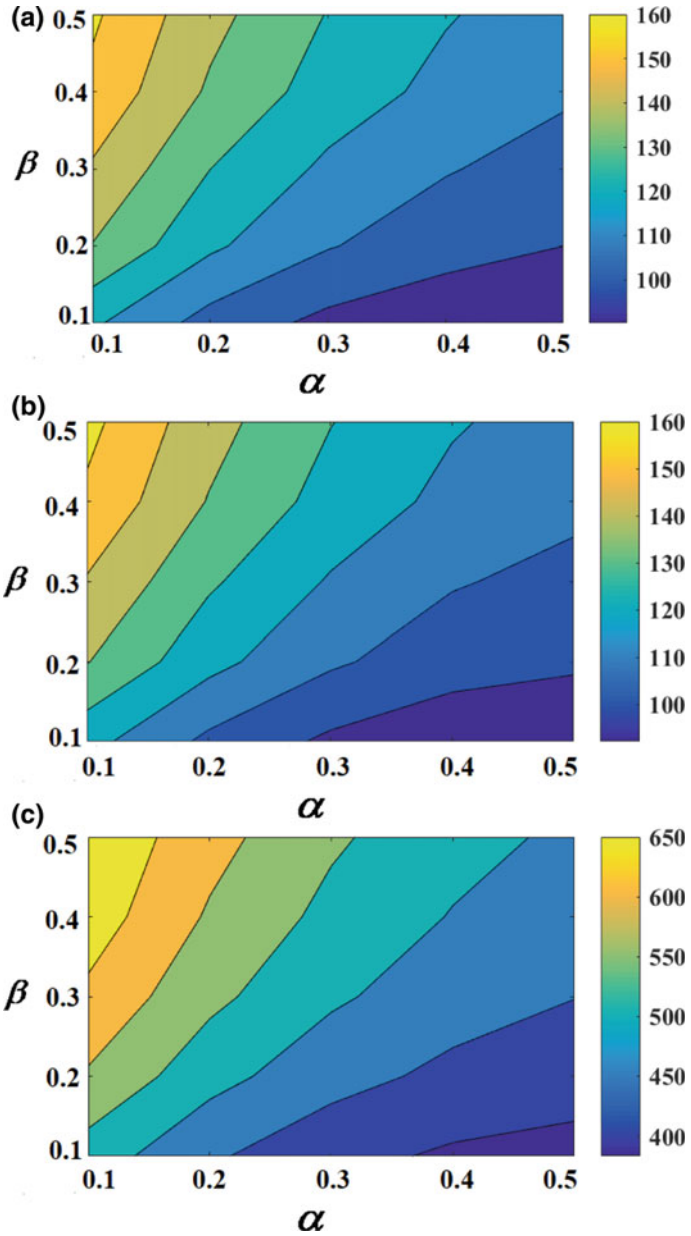


Fig. 5 Contour plot for the natural frequencies showing the effect of relative thickness of various component of hybrid hyperbolic paraboloid shells (here, α = upper facesheet thickness/total thickness and β = lower facesheet thickness/total thickness)

4 Conclusions

Based on linear regression model (LRM) integrated with FE modeling, the random free vibration of hybrid hyperbolic paraboloid shell is studied showing the effect of relative thickness of various components of these hybrid structures. The LRM surrogate is made into use so as to increase the computational efficiency by reducing the iteration time (from 10,000 samples to 256 samples) without hindering with the precision of the outcomes. The novelty of current work includes the study of the relative outcome of various component of hybrid on stochastic natural frequencies. Due to the complex geometric configuration and manufacturing technique of this hybrid structure, we can observe random behavior of these structures which are unavoidable. These studies are done to guarantee the reliability of these structures. The parametric analysis presented here in terms of the contour plots will help the designers to have a comprehensive idea regarding the variation of natural frequencies in the entire design space of layer-wise thickness. Based on these outcomes, we can further extend our study for different geometric configurations.

Acknowledgements The first author acknowledges MHRD for the monetary support provided for this work.

References

1. Pandey A, Muchhala D, Kumar R, Sriram S, Venkat AC, Mondal DP (2020) Flexural deformation behavior of carbon fiber reinforced aluminium hybrid foam sandwich structure. *Compos B Eng* 183:107729
2. Kumar RR, Vaishali, Pandey KM, Dey S (2020) Effect of skewness on random frequency responses of sandwich plates. In: Singh B, Roy A, Maiti D (eds) *Recent advances in theoretical, applied, computational and experimental mechanics. Lecture notes in mechanical engineering*. Springer, Singapore. https://doi.org/10.1007/978-981-15-1189-9_2
3. Vaishali, Mukhopadhyay T, Karsh PK, Basu B, Dey S (2020) Machine learning based stochastic dynamic analysis of functionally graded shells. *Compos Struct* 237:111870
4. Vaishali, Mukhopadhyay T, Kumar RR, Dey S (2020) Probing the multi-physical probabilistic dynamics of a novel functional class of hybrid composite shells. *Compos Struct* 113294
5. Siwowski T, Rajchel M (2019) Structural performance of a hybrid FRP composite–lightweight concrete bridge girder. *Compos B Eng* 174:107055
6. Loy CT, Lam KY, Reddy JN (1999) Vibration of functionally graded cylindrical shells. *Int J Mech Sci* 41(3):309–324
7. Dey S, Mukhopadhyay T, Sahu SK, Adhikari S (2018) Stochastic dynamic stability analysis of composite curved panels subjected to non-uniform partial edge loading. *Eur J Mech-A/Solids* 67:108–122
8. Karsh PK, Mukhopadhyay T, Dey S (2018) Stochastic dynamic analysis of twisted functionally graded plates. *Compos B Eng* 147:259–278
9. Baferani AH, Saidi AR, Ehteshami H (2011) Accurate solution for free vibration analysis of functionally graded thick rectangular plates resting on elastic foundation. *Compos Struct* 93(7):1842–1853

A Review: High Amplitude Vibration and Jump Phenomena Attenuation Methods in Different Dynamic Systems



Mohd Anis Ansari, Prabina Kumar Meher, Alfa Bisoi,
and Agnimitra Biswas

Abstract In this review paper, the research findings regarding the jump phenomena, vibration issue and a broad range of attenuation techniques for the issues in different dynamic systems are well succinct. In the field of dynamics, the interaction between the drive and the driven source is always an interesting point of research to perceive the characteristic of non-ideal vibrating systems. In this article, we broadly categorized the investigation and vibration attenuation techniques for different dynamic system into three types, namely optimization of the system design parameter, optimization of drive parameter and smart methods. In the first category, various research articles are briefed to deliver the optimization technique for foundation element parameters such as spring, damper and bearing to reduce heavy-duty vibration amplitude. In the second category, a bunch of research findings are described to showcase that optimizing the electrical input and drive torque may help to attenuate resonant vibration. In the third part, some smart methods like the use of a magnetic bearing, magneto-rheological damper and shape memory alloy to suppress the chaotic behavior of the system in the resonance region are addressed. Nowadays, practice of the smart technique is growing faster and it is an emerging research option for the attenuation of the vibration in highly dynamic systems.

Keywords Ideal and non-ideal · Linear and nonlinear · Vibrating structure · Sommerfeld effect

M. A. Ansari · P. K. Meher (✉) · A. Bisoi · A. Biswas
Mechanical Engineering, National Institute Technology, Silchar, India
e-mail: prabinmeher90@gmail.com

M. A. Ansari
e-mail: mohd.anis68@gmail.com

A. Bisoi
e-mail: alfabisoi@mech.nits.ac.in

A. Biswas
e-mail: agnibis@mech.nits.ac.in

1 Introduction

Fault-free maneuvering of dynamic systems is difficult to achieve. The dynamics of the systems are complex due to the coupling of lateral, torsional, axial vibrations. Rotor dynamic systems are one of those systems and the impact of source dynamics on systems also played a significant role in the modeling, which also add more complexity to the system. Rotor dynamic systems are significant machine element which is used in various applications, such as in household element, particle separator, turbines, pumps and helicopter rotors. Failure of the dynamic systems happens mostly near the resonance region. In the mechanical system-source arrangement as in Fig. 1, the maximum power also gets consumed to survive the resonance. For a significant power input, it is able to transit through resonance and the system speed jumps to a higher value from resonance (see in Fig. 2). A German scientist named Arnold Sommerfeld in 1904 was the first to give conclusive evidence about the jump phenomenon that occurred in the region of resonance [1].

This jump phenomenon is popularly known as the Sommerfeld effect. Jump phenomena also described an important issue, that is regarding the reduced working speed range in the post-resonance region. Therefore, jump phenomena attenuation is a difficult and necessary task to make the system dynamically efficient and economical. In this introductory segment, some research regarding the occurrence of jump phenomena in various dynamic systems and its consequences is summarized.

Fig. 1 Rotor shaft system driven by DC motor

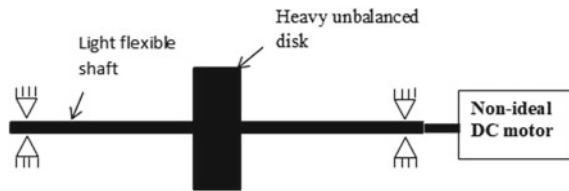
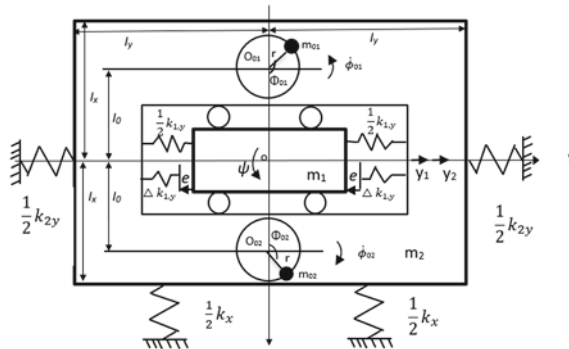


Fig. 2 Dynamical model of considered vibrating system



An internally damped rotor placed symmetrically on a flexible shaft driving by a non-ideal DC motor is considered for investigation by Sommerfeld [2]. The gyroscopic effect of the rotor is taken into consideration, and additional coupling is observed due to the coupling by the researcher. From the analysis, they observed that an increase in the power supply near critical speed leads to an increase in the flexural vibration instead of increasing the rotational speed of the motor. They also provide the concept of stability threshold that motor speed cannot pass the stability threshold. Dasgupta et al. [3] considered the dynamics of two externally and internally damped rotationally symmetric planar systems. There the researchers tried to validate the manifestation of the Sommerfeld effect by comparing both analytical and numerical simulation results. The study also showed the influence of material damping of the system on the stability threshold speed of the systems and cease of jump phenomena at the stability threshold. In their analysis with dynamic system, i.e., unbalanced motor at the tip of a cantilever beam also provides the information about the acuteness of Sommerfeld effect increased due to the additional gyroscopic effect. Tsuchida et al. [4, 5] investigated the pattern of vibration observed for a non-ideal two degree of freedom system of 1:1 internal resonance. Linear and nonlinear torque models are taken into consideration for numeral simulation. Before the resonance, at resonance and after the resonance regions were taken into account for analysis. At resonance, they observed that stronger nonlinearity instigates the jump phenomena and the Sommerfeld effect changes the regular vibration to a chaotic one. Sado and Kot [6] have considered a highly dynamic non-ideal two-degree freedom system to study the characteristic of vibration amplitude at the resonance region. The investigated system consisted of a pendulum of a certain mass and length and a body of a certain mass suspended on a flexible element. The system was excited by a non-ideal source (DC motor) with an unbalanced mass. After analysis, they conclude that chaotic or quasi-periodic vibration will occur always during the strong interaction between the non-ideal source and the body. They also observed that vibration amplitude jump can be significantly visible for a quasi-static analysis of the system and recommended the necessity of the study of nonlinear source-system interaction. An experimental investigation to study the nonlinear characteristic of a non-ideal vibrating system is done by El-badawy [7]. He has performed an experimental analysis on a setup, which was consisting of a cantilever beam and a large motor attached to its free end. The major intention of this analysis is to characterize the Sommerfeld effect. Both static and dynamic analyses of the system have been done, and the author compared both static and dynamic response curves in terms of power versus rotational speed. Nonlinearity is found when the motor frequency approaches the resonant frequency in dynamic response curve which is one of the main characteristics of the Sommerfeld effect. A structural system having two degrees of freedom excited with a non-ideal source is considered for the analysis of the Sommerfeld effect. An analytically obtained solution for the resonant regime is compared with the numerical solution and shows good agreement. Sommerfeld effect appears only one time when the x and y direction frequency is the same but the Sommerfeld effect occurs twice for different value of torque parameter when the frequency of x and y

direction is different. The researcher also observed a significant jump in vibration amplitudes at resonance in the coupled system [8].

The severity of the Sommerfeld effect is observed with respect to different unbalance position in a two-disk rotor system that is run by a non-ideal DC motor by using the semi-analytical and numerical method. It is investigated that the interference of two close frequencies with the jump phenomenon is related to the Sommerfeld effect. The most severe condition of the Sommerfeld effect for the in-phase and out-phase unstable position is the first and second critical speed of the system, respectively. This is much easier to deal with the discrete rotor model for the investigation of Sommerfeld effect characteristics by using the power balance principle [9]. The same research group also investigated characterizing the Sommerfeld effect in an overhung rotor system that is connected with a non-ideal driving source, i.e., DC motor. They detected a jump phenomenon at forward critical speed and observed that motor cannot accelerate quickly when the inertia of the rotor is high. The gyroscopic effect in the overhung system is very high and that adds another coupling in the system equation [10]. A study on Sommerfeld effect with two vibrating systems excited by two separately induction motors is analyzed experimentally by Zhang et al. [11]. The main motive for the investigation is to validate Sommerfeld effect numerically as well as experimentally. After the analysis, authors commented that temperament of amplitude was high at resonance region and it came down to zero after passing the resonant region. Sommerfeld effect added more complexity in vibration analysis of the nonlinear system. Many authors provided the significance of jump phenomena and its analysis methods for nonlinear systems in their research, which is summarized as follows: Krasnopolskay [12] investigated about nonlinear vibration that occurs on acoustic medium. He considered a hydro-elastic infinite system for the study. Also, two types of mathematical model were considered. The first one when the plate was subjected to a point excitation by a non-ideal source supported by an elastic foundation, and the second one it was subjected to a direct excitation without the foundation. After analysis, author commented that for the first case, chaos could occur due to excitation of foundation. And for second case, chaos might occur due to rotation of the shaft. In 2003, Dantas and Balthazar [13] investigated about stability criteria on a non-ideal dynamic problem with the help of Hopf bifurcation mathematical theory. A DC motor with an eccentric mass place on a spring is considered for analysis. After the analysis, authors suggested that one can analyze a non-ideal problem with the help of Hopf bifurcation because the appearance of Hopf bifurcation is also a manifestation of Sommerfeld effect. Bolla et al. [14] in 2007 studied on a nonlinear vibrating system with a non-ideal source of excitation. The investigating system consists of a DC motor with eccentricity attached to a cantilever beam. The above-mentioned model is already discussed experimentally by Mattos et al. [15]. So, for current study, authors tried to analyze the above-mentioned system numerically as well as analytically with a simplified model. To make the system more realist, author chooses cubic nonlinearity for spring and quadratic nonlinearity for DC motor. The analytical solution is obtained by Multiple Scales Method. Stability criteria also discussed through Hopf bifurcation technique. The result showed a good match with the experimental one. The unstable periodical orbits with more

than one direction are used to explain the evolution between chaos and hyperchaos response of the system for the Sommerfeld effect. There are four stability regions are observed for the control parameter ν in the range of 0 to 10. The first region (0–3) is showing the stable region at a particular value of the influence parameter α and β , second (3–6), and fourth (8–10) is found some instability in the structural behavior, the third region is (6–8) showing chaotic behavior [16]. Numerical and analytical methods are applied to find out the dynamic characteristics of the rotor system with a flexible shaft and rigid disk. Three methods are used for the resonant curve, the method of multiple scales (MMS), Matcont, and step-by-step method in MATLAB software. Method of multiple scales is showing very effective results in comparison with the other two methods at the resonant condition. It is observed that the dynamic response of the system is highly affected by the variation in the unbalance mass and shaft diameter [17]. A nonlinear vibrating system having three DOF is connected to the non-ideal drive source. The decomposition concept is applied to understand the rotor fluctuations distinctly, disregarding its rotational speed. The possible amplitude of steady-state vibration is also derived analytically and observed that steady-state motion is not possible at some range of frequency near to the resonance point. It can be related to the Sommerfeld effect in the nonlinear vibrating system [18]. Three-dimensional micro-rotating Rayleigh beam with rotary inertia and the gyroscopic effect is analytically investigated based on modified stress coupled theory taking account of the small-scale effect of vibration. Hamilton principle is used for the derivation of nonlinearly coupled three-dimensional governing equation of motion and its boundary condition. To find the nonlinear vibration characteristic, Galerkin and multiple scale methods are imposed in the differential equation. It was found that the length scale parameter is an important consequence on the linear as well as the nonlinear natural frequency of clamped–clamped and hinged–hinged micro rotating-beam [19]. A center manifold theory and a bifurcation technique are used in a simply supported shaft including internal damping to observe the rotating Shaft behavior in the neighboring point of Hopf bifurcation and double zero eigenvalues. If the value of external damping is zero, the trivial solution of the shaft is stable when the whirling speed of the shaft is not exceeded of the critical speed and if the speed is greater than the critical speed the shaft is whirling synchronously. If the external damping is considered, the radius of the cycle depends on the spinning speed and the quotient of external and internal damping value. It was observed that the precession rate is directly proportional to the external damping coefficient while inversely proportional to the internal damping coefficient [20].

From the above literature, it is observed that significant Sommerfeld effect appears at the critical speed region. However, the prediction of critical speed in a flexible dynamic system is not easy. In [21], researchers have developed some methods related to the Southwell plot which was used for the prediction of the first critical speed of the three different types of dynamic systems. The first two were theoretical analysis of Jeffcott rotor connected with external damping and shaft bow at low rotational speed and the third one was the experimental analysis of Jeffcott rotor with centrally placed disks. For the initial two systems, critical speed was predicted from the slope of the fitted curve, and in the third case, linear or nonlinear type

extrapolation of data point method has been used for critical speed prediction. In all three cases, the used method is showing a good observation of the critical speed of the system at a low rotational speed. Jump phenomena prediction and overcoming from its effect are highly essential in motorized rotor dynamic systems. In this paper, various methods for a smooth operation through the resonance are summarized.

2 Jump Phenomena Attenuation Methods

In the above segment, it is observed that the connotation of jump phenomena or Sommerfeld effect cannot be ignored for a fault-free maneuver of dynamic systems. Many researchers have developed a variety of methods to avoid the vibration chaos which is occurred due to the Sommerfeld effect. Some of the important findings related to jump phenomena attenuation and high vibration amplitude control near resonance are summarized in this segment.

In multiple resonant states, a nonlinear characteristic was investigated in a vibrating system excited by two different external exciters shown in Fig. 2. The study carried out to deliver the idea that stability and synchronization criteria are achieved by keeping zero phase difference in the exciter input. They have suggested choosing the working region in stable condition and at the nonlinear condition of the system, and the vibration stability can be kept in harmony by varying the shear rubber spring foundation stiffness [22].

In 1995, Dimentberg et al. [23] have performed an experimental, as well as the numerical, study on dynamics of unbalanced shaft excited by a non-ideal power source. The analysis is mainly focused on the region of resonance. Here, the system is consisting of an unbalanced shaft attached on a rigid base supported by damper and spring. And after the investigation, authors found that the rotation speed at the resonance region strongly influences by damping ratio and non-dimensional unbalance parameter. Also, the authors suggested that one can ensure easy passage through resonance by switching system stiffness. According to Dimentberg et al. by adding some stiffness to a system designed stiffness before starting for making a safe passage through resonance and after smooth passage, one can remove the additional stiffness. Gu et al. in 1998 [24] investigated extensively to study the chaotic behaviors in the machine. Chaotic vibration of machine could be also named as one of the primary characteristics of Sommerfeld effect. They considered two systems namely the impact beam system and spatial slider-crank mechanism. For both systems, the chaotic behaviors were studied as a function of clearance size, component dimension, and driving speed. Chaotic vibration is found in both the cases, and they confirmed it by comparing the obtained result from simulation and experiment. They divided their study into three categories namely type I response, type II response and type III response. And from the obtained result, it shows that (Table 1).

And finally, the authors commented that these were inevitable and advised design engineers to give more emphasis on fatigue life and reliability of machine that shows chaotic behavior to avoid certain catastrophic failures. A two-dimensional analysis is

Table 1 Different types of response behavior

Sr. No	Response type	Descriptions
1	Type I response	Periodic and non-sensitive to initial condition and small variation in parameter
2	Type II response	Periodic but near chaotic behavior also found and non-sensitive to initial condition but sensitive to small variation
3	Type III response	Unpredictable, more chaotic vibration and sensitive to both initial condition as well as small variation

carried out of a vibrating body attached with a spring-damper system that is connected with a non-ideal source drive having an unbalanced mass for the observation of jump phenomenon as shown in Fig. 3.

An experiment is also performed for the supporting of obtained data from numerical analysis. The concentrated mass is fixed at two positions, one is 35 mm and second is 160 mm from the right end of the structural frame. It was found out that the second natural frequency is reduced from 30 to 23 Hz at both positions but the first natural frequency is altered by placing mass at the second position [25]. Sommerfeld effect was analyzed numerically and experimentally in a cantilever beam with a non-ideal DC motor attached at its free end which is supported by single DOF of spring-mass damper system. It is observed that the solution obtained by the numerical and experimental analysis is a supporting point to explain the dynamic behavior at resonance condition and exploring the sensitivity of the system by changing the system parameter like a moment of inertia, damping coefficient, motor constant, etc. [26]. A study on Sommerfeld effect is performed numerically on a single degree of freedom systems connected to a DC motor as shown in Fig. 4.

Two different types of mechanical oscillator are used for investigation (i) A slotted cam follower mechanism, (ii) A scotch yoke mechanism with a variation in speed as input. First, an analytical analysis is done after that it was validated with the numerical result and finally authors were commented that while dealing with real nonlinear system basic parameter like joint clearance, imperfection joint should be taken care as well as friction between the slots [27]. A study is carried out for

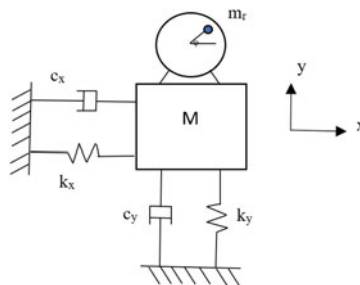


Fig. 3 Discrete parameter system with two-degree-of-freedom and coupled non-ideal unbalanced motor

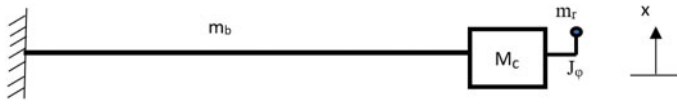
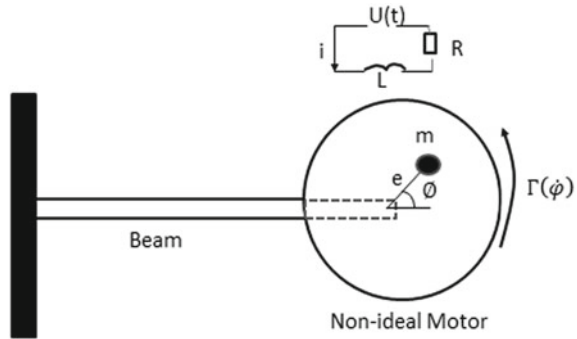


Fig. 4 Cantilever beam with a concentrated mass and an unbalanced DC motor

the observation of the rotor stuck problem near the resonant regime in the rotating structure supported by the elastic foundation. A hydraulic absorber is used as a damper for the dissipation of energy by varying the damping property of the system. If the value of the energy dissipation increases, the Sommerfeld effect gets down or completely vanishes that gives the idea of synchronisation of the vibrating structure. It was observed that there are two necessary conditions for the stable synchronisation and value of both conditions should be less than unity. The first one is stable phase synchronisation and the second one is the difference in the coefficient of resonating excitation and coefficient of energy dissipation [28]. A Sommerfeld effect is analyzed in unbalanced rotor attached with an asynchronous motor having limited power connected with the highly damped foundational system. Author wants to avoid the Sommerfeld effect by using the vibrational torque equation and the friction element spring. This friction element spring can avoid the resonance in two ways: The first one is the constant switching of the Eigen frequency and sliding friction of the system at each oscillating period, this prevents the generation of large amplitude and the second one is the energy dissipation during sliding of the foundation [29]. Zukovic and Cveticanin [30] studied on the Sommerfeld effect by considering a mechanical model couple to a non-ideal motor. The model consisting of a fluctuating mass coupled to an unbalanced eccentric motor and whole the system is connected to a fixed surface by employing spring and damper. Here, the authors considered a clearance value at the connection between the vibrating system and the spring to investigate the Sommerfeld effect. They considered a range of 0–1 by varying intermediates value of clearance. At zero clearance value, the maximum amplitude is found in the region of resonance. But at 0.1 clearance value, the maximum amplitude came close to the zero clearance value. Still, some chaotic vibration is observed at 0.1 clearance values as it could not overcome the maximum amplitude. And at last, for the regulation of the chaotic behaviors, an energy-based control technique is discussed. Varanis et al. [31] introduced a novel way to characterize the Sommerfeld effect. They used wavelet packet transform and continuous wavelet transforms for describing the nonlinear phenomenon. The experimental systems consisting of a three-story building and a portal frame separately excited by a DC motor. After the analysis, authors were commenting that both methods showed decent temperament to study the nonlinearity of a vibrating system. Out of both proposed method, wavelet packet transform turn out as the best method. Arbex et al. [32] analyzed a unique mechanical system for the study of jump phenomenon which is widely known as the Sommerfeld effect. They consider the magnetic repulsion technique instead of spring and damper. The oscillatory system attached with a magnet whose North Pole is facing toward the South Pole of another base magnet or vice versa. The whole system

Fig. 5 Model of the non-ideal cantilever beam



is excited through a DC motor. They discussed two control strategies to minimize the amplitude namely (i) passive control and (ii) semi-active control. In passive control method, an additional pendulum is attached to the system. Similarly, in the semi-active method, a governable electromagnetic suspension is used. From the obtained result, it is observed that the active control method is more efficient than passive control. Also, adding an active control method to the system on an already applied passive control method showed good efficacy in terms of minimizing the amplitude of the vibration. Felix et al. [33] investigated cantilever beam with nonlinear stiffness and damping model by Duffing–Rayleigh equation contacted to a non-ideal source shown in Fig. 5. So, from the result, it has been observed that Sommerfeld effect can reduce when the value of the nonlinear stiffness is less than one. And also, some special condition has been derived from eliminating the signs of Sommerfeld effect by increasing the nonlinear damping.

An investigation is carried out of the interaction between the non-ideal drive source and the nonlinear nature of the oscillator for the behavior of the Sommerfeld effect. They considered the three types of nonlinearity value, i.e., less than 1 equal to and greater than 1 having different stiffness value and the controlling parameter of these DC motor is the input voltage. It was observed that the Sommerfeld effect is available in all three cases only the difference is shifting of the frequency amplitude curve from right to left as we decrease the order of nonlinearity from greater than one to less than one [34]. A study on the attenuation of the Sommerfeld effect with the help of passive control is investigated by Shina et al. [35]. A system consisting of two eccentric rotors excited separately by two DC motor placed on a common foundation. A secondary vibration absorber and an additional spring-mass system (nonlinear energy sinks) are connected to the main system for reducing the amplitude of vibration. Finally, the authors have suggested that with the help of passive control mechanism, we can reduce the temperament of vibration up to a certain extent but cannot fully suppress chaosity of the foundation. Frolov and Krasnopol [36] investigated the Sommerfeld effect by considering a system consisting of an acoustic medium, an infinite elastic plate and a non-ideal source for excitation. Internal damping is neglected for the analysis. Here, the author analyzed how the elastic plate behaves when excited through a fluid medium as one side of the plate, in contact with the fluid. A study

on Sommerfeld effect is performed by Jha and Dasgupta [37]. A rotor placed at the middle of a simply supported beam is considered for analysis. A DC motor was used for excitation. Fractional-order external damping method was used for minimization of Sommerfeld effect. From the result, it is established that by increasing the fractional-order constraint, one can attenuate the Sommerfeld effect up to a certain degree.

Dynamics of the power source add another degree of freedom to the system equation and optimizing the source parameter also help in smooth transit through the critical speed region. Observations of many research article, highlighting the source effect in lessening the effect of jump phenomena, are summarized. A group of researcher has studied the Sommerfeld effect in a dynamic vibration-absorbing system in two stages connected with spring having a different mass of the blocks. Two types of excitation sources, i.e., ideal and non-ideal excitation are used in the analysis. Ideal excitation is used as a harmonic force and non-ideal excitation is used as a DC motor. It is observed that the non-ideal source of excitation gives a higher rate of displacement than the ideal excitation [38]. The obtained response characteristic from the FE model with the ideal drive is used for the prediction of the spin speed of the rotor and the vibrational amplitude of a non-ideal system for a particular value of power supply. A Bond graph model is used in transient analysis of the rotor system for the prediction of threshold power requirement at resonance condition [39]. Iwatsubo et al. [40], in 1972, discussed on non-stationary vibration of an asymmetric rotor attached to a non-ideal source of excitation by altering the rate of the acceleration for minimizing the response of the structure during passage through resonance. In this paper, the chaotic behaviors of the rotor with unequal shaft stiffness, driven by a DC motor, are studied. After the theoretical and experimental analysis, authors comment that the asymmetric rotor system with a limited power supply has an unstable region due to asymmetry of the shaft. The phase angle of eccentricity plays a major role in non-stationary vibration of the rotor. An investigation of the characteristics of the Sommerfeld effect is carried out of a vibrating structure attached with spring damper system connected with a non-ideal driving source, i.e., DC motor by applying various controlling parameter like magnetizing the pole, Shunt and series wound of the DC motor. The obtained result is validated through ADAMS and Bond Graph Model. It was found that the jumping value of the amplitude is the lowest when the system connected with the DC shunt motor and highest when the system connected with the DC series motor. So according to authors, for making a safe passage through resonance, one can use DC series motor initially to boost the torque and switch back to DC shunt motor just before the resonance region and again switch back to DC series motor just after the resonance region [41]. A semi-analytical method is used for the Sommerfeld effect of the two rigid disks having eccentricity mounted on a simply supported flexible shaft connected with a non-ideal drive source. A controlling parameter of the speed regulation of DC motor is the supply voltage for the attenuation of the Sommerfeld effect. They validated the result obtained from the theoretical analysis with the FE model and the Bond Graph model for the Sommerfeld effect. In the context of designing (size of the actuator) and computational analysis, the applied approach is very efficient and beneficial to

find out the resonating behavior of any type of multi-disk system of the rotor [42]. They studied the characteristics of Sommerfeld effect in an eccentric disk mounted asymmetric position on the rigid shaft supported by flexible bearing that is driven by a DC motor. A Sommerfeld effect is found at first forward and backward whirl critical speed. Existence of stability criteria, it was observed that when the two critical speed is closer to each other there are four stable and two unstable regulating speed simultaneously occur at a specific range of the applied voltage but when these two critical speeds not close to each other the stability of regulating speed just showing half of the previous i.e. two stable and one unstable at a two different interval of applied voltage [43]. Tusset et al. [44] investigated on a simple portal frame about its chaotic behavior connected to a DC motor. They used both active and passive control strategy for suppressing the behavior. In passive control, they added a spring-mass system (sub-structure) to the original model and successfully reduced the amplitude. Lyapunov exponent is used for characterizing the stability of the system. In the active control, an additional MR damper is used to the original model to control the electric current. Efficacy in the result for both the control strategy has been seen. Shina et al. [45] have performed an analysis on a single degree of freedom system excited by a non-ideal source. A slider-crank reciprocating mechanism is considered for analysis where the DC motor is connected to the crank and the whole system is connected with spring and damper. The current objective is to investigate whether a particular supply power can make a safe passage through the resonance region. As we know that dissipated power is always constant irrespective of the supply voltage. By changing the input supply voltage authors found that at 71.6 V is the threshold voltage which can overcome the resonance region. So according to authors, any voltage higher than the threshold voltage will guarantee a smooth transition through resonance. A new method is imposed for the rotor motor system which is related to the speed gradient energy control method and averaging method in multidimensional analysis. The purposed method is very effective for the reduction in controlling torque [46]. A non-ideal model of motor oscillator system having two degrees of freedom is studied. The torque developed by the motor is the nonlinear function of angular velocity that is assumed for the analysis of the Sommerfeld effect. It is found that the torque of the motor is getting higher at a lower order of nonlinearity for a constant frequency. The parameter value which suppresses the Sommerfeld effect is presented in the steady-state response of oscillator for all the value of the driving torque [47].

Smart Techniques

In some research articles, advanced technique, smart damper, smart bearings and shape memory alloy are considered for the attenuation of Sommerfeld and reducing the resonant vibration in dynamic systems. Many such findings are addressed in this segment.

Castao et al. [48] tried to surpass the high vibration amplitude at the resonance region with the help of magneto-rheological damper (MR damper). The system is consisting of an oscillator, a nonlinear spring, and a magneto-rheological damper connected to a limited power supply DC Motor. Their findings have described the technique of increasing the damping factor of the MR damper by changing the current,

which leads to a decrease in the Sommerfeld effect by reducing the amplitude of vibration near the resonance region. A semi-active approach is used in a non-ideal system for the reduction in resonating vibration in a non-ideal structure with MR damper. A comparison is carried out with and without MR damper for the Sommerfeld effect in a non-ideal vibrating system. The undesirable oscillation is suppressed with the help of MR damper by varying the viscosity of MR fluid which depends on the supply current or voltage. In the case of MR damper, the Sommerfeld effect is avoided at a particular value of current supply which means MR damper is efficient to suppress the energy consumption of DC motor at resonance condition [49]. Another non-ideal kind of dynamical system is investigated by Wauer and Suherman [50]. The system consists of a simple supported vertical shaft with damping, and it was presumed that the bending stiffness of shaft can be altered from one numeric value to another by using shape memory alloy. To avoid the passage through resonance, the bending stiffness was altered at a certain time as the speed of shaft increases. Dynamic behavior of an overhung disk having flexible shaft has been studied by using the full spectrum analysis in theoretical, as well as experimental, observation. A full-spectrum analysis is used in the system to investigate the backward whirl vibration affected by the interaction of the anisotropy of bearing stiffness, shaft flexibility, and the gyroscopic effect. The tracking filter is used for the isolation of synchronous and non-synchronous whirl vibration and the measurement of an accurate phase angle. The rapid decrement of the vibration amplitude of positive frequency between two natural frequencies in experimental as well as a theoretical model is observed [51]. A flexible shaft with internal damping having eccentricity driven by a DC motor is used for the analysis of the Sommerfeld effect by providing an external damping system as a magnetic bearing. The magnetic bearing is actuated with the help of supply current. It was found that by increasing the supply current, the jumping effect of amplitude is gradually decreasing. The range of current supply is from 0 to 4A, and it is found that at 3.43A, the jump phenomenon of amplitude is almost disappeared [52]. In future, use of the smart technique in rotor-motor analysis may be the suitable option to attenuate the higher vibrational amplitude and to make a quick escape from the resonance region without being stuck for a long time (Table 2).

In this article, major possible way of vibration attenuation methods is summarized. Further, in this assessment of vibration and jump phenomena control, it is understood that many research possibilities exist that need further research. These investigations may be carried out by the young researchers to seal the observed gaps. Vibration and jump phenomena control through variation in the system parameters is experimentally possible by manual reconfiguration of the original system. Conversely, there is not much research work done to explain the possible difficulty to change the system parameter manually on a final manufactured product. On the other hand, we may take the help of vibration observer or isolator, for vibration control, it would also restrict the range to very small unit. In another set research work related vibration attenuation by adjusting the drive parameter, the researchers have suggested additional configuration to the original motors, which may lead to excess cost and additional weight to the system. Thus, optimal methods with minimal weight and less cost are required to be investigated for considering this study. Finally, various smart methods

Table 2 Summary of the optimization parameter for attenuation type

Attenuation type	Methods	Research groups
Type I and type II response	Attenuation of vibration and jump phenomena using the system parameters	Zhang et al. [22], Dimentberg et al. [23], Gu et al. [24], Goncalves et al. [25], Goncalves et al. [26], Sinha et al. [27], Kovriguine [28], Alexander and Drozdetskaya [29], Zukovic and Cveticanin [30], Varanis et al. [31], Arbex et al. [32], Felix et al. [33], Cveticanin and Zukovic [34], Shina et al. [35], Frolov and Krasnopol [36], Jha and Dasgupta [37], Fernando et al. [38]
	Attenuation of vibration and jump phenomena using the drive parameters	Karhikeyan et al. [39], Iwatsubo et al. [40], Bisoi et al. [41], Bisoi et al. [42], Bharti et al. [43], Tusset et al. [44], Shina et al. [45], Fradkov et al. [46], Cveticanin and Zukovic [47]
Type I, II and III response	Attenuation of vibration and jump phenomena using the Smart parameters	Castao et al. [48], Piccirillo et al. [49], Wauer and Suherman [50], Wu et al. [51], Jha and Dasgupta [52]

for vibration and jump phenomena control are addressed in this article. However, it is observed that only use of electro-magnetic bearing, magneto-rheological damper and smart materials for suspension may not provide adequate vibration management irrespective of its cost. In addition, it is largely observed that not much research is present related to the amalgamation of the above methods.

3 Conclusions

In this article, assortments of research articles are abridged addressing the vibration issue, Sommerfeld effect and the attenuation technique of the same for linear and nonlinear dynamic systems. Dynamic systems are easily prone to vibration. For example, a simple manufacturing fault in dynamic system can create unbalance which leads to vibration in the system. At resonance, that vibration amplitude becomes very high which creates chaos and that leads to system failure. In drive-rotor systems, speed jump happens at the resonance due to profound foundation vibration. It is important to develop vibration control techniques to accelerate dynamic systems through heavy vibration.

In this paper, different types of developed analytical techniques to solve the complex equation of motion of highly dynamic systems are addressed. Many articles are summarized to deliver a vast range of idea such as optimizing the foundation spring-damper parameters, balancing the rotor system, drive speed control, optimization of input torque for heavy-duty vibration control and transit through jump phenomena. For a different type of dynamic systems, active, semi-active and smart vibration control techniques given by various researcher are well briefed in this article. In this article, the major research gaps are identified, that will assist the young researchers to developed interest in this field.

References

1. Sommerfeld A (1902) Contributions to the dynamic expansion of strength theory. *Phys J* 3:266–284
2. Samantary A (2009) Steady-state dynamics of a non-ideal rotor with internal damping and gyroscopic effects. *Nonlinear Dyn* 56:443–451
3. Dasgupta S, Samantaray A, Bhattacharyya R (2010) Stability of an internally damped non-ideal flexible spinning shaft. *Int J Non-Linear Mech* 2010:286–293
4. Tsuchida M, Guilherme L, Balthazar M (2005) On chaotic vibrations of a non-ideal system with two degrees of freedom. *J Sound Vib* 282:1201–1207
5. Tsuchida M, Guilherme K, Balthazar J, Silva G, Cheshankov B (2003) On regular and irregular vibrations of a non-ideal system with two degrees of freedom. 1:1 resonance. *J Sound Vib* 260:949–960
6. Sado D, Kot M (2007) Chaotic vibration of an autoparametrical system with a non ideal source of power. *J Theor Appl Mech* 45:119–131
7. El-badawy A (2007) Behavioural investigation of a nonlinear nonideal vibrating system. *J Vib Control* 13:203–217
8. Cveticanin L, Zukovic M, Cveticanin D (2017) Two degree of freedom oscillator coupled to a non-ideal source. *Int J Non-Linear Mech* 94:1–21
9. Bisoi A, Samantaray AK, Bhattacharyya R (2017) Sommerfeld effect in a two-disk rotor dynamic system at various unbalance conditions. *Meccanica* 53:681–701
10. Bisoi A, Samantaray AK, Bhattacharyya R (2017) Sommerfeld effect in a gyroscopic overhung rotor-disk system. *Nonlinear Dyn* 88(3):1565–1585
11. Zhang X, Li Z, Li M, Wen B (2020) Stability and sommerfeld effect of a vibrating system with two vibrator driven separately by induction motors. *IEEE*. <https://doi.org/10.1109/TMECH.2020.3003029>
12. Krasnopolskaya S (1994) Acoustic chaos caused by the sommerfeld effect. *J Fluids Struct* 8:803–815
13. Dantas H, Balthazar M (2003) On the appearance of a Hopf bifurcation in a non-ideal mechanical problem. *Mech Res Commun* 30:493–503
14. Bola R, Balthazar M, Felix P (2007) On an approximate analytical solution to non-linear vibrating problem excited by a non-ideal motor. *Nonlinear Dyn* 50:841–847
15. Mattos CM, Balthazar M (1999) On the dynamics of an armature controlled DC motor mounted on an elastically supported Table. In: 15th Brazilian Congress of Mechanical Engineering, Aguas de Lindoia, Sao Paulo, 22–26 Nov pp. 1–10
16. Munteanu L, Brisani C, Chiroiu V, Dumitriu D, Ioan R (2014) Chaos–hyperchaos transition in a class of models governed by sommerfeld effect. *Nonlinear Dyn* 78:1877–1889
17. Shad MR, Michon G, Berlioz A (2011) Modeling and analysis of nonlinear rotordynamics due to higher order deformations in bending. *Appl Math Model* 35:2145–2159

18. Jan A, Roman S, Grażyna S (2015) Decomposition of governing equations in the analysis of resonant response of a nonlinear and non-ideal vibrating system. *Nonlinear Dyn* 82:299–309
19. Asghari M, Hashemi M (2017) The couple stress-based nonlinear coupled three-dimensional vibration analysis of microspinning Rayleigh beams. *Nonlinear Dyn* 87:1315–1334
20. Hosseini S (2013) Dynamic stability and bifurcation of a nonlinear in-extensional rotating shaft with internal damping. *Nonlinear Dyn* 74:345–358
21. Lawrence NV, Josiah DK, Raymond HP (2016) A new method for predicting critical speeds in rotordynamics. *J Eng Gas Turbines Power* 138:22541–22546
22. Zhang X, Wen B, Zhao C (2016) Theoretical study on synchronization of two exciters in a nonlinear vibrating system with multiple resonant types. *Nonlinear Dyn* 85:141–154
23. Dimentberg MF, McGovern L, Norton R, Chapdelaine J, Harrison R (1997) Dynamics of an unbalanced shaft interacting with a limited power supply. *Nonlinear Dyn* 13:171–187
24. Gu P, Dubowsky S, Mavroidis C (1998) The design implication of chaotic and near chaotic vibrations in machines. In: *Proceeding of the 1998 ASME design technical conferences*, Atlanta, GA. 13–16 Sept, pp 1–11
25. Goncalves PJP, Silveira M, Petrocino EA, Balthazar JM (2016) Double resonance capture of a two degree of freedom oscillator coupled to a non-ideal motor. *Meccanica* 51:2203–2214
26. Gonçalves P, Silveira M, Junior B, Balthazar J (2014) The dynamic behavior of a cantilever beam coupled to an on-ideal unbalanced motor through numerical and experimental analysis. *J Sound Vib* 333:5115–5129
27. Sinha A, Bharti S, Samantarya A, Bhattacharya R (2020) Sommerfeld effect in a single-DOF system with base excitation from motor driven mechanism. *Mech Mach Theory* 148:103–108
28. Kovrigin DA (2012) Synchronization and sommerfeld effect as typical resonant patterns. *Arch Appl Mech* 82:591–604
29. Alexander F, Drozdetskaya O (2016) On the averaging in strongly damped systems: the general approach and its application to asymptotic analysis of the Sommerfeld effect. In: *IUTAM 19 symposium analytical methods in nonlinear dynamics*, vol. 43, pp 43–52
30. Zukovic M, Cveticanin L (2009) Chaos in non-ideal mechanical system with clearance. *J Vib Control* 15(8):1229–1246
31. Varanis M, Balthazar J, Silva A, Mereles A, Pederiva R (2018) Remark on sommerfeld effect characterization in the wavelet domain. *J Vib Control* 1–11
32. Arbex H, Balthazar J, Pontes jr B, Brasil R, Felix J, Tusset A, Bueno A (2014) On nonlinear dynamics behaviour and control of a new model of magnetically leitated vibrating system excited by an unbalanced DC motor of limited power supply. *Brazilian Soc Mech Sci Eng* 37:1139–1150
33. Felix J, Balthazar JM, Brasil R (2009) Comments on nonlinear dynamics of a non-ideal duffing-rayleigh oscillator: Numerical and analytical approaches. *J Sound Vib* 319:1136–1149
34. Cveticanin L, Zukovic M (2015) Non-ideal mechanical system with an oscillator with rational nonlinearity. *J Vib Control* 21:2149–2164
35. Shina A, Samantarya AK, Bharti SK, Bhattacharya R (2018) Sommerfeld effect and passive energy reallocation in self synchronizing system. *ASME*, pp 1–10
36. Frolov KV, Krasnopolskaya TS (1988) Sommerfeld effect in system without internal damping. *Plenum Publishing Corporation* 23:19–24
37. Jha AK, Dasgupta SS (2020) Suppression of sommerfeld effect in a non-ideal discrete rotor system with fractional order external damping. *European J Mech* 79(103873)
38. Fernando HM, Bento RP, Silveira M (2013) Influence of ideal and non-ideal excitation sources on the dynamics of a nonlinear vibro-impact system. *J Theor Appl Mech* 51:763–774
39. Karthikeyan M, Bisoi A, Samantarya A, Bhattacharya R (2015) Sommerfeld effect characterization in rotors with non-ideal drive from ideal drive response and power balance. *Mech Mach Theory* 91:269–288
40. Iwatsubo T, Kanki H, Kawai R (1972) Vibration of asymmetric rotor through critical speed with limited power supply. *J Mech Eng Sci* 14(3):184–194
41. Bisoi A, Samantarya A, Bhattacharya R (2017) Control strategies for DC motors driving rotor dynamic systems through resonance. *J Sound Vib* 411:304–327

42. Bisoi A, Samantaray AK, Bhattacharyya R (2014) Sommerfeld effect characterisation in multi-disk rotor dynamic system with non-ideal drive through semi-analytical methods. In: Proceedings of ICTACEM, IIT Kharagpur
43. Bharti SK, Bisoi A, Sinha A, Samantaray A, Bhattacharyya R (2019) Sommerfeld effect at forward and backward critical speeds in a rigid rotor shaft system with anisotropic supports. *J Sound Vib* 442:330–349
44. Tusset AM, Balthazar JM, Felix J (2012) On elimination of chaotic behaviour in a non-ideal portal frame structural system using both passive and active controls. *J Vib Control* 19(6):803–813
45. Shina A, Bharati SK, Samantary AK, Chakraborty G, Bhattacharya R (2018) Sommerfeld effect in an oscillator with a reciprocating mass. *Nonlinear Dyn* 93:1719–1739
46. Fradkov A, Tomchina O, Tomchin D (2011) Controlled passage through resonance in mechanical systems. *J Sound Vib* 330:1065–1073
47. Cveticanin L, Zukovic M (2015) Motion of a motor-structure non-ideal system. *European J Mech A/Solids* 53:229–240
48. Castao KA, Goes LC, Balthazar JM (2010) A note on the attenuation of the sommerfeld effect of a non-ideal system taking into account a MR damper and the complete model of a DC motor. *17(7):1112–1118*
49. Piccirillo V, Tusset AM (2014) Dynamical jump attenuation in a non-ideal system through a magnetorheological damper. *J Theor Through Magnetorheological Damper* 52:595–604
50. Wauer J, Suherman S (1997) Vibration suppression of rotating shafts passing through resonances by switching shaft stiffness. *J Vib Acoust* 120:170–180
51. Wu X, Naugle C, Meagher J (2016) A full spectrum analysis methodology applied to an anisotropic overhung rotor. *J Appl Mech Eng* 5:1–10
52. Jha AK, Dasgupta SS (2019) Attenuation of sommerfeld effect in an internally damped eccentric shaft-disk system via active magnetic bearings. *Meccanica* 54:311–320

Investigation and Characterization of Coir Fiber Reinforced Polymer Composite Under Cyclic Loading



Kshounish Brahma, Sumit Bhowmik, and Krushna Gouda

Abstract In the last few decades natural fiber reinforced polymeric composites have undergone wide amount of research in engineering and science. This is due to its durability, eco-friendly with nature, low cost, recyclability, biodegradability and high specific strength. The aim of the present research is to investigate the fatigue properties of the coir reinforced polymeric composites under cyclic loading. Composites samples are fabricated with four different weight fractions of coir fiber (10%, 20%, 30% and 40%) and different mechanical properties like tensile and fatigue analysis are evaluated with the help of universal testing machine (UTM). The experiments suggest that there is gradual increment in tensile strength as fiber loading is increasing up to 30% of fiber loading then there is drop in tensile strength for 40% fiber weight content. The fatigue analysis is performed with three different loading levels which is determined from the tensile test. It is seen that as the loading level increases the fatigue life of the composite decrease. It is concluded that changing loading levels have impact on the load bearing capacity of the composite.

Keywords Natural fiber · Composite · Coir fiber · Epoxy · Tensile test · Fatigue test

1 Introduction

Nowadays in our modern world requirement of certain unique material properties is essential for different areas of application, which is not possible to obtain from our conventional metals, ceramics, alloys etc. Like in aerospace and construction industries the requirement of light weight material has become a necessity. This can be achieved by unusual combining of different material properties. This is how composites are made, it is basically combining two or more materials with different properties in order to achieve extraordinary and unusual properties. The simplest composite consists of two different materials, one being the matrix phase and the other being

K. Brahma (✉) · S. Bhowmik · K. Gouda
Mechanical Engineering Department, NIT Silchar, Silchar, India
e-mail: khobrahma@gmail.com

© The Author(s), under exclusive license to Springer Nature Singapore Pte Ltd. 2023
T. S. Sudarshan et al. (eds.), *Recent Advancements in Mechanical Engineering*,
Lecture Notes in Mechanical Engineering,
https://doi.org/10.1007/978-981-19-3266-3_29

377

the reinforcing phase. The reinforcing phase is hard in nature and is embedded in the matrix phase which is ductile in nature. Some of the unique features of composites are high fatigue strength, high specific strength and modulus, high corrosive resistance, anisotropic in nature etc. [1]. There are various types of composites but due to environmental pollution growing at a rapid rate, there has come the need for Natural constituent based composites. This has led to the increasing demand for polymer composites with organic fillers [2]. These Natural constituents are mainly composed of hemicelluloses, lignin and celluloses [3]. But this type of structure has poor wetting property and more moisture absorption which leads to matrix debonding [4–6]. The most commonly used natural fibers are mostly plant based, be it jute, hemp, bamboo, coir, wood etc. These fibers have been extensively studied due to it being used as reinforcement in thermosets and thermoplastics for various applications.

From the above mentioned fibers, coir fiber has excellent durability, good weathering capacity and it has very less water absorption capacity [7] compared to other fibers. Also these coir fibers are extracted from agro wastes i.e., from the outer husk of the coconut fruit. So this agro waste is utilized as a reinforcement in thermoplastics and thermosets to synthesize a composite which will provide immense industrial value. Also these will also provide revenue for the farming industry [8]. It can be said that coir fiber is a value added product. Also due to the cheapness of coir fiber, it is finding immense importance as a substitute for glass fiber which is costly in automobile industries [9]. In order to use the above natural fiber reinforced composite in various application one needs to know the mechanical properties, so researchers have done extensive research. These mechanical properties are flexural modulus, tensile strength, fatigue behavior etc. [10–14]. To know more about the mechanical properties, different research works are carried out and also improvement of these mechanical properties is important because of the growing needs of the composites working in severe conditions. Although natural constituent reinforced composites are quite promising, current natural constituent reinforced composites may not permit their use in load demand application.

Natural constituent based composite can suffer under fatigue load like other composites. So study of fatigue behavior has become more and more important. Also nowadays composites are of huge demand, so most of the material that are required for various parts are made of composites and most of these are subjected to cyclic loading. This has made it necessary to study the fatigue behavior of composites. Cyclic loading on the parts made of composites causes progressive damage. So, to prevent and to take precautionary measure prediction of fatigue life has become important. We need to know the response of the material undergoing repetitive loading. The four modes of failure due to fatigue are delamination, fiber breakage, cracking and interfacial debonding [15]. The failure due to fatigue occurs without any warning [16]. The fatigue behavior is generally of three stages initially under cyclic loading, damage gets accumulated along the matrix in the form of intra-laminar cracking, then a steady damage growth rate can be seen in the second stage with little accumulated damage and lastly debonding and inter laminar cracks increases rapidly at the last stage which results in fiber bundles pull-out and delamination [17]. The cracks initiated are dependent on the fiber modulus and matrix ductility [18]. This Fatigue behavior

can be influenced by many ways, one being aspect ratio of the fiber which can be manipulated in order to increase the fatigue strength. Another important factor is the interface between the matrix and the fiber. By adding silane coupling agent the fatigue strength can be increased. It can also be influenced by frequency. Increasing the cyclic frequency leads to decrease in fatigue life [19].

Based on the above specifics discussed, this research work is to fabricate a mechanically feasible polymer-based composite with agro waste like coir fiber being used as the reinforcement. Accounting the durability in harsh environment, its less water absorption capacity, cellulose content and availability as agro-waste, coir Fibers are used as reinforcement [20]. Due to great dimensional stability after curing, easy processing and good mechanical properties, thermoset epoxy polymeric resin is selected as the matrix for the composite. The composite samples are prepared according to different weight percentages i.e., 10%, 20%, 30% and 40% along with neat epoxy samples. These samples are subjected to tensile testing with constant cross speed to find the ultimate tensile strength (UTS). The fatigue test is done to determine the fatigue life of the samples under different loading levels. These loading levels are determined from the above found UTS. The results of the testing mentioned above are given in the subsequent sections. Basically the main aim of this research work is to know the fatigue life of the coir reinforced polymeric composite, which will help in determining its feasibility in structural applications. The results are compared for different fiber loadings and the best result is noted. Also the conclusion of the research done is mentioned at the ending of this work.

2 Materials and Methods

The reinforcement and the matrix used are coir fiber and thermoset epoxy resin, respectively. Coir is found in countries with tropical climate like Thailand, India etc. [21]. Coir fiber has relatively low tensile strength and also other mechanical properties are also moderate. This is basically because of its hemicellulose and cellulose content being less than other fibers. But the lignin content is very high in coir fibers, this provides high durability, less wear and high water resistant [22–25]. These fibers also have high elongation at break. Because of the water resistant properties these fibers are more and more used as reinforcement for composites. And as it is known that coir is basically is an agro waste, so by using the coir fiber in various applications, value is added to this agro waste. This not only boost the agricultural sector of the world, but also the industrial sectors. So here, the research work currently focuses on fabricating a composite, reinforced with coir fiber as the reinforcement. These will allow to know if it is feasible to synthesize a product which can be used in various structural applications.

The matrix that is used to fabricate the composite comes in two part system, i.e., araldite ‘LY556’ and hardener ‘HY917’ having mixed viscosity between 1500 and 3000 centi poise (cP) at room temperature. The epoxy is based on Bisphenol-A. The density of the resin and hardener are 1.15 and 1.20 g/cc, respectively. The

reason for using this epoxy as matrix is because of its relatively moderate viscosity which helps in proper alignment of the coir fibers. This will impart better mechanical properties. This epoxy also has good fiber impregnation. The matrix used also has a very good dimensional stability. This helps in synthesizing samples into its proper dimensions with accuracy. The curing process for this matrix is easy. It gets cured at room temperature. The epoxy also has good tensile strength, flexural strength. The coconut fruit and stem are obtained from local markets in the state of Assam. From the outer part of the coconut fruit the coir fiber are extracted. After extraction the fiber is dried at room temperature for removing moisture. Then the fibers are evenly chopped with length between 120 and 140 mm for getting a uniform length of Fibers throughout the composites. Now the fibers are treated with alkali solutions. The fibers are washed continuously for a number of times to remove dirt and debris present and then submerged in to NaOH solution of 5% weight for 30 min at 20 °C and followed by washing with tap water for the leaching of the absorbed alkali in the fibers. Then these fibers are naturally dried for 24 h at room temperature and again dried in an oven at 50 °C for 8 h. Finally the fibers are sealed in a plastic bag to avoid moisture contamination and keep it for further use in mechanical testing. The samples are prepared with different fiber weight %. The weight % taken are 10%, 20%, 30% and 40%. The samples are prepared according to ASTM standards. The fabrication of the composite by using hand layup technique. Firstly a mold consisting of bottom and upper die is prepared which is of cast iron. The dimension of the mold are 200 mm, 200 mm and 10 mm. The surfaces of the molds are first cleaned with the help of acetone to remove dirt and also wax is used to make a smooth surface. The molds are coated with a thin layer of polyvinyl alcohol (PVA), for easy removal of the mold. Then epoxy resin araldite 'LY556' is mixed with the hardener 'HY917' in the ratio 10:1 with the help of a stirrer rod. The Coir fibers of uniform length (120–140 mm) are oriented in unidirectional manner over the lower molds and properly mixed epoxy resin and hardener are spread uniformly over the Fibers. In this way three layers are done to get the required thickness. A roller is used to blend the epoxy and fiber together in order to fill the voids. Then the upper die is placed over the mixture. The required pressure is given with the help of H8 nut and bolts. Curing takes place under this light pressure for about 12 h. Then specimen is removed from the mold. Then again cured at 150 °C for 3 h and finally cooled down to room temperature. Same process is used for different weight fractions mention above for coir fibers. Finally the samples are cut down to ASTM standards for different testing methods.

3 Testing and Characterization

3.1 Water Absorption Test

Water absorption test is used to determine the amount of water absorbed under specified conditions. The test was done according to ASTM D570 with the sample

size in circular disk of 0.250" [26]. Factors affecting water absorption include: type of plastic, additives used, temperature and length of exposure. The data collected sheds light on the performance of the materials in water or humid environments. This test is done to basically see the water absorption capacity of the coir fiber reinforced composite. The water absorption percent (WA) are found out with following Eq. (1) where, W_w = wet weight, W_d = dry wet of the sample composite.

$$WA = \frac{W_w - W_d}{W_d} \times 100 \quad (1)$$

3.2 Density and Void Test

This test was to determine the void present in the fabricated composites and test was done according to ASTM D2734-09 [27]. Here the theoretical density of both the fiber and epoxy has to be known. When the fibers are incorporated in the matrix, then due to trapped air or other volatiles there maybe voids or micro voids. This voids significantly the mechanical properties of a composite. Due to this voids there is difference in actual and theoretical density. The theoretical density can be calculated from Eq. (2).

$$T_d = \frac{D_e \times W_e + D_f \times W_f}{W_e \times W_f} \quad (2)$$

where T_d = theoretical density, D_e = density of resin, W_e = resin in composite, weight %, D_f = density of reinforcement, and W_f = reinforcement in composite, weight %. The actual density (A_d) is measured by specific gravity test based on Archimedes principle. The Void content (V) percentage is then calculated as follows

$$V = \frac{100(T_d - A_d)}{T_d} \quad (3)$$

3.3 Mechanical Test

The tensile test was done with the help of universal testing machine (Instron 8801) and tests have been performed according to ASTM D3039 [28] with the specimens dimensions of 250 mm × 25 mm × 5 mm. Five samples for each weight fraction of fibers were tested at a constant cross-speed of 1 mm/min. Tensile test was done to find the ultimate tensile strength (UTS), tensile strain. The UTS will help in setting the loading level for fatigue testing. The *fatigue testing* was done according to ASTM

Table 1 Water absorption test results

Fiber content (%)	Dry weight (gm)	Wet weight (gm)	Water absorption
10	14.25	14.28	0.21
20	14.36	14.40	0.27
30	14.40	14.45	0.34
40	14.65	14.72	0.47

D3479 and samples sizes are similar to tensile test [29]. The fatigue test is done for three different loading levels determined from the above tensile test. The test is conducted UTM -Instron 8801, with stress ratio $R = 0.1$ and constant amplitude. The frequency is kept at 5 Hz throughout the tests, this is to avoid self-generation of heat. The fatigue test was done to find the fatigue life of the composites for different weights % variation to give an understanding of their appropriateness under cyclic loading.

4 Results and Discussion

4.1 Water Absorption Test

The sample is first dried in an oven, to remove unnecessary moisture and then immersed in water for 24 h at 23 °C. After that it is removed and immediately weight of the specimen is measured. This is repeated for all the respective weight fraction of fiber samples. The results of the test is given in Table 1. From the results it is seen that as the Fiber weight % increases the water absorption of the composite goes on increases because as the fiber content increases, there is less polymer content and there is also fiber agglomeration. This creates voids in which the water is trapped, thereby having more water absorption than that of the other coir fiber weight %.

4.2 Void Test

The void content in a composite can be estimated by comparing the theoretical density with its actual density. The actual density (A_d) is measured by a specific gravity test based on Archimedes principle. Calculated values of densities and void % is shown in Table 2. From the results, it is observed that there is an increase in percentage of voids with the increase in fiber content. It may due to the improper fiber volume fraction or insufficient resin or may be due to the accumulation of fibers at a particular area at higher percentage due to which the resin and hardener could not mix properly. Another reason for high void content maybe due to the fabrication process used. Here

Table 2 Void test results

Fiber content (%)	Theoretical density (gm/cc)	Actual density (gm/cc)	Void %
10	1.213	1.195	1.48
20	1.235	1.190	1.89
30	1.263	1.184	2.39
40	1.286	1.178	2.88

hand layup technique is used. But if we used vacuum bagging (autoclave) there will be less void, because the trapped air that causes most of the void will be removed. In autoclaves there are range of temperatures and pressures which is used to remove the void content in the composite. This is not possible for simple hand layup method. A high void content usually leads to greater susceptibility to water diffusion, lower fatigue resistance and increased variation (scatter) in mechanical properties.

4.3 Tensile Test

From the results it is analyzed that the tensile strength of the composite goes on increasing gradually as we increase the fiber weight % content and then gradually decreases. The value ultimate tensile strength (UTS) for neat epoxy is 20 MPa, as we increase the coir fiber weight % to 10%, the UTS becomes 80.01 MPa, this spike in UTS is the load transferring ability of the coir fiber. When the coir weight % is increased to 20%, there is about 30% increase in UTS, the value is 105 MPa. Again as we keep on increasing the weight % to 30%, there is about 10% increase, the value gets to 115 MPa. As it can be seen from the above table for void, the void increases as the fiber weight % increases. The acceptable limit for void % is 4–5%. So here the increasing void % is not significant enough to decrease the UTS. Also the decrease in strength on composites not only depends on void % but also due to other defects like agglomeration, non-uniform distribution of matrix etc. so, here the other defects may not be present [30]. Hence the increment of UTS with increasing fiber %. The layer of coir fibers is able to withstand the voids in the composite and as there is uniform stress transfer between the coir and matrix, the void does not affect the UTS. This shows a positive interfacial bond between polymer and the coir fiber. But there is a decrement of 10% in UTS as the weight % becomes 40% (107 MPa) as compared to 30% weight fraction of fibers. This showed that as we increase the weight percentages, there is greater fiber accumulation and less amount of polymer left in the composite. This decreases the uniform stress distribution of the polymer matrix to the fiber. The result is given below in Table 3. The stress–strain graph is shown below in Fig. 1.

Table 3 UTS for different fiber weights %

Fiber content (%)	Speed (mm/min)	UTS (MPa)
10	1	80
20	1	105
30	1	115
40	1	108

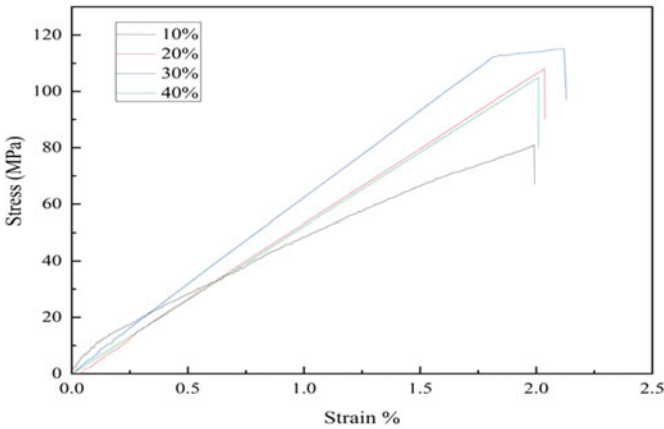


Fig. 1 Tensile stress versus tensile strain curve for different fiber weight fractions

4.4 Fatigue Testing

The test is carried out by taking three different loading levels 35%, 50% and 65% of tensile test. These loading levels are selected in such a way that each of them is less than the UTS of the different fiber %. The loading levels were taken as 35%, 50% and 65% of the UTS of 30% fiber content composite. It is seen that at 35% loading level as the fiber weight % is increased from 10 to 20% then to 30%, there improvement in fatigue life. Similarly there is improvement in fatigue life for 50% loading level as well as for 65% loading level. This shows that increasing the fiber volume % increases the fatigue life. The values of fatigue life are shown in Table 4. From the void test results, it is seen that as fiber % is increased, void increases. As discussed above the void % is not significant enough for the fatigue life of the

Table 4 No. of cycles to failure for different weights % at different loading levels

Loading level (%)	Fatigue life (no. of cycles to failure)		
	10% fiber	20% fiber	30% fiber
35	40,000	45,000	50,000
50	10,000	15,000	20,000
65	1000	1538	2456

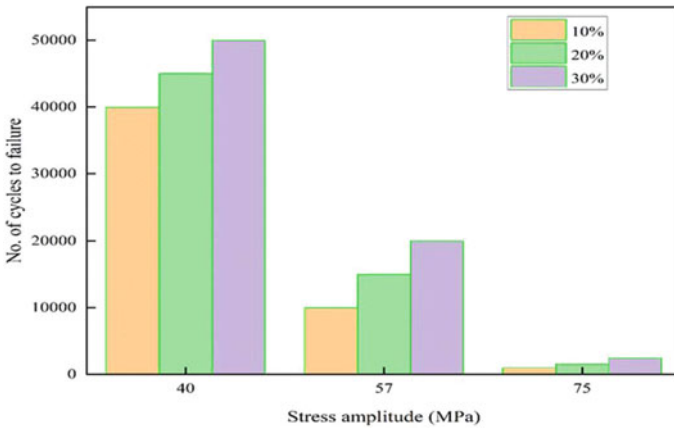


Fig. 2 Comparison of the no. of cycles to failure at different stress amplitudes

composite to decrease as the allowable void % is 4–5% [30]. Also the void % is not the only factor deciding the fatigue life of a composite, there are other defects as well. Since the other defects are not significant as discussed in the previous section, the fatigue life will not decrease with increasing fiber %.

However, as the loading levels increase for each fiber weight %, there is decrease in fatigue life as seen in the above table. Since the UTS of 40% fiber content showed to decrease from 30% fiber content, so fatigue testing is not done. The positive increase in fatigue life for each loading level as the fiber weight % is increased shows that there is positive interfacial bond between matrix and the coir fiber. The pattern of the no. of cycles to failure for different fiber weight fractions at different stress amplitude is given in Fig. 2.

5 Conclusion

From the present research this can be concluded that coir fiber has a positive impact as reinforcement in thermoset polymer. This composite demonstrated comparable mechanical properties and also due to its low cost can be used in place of other synthetic fiber to develop composites. Based on the experiment results the following conclusions are made.

- I. The water absorption of the coir fiber reinforced composite goes on increasing as the fiber weight % goes on increasing, due to the fiber agglomeration at higher weight % and so voids are created thereby entrapping the water in it.
- II. The void content of the developed composite kept on increasing as the fiber weight % kept on rising; the void content for 10 weight % is 1.48, while that of 40 weight % is 2.88. This showed that as the fiber content increases the fiber

gets accumulated in a particular area without getting uniformly distributed. This does not allow the epoxy and hardener to mix properly, thereby making the composite lose some of its mechanical properties.

- III. The ultimate tensile strength of the developed composite at constant crosshead speed 1 mm/min, are increasing as the fibers weight % are increasing up to 30% after increasing the fiber weight, the decrements in UTS are found due to polymer content getting less due to which there is less uniform stress transfer from the polymer matrix to the fiber.
- IV. The no. of cycle to failure kept on decreasing as the load levels kept on increasing for each fiber weight %. The lowest being at 65% loading level and highest at 35% loading level for each individual fiber content. Also for a particular loading level, there is an increment in fatigue life as the fiber content increases.

This paper gives a perspective that coir fiber can be used for improving the performance of epoxy polymer in cyclic condition. So, it is possible to develop a new product. Even though this paper gives a prospective use of coir fiber as reinforcement for few applications areas like automobile industries and shipping industries which may replace the glass fiber.

Acknowledgements The authors acknowledge Machine element laboratory for the necessary equipment for the experiments. The authors thank the Ministry of Human Resource Development (MHRD) for the funding to perform the above testing.

References

1. Callister WD (2014) *Materials science and engineering: An introduction*. 2nd edition. Wiley, New Jersey
2. Mantia FPL, Morreale M (2011) Green composites (2011): A brief review. *Composites: Part A*, 42, 579–588. <https://doi.org/10.1016/j.compositesa.2011.01.017>
3. Thakur VK, Thakur MK (2014) Processing and characterization of natural cellulose fibers /thermoset polymer composites. *Carbohydr Polym* 109:102–117. <https://doi.org/10.1016/j.carbpol.2014.03.039>
4. Kabir MM, Wang H, Lau KT, Cardona F (2012) Chemical treatments on plant-based natural Fibre reinforced polymer composites: An overview. *Compos Part B*, 43, 2883–2892. <https://doi.org/10.1016/j.compositesb.2012.04.053>
5. Doan TTL, Gao SL, Mader E (2006) Jute/polypropylene composites I. Effect of matrix modification. *Compos Sci Technol* 66:952–963. <https://doi.org/10.1016/j.compscitech.2005.08.009>
6. Bledzki AK, Gassan J (1999) Composites reinforced with cellulose based fibers. *Prog Polym Sci* 24:221–274. [https://doi.org/10.1016/S0079-6700\(98\)00018-5](https://doi.org/10.1016/S0079-6700(98)00018-5)
7. Dhawan V, Singh S, Singh I (2013) Effect of natural fillers on mechanical properties of GFRP composites. *J Compos*
8. Kumar R, Kumar K, Bhowmik S (2018) Assessment and response of treated *Cocos nucifera* reinforced toughened epoxy composite towards fracture and viscoelastic properties. *J Polym Environ* 26(6):2522–2535

9. Mohanty AK, Misra M, Drzal LT (eds) (2005) Natural fibers, biopolymers, and biocomposites. CRC press
10. Bajpai PK, Singh I, Madaan J (2013) Tribological behavior of natural fibre reinforced PLA composites. *Wear* 297:829–840. <https://doi.org/10.1016/j.wear.2012.10.019>
11. Hossain MR, Islam MdA, Vuurea AV, Verpoest I (2013) Tensile behavior of environment friendly jute epoxy laminated composite. *Procedia Eng* 56:782–788. <https://doi.org/10.1016/j.proeng.2013.03.196>
12. Fiore V, Scalici T, Vitale G, Valenza A (2014) Static and dynamic mechanical properties of ArundoDonax fillers-epoxy composites. *Mater Des* 57:456–464. <https://doi.org/10.1016/j.matdes.2014.01.025>
13. Mirmehdi SM, Zeinaly F, Dabbagh F (2014) Date palm wood flour as filler of linear low-density polyethylene. *Compos B* 56:137–141. <https://doi.org/10.1016/j.compositesb.2013.08.008>
14. Brown R (1999) Handbook of polymer testing—Physical methods. Marcel Dekker, Inc.
15. Pandita SD, Verpoest I (2003) Tension-tension fatigue behaviour of knitted fabric composites. *Compos Struct* 2004(64):199–209. <https://doi.org/10.1016/j.compstruct.2003.08.003>, doi:10.1016/j.compstruct.2003.08.003
16. Leigh S, Phoenix SL (2000) Modelling the statistical lifetime of glass fiber/polymer matrix composites in tension. *Compos Struct* 48:19–29. [https://doi.org/10.1016/S0263-8223\(99\)00069-0](https://doi.org/10.1016/S0263-8223(99)00069-0)
17. Vieille BW, Albouy W (2014) About the applicability of a simple model to predict the fatigue life and behavior of woven-ply thermoplastic laminates at T >T_g. *Compos Part B*, 61:181–190. <https://doi.org/10.1016/j.compositesb.2014.01.050>
18. Gassan J (2002) A study of Fibre and interface parameters affecting the fatigue behaviour of natural fibre composites. *Compos Part A Appl Sci Manuf* 2002(33):369–374. [https://doi.org/10.1016/S1359-835X\(01\)001166](https://doi.org/10.1016/S1359-835X(01)001166)
19. Chandra R, Singh SP, Gupta K (1999) Damping studies in fiber-reinforced composites—a review. *Compos Struct* 1999(46):41–51. [https://doi.org/10.1016/S0263-8223\(99\)00041-0](https://doi.org/10.1016/S0263-8223(99)00041-0)
20. Wang W, Huang G (2009) Characterisation and utilization of natural coconut fibers composites. *Mater Des* 30(7):2741–2744
21. Arancon RN (2007) Natural fibre production and food security: Coir in Asia and the Pacific. Asian and Pacific Coconut Community, Jakarta
22. Siddika S, Mansura F, Hasan M, Hassan A (2014) Effect of reinforcement and chemical treatment of fiber on the properties of jute-coir fiber reinforced hybrid polypropylene composites. *Fiber Polym* 15(5):1023–1028
23. Yan L, Su S, Chouw N (2015) Microstructure, flexural properties and durability of coir fibre reinforced concrete beams externally strengthened with flax FRP composites. *Compos B Eng* 80:343–354
24. Geethamma VG, Joseph R, Thomas S (1995) Short coir fiber-reinforced natural rubber composites: effects of fiber length, orientation, and alkali treatment. *J Appl Polym Sci* 55(4):583–594
25. Geethamma VG, Kalaprasad G, Groeninckx G, Thomas S (2005) Dynamic mechanical behavior of short coir fiber reinforced natural rubber composites. *Compos A Appl Sci Manuf* 36(11):1499–1506
26. Standard test method for water absorption of plastic, (2018) ASTM D570–98
27. Standard test methods for void content of reinforced plastics D2734-94
28. Standard test methods for tensile properties of polymer matrix composites, D3039M-14
29. Standard test method for tension tension fatigue of polymer matrix composite materials, D3479/D3479M-96
30. Gouda K, Bhowmik S, Das B (2020) Thermomechanical behavior of graphene nanoplatelets and bamboo micro filler incorporated epoxy hybrid composites. *Mater Res Expr* 7(1):015328

Acoustic Analysis of Effect of Louver Window Material in Noise Attenuation



G. Avinash, Santosh Kumar, B. Goutham Krishna, B. Mohammed Akram, Karan Manoj, R. Eshanth, and N. S. Sriprasad

Abstract Applications of louver designs in modern structures have increased extensively in recent times owing to their flexibility of controlling the amount of air flow and sunlight into the building. They also tackle a parallel challenge of involving noise pollution within the region. The phenomenon of noise attenuation over louver windows is investigated using numerical methods to improve the understanding of challenges faced in this scenario. A source of sound is placed on one side of the louver setup, and a microphone is placed on the other side to record the transmitted sound levels. Sound pressure levels are measured for frequencies ranging from 100 to 6000 Hz in intervals of 50 Hz for louver configurations consisting of 6 and 12 louvers. The angle of louvers is varied from 0° to 90° in steps of 15°. Their corresponding attenuations are noted, and the insertion losses are calculated. In the 12-louver configuration, the results validated the model by exhibiting a trend similar to that established through experiments in literature. It is found that the louvers recorded an insertion loss of 0.22%, 5.22%, and 12.89% when the louvers are arranged at angles of 30°, 60°, and 90°, respectively. The 6-louver configuration is used to understand the effect of coating materials in noise mitigation. Of the materials tested, jute is found to have the best sound attenuation effect. The property of flow resistivity is found to be of key significance in noise attenuation.

Keywords Louver · Acoustics · Noise attenuation · Insertion loss · Flow resistivity

G. Avinash (✉) · B. Goutham Krishna · B. Mohammed Akram · K. Manoj · R. Eshanth · N. S. Sriprasad
Mechanical Engineering Department, BMSIT & M, Bengaluru, India
e-mail: avinash.govindaraju@bmsit.in

S. Kumar
Mechanical Engineering Department, Indian Institute of Science, Bengaluru, India
e-mail: santoshkumar@iisc.ac.in

© The Author(s), under exclusive license to Springer Nature Singapore Pte Ltd. 2023
T. S. Sudarshan et al. (eds.), *Recent Advancements in Mechanical Engineering*,
Lecture Notes in Mechanical Engineering,
https://doi.org/10.1007/978-981-19-3266-3_30

389

1 Introduction

A louver or louvre is a window blind or shutter with horizontal slats that are angled to admit light and air but keep out rain and direct sunshine. Louver windows are used in a wide variety of buildings such as schools, factories, and commercial buildings for enhancement of natural ventilation and daylight. The direction of airflow and distribution of daylight in the building can be controlled by adjusting the angle of louver panels. However, it is observed that sound is still able to pass through the louver panel even when it is fully closed. In accordance with increasing awareness about the issue of environmental noise pollution, more attention is being paid to prevention strategies employed in the control of noise pollution. Louvers are rarely seen as primary design elements in the language of modern architecture for control of noise pollution but rather a utility device. This prevalent issue is addressed in the present study by investigating the sound attenuation occurring in such window louver configurations.

Several studies have been reported in the past about the general performance of louver windows, for example, heat transfer capability, daylight distribution, and ventilation. Amrita Prabhu et al. [1] studied acoustic enclosures intended for noisy chemical engineering equipment made out of natural fibre materials such as corn cobs, corn stovers and banana stalks. Bansod et al. [2] studied acoustic characterization of jute using experimental and numerical techniques. Lee et al. [3] performed experimental and numerical studies of acoustic and ventilation performances of glass louver window. Results showed that the louver window was able to attenuate 1.4%, 5.5%, and 12.0% of the noise when panels were partially and fully closed at 30°, 60°, and 90°, respectively, as against 0° panel inclination. Sakamoto and Aoki [4] performed numerical and experimental study on noise shielding effect of eaves/louvers attached to building façade. Results showed that louvers with horizontal short fins and inclined eaves are effective at high stories while inclination angle of louvers affects noise reduction capabilities. Prabhakaran et al. [5] investigated the sound and vibration damping properties of flax fibre-reinforced composites. Results showed that by using natural fibre-based composite materials, it is possible to create a composite laminate with superior acoustic and vibration damping performance without compromising stiffness-to-weight ratios. Other works concerning the study of louvers include Santoni et al. [6] and by Hayne et al. [7]. Mastumoto et al. [8] estimated the efficiency of highway noise barrier with horizontal louvers using two different sound-absorbing materials. They concluded that by applying an absorptive material to the blade surface efficiency of barrier with a horizontal louver increases. The present work differs from those mentioned in literature by employing coatings of different materials over the louvers. Further, a numerical analysis is performed by gauging the sound attenuation occurring over these louvers at smaller incremental angles.

2 Methodology

A numerical method is employed for the investigation of attenuation in sound pressure levels over louver configurations. The simulations are carried out in an acoustic software called 'ACTRAN'. Acronym of ACoustic TRANsmission (ACTRAN) also known as the Acoustic NASTRAN is a finite element-based computer-aided engineering software used in modelling acoustic behaviour of mechanical systems and components. The use of finite elements enables the simulation of complex noise sources, combination of multiple materials in the same model, and handling of multi-million degrees-of-freedom.

- The point S (source) and M (microphone position) are fixed and independent of the angle or any other variable, i.e., position of microphone is at the same height as that of the centre of the box ($Y/2$).
- The louvers are rotated about their mid-point.
- Values of A and B are 0.5 m and 1 m, respectively, for all cases.
- Value of $h = 0.0026$ m for all cases.

Figure 1 shows the setup consisting of 12-louvers which are arranged in parallel one below the other. The louvers are rotated about their centre positions from an angle of 0° to 90° in steps of 15° . On one side of the vertical plane, an omni-directional source of sound is placed at a distance of 0.5 m, and on the other side, a sound level metre (microphone) is placed at a distance of 1.0 m. Both the instruments are placed such that they coincide with the central axis of the louver setup. The input parameter is the sound emitted from the omni-directional source which has a uniform amplitude of 1 Pa across the frequency range. The analysis is conducted for a frequency range of 100–6000 Hz in intervals of 50 Hz. The analysis is done in frequency domain, and the acoustic propagation in this domain is given by Helmholtz equation. The output is measured in weighted decibels (dBA) at the microphone placed on the other side of the louver axis. Weighted decibel scale is based on the intensity of sound and perception capability of the human ear.

The noise attenuation performance of louver windows in this study is examined in terms of insertion loss (IL) and acoustic performance (A), which are given by Eqs. (1) and (2), respectively,

$$IL = SPL(0^\circ) - SPL(30^\circ, 60^\circ, 90^\circ) \quad (1)$$

where SPL refers to sound pressure level measured in dBA.

$$A = \frac{LA_{eq}(0^\circ) - LA_{eq}(30^\circ, 60^\circ, 90^\circ)}{LA_{eq}(0^\circ)} \quad (2)$$

where LA_{eq} is the equivalent sound pressure level or mean value measured in dBA.

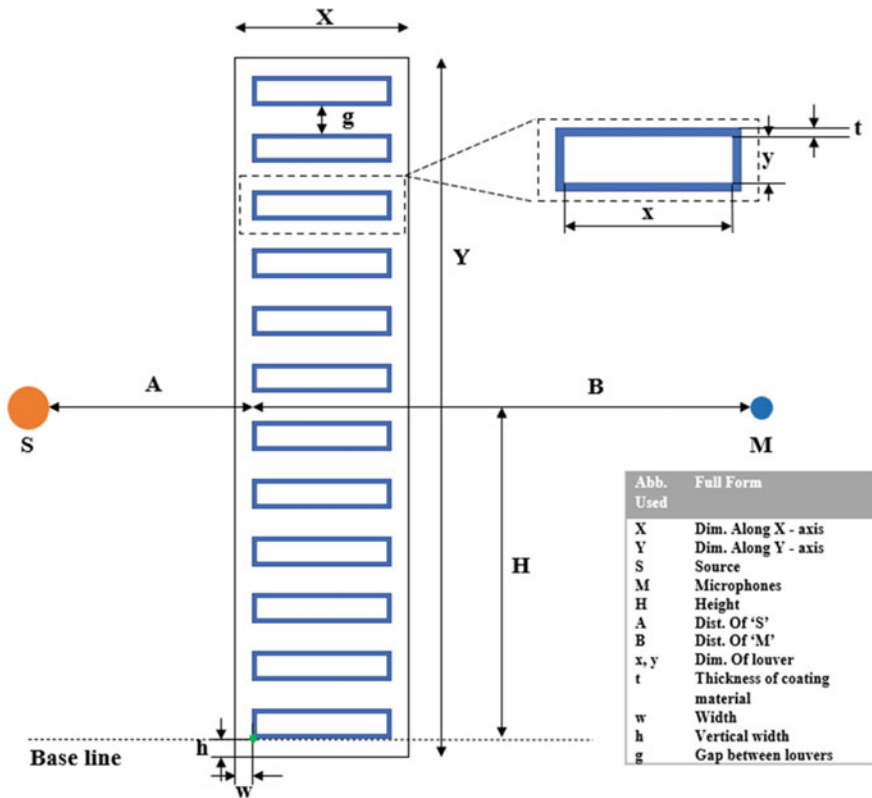


Fig. 1 General setup

2.1 Different Sound-Absorbing Coating Materials

In order to improve the understanding of effect of louver material on noise attenuation, coatings of different materials are used in the present study. Each material possesses different properties that vary the noise shielding effect, in turn producing varying sound attenuation capability. The materials selected are porous in nature and made of natural fibres. The materials used along with their properties are listed in Table 1. The materials are selected based on studies from Amrita Prabhu et al. [1] and Bansod et al. [2]. Figures 2, 3, and 4 represent 12-louver setup without any coating material, 6-louver setup without any coating material, and 6-louver setup with coating material, respectively. The 12-louver setup is used in validation, while the 6-louver setup is used for all other simulations. The mesh size used is 14.5 mm throughout the domain for all cases. A mesh size of 6 mm is used in the region of coating material as a finer mesh is required to capture the physics better across this region.

Table 1 Material properties

Sr. No.	Material	Density (kg/m ³)	Young's modulus (Pa)	Poisson's ratio	Flow resistivity (Nsm ⁻⁴)	Tortuosity	Porosity
1.	Coconut fibre	821	7.06E+08	0.3	1680	1.07	0.88
2.	Banana fibre	1012	8.72E+09	0.36	11,700	1.1	0.86
3.	Corn cobs	882.44	5E+08	0.3	4500	1.15	0.68
4.	Corn stover	313.885	2.05E+08	0.32	3000	1.1	0.76
5.	Jute	411	2E+10	0.3	19,790	1.1	0.7003

Fig. 2 12-louver setup (all dimensions are expressed in metres)

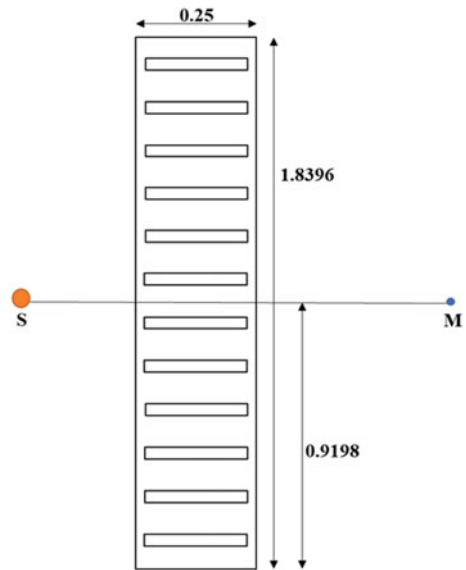


Fig. 3 6-louvers setup (all dimensions are expressed in metres)

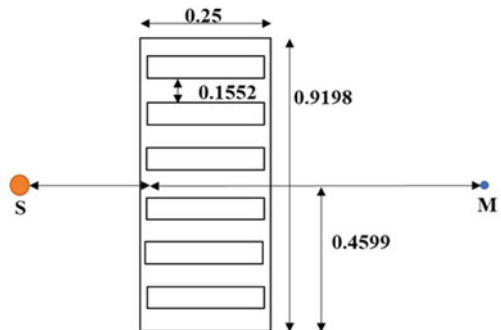
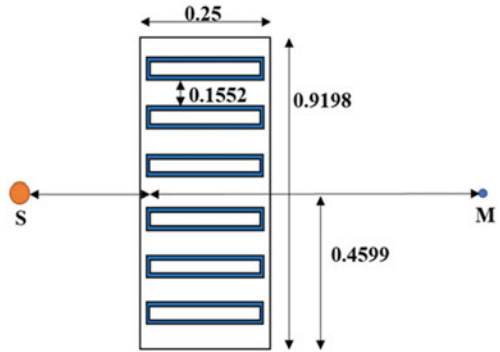


Fig. 4 6-louvers setup with sound-absorbing material coating (all dimensions are expressed in metres)



3 Results

3.1 Validation

In order to validate the setup in the present study, simulations were carried out to compare with results of Lee et al. [3]. As described previously, the investigation consisted of an arrangement of 12-louvers placed on a wall with a source of sound and microphone on its either side. The input frequencies are varied, and their corresponding attenuations are noted. Figure 5 represents the sound pressure levels for frequencies ranging from 100 to 6000 Hz for the angular orientations of the louvers at 0°, 30°, 60°, and 90°. Figure 5a shows the experimental results of Lee et al. [3], while their corresponding results using simulations from the present study are shown in Fig. 5b.

The sound pressure levels of 0° and 30° overlap in both cases, and the common point of dip is near 4000 Hz. In the case of 30°, it is observed that the experimental results and the simulation results have a common area of attenuation after the 4000 Hz frequency mark. Abrupt variations are observed in the 60° louver configuration. In the experimental results, for the 60° louver setup, sound pressure levels do not

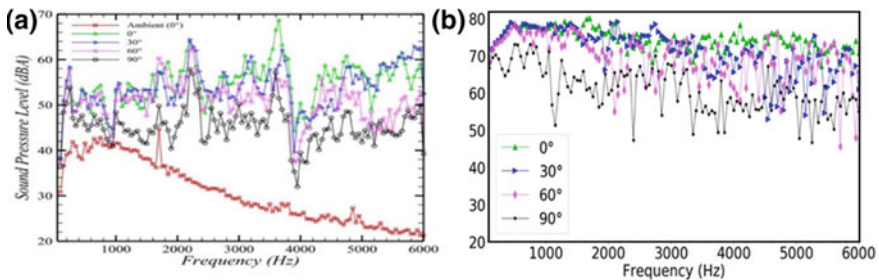


Fig. 5 Variation of sound pressure level with respect to frequency for **a** experimental results of Lee et al. [3] and **b** numerical results of present study

undergo much attenuation until the 3900 Hz frequency range, and the simulation results are attenuated from the frequency range of 1900 Hz. There are irregularities as the frequencies increase, and the highest attenuation is achieved at 2300 Hz. The attenuation trends are consistent post the 4000 Hz frequency range.

The trend of 90° louver configuration forms the best comparison with the results of Lee et al. [3]. The initial dip is observed at a frequency of 900 Hz in both the studies. The variations continue to occur in both the plots at similar frequencies and show a common dip close to the 4000 Hz frequency range. It is important to note that the values in the two studies would not form a one-to-one correspondence owing to difference in perturbations present in the natural environment and that of the simulated domain.

Results from Lee et al. [3] explain the sound pressure levels and insertion losses for 0°, 30°, 60°, and 90°, respectively. Figure 6 describes the insertion loss variation of Lee et al. [3], and Fig. 7 describes the same obtained from the present study. It is

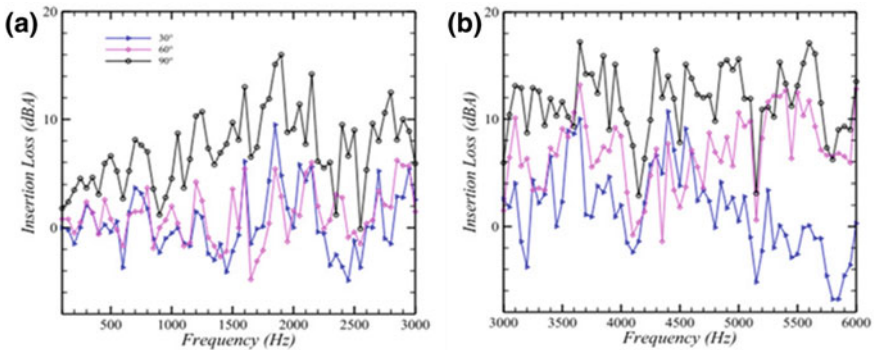


Fig. 6 Variation of insertion loss with respect to frequency for experimental results of Lee et al. for **a** 100–3000 Hz and **b** 3000–6000 Hz

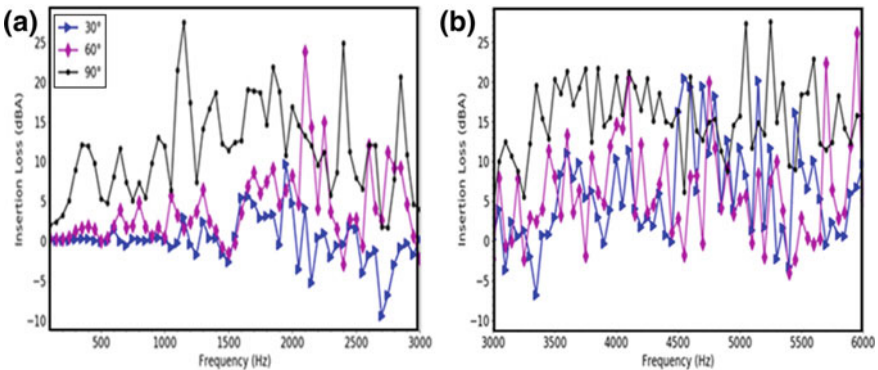


Fig. 7 Variation of insertion loss with respect to frequency for numerical results of present study for **a** 100–3000 Hz and **b** 3000–6000 Hz

Table 2 Percentage attenuation comparison

Angle (°)	Attenuation (Lee et al. [3]) (%)	Attenuation (Present study) (%)
30	1.4	0.216
60	5.5	5.216
90	12.0	12.896

of prime significance to note that the insertion loss values project a near exact match for 60° and 90° and a close match for 30°. It thus provides the basis in validating the setup of the simulations used in this study which can be further applied for different configurations. Table 2 compares percentage attenuation of Lee et al. [3] and present study.

3.2 Varying Sound-Absorbing Coatings

The mentioned figures depict the graphs of sound pressure levels (dBA) versus frequency (ranging from 100 to 6000 Hz in intervals of 50 Hz) for different material coatings at all angular orientations. In general, the sound pressure levels have a maximum value for 0° angular orientation as there is a lot of gap between consecutive louver panels. For the 90° angular orientation, the sound pressure levels are minimum as the gap between consecutive louvers is the least, thereby reducing the intensity of sound passing through them.

Figure 8a represents the 6-louver setup without any sound-absorbing coating which is considered as the base case for comparison. From the trend shown, the mean value of sound pressure level measured for the 0° angular orientation is the maximum having a value of 75.154 dBA. The mean value of sound pressure level for 90° angular orientation is the least with a magnitude of 63.2383 dBA. This occurs due to presence of very less gap between consecutive louvers which offers high resistance to the transmitted sound. In general, a gradual decrease in pressure levels is noticed as the angular orientation increases from 0° to 90°. Figure 8b represents the 6-louver

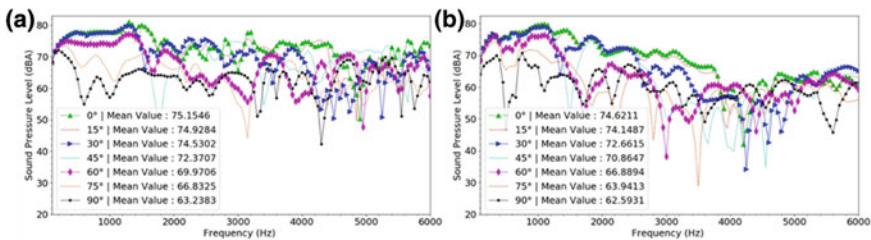


Fig. 8 Variation of sound pressure level with respect to frequency for **a** base case, **b** jute as coating material

setup having a coating material made of jute. The coating has a thickness of 10 mm and is covering each louver panel on all of its four sides. Due to material properties of jute, the sound attenuation ability of the louvers is increased. As shown in the graph, there are multiple dips in the sound pressure levels for a frequency below 5000 Hz with least sound pressure value of 28.5 dBA for an angular orientation of 75° and at a frequency of 3450 Hz.

Figure 9a represents the 6-louver setup having a sound-absorbing material coating made of corn stover. A general decrease in sound pressure values is noticed with the increase in angular orientation. The least value of sound pressure is obtained at a frequency of 4600 Hz measured at an angle of 90° with a value of 26 dBA. Figure 9b represents the material coating made of corn cob. The trend is very similar to that of the previous case except that the least sound pressure value is 32 dBA and is located at a frequency of 3250 Hz for an angular orientation of 90°.

Figure 10a represents the setup having a sound-absorbing material coating made of coconut fibre. Compared to other material coatings, there are no steep dips in the pattern of sound pressure levels. Alternate peaks and dips are observed at different frequency levels for each angular orientation. However, such fluctuations are gradual for one particular angle. Steep dips in pressure levels are seen only when angle of orientation is 45° and above. Figure 10b represents the setup having banana fibre as the coating material. Unlike the previous trends, there are steep dips in the sound

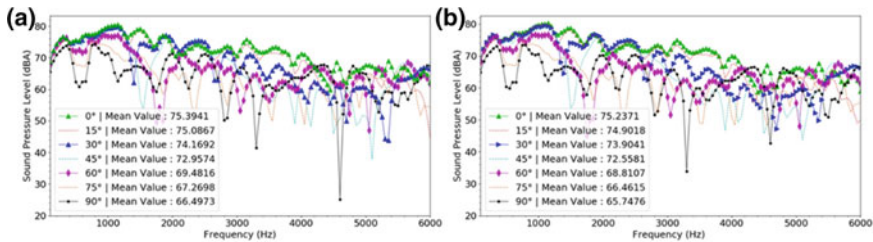


Fig. 9 Variation of sound pressure level with respect to frequency for a corn stover as coating material, b corn cob as coating material

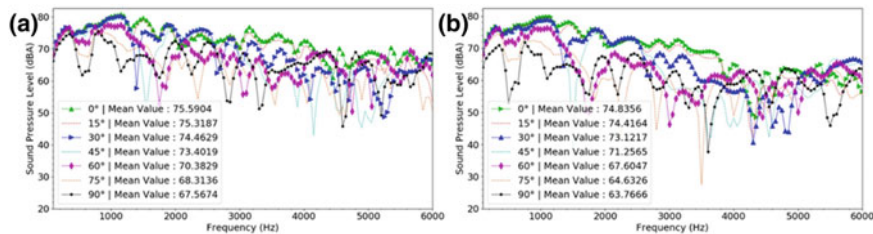


Fig. 10 Variation of sound pressure level with respect to frequency for a coconut fibre as coating material, b banana fibre as coating material

pressure levels seen for angles having values 30° and above. The least sound pressure value of 26 dBA is noticed for a frequency of 3500 Hz.

3.3 Mean Value Versus Angles

Figure 11 represents the variation in sound pressure level with increasing angle of louvers. The attenuation obtained using different materials is compared with the base case. The plot shown can be used to determine the best sound attenuation case. It is observed that a gradual decrease in sound pressure levels with angular orientation is consistent for all cases. However, there appears to be crossovers in trend lines at certain angular orientations for few of the materials.

As seen in the plot, the case having coconut fibre as the material coating shows the least sound attenuation performance. This occurs because unlike the other materials, coconut fibre is made from the hard shell of coconut and once processed and softened in water; it results in a strong and tough fibre that offers durability. It is, however, very light in nature and hence has less flow resistivity.

In general, once the angle is increased above 45°, there is a steep decrease in sound pressure levels. This occurs because the sound pressure waves are reflected and not absorbed as done in lower angular orientations. As the louver is rigid, the sound bounces off its outer surface, but for angular orientations of 30° and below, the reflected sound waves are incident on the lower surfaces of the upper louvers and undergo reflection once again, thereby transmitting the sound in the intended path. However, the base case shows a gradual crossover in sound pressure levels at multiple locations due to the absence of a coating material.

The best case is when jute is used as coating material which gives the highest sound attenuation performance. As seen in the graph, the sound pressure levels are much lesser compared to the other cases. This occurs due to high flow resistivity of jute. Flow resistivity is the airflow resistance within unit thickness, and it portrays the air

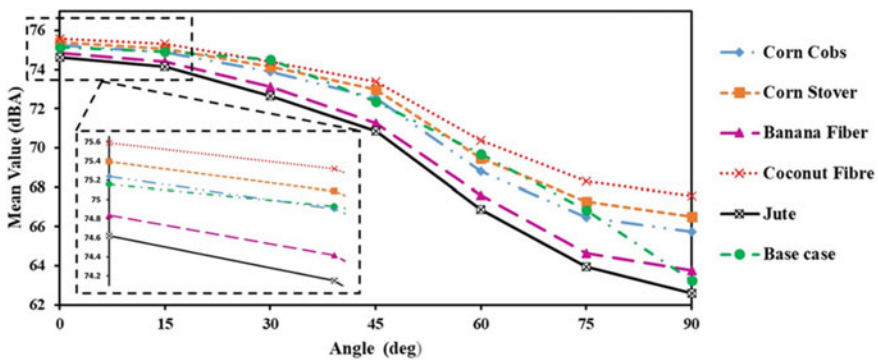


Fig. 11 Mean value in dBA versus angles in deg graph

permeability through porous materials. Unlike other materials used for coating material, jute is very soft and silky in texture. The fibres of jute are primarily composed of the plant materials cellulose and lignin. Due to high value of flow resistivity, the sound waves passing through the material are restricted. As there is less permeability, the material particles do not have sufficient space to vibrate across their mean position to transmit the sound. Hence, jute having the highest flow resistivity provides the best sound attenuation performance.

3.4 Pressure Plots

Figures 12 and 13 are visual representations of the sound pressure distribution as it passes across the louver panel. The different colours represent the intensity of pressure levels within the domain. All values specified in pressure maps are expressed in dBA. Figures 12 and 13 represent the averaged pressure distribution for the case with coconut fibre and jute as coating material, respectively.

For all cases, at 0° , it is seen that the intensity of pressure waves is less as there is no obstruction to the sound waves. As the angle increases from 0° to 90° , the intensity of pressure adjacent to the louver surface increases and reaches a maximum value at an angle of 90° . This occurs due to the obstruction of sound waves across the vertical region as there is minimum gap present between consecutive louvers.

It can be observed that for each angle, jute (Fig. 12) produces a higher noise mitigation compared to coconut fibre (Fig. 13) which is corroborated by an increase in area of the low-pressure intensity domain (blue region) beyond the louver region to its right. In addition, the case of 90° can be considered to understand the restriction

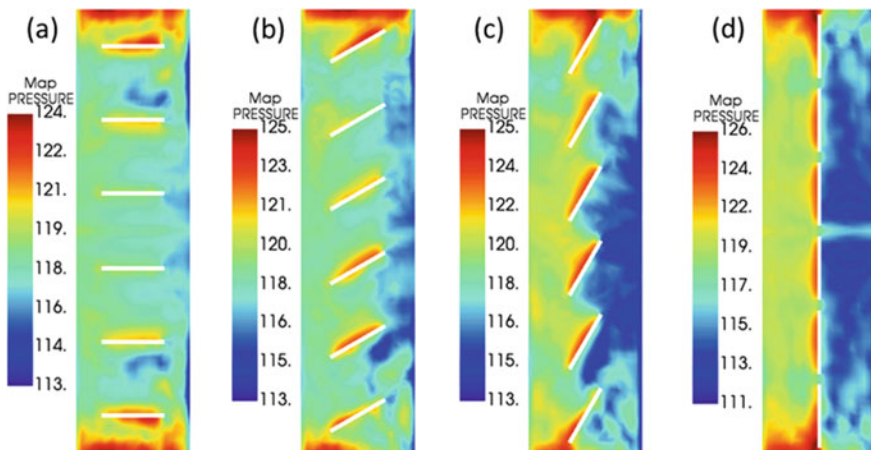


Fig. 12 Averaged pressure plots for coconut fibre as coating material for a 0° , b 30° , c 60° , d 90°

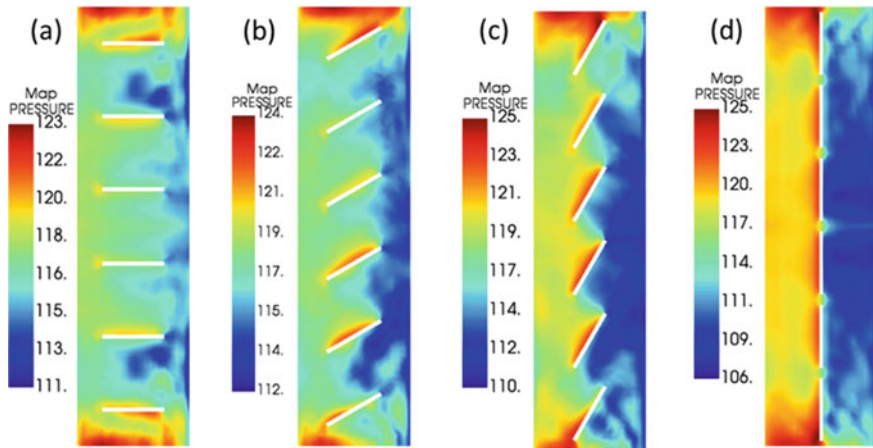


Fig. 13 Averaged pressure plots for jute fibre as coating material for **a** 0° , **b** 30° , **c** 60° , **d** 90°

of sound waves transmitted which is indicated by an elevated concentration of high pressure intensity domain to the left of louvers.

4 Conclusion

Considering the widespread application of louver windows, this paper describes the sound attenuation occurring over different louver coating materials at varying angles. Two types of louver configurations are considered, one containing 12-louvers and the other having 6-louvers. The angle of louvers is varied from 0° to 90° in steps of 15° . Based on past work in literature, five different substances are used as the material of coating over louvers, namely jute, corn cobs, banana fibre, coconut fibre, and corn stover. The input frequencies are varied from 100 to 6000 Hz in steps of 50 Hz, and their corresponding attenuations are noted.

The 12-louver configuration is used to validate the model by simulating an experimental setup from literature. The trend of sound pressure levels and values of insertion losses at various angles provided a good match with the experimental results. With respect to the effect of angle, it can be concluded that the 90° louver setup is the most efficient configuration when it comes to sound reduction capability. Although the 90° setup restricts sound produced by the source more than other angles, it results in poor ventilation in the room. The 60° louver setup can be considered as the optimum setup as it provides good sound attenuation characteristics in addition to providing adequate ventilation.

In order to understand the effect of coating material of louvers on sound attenuation, the 6-louver configuration is used. Jute is found to have the best noise attenuation property in comparison with other materials tested. Consistently, coconut fibre

produces the least noise attenuation effects. It is observed that despite each of the material having varying values of density, Young's modulus, and flow resistivity, the effect of flow resistivity is most profound. As sound waves travel through a medium, a higher flow resistivity results in higher restraint for the movement of air. This in turn reduces the air permeability through the substance, thereby constraining the sound waves passing through them.

Acknowledgements The authors would like to thank Mr. Vivek, Business Development Manager-Acoustics, Hexagon MSC Software, Bangalore, in executing this research work. Appropriate permission has been obtained from Hexagon MSC Software for the text and figures used here. A disclaimer document in this regard has been attached.

References

Journal Articles

1. Amrita Prabhu K, De Maria FR, Manoj K, Satish N, Sai Harshitha S, Siddiqui S, Vivek (2020) Analysis of prepared acoustic boards from natural waste materials using ACTRAN software and its application. *Glob J Mater Sci Eng* 01:23–30
2. Bansod PV, Mittal T, Mohanty AR (2016) Study on the acoustical properties of natural jute material by theoretical and experimental methods for building acoustics. *Acoust Aust*
3. Lee HM, Lim KM, Lee HP (2017) Experimental and numerical studies of acoustical and ventilation performances of glass louver window. *J Vibroeng* 19
4. Sakamoto S, Aoki A (2015) Numerical and experimental study on noise shielding effect of eaves/louvers attached on building façade. *Int J Build Sci Appl*
5. Prabhakaran S, Krishnaraj V, Senthil Kumar M, Zitoune R (2014) Sound and vibration damping properties of flax fibre reinforced composites. *Procedia Eng* 97:573–581
6. Santoni A, Martello NZ, Fausti P, Secchi S (2015) The use of sound absorbing shading systems for the attenuation of noise on building façades an experimental investigation. *Buildings* 5:1346–1360
7. Hayne M, Tan D, Devereux R, Mee DJ (2019) Static insertion loss, transmission loss and noise reduction testing of an acoustic louvre. *Proc Acoust*

Conference Papers

8. Mastumoto T, Yamamamoto K, Ishikita H (2000) Efficiency of highway noise barrier with horizontal louvers—a study by full-scale model experiment. In: *The 29th international congress and exhibition on noise control engineering, France, 27–30 Aug 2000*

Dock Detection for an Underwater Autonomous Vehicle Using Deep Learning in a Simulated Environment



Swastik Jena and Saikat Ranjan Maity

Abstract Autonomous underwater vehicles (AUVs), which are fundamentally self-swimming robots, have a wide range of scientific, military, and commercial uses due to their presence and improved performance over traditional search and survey methods as well as their potential capabilities and significant cost-performance improvements over the traditional means. They are a very useful tool for deep-sea exploration and reconnaissance missions. AUVs are capable of eliminating wastage of resources and reducing the risk to human life underwater. The construction of a reliable AUV requires a comprehensive system design and a lot of expensive testing at sea where system details can be verified. Modelling and simulation provide a cost-effective measure of the initial design, system: both hardware and software, and mechanical testing and verification, thereby minimizing the number of potential failures in marine tests. Accurate simulation can help developers find hidden errors in embedded AUV software and gain an understanding of AUV performance and capabilities. This project makes an attempt at real-time simulation and dock detection for AUVs so that they can dock underwater and prolong their subsea times. The proposed system utilises the powerful rendering capabilities of Unity along with MATLAB and Tensorflow. The modelling section incorporates the environment and camera features. The simulation component consists of testing the dock detection algorithm using the camera feedback from the AUV.

Keywords Autonomous underwater vehicles · Underwater simulation · Dock detection · Deep learning · Unity

S. Jena (✉) · S. R. Maity
Department of Mechanical Engineering, National Institute of Technology Silchar, Silchar, India
e-mail: swastik_ug@mech.nits.ac.in

S. R. Maity
e-mail: sрмаity@mech.nits.ac.in

© The Author(s), under exclusive license to Springer Nature Singapore Pte Ltd. 2023
T. S. Sudarshan et al. (eds.), *Recent Advancements in Mechanical Engineering*,
Lecture Notes in Mechanical Engineering,
https://doi.org/10.1007/978-981-19-3266-3_31

403

1 Introduction

A large part of the ocean and its biodiversity is still a mystery to mankind. Researchers have come a long way from using ships to photograph the depths to developing autonomous underwater vehicles (AUVs) to conduct experiments. The AUVs immensely reduce the risk to human life while increasing the range and scope of the experiments that can be conducted at the same time. They are much more suited for exploring the aquatic environment and unknown depths of the ocean.

For an AUV to be completely autonomous, it must be capable of searching a designated area, come back to its docking station and dock at the said station to recharge the batteries to prolong its diving time. Performing such tests while in the developmental stages of the vehicle would consume an immense amount of resources each time the vehicle needs to be submerged in water. Therefore, physically testing the vehicle each time is not a viable solution considering the cost of each experiment, time constraints, maintenance and limited resources. To tackle the above-mentioned problems and save resources, this paper proposes an open-source underwater vehicle simulator for visual servoing and docking.

This project presents a docking system based on optical guidance which uses artificial neural networks to identify the docking station and provides the underwater environment in Unity 3D, a widely used game engine to simulate and test the AUV before entering physical testing. The AUV is propelled by 5 thrusters which grant it 6 degrees of motion underwater. It has a camera mounted on its nose and one on the underside to provide images of its surroundings, which are processed to identify the docking station and help it to dock on the station.

2 Literature Review

Experimenting with AUVs can be very expensive and drubbing. Simulation of the AUV can not only reduce the cost but also help in the validation process. An approach to work on the simulation of AUVs can be seen in MORSE [1]. MORSE is an open-source robotics simulator based on component-based architecture and uses software-in-the-loop. It provides several features for simulation: sensors, actuators, environments (aerial, ground, maritime), and can allow multiple robots to be simulated at the same time. MORSE uses Blender's game engine to provide graphical display and python scripts to improve its functionality. Prats et al. proposed a software tool called UWSim [2], a hardware-in-the-loop simulator for underwater robotic missions. UWSim can recreate a virtual underwater scenario that can be constructed using standard modelling tools. This simulator provides underwater and surface vehicles, robotic manipulators and sensors that can be used through a network interface. Similar to MORSE, UWSim is also an open-source software. A much earlier example of 3D robotic simulator is Gazebo [3] proposed by Koenig and Howard in their study in 2004. Gazebo is a 3D dynamic multi-robot simulator proficient

in complex environment simulations. It contains detailed control and high fidelity. The open-source status of Gazebo has led to its gradual development over the years, and the simulator continues to be used till date. This tool has helped bridge the gap between theoretical designs and hardware testing. It aids data visualisation, simulation of hard-to-reach environments and reverse engineering applications. It is a simple and scalable tool that is now backed by a large community of robot enthusiasts. OpenSim [4] and Darwin2K [5] are two other open-source simulators similar to Gazebo. OpenSim, developed by David Jung, is a generic open-source simulator with objectives and design akin to Gazebo. It has additional features designed for constructing and debugging joint chains in robots. Darwin2K was developed by Chris Leger for his work on evolutionary robotics. This simulator was focussed on evolutionary synthesis, design, and optimization. It can model motor and gear heads in fine detail accurately and also provide estimates of stress analysis on the structural bodies.

Olivier Kermorgant [6] in his study on simulators for underwater vehicle manipulators in 2015 presented an integrated system composed of ROS, Gazebo and UWSim. This holistic approach allowed the user to obtain realistic rendering of dynamic multi-robots along with contact physics, buoyancy, hydrodynamic damping and low-level PID control. The study presented an example of the simulation of a black box recovery mission. The proposed system conveniently merges together the dynamic simulation capabilities of Gazebo and the realistic underwater rendering of UWSim. URSim [7] represents another open-source robot simulator developed along similar lines. This framework uses ROS and Unity3D to simulate dynamic 3D systems which are capable of feedback control and underwater mission planning for robots. It also has the algorithms to support underwater sensors, underwater physics and collision kinematics. URSim utilises the game and physics engines of Unity3D to recreate the environments with close to realistic detail. Setting up the AUV for charging its batteries and data transfer underwater is helpful for applications that require long-term recognition. This system can reduce the need for regular launches and upgrades and enables AUVs to stay permanently in one place to be ready to operate underwater. Sans-Muntadas et al. [8] proposed a system to acquire data and train a convolutional neural network (CNN) to dock the AUV. The proposed system used raw images from the front-facing camera as input to feed the CNN which then directed the controller to dock the AUV.

3 Unity 3D

3.1 Overview

Unity 3D is a multi-platform compatible game engine which supports more than 25 platforms. Its 3D development platform has a wide range of development tools including physics engines which can be used to simulate 3D CAD models. Unity's

rendering capabilities also aid to produce visuals similar to the real world reducing the differences between simulation and physical testing in visual servoing. Unity 2013 had an integrated development kit from Facebook focussed on games. This tool featured applications like tracking advertising campaigns and deep linking, where social media posts of specific segments within the game were directly linked to users. It also allowed the users to share in-game-images easily. Facebook also developed a new desktop-level gaming platform with Unity in the year 2016. In this collaboration, Unity developers could more quickly export and publish games to Facebook and Unity provided support for Facebook's gaming platforms. Later in 2018, Unity added the Scriptable Render Pipeline which allowed developers to create better high-end graphics. The High-Definition Rendering Pipeline was focussed towards console PC and console experiences, and the Lightweight Rendering Pipeline was aimed at mobile platforms, virtual reality, augmented reality, and mixed reality. Imitation learning which a famous machine learning tool was added to Unity in the year 2018 along with other ML tools. These tools helped AI bots to learn from real players habits and then go on to play the game themselves. Other ML applications such as templates for new developers and support for Magic Leap were also implemented. Unity dominated the 2018 mobile games market where around half of the games were made using Unity. The open-source Unity Machine Learning platform connects to machine learning programmes, including Google's TensorFlow. It is also used to a great extent in developing and simulating robots and self-driving cars.

The Unity Asset Store is a great marketplace for the Unity community where the creators can buy and sell user-generated assets to other creators and game makers. The Unity Asset Store includes 3D and 2D assets as well as pre-structured environments for developers to choose from. The Unity Asset Store was launched in 2010, and by 2018, there had been approximately 40 million downloads on the digital store. The asset store now contains many pre-designed tools for project development and makes the task of creating a project easier.

3.2 Modelling in Unity

Unity engine supports the C# programming language for API scripting. Although it used to offer JavaScript as well, that was deprecated in 2017. Several APIs are provided to reproduce physics like that of the real world in the form of RigidBody, Time, Transform, Materials, etc. A new project was created using Unity 2019.4.10f1. The UUV prefab model which was downloaded from the unity asset store was imported into the scene. A mesh renderer and Shader were applied to the bot to simulate rigid body properties. A camera was attached to the front end of the bot. The background of the camera was set to a deep blue to represent the sea, and its field of view was shortened to account for the poor visibility of the water. The environment has been simulated considering the low lighting conditions under the sea, and a post-processing stack has been added to the camera to reduce visibility in order to reproduce the actual scene. The ocean floor has been made of planes with

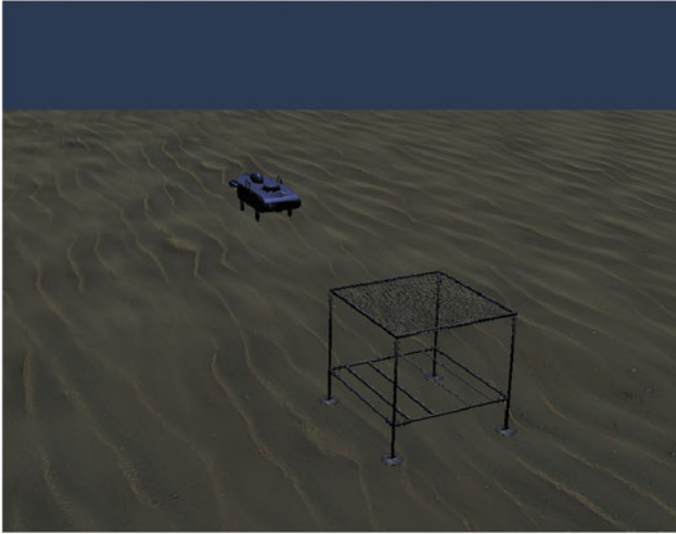


Fig. 1 Simulation of the AUV and Dock in Unity

the sand texture from the asset store to simulate the ocean bed. The dock has been placed on the virtual ocean bed. A sample of the environment is shown in Fig. 1 which contains the AUV and the docking station. The UUV can be controlled with input from MATLAB. Communication with MATLAB is established over TCP/IP where Unity is acting as the server and MATLAB is acting as the client. Once the simulation is started in Unity, the TCP starts to listen for the client. At the same time, the MATLAB code containing the `tcpipClient` is executed so that it starts relaying the coordinates and angles of the bot in real time.

4 Dock Detection

The object detection algorithm used is YOLOv3 [8] which is a state-of-the-art, open source, real-time object detection system. It is based on the 53-layered Darknet algorithm with the exception that it has 53 additional layers, making it a 106-layered convolutional neural network. It was chosen because of its speed and accuracy. The algorithm uses a single neural network on the full image to perform the detection. The image is divided into regions, and bounding boxes are drawn over regions with probabilities. YOLOv3 is the third version of YOLO with better training methods and improved performance. Tensorflow and OpenCV (Python libraries) were used in this project to re-train the model and detect the dock in simulation time. Multiple images of the docking station were captured from various angles to make up the training dataset. The dataset was further augmented to improve the training efficiency and

enhance the performance of the neural network in identifying the dock. Figure 2 depicts a raw image of the docking station, and Fig. 3 shows an augmented version of the same image.

The images were augmented, and the sample number increased to 264 samples to improve the performance of the model. The model was thereafter trained with the created dataset using Tensorflow. The training of the model using transfer learning on a GPU took around 4 h. The results of the training acquired from tensorboard are shown in Fig. 4. The training results are close to ideal due to the fact that the images

Fig. 2 A raw sample image of the dock

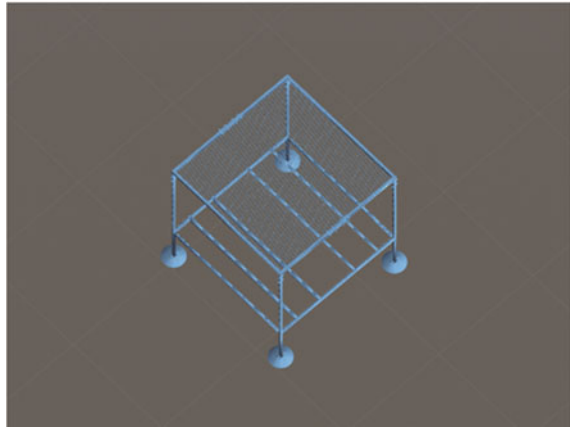
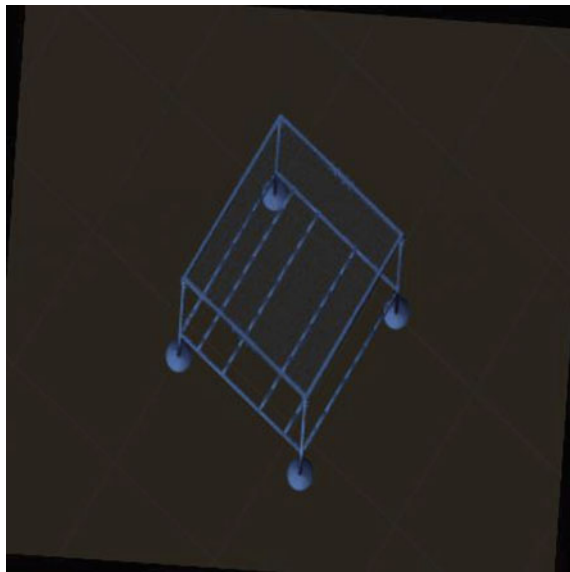


Fig. 3 An augmented sample image of the dock



loss

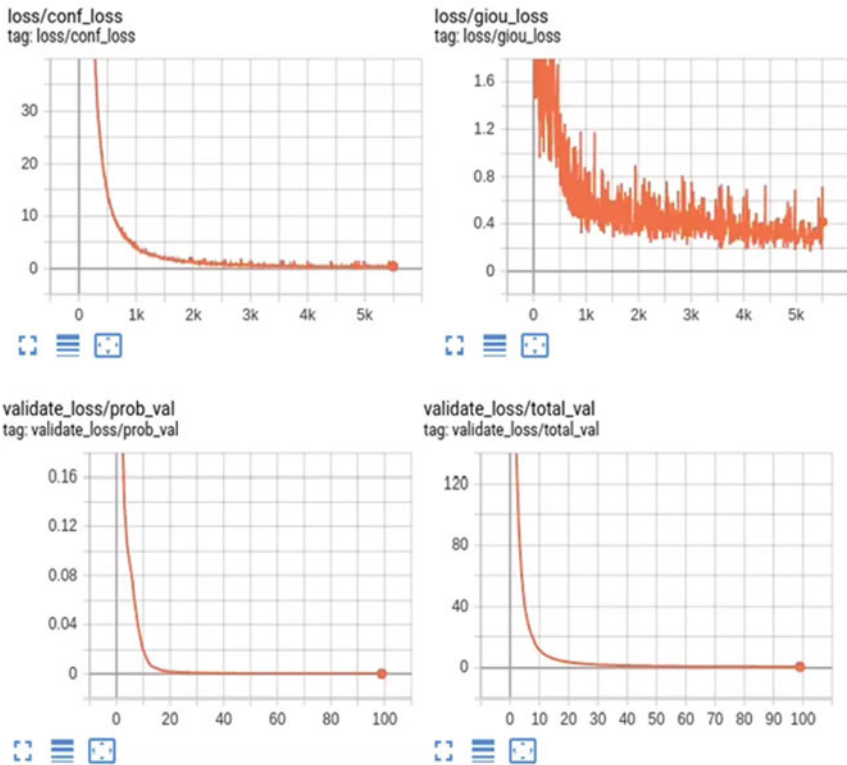


Fig. 4 Training results obtained from Tensorboard

were taken from a single source. Increasing and variegating the dataset would lead to more realistic training of the neural network.

The re-trained model was tested to detect the docking station inside the simulation environment. It was observed that the model could be used in real time and promising results were obtained on the test.

5 Results and Discussion

The developed simulation system in the study demonstrates the visual servoing potential of conventional AUVs. It provides a complete overview of vehicle performance-related functions such as tracking, finding and passing underwater gates, detecting and striking underwater buoys. These activities represent typical independent self-assessment activities, mapping, route planning, local practice, avoidance obstacles and target identification. They serve as proof of concept and can be extended to actual



Fig. 5 Screenshot of the algorithm detecting the dock in simulation

commercial, military and research activities for surveillance, recognition, intelligence collection and delivery. Experiments of the acquisition of ports conducted at the simulation site yielded satisfactory results. Neural network accuracy increases to 94%, and the system frame remains unchanged at 17 FPS. The current launch can be used for visual representation of underwater vehicles. The AUV-supported capsule in the visual environment can be modified by importing custom vehicle models into the scene. A screenshot of the result is given in Fig. 5.

6 Conclusion and Future Scope

In this paper, a Unity3D and MATLAB-based simulation model is shown. This hybrid simulation programme is a framework to replicate complex robotic operations in the physical environment inside a software. This provides a sandbox environment for robust software testing of the constructed model that exhibits vehicle performance similar to that in the case of a real-world scenario.

In the space of future development, there are certain elements that could be added to the current project. Some of these are-

1. Extensive sensor support such as Doppler velocity log, Side-scan SONAR and Multibeam Sonar
2. Underwater acoustic communication support
3. Feature to add a robotic manipulator arm
4. Support for ROS to make the system modular
5. Underwater environment design to replicate real-life ocean floor.

References

1. Echeverria G, Lassabe N, Degroote A, Lemaignan S (2011) Modular open robots simulation engine: MORSE. In: 2011 IEEE international conference on robotics and automation. Shanghai, pp 46–51
2. Prats M, Pérez J, Fernández JJ, Sanz PJ (2012) An open source tool for simulation and supervision of underwater intervention missions. In 2012 IEEE/RSJ international conference on intelligent robots and systems. Vilamoura, pp 2577–2582
3. Koenig N, Howard A (2004) Design and use paradigms for Gazebo, an open-source multi-robot simulator. In 2004 IEEE/RSJ international conference on intelligent robots and systems (IROS) (IEEE Cat. No.04CH37566). Sendai, pp 2149–2154
4. Smith RL (2014) OpenDE homepage, 2014. [Online] Available from: <http://opende.sourceforge.net>. [Accessed 05 Nov 2020].
5. Kermorgant O (2014) A dynamic simulator for underwater vehicle-manipulators. In: International conference on simulation, modeling, and programming for autonomous robots Simpar. Bergamo, Italy, pp 25–36
6. Lachele J, Franchi A, Bühlhoff HH, Giordano PR (2012) SwarmSimX: Real-time simulation environment for multi-robot systems, simulation, modeling, and programming for autonomous robots. Springer, Berlin, pp 375–387
7. Katara P, Khanna M, Nagar H, Panaiyappan A (2019) Open source simulator for unmanned underwater vehicles using ROS and Unity3D. In: 2019 IEEE underwater technology (UT). Kaohsiung, Taiwan, pp 1–7
8. Sans-Muntadas A, Kelasidi E, Pettersen KY, Brekke E (2019) Learning an AUV docking maneuver with a convolutional neural network. *IFAC J Syst Control* 8(100049):1–5
9. McMillan S, Orin DE, McGhee RB (1995) Efficient dynamic simulation of an underwater vehicle with a robotic manipulator. In: *IEEE transactions on systems, man, and cybernetics*, vol. 25, Aug 1995, pp 1194–1206
10. Peng S, Liu J, Wu J, Li C, Liu B, Cai W, Yu H (2019) A low-cost electromagnetic docking guidance system for micro autonomous underwater vehicles. *Sensors* 19(3):682

Performance Evaluation of Evacuated Tube Containing Heat Pipe Solar Collector-Based Solar Dryer



Adarsh Abi Mathew, R. Anandu Krishna, R. Sivakumar, and T. Venugopal

Abstract The drying kinetics of *Allium cepa* was studied using an evacuated tube heat pipe solar dryer (ETHPSD). The performance analysis of the present solar collector was analyzed at the no-load condition of the dryer using 0.0105 kg/s, 0.0211 kg/s, and 0.0316 kg/s air flow rates. The maximum temperature of the air measured at the outlet of the solar collector and the drying chamber during allium cepa drying was 58°C and 55 °C, respectively, at 0.0105 kg/s air flow rate. The ambient temperature measured was between 32°C and 35 °C. The average intensity of solar radiation measured during the experimental period was 695 W/m². The drying process done in ETHPSD took 8 h to reduce the moisture content present in *Allium cepa* from an initial value of 89% (wb) to 8.9% (wb). In the present study, the experimental and theoretical moisture ratio for allium cepa was analyzed using six thin-layer drying models. The Newton model exhibits an exact fit holding a higher $R^2 = 0.982$, lowest $\chi^2 = 0.087$, and RMSE = 0.276. A comparable anti-diabetic inhibition property was obtained before and after the drying of allium cepa in ETHPSD.

Keywords Evacuated tube collector · Heat pipe · Solar dryer · Thin-layer drying model

A. A. Mathew (✉) · R. A. Krishna · R. Sivakumar · T. Venugopal (✉)
SMEC, VIT, Chennai, India
e-mail: adarsh.abimathew2016@vitstudent.ac.in

T. Venugopal
e-mail: venugopal.t@vit.ac.in

R. A. Krishna
e-mail: anandukrishna.r2016@vitstudent.ac.in

R. Sivakumar
e-mail: sivakumar.r@vit.ac.in

Nomenclature

ETHPSD	Evacuated tube heat pipe solar dryer
M_{in}	Initial moisture content of product (%)
W_i	Initial weight of product (kg)
W_f	Final weight of product in (kg)
M_t	Instantaneous moisture content of product (%)
\dot{m}_a	Air mass flow rate (kg/s)
C_{pa}	Specific heat of air (kJ/kg ° C)
T_{oa}	Air inlet temperature (C)
T_{ia}	Air outlet temperature (C)
M_w	Mass of water evaporated (kg)
A_c	Solar collector surface area (m ²)
I	Intensity of solar radiation (W/m ²)
L_v	Latent heat of vaporization of water (J/kg)
t_d	Drying time (h)
δ	Standard deviation
N_0	No of sets
M	Moisture content at time t
M_e	Equilibrium moisture content

1 Introduction

The latest researches point out that energy consumption throughout the globe is becoming twofold every 20 years [1]. The world is facing problems due to pollution and threat to the environment due to the uncontrolled use of fossil fuels. The preference for renewable energy, mainly solar energy, has increased during recent years [2]. About 3.6% of the energy available in the world is used for agricultural product drying [3]. The pertinent method for storing consumable agricultural products is drying them with the help of well-designed machines having minimum consumption of energy. Solar drying is an encouraging technique preferred over the traditional method of drying under the sun due to the improved quality of products and drying time [4]. Despite all the benefits of solar dryers, only a little development has occurred in solar dryers due to their low efficiency [5]. So, the agricultural products were forced to dry in fossil fuel-powered dryers. This raised the concern of having a proper design for solar dryers that are economic and energy-efficient [6]. The simplest, efficient, and economical technique of exploiting solar energy is by converting it into thermal energy using a solar collector (Velmurugan and Kalaivanan 2015; Hematian and Bakhtiari 2015). Various collector configurations in solar dryers help to attain a different temperature range suitable for drying different products. The most commonly used solar collector is a flat plate collector. It is mainly benefited by operations within the temperature range of 20°C–80 °C [7]. Another type of solar

collector that is gaining attention is the evacuated tube solar collector [8]. It is having an operating temperature range of 50°C–200 °C [9]. The major drawbacks of flat plate collectors are the absence of sun-tracking and convective heat loss through the glass cover, whereas evacuated tube solar collector overcomes this drawback by maintaining vacuum in-between the glass tubes. Evacuated tubes can collect direct as well as diffuse radiations [10].

Thus, in this experimental study, an evacuated tube heat pipe solar dryer was developed and its performance was studied with different inlet air mass flow rates. In this study, the quality analysis of allium cepa was done to study the feasibility of using the dryer for industrial purposes. The moisture ratio obtained through the drying experiments of allium cepa is applied to the six selected mathematical models.

2 Experimental Setup

2.1 Evacuated Tube Heat Pipe Solar Dryer

The experiments were conducted at Vellore Institute of Technology—Chennai, Chennai, Tamil Nadu, India (12.8406° N, 80.1534° E). A solar drying system incorporated with an evacuated tube heat pipe solar collector was used to conduct the drying experiments (Fig. 1). ETHPSD is mainly comprised of evacuated tubes containing

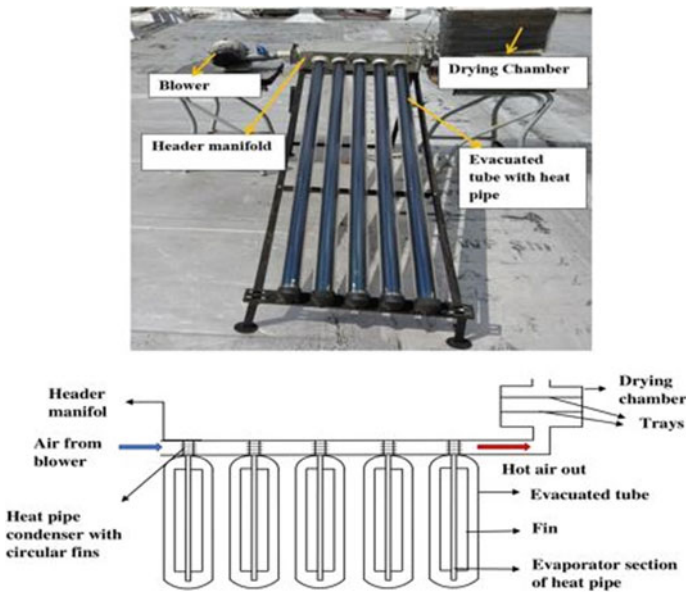


Fig. 1 Evacuated tube heat pipe solar dryer

heat pipes solar collector, a drying chamber, and an air blower. The main features of the collector used in the system that distinguishes it from a conventional flat plate collector are as given below.

- The collector consists of five evacuated tubes with copper heat pipes.
- The working medium filled in the heat pipe was water.
- The copper heat pipes having high thermal conductivity transfer maximum heat produced in the evacuated tubes to the header manifold.

The solar collector consists of five evacuated glass tubes made up of borosilicate glasses having length 1.5 m, outer and inner diameter of 58 mm, 47 mm, respectively. Copper heat pipes with length 1.3 m, evaporator section diameter 9 mm, condenser section diameter 15 mm were inserted individually inside each evacuated tube. Aluminum fins of size 150 mm × 58 mm and thickness 1 mm were attached with the heat pipe. One end of evacuated tubes and heat pipes is connected to a rectangular header manifold channel with dimensions 150 mm × 150 mm × 500 mm, and the other end was supported by a frame. A polyurethane foam insulation was provided above the manifold to prevent heat loss. A blower was fixed at one end of the collector manifold to blow the air at different flow rates and the other end of the manifold was connected to the drying chamber. Fifteen circular aluminum fins of diameter 50 mm and thickness 1 mm are connected to each heat pipe's condenser section. The drying chamber was made up of aluminum of size 400 mm × 300 mm × 300 mm. Two aluminum wire mesh trays of size 300 mm × 200 mm were used inside the drying chamber to store the products to be dried.

2.2 Working Methodology

The solar radiation that is falling on the evacuated tube raised the temperature within it and the absorbed heat was transferred to the heat pipe. Thus, the working fluid water which is stored in the heat pipe gets heated up. The evacuated tubes are made of borosilicate glass. A three-target as selective coating material Al N/Al N-SS/Cu with 0.96 absorptivity and 0.06 emissivity was coated in the inner glass tube. Aluminum fins are attached to each heat pipe to boost up the rate of heat transfer.

As the solar radiation falls on the evacuated tubes, the temperature within the evacuated tube rises and the heat is transferred to the heat pipe placed within the glass tube. The water present within the heat pipe absorbs the latent heat and evaporates at normal operating conditions. The vapor rises upwards carrying a large amount of energy to the condenser section of the heat pipe. The heat is then transferred to the air. The vapor thus condenses and returns. The heating process is repeated. The hot air is transferred to the drying chamber.

Fig. 2 Allium cepa cut into small pieces



2.3 Drying Product and Quality Analysis of Product Dried in ETHPSD

Allium cepa was dried in ETHPSD and under the open during the study (Fig. 2). Allium cepa is considered an anti-diabetic medicinal product for controlling diabetes [11]. One of the methods for treating diabetes is detaining the absorption of glucose by inhibiting α -amylase, α -glucosidase, and carbohydrate hydrolyzing. α -Amylase is an enzyme in the digestive system that initiates glucose absorption. Allium cepa contains α -amylase inhibition assay that can decelerate glucose absorption [12]. Quality analysis of allium cepa dried in ETHPSD will help in studying the feasibility of using the dryer for industrial applications. In this study, the quality analysis of the dried product was done by analyzing the presence of α -amylase inhibition assay.

2.4 Drying Procedure

The performance study of the solar collector was done using 0.0105 kg/s, 0.0211 kg/s, and 0.0316 kg/s mass flow rate of air. The variation in temperature of evacuated glass tubes, condenser, and evaporator section of heat pipe fins, inlet, and outlet air was analyzed. Allium cepa was dried in ETHPSD using the flow rate that delivered maximum air temperature. The drying experiments were conducted by drying 200 g of sliced allium cepa (Fig. 2) under the open sun and in ETHPSD.

3 Performance Analysis of Ethpsd

3.1 Solar Collector and Dryer Performance

Total heat absorbed by the solar collector system

$$Q_{abs} = A_c \times I$$

Total useful heat gain by the air passing through the collector is given by

$$Q_u = A_{\text{air}} \times c_{\text{pa}}(T_{\text{oa}} - T_{\text{ia}})$$

Collector efficiency

Collector efficiency is the ratio of useful heat gained by the air to total heat absorbed [13].

$$\eta_{\text{coll}} = \frac{Q_u}{Q_{\text{abs}}}$$

Solar dryer efficiency

$$\eta_d = \frac{M \times W \times Lv}{I \times A_c \times t_d}$$

3.2 Drying Kinetics

The drying kinetics of allium cepa was determined as.

Initial moisture content [14]

$$M_{\text{in}} = \frac{(W_i - W_f)}{W_i}$$

Instantaneous moisture content [15]

$$M_t = \left(\frac{(M_{\text{in}} + 1)W_t}{W_i} \right) - 1$$

The drying kinetics and moisture ratio of drying products at a specific time can be predicted using empirical correlations. The drying characteristics of allium cepa were studied using thin layer drying models, as shown in Table 1.

The experimental moisture ratio (MR) can be defined as follows [17]:

$$MR = \frac{M - M_e}{M_o - M_e}$$

But M_e found to be negligible, so the moisture ratio can be simplified as

$$MR = \frac{M}{M_o}$$

Table 1 Drying models

Model	Equation	Reference
Newton	$MR = \exp(-kt)$	[16]
Henderson and Pabis	$MR = a \exp(-kt)$	
Page	$MR = \exp(-kt^n)$	
Two-term exponential	$MR = a \exp(-kt) + (1 - a)\exp(-kat)$	
Logarithmic	$MR = \exp(-kt) + c$	
Wang and Singh	$MR = 1 + at + bt^2$	

The coefficient and the constants of the models were obtained by nonlinear regression analysis. The RMSE (root of mean square error), χ^2 (reduced chi-square), and R^2 (coefficient of determination) were analyzed to check the goodness of the fit [17].

4 Result and Discussion

4.1 Performance of Evacuated Tube Heat Pipe Solar Collector at No-Load Condition of the Dryer by Varying Inlet Airflow Rates

The performance of the solar collector of ETHPSD with no load condition was analyzed by varying the inlet airflow rates. Performance of collector with airflow rate 0.0105 kg/s, 0.0211 kg/s, and 0.0316 kg/s was analyzed (Table 2). The inlet temperature and outlet temperature of the air were varying with time (Fig. 3). It was detected that the maximum outlet air temperature was logged at an airflow rate of 0.0105 kg/s. At low velocity, the air was able to reside within the header manifold for a longer time to absorb more heat from the heat pipe. Drying experiments in ETHPSD were steered with an inlet air mass flow rate of 0.0105 kg/s. Figures 4

Table 2 Performance analysis of solar collector

Parameters	Low flow rate (0.0105Kg/s)	Medium flow rate (0.0211Kg/s)	High flow rate (0.0316Kg/s)
T_{In} (°C)	33–35.8	33–36	33–35.5
$T_{Out\ max}$ (°C)	59	53	49
I_{Max} (W/m ²)	1020	1035	1015
ΔT_{Max} (°C)	24	17.1	14
ΔT_{Avg} (°C)	18	11	9
$Q_{Useful\ max}$ (W)	253	365	466
Avg $\eta_{Collector}$ (%)	27	30.8	40

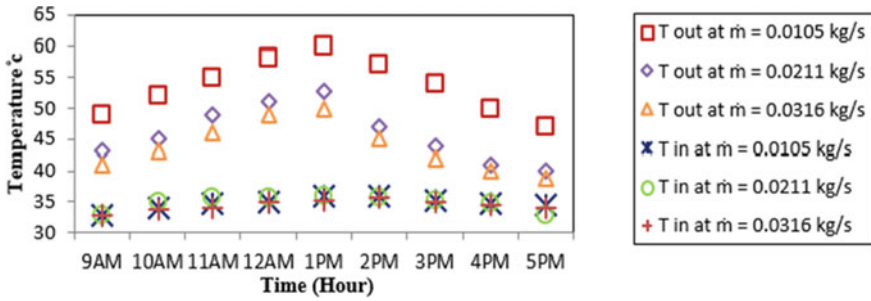


Fig. 3 Inlet and outlet temperature of the air

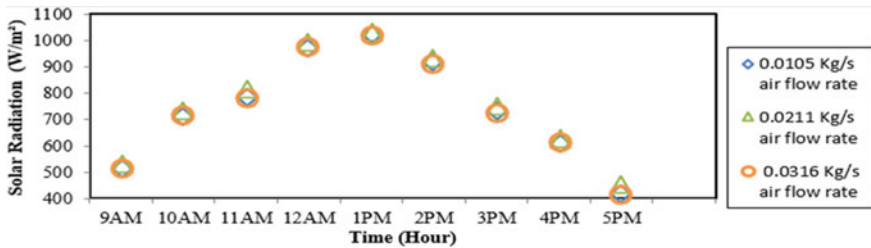


Fig. 4 Variation of intensity of solar radiation with time

and 5 show the evacuated tube temperature and solar radiation intensity. The highest solar radiation intensity was observed at 1 pm and the lowest at 5 pm. The highest temperature recorded from the evacuated tube was 170 °C.

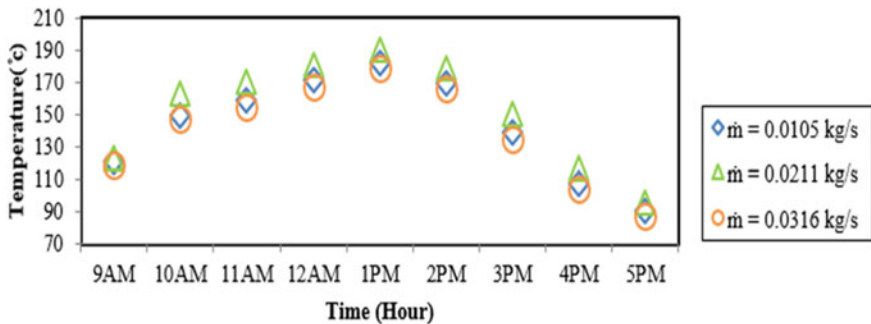


Fig. 5 Variation of evacuated tube temperature with time

4.2 Performance Analysis of ETHPSD and Drying Characteristics of Allium Cepa

The average solar irradiance available during the period of study was 695 W/m². The highest temperature of drying air delivered by the solar collector was 58 °C. The RH inside the drying chamber has always been on a lower side compared to the RH of ambient air. The moisture from the product will be expelled out at a faster rate with Lower RH (Fig. 6). The maximum and average temperature recorded in evacuated tube temperature, heat pipe temperature, and fin temperature is as shown in Table 3.

The maximum temperature recorded at the top tray and bottom trays were 51 °C and 55 °C, respectively. Allium cepa was dried to a final mass of 22 g in ETHPSD from an initial mass of 200 g in 8 h drying time (Figs. 7 and 8). The initial and final moisture content present in allium cepa obtained during the study was 89% and 8.9%, respectively (Fig. 9). During the drying experiment conducted for drying allium cepa in ETHPSD, the average collector efficiency was 31.5%. The dryer efficiency was observed as 6.2%, respectively. Allium cepa kept under open sun took 14 h for drying.

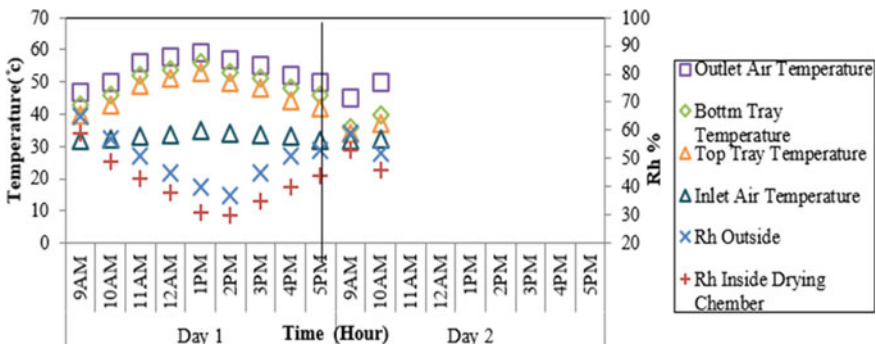


Fig. 6 Variation of temperatures and relative humidity with time

Table 3 Evacuated tube, fin, and heat pipe temperature during allium cepa drying

Parameters	Maximum temperature (°C)	Average temperature (°C)
Evacuated tube	167	130
Fin	163	127
Heat pipe evaporator section	160	123
Heat pipe condenser section	151	113

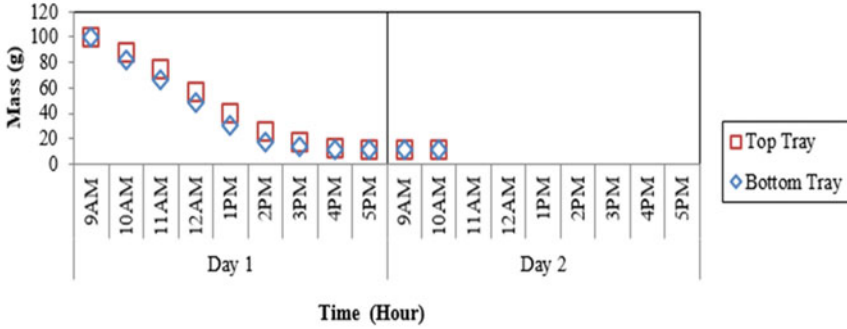


Fig. 7 Variation in mass of allium cepa at top and bottom tray with time

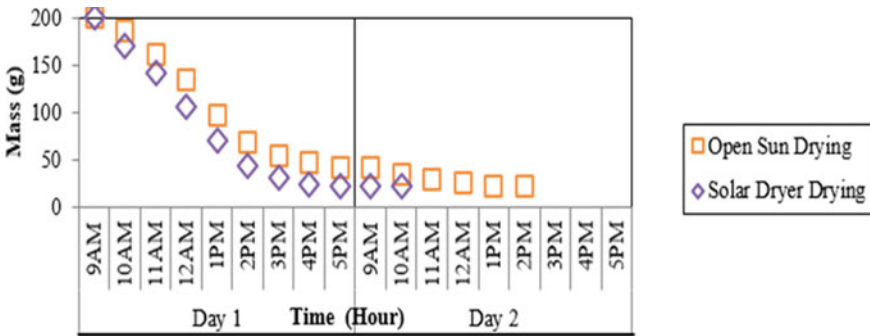


Fig. 8 Variation in the mass of allium cepa when dried in the solar dryer and under the open sun

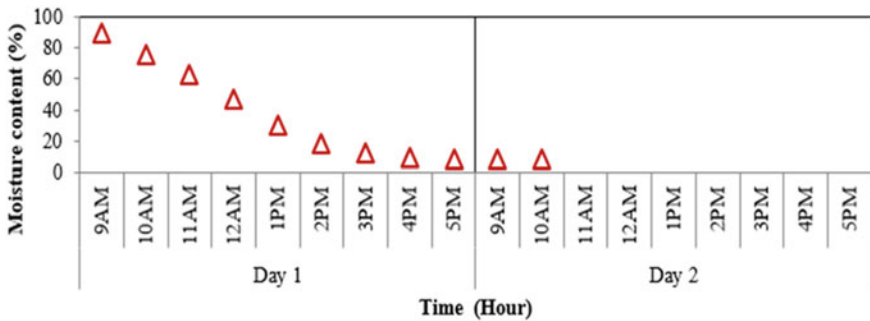


Fig. 9 Variation of moisture content in allium cepa with time

4.3 Drying Kinetics for Allium Cepa

The moisture ratio obtained through the drying experiments of allium cepa is applied to the six selected mathematical models. The mathematical model that has a high R^2

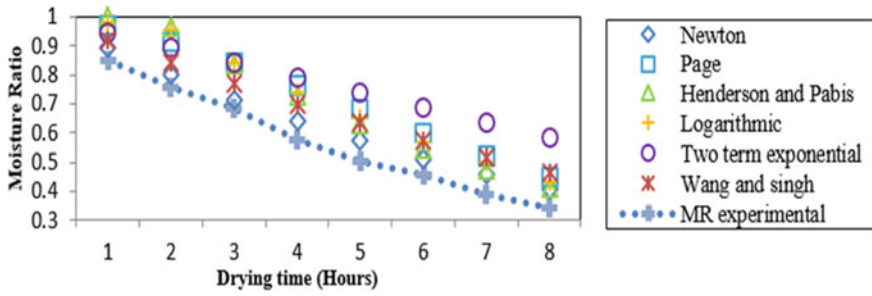


Fig. 10 Predicted and experimental moisture ratio

value, lower reduced χ^2 , and RMSE value is taken as the finest model that can depict the drying characteristics of the sample [16]. The Newton model fairly demonstrates the drying kinetics of allium cepa with R^2 of 0.982593724, χ^2 of 0.087489304, and RMSE of 0.276682382, respectively. Figure 10 shows the predicted and experimental moisture ratio during allium cepa drying.

4.4 Quality Analysis

The α -Amylase inhibition assay was 3.78% for allium cepa dried in ETHPSD, whereas those dried under open sun gave 3.21%. Allium cepa contains a 4.89% α -Amylase inhibition assay before drying (Fig. 11). During the study, it was noted that α -Amylase inhibition assay was retained more in allium cepa dried in ETHPSD. Temperature plays an indispensable part in α -Amylase activity. α -Amylase inhibition assay is reduced with raise in temperature. Uniform air flow rate into the drying chamber and maintaining uniform temperature helped to obtain improved α -Amylase inhibition assay for allium cepa dried in ETHPSD. Thus, ETHPSD showed a better

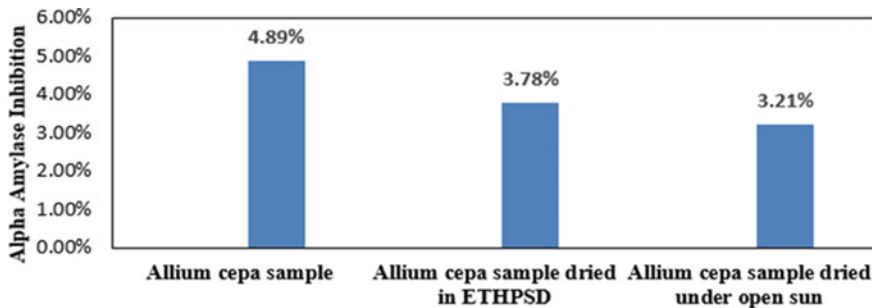


Fig. 11 α -Amylase inhibition assay for allium cepa



Fig. 12 Appearance of ETHPSD and under open dried allium cepa

ability to retain α -Amylase inhibition assay. The appearance of ETHPSD and under open dried allium cepa is as shown in Fig. 12.

A performance study on the modified evacuated tube containing heat pipe solar collector and solar dryer with thermal energy storage has been carried out by Adarsh Abi Mathew and Venugopal. T [18, 19].

5 Conclusions

The main conclusions drawn from the present study are:

- A low inlet air flow rate resulted in a higher temperature difference between inlet and outlet air. The average and maximum temperature differences were recorded as 18 °C and 24 °C, respectively.
- Drying time was observed to be less with ETHPSD which was 8 h when compared to open sun drying of 14 h.
- The average collector and dryer efficiency recorded during the study was 31.5% and 6.2%, respectively.
- The Newton model demonstrated the solar drying of allium cepa with correlation $R^2 = 0.982$, $\chi^2 = 0.087$ and $RMSE = 0.276$.
- α -Amylase inhibition assay obtained was 3.78% for allium cepa dried in ETHPSD, whereas under the open sun the value is 3.21%. α -Amylase inhibition in allium cepa before drying was 4.89%.

On the whole, it can be concluded that the ETHPSD took less drying time when compared to open sun drying. A low airflow rate resulted in higher output air temperature from the collector. Anti-diabetic inhibition content and nutrition content in allium cepa didn't show much variation after drying in the dryer. The Newton model demonstrated the solar drying kinetics of allium cepa.

References

1. Motahayer M, Arabhosseini M, Samimi-Akhijahani A, Khashechi H (2018) Application of computational fluid dynamics in optimization design of absorber plate of solar dryer. *Iran J Biosyst Eng* 49(2):285–294
2. Arabhosseini A, Samimi-Akhijahani H, Motahayer M (2019) Increasing the energy and exergy efficiencies of a collector using porous and recycling system. *Renew Energy* 132:308–325. <https://doi.org/10.1016/j.renene.2018.07.132>
3. Trostle R (2010) Global agricultural supply and demand: factors contributing to the recent increase in food commodity prices. *Rev Diane Publ*
4. Akmak G, Yildiz C (2011) The drying kinetics of seeded grape in solar dryer with PCM-based solar integrated collector. *Food Bioprod Process* 89(2):103–108. <https://doi.org/10.1016/j.fbp.2010.04.001>
5. Ghaffari A, Mehdipour R (2015) Modeling and improving the performance of cabinet solar dryer using computational fluid dynamics. *Int J Food Eng* 11(2):157–172. <https://doi.org/10.1515/ijfe-2014-0266>
6. Bala S, Janjai BK (2005) Solar drying of fish (Bombay Duck) using solar tunnel drier. *Int Energ J* 6(2)
7. Sharma N, Diaz G (2011) Performance model of a novel evacuated-tube solar collector based on minichannels. *Sol Energy* 85:881–890. <https://doi.org/10.1016/j.solener.2011.02.001>
8. Ghoneim AA (2018) Performance optimization of evacuated tube collector for solar cooling of a house in hot climate. *Int J Sustain Energy* 37(2):193–208. <https://doi.org/10.1080/14786451.2016.1256886>
9. Tyagi VV, Kaushik SC, Tyagi SK (2012) Advancement in solar photovoltaic/thermal (PV/T) hybrid collector technology. *Renew Sustain Energy Rev* 16:1383–1398. <https://doi.org/10.1016/j.rser.2011.12.013>
10. Morrison GL, Tran NH, Mckenzie DR, Onley IC, Collins RE (1984) Long term performance of evacuated tubular solar water heaters in Sydney, Australia. *Sol Energy* 32(6)
11. Jevan C (2017) Anti-diabetic effects of *Allium cepa* (onions) aqueous extracts on alloxan-induced diabetic *Rattus norvegicus*. *J Med Plants Res* 5(7):1134–1139
12. Rhabasa-Lhoret R, Chiasson JL (2004) α -glucosidase inhibitors. In: Defronzo RA, Ferrannini E, Keen H, Zimmet P (eds) *Title, tuberculosis and diabetes mellitus* 1(3):901–914
13. Bai Y, He X, Liu Y, Duan J, Wang Y, Han X (2018) Experimental investigation of a solar thermal storage heater assembled with finned heat pipe and collective vacuum tubes. *166(May):463–473*
14. Lakshmi DVN, Muthukumar P, Layek A, Nayak PK (2018) Drying kinetics and quality analysis of black turmeric (*Curcuma caesia*) drying in a mixed mode forced convection solar dryer integrated with thermal energy storage. *Renew Energy*. <https://doi.org/10.1016/j.renene.2017.12.053>
15. Vijayan S, Arjunan TV, Kumar A (2016) Mathematical modeling and performance analysis of thin layer drying of bitter gourd in sensible storage based indirect solar dryer. *Innov Food Sci Emerg Technol* 36:59–67. <https://doi.org/10.1016/j.ifset.2016.05.014>
16. Dhanushkodi S, Wilson VH, Sudhakar K (2017) Mathematical modeling of drying behavior of cashew in a solar biomass hybrid dryer. *Resource-Efficient Technol* 3(4):359–364. <https://doi.org/10.1016/j.refit.2016.12.002>
17. Umayal Sundari A, Neelamegam P, Subramanian CV (2014) Drying kinetics of muscat grapes in a solar drier with evacuated tube collector. *Int J Eng Trans B Appl* 27(5):811–818. <https://doi.org/10.5829/idosi.ije.2014.27.05b.18>
18. Mathew AA, Thangavel V (2021) A novel thermal energy storage integrated evacuated tube heat pipe solar dryer for agricultural products: Performance and economic evaluation. *Renew Energy* 179:1674–1693. <https://doi.org/10.1016/j.renene.2021.07.029>
19. Abi Mathew A, Thangavel V (2021) A novel thermal storage integrated evacuated tube heat pipe solar air heater: Energy, exergy, economic and environmental impact analysis. *Sol Energ* 220(March):828–842. <https://doi.org/10.1016/j.solener.2021.03.057>

Study and Management Aspects of Reserves, Production, Consumption and Life of Oils of the World



Sameer Kumar Anand and Soupayan Mitra

Abstract As the energy demands of the world are increasing, researchers are in search of those energy resources which are economical, easily accessible, versatile, easy to transport and produce very less residue and pollution on energy generation. Oil has been the world's major commercial energy source from many decades and is likely to dominate in the twenty-first century as well. Oil accounts for nearly 40 percent of world's energy mix. The aim of this research is to focus on availability of proved oil reserves along with production and consumption of oil in different regions and countries of the world. An effort has also been made to find the global position of India in terms of proved oil reserves, production and consumption of oil in the world. At the end, life of available proved oil reserves in the world is found out at the production rate of oil as in 2018. The management policy that may be adopted to use oil in a better way, considering environmental pollution, are also discussed.

Keywords Oil consumption · Oil production · Oil reserves · World

1 Introduction

Oil is one of the most important and widely used energy resources all over the world. In today's globally rapid development environment, oil is a major contributor to the world economy [1]. Oil accounts for nearly 40% of the world's energy mix. Crude oil or oil reserves are finite non-renewable energy resources and it will not be able to meet energy demands at the present or current rate in future. Ferreira [2] defines reserves as the mineable (recoverable) portion of a mineral resource (or energy resource) and classifies them as proven or probable. According to the data published by BP (British Petroleum), more than half of the world's discovered conventional oil reserves are located in five Persian Gulf states, all of which are OPEC (Organization of the Petroleum Exporting Countries) members [3]. McMichael [4] states that oil reserves

S. K. Anand (✉) · S. Mitra

Department of Mechanical Engineering, Jalpaiguri Government Engineering College, Jalpaiguri, West Bengal, India

e-mail: nceianska2k15@gmail.com

are among the most fundamental elements of the international oil industry. Oil, as an energy resource, has lots of advantages over coal and other energy resources. The cost of oil is not comparatively too high this time. Aguilera [5], Doshi et al. [6], Toews et al. [7], EIA (Environment Impact Assessment) [8], Willigers [9], Gulen [10], and McGlade [11] indicated the evidence of a relationship between oil prices and oil production costs. In addition, forecasting oil price is a difficult task for long-term investments—e.g., the development of oil projects that lasts around 30 years and uncertainty should not be ignored, as stressed by Pindyck [12], Radchenko [13], Postali et al. [14], Hamilton [15], Meade [16], and Larsson et al. [17].

World oil reserves are unevenly distributed between 70,000 fields [18]. Around 50% of the total proved oil reserves are present in the Middle East region, and more than one-fourth of the total proved oil reserves in the world are found in South and Central America and North America. This clearly shows distribution of proved oil reserves in different regions of the world is very uneven. Similarly, Venezuela, Saudi Arabia, Canada, and Iran have more than 50% of the total proved oil reserves of the world, while the rest of the countries of the world have the remaining 50% of the total proved oil reserves of the world.

In total, 507 fields are classified as ‘giant’ and account for 60% of conventional oil production [19]. The top 110 producing fields constitute over 50% of global supply, the top 20 contribute 27%, and the most productive 10 fields contribute 20% [18]. The top 110 producing fields constitute over 50% of global supply, the top 20 contribute 27%, and the most productive 10 fields contribute 20% [18]. Of the 507 giant oil fields, 430 are in production [19], of which 261 are in decline [20]. In recent years, however, concerns have grown over the environmental consequences of burning large volumes of oil, and whether reserves have the capacity to service growing demand ([19, 21–25]) (Table 1).

2 Study Procedure

The study and management aspects of reserves, production, consumption, and life of oil fields in the world were done with the help of various secondary data of British Petroleum Statistical Review of World Energy, 2019. The study and management of various aspects of oil reserves of the world was possible only after studying quality research of various researchers in the field of various aspects of oils, energy management, renewable and non-renewable resources of energy, management policies for sustainable use of energy and recent works or advancements in the field of renewable energies like solar energies, hydro energies, wind energies etc. After studying quality research, it was found that in each case, i.e., reserves, or production, or consumption of oil, only the top ten countries in the world dominated over there. So, this research paper was mainly focused on the top ten countries in each case. In our study, the main aim was focused on the data of 2018 in every aspect, but previous three years’ secondary data from 2015 to 2017 were also taken for comparative study of production and consumption in oil of the world so that life of proved

Table 1 Top ten countries having highest proved oil reserves at the end of 2018

Rank	Country	Thousand million barrels	Thousand million tonnes	Share of total (in %)	R/P ratio
1	Venezuela	303.3	48.0	17.5	•
2	Saudi Arabia	297.7	40.9	17.2	66.4
3	Canada	167.8	27.1	9.7	88.3
4	Iran	155.6	21.4	9.0	90.4
5	Iraq	147.2	19.9	8.5	87.4
6	Russia	106.2	14.6	6.1	25.4
7	Kuwait	101.5	14.0	5.9	91.2
8	United Arab Emirates	97.8	13.0	5.7	68.0
9	United States	61.2	7.3	3.5	11.0
10	Libiya	48.4	6.3	2.8	131.3
22	India	4.5	0.6	0.3	14.1

Source BPSRWE, 2019 [26]

Reserves-to-production (R/P) ratio—It is the ratio of total proved reserves of a country at the end of 2018 to production of oil in 2018. This forecasts the life of the oil reserves that will last in future at the current production

• More than 500 years

oil reserves could be estimated at the current production rates as in 2018 as well as the life of proved oil reserves at an increasing rate year by year. Actually, how much demand for oil has increased as obtained from Tables 2 and 3, was also helpful for knowing the increasing demands of oil as an energy resource. After all these studies,

Table 2 Top ten oil producer countries (in million tonnes) in 2018 rankwise

Rank	Country	2015	2016	2017	2018	Share % of 2018
1	United States	566.6	541.9	573.9	669.4	15.0
2	Saudi Arabia	568.0	586.7	559.3	578.3	12.9
3	Russia	541.8	555.9	554.3	563.3	12.6
4	Canada	215.6	218.0	235.4	255.5	5.7
5	Iraq	195.6	217.6	222.2	226.1	5.1
6	Iran	180.2	216.3	235.6	220.4	4.9
7	China	214.6	199.7	191.5	189.1	4.2
8	United Arab Emirates	176.1	182.4	176.2	177.7	4.0
9	Kuwait	148.1	152.5	144.8	146.8	3.3
10	Brazil	132.2	136.2	142.3	140.3	3.1
23	India	41.2	40.2	40.4	39.5	0.9

Source BPSRWE, 2019 [26]

Note 'Share of 2018' represents % contribution of a country of total oil produced in 2018 individually

Table 3 Top ten oil consumer countries (in million tonnes of oil equivalent) in 2018 rankwise

Rank	Country	2015	2016	2017	2018	Share % of 2018
1	United States	884.5	893.3	902.0	919.7	19.7
2	China	573.3	587.0	610.7	641.2	13.8
3	India	199.8	219.5	227.1	239.1	5.1
4	Japan	196.5	191.0	187.8	182.4	3.9
5	Saudi Arabia	173.5	171.5	168.8	162.6	3.5
6	Russia	149.4	153.1	151.5	152.3	3.3
7	Brazil	140.6	132.7	136.1	135.9	2.9
8	South Korea	120.2	129.3	130.0	128.9	2.8
9	Germany	114.2	116.5	119	113.2	2.4
10	Canada	107.0	108.7	108.8	110.0	2.4

Source BPSRWE, 2019 [26]

Note 'Share of 2018' represents % contribution of a country of total oil consumed in 2018 individually

the R/P ratio i.e., Reserves-to-production ratio of World's proved oil reserves, was calculated. That really shocked the point of future perspective of energy resources and that forced them into the condition of going through the management aspects of reserves, production, consumption, and life of oil of the world. Management aspects of oil were also focused on global serious issues like global warming, ozone layer depletion, climate change and acid rain, which were caused due to the consumption of oil.

3 Oil Reserves in World

At the end of 2018, total proved oil reserves in the world were 1729.7 thousand million barrels, or 244.1 thousand million tonnes [26]. Oil reserves were randomly distributed in different regions and countries of the world. More than 85% of total proved oil reserves were found in top ten leading proved oil reserves country of the world (Table 1). Venezuela was the leading proved oil reserve country with a share of 17.5% of the total proved oil reserves in the world, followed by Saudi Arabia, Canada, Iran, and Iraq, respectively (Table 1). China, as well as India, were not included in the top ten proved oil reserve countries of the world in 2018. India is in 22nd position in the world, having the highest proved oil reserves. Australia, China, India, Indonesia, Germany, Ukraine, Poland, and Kazakhstan were included in the list of the top ten highest proved coal reserves in the world at the end of 2018 [26], but these countries were not included in top ten highest proved oil reserves of the world at the end of 2018. This statistics shows that countries having high proved coal reserves doesn't mean that they will have high proved oil reserves. Likewise, India was the 5th most leading country having the highest proved coal reserves in the world

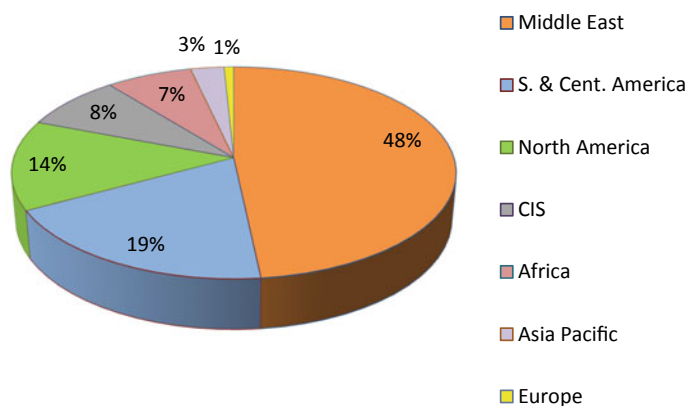


Fig. 1 Region wise percentage distribution of proved oil reserves in world (2018). *Source* BPSRWE, 2019 [26]

[26], but unfortunately, India was not in the list of the top ten highest oil reserves countries at the end of 2018 (Table 1). India had only 4.5 thousand million barrels or 0.6 thousand million tonnes of oil, which is only 0.3% of the total proved oil reserves of world in 2018.

Region wise percentage distribution of proved oil reserves in world at the end of 2018 are shown in Fig. 1. Middle East, individually, contributed around half of the total proved oil reserves of the world (Fig. 1). There were lots of major countries in Middle East which had proved oil reserves. Major countries of the Middle East for proved oil reserves are Saudi Arabia, Iran, Iraq, Kuwait, and United Arab Emirates (UAE). Rest of the regions of the world, such as South and Central America, North America, Commonwealth of Independent States etc. contributed the remaining 50% proven oil reserves. Europe had the lowest proved oil reserves at the end of 2018. Norway was the major country in Europe which has proven oil reserves in 2018.

4 Production of Oil in World

In 2018, total oil produced in the world were 4474.3 thousand million tonnes [26]. Oils were randomly produced in different regions and countries of the world. Around 70% of total oil produced in the world in 2018 were found in top ten leading oil producer country of the world (Table 2). United States was the leading oil producer country with share of 15.0% of the total oil produced in the world in 2018 followed by Saudi Arabia, Russia, Canada, Iraq and Iran respectively (Table 2). China, United States and Russia were only three countries who were included in top ten oil producer countries as well as in top ten coal producer countries of the world in 2018 [26]. In 2018, India was 23rd highest oil producer country of the world but, China produced more than four times than India produced oil in 2018. India produced

only 39.5 million tonnes oil in 2018 with share of only 0.9% of the total oil produced in the world.

Top ten oil producer countries and region wise percentage distribution of oil producers in the world in 2018 are shown in Table 2 and Fig. 2 respectively. From these, it can be concluded that only Middle East produced one third of the total oil produced in world in 2018. Major oil producer countries of Middle East were Saudi Arabia (12.9%), Iraq (5.1%), Iran (4.9%), United Arab Emirates (4.0%) and Kuwait (3.3%). North America region, individually, contributes around one fourth (23%) of the total oil produced in world in 2018. In North America, United States (15.0%) and Canada (5.7%) are the major oil producer country which are also listed in top ten oil producer countries of the world in 2018. Rest of the regions of the world such as Commonwealth of Independent States, Africa, Asia Pacific, South and Central America and Europe respectively consumed 15.8%, 8.7%, 8.1% and 3.6% of total oil produced in world in 2018. Out of 15.8% of total oil produced by Commonwealth of Independent States (CIS), Russia, individually, produced around 80% of total oil produced by Commonwealth of Independent States. Nigeria (2.2%), Angola (1.7%) and Algeria (1.5%) were the major oil producer countries in Africa region while, China (4.2%), India (0.9%) and Indonesia (0.9%) were the major oil producer countries of Asia Pacific region of the world in 2018. From Asia Pacific, China was only country that was listed in top ten oil producer country of the world in 2018, but India, which is one the biggest country, was not included in top ten list. In South and Central America region, Brazil (3.1%), Venezuela (1.7%) and Colombia (1.0%) were major oil producer countries. Norway, individually, produced 50% of the total oil produced by Europe region in 2018.

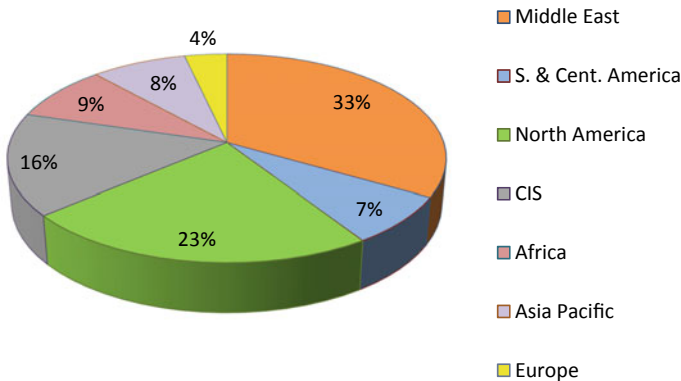


Fig. 2 Region wise percentage distribution of oil producers in world (2018). *Source* BPSRWE, 2019 [26]

5 Consumption of Oil in World

In 2018, 4662.1 million tonnes of oil equivalent oils were consumed by different countries of world [26]. Like random distribution of proved oil reserves and production of oil in different regions and countries of the world in 2018, oils were also randomly consumed in different regions and countries of world. Top ten leading oil consumer countries of the world consumed around 60% of total million tonnes of oil equivalent of oil consumed in 2018 (Table 3). Like United States, the most leading oil producer country of the world, United States was also the most oil consumer country of the world in 2018. United States consumed 19.7% of the total oil consumed in world in 2018 which is around one-fifth of the total oil consumed in world in 2018 followed by China, India, Japan, Saudi Arabia, Russia, Brazil, South Korea, Germany and Canada with share of 13.8%, 5.1%, 3.9%, 3.5%, 3.3%, 2.9%, 2.8%, 2.4% and 2.4% respectively (Table 3).

India, United States, Japan, South Korea, Germany, China and Russia were those countries who were included in top ten oil consumer countries as well as in top ten coal consumer countries of world in 2018 [26]. In 2018, India was 3rd (third) highest oil consumer country of the world and China was 2nd (second) highest oil consumer country of the world but the difference in consumption of oil by these two countries was very large. China consumed around more than 2.5 times the oil consumed by India in 2018. India consumed only 239.1 million tonnes of oil equivalent in 2018 with share of only 5.1% of the total oil consumed in the world while China consumed 641.2 million tonnes of oil equivalent in 2018 with share of only 13.8% of the total oil consumed in the world (Table 3).

Top ten oil consumer countries and region wise percentage distribution of oil consumers in the world in 2018 are shown in Table 3 and Fig. 3 respectively. Asia Pacific and North America consumed more than 60% of oil consumed in world in 2018 (Fig. 3). China (13.8%), India (5.1%), Japan (3.9%), South Korea (2.8%)

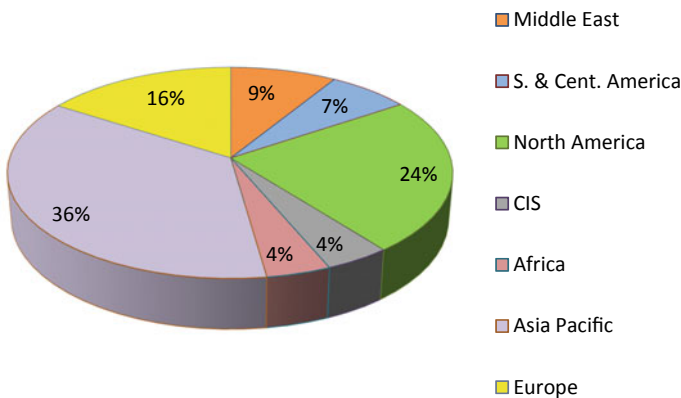


Fig. 3 Region wise percentage distribution of oil consumers in world (2018). *Source* BPSRWE, 2019 [26]

and Indonesia (1.8%) were the five major oil consumer countries in Asia Pacific while United States (19.7%), Canada (2.4%) and Mexico (1.8%) were major oil consumer countries in North America in 2018. Other than Asia Pacific and North America, remaining regions consumed around 40% of the oil consumed in world in 2018. Europe, Middle East, South and Central America and Commonwealth of Independent States respectively consumed 15.9%, 8.8%, 6.8% and 4.2% of the total oil consumed in world in 2018 (Fig. 3). In Europe region, whose oil consumption in 2018 was 15.9% of the total oil consumed in world, included major oil consumer countries such as Germany, United Kingdom and France which consumed 2.4%, 1.7% and 1.7% of total oil consumed in world in 2018. Iran (1.8%) and United Arab Emirates (1%) were the major oil consumer countries from Middle East. Brazil, individually, consumed more than 40% of the total oil consumed in South and Central America while Russia, individually, consumed around 80% of the total oil consumed in Commonwealth of Independent States in 2018. In Africa region, Egypt (0.8%) was the major oil consumer country.

6 Life of Oil Reserves in Future

The life of oil reserves is represented by the R/P ratio i.e., Reserves-to-Production ratio. Reserves-to-Production ratio may be defined as ratio of available oil proved reserves in last year to production of oil reserves in last year. The formula used for finding the life of oil reserves is

$$\text{Life (in years)} = \frac{\text{Available proved oil reserves in last year (R)}}{\text{Production of oil in last year (P)}}$$

From this formula, the life of oil reserves of the world was only 50 years in 2018. Venezuela, which was the world's leading proved oil reserves country, had more than 500 years of life. India, which is one of the oil consumer countries, had life of only 14.1 years. Both Russia and United States, which is one of the major nuclear power countries had an average life of oil reserves of 25.4 and 66.4 years, respectively.

7 Conclusions

From the foregoing study and analysis, the following conclusions and comments may be made:

- (a) More than 85% of the total proved oil reserves are found in the top ten oil producing countries of world. This clearly shows the uneven/random distribution of oil reserves in different countries of the world. This uneven distribution sometimes causes concern about the timely availability of oils and it is found

that sometimes the supply chain is broken down, causing production loss in distant countries.

- (b) The contribution of Venezuela, Saudi Arabia, Canada, Iran, and Iraq to total proved oil reserves in 2018 is very good, but most populated countries like China and India have a very small share of total proved oil reserves. India contributes only 0.3% of total proved oil reserves in the world and holds the 22nd position in the world.
- (c) The top ten oil producer countries and the top ten oil consumer countries contribute around 70% and 60%, respectively.
- (d) Based on available proved oil reserves and current production of oil in the world, the life of oil in the world is about 50 years.
- (e) For energy security and sustainable development points of view, almost every country of the world should very seriously focus on alternative sources of energy, especially, renewable sources of energy such as solar energy, wind energy, tidal energy, geothermal energy, small hydro energy, and bioenergy.
- (f) Oil causes pollution in huge quantities, which is very unsafe for the environment and health. When oil is burned for electricity, sulphur dioxide, mercury compounds, and nitrogen oxides are produced. This pollution is a major cause of serious global environmental issues such as global warming, ozone layer depletion, climate change and acid rain.

To address the above issues, the following management aspects, or policies may be adopted:

- (i) Emphasis should be given to reduce oil as a fuel in power plants. Instead of oil, focus should be concentrated on environmentally friendly energy sources like renewable energy sources like hydro energy, solar energy, wind energy etc.
- (ii) The most common fuel for generating power in the world is coal, though it is the dirtiest fuel. However, coal will dominate, at least in near future too, in spite of its gradual replacement by alternative energy sources like renewable energy and hydro energy sources. The available immediate solution tactics is to adopt clean coal technologies, IGCC (Integrated Gasification Combined Cycle) systems and carbon sequestration in every possible way while burning coal as fuel in power plants. Replacing coal-based plants with oil will not be a viable solution. Oil should be reserved for transportation and other special requirements only.
- (iii) High taxes should be imposed on oil based non-performing plants in respect of pollution norms.
- (iv) Proper pollution reduction equipment should be used, which is sustainable for the environment.
- (vi) Old power plants should either be properly renovated or dismantled from pollution reasons and to enhance efficiency, thereby fuel requirements will be less.

Acknowledgements The authors would like to thank Prof. Dr. M.P. Mandal, Assistant Professor-cum-Junior Scientist for their valuable and constructive suggestions during the planning and development of this research work.

References

1. Aydin G (2015) Production modeling in the oil and natural gas industry: an application of trend analysis. *Pet Sci Technol* 32(5):555e64
2. Ferreira DF (2009) In: Komedi C (ed) Oil and gas production in marginal fields: a nascent market in Brazil
3. BP (2017) BP statistical review of world energy, June
4. McMichael C (1997) The SPE/WPC reserve definitions: the impact on past and future book evaluations. SPE Hydrocarbon Economics and Evaluation Symposium, Dallas, USA. pp 185–192. <https://doi.org/10.2118/37957-MS>
5. Aguilera RF (2014) Production costs of global conventional and unconventional petroleum. *Energy Police* 64:134–140
6. Doshi H, Kumar P, Yerramilli V (2014) Uncertainty and capital investment: real options or financial frictions. SSRN Scholarly Paper ID 2315217
7. Toews G, Naumov A (2015) The relationship between oil price and costs in the oil and gas industry. Departments of Economics, OxCarre Research Paper 152, University of Oxford
8. EIA (2014) Short-term energy outlook market prices and uncertainty report
9. Willigers BJA (2009) Enhanced economic modeling by correlated stochastic models of E&P costs and hydrocarbon prices: the limitations of fixed price decks and the versatility of least-squares monte carlo simulation, SPE, p 121442
10. Gülen G (2014) Global hydrocarbon model: upstream module design considerations, energy information administration (EIA)
11. McGlade CE (2013) Uncertainties in the outlook for oil and gas, doctor of philosophy's Thesis University College London, UCL Energy Institute
12. Pindyck RS (1999) The long-run evolution of energy prices. *Energy J* 20(2)
13. Radchenko S (2005) The long-run forecasting of energy prices using the model of shifting trend. University of North Carolina at Charlotte
14. Postali FAS, Picchetti P (2006) Geometric Brownian Motion and structural breaks in oil prices: a quantitative analysis. *Energy Econ* 28:506–522
15. Hamilton JD (2008) Understanding crude oil prices, national bureau of economic research. University of California, 2008 working paper 14492
16. Meade N (2010) Oil prices—Brownian motion or mean reversion? A study using a one year ahead density forecast criterion. *Energy Econ* 32:1485–1498
17. Larsson K, Nossman M (2011) Jumps and Stochastic volatility in oil prices: time series evidence. *Energy Econ* 33:504–514
18. IEA (2008) World energy outlook 2008. International Energy Agency. Paris, France
19. Robelius F (2007) Giant oil fields—The highway to oil: Gint oil fields and their importance for future oil production. Uppsala University, Teknisk-naturvetenskapliga vetenskapsområdet, Physics, Department of Nuclear Physics. Uppsala Universitet, Uppsala
20. Hook M, Hirsch R et al (2009) Giant oil field decline rates and their influence on world oil production. *Energy Policy* 37(6):2262–2272
21. Alekkett K (2007) Peak oil and the evolving strategies of oil importing and exporting countries: facing the hard truth about an import decline for the OECD countries. Joint Research Centre Discussion Papers. International Transport Forum, OECD/ITF
22. Campbell CJ, Laherrere JH (1998) Preventing the next oil crunch—the end of cheap oil. *Sci Am* 278:77–83

23. Laherrere J (2009) Oil peak or plateau St. Andrews Economy Forum. ASPO France, France
24. Sperling D, Gordon D (2007) Two billion cars. Oxford University Press, New York
25. USGAO (2007) Crude Oil: uncertainty about future oil supply makes it important to develop a strategy for addressing a peak decline in oil production. United States Government Accountability Office, Washington
26. BPSRWE (2019) BP statistical review of world energy, 68th Edition

Prediction of Remaining Useful Life (RUL) of Bearing Using Exponential Degradation Model



Keval Bhavsar  and Vinay Vakharia 

Abstract Prognostics and Health Management (PHM) plays a vital role in the reduction of maintenance as the fault can be identified prior due to condition monitoring and its remaining useful life is predicted based on the condition of the component. Fault prognosis and condition monitoring uses the previous data and predicts the remaining useful life (RUL) of the component using various regression/degradation model. Bearing is one of the most important part of any rotating mechanical machine, so it is important to monitor its condition to ensure the best utilization and identify its remaining life to reduce the downtime. In this paper, statistical features are calculated from the denoised vibration data on which monotonicity analysis is performed to select the feature. That are then used to train the degradation model and predict the RUL for the degrading bearings. The degradation model is validated using the FEMTO bearing dataset provided by the National Aeronautics and Space Administration.

Keywords Remaining useful life · RUL · Bearing · PHM · Prognostics and health management · Exponential degradation model

1 Introduction

In recent years, Prognostics and health management (PHM) has gotten broad consideration in the improvement in accuracy and reduction of maintenance costs [1, 2]. PHM is a combination of condition monitoring, Fault diagnosis and prognosis with decision support [3]. The aim of Remaining Useful Life (RUL) is to assess the degradation performance of the machine and detect the upcoming failure [4]. There are three main approaches for performing fault diagnosis, they are model-based approach, data-driven approach and hybrid approach. Generally, the data-driven approach is used as it gives more accuracy.

K. Bhavsar · V. Vakharia (✉)

Department of Mechanical Engineering, Pandit Deendayal Energy University, Gandhinagar, Gujarat, India

e-mail: vinayvakharia4343@gmail.com

Prediction of RUL for a bearing is done to reduce the machine downtime and cost of maintenance. RUL of a bearing can be predicted by using vibration, acoustic, pressure, oil analysis and temperature. Generally, the data-driven approach and analysis of vibration data is used to predict the RUL, as the measurement of vibration can be taken accurately and timely [5, 6].

Xiang Li et al. (2019), proposed the time–frequency domain information to perform the prognostic of bearing and a CNN is used for multi-feature extraction [7]. Weiwen Peng et al. (2019) proposed time–frequency representation generated using the wavelet transform of the degradation data and multi-scale convolution neural network is used to predict the RUL [8]. Mehdi Behzad et al. (2018) proposed the used of kurtosis, root mean square (RMS) and a high-frequency root mean square (HFRMS) to train and predict the RUL from a feed-forward neural network [9]. Yaguo Li et al. (2020) proposed a hybrid prognostic approach where degradation data are sparsely using relevance vector machine regression and RUL is predicted using the exponential degradation model [10]. Gaoliang Peng et al. (2020) proposed the use of five bandpass energy of a frequency spectrum as features and used linear regression to predict the RUL [11]. Tahar Boukra and Abdessalam Lebaroud (2017) proposed the use of the cumulative form of standard trigonometric function on the extracted features and used the neuro-fuzzy system and particle filtering to predict the RUL [12]. Wentao Mao et al. (2018), proposed a LSTM model for predicting the RUL and used the Hilbert Hung Transform for training the model [13]. Youngji Yoo and Jun-Geol Baek (2018) proposed continuous wavelet transform of the vibration signal to generate the 2-D image and fed the wavelet power spectrum to the convolutional neural network (CNN) predict RUL [14].

In this paper, the first section is about the FEMTO bearing dataset. The second section is about the preprocessing of the data where denoising is done using the clip feature after that statistical features like root mean square and kurtosis are extracted. The third section is about the RUL prediction where Exponential Degradation Model is used, followed by the last section of results where the predicted RUL is compared with the True RUL for the bearings.

2 Dataset

The FEMTO bearing dataset of Prognostic and Health Management (PHM)'s IEEE challenge 2012, provided by National Aeronautics and Space Administration is used [15]. Fig. 1 is an experimental setup of Pronostia which is used for testing and validation of bearing's fault detection and prognostics.

Table 1 shows the FEMTO bearing dataset generated on pronostia which has acceleration values collected at a sampling frequency of 25.6 kHz as data for a total of seventeen bearings, of which seven bearings in each condition 1 and 2, while three bearings for condition 3. Vibration signal is plotted against time for bearing 1_3 is shown in Fig. 2.

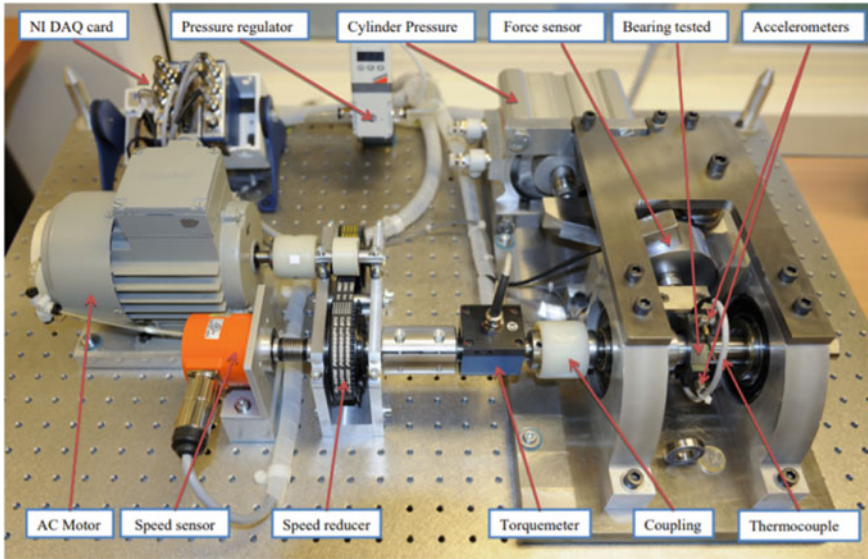


Fig. 1 Overview of Pronostia

Table 1 Datasets

	Operating Condition		
	condition 1	condition 2	Condition 3
Radial load (N)	4000	4200	5000
Speed (RPM)	1800	1650	1500
Training sets	Bearing_1_1	Bearing_2_1	Bearing_3_1
	Bearing_1_2	Bearing_2_2	Bearing_3_2
	Bearing_1_3	Bearing_2_3	Bearing_3_3
	Bearing_1_4	Bearing_2_4	
	Bearing_1_5	Bearing_2_5	
	Bearing_1_6	Bearing_2_6	
	Bearing_1_7	Bearing_2_7	

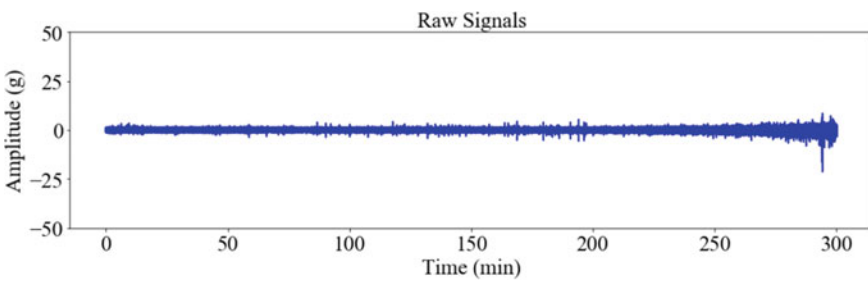


Fig. 2 Vibration signal of bearing 1_3 in the time domain

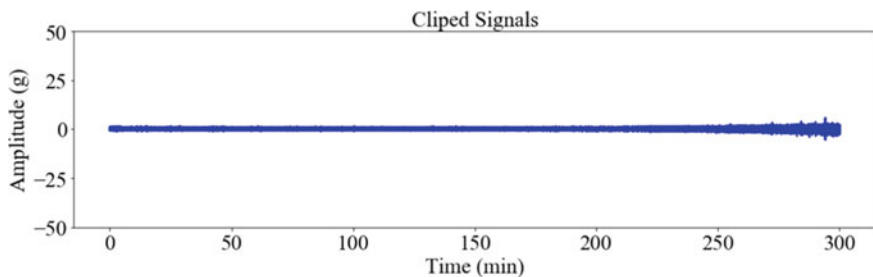


Fig. 3 Clipped vibration signal of bearing 1_3 in the time domain

3 Data Denoising and Statistical Feature Extraction

Denoising is a technique in which the noise is reduced from the data. It can be done using clipping and moving average method. In this paper, clipping technique is used in which data outside the bound is converted to the boundary value as shown in Fig. 3.

Statistical Features used in this paper are the time domain features like mean, sum, skewness, kurtosis, maximum amplitude, minimum amplitude and root mean square. The formulas of all the features extracted from the vibration data of bearing are given in Table 2 and the feature table of bearing 1_3 is shown in Table 3.

Monotonicity analysis, a feature ranking method which gives the monotonic trend of the feature as a system gets closer to the failure point. If the feature is having a monotonic trend (value closer to 1) then it traces the degradation process. Monotonicity analysis is performed on the feature vector for reducing the number of features. Features namely RMS, Kurtosis and Maximum having monotonic trends (shown in Fig. 4) are selected are fed to the model.

Along with features, First prediction point (FPT) (a point from where the degradation is started) and Last prediction point (LPT) (a point where bearing fails), calculated from the data are also fed to the model.

4 Exponential Degradation Model

A degradation model is used when a safety failure threshold is available. RUL is estimated when the monitored signal crosses the safety threshold (calculated from training dataset). In this paper, exponential degradation model is used because the bearing is experiencing the cumulative degradation. The degradation model is based on Eq. (11) and the curve is shown in Fig. 5.

$$Y = B * e^{AT} \quad (11)$$

Table 2 Statistical features/Time domain features

Name	Description	Formula
Mean	The average value of the vibration signal	$x_m = \frac{1}{K} * \sum_{k=1}^K x(k)$ (1)
Standard deviation (std)	Deviation from the mean value of the vibration signal	$x_{std} = \sqrt{\frac{\sum_{k=1}^K (x(k)-x_m)^2}{(K-1)}}$ (2)
Variance	Square of std	$x_{std} = \frac{\sum_{k=1}^K (x(k)-x_m)^2}{(K-1)}$ (3)
Sum	Sum of signal	$Sum = \sum_{k=1}^K x(k)$ (4)
Skewness	A measure of lack of symmetry	$x_{skew} = \frac{\sum_{k=1}^K (x(k)-x_m)^3}{(K-1)*x_{std}^3}$ (5)
Kurtosis	A measure of the spikiness of the signal relative to a normal distribution	$x_{kurt} = \frac{\sum_{k=1}^K (x(k)-x_m)^4}{(K-1)*x_{std}^4}$ (6)
Root mean square (RMS)	The square root of the mean of squares of a signal	$x_{rms} = \sqrt{\frac{\sum_{k=1}^K (x(k))^2}{K}}$ (7)
Peak to peak value	Difference between maximum and minimum peak values	$x_{ppv} = x_{max} - x_{min}$ (8)
Maximum amplitude	Value of the maximum amplitude of the signal	$x_{max} = \max(x(k))$ (9)
Minimum amplitude	Value of the minimum amplitude of the signal	$x_{min} = \min(x(k))$ (10)

where Y = degradation; T = data; and A and B = parameters to be estimated by the regression method based on historical data.

5 Result and Discussion

Predicted RUL is predicted/calculated by fitting the exponential degradation model shown in the previous section which is compared with the True RUL of the bearing. The error is calculated based on an equation such as:

$$\% \text{ Error} = \frac{RUL_{True} - RUL_{Predicted}}{RUL_{True}} \tag{12}$$

And the overall score is calculated based on an equation such as:

$$Score = \frac{\sum_{i=1}^{11} Z_i}{11} \tag{13}$$

Table 3 Statistical/Time domain feature of bearing 1_3

Data	Kurt	SD	Mean	Var	Skew
1	-0.1075	0.412402	0.001173	0.170076	-0.00633
2	-0.00105	0.388173	9.02E-05	0.150678	0.031593
3	0.038631	0.384075	0.012569	0.147514	0.057434
4	0.085079	0.375633	0.009456	0.1411	-0.0438
5	0.015822	0.396988	0.004699	0.157599	-0.02949
1798	0.034831	0.699871	0.008433	0.489819	-0.11621
1799	0.126685	0.808148	0.000823	0.653104	-0.06208
1800	0.785421	0.840164	-0.01117	0.705875	-0.61168
1801	-0.08492	0.812163	0.015807	0.659608	-0.01193
1802	2.188013	0.81028	0.015343	0.656554	-0.57617
Data	RMS	Peak2Peak	Max	Min	Sum
1	0.412404	2.216	1.116	-1.1	3.004
2	0.388173	2.193	1.149	-1.044	0.231
3	0.384281	2.121	1.134	-0.987	32.176
4	0.375752	2.166	1.107	-1.059	24.208
5	0.397016	2.202	1.12	-1.12	12.03
1798	0.699922	3.915	1.958	-1.958	21.589
1799	0.808149	4.599	2.348	-2.251	2.107
1800	0.840238	4.862	3.017	-3.017	-28.587
1801	0.812317	4.369	2.405	-2.405	40.465
1802	0.810426	5.789	3.548	-3.548	39.279

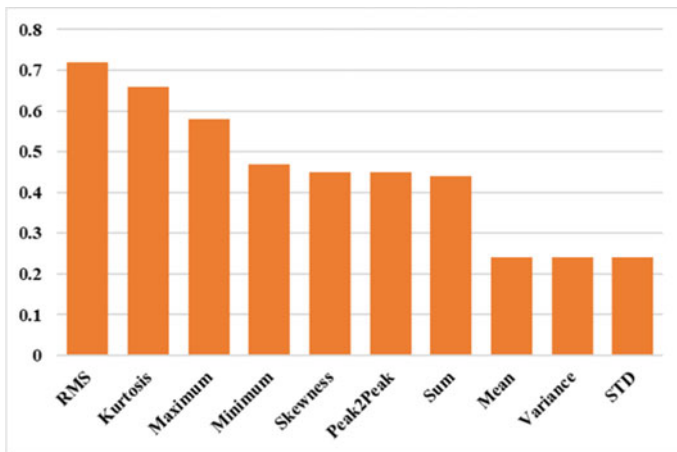


Fig. 4 Monotonicity analysis

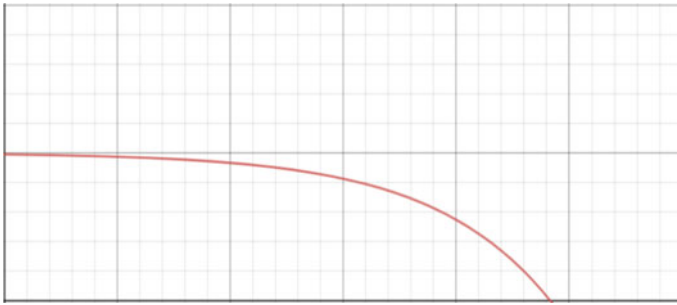


Fig. 5 Exponential degradation model

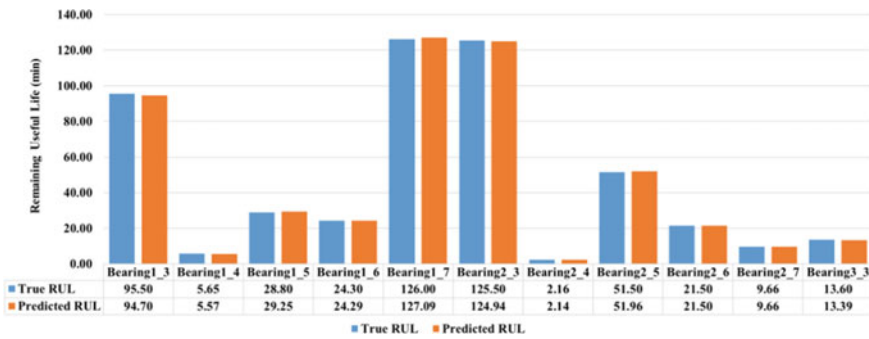


Fig. 6 Graph of the predicted RUL and true RUL

where Z_i is a scoring function that is based on equation such as:

$$Z_i = \begin{cases} \exp^{-\frac{\ln(0.5) * \text{Error}}{5}}, & \text{Error} \leq 0, \\ \exp^{\frac{\ln(0.5) * \text{Error}}{20}}, & \text{Error} > 0. \end{cases} \quad (14)$$

The graph shows the comparison between true RUL and RUL predicted by the exponential degradation model for the FEMTO bearing dataset is shown in Fig. 6. The score of the model is 0.97 shown in Table 4, which is calculated using Eqs. (13) and (14).

6 Conclusion

Prognostic and Health Management plays an important role in reducing the maintenance downtime as well as cost. RUL is predicted using the FEMTO bearing dataset. Statistical/Time-domain features are calculated after doing denoising of the vibration data from that maximum, kurtosis and RMS are selected using the monotonicity

Table 4 Error in percentage with the overall score of the model

Name	True RUL	Predicted RUL	%Error
Bearing1_3	95.5	94.7	0.84
Bearing1_4	5.65	5.57	1.42
Bearing1_5	28.8	29.25	-1.56
Bearing1_6	24.3	24.29	0.04
Bearing1_7	126	127.09	-0.87
Bearing2_3	125.5	124.94	0.45
Bearing2_4	2.16	2.14	0.93
Bearing2_5	51.5	51.96	-0.89
Bearing2_6	21.5	21.50	0.00
Bearing2_7	9.66	9.66	0.00
Bearing3_3	13.6	13.39	1.54
Score			0.97

analysis. Exponential degradation model is used to predict the RUL as the bearings are experiencing cumulative degradation. The score of 0.97 is achieved by the model.

Acknowledgements Authors would like to thank Prof. Patrick Nectoux and his colleagues for doing the experiment at FEMTO-Institute and National Aeronautics and Space Administration (NASA) for providing the dataset.

References

1. Heng A, Zhang S, Tan ACC, Mathew J (2009) Rotating machinery prognostics: State of the art, challenges and opportunities. *Mech Syst Signal Process* 23(3):724–739. <https://doi.org/10.1016/j.ymssp.2008.06.009>
2. Lee J, Wu F, Zhao W, Ghaffari M, Liao L, Siegel D (2014) Prognostics and health management design for rotary machinery systems—Reviews, methodology and applications. *Mech Syst Signal Process* 42(1–2):314–334. <https://doi.org/10.1016/j.ymssp.2013.06.004>
3. Benkedjough T, Medjaher K, Zerhouni N, Rechak S (2013) Remaining useful life estimation based on nonlinear feature reduction and support vector regression. *Eng Appl Artif Intell* 26(7):1751–1760. <https://doi.org/10.1016/j.engappai.2013.02.006>
4. Qiu H, Lee J, Lin J, Yu G (2003) Robust performance degradation assessment methods for enhanced rolling element bearing prognostics. *Adv Eng Inform* 17(3–4):127–140. <https://doi.org/10.1016/j.aei.2004.08.001>
5. Pham HT, Tran VT, Yang B-S (2010) A hybrid of nonlinear autoregressive model with exogenous input and autoregressive moving average model for long-term machine state forecasting. *Expert Syst Appl* 37(4):3310–3317. <https://doi.org/10.1016/j.eswa.2009.10.020>
6. Jardine AKS, Lin D, Banjevic D (2006) A review on machinery diagnostics and prognostics implementing condition-based maintenance. *Mech Syst Signal Process* 20(7):1483–1510. <https://doi.org/10.1016/j.ymssp.2005.09.012>
7. Li X, Zhang W, Ding Q (2019) Deep learning-based remaining useful life estimation of bearings using multi-scale feature extraction. *Reliab Eng Syst Saf* 182:208–218. <https://doi.org/10.1016/j.res.2018.11.011>

8. Zhu J, Chen N, Peng W (2019) Estimation of bearing remaining useful life based on multiscale convolutional neural network. *IEEE Trans Ind Electron* 66(4):3208–3216. <https://doi.org/10.1109/TIE.2018.2844856>
9. Behzad M, Arghand HA, Rohani Bastami A (2018) Remaining useful life prediction of ball-bearings based on high-frequency vibration features. *Proc Inst Mech Eng Part C J Mech Eng Sci* 232(18):3224–3234, Sep 2018. <https://doi.org/10.1177/0954406217734885>
10. Wang B, Lei Y, Li N, Li N (2020) A hybrid prognostics approach for estimating remaining useful life of rolling element bearings. *IEEE Trans Reliab* 69(1):401–412. <https://doi.org/10.1109/TR.2018.2882682>
11. Chen Y, Peng G, Zhu Z, Li S (2020) A novel deep learning method based on attention mechanism for bearing remaining useful life prediction. *Appl Soft Comput* 86:105919. <https://doi.org/10.1016/j.asoc.2019.105919>
12. Boukra T, Lebaroud A (2017) New trend in enhancing the remaining useful life prediction. *Proc Eng Technol PET* 25:36–40
13. Mao W, He J, Tang J, Li Y (2018) Predicting remaining useful life of rolling bearings based on deep feature representation and long short-term memory neural network. *Adv Mech Eng* 10(12):168781401881718. <https://doi.org/10.1177/1687814018817184>
14. Yoo Y, Baek J-G (2018) A novel image feature for the remaining useful lifetime prediction of bearings based on continuous wavelet transform and convolutional neural network. *Appl Sci* 8(7):1102. <https://doi.org/10.3390/app8071102>
15. “FEMTO Bearing Data Set,” NASA ames prognostics data repository. <http://ti.arc.nasa.gov/project/prognostic-data-repository>

Analysis of Tool Defect in Ultrasonic Machining Process Through Numerical Modelling



Mehdi Mehtab Mirad, Jiomani Talukdar, and Bipul Das

Abstract Ultrasonic machining is a non-traditional machining method which is extensively used for the machining of fragile materials such as semiconductor materials, glass, and ceramics. The work and tool material properties impact the machining performance to a greater level. The tool profile is another important factor that can influence the machining in the ultrasonic machining process. The most significant aspect of tool design is the determination of resonant length and resonant frequency of the tool. The conical tool profile is considered here for the investigation. Depending on the dimensions of the tool, the tool profile is designed. Modal analysis is performed using finite element method. The dimensions of the tool under the frequency of 19.5–20 kHz are selected. Modal analysis is executed to define the natural frequencies as well as mode shapes of the tool. In the harmonic response analysis, stress and deformation behaviour are obtained for the tool profile. After the stresses are generated, a line defect is introduced at the highest stressed point in the tool profile. The defects are made in two different orientations i.e. one along the longitudinal direction and another is perpendicular to the longitudinal axis with respect to the oscillation of the tool. The maximum stress generated in tool is found to be 639.57 MPa at the defect location that is perpendicular to the longitudinal axis with respect to the tool oscillation.

Keywords Tool profile · Resonant frequency · Resonant length · Modal analysis · Harmonic response analysis

1 Introduction

Non-traditional machining techniques such as laser beam machining and electric discharge machining can be used for machining hard and fragile materials. Even these processes are having various assumptions. Ultrasonic machining (USM) is an alternate method for machining both the conductive and nonconductive hard

M. M. Mirad · J. Talukdar · B. Das (✉)

Department of Mechanical Engineering, National Institute of Technology Silchar, Silchar, India
e-mail: bipul@mech.nits.ac.in

© The Author(s), under exclusive license to Springer Nature Singapore Pte Ltd. 2023
T. S. Sudarshan et al. (eds.), *Recent Advancements in Mechanical Engineering*,
Lecture Notes in Mechanical Engineering,
https://doi.org/10.1007/978-981-19-3266-3_35

449

and fragile materials. In this process, a vibrating tool is changing the ultrasonic frequencies to eliminate the material from the work surface.

Aher et al. [1] investigated the effects of several process constraints such as tool feed rate, power rating, and abrasive grain size to produce a stepped hole profile. These effective parameters are studied through graphical illustration. Singh et al. [2] performed the modal analysis to develop two different horn profiles such as stepped and exponential horn with the help of FEM-based method. The mode shapes and natural frequencies for both the tool profiles are considered. The tool profiles are made up of titanium and aluminium. The stepped horn profile with titanium is generated at a higher natural frequency for all six modes. Sarraf [3] investigated the combination of several vibration modes to design the operative resonant horns for high power ultrasonic uses such as cleaning, welding, metal forming, and surgical devices. The suggested modifications included the cutting of holes and reduction in the cross-sectional area that can regenerate the longitudinal mode of vibration into a longitudinal–torsional mode. Behera et al. [4] performed a design for the horn profile based on finite element analysis using ANSYS environment. The natural frequency is calculated for the resonance regime. The aluminium and carbon steel are considered as the material of the horn. The frequencies at mode 5 for both aluminium and carbon steel are found closest to the operating frequency of 25,000 Hz. The amplitude of vibration is maximum at the tip which is greater than that of input and zero at the conical section where the nodal point appears. The amplitude of vibration at the tip of aluminium horn is more than that of the carbon steel horn.

Stanasel et al. [5] have been designed an ultrasonic horn for application in the automotive industry. The numerical analysis is carried out to determine the velocity, amplitude, acceleration, mechanical impedance, and stress of the horn. Wang et al. [6] analysed a FEM-based model for a finned-tube heat exchanger. The vibration analysis is carried out using COMSOL 3.5. The results showed that in the heat exchanger, the vibration modal difference is more between the high- and low-frequency vibration modes. Addepalli [7] studied different shapes of the horn to identify the different modes for longitudinal vibrations. The modal analysis is performed for the mode shapes as well as the natural frequencies of the different shaped horns. The different modes are created at different natural frequencies and the preferred frequency is the mode at which the longitudinal vibration is obtained. So, the desired longitudinal mode of vibration is observed at 1st mode for conical, exponential, and cylindrical horn and 5th mode for stepped horn. Kumar et al. [8] have been designed a new stepped horn profile for ultrasonic welding in terms of displacement amplitude and von Mises stress by using harmonic and modal analysis. The results showed that the displacement amplitude and von Mises stress of the stepped horn are more than the other profile horns. The new stepped horn is increased by 19% of natural frequency by existing other horns.

The aforementioned survey of available literature revealed that the numerical investigations carried out in the field of USM have not considered the analysis of tool for investigating the machining performance. Moreover, no study has revealed the behaviour of the tool under the presence of defect. Thus, in this study, the behaviour of the tool is investigated under the presence of line defect. Numerical investigation

was carried out to understand the effect of defect in the tool through vibration analysis and stress profile of the tool in the vicinity of the defect.

2 Numerical Analysis

Numerical analysis is carried out using finite element modelling of the tool designed for the investigation. Commercial FEM simulation package COMSOL and ANSYS is used for obtaining the modal as well as harmonic analysis. Stress modelling of the tool under the influence of defects in the tool is carried out using ANSYS software package. The framework followed for the numerical modelling is presented in the following sections.

2.1 Tool Design

The design of a tool is a complicated process. It involves the selection of correct material and tuning the tool to a specific frequency range. Conical tools have a cross-sectional area that changes with length. The gradual transition of cross-sectional area in the conical tool distributes the stress over a greater length. A significant aspect of tool design is the intention of the precise resonant length. This resonant length is equal to the multiple of half of the wavelength of the structure. The schematic representation of the conical tool is shown in Fig. 1.

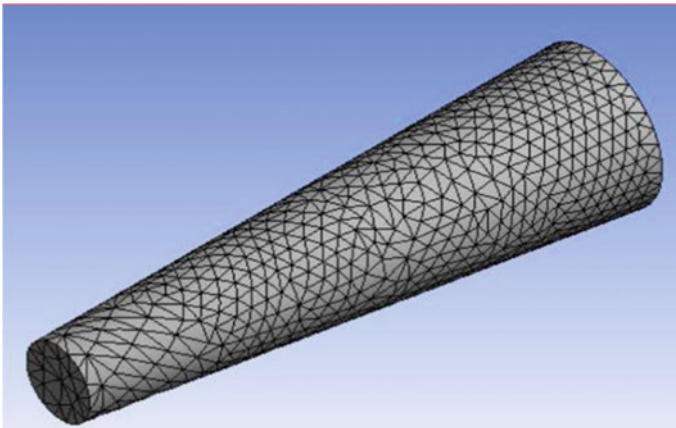


Fig. 1 Schematic representation of a conical tool

Table 1 Dimension of the tool

Tool profile	Tool length (mm)	Tool diameter (mm)
Conical	145	$D_1 = 20, D_2 = 10$

Table 2 Properties of the tool material

Material	Modulus of elasticity (E)	Poisson's ratio	Density (ρ)	Ultimate tensile strength
Tungsten carbide (WC)	530 GPa	0.31	15,630 kg/m ³	344 MPa

2.2 Tool Length Calculation

The desired length of a conical tool profile is measured by the multiplication of resonant length for the exponential shape of a tool by a factor of 1.1. The resonant length of an exponential tool profile is given by Eq. (1).

$$L = \frac{C}{f \left\{ \sqrt{1 + \left(\ln\left(\frac{N}{2\pi}\right)\right)^2} \right\}} \tag{1}$$

where, C, f, N represent the wave speed in m/s, frequency in Hz and diameter ratio, respectively. The wave speed can be measured with Eq. (2).

$$C = \sqrt{\frac{E}{\rho}} \tag{2}$$

where, E, ρ represent the modulus of elasticity in GPa and density of the material in kg/mm³.

The dimensions and properties of the tool considered for this investigation are presented in Tables 1 and 2, respectively.

2.3 Modal Analysis

This analysis is used to define the mode shapes as well as natural frequencies of a system; it reflects the features of a free vibration system. In other words, it will generate the natural frequency of the structures for different mode shapes or modes of frequency. The equations which are related to modal analysis are taken from Eigen systems. These equations are comprising of Eigen values and Eigen vectors. It signifies the frequencies and consistent mode shapes accompanying the structural

measure. The modal displacement in the vibrated tool takes place in the direction of x , y , and z . The modal analysis equation is given in Eq. (3).

$$(K - \omega_i^2 M) \cdot \phi_i = 0 \quad (3)$$

where, K , ω_i , M , ϕ_i represent stiffness matrix, rounded natural frequency of mode i , mass matrix and shape vector of mode i , respectively, and i is the frequency range in which the Eigen values and the Eigen vectors are to be measured through numerical investigation.

2.4 Harmonic Analysis

The analysis of harmonic is used to evaluate the response of the load structure at a given frequency. It determines the dynamic behaviour of the structure by testing whether the structure is fatigue, resistant to resonance, and other adverse effects. The fundamental equation of the vibrant finite element analysis is given in Eq. (4).

$$M \ddot{X} + C \dot{X} + K X = F(t) \quad (4)$$

where, M represents discrete mass matrix, K represents overall stiffness matrix and C represents damping matrix of the model. X and $F(t)$ represent displacement vector matrix and external excitation force, respectively.

3 Results and Discussion

The results obtained from the numerical investigation of the tool under the influence of defects in the USM tool are presented in terms of modal and harmonic analysis. Stress analysis results are also furnished to understand the behaviour of the tool under the influence of defect and loading conditions experienced during USM process.

3.1 Modal Analysis

The tool in the USM should possess a longitudinal mode of vibration. Based on the length of the tool obtained by mathematical modelling, the tool profile is designed in Solidworks and analysis has been performed using ANSYS 18.1 workbench. The modes and frequencies obtained by ANSYS software for conical tool profile are given in Fig. 2.

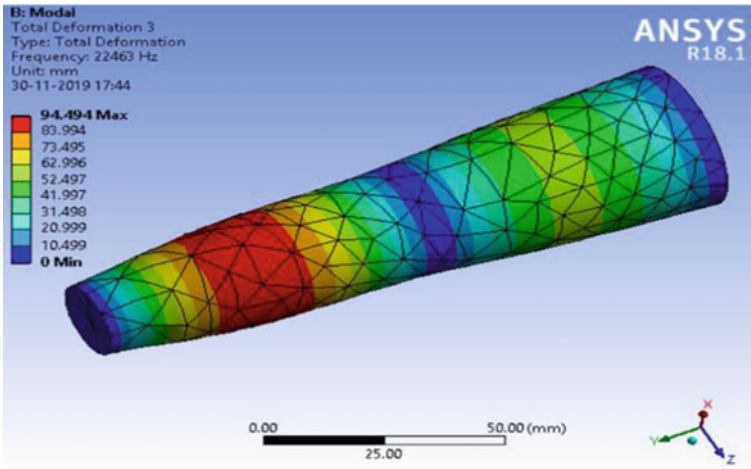


Fig. 2 Deformation profile of the conical tool

Table 3 Result of modal analysis of conical tool

Mode	1	2	3	4
Frequency (Hz)	19,536	19,540	22,463	27,194

This work exposes that several frequencies generated at several modes in the conical tool profile. The preferred mode at which axial mode of vibration is generated in the third mode. In the specific tool profile, the axial mode has a frequency of 22,463 Hz and the other two non-axial modes are having frequencies of 19,540 Hz and 27,194 Hz. The frequency gap between the axial and non-axial modes in the tool profile prevents the modal coupling and it confirms the safety of the tool in the deal (Table 3).

3.2 Harmonic Response Analysis

In ANSYS Workbench, the harmonic analysis is used to achieve a steady-state response of a modal subjected to a load that changes harmonically in time. Harmonic analysis of the conical tool profile is carried out to determine the stress proficiency and displacement by the tool during the examination for a given frequency. The suitable boundary conditions are used to define the harmonic response analysis of the tool. The harmonic response analysis of the conical tool profile is shown in Fig. 3.

The peak points are observed at the mode frequencies of the axial modes in the frequency response curves. The stresses are generated in the tool can be found by the harmonic response analysis. An enlarged assessment of the stress region with

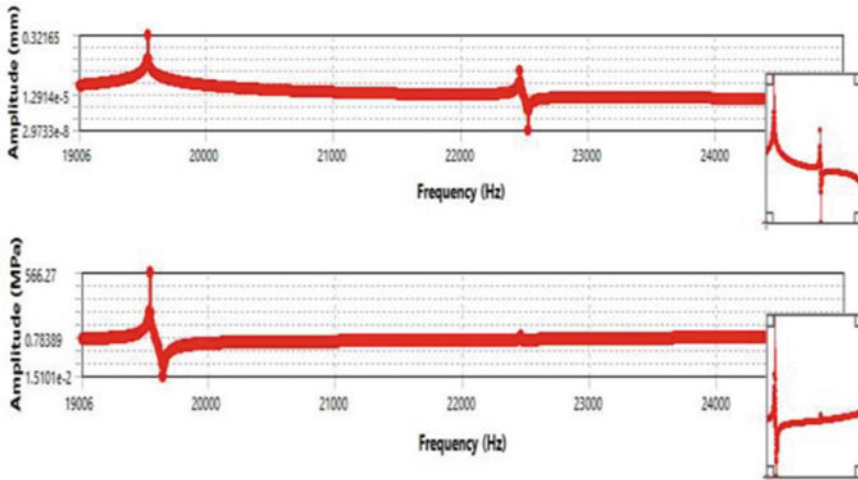


Fig. 3 Harmonic analysis of the conical tool

von Mises stress values is presented in Fig. 4 for the conical tool profile. The higher stresses are placed in a thin region where the deviation of tool thickness reveals a variation in trend.

After the stresses are generated, a defect is introduced at the highest stressed point in the tool profile. The defect is made in the form of a rectangular slot with 10 mm length, 2 mm width, and 2 mm depth as its dimensions. The defects are made in two different orientations, i.e. one is along with the longitudinal direction and another is perpendicular to the longitudinal axis. After generating the defects, the von Mises stresses for both the tool profiles are calculated which is shown in Fig. 5.

In the specific tool profile, it is seen that the highest stress is generated in the tool with the defect of the orientation which is perpendicular to the longitudinal axis and

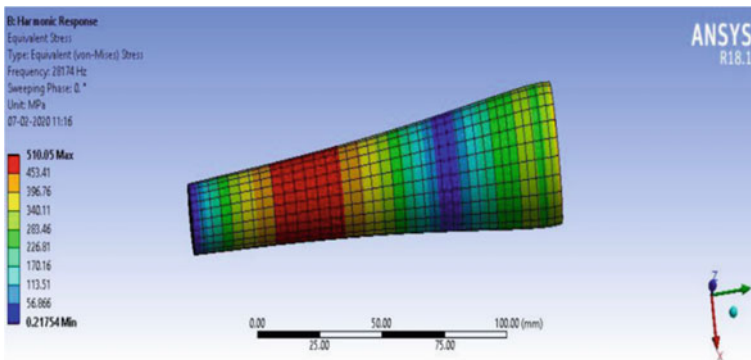


Fig. 4 Stress profile of the conical tool observed during the numerical modelling

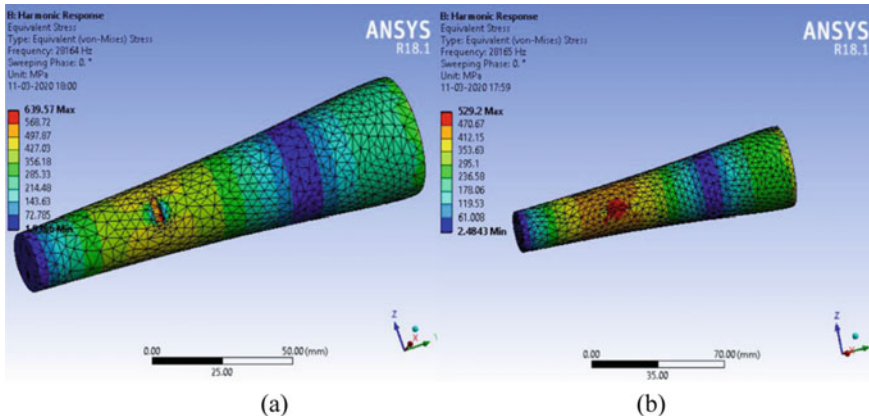


Fig. 5 Stress profiles of conical tool with defects **a** defect in an oblique direction **b** defect in a longitudinal direction

its value is 639.57 MPa. The generated stress value is more than the ultimate tensile strength of the material which is 344 MPa.

3.3 Harmonic Response Curves

By using modal analysis, it can spot the different frequencies of the mode shapes, so it gets a range of frequencies that contains the modes. In the frequency response, it is efficient to choose the frequency range for the performance of the analysis. So, if the modal frequencies are in the range and which are resonated with the load, the peaks can be seen at the mode frequencies in the frequency response graph which is shown in Fig. 6.

The peaks in the modal frequencies for the axial modes of vibration are higher than the peaks in the modal frequencies for the non-axial modes. The axial modes have a higher amplitude value as compared to the amplitude of the non-axial modes.

4 Conclusions

The tool in the ultrasonic machining is an important element for the proper functioning of the process. Hence, the study of the effects of a conical tool profile is carried out by numerical simulation using finite element analysis. The modal analysis of the tool is developed in the different axial and non-axial modes in the tool profile. The preferred mode at which axial mode of vibration is generated in the third mode. In the specific tool profile, the axial mode has a frequency of 22,463 Hz and the other

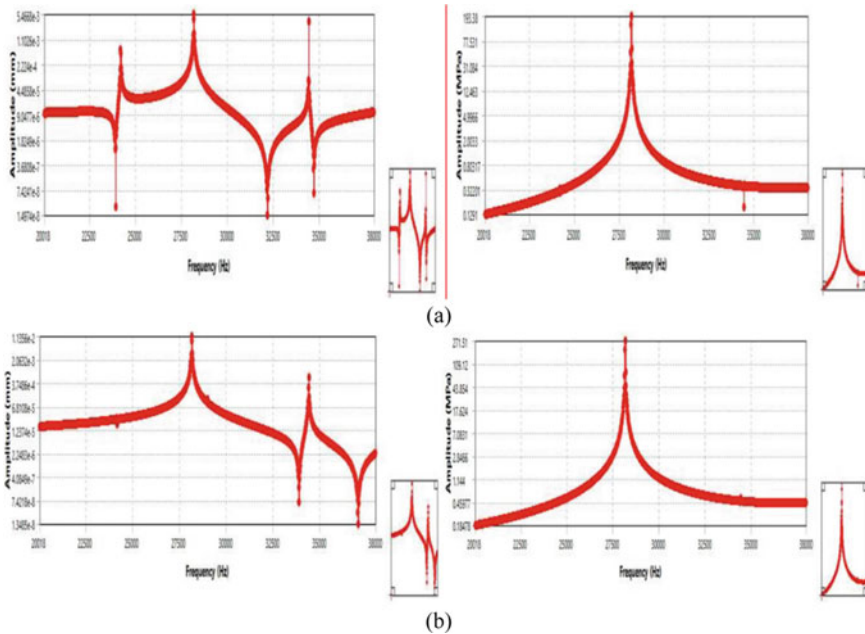


Fig. 6 Frequency response curves for the conical tool with defects **a** defect present in oblique direction **b** defect in a longitudinal direction to the oscillation axis

two non-axial modes having frequencies of 19,540 Hz and 27,194 Hz are developed. By the harmonic analysis, stress and deformation profiles are obtained for the tool profile. It is revealed that the maximum stress is generated in the narrow region of the tool. The generated maximum stress is 639.57 MPa in the defect location which is perpendicular to the longitudinal axis. The frequency response curve revealed that the peaks are generated at the modal frequencies of the tool profile.

References

1. Aher B, Ghodke V, Ahirrao J (2016) Ultrasonic machining. In: International conference on emerging trends in engineering and management research. Nashik, 23rd March 2016, pp 1311–1318
2. Singha DP, Mishrab S, Porwal RK (2019) Modal analysis of ultrasonic horn using finite element method. *Mater Today Proc* 18(7):3617–3623
3. Sarraf ZS (2018) Design and analysis of ultrasonic horns operating in multiple vibration modes. *Appl Eng* 2(2):28–32
4. Behera B, Sahoo S, Patra L, Rout M, Kanaujia K (2011) Finite element analysis of ultrasonic stepped horn. In: Proceedings of the 5th international conference on advances in mechanical engineering. Gujarat, India, 06–08 June 2011
5. Stanasel I, Buidos T, Blaga F (2014) Design and fem simulation of ultrasonic welding horn. *Nonconventional Technol Rev* 51–55

6. Wang D, Tao T, Xu G, Kang S, Luo A (2012) Vibration modal analysis for a finned-tube heat exchanger based on COMSOL. In: Recent advances in computer science and information engineering. China, pp 361–366
7. Addepalli SN (2016) Modal analysis of horns used in ultrasonic vibration assisted drilling. *Int J Innov Eng Technol* 294–298
8. Kumar S, Ding W, Sun Z, Wu CS (1972) Analysis of the dynamic performance of a complex ultrasonic horn for application in friction stir welding. *Int J Adv Manuf Technol* 1269–1284; Peck RB (1972) *Foundation engineering*, 2nd edn. McGraw-Hill, New York, pp 230–292

An Overview: Natural Fiber Composites as Eco-Friendly Materials, Their Properties, Chemical Treatments, Applications



Rafid Sobhan, Afsana Mustari, Prajjayini Chakma, and N. R. Dhar

Abstract Environmental pollution has become a major concern in the modern world. So the use of natural fiber composites is growing rapidly worldwide because of their eco-friendly characteristics. Their biodegradable nature, lightweight, low production cost also make them remarkable to use in the aerospace and automobile sectors. However, it is challenging to use natural fiber composites for their various limitations, for example poor moisture absorption capability, high hydrophilic nature, lower strength than synthetic fibers, and many more. But these limitations can be resolved by following different measures. In this research work, we have analyzed different sources, properties of natural fiber composites. The influence of various chemical treatment methods on natural fiber composites has also been reviewed. Finally, we have summarized various applications of these composites in different industries and evaluated their potential as environment-friendly materials.

Keywords Natural fiber composites · Chemical treatment · Alkaline · Silane · Applications · Eco-friendly materials

R. Sobhan (✉) · A. Mustari · P. Chakma
Aeronautical Engineering Department, Military Institute of Science and Technology, Dhaka,
Bangladesh
e-mail: rafidsobhan7@gmail.com

A. Mustari
e-mail: Afsanaitul@gmail.com

P. Chakma
e-mail: susandhk2016@gmail.com

N. R. Dhar
Industrial and Production Engineering Department, Bangladesh University of Engineering and
Technology, Dhaka, Bangladesh
e-mail: nrdhar@ipe.buet.ac.bd

1 Introduction

Traditional materials were widely used in the manufacturing industry in earlier days to produce different industrial accessories. But they started to lose their appeal after the introduction of polymers and composite materials. Eventually, composite materials started growing rapidly due to their different advantageous properties [1]. And, they successfully replaced different ferrous and non-ferrous metals in the industries. The development of composite materials first took place in the 1940s while using the fibers as reinforcement [2]. They comprise multiple phases that show enhanced properties in the composite materials than the individual phases when they are used alone. Composite materials basically contain two components. One is reinforcement and the other is matrix [3]. Reinforcement part takes the majority of the load whereas the less amount of load is distributed to the matrix part.

Various fibers are commonly used as composite material reinforcements. Among them, different manufacturing industries use natural fibers and synthetic fibers mostly. Previously, various synthetic fibers like carbon, glass, metals, ceramics were the ultimate choice in the manufacturing industry [4]. Day by day, natural fibers have turned into the perfect alternatives to the synthetic fibers because of the environmental concerns going all around the world. They have low density and abrasiveness and are light in weight [5]. Also, they are partially recyclable and renewable [6]. The biodegradable nature of natural fibers helps to build a strong ecosystem. Additionally, their low cost, CO₂ neutrality, high flexibility, CO₂ neutrality, low relative density and ease of manufacturing process make them reliable to all [7–11]. The fiber content available in natural fiber composites minimizes the harmful base polymer contents in composite materials.

However, they have got some limitations which refrain them from being perfect materials to be utilized in different industries. They possess lower mechanical properties than synthetic fibers [12]. They have poor moisture resistance. Also, their hydrophilic nature causes a major concern while making composites [13].

But it is inevitable that natural fibers can bring the ecological balance what the modern researchers are exactly looking for. For this reason, so many researchers conducted research works worldwide to minimize the negative impact of using natural fibers. But most of the research works pointed out the chemical treatment methods to improve various properties of natural fiber composites. This review paper summarizes different aspects of these composites, elaborating their sources, types, reinforcement, properties, reported works on various chemical treatment methods, their application in different industries, and their potential as eco-friendly materials. Also, this paper will provide an overall analysis of how global warming and CO₂ emission can be mitigated by enhancing the use of natural fiber composites in different industries, eventually establishing them as the ideal materials for twenty-first century.

2 Natural Fibers

Natural fibers have different sources of origin such as plants, minerals, and animals which make them versatile in characteristics and usage. On the other hand, synthetic fibers are produced artificially by a process called synthesis (different chemical reactions). There are so many plant fibers from which natural fibers can be obtained, for example Leaf fibers (sisal, pineapple, banana), bast fibers (hemp, jute, ramie, flax), seed fibers (kapok, cotton, coir), Reed fibers (rice, wheat) and others [14]. Animal fibers are classified into three different types: avian fiber (bird feathers), animal fiber (goat, sheep wool), and silk fiber (dried saliva of bugs) [15, 16].

Generally, natural fiber strength is dependent on the spiral angle and the cellulose content. Regarding the geometry, they are not uniform similar to glass or carbon fibers. Rather, they are bundles of elementary fibers, consisted of defects and voids. In natural fibers, available bonding sites and surface energy vary to create these elementary fiber bundles [17]. Mechanical properties in these fibers rely on both the fiber composition quality and the plant age. Hence, it becomes challenging to obtain the same mechanical properties after repeated testing [18].

Each natural fiber possesses some specific physical properties, as shown in Table 1. Bast fibers mainly exhibit better flexural strength and elastic modulus than other types of natural fibers whereas leaf fibers show improved impact properties than other fibers [19]. The properties of natural fibers vary on different parameters. Some of them are form and type of fibers, cultivation condition, moisture content, extracting process and many more [20–22].

When the fibers are used as a reinforcement, they increase the functional range of polymer properties. Factors that need to be considered are the chemical nature of the fibers and the matrix, fiber length and aspect ratio, fiber distribution orientation and, the surface texture of the fibers, fiber volume fraction, interfacial adhesion, type of molding, molding conditions, and void content.

The reinforcement of natural fiber can be done in three different ways: using continuous, discontinuous, and hybrid fiber. The orientation of fiber is maintained

Table 1 Natural fiber physical properties [1, 3, 23–28]

Fiber type	Density (g/cm ³)	Diameter (μm)	Length (mm)	Tensile strength (MPa)	Young's modulus (MPa)	Elongation (%)	Moisture content (%)
Hemp	1.48	25–500	5–55	550–900	70	1.6–4.5	8
Flax	1.50	12–600	5–900	345–1100	27.6	1.2–3	7
Jute	1.48	20–200	1.5–120	410–780	26.5	1.5–3.1	12
Sisal	1.3–1.5	8–200	900	507–855	9.4–28	1.9–3	11
Banana	1.35	12–30	300–900	529–914	27–32	5–6	10–11
Coir	1.25	10–460	20–150	170–230	146	15–25	10
Ramie	1.5	20–80	900–1200	400	44	2–4	12–17
Cotton	1.51	10–45	10–60	400	12	2–10	33–34

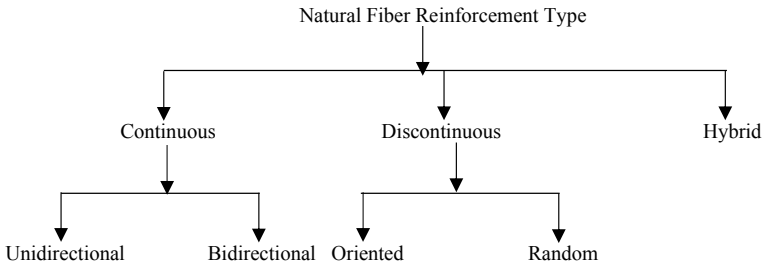


Fig. 1 Types of natural fiber reinforcement

only in one direction in continuous natural fiber composites. In discontinuous fiber composites, fibers are normally short in size that prevents individual fibers from entangling to maintain the fibrous nature. Since discontinuous fibers can be procured easily, they show better mechanical properties than continuous fibers [29]. A schematic representation of different reinforcement type of natural fiber composites is shown in Fig. 1.

3 Chemical Treatment

While making composites, fiber selection is a crucial step. Researchers have to keep in mind the mechanical, physical, chemical properties of the fibers to fulfill their criteria. The biodegradable nature of natural fibers has a significant role in introducing them as the reinforcement in composite materials. Synthetic fibers are neither recyclable nor biodegradable. Hence, instead of synthetic fibers, researchers are showing interest in natural fibers to achieve the desired characteristics of the composites. In that case, chemical properties of natural fibers have a crucial part to make the composites environmentally efficient. Table 2 shows Cellulose, Lignin, and Hemicellulose as the main constituents of different natural fibers:

Table 2 Chemical composition of natural fibers [30]

Fiber type	Cellulose	Lignin	Hemicellulose
Hemp	57–77	3.7–13	14–22.4
Flax	71	2.2	18.6–21.6
Jute	59–71.5	11.8–13	13.6–20.4
Sisal	78	12.1	25.7
Banana	62–64	5	19
Coir	37	42	20
Ramie	68.6–91	0.6–0.7	5–16.7
Cotton	82.7–90	<2	5.7

However, some of the major disadvantages of the natural fiber composites are low thermal stability, poor moisture, and water absorption, poor fiber-matrix interfacial bonding [31–33]. Also, the reduction of mechanical strength of natural fiber composites takes place because of the natural fibers being hydrophilic [34]. That's why researchers have implemented various chemical treatment methods to optimize the natural fiber composites. Among them, we will review some of the commonly used effective chemical treatment techniques to improve their properties:

3.1 Alkaline Treatment

Alkalization is a widely used chemical treatment process used in natural fibers to improve their surface. The process uses Sodium Hydroxide (NaOH) as a chemical reagent to alter the natural fiber structure [35]. Mishra et al. [36] and Ray et al. [37] used 5% aqueous NaOH solution to treat sisal and jute fibers at room temperature. Morrison et al. [38] followed a similar treatment to flax fiber. The studies reported that alkaline treatment causes the increase of amorphous cellulose content in crystalline cellulose.

Mwaikambo and Ansell [39] analyzed the effect of NaOH on kapok, hemp, sisal, and jute at 20 °C for 48 h. Thermal characteristics, reactivity, crystallinity morphology of both treated and untreated natural fibers were investigated. The analysis concluded that natural fibers that were chemically treated exhibit improved adhesion of fiber-resin, leading to interfacial energy increase and therefore show better mechanical and thermal properties.

Rashid et al. [40] experimented the chemical treatment of Sugar Palm Fiber with seawater, alkali and observed various properties of the fiber. Application of the alkalization process enhanced their adhesion properties but minimized their thermal stability whereas after treating the fibers with seawater, only physical change took place in the composites.

Siddika et al. [41] reported tensile, impact, flexural, and hardness properties of jute-coir hybrid PP composites by varying the coir, jute contents, and NaOH treatment concentration. The study revealed improved mechanical properties of the composites with 5% NaOH treatment as compared to 10% NaOH treatment.

Sawpan et al. [42] and Boopathi et al. [43] added 5% NaOH solution in hemp fiber and Borassus fiber composites respectively. The experiments concluded with the enhancement in the tensile properties of both of them. Similarly, kenaf fiber and hybrid jute-sisal epoxy composites exhibit enhanced mechanical properties after treating both of them with 5% NaOH solution [44, 45].

3.2 Silane Treatment

Silane is one type of coupling agent that allows the fibers adhering to a polymer matrix to stabilize the composites. In the fiber-matrix interface of the composites, cellulose hydroxyl groups get reduced with the addition of silane.

Atiqah et al. [46] treated the sugar palm fibers with 6% NaOH and 2% silane for 3 h. The researchers observed an improvement in the tensile strength of silane treated SPF composites than alkali treated, alkali-silane treated, and untreated composites.

Fathi et al. [47] examined the flax-bio epoxy interface by treating with TEMPO oxidation and amino silane. The experiment concluded that oxidized silanized composite shows improved adhesive properties between fiber/matrix than TEMPO mediated oxidation process.

Feng et al. [48] studied the treatment of 3% silane and 5% alkaline solution on Kenaf and PALF fibers. The findings evidenced that the mechanical properties of both composites experience notable improvement after the chemical treatment. Also, after comparing with NaOH treated composites, silane treated composites show superior mechanical properties.

3.3 Acetylation Treatment

Acetylation is an esterification process to plasticize the cellulosic fibers. The process introduces an acetyl group on the fiber surface and minimizes the hydrophilicity of the fibers to stabilize the composites.

Zaman and Khan [49] fabricated matted banana composites to observe various mechanical properties of them. The results showed that after acetylation treatment, fiber composites achieve better mechanical properties than the non-treated and alkali-treated composites.

Bledzki et al. [50] evaluated acetylation treatment impact on flax-polypropylene composites and analyzed different mechanical properties of them. For adding acetylation up to 18% degree, tensile and flexural properties of flax-PP increase, and then, the properties start to decrease.

3.4 Peroxide Treatment

Peroxide is one type of functional group that decomposes to create free radicals. Then, reaction takes place between the free radicals and hydrogen group inherent in the cellulose fibers and matrix. In general, fibers are treated with peroxide after the alkaline treatment.

Then et al. [51] observed the influence of alkaline-peroxide in oil palm mesocarp composites. The observation indicated a major development in the tensile strength of

the biocomposites. The results also noticed better fiber-matrix interfacial adhesion in the composites.

Razak et al. [52] treated kenaf fiber composites with bleaching method and used hydrogen peroxide via alkaline medium. From the experiment, surface roughness was found getting increased for employing the bleaching treatment and a notable improvement was observed in the mechanical properties of kenaf fiber composites.

3.5 Benzoylation Treatment

It is a chemical compound used to minimize any fiber's hydrophilic nature. Benzoylation treatment improves the fiber-matrix bonding and thereby increases the composite strength.

Zhang et al. [53] optimized sisal fiber plasticized composites by benzoylation process to convert them into thermally formidable materials. The treatment of NaOH and benzoyl chloride resulted in elevated mechanical properties with biodegradable nature.

Sreekumar et al. [54] carried out chemical treatment on sisal fiber reinforced composites with various physical treatments for example permanganate, mercerization, benzoylation, 100° heating, and vinyl tris (2-ethoxymethoxy). Storage modulus, damping factor, loss modulus, etc. dynamic properties were observed after treating the composites. All treatments showed higher damping nature in the composites except alkali treatment whereas storage modulus was found maximum in benzoylated treated fibers.

3.6 Potassium Permanganate Treatment

It is basically a chemical reagent to improve fiber/matrix interfacial interaction in the composites. This treatment decreases the hydrophilic tendency in fibers, leading to a reduction of their water absorption properties.

Arsyad [55] treated coconut fiber composites to observe the effect of NaOH and potassium permanganate solution of various concentrations on them. The test concluded that tensile stress increases with NaOH treatment but decreases after treating with Potassium Permanganate in the coconut fibers.

Mohammed et al. [56] determined the tensile behavior of sugar palm fiber composites with the surface treatment of alkaline and KMnO_4 . 6% of NaOH solution and 0.033, 0.0666, and 0.125% of KMnO_4 concentration were used as chemical treatments on the composites. The results showed an enhancement in all types of tensile properties of the composites except tensile strain. Only tensile strain experienced a downgrade after increasing the concentration of potassium permanganate in the composites.

3.7 Stearic Acid Treatment

Stearic acid is one type of fatty acid which is used mostly in biocomposite applications. The reaction between the hydroxyl group in the natural fibers and carboxyl group in the stearic acid minimizes the moisture content of the fibers.

Salem et al. [57] applied stearic acid of various concentrations on kenaf fiber composites and observed their water absorption nature. The study revealed that the treatment of stearic acid decreases the water absorbing tendency of the composites.

Dogan et al. [58] investigated jute fiber composites with stearic acid based on Azide method. The experiment showed that tensile strength of the jute fiber composites improves after using stearic acid. In addition, noticeable enhancement was observed in the elastic modulus of the composites.

4 Applications

Natural fibers are strong, lightweight, cost-effective, and most importantly, eco-friendly. That's why they have been replacing glass and other synthetic fibers in a wide range of engineering applications, for example automobiles, construction, packaging, and many more, as shown in Table 3. That being the case, "European Guideline 2000/53/EG" was introduced in order to improve automotive recyclability from 85% in 2005 to 95% by 2015 for a vehicle by weight.

Natural fibers have potentially shown their worth in replacing common synthetic fibrous materials especially for using in acoustic absorption. In commercial acoustic absorption, natural fibers are mixed with various additives. Fibers such as hemp, kenaf, coir, corn, sugar cane, and jute composites are manufactured with resin-coated

Table 3 Applications of natural fiber composites in different industries [1, 55–59]

Fiber type	Applications
Hemp	Racing bi-cycle, snowboarding, textiles, furniture, cordage
Flax	Seatbacks, spare-tire covers, window frame, fencing, decking, panels, racing bicycle, fork, seat post, tennis racket
Jute	Door frames, packaging, roofing sheets, frontal bonnet of off-road vehicle (Buggy), drain pipes, and water pipes
Sisal	Doors, panels, roofing sheets, shutting plate, paper, and pulp manufacturing
Kenaf	Phone casing, door panel, insulations, animal bedding, packing material
Coir	Helmet, projector panel, stabilizer casing, mirror casing, storage tank, brushes and brooms, seat cushions, mattress
Ramie	Clothing, industrial sewing thread, fishing nets, ropes, packing materials
Cotton	Furniture, textile, and yarn

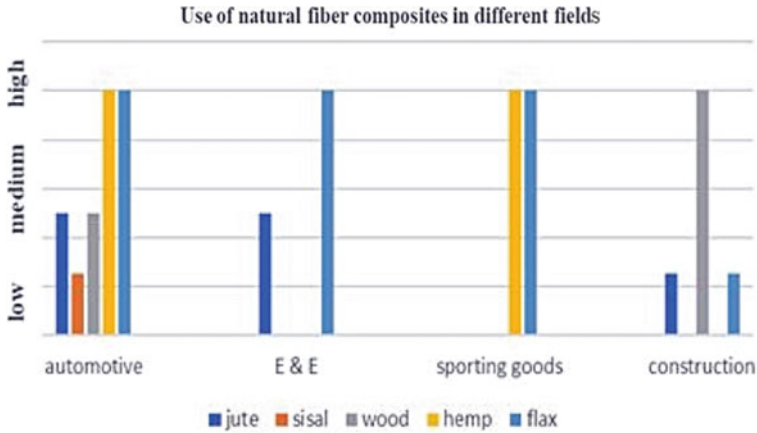


Fig. 2 Use of different natural fiber composites in different fields [60]

fiber, rubber granular, and veneer materials. These natural fiber composites show good quality sound absorption properties by themselves.

Figure 2 shows the graphical representation of using different natural fiber composites in various industries:

5 Environmental Awareness

Natural fiber composites have environmental superiority as compared to synthetic fibers. During primary fiber production, natural fibers absorb CO₂ and emit Oxygen. Thus, natural fibers have lower CO₂ footprint that results in the enhanced life cycle of the composites. Also, the composites that are made of natural fibers are recyclable after the consumption. Even if when natural fibers are no more recyclable, disposing them is convenient as green plants can consume them and thus the ecosystem remains stable.

On the other hand, synthetic fibers emit a massive amount of CO₂ during material production and manufacturing process. So the CO₂ footprint of these fibers is very high that causes the degradation of environment. Thus, the green globalization is greatly hampered by the synthetic fibers [61].

6 Conclusions

In terms of being biodegradable, eco-friendly, renewable, affordable, natural fiber composites have various advantageous properties, making them attractive alternatives to replace synthetic fibers in different industries. However, the poor wettability

and moisture resistance of natural fibers restrain them from being used in composites in many cases. That's why our review paper has highlighted the effect of chemical treatments in natural fiber composites to develop their properties. From the analysis, we can draw some major conclusions that are given below:

- All types of chemical treatment processes perform remarkably well to improve different properties of natural fiber composites.
- Silane treatment is found the most suitable chemical treatment process that is followed by Alkaline treatment.
- The eco-friendly nature of natural fibers is growing interest in the researchers to enhance their use for the betterment of environment.
- The tendency to reinforce natural fibers in composites is increasing every day and it is expected that with their improved properties, industries will be keen to use them more in the near future.

However, based on this review, there are some research scopes which need to be pointed out in future. Most of the researchers mainly used different chemical modification methods to enhance various properties of natural fiber composites. So further research works are recommended to improve their properties with the inclusion of filler materials, additives, or coupling agents. Also, thermal properties have been less explored than the mechanical properties of the composites. So extended investigations are required to enhance the thermal properties of these composites.

References

1. Santhosh Kumar S, Hiremath SS (2020) Natural fiber reinforced composites in the context of biodegradability: a review 322(1567)
2. Yao J, Zhou Z, Zhou H (2019) Highway engineering composite material and its application
3. Madhukiran J, Rao SS, Madhusudan S (2013) Fabrication and testing of natural fiber reinforced hybrid composites banana/pineapple 3:2239–2243
4. Jariwala H, Jain P (2019) A review on mechanical behavior of natural fiber reinforced polymer composites and its applications. *J Reinf Plast Compos* 38(10):441–453. <https://doi.org/10.1177/0731684419828524>
5. Jayabal S, Natarajan U, Murugan M (2011) Mechanical property evaluation of woven coir and woven coir-glass fiber-reinforced polyester composites. *J Compos Mater* 45(22):2279–2285. <https://doi.org/10.1177/0021998311401080>
6. Kalia S et al (2011) Cellulose-based bio- and nanocomposites: a review. *Int J Polym Sci* 2011. <https://doi.org/10.1155/2011/837875>
7. Biagiotti J, Puglia D, Kenny JM (2004) A review on natural fibre-based composites-part I. *J Nat Fibers* 1(2):37–68. [Online]. Available: https://doi.org/10.1300/J395v01n02_04
8. Joshi SV, Drzal LT, Mohanty AK, Arora S (2004) Are natural fiber composites environmentally superior to glass fiber reinforced composites? *Compos Part A Appl Sci Manuf* 35(3):371–376. <https://doi.org/10.1016/j.compositesa.2003.09.016>
9. Ratna Prasad AV, Mohana Rao K (2011) Mechanical properties of natural fibre reinforced polyester composites: jowar, sisal and bamboo. *Mater Des* 32(8–9):4658–4663. <https://doi.org/10.1016/j.matdes.2011.03.015>

10. Sarikaya E, Çalioğlu H, Demirel H (2019) Production of epoxy composites reinforced by different natural fibers and their mechanical properties. *Compos Part B Eng* 167(15):461–466. <https://doi.org/10.1016/j.compositesb.2019.03.020>
11. El-Shekeil YA, Sapuan SM, Abdan K, Zainudin ES (2012) Influence of fiber content on the mechanical and thermal properties of kenaf fiber reinforced thermoplastic polyurethane composites. *Mater Des* 40:299–303. <https://doi.org/10.1016/j.matdes.2012.04.003>
12. Sanjay MR, Arpitha GR, Yogesha B (2015) Study on mechanical properties of natural—glass fibre reinforced polymer hybrid composites: a review. *Mater Today Proc* 2(4–5):2959–2967. <https://doi.org/10.1016/j.matpr.2015.07.264>
13. Selke SE, Wichman I (2004) Wood fiber/polyolefin composites. *Compos Part A Appl Sci Manuf* 35(3):321–326. <https://doi.org/10.1016/j.compositesa.2003.09.010>
14. Rowell RM (2008) Natural fibres: types and properties. *Prop Perform Nat Compos* 3–66. <https://doi.org/10.1533/9781845694593.1.3>
15. Abdul Khalil HPS, Bhat IUH, Jawaid M, Zaidon A, Hermawan D, Hadi YS (2012) Bamboo fibre reinforced biocomposites: a review. *Mater Des* 42:353–368. <https://doi.org/10.1016/j.matdes.2012.06.015>
16. Ayrimis N, Ashori A (2015) Alternative solutions for reinforcement of thermoplastic composites. *Nat Fiber Compos* 65–92. <https://doi.org/10.1201/b19062-4>
17. Fuqua MA, Huo S, Ulven CA (2012) Natural fiber reinforced composites. *Polym Rev* 52(3–4):299–320. <https://doi.org/10.1080/15583724.2012.705409>
18. Bergeret A, Tran T, Papanicolaou GC (2014) Green composites from natural resources. Chapter: Valorization of agricultural by-products in poly (lactic acid) (PLA) to develop <https://doi.org/10.13140/2.1.1271.2969>
19. Athijayamani A, Thiruchitrambalam M, Natarajan U, Pazhanivel B (2009) Effect of moisture absorption on the mechanical properties of randomly oriented natural fibers/polyester hybrid composite. *Mater Sci Eng A* 517(1):344–353. <https://doi.org/10.1016/j.msea.2009.04.027>
20. O'Donnell A, Dweib MA, Wool RP (2004) Natural fiber composites with plant oil-based resin. *Compos Sci Technol* 64(9):1135–1145. <https://doi.org/10.1016/j.compscitech.2003.09.024>
21. Ochi S (2008) Mechanical properties of kenaf fibers and kenaf/PLA composites. *Mech Mater* 40(4–5):446–452. <https://doi.org/10.1016/j.mechmat.2007.10.006>
22. Pickering KL, Beckermann GW, Alam SN, Foreman NJ (2007) Optimising industrial hemp fibre for composites. *Compos Part A Appl Sci Manuf* 38(2):461–468. <https://doi.org/10.1016/j.compositesa.2006.02.020>
23. Wambua P, Ivens J, Verpoest I (2003) Natural fibres: can they replace glass in fibre reinforced plastics? *Compos Sci Technol* 63(9):1259–1264. [https://doi.org/10.1016/S0266-3538\(03\)00096-4](https://doi.org/10.1016/S0266-3538(03)00096-4)
24. Mohanty AK, Misra M, Hinrichsen G (2000) Biofibres, biodegradable polymers and biocomposites: an overview. *Macromol Mater Eng* 276–277:1–24. [https://doi.org/10.1002/\(SICI\)1439-2054\(20000301\)276:1%3c1::AID-MAME1%3e3.0.CO;2-W](https://doi.org/10.1002/(SICI)1439-2054(20000301)276:1%3c1::AID-MAME1%3e3.0.CO;2-W)
25. Ramesh M, Palanikumar K, Reddy KH (2013) Mechanical property evaluation of sisal-jute-glass fiber reinforced polyester composites. *Compos Part B Eng* 48:1–9. <https://doi.org/10.1016/j.compositesb.2012.12.004>
26. Pickering KL, Efendy MGA, Le TM (2016) A review of recent developments in natural fibre composites and their mechanical performance. *Compos Part A Appl Sci Manuf* 83:98–112. <https://doi.org/10.1016/j.compositesa.2015.08.038>
27. Karthi N, Kumaresan K, Sathish S, Gokulkumar S, Prabhu L, Vigneshkumar N (2019) An overview: natural fiber reinforced hybrid composites, chemical treatments and application areas. *Mater Today Proc* 27:2828–2834. <https://doi.org/10.1016/j.matpr.2020.01.011>
28. Peças P, Carvalho H, Salman H, Leite M (2018) Natural fibre composites and their applications: a review. *J Compos Sci* 2(4):66. <https://doi.org/10.3390/jcs2040066>
29. Kandemir A, Pozegic TR, Hamerton I, Eichhorn SJ, Longana ML (2020) Characterisation of natural fibres for sustainable discontinuous fibre composite materials. *Materials (Basel)* 13(9). <https://doi.org/10.3390/ma13092129>

30. Reddy RA, Yoganandam K, Mohanavel V (2020) Effect of chemical treatment on natural fiber for use in fiber reinforced composites—review. *Mater Today Proc* 33. <https://doi.org/10.1016/j.matpr.2020.02.982>
31. Ho MP et al (2012) Critical factors on manufacturing processes of natural fibre composites. *Compos Part B Eng* 43(8):3549–3562. <https://doi.org/10.1016/j.compositesb.2011.10.001>
32. Bajpai PK, Singh I, Madaan J (2013) Tribological behavior of natural fiber reinforced PLA composites. *Wear* 297(1–2):829–840. <https://doi.org/10.1016/j.wear.2012.10.019>
33. Ridzuan MB, Daud Z, Ahmad Z, Md Nordin NA, Zakariah Z (2018) Development of natural fiber as a filter media in removing organic pollutants from greywater. *Defect Diffus Forum* 382:302–306. <https://doi.org/10.4028/www.scientific.net/DDF.382.302>
34. Wang B, Panigrahi S, Tabil L, Crerar W (2007) Pre-treatment of flax fibers for use in rotationally molded biocomposites. *J Reinf Plast Compos* 26(5):447–463. <https://doi.org/10.1177/0731684406072526>
35. Sgriccia N, Hawley MC, Misra M (2008) Characterization of natural fiber surfaces and natural fiber composites. *Compos Part A Appl Sci Manuf* 39(10):1632–1637. <https://doi.org/10.1016/j.compositesa.2008.07.007>
36. Mishra S, Misra M, Tripathy SS, Nayak SK, Mohanty AK (2001) Graft copolymerization of acrylonitrile on chemically modified sisal fibers. *Macromol Mater Eng* 286(2):107–113. [https://doi.org/10.1002/1439-2054\(20010201\)286:2%3c107::AID-MAME107%3e3.0.CO;2-0](https://doi.org/10.1002/1439-2054(20010201)286:2%3c107::AID-MAME107%3e3.0.CO;2-0)
37. Ray D, Sarkar BK, Rana AK, Bose NR (2001) Effect of alkali treated jute fibres on composite properties. *Bull Mater Sci* 24(2):129–135. <https://doi.org/10.1007/BF02710089>
38. Morrison WH, Akin DE (2001) Chemical composition of components comprising bast tissue in flax. *J Agric Food Chem* 49(5):2333–2338. <https://doi.org/10.1021/jf001474k>
39. Mwaikambo LY, Ansell MP (2002) Chemical modification of hemp, sisal, jute, and kapok fibers by alkalization. *J Appl Polym Sci* 84(12):2222–2234. <https://doi.org/10.1002/app.10460>
40. Rashid B, Leman Z, Jawaid M, Ghazali MJ, Ishak MR (2016) Physicochemical and thermal properties of lignocellulosic fiber from sugar palm fibers: effect of treatment. *Cellulose* 23(5):2905–2916. <https://doi.org/10.1007/s10570-016-1005-z>
41. Siddika S, Mansura F, Hasan M, Hassan A (2014) Effect of reinforcement and chemical treatment of fiber on the properties of jute-coir fiber reinforced hybrid polypropylene composites. *Fibers Polym* 15(5):1023–1028. <https://doi.org/10.1007/s12221-014-1023-0>
42. Sawpan MA, Pickering KL, Fernyhough A (2011) Effect of various chemical treatments on the fibre structure and tensile properties of industrial hemp fibres. *Compos Part A Appl Sci Manuf* 42(8):888–895. <https://doi.org/10.1016/j.compositesa.2011.03.008>
43. Boopathi L, Sampath PS, Mylsamy K (2012) Investigation of physical, chemical and mechanical properties of raw and alkali treated Borassus fruit fiber. *Compos Part B Eng* 43(8):3044–3052. <https://doi.org/10.1016/j.compositesb.2012.05.002>
44. Mahjoub R, Yatim JM, Mohd Sam AR, Hashemi SH (2014) Tensile properties of kenaf fiber due to various conditions of chemical fiber surface modifications. *Constr Build Mater* 55:103–113. <https://doi.org/10.1016/j.conbuildmat.2014.01.036>
45. Gupta MK, Srivastava RK (2016) Mechanical, thermal and water absorption properties of hybrid sisal/jute fiber reinforced polymer composite. *Indian J Eng Mater Sci* 23(4):231–238
46. Atiqah A, Jawaid M, Ishak MR, Sapuan SM (2018) Effect of alkali and silane treatments on mechanical and interfacial bonding strength of sugar palm fibers with thermoplastic polyurethane. *J Nat Fibers* 15(2):251–261. <https://doi.org/10.1080/15440478.2017.1325427>
47. Fathi B, Foruzanmehr M, Elkoun S, Robert M (2019) Novel approach for silane treatment of flax fiber to improve the interfacial adhesion in flax/bio epoxy composites. *J Compos Mater* 53(16):2229–2238. <https://doi.org/10.1177/0021998318824643>
48. Feng NL, Malingam SD, Razali N, Subramonian S (2020) Alkali and silane treatments towards exemplary mechanical properties of kenaf and pineapple leaf fibre-reinforced composites. *J Bionic Eng* 17(2):380–392. <https://doi.org/10.1007/s42235-020-0031-6>
49. Zaman HU, Khan RA (2019) Acetylation used for natural fiber/polymer composites. *J Thermoplast Compos Mater*. <https://doi.org/10.1177/0892705719838000>

50. Bledzki AK, Mamun AA, Lucka-Gabor M, Gutowski VS (2008) The effects of acetylation on properties of flax fibre and its polypropylene composites. *Express Polym Lett* 2(6):413–422. <https://doi.org/10.3144/expresspolymlett.2008.50>
51. Then YY, Ibrahim NA, Zainuddin N, Chieng BW, Ariffin H, Wan Yunus WMZ (2015) Influence of alkaline-peroxide treatment of fiber on the mechanical properties of oil palm mesocarp fiber/poly(butylene succinate) biocomposite. *BioResources* 10(1):1730–1746. <https://doi.org/10.15376/biores.10.1.1730-1746>
52. Razak NIA, Ibrahim NA, Zainuddin N, Rayung M, Saad WZ (2014) The influence of chemical surface modification of kenaf fiber using hydrogen peroxide on the mechanical properties of biodegradable kenaf fiber/poly (lactic acid) composites. *Molecules* 19(3):2957–2968. <https://doi.org/10.3390/molecules19032957>
53. Zhang MQ, Rong MZ, Lu X (2005) Fully biodegradable natural fiber composites from renewable resources: all-plant fiber composites. *Compos Sci Technol* 65(15–16):2514–2525. <https://doi.org/10.1016/j.compscitech.2005.06.018>
54. Sreekumar PA et al (2009) Dynamic mechanical properties of sisal fiber reinforced polyester composites fabricated by resin transfer molding. *Polym Compos* 30(6):768–775. <https://doi.org/10.1002/pc.20611>
55. Arsyad M (2019) Sodium hydroxide and potassium permanganate treatment on mechanical properties of coconut fibers. *IOP Conf Ser Mater Sci Eng* 619(1). <https://doi.org/10.1088/1757-899X/619/1/012011>
56. Mohammed AA, Bachtiar D, Rejab MRM, Hasany SF (2017) Effect of potassium permanganate on tensile properties of sugar palm fibre reinforced thermoplastic polyurethane. *Indian J Sci Technol* 10(7):1–5. <https://doi.org/10.17485/ijst/2017/v10i7/111453>
57. Salem IAS, Rozyanty AR, Betar BO, Adam T, Mohammed M, Mohammed AM (2017) Study of the effect of surface treatment of kenaf fiber on chemical structure and water absorption of kenaf filled unsaturated polyester composite. *J Phys Conf Ser* 908(1). <https://doi.org/10.1088/1742-6596/908/1/012001>
58. Dogan SD, Tayfun U, Dogan M (2016) New route for modifying cellulosic fibres with fatty acids and its application to polyethylene/jute fibre composites. *J Compos Mater* 50(18):2477–2485. <https://doi.org/10.1177/0021998315604706>
59. Shalwan A, Yousif BF (2013) In state of art: mechanical and tribological behaviour of polymeric composites based on natural fibres. *Mater Des* 48:14–24. <https://doi.org/10.1016/j.matdes.2012.07.014>
60. Brief L (2011) Opportunities in natural fiber composites, pp 1–35
61. Shahinur S, Hasan M (2020) Natural fiber and synthetic fiber composites: comparison of properties, performance, cost and environmental benefit. Elsevier Ltd.

Additive Manufacturing of Fiber Reinforced Composite: Material, Methods Challenges and Future Works



Kamal Kumar Ojha, Srinath Chowdarpally, and Vishal Francis

Abstract Flexibility to design and ease to manufacture complex and customized features has asphalted Additive manufacturing (AM) path in various applications starting from defense, automotive to biomedical. However, the properties of AM parts lack integrity due to its layer manufacturing nature. The presence of fibers can enhance the properties of AM parts. The present paper discusses the fabrication of Fiber Reinforced Composite (FRCP) via AM techniques. Various AM methods used for manufacturing of F.R.C.P as well as issues faced are discussed along with detailed discussion on understanding anisotropic behavior in AM. This article overviews the challenges as well as future works in AM for fiber reinforced composites.

Keywords Additive manufacturing · Anisotropic · Fiber reinforced polymer composites

1 Introduction

History of composite started with mud houses made of bamboo and mud, laminated wood, Forged Sword. In the year 1930 years the concept of glass fiber reinforced fiber was introduced. Composites are resultant of mixing of two constituents at macroscopic level, which are not soluble to each other. Fiber Reinforced Polymer Composite is formed by taking fiber as reinforcement and polymer as matrix is called F.R.C.P. Stereo lithography was commercialized in 1987. Stereo lithography solidifies polymer (Light Sensitive) by using Laser. The year 1991 was a hallmark were three different AM technologies were begin materialized F.D.M (fused deposition

K. K. Ojha (✉) · V. Francis
Mechanical, L.P.U, Phagwara, India
e-mail: kamalojha.lpu.co@gmail.com

V. Francis
e-mail: vishal.24813@lpu.co.in

S. Chowdarpally
Mechanical, M.C.E.T Hyderabad, Hyderabad, India

modeling) produces part layer by layer, extruding thermoplastic materials S.G.C (Solid ground curing) solidifies the complete layer by passing UV light on a UV-sensitive liquid polymer L.O.M (Laminated object Manufacturing) uses guided lasers to cut material. Henceforth further AM technologies came into picture [1, 2] Fiber Reinforced Composites (F.R.C.P) have attracted both researchers as well as industrialist owing excellent strength to weight to ratio. Conventional manufacturing process like spray-up, hand lay-up, vacuum-bag molding, encounters a major problem that is need of mold which thwart the process by making it tedious and costly. Above all mentioned problems are eradicated using computer generated S.T.L file to fabricate layer by layer using AM Technique. Tailored property can be achieved by altering fiber volume fraction and changing fiber orientation. Conventional Manufacturing process encompasses two sub process, firstly the material is laid up hence forth it is consolidated. Consolidation process requires external pressure and dependency of mold is there which is expensive [1]. Additive manufacturing process encompasses low investment cost to manufacture F.R.C.P layer by layer. Conventional manufacturing process like spray-up, hand lay-up, vacuum-bag molding, encounters a major problem that is need of mold which thwart the process by making it tedious and costly. Above all mentioned problems are eradicated using computer generated S.T.L file to fabricate layer by layer using AM Technique [3]. Composites comprises of reinforcement (fiber, particle, and flake) and matrix (polymer, metal ceramic, carbon. Polymer (epoxy, polyester, and urethane) Reinforced (graphite, aramids, boron). Aramids fiber are of two types Kevlar 29 and Kevlar 49) in which reinforcement is embedded [4]. Commonly used fibers are glass fiber, Kevlar fiber and carbon fiber. Carbon fiber when reinforced with Onyx provides strength up to 800 MPa. High impact resistance parts can be produced by keeping Kevlar as reinforcement and strength up to 610 MPa can be achieved. High strength High Temperature Fiberglass can work both in area of high strength as well as high Temperature and provides strength up to 600 MPa. Fiberglass can provide strength up to 590 MPa. The extraordinary properties displayed by Kevlar makes it an ideal candidate military and industrial application. The high ratio of tensile to shear modulus results in anisotropic property of Kevlar [2]. Matrix Material used are nylon, PLA, Polyester, Vinyl ester, ABS, and Polycarbonate. Matrix material insure that the fibers are aligned, able to transfer stress and protect Composite from environment. There must not be any thermal, chemical and physical reaction between matrix and the reinforcement. Matrix selection process are processing properties, printability characteristics and thermal properties.

Fiber are characterized into two categories chopped fiber (Discontinuous) and continuous fiber. The minimum length required to transfer entire load from matrix to fiber is called critical length. The length versus diameter ratio >100 is termed as Continuous fiber [3]. The length of the fiber must be 15 times than that of the critical length is considered optimal. Fiber length more than the optimal length are continuous. Discontinuous fiber are shorter than critical length. Hence less effective in strengthening and provide less stiffness. However they are cheaper faster and easier to fabricate. Simpler processing is obtained from short fiber as more freedom in material replacement and material deposition Pores are also less in case of short

fiber [4]. The length of the fiber between L and L_C is termed as short fiber. Continuous fiber provides more strengthening than fiber composite. Fiber are extravagant for engineering analysis as they provide outstanding strength to weight ratio. Their strength even par with metal. Major problem encountered with continuous fiber is deposition rate and minimal continuous radius. However in tension only. Fiber are extremely weak to resist bending, compression, and shear. When Fiber are bonded with the matrix and oriented in such a fashion to extract its tensile properties it gives extravagant properties. In case of chopped (discontinues) fibers, fiber is mixed with thermoplastic, ABS, PLA or Nylon. The mixed fiber are extruded into a spool for further additive manufacturing Process. This process aviates properties like thermal, strength, stiffness, dimensional stability and print quality. However discontinues fiber is unable to leverage strength of the composite. The strength of composite is what it is holding it together like thermoplastic. Continuous fiber reinforced composite is provides strength as fiber are continuously laid to give strength not the thermo-plastic. When the fiber length $L > 30L_C$ ($L_C = 115 \mu\text{m}$) is called continuous fiber [5]. Continuous fiber reinforced composite has been manufactured by fused filament fabrication.

2 Additive Manufacturing Process

Additive manufacturing Process of Fiber Reinforced Composite is segregated into four major categories as shown in Fig. 1. Four broader category of these are material extrusion, vat polymerization, powder bed fusion and sheet lamination. Table 1 shows the summary of Additive manufacturing process.

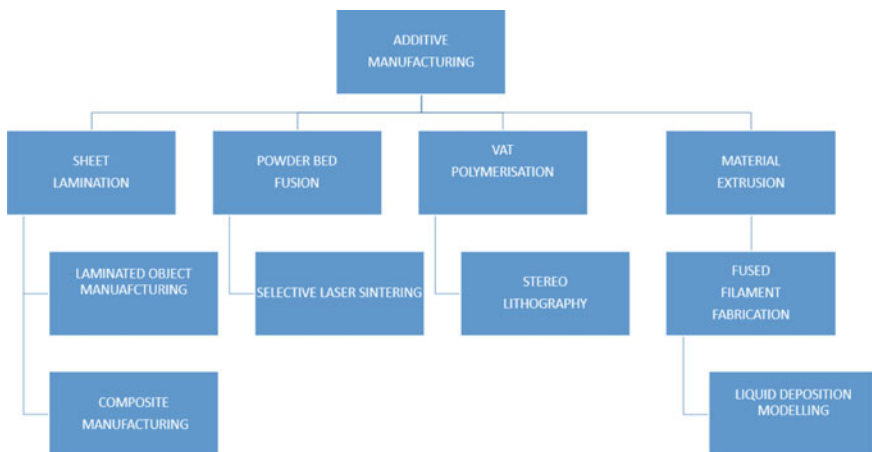


Fig. 1 Different additive manufacturing process of fiber reinforced composites

Table 1 Advantages and disadvantages of various additive manufacturing process

S. No.	Methods	Mechanism	Advantages	Disadvantages
1	Material extrusion	Extrusion	<ul style="list-style-type: none"> • Low cost • Improved mechanical properties • Aligned fiber • No support structure • Good geometrical accuracy 	<ul style="list-style-type: none"> • Nozzle clogging • Poor wettability • Porosity • Delamination • Complex parts can't be manufactured • High wastage • Agglomeration • Layer by layer effect
2	Powder bed fusion	Sintering	<ul style="list-style-type: none"> • High resolution, • High dimensional accuracy • Easy • No tooling • Post treatment • Improved mechanical properties • Better surface quality • High deposition rate 	<ul style="list-style-type: none"> • Porosity • Poor surface finish • Poor mechanical properties • Complexity • Warpage • Anisotropic absent • Stair stepping effect • Low elastic modulus • Lower strength • High porosity
3	Vat Polymerization	Photo Polymerization	<ul style="list-style-type: none"> • High resolution • Nozzle clogging • Low porosity • Complex geometries • High resolution geometry • Improved mechanical property 	<ul style="list-style-type: none"> • Wrapping • Segregation of fibers • Support structure required • Fiber misalignment • High fiber loading • Poor binding • Entrapped air • Limited material
4	Sheet lamination	Sheet lamination	<ul style="list-style-type: none"> • Complex parts can be manufactured • Non-toxic involvement • High mechanical properties • Stair case effect reduced • Low cost • Less resolution 	<ul style="list-style-type: none"> • Wastage • Internal cavity produced • Unable to build complex parts

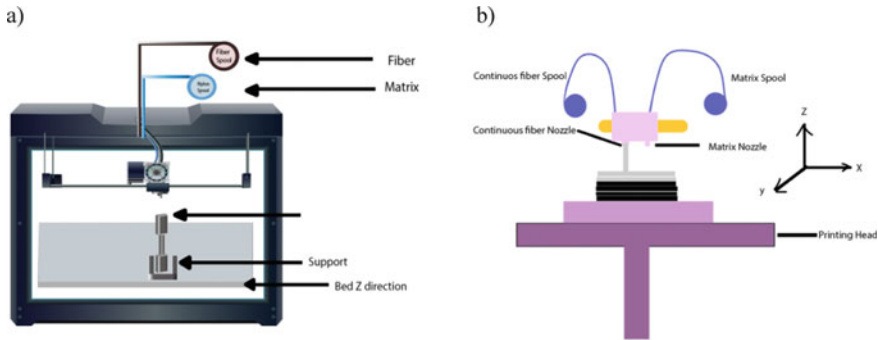


Fig. 2 a Fused deposition modeling with double extruder b flow diagram of fused deposition modeling with double extruder (Modeled using adobe illustrator)

(a) Material Extrusion

Material extrusion process as shown in Fig. 2a, deposition of material takes place due to shear force between nozzle and fiber. Prior Extrusion thermoplastic is heated [6, 7]. Extrusion in paste form is known as liquid deposition modeling and that in filament form is called Fused Deposition modeling [8]. Conventional F.D.M process from plastic filaments [9] use single filament to fabricate composite by combining both matrix and reinforcement. Mark forged (Mark One) 3D Printer uses two nozzle one for reinforcement and other for fiber to fabricate composite as shown in Fig. 2b, Weight percentage, Fiber layer and orientation can be controlled to enhance various mechanical properties [8]. Some commonly used fibers are Kevlar, Carbon fiber, High strength High Temperature Fiber Glass. Thermoplastic polymer used are acrylonitrile butadiene styrene (ABS), poly-acetic acid (PLA), polypropylene (PP), polyether ketone (PEEK) and Ultem [1, 10]. In fiber reinforced composite matrix fiber supports the load and the thermoplastic plays dual role of protecting the fiber and transferring the load [11].

Simplicity lack of support structure, good geometrical accuracy and low cost is the main benefit of FDM. Fibers are aligned due to shear force of the nozzle and the extruder. Increase in wt% of matrix resulted in void formation because of interaction between reinforcement and matrix. Improve in tensile properties was observed in case of reinforced continuous fiber [12]. Tensile Strength up to 198 MPa, 8.46 MPa with 33% isotropic pattern. Carbon fiber reinforced composite and tensile strength up to 110 MPa, elastic modulus 4.23 GPa in case of Kevlar was reported using Kevlar fiber reinforcement composite [13]. Kevlar fiber reinforced composite can increase up to 27 GPa [8]

Delamination occurs due to porosity which reduces the tensile strength [7]. Limited thermoplastic material, layering effect and nozzle clogging due to fiber loading are the major drawback reported [7, 14]. Composite manufactured via F.D.M lacks strength in Z direction [8].

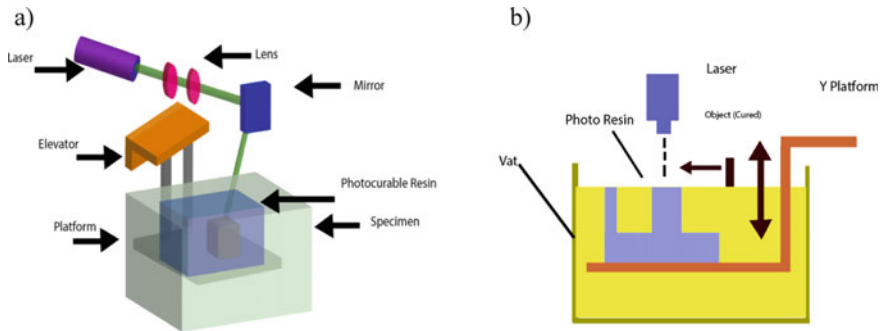


Fig. 3 a Vat Polymerization process b flow diagram of Vat Polymerization process (Modeled using adobe illustrator)

(b) Vat Polymerization

Vat Polymerization as shown in Fig. 3a uses ultraviolet light to cure photo-reactive polymer [15]. Discontinuous as well as continuous F.R.C.P have been successfully manufactured using Vat Polymerization [6, 7] Matrix material used for fabrication comprises of photosensitive acrylate resin [16], polyester resin and photo curable epoxy resin [17]. Some commonly used fiber are glass fibers, carbon fibers [18]. Fabrication of F.R.C.P have been achieved by two methods. Firstly mixing the fiber reinforcement and the matrix. Secondly by dispersing the fiber on the resin surface as shown Fig. 3a.

Increase in mechanical properties were reported in the literature. Layering effect is not evident. Higher resolution parts has been manufactured due to the absence of layering effect [6]. Parts with low porosity was evident [16]. Fabrication accuracy is extremely high to the absence of heat shrink ability [19]. Tensile Strength of 62.3 MPa was achieved using discontinuous carbon fiber. The major drawback is that it is limited to photo curable material. Wrap and distort due to scattering of ultraviolet rays leads to weak mechanical properties and shrinkage [17]. Mechanical properties are inferior as compared to conventional manufacturing process [19]. To enhance the mechanical properties post processing is required [16].

(c) Powder Bed Fusion

Powder Bed Fusion as shown in Fig. 4a process uses electron beam or laser technology to fuse plastic powder together [20]. It is further branched into two categories electron beam melting (E.B.M), selective laser sintering (SLS). Selective laser Sintering use laser technology to sinter wide varieties of material like metal ceramic as well as polymer [21]. Electron Beam technology sinter the material by enhancing the heat energy [6, 8]. In a controlled environment as mentioned in Fig. 4b. Fiber powder are dispersed across platform henceforth laser fuse the powder to create the geometry. Build platform is lowered continuously to get the desired shape. Discontinuous fiber are preferred for sintered by selective laser sintering process [22, 23]. Thermo-plastic Resin for Matrix material used in Selective laser sintering as reported in the

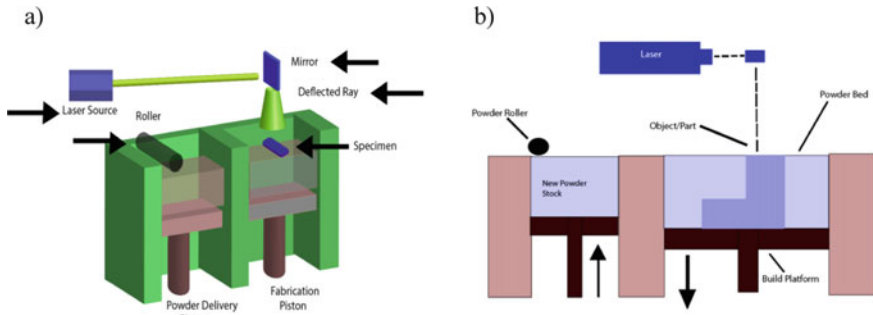


Fig. 4 a Powder bed fusion process b flow diagram of powder bed fusion process (Modeled using adobe illustrator)

literature are polyamide, polystyrene, polyethylene, polyoxymethylene, polyamide, poly butylene terephthalate, Poly ether ketone and poly ether ether ketone [24].

The parts manufactured by Selective laser sintering are comparable to Extrusion based process with high geometric accuracy and superior mechanical properties [23]. Complex structure can be built without any tooling [25].

However mechanical properties are inferior when compared to Conventional manufacturing process [26]. Porosity (dependent on the powder flow ability) affects the mechanic property (tensile strength, charpy impact test, flexural strength, break at elongation) [27]. Anisotropic behavior that shows different directional properties cannot be achieved through Powder Bed Fusion [28].

(d) Sheet Lamination

In Sheet lamination as shown in Fig. 5a fabrication of sheet is achieved through Bonding of sheets. Laminated object manufacturing and composite-based additive manufacturing process fall into this category. Laminated object manufacturing have higher strength as compared to composite-based additive manufacturing process due to aligned fiber [22]. In sheet lamination process sheet of binding material are

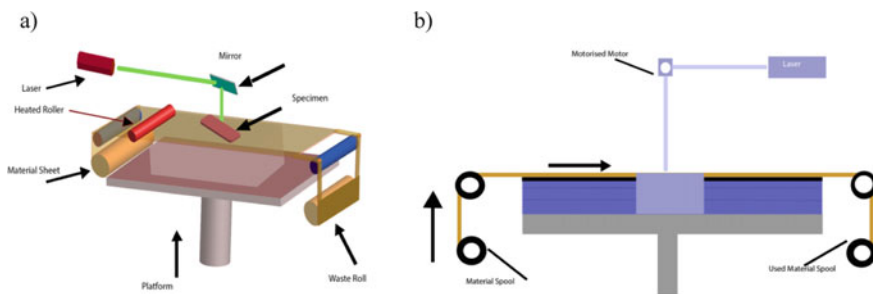


Fig. 5 a Sheet lamination process, b sheet lamination process line diagram (Modeled using adobe illustrator)

sliced using either knife or laser. Aqueous bases solution is deposited on the sheet followed by deposition of thermoplastic powder. Fiber sheet are stacked and bonded by applying external pressure shown in Fig. 5b. Fiber sheet of both discontinuous as well as continuous has been used. Aligned fiber followed by minimum stair case has been achieved. The major advantages shown by laminated object manufacturing is producing high strength part without aid of any mechanical support [29].

The Major drawback with this process is large amount of shrinkage which is the result of thermal post-processing leading to dimensional accuracies [30].

2.1 Future Work

Majority of the research work carried out in the realm of F.R.C.P manufactured by additive manufacturing process is in the area of short fibers and that too Carbon Fiber [10]. Also minority work has been done in the area of F.R.C.P with Kevlar as the reinforcement. The Main objective of F.R.C.P is to obtain high specific modulus and high strength to weight ratio. To achieve this interfacial bonding is extremely important. The applied strength is obtained when the applied load is transmitted from matrix to fiber. Additive manufacturing of F.R.C.P generally compromises of base material such as glass fiber, carbon fiber. Anisotropic capabilities of AM techniques must be surveyed to fabricate F.R.C.P

2.2 Future Trends in Additive Manufacturing Process

The digital area of Industry 4.0 is being led by additive manufacturing process. Elimination of tools, jigs, fixture and dependency on high cost mold. Additive manufacturing will become simple as a click of button leading to manufacturing.

3 Conclusion

This report tried to encapsulate a brief overview of recent advancement of fabrication of continuous fiber via AM process. Addition of reinforcement helps in achieving tailored made property. The advantages and disadvantages of various AM techniques have been briefly discussed. Selection of appropriate AM technique with correct matrix and reinforcement is needed to get enhanced mechanical properties. Continuous fiber in comparison with discontinuous fiber show better property.

- Void Unfilled spaces (Void) decrease the mechanical strength of F.R.C.P. Cracks and pores are result of the way the material is being fabricated. Unwanted voids are present in polymer matrix. The way the manufacturing is done can also induce

porosity. Technical factor like thickness of the matrix, layer temperature of the nozzle and all such factors may increase pore formation [31]. Porosity increases with increase in fiber content up to 15%. However, porosity was maximum in case of 10% reinforcement [3].

- Fiber Length: FRCP up to 150 μm shows superior Young's modulus and tensile strength in comparison with 100 μm , both are 7 μm diameter [32]. 150 μm shows less toughness, ductility compared to μm , both having 7 μm diameter [3].
- Interfacial properties: The failure of the composite material which takes place by interface delamination which takes place at fiber matrix interaction. Hence interfacial bonding is governed by the way interface is formed [11]. Fiber matrix interfacial shear stress controls the stability and functional performance [2]. Interfacial strength is enhanced when interfacial shear stress is decreased [12, 13]. Mechanical characterization to know the mechanical properties like tensile and flexure properties is the hub of maximum research. Few research has been done in the area of interface of composite [6]. SEM analysis aid in understanding strength variation in case of F.R.C.P.
- Anisotropic properties of the Kevlar is obtained by aligning fiber in different direction in F.R.C.P. The Longitudinal tensile strength will be extremely high in compare to the transverse strength.

Authors Contribution All authors contributed equally for the preparation of the manuscript.

Conflict of Interest The author declare no conflict of interest.

References

1. Blok LG, Yu H, Longana ML, Woods BKS (2020) Development of discontinuous fibre reinforced thermoplastic feedstocks for high performance 3D printing. In: ECCM 2018—18th European conference on composite materials, pp 1–8
2. Singh TJ, Samanta S (2015) Characterization of kevlar fiber and its composites: a review. *Mater Today Proc* 2(4–5):1381–1387. <https://doi.org/10.1016/j.matpr.2015.07.057>
3. Ning F, Cong W, Qiu J, Wei J, Wang S (2015) Additive manufacturing of carbon fiber reinforced thermoplastic composites using fused deposition modeling. *Compos Part B Eng* 80:369–378. <https://doi.org/10.1016/j.compositesb.2015.06.013>
4. Nawafleh N, Celik E (2020) ur na I P. *Addit Manuf* 101109. <https://doi.org/10.1016/j.addma.2020.101109>
5. Lu ZL, Lu F, Cao JW, Li DC (2014) Manufacturing properties of turbine blades of carbon fiber-reinforced SiC composite based on stereolithography. *Mater Manuf Process* 37–41. <https://doi.org/10.1080/10426914.2013.872269>
6. Ngo TD, Kashani A, Imbalzano G, Nguyen KTQ, Hui D (2018) Additive manufacturing (3D printing): a review of materials, methods, applications and challenges. *Compos Part B* 143:172–196. <https://doi.org/10.1016/j.compositesb.2018.02.012>
7. Vaidyanathan R, Barrera EV, Shofner ML (2003) Single wall nanotube and vapor grown carbon fiber reinforced polymers processed by extrusion freeform fabrication 34:1207–1217. <https://doi.org/10.1016/j.compositesa.2003.07.002>

8. Dong G, Tang Y, Li D, Zhao YF (2018) Mechanical properties of continuous kevlar fiber reinforced composites fabricated by fused deposition modeling process. *Proc Manuf* 26:774–781. <https://doi.org/10.1016/j.promfg.2018.07.090>
9. Dudek P (2013) Agh university of science and technology, faculty of mechanical engineering and robotics, al. a. mickiewicza 30:30-059 Kraków, Poland. <https://doi.org/10.2478/amm-2013-0186>
10. Goh GD, Yap YL, Agarwala S, Yeong WY (2019) Recent progress in additive manufacturing of fiber reinforced polymer composite
11. Shubhra QTH, Alam A (2011) Mechanical properties of polypropylene composites: a review. <https://doi.org/10.1177/0892705711428659>
12. Van Der Klift F, Koga Y, Todoroki A, Ueda M, Hirano Y, Matsuzaki R (2016) 3D printing of continuous carbon fibre reinforced thermo-plastic (CFRTP) tensile test specimens. <https://doi.org/10.4236/ojcm.2016.61003>
13. Dickson AAN, Barry JN, Dickson AAN, Dowling DP (2017) Fabrication of continuous carbon, glass and kevlar fibre reinforced polymer composites using additive manufacturing. *Addit Manuf*. <https://doi.org/10.1016/j.addma.2017.06.004>
14. Mohamed OA, Masood SH, Bhowmik JL (2015) Optimization of fused deposition modeling process parameters: a review of current research and future prospects. <https://doi.org/10.1007/s40436-014-0097-7>
15. West AP, Sambu SP, Rosen DW (2001) A process planning method for improving build performance in stereolithography 33
16. Zheng Z et al (2016) Shear induced alignment of short nano fibers in 3D printed polymer composites. *Nanotechnology* 27(49):1–8. <https://doi.org/10.1088/0957-4484/27/49/495302>
17. Cheah CM, Fuh JYH, Nee AYC, Lu L (1996) Mechanical characteristics of fiber-filled photopolymer used in stereolithography 112–119
18. Plymill A, Minneci R, Greeley DA, Gritton J (2016) Graphene and carbon nanotube PLA composite feedstock development for fused deposition modeling
19. Sano Y, Matsuzaki R, Ueda M, Todoroki A, Hirano Y (2018) 3D printing of discontinuous and continuous fibre composites using stereolithography. *Addit Manuf* 24(May):521–527. <https://doi.org/10.1016/j.addma.2018.10.033>
20. Kruth JP, Wang X, Laoui T, Froyen L (2003) Lasers and materials in selective laser sintering 23(4):357–371
21. Jing W, Hui C, Qiong W, Hongbo L, Zhanjun L (2016) *PT. Mater Des*. <https://doi.org/10.1016/j.matdes.2016.12.037>
22. Chapiro M (2016) Current achievements and future outlook for composites in 3D printing. *Reinf Plast* 00(00):2–5. <https://doi.org/10.1016/j.repl.2016.10.002>
23. Paolini A, Kollmannsberger S, Rank E (2019) Additive manufacturing in construction: a review on processes, applications, and digital planning methods. *Addit Manuf* 30:100894. <https://doi.org/10.1016/j.addma.2019.100894>
24. Wang Y, Rouholamin D, Davies R, Ghita OR (2015) Powder characteristics, microstructure and properties of graphite platelet reinforced poly ether ether ketone composites in high temperature laser sintering (HT-LS). *JMADE* 88:1310–1320. <https://doi.org/10.1016/j.matdes.2015.09.094>
25. Zhu W A novel method based on selective laser sintering for preparing high-performance carbon fibres_polyamide12_epoxy ternary composites_Enhanced Reader.pdf
26. Athreya SR, Kalaitzidou K, Das S (2011) Mechanical and microstructural properties of Nylon-12/carbon black composites: selective laser sintering versus melt compounding and injection molding. *Compos Sci Technol* 71(4):506–510. <https://doi.org/10.1016/j.compscitech.2010.12.028>
27. Li N, Li Y, Liu S (2016) Rapid prototyping of continuous carbon fiber reinforced polylactic acid composites by 3D printing. *J Mater Process Tech*. <https://doi.org/10.1016/j.jmatprotec.2016.07.025>
28. Wang Y, Xu Z, Wu D, Bai J (2020) Current status and prospects of polymer powder 3D printing technologies. *Materials (Basel)* 13(10). <https://doi.org/10.3390/ma13102406>

29. Vaezi M, Seitz H, Yang S (2012) A review on 3D micro-additive manufacturing technologies. <https://doi.org/10.1007/s00170-012-4605-2>
30. Mani M, Lyons KW, Gupta SK (2014) Sustainability characterization for additive manufacturing 119:419–428
31. Zindani D, Kumar K (2019) An insight into additive manufacturing of fiber reinforced polymer composite. *Int J Light Mater Manuf* 2(4):267–278. <https://doi.org/10.1016/j.ijlmm.2019.08.004>
32. Fidan I, Imeri A (2019) The trends and challenges of fiber reinforced additive 1(931)

Numerical Investigation of the Effect of Developed Thermal Stress on Ultrasonic Horn Material



Guddakesh Kumar Chandan and Chinmaya Kumar Sahoo

Abstract In ultrasonic machining, the horn is used to transfer frequency and therefore has a critical role in dictating the machining performance. The design and material behaviour of ultrasonic horn have been explored through experimental and numerical methods by different research groups. However, the primary effect of temperature and thermal stress developed within the horn has been paid less attention. Therefore, the present study addresses the impact of thermal stress on a cylindrical horn using a three-dimensional numerical model for different horn materials viz. aluminium, titanium, and steel (AISI-4063). The numerical analysis results showed that natural frequency decreased with an increase in temperature irrespective of material selection. Furthermore, the amplitude and von Mises stress show growth with an increase in temperature. Moreover, titanium horn showed a minimum acoustic loss in terms of frequency followed by steel and aluminium due to material damping. Further, temperature change during the ultrasonic process has less effect on the titanium horn, followed by aluminium and steel due to its low thermal conductivity.

Keywords Ultrasonic horn · COMSOL Multiphysics · Thermal stress · Modal analysis

1 Introduction

In ultrasonic machining process, a horn is subjected to high frequency and high thermal stress due to a temperature rise. Apart from the horn design, horn material and operating condition are the factors for the temperature rise and significantly affect the performance of horn [1]. In ultrasonic operations, when the tool holder/horn actuates at a natural frequency around 20 kHz, a minute variation in thermal stress can affect the ultrasonic horn performance. Therefore, designers dedicated their time

G. K. Chandan · C. K. Sahoo (✉)

Department of Mechanical Engineering, National Institute of Technology Silchar, Silchar, Assam 788010, India

e-mail: chinmaya.cks@gmail.com

and effort to study the characteristics of thermal stress with a change of temperature. Several researchers have reported the relevant research on the thermal stress generation in horn [2–5]. Johnston and Young [2] pioneered the area of cavitation erosion by adding the influence of pressure and temperature. The authors reported about increase in material removal rate (MRR) with varying pressure and temperature. Hammitt and Rogers [3] experimented on bronze (SAE-660) with temperature range (55° F–250° F) with and without variation in pressure (1–4 atm) for 20 kHz vibration and it has been observed that the temperature and pressure significantly affect maximum damage rate of bronze material. Auret et al. [4] investigated erosion characteristics of stainless steel for different temperature ranges. It has been reported that MRR was highest near 50 °C. Liu et al. [5] analysed the relation between modal frequencies and temperature of the beam and reinforced concrete slab. Furthermore, they proposed regression models for accurate quantification of the temperature effect on natural frequencies of the beam and reinforced concrete slab. Nagalingam and Yeo [6] investigated the cavitation collapse mechanism for different temperatures and pressure for steel and aluminium alloys using ultrasonic machining. It has been found that the increase in MRR was observed up to 50 °C and 400 kPa and then decreased with increment in fluid temperature. Ahmed [7] studied the influence of pressure and temperature in cavitation erosion for aluminium metal and reported the effect of temperature on impact pressure. Rani and Rudramoorthy [8] studied the influence geometry of horn (i.e. catenoid, Bezier, cylindrical, stepped, Gaussian) for amplitude and von Mises stress for welding. Among all horn design, Bezier horn illustrates higher amplitude within the considerable stress. Rani et al. [9] also studied thermoelastic heating of stepped horn. Furthermore, it has been observed that titanium has better energy utilization with minimum acoustic loss among mild steel, aluminium, and stainless steel.

Although the performance parameters related to USM are well documented in the theoretical and experimental study, most of the researchers considered temperature as constant, which is a bit of simplification in the real world. Furthermore, it has been observed that the working temperature of USM can vary during the machining process. However, in the literature, the topic of thermal stress developed during the ultrasonic machining process has been given less attention. Therefore, the present study attempts to analyse the thermal stress generated in a cylindrical horn made of aluminium, titanium, and steel (AISI-4063) using a three-dimensional numerical model.

2 Numerical Analysis

The geometry of ultrasonic cylindrical horn is developed with length and diameter are 130 and 35 mm, respectively, in the FEM environment, as shown in Fig. 1 [8]. The selection of cylindrical horn is supported by the fact that manufacturing of cylindrical horn is simple and easily customized. Finite element software (COMSOL Multiphysics) is used to analyse thermal stress in ultrasonic cylindrical horn model. Three

Fig. 1 Schematic diagram of a cylindrical ultrasonic horn

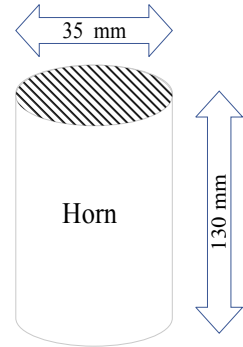


Table 1 Properties of horn materials

Material	Aluminium	Titanium	Steel
Density (Kg/m ³)	2740	4430	7800
Young's modulus (GPa)	74.5	114	210
Poisson's ratio	0.33	0.34	0.33
Thermal conductivity (w/m-k)	205	7.1	46
Specific heat (J/Kg-k)	897	553	466
Coefficient of thermal expansion (1/k)	24×10^{-6}	8.7×10^{-6}	12×10^{-6}

distinct models of COMSOL viz. solid mechanics, heat transfer in solids, and pressure acoustics frequency domain are coupled together for the present investigation.

Three different materials, i.e. aluminium, steel, and titanium are configured to analyse the influence of temperature in the ultrasonic horn. Table 1 presents the properties of various materials [8–10].

For the mathematical solution of the horn, the following assumptions are listed.

- i. Linear elastic material property is assumed.
- ii. Atmospheric pressure is assumed to be 1 atm.
- iii. The ambient temperature is assumed to be 294° K, i.e. 21 °C.
- iv. Variation of temperature during the machining process is assumed to be 10 °C, 30 °C, and 50 °C [6].

2.1 Governing Equation

The governing equations consist of the heat transfer equation for solids and the equation of motion for free vibration, as discussed in this section [11, 12].

Heat Transfer in Solids

$$\rho C_p \mu \nabla T + \nabla \cdot q = Q + Q_{ted} \tag{1}$$

where ρ , C_p , u , T , q , Q , Q_{ted} are density, specific heat capacity at constant stress, velocity, temperature, heat flux by conduction, additional heat sources, thermoelastic damping, respectively.

Equation of motion for free vibration

$$M\ddot{u} + B\dot{u} + Ku = 0 \quad (2)$$

where M , \ddot{u} , B , \dot{u} , K , u denote inertial force, acceleration, damping force, velocity, stiffness, and displacement, respectively.

For natural frequency in the object,

$$-\rho\omega^2u = \nabla \cdot S \quad (3)$$

where ρ , ω , u , S indicate the density of the material, angular frequency, displacement, stress, respectively.

For the travel of frequency in the wall of the following equation used,

$$\nabla \cdot \left(-\frac{1}{\rho_c}(\nabla P_t - q_d) \right) - \frac{K_{\text{eq}}^2 P_t}{\rho_c} = Q_m \quad (4)$$

where ρ_c , q_d , Q_m , P_t , K_{eq} show the density of the material, dipole domain source, monopole domain source, total pressure, wavenumber used in the equation, respectively.

2.2 Boundary Condition

The boundary conditions used to solve Eqs. (1)–(4) are summarized as follows:

- i. The top portion of the horn is attached to the transducer.
- ii. Boundary standard component of velocity and acceleration is considered as zero, i.e.

$$-n \cdot \left(-\frac{1}{\rho_c}(\nabla P_t - q_d) \right) = 0.$$

- iii. Ambient temperature is applied to the entire geometry.

Table 2 Effect of mesh size on the horn performance

Number of elements	Total displacement (μm)	Number of elements	Total displacement (μm)
40,158	20.1267	57,059	20.1257
43,490	20.126	62,704	20.1252
47,379	20.1262	69,085	20.1252
52,400	20.125	76,586	20.1252

2.3 Numerical Analysis

COMSOL Multiphysics (commercial FEM software) was used to solve the governing Eqs. (1)–(4) considering the boundary conditions for cylindrical horn made of different materials, i.e. steel, aluminium, and titanium. The free tetrahedral mesh was considered for the entire horn geometry. Before conducting a simulation of modal and thermal stress analysis, a mesh sensitivity test was performed. Mesh size range was varied between 3 and 4 mm for that number of elements generated, i.e. between 5505 and 76,586, respectively. The effect of the number of the element was analysed by varying the mesh size, and it was observed that at a mesh size of 3 mm, i.e. no of elements at 76,586, the variation of the result is minimum considering computational time. So the mesh size of 3 mm was selected for the analysis. The effect of no of elements and total displacement is shown in Table 2.

The effect of the present study is obtained through performing two tasks, i.e. modal analysis and thermal stress analysis. The simulation time for modal analysis is about 8 min, and the thermal study is about 32 min.

2.4 Model Validation

Before discussing the results obtained from the current study, the correctness of the numerical research needs to be ascertained. The value of amplitude and von Mises stress of the current model has been validated with the earlier published article [8]. The amplitude and von Mises stress value variation is significantly less (below 0.5%). So the current model is considered for detecting the effect of a rise in temperature on the ultrasonic horn performance (Table 3).

Table 3 Comparison of displacement amplitude and von Mises stress with an earlier study [8]

Parameters	Reference article [8]	Present study
Amplitude in microns	20	20.1
von Mises stress in MPa	40	40.1

3 Results and Discussion

The present investigation briefly discusses the effect of temperature on acoustic characteristics of the ultrasonic horn. Three distinct COMSOL models viz. solid mechanics, heat transfer in solids, and pressure acoustics frequency domain were coupled to investigate the effect in terms of natural frequency, amplitude, and von Mises stress. In this context, three materials viz. aluminium, titanium, and steel (AISI-4063) were investigated. The results obtained from the present investigation are illustrated in Table 4. At ambient temperature (21 °C), the value of natural frequency is 18,445, 19,512, and 18,354 for aluminium, titanium, and steel, respectively. Detailed analysis of the natural frequency on the horn material at constant environmental temperature has been discussed in authors' previously published article [10].

The results obtained in Table 4 are presented in terms of well-characterized bar charts, line plots for illustrating a comparative assessment of three horn materials when subject to the thermal environment. The discussion has briefly defined the effect of temperature in terms of modal analysis and thermal stress analysis, as presented in the subsequent section.

3.1 Modal Analysis

Modal analysis is instrumental in determining the natural frequency of a system and is further utilized in the study, control, design, and diagnosis of vibration [8]. Thereby, the present investigation conducted a modal analysis to determine the natural frequency, as shown in Fig. 3. It has been observed from Fig. 3 that there is a reduction in the natural frequency while increasing temperature. At ambient temperature (21 °C), the value of natural frequency is 18,445, 19,512, and 18,354

Table 4 Dynamic analysis for change in temperature for different horn materials

S. No.	Material	Change in temperature (°C)	Natural frequency (kHz)	Amplitude (μm)	von Mises stress (MPa)
1	Aluminium	304	18,330	20.1	40.1
		324	18,163	52.2	51.4
		344	17,975	84.3	64.1
2	Titanium	304	19,496	7.3	22.3
		324	19,465	18.9	28.6
		344	19,434	30.5	35.5
3	Steel (AISI-4063)	304	18,330	10.1	56.5
		324	18,282	26.1	72.5
		344	18,235	42.1	90.4

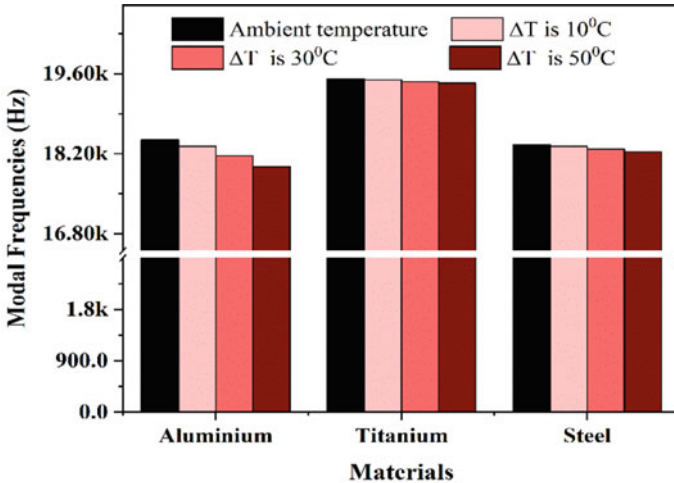


Fig. 3 Effect of temperature on the natural frequency for Al, Ti, and steel horn material

for aluminium, titanium, and steel, respectively. In contrast, the increase in temperature up to 10 °C, 30 °C, 50 °C by performing modal analysis the value of natural frequency of aluminium, titanium, and steel are reduced to 0.62%, 0.08%, and 0.13% simultaneously. It is noteworthy to mention that the material which has the highest density (steel) has the least natural frequency.

Additionally, damping is only significant where the high frequency is used and that in the case of ultrasonic. So, materials damping plays a crucial role in defining the frequency reduction. Furthermore, it has been observed that the titanium horn shows the least effect on frequency variation with the rise in the temperature followed by steel and aluminium. It is noted that the titanium horn has the least thermal conductivity compared to Al and steel [9]. Therefore, the Ti horn is most resistance to the temperature variation.

3.2 Thermal Stress Analysis

Thermal stress analysis is used to determine the effect of temperature rise in horn materials. Figure 4 shows the impact of the horn temperature on the generated amplitude and von Mises stress for Al, Ti, and steel horn. The effect of change in temperature in the horn with different materials, i.e. aluminium, titanium, and steel, was analysed through thermal stress analysis. It needs to be noted that the ambient temperature considered for the investigation is 294° K, i.e. 21 °C. At ambient temperature (21 °C), the value of the amplitude is 18.9, 6.58, and 9.79 for aluminium, titanium, and steel, respectively.

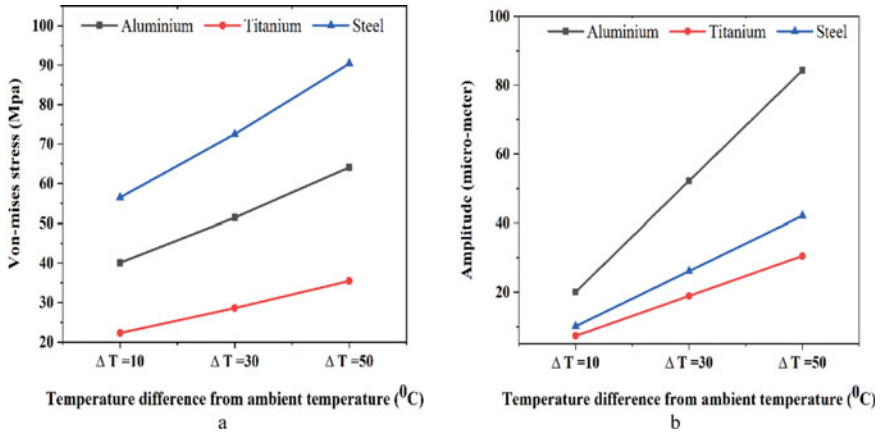


Fig. 4 Effect of temperature on a von Mises stress and b amplitude

While the increase in temperature from (0–50) °C by performing thermal stress analysis the value of the amplitude of aluminium, titanium, and steel are get increased up to 446.03.4%, 463.52%, and 430.03% simultaneously, it is observed that aluminium has the highest effect on amplitude, with a temperature rise, followed by steel and titanium. The variation in the amplitude is due to material thermal conductivity. Furthermore, it is observed that steel shows highest von Mises stress for variation in temperature followed by aluminium and titanium, respectively. So from observation, it is noteworthy to mention that among all horn material, steel shows a moderate effect on amplitude while increment in temperature compared with aluminium and titanium. Furthermore, steel horn shows a high von Mises stress followed by aluminium and titanium. Aluminium shows the highest amplitude, but it offers a high variation in amplitude with the increase in horn temperature, and titanium horn shows the least effect due to increment in temperature.

4 Conclusion

The present work showed the effect of increment in temperature on cylindrical horn material (made of aluminium, titanium, and steel) during ultrasonic operation. During the ultrasonic process, the rise in temperature plays a crucial role in the variation of the natural frequency, von Mises stress, and amplitude for different horn materials. The result of the numerical analysis can be considered as follows:

- I. Natural frequency decreased with an increase in temperature irrespective of material selection. Furthermore, the magnitude of amplitude and von Mises stress increases with an increase in the surrounding temperature of the horn.
- II. Titanium horn showed a minimum acoustic loss in terms of frequency followed by steel and aluminium. Further, titanium horn shows the lowest variation (of

- amplitude and von Mises stress) with the increase in temperature due to low thermal conductivity while comparing with aluminium and steel.
- III. Titanium is observed to be one of the best materials for ultrasonic horn in all thermal conditions as the amplitude and von Mises stress both are minimal for the investigated thermal environment.

References

1. Shan T, Qi X, Cui L, Zhou X (2017) Thermal behavior modeling and characteristics analysis of electrothermal microactuators. *Microsyst Technol* 23(7):2629–2640
2. Johnston J, Young S (1969) Effect of temperature and pressure on cavitation damage to a cobalt base alloy in sodium. NASA Technical note no TN D-5273
3. Hammitt FG, Rogers DO (1970) Effects of pressure and temperature variation in vibratory cavitation damage test. *J Mech Eng Sci* 12(6):432–439
4. Auret JG, Damm OFRA, Wright GJ, Robinson FPA (1993) Cavitation erosion of copper and aluminium in water at elevated temperature. *Tribol Int* 26(6):421–429. [https://doi.org/10.1016/0301-679X\(93\)90082-C](https://doi.org/10.1016/0301-679X(93)90082-C)
5. Liu H, Wang X, Jiao Y (2016) Effect of temperature variation on modal frequency of reinforced concrete slab and beam in cold regions. *Shock Vib*
6. Nagalingam AP, Yeo SH (2018) Effects of ambient pressure and fluid temperature in ultrasonic cavitation machining. *Int J Adv Manuf Technol* 98(9):2883–2894
7. Ahmed S (1998) Investigation of the temperature effects on induced impact pressure and cavitation erosion. *Wear* 218:119–127
8. Rani MR, Rudramoorthy R (2013) Computational modeling and experimental studies of the dynamic performance of ultrasonic horn profiles used in plastic welding. *Ultrasonics* 53:763–772
9. Rani MR, Prakasan K, Rudramoorthy R (2015) Studies of thermo-elastic heating of horns used in ultrasonic plastic welding. *Ultrasonics* 55:123–132
10. Chandan GK, Sahoo CK (2021) Numerical analysis on a selection of horn material for the design of cylindrical horn in ultrasonic machining. In: *Recent advances in mechanical engineering*. Springer, Singapore, pp 127–136
11. COMSOL, Acoustics module user's guide version 5.4, 1998–2018
12. COMSOL, Structural mechanics module user's version 5.4, 1998–2018

Corrosion in Thermal Pipes: An Investigation on Problems and Causes



A. Hari Ganesh, R. D. Mishra, and S. Kar

Abstract Corrosion is one of the primary causes for failures of underground metal pipes. The literatures on corrosion of pipes indicate that the effect of corrosion on the mechanical properties of pipe materials is highly harmful and needs prevention. However, very few research work is available on corrosion effect related to various corrosion related failures. The aim of this paper is to present a comprehensive investigation on various corrosion induced failure, synthesized corrosion inhibitor and corrosion resistance coatings for reduction this environmental impact. In this paper, the mechanism of corrosion in concrete structures is studied and analysed. In addition, kinetics of corrosion, and reactions of the concrete structures that resulted in corrosion failure are discussed. Further, the study also encompasses boiler corrosion, types and preventive measures for minimizing corrosion and preventing catastrophic failure.

Keywords Corrosion · Oxidation · Oxygen corrosion · Carbonic acid corrosion · Boiler · Stress corrosion cracking · Prevention

1 Introduction

In different useful/daily life applications like as petroleum, maritime, and transport, the special mechanical properties of metals are greatly respected and helpful. The main issue that has posed many questions, though is that corrosive animals may attack much of the metals in the natural world, which not only contributes to undesirable destruction but also damages human protection [1–4]. The use of organic coatings is a realistic and possibly cost-effective solution that has drawn

A. Hari Ganesh (✉)

Power Mech Projects Limited, 2×800 MW, Yeramarus Thermal Power Station, Raichur,
Karnataka 584134, India
e-mail: ahariganesh@yahoo.com

R. D. Mishra · S. Kar

Department of Mechanical Engineering, National Institute of Technology, Silchar 788010, India
e-mail: rdmisra@mech.nits.ac.in

a lot of researchers' interest [5, 6]. Few of the special characteristics of epoxy coatings, like strong acid/alkaline stability, excellent adhesion and high mechanical properties, have successfully coated much of the metal substances to shield them [7–10]. Researchers have applied diverse techniques to achieve an extended protection against corrosion. Among them, the incorporation of the barrier nanofiller and nanopigment (i.e. graphene oxide (GO), halloysite, and clay [11]), active nanopigment (i.e. zincphosphate [11], polyaniline) and hybrid pigment/filler (with both inhibition and barrier functions [12]) would be beneficial for improving the protection ability of the coatings. MOFs, metallic ions (or oxide clusters) associated by organic ligands, have recently been developed as novel hybrid materials. Because of the unique properties, they are used in various applications like gas storage [13], waste water treatment] and drug delivery. MOFs are also applied in organic coatings and have shown excellent compatibility [14, 15]. The corrosion retardation effect of MOFs has recently gained considerable attention. Ramadan zadeh et al. [16] used ZIF-8 decorated graphene oxide (GO). MOF-5 was used by Cao et al. [17] as a nanocontainer of benzotriazole. In addition, GO was further combined with the resulting compounds and then integrated into an epoxy coating to create a nanocomposite with active (inhibition) and passive (barrier) corrosion retardation efficiency.

Recently, many investigations have concerned the detection of incidents of breakdown of electric power plants. In steam power plants, steam generators are the main equipments whose breakdown results in the elimination of the entire unit from the network [18]. In heat exchangers such as boiler tubes, steam superheater elements and chemical plant reformer tubes, tubes subjected to high internal pressures are crucial components. Boiler tubes are exposed internally to the fast flowing steam pressure and temperature, and on the surface to the elevated combustion fuel temperature. The in/outside of the tubes may be seriously compromised by corrosive organisms found in both ecosystems. Superheater tubes are often vulnerable to multiple faults, which often include issues with creep loss. The failures that occur under varying temperatures and time conditions were deducted from the fracture morphology and microstructure adjustment [19]. One of the key reason for the shutdown and taking away of steam generators from the path and, subsequently, the elimination of the device from the network is the incidence of leak due to the failure of boiler tubes, particularly in superheater tubes and reheater tubes [20]. In general, boiler tubes are subject to high internal pressure and temperature, and to much higher outer atmospheric temperatures. The mainly significant explanation for the damage of the heatertubes is that the temperature of the metallic pipe reaches specified strength level. The metal temperature may rise steadily through the years with development of the oxide layer on the tubing, otherwise it may also rise abruptly as a result of reduce in the flow of gas or the cooling internally. The failure study of the irregular corrosion of the economizer tubes of the waste heat steam generator was conducted by Ding et al [21] to determine the root causes of the corrosion of SA106 GrA steel.

Pipe lines are vital material which plays a key position in the nation's financial system, social well-being and quality of life. Largely pipelines are prepared with

metals, such as castiron and ssteel, and are found *u/g* in the earth. About 85% of the water distribution lines are castiron and concrete.

1.1 Carbon Steel Corrosion Mechanisms in Concrete

The RC systems' service life can be divided into two significant periods, as indicated by Tuutii [22]: the activation phase and the propagation-phase. It relates to the penetration of aggressive-agents, CO₂ and chloride, into the rebar of concrete material, resulting in passive film's incremental degradation on the steel surface. Before the degree of corrosion exceeds the maximum failure allowed by construction standard values, the propagation stage is the active corrosion condition. If the current density is less than 0.1mA cm⁻², and in the active state, if the value is more significant than 1 mA cm⁻², steel corrosion is typically considered passive. [23]. Other models considered the improvement in the corrosion rate during the service life of reinforced concrete [24–26] based on the Tuutii model or included additional stages in the concept of service life for differentiating rust-expansion, cover-cracking, and spalling/delamination (Fig. 1) [27–29]. However, because the corrosion rate can be increased by concrete cracking and spalling, the degree of deterioration is not sequential, on the other hand the rise of rust materials in broken concrete can pack the pores, therefore falling the corrosion rate.

It takes knowledge of the two critical steel corrosion stages in concrete to estimate the service life of reinforced concrete [30].

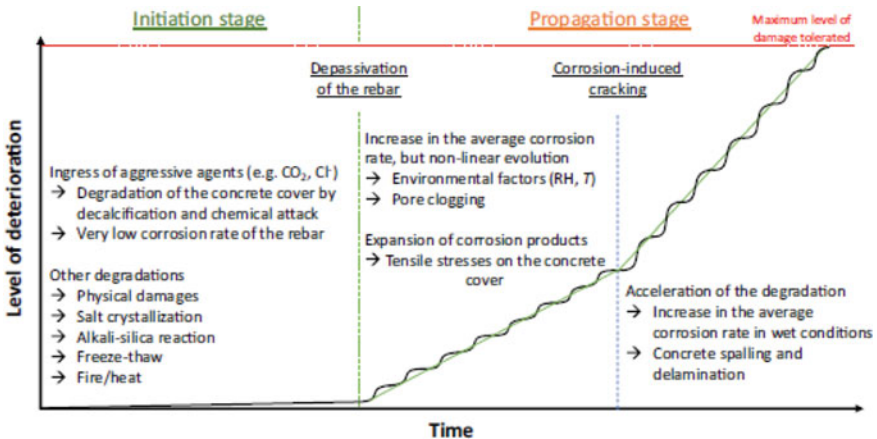


Fig. 1 Schematic representation of RC structures' service life, adapted from the diagram of Tuutii

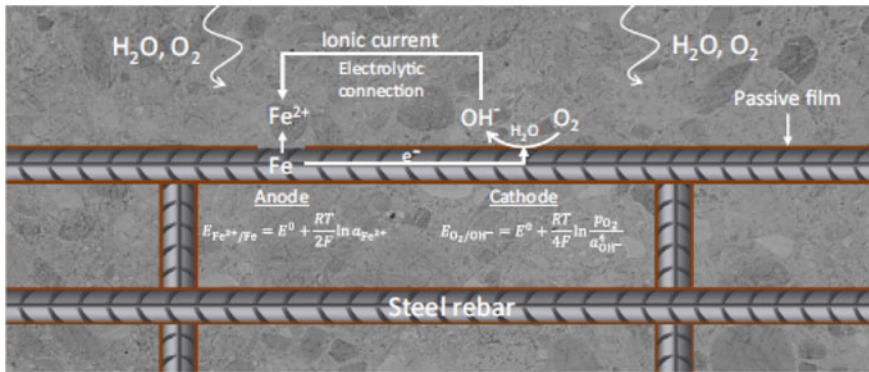


Fig. 2 Schematic depiction of steel corrosion in concrete among the cathodic, anodic sites, including iron oxidation, oxygen reduction, electrical relation, and ionic current

1.2 Thermodynamic, Electro-chemical and Kinetic Corrosion

Steel concrete corrosion is an electro-chemical procedure which involves the iron anodic dissolution, the general oxygen reduction in cathodic [31, 32]. Water/proton reduction can also be observed [33], depending on oxygen availability and steel surface surrounding pH. At last, between cathode and anode electrical connection, an electrolytic atmosphere for the ion transfer in the solutions is needed to transfer electrons. (Fig. 2).

In the Fe/H₂O structure (Pourbaix or potential pH), the concrete fundamental steel corrosion principle can be explained [54]. Species predominance may differ depending on the experimental conditions, i.e. the total temperature and Fe content. Under alkaline conditions, the thin (~15–10 nm) and the passive film formed on the surface of the steel is maintained. In case of passive layer, iron is in the realm of corrosion and passivation (< 0.1 mA cm², “passive rebar”) is slow. Very badly, chronic reinforced concrete corrosion impacts the passive layer durability under conditions that involve CO₂ and Cl⁻. In the corrosion domain, iron differs, resulting in corrosion increase in rate (> 1 mA cm², ‘strongly corroding rebar’), a steady decrease in steel cross sections manufacture of products of corrosion.

2 Mechanisms of Corrosion

2.1 Carbonation

Initiation of corrosion causes various aspects, such as CO₂ intake in the environment, superior diffusion rate in the 70–50% relative humidity range, water dissolution as

carbonic acid, concrete de-calcification, Ca-bearing hydrated phase reaction, pore solution pH reduction, rebar depassivation.

Corrosion propagation.

For RC systems exposed to the environment, the oxidization rate is caused by the content of water and pore size sharing in rebar's surrounding area. Clogging pore.

- In the concrete cover, tensile tension
- Formation of cracks caused by corrosion
- Increase in the mean rate of corrosion
- Spalling and delamination of concrete

2.2 Chloride

- Chloride induces corrosion in the Cl-inflow component from the environment of marine or the salts of de-icing usage, Un equal Cl-infiltration into the material up to the rebar, De-passivation/passivation sequence till the chloride substance is sufficiently more.
- Rebar De-passivation
- Mechanism of Auto catalytic pitting in the vicinity of interfacial air voids, most bottomless pits are typically observed in macrocell formation with more rate of corrosion.

2.2.1 Nature and Reactivity of Corrosion Products and Their Effect on Material Durability

Total oxidation results in oxides of Fe(III), oxy hydroxides being formed, jointly referred to as "rust" with a high oxygen supply. The occurrence of Corrosion Products is largely based on the bar nature and the climate conditions. It functions as a porous electrode, capable of reducing oxygen [34]. Notably, where rust is present, the reduction of O₂ trade current density is higher than a face where a millscale takes place [35]. The decrease in rust, especially FeOOH looked as the iron dissolution-related cathodic-reaction [36].

2.2.2 Electric Procedures for Non-Destructive Monitoring of Corrosion and Assessment

A vital issue for estimating reinforced concrete structures' service life is non-destructive testing (NDT) and evaluation of steel corrosion in the concrete [37]. Among the different approaches, electrical methods make it possible to assess the rate of corrosion, a metric of primary importance at the point of propagation to measure the service life of RC systems. These methods require the use of two, three,

or four electrode combinations of an electrical system to assess three primary parameters: E_{corr} corrosion potential, q concrete resistance, and R_p polarization resistance [38]. The various methods presented in this section are described in Table 1. With their methodology and critical advantages and disadvantages.

Table 1 List of few electrical procedures for the assessment of the corrosion rate of steel in concrete structure, with their main Pros and con

Process	Procedure	Pros and con
Rust half cell	dimension of the probable distance among the reference electrode and a rebar open-circuit located on or embedded in the surface of concrete	<ul style="list-style-type: none"> • Quick calculation • Enable the key deficiency point in a higher risk of the corrosion to be established • No quantitative corrosion rate details • Effects should viewed in possible gradient only • The rebar electrical link is essential • Dimensions should be done on the concrete surface using at least two reference electrodes, and the effects should be evaluated as potential vectors [71–74]
Resistivity (Configuration of wenner)	DC or AC injection among the 2 external electrodes and calculation of the potential difference among the 2 outer electrodes Normal value: 0.01 less than f (kHz) less than 10	<ul style="list-style-type: none"> • Quick calculation • Enable critical flaw points with a more risk of rust to be established • It is possible to estimate the corrosion rate depended on suggestions and similarity with concrete resistivity • No single association among the 2 values could be determined
LPR—linear polarization resistance	Cathodic and anodic path surround the corrosion potential, linear sweep voltammetry Normal parameters: Level of sweep = 10.0 mV/min	<ul style="list-style-type: none"> • Quick calculation • Good agreement in the event of active corrosion with gravimetric loss • The electrical link to the rebar is essential • Another process must measure concrete resistivity to compensate for the ohmic decrease • It is not easy to establish the polarized zone on reinforced concrete construction

(continued)

Table 1 (continued)

Process	Procedure	Pros and con
Electro-chemical impedance spectroscopy (EIS)	Injection and calculation of the final current among the reference electrode and a rebar between the alternating potential among there bar, a counter electrode during Customary values: $E = 10.0$ mV RMS 10^{-3} less than f (Hz) less than 10^5	<ul style="list-style-type: none"> • Effective concurrence in the event of Passive and active corrosion with gravimetric loss • Measurement length is long • It is not easy to establish the polarized zone on Reinforced Concrete construction

2.3 Corrosion Measurement

The measurement is carried out by configuring two electrodes, linking the rebar, the cell 1st and 2nd half, the reference electrode (RE), using a high impedance voltmeter [39]. The process was first cited as the primary test method of ASTM C876 for the uncoated concrete reinforced steel half-cell power. This approach's advantages are to ensure operator safety, particularly in areas that are difficult to access, and to reduce the overall cost of the inspection potentially.

2.4 Analysis and Suggestions Interpretation

As corrosion along the rebar is non-uniform, variations in electro-chemical and potential values among passive areas and actively corroding area are required. Electrical current that passes between these regions will affect the propagation of the material's equipotential lines.

RILEM guidelines [40] and the updated ASTM C876 standard [41] suggest the use of potential gradients for better visibility in a more risk of corrosion area.

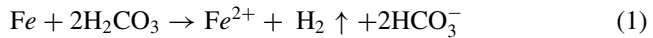
3 Boiler Introduction

The trouble free and efficient operation of steam generators (boilers) is essential while industrial plants generate energy or steam is required for process activities. It is therefore necessary for engineers to know the factors that contribute to the fouling and corrosion of different sections of the boiler and know the techniques that lead to the hassle free operation of steam generator.

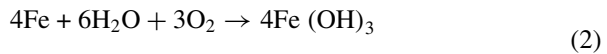
3.1 Corrosion Problems in the Condensate Systems

The steam/condensate systems form an essential part of the water boiler scheme. In the condensate process, everywhere that the steam condenses to form liquid water is used. When the vapour leaves the low-pressure turbine, it contains droplets of water. Consequently, it is not appropriate to expose these materials to corrosion. In the condensing device, the majority of the corrosion content found in the boiler originates. In the condensate environment, high levels of iron oxide are produced. The significant corrosion reactions are the following:

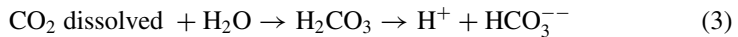
(1) Carbonic acid corrosion:



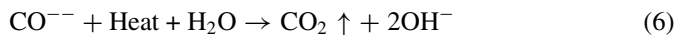
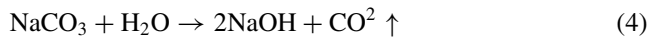
(2) Oxygen corrosion:



Carbon dioxide reacts to form weakly ionized carbonic acid:



The water's pH is lowered, and its corrosivity is elevated. One ppm of dissolved CO_2 can reduce the pH from 6.5 to 5.5. At times, ammonia can be present, forming NH_4OH with water.



3.2 Prevention of Corrosion of Condensate

The subsequent procedure can practice to avoid Condensate system corrosion:

1. Elimination of oxygen and carbon dioxide contamination by mechanical and chemical methods (or minimization). Using deaeration, sodium sulphite above

hydrogen, oxygen is reduced. Demineralization, soda-limes softening, split-stream softening, used to remove carbonate and bicarbonate. The process above also decreases alkalinity.

2. System air leakage to be minimized.

4 Steam Generators Corrosion Issues

4.1 O_2 Corrosion

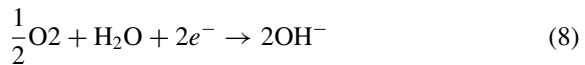
Entire Steam generator structure is typically vulnerable to oxygen-induced oxidation, majorly in the form of pit. Pitting corrosion is caused by superheater tubes due to atmospheric oxygen and concentrated moisture. On superheaters, saturated steam is fired, leaving the steam drum. Bottomless pits are formed in locations wherever moisture is formed. A description of the corrosion mechanism that leads to boiler pitting is given below. In the section on modes of corrosion, the issue of pitting has been extensively discussed.

- (1) In the anodic reaction, Fe is oxidized to Fe^{2+}



Iron is dissolved as a result of this anodic reaction.

- (2) The cathodic reaction is the reduction of oxygen:



Steam Generator (boilers) pitting can be eliminated by below procedures:

- (1) Remove O_2 chemically or mechanically by deaeration. Removing must be performed correctly.
- (2) Raise the boiler water's pH.
- (3) Have a Fe_3CO_4 passive film on the surface of the metal or a chemical film. Depending on the defensive quality of Fe_3CO_4 film ($3Fe + 4H_2O \rightarrow Fe_3O_4 + 4H_2$). Stress corrosion cracking (SCC) is combination of corrosion and pressure.

5 Case Study

A study in real-time corrosion sources identification; testing and providing solution to avoid such kind of situations in the future are discussed. Pipe thickness measured

to identify the corrosion level as below (Fig. 4) at cooling water piping in power plant, Karnataka. If thickness falls below 20% of nominal thickness, then pipe need to replace/ repair. Instead of replacement the anti-corrosive coating can be applied

5.1 Measurement of Pipe Thickness Reference to Corrosion with Ultrasonic Thk. Gauge (TT100)

See Figs. 3, 4, 5 and 6

Product title: Polyglass VEHA (Corrocoat) Vinyl ester/acrylic glass flake, Type A two-pack, for hand use.

Surface preparation Gritblast steel to ISOstandard8501-1 Sa 2.5 near 3/equivalent, priorto usage.

Application 2 or above coats of VEHA polyglass can be added when used alone.



Fig. 3 Pipe thickness measurement



Fig. 4 Pipe thickness measurement



Fig. 5 Cooling water pipe corrosion at power plant



Fig. 6 After CorroKote application on cooling water pipe

5.2 Pot Life

At 20 °C for 60 min. With temperature increases, pot life can decrease dramatically and expand with temperature decreases. For hot climates, inhibitors are available to prolong pot life. The inhibitor is blended long before the catalyst is used.

6 Conclusion

The paper deals with different sources of corrosion, mechanisms of corrosion. The review briefs about corrosion significance in concrete structure of various phases. The various forms of corrosion issues occurred, measuring methods of corrosion and also problems occurred due to corrosion and rectification measures are explored. As a part of the review a typical corrosion issues occur in boilers and the respective methods of avoiding corrosion are also presented. A case study regarding corrosion

effect in industry is also discussed, and the following inferences from above the case study are presented:

From the above study, it is obvious that corrosion has a detrimental impact on the surface of metallic pipes leading to weakening of mechanical properties of the underground structure. Further, stress corrosion leads to surface embrittlement that might lead to catastrophic failure. Further, underground Steel pipes are highly prone to corrosion and immediate failure like bursting, Anti corrosive coatings like cementing, gunneting, wrap coating are few earlier methods that have shown limited improvement. However, in the above case corrocoat has been applied as an anti-corrosive coating that has shown significant amount of corrosion resistance to the environment.

References

1. Yang T, Cui Y, Li Z, Zeng H, Luo S, Li W (2018) Enhancement of the corrosion resistance of epoxy coating by highly stable 3, 4, 9, 10-perylene tetracarboxylic acid functionalized graphene. *J Hazard Mater* 357:475–482. <https://doi.org/10.1016/j.jhazmat.2018.06.038>
2. Mansour RB, Ouzzane M, Aidoun Z (2014) Numerical evaluation of ejector-assisted mechanical compression systems for refrigeration applications. *Int J Refrig* 43:36–49. <https://doi.org/10.1016/j.ijrefrig.2014.04.010>. This
3. Zhou C, Li Z, Li J, Yuan T, Chen B, Ma X, Jiang D, Luo X, Chen D, Liu Y (2020) Epoxy composite coating with excellent anticorrosion and self-healing performances based on multi-functional zeoliticimidazolate framework derived nano containers. *Chem Eng J* 385. <https://doi.org/10.1016/j.cej.2019.123835>
4. Cui M, Ren S, Zhao H, Xue Q, Wang L (2018) Polydopamine coated graphene oxide for anti-corrosive reinforcement of water-borne epoxy coating. *Chem Eng J* 335:255–266. <https://doi.org/10.1016/j.cej.2017.10.172>
5. Montemor MF, Snihirova DV, Taryba MG, Lamaka SV, Kartsonakis IA, Balaskas AC, Kordas GC, Tedim J, Kuznetsova A, Zheludkevich ML, Ferreira MGS (2012) Evaluation of self-healing ability in protective coatings modified with combinations of layered double hydroxides and cerium molybdate nanocontainers filled with corrosion inhibitors. *Electrochim Acta* 60:31–40. <https://doi.org/10.1016/j.electacta.2011.10.078>
6. Hao Y, Liu F, Han EH, Anjum S, Xu G (2013) The mechanism of inhibition by zinc phosphate in an epoxy coating. *Corros Sci* 69:77–86. <https://doi.org/10.1016/j.corsci.2012.11.025>
7. Javidparvar AA, Naderi R, Ramezanzadeh B (2019) Epoxy-polyamide nanocomposite coating with graphene oxide as cerium nanocontainer generating effective dual active/barrier corrosion protection. *Compos Part B Eng* 172:363–375. <https://doi.org/10.1016/j.compositesb.2019.05.055>
8. Chen B, Wu Q, Li J, Lin K, Chen D, Zhou C, Wu T, Luo X, Liu Y, A novel and green method to synthesize a epoxidized biomass eucommia gum as the nanofiller in the epoxy composite coating with excellent anticorrosive performance. *Chem Eng J* 379. <https://doi.org/10.1016/j.cej.2019.122323>
9. Zhang Y, Zhao M, Zhang J, Shao Q, Li J, Li H, Lin B, Yu M, Chen S, Guo Z (2018) Excellent corrosion protection performance of epoxy composite coatings filled with Silane functionalized silicon nitride
10. Nikpour B, Ramezanzadeh B, Bahlakeh G, Mahdavian M (2017) Synthesis of graphene oxide nanosheets functionalized by green corrosion inhibitive compounds to fabricate a protective system. *Corros Sci* 127:240–259. <https://doi.org/10.1016/j.corsci.2017.08.029>
11. Behzadnasab M, Mirabedini SM, Esfandeh M (2013) Corrosion protection of steel by epoxy nanocomposite coatings containing various combinations of clay and nanoparticulate zirconia. *Corros Sci* 75:134–141. <https://doi.org/10.1016/j.corsci.2013.05.024>

12. Shao Y, Jia C, Meng G, Zhang T, Wang F (2009) The role of a zinc phosphate pigment in the corrosion of scratched epoxy-coated steel. *Corros Sci* 51:371–379. <https://doi.org/10.1016/j.corsci.2008.11.015>
13. Sanaei Z, Bahlakeh G, Ramezanzadeh B (2017) Active corrosion protection of mild steel by an epoxy ester coating reinforced with hybrid organic/inorganic green inhibitive pigment, Elsevier B.V. <https://doi.org/10.1016/j.jallcom.2017.09.095>
14. Alezi D, Belmabkhout Y, Suyetin M, Bhatt PM, Weseliński LJ, Solovyeva V, Adil K, Spanopoulos I, Trikalitis PN, Emwas AH, Eddaoudi M (2015) MOF crystal chemistry paving the way to gas storage needs: aluminum-based soc-MOF for CH₄, O₂, and CO₂ storage. *J Am Chem Soc* 137:13308–13318. <https://doi.org/10.1021/ja710973k>
15. Xu AW, Wang X, Wu Y, Li W, Chen C, SC (2018). <https://doi.org/10.1016/j.jhazmat.2018.09.08610.1016/j.jhazmat.2018.09.086>
16. Editors G, Jang BW, Gl'aser R, Liu C, Jang BW, Gl'aser R, Liu C, Capelsanchez MC, Camposmartin JM, Fierro LG, Sci EE, L'eonard A, Rooke JC, Meunier CF, Sarmento H, Descy J, Su B, Harvey BG, Quintana RL, Jae J, Tompsett GA, Lin Y, Torren R, Shen J, Zhang T, Yang B, Charles E, Conner WC, Huber GW (2010) This paper is published as part of an energy & environmental science themed issue on: fuels of the future purification selecting metal organic frameworks as enabling materials in mixed matrix membranes for high efficiency natural gas purification. <https://doi.org/10.1039/c003390c>
17. Ramezanzadeh M, Ramezanzadeh B, Mahdavian M, Bahlakeh G (2020) Development of metal-organic framework (MOF) decorated graphene oxide nanoplateforms for anticorrosion epoxy coatings. *Carbon N Y* 161:231–251. <https://doi.org/10.1016/j.carbon.2020.01.082>
18. Cao K, Yu Z, Yin D, Chen L, Jiang Y, Zhu L (2020) Progress in organic coatings fabrication of BTA-MOF-TEOS-GO nanocomposite to endow coating systems with active inhibition and durable anticorrosion performances. *Prog Org Coat* 143
19. SaadAbou-elazm A, El Mahallawi I, Abdel-Karim R, Rashad R (2009) Failure investigation of secondary superheater tubes in a power boiler. *Eng Fail Anal* 16:433–448
20. Husain A, Habib K (2005) Investigation of tubing failure of superheater boiler from Kuwait desalination electrical power plant. *Desalination* 183:203–208
21. Othman H, Purbolaksono J, Ahmad B (2009) Failure investigation on deformed superheater tubes. *Eng Fail Anal* 16:329–339
22. Ding Q, Tang X-F, Yang Z-G (2017) Failure analysis on abnormal corrosion of economizer tubes in a waste heat boiler. *Eng Fail Anal* 73:129–138
23. Tuutti K (1982) Corrosion of Steel in Concrete, Swedish Cement and Concrete Research Institute, Stockholm
24. Andrade C, Alonso C, Gulikers J, Polder R, Cigna R, Vennesland Ø, Salta M, Raharinaivo A, Elsener B (2004) Test methods for on-site corrosion rate measurement of steel reinforcement in concrete by means of the polarization resistance method. *Mater Struct* 37:623–642
25. Qing Li C (2004) Reliability based service life prediction of corrosion affected concrete structures. *J Struct Eng* 130:1570–1577. [https://doi.org/10.1061/\(ASCE\)0733-9445\(2004\)130:10\(1570\)](https://doi.org/10.1061/(ASCE)0733-9445(2004)130:10(1570))
26. Raupach M (2006) Models for the propagation phase of reinforcement corrosion—an overview. *Mater Corros* 57:605–613. <https://doi.org/10.1002/maco.200603991>
27. Otieno MB, Beushausen HD, Alexander MG (2011) Modelling corrosion propagation in reinforced concrete structures—a critical review. *Cem Concr Compos* 33:240–245. <https://doi.org/10.1016/j.cemconcomp.2010.11.002>
28. Chen D, Mahadevan S (2008) Chloride-induced reinforcement corrosion and concrete cracking simulation. *Cem Concr Compos* 30:227–238. <https://doi.org/10.1016/j.cemconcomp.2006.10.007>
29. Chen F, Baji H, Li C-Q (2018) A comparative study on factors affecting time to cover cracking as a service life indicator. *Constr Build Mater* 163:681–694. <https://doi.org/10.1016/j.conbuildmat.2017.12.120>
30. Alexander M, Beushausen H (2019) Durability, service life prediction, and modelling for reinforced concrete structures—review and critique. *Cem Concr Res* 122:17–29. <https://doi.org/10.1016/j.cemconres.2019.04.018>

31. Isgor OB, Razaqpur AG (2006) Modelling steel corrosion in concrete structures. *Mater Struct* 39:291–302. <https://doi.org/10.1007/s11527-005-9022-7>
32. Hausmann DA (1967) Steel corrosion in concrete. How does it occur? *J Mater Prot* 6:19–23
33. Stratmann M, Müller J (1994) The mechanism of the oxygen reduction on rustcovered metal substrates. *Corros Sci* 36:327–359. [https://doi.org/10.1016/0010-938X\(94\)90161-9](https://doi.org/10.1016/0010-938X(94)90161-9)
34. Hansson CM (1984) Comments on electrochemical measurements of the rate of corrosion of steel in concrete. *Cem Concr Res* 14:574–584. [https://doi.org/10.1016/0008-8846\(84\)90135-2](https://doi.org/10.1016/0008-8846(84)90135-2)
35. González JA, Miranda JM, Otero E, Feliu S (2007) Effect of electrochemically reactive rust layers on the corrosion of steel in a Ca(OH)₂ solution. *Corros Sci* 49:436–448. <https://doi.org/10.1016/j.corsci.2006.04.014>
36. Stefanoni M, Angst U, Elsener B (2015) Local electrochemistry of reinforcement steel—distribution of open circuit and pitting potentials on steels with different surface condition. *Corros Sci* 98:610–618. <https://doi.org/10.1016/j.corsci.2015.06.004>
37. Ji Y, Zhan G, Tan Z, Hu Y, Gao F (2015) Process control of reinforcement corrosion in concrete. Part 1: effect of corrosion products. *Constr Build Mater* 79:214–222. <https://doi.org/10.1016/j.conbuildmat.2014.12.083>
38. Luo D, Li Y, Li J, Lim K-S, Nazal NAM, Ahmad H, Luo D, Li Y, Li J, Lim K-S, Nazal NAM, Ahmad H (2018) A recent progress of steel bar corrosion diagnostic techniques in RC structures. *Sensors* 19:34. <https://doi.org/10.3390/s19010034>
39. Andrade C, Martínez I (2010) Techniques for measuring the corrosion rate (polarization resistance) and the corrosion potential of reinforced concrete structures. *Non-Destructive Eval Reinf Concr Struct*, 284–316. <https://doi.org/10.1533/9781845699604.2.284>
40. Pour-Ghaz M, Isgor OB, Ghods P (2009) Quantitative interpretation of half-cell potential measurements in concrete structures. *J Mater Civ Eng* 21:467–475. [https://doi.org/10.1061/\(ASCE\)0899-1561\(2009\)21:9\(467\)](https://doi.org/10.1061/(ASCE)0899-1561(2009)21:9(467))
41. Elsener B, Andrade C, Gulikers J, Polder R, Raupach M (2003) Half-cell potential measurements—potential mapping on reinforced concrete structures. *Mater Struct* 36:461–671
42. ASTM C876–09, Standard test method for corrosion potentials of uncoated reinforcing steel in concrete. <https://www.astm.org/Standards/C876.htm>

Comparative Analysis of Hybrid Renewable Energy System Using Homer: A Case Study of Silchar, India



Anil Kumar Singh Maisanam, Agnimitra Biswas,
and Kaushal Kumar Sharma

Abstract The decentralization of power is nowadays gaining wide acceptability due to its economic benefits. However, using a single renewable source for electricity generation makes the system unreliable as the availability of renewable energy sources is highly nonuniform. Therefore, two or more renewable energy sources can be integrated along with a suitable energy storage unit to improve reliability, make the system economic, and increase efficiency. The selection of energy sources for a standalone application depends on the locally available renewable sources. Hence, in this study, 2 different hybrid systems are designed and compared considering the total net present cost (TNPC) and loss of power supply probability (LPSP) to investigate the performance of these systems. For optimal sizing of the hybrid system, the HOMER software package is used as it is simple, easy to use, and widely accepted. The design variables considered are the number of PV panels, wind turbines units, biogas generator power, and the storage unit capacity. It is found that the PV-BG-PHS system is better when compared to PV-WT-PHS on a techno-economic basis.

Keywords Hybrid renewable energy system · HOMER · Net present cost · Loss of power supply probability

1 Introduction

Energy insecurity is a major hurdle to the region's rapid growth. In a developing country like India, electrification of the rural area is very important to improve the quality of life and increase the job opportunities in rural areas. However, due to the

A. K. S. Maisanam (✉) · A. Biswas · K. K. Sharma
Mechanical Engineering, National Institute of Technology, Silchar, India
e-mail: maisanam_rs@mech.nits.ac.in

A. Biswas
e-mail: agnibis@mech.nits.ac.in

K. K. Sharma
e-mail: kks@mech.nits.ac.in

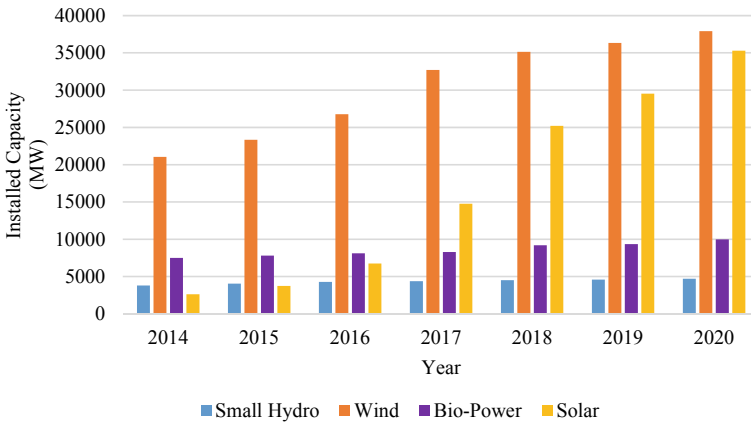


Fig. 1 Renewable energy installed capacity and their composition

difficult terrain as well as the high cost involved in grid extension, 100% electrification is still a challenge [1]. Power decentralization is one of the solutions to address the problem, and increasing the utilization of renewable energy sources is a vital step towards it. However, the penetration of renewable energy systems is still a challenge as the availability of renewable energy is highly nonuniform, which decreases the reliability of renewable energy systems [2]. Therefore, a standalone system where more than one renewable energy resource is integrated has the potential to improve reliability and make the system economic and efficient [3]. To design HRES, optimal sizing of various components is essential to avoid over-sizing of the system. Various combinations of renewable energy sources were used to analyze the efficiency of the HRES. The most common renewable energy used for the generation of electricity is solar and wind energy. The installed capacity of different types of renewable energy is presented in Fig. 1, and it is observed that solar and wind energy is the major contributor to renewable energy generation. However, the availability of such energy sources is highly location specific which makes the selection a difficult task.

The sizing of HRES can be performed using a software package or by using evolutionary algorithms. Due to multiple advantages of the HOMER software package, for the present work, the performance analysis of the hybrid system is carried out in it. HOMER is a software package that involves planning, designing, and optimization standalone energy systems [4]. This tool can perform component sizing of both grid-connected and off-grid power systems [5]. Simulation, optimization, and sensitivity analysis are the three main features of HOMER software [6]. It is attractive, user-friendly GUI, and simple to use feature which makes the package very handy. It does not necessitate any know-how of programming languages due to which it is used widely in the energy system design. Moreover, the different time step options and optimization through sensitivity analysis using limited input are one of its added features which makes it a suitable optimization tool [7, 8].

Numerous study of HRES optimization via HOMER software is available. Ahmed et al. [9] investigated the feasibility of a megawatt-scale HRES consisting of photovoltaic (PV), biogas (BG), and wind turbine (WT) for electrification of Kallar Kahar in Pakistan. The proposed energy mix of PV-WT-BG was found commercially viable although certain factors such as political will, regulatory issues, and availability of potential investors can be a challenge to such a megawatt-scale project which requires multimillion-dollar investments [9]. Mehrpooya et al. [10] investigated diesel–battery system, PV-battery system, PV-hydrogen storage system, diesel system considering technical, financial, and environmental parameters. Their analysis concludes that the sizing of the PV system increases when the diesel system is replaced by a battery system; however, HRES has an economic advantage over conventional systems owing to environmental factors. Rajbongshi et al. [11] studied HRES integrated with the electricity grid to improve the reliability and quality. Further, the analysis also included the determination of breakeven distance, which gives a different dimension in the hybrid system selection problem. Finally, the study concluded that grid-connected HRES is more economic than off-grid HRES. Shahzad et al. [12] investigated the feasibility of a hybrid system considering technical and economic parameters. Their study mainly contributed towards meeting the residential as well as an agricultural load of a rural area in Pakistan. Ali and Shania [13] designed an off-grid HRES for a West Australian town considering economic and sustainability factors. Further, a comparison between the energy cost of HRES and the conventional system is carried out which shows that an optimized combination of DG-PV-WT-BES can provide electricity at a competitive price. Singh and Baredar [14] studied HRES system consisting of PV, BG, and fuel cell and found that varying load demand can be successfully met using the proposed system. Many other studies are available in the literature, which focuses on the design of reliable, economic, and sustainable HRES [8, 15–19]. Various literature can be found which deals with the optimization of different types of load such as a village load, agricultural load [12], telecommunication station load [20], and water supply station load [21] which are available. However, a comparison of various locally available renewable energy resources for HRES design needs to be explored which has been ignored in most of the studies. Therefore, the present work is performed by choosing the renewable energy options which are commonly used to design renewable energy systems. Hence, two different hybrid system designs are conceptualized considering wind, solar, and biomass energy and their technical and economic performance are analyzed in HOMER software package. Finally, the best combination of HRES is determined and the optimal HRES size is determined.

2 Detail Load Demand of the Site

The site is located at the Borakhai division 2 village, near the National Institute of Technology Silchar (NITS), Assam, India. The region is 25 m above the sea level, and the average temperature varies from 21 to 32 °C. The people living in this village

mainly depend on farming. A cluster of 63 houses is present in the location, and there is a lower primary school. The load demand of a typical house and the school is simulated as shown in Table 1. According to the different load demand during a year, four types of load patterns have been generated which are presented in Fig. 2.

Table 1 Estimated load demand data

Energy consumption sector	Electrical equipment	Power rating (W)	No. of units	Operating hour per day (h/day)			
				Pattern I (Mar–Jun)	Pattern II (Jul–Sept)	Pattern III (Oct–Nov)	Pattern IV (Dec–Feb)
Domestic load—residential load (A)	LED bulb	12	3	6	5	7	8
	Fan	75	2	15	16	11	0
	Mobile charging point	10	2	2	2	2	2
	TV	55	1	11	10	9	15
				Apr-sept	Summer break	Winter break	Dec–Feb
Community load—School (B)	Florescent tube light	40	11	4	1	1.5	4.5
	Fan	75	11	5.5	2	0	0
	Pump	3730	1	2	1	1	2

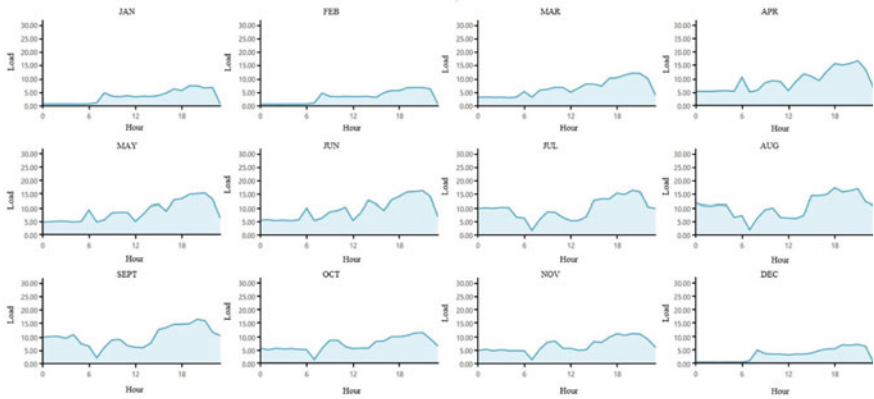


Fig. 2 Monthly average load demand curve

3 Description of System Components

The hybrid system consists of four main components, i.e. two generating components, one inverter, and one storage unit. Reliability is a major challenge in the penetration of such systems, and hence a storage unit is integrated to improve that. The reason behind the integration of a storage unit with an hybrid system is to integrate into the HRES to improve the overall reliability of the system. Details of the various components of HRES considered in the present study are discussed in the subsequent section.

3.1 Solar Photovoltaic

Solar photovoltaic (PV) panels are the devices used to convert solar energy into electricity. The PV power output at a location is directly proportional to the available solar radiation intensity, so the location-specific solar energy data are taken from the author’s earlier published work [22] and are represented in Fig. 3. Using the above data, the PV output is calculated in HOMER software as given below:

$$P_{pv}(t) = Y_{pv} f_{pv} \left(\frac{I_{\text{tilt}}(t)}{I_{\text{STC}}} \right) [1 + \beta_T (T_{\text{cell}}(t) - T_{\text{cell_STC}})] \tag{1}$$

where Y_{pv} is the rated capacity of the PV (kW), f_{pv} is the derating factor (%), $I_{\text{tilt}}(t)$ is the incident radiation at instant ‘t’, I_{STC} is the irradiation intensity at standard test condition, β_T is the PV temperature coefficient (%/°C), $T_{\text{cell_STC}}$ is the PV cell temperature at 25 °C, and $T_{\text{cell}}(t)$ is the PV cell temperature at any instant ‘t’ which is given by:

$$T_{\text{cell}}(t) = T_{\text{amb}} + \left(\frac{\text{NOCT} - 20}{0.8 \times I_{\text{STC}}} \right) \times I_{\text{tilt}}(t) \tag{2}$$

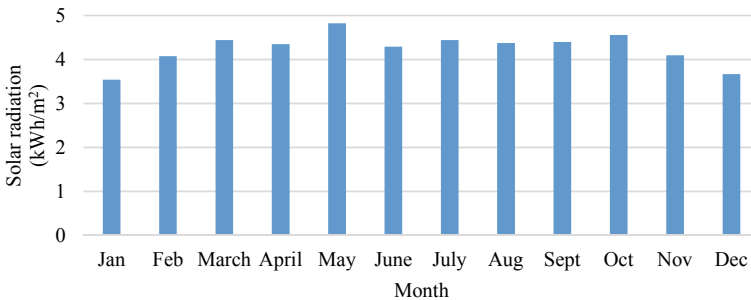


Fig. 3 Monthly averaged solar radiation data

where T_{amb} is the average temperature and NOCT is the nominal operating cell temperature.

3.2 Wind Turbine

The wind turbine is the device, which converts wind energy into electrical energy. In the HOMER software, the power output of a wind turbine is determined in three steps. First, the wind speed at a certain hub height is calculated. Wind speed calculation can be performed using either the logarithmic law or the power law. The mathematical equations used are expressed as:

$$U_{hub} = U_{anem} \frac{\ln(Z_{hub}/Z_0)}{\ln(Z_{anem}/Z_0)} \tag{3}$$

$$U_{hub} = U_{anem} \left(\frac{Z_{hub}}{Z_{anem}} \right)^\alpha \tag{4}$$

Second, the amount of power produced at standard air density is determined. Finally, the adjusted power is calculated using the actual air density data. The wind turbine power output is expressed as follows:

$$P_{WTG} = \left(\frac{\rho}{\rho_0} \right) \cdot P_{WTG_STP} \tag{5}$$

The wind energy potential of the location is presented in Fig. 4.



Fig. 4 Wind speed data

3.3 Biogas Generator

In this study, a generic biogas generator is considered which produces an AC output. The lifetime of the generator is taken as 15,000 h and the overall conversion efficiency as 21% [22]. The power generated is calculated as given below:

$$E_{bg}(t) = \eta_{bg} \times \frac{CV_{bg}}{CF} \times F_{bg}(t) \quad (6)$$

where η_{bg} is the conversion efficiency, CV_{bg} is the calorific value of the biogas (kJ/m^3) which is 4700 kcal/m^3 , CF is the conversion factor (860) for converting kcal to kWh, and $F_{bg}(t)$ is the rate of fuel consumption (m^3/h).

3.4 Pumped Hydro Storage

Pumped hydro storage (PHS) is the most mature and reliable technology available for energy storage. In this system, water is stored at a certain height using the excess amount of energy generated from solar PV. Whenever there is low energy production, the stored water is allowed to pass through the turbine which generates energy. The amount of energy stored in the PHS is given by:

$$P_{phs} = \rho g Q H \eta_{gen} \quad (7)$$

where ρ is the density of the working fluid, i.e. water (1000 kg/m^3), g is the acceleration due to gravity (m/s^2), Q is the mass flow rate (m^3/s), H is the head of the water, and η_{gen} is the efficiency of the generator.

3.5 Converter

PV output is obtained in the form of DC but the load demand is AC. Therefore, an inverter is required for the conversion of AC into DC. The lifetime and the inverter efficiency are taken as 20 years and 90% [22]. The choice of converter size depends on the peak load. The rating of an inverter is generally determined using the following relationship:

$$P_{conv} = \frac{P_{peak}}{\eta_{inv}} \quad (8)$$

where P_{peak} is the peak load demand (kW) and η_{inv} is the inverter efficiency.

4 Criteria Considered for Homer Analysis

In the present study, the techno-economic performance of HRES has been evaluated. The technical parameter considered in this study is known as the loss of power supply probability (LPSP). The economic parameter considered in this study is known as the total net present cost. A detailed discussion of these parameters is included in the subsequent section.

4.1 Loss of Power Supply Probability

Loss of power supply probability (LPSP) is the ratio of the total unmet load to the load demand. It is given by:

$$\text{LPSP} = \frac{\sum_{t=1}^T \text{LPS}(t)}{\sum_{t=1}^T E_{\text{load}}} \quad (9)$$

where LPSP is the loss of power supply and E_{load} is the total load demand.

4.2 The Total Net Present Cost

The total net present cost (TNPC) of a system can be defined as the cost of all the components of the system converted to its present value that it incurs during its operational life, subtracting the present value of revenue it generates over its lifetime. Costs include capital costs, operation and maintenance costs, replacement costs, emissions penalties, fuel costs. Revenues include salvage value of the components and total energy units sold to grid. The TNPC is calculated in HOMER software as given below:

$$C_{\text{TNPC}} = \frac{C_{\text{TAC}}}{\text{CRF}} \quad (10)$$

where C_{TAC} is the total annualized cost of the system and CRF is the capital recovery factor and is given by:

$$\text{CRF} = \frac{i(1+i)^N}{(1+i)^N - 1} \quad (11)$$

where i is the annual interest rate and N is the project life.

4.3 Levelized Cost of Energy

Levelized cost of energy (LCOE) can be defined as the ratio of the annualized cost of the system and the total energy served during the year, which can be given as:

$$LCOE = \frac{TAC}{\text{Total energy served}} \tag{12}$$

5 Results and Discussions

The HRES configurations compared in the present study are shown in Fig. 5. The techno-economic performance of the two systems has been analyzed. Figure 5a represents the HRES system consisting of PV, biogas, and PHS as the storage unit, and Fig. 5b represents the system consisting of PV, wind turbine, and PHS system. For the analysis, the project lifetime is considered to be 25 years, it is assumed that all the system components serve their full life, the capacity shortage is considered to be 2%, discount rate, and the inflation rate is considered as 6% and 4%, respectively.

The two-system configuration is analyzed in the HOMER software using the technical and economic details given in Table 2. The optimal configuration of PV-BG-PHS is found to be 64.4 PV, 8 kW BG, 3 strings of PHS, and a 21.6 kW converter. The total energy produced from PV is 85467 kW h/year, and BG produces 16605 kW h/year. The excess energy production is found to be 13881 kW h/year, and the unmet load is 31.1 kW h/year. The cost summary of the PV-BG-PHS system is presented in Table 3. The state of charge (SOC) of the PHS is also presented in Fig. 6. It can be observed that during the initial months of January–March, the SOC of PHS

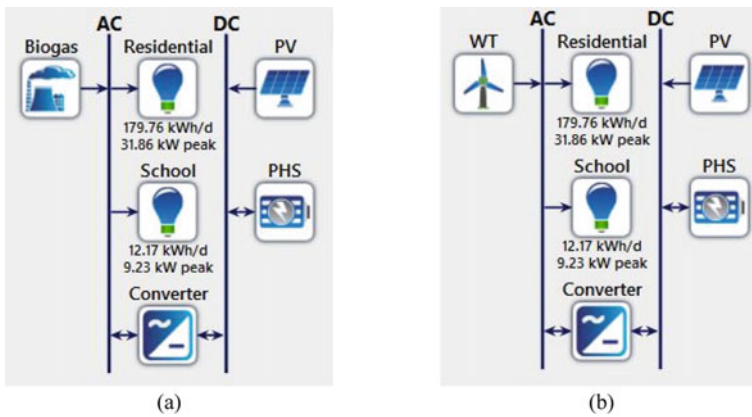


Fig. 5 HRES system configurations a PV-BG-PHS and b PV-WT-PHS

Table 2 Technical and economic data of HRES components [16, 22]

Component	Specification	Value
PV panel	Power rating	1 kW
	Derating factor	88%
	Capital cost	1200 (\$/kW)
	Operation and maintenance cost	4 (\$/year)
	Life time	25 years
Wind turbine	Power rating	1 kW
	Hub height	50 m
	Overall efficiency	26%
	Lifetime	20 years
	Capital cost	2300 (\$/kW)
	Operation and maintenance cost	2 (\$/year)
	Replacement cost	1500 (\$/kW)
Biogas generator	Overall efficiency	21%
	Calorific value of biogas	5.47 kW h/m ³
	Cost of fuel	5 (\$/ton)
	Capital cost	2300 (\$/kW)
	Operation and maintenance cost	2 (\$/year)
	Replacement cost	1500 (\$/kW)
	Lifetime	15,000 h
Converter	Inverter efficiency	90%
	Lifetime	20 years
	Capital cost	465 (\$/kW)
	Operation and maintenance cost	1 (\$/year)
	Replacement cost	465 (\$/kW)
Pumped hydro storage	Capital cost	3256 (\$/kW)
	Operation and maintenance cost	3 (\$/year)
	Lifetime	35 years

fluctuates between 80 and 100% as during the winter months energy demand drops. As the energy demand increases during the summer months, discharge from the PHS system takes place frequently which can be observed in Fig. 6.

The optimal HRES size consisting of the PV-WT-PHS is found to be 80 kW PV, 1 kW WT, 39 strings of PHS, and a 28 kW converter. The total generation from the hybrid system is observed to be 106,396 kW h/year, out of which the PV system

Table 3 Cost summary of PV-BG-PHS system

Components	Capital cost (\$)	Replacement cost (\$)	O and M cost (\$)	Fuel Cost (\$)	Salvage value (\$)	Total (\$)
BG	18400.00	37888.00	31026.04	3789.27	0.00	91,103.31
PV	1,48,014.47	0.00	3327.76	0.00	0.00	1,51,342.22
Converter	10067.22	3209.50	279.88	0.00	-1,808.76	11,747.84
PHS	9,768.00	0.00	116.35	0.00	0.00	9,884.35
Total	1,86,249.69	37560.62	30437.40	3257.41	-4,872.23	2,52,632.89

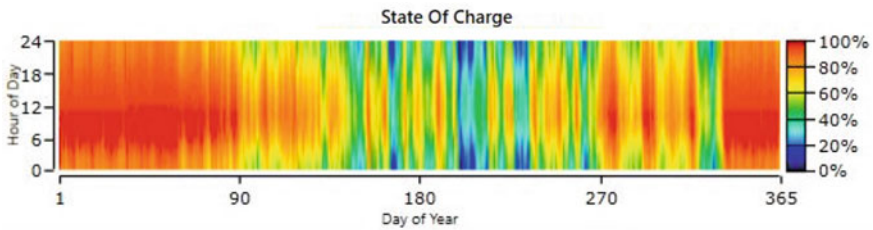


Fig. 6 State of charge of the storage unit during a year

contributes 99% and the remaining 1% is produced by the wind turbine system. Such low energy generation is due to the low wind speed potential of the location. For this system, the amount of excess electricity produced is 16330 kW h/year and the unmet load is 14.4 kW h/year. The capacity shortage is found to be 0.0951%. The state of charge of the PHS system is presented in Fig. 7, and it is observed that the charge–discharge trend is similar to the PV-BG-PHS system. The detailed cost summary of the hybrid system is given in Table 4.

The comparison of both the systems in terms of their technical and economic parameters shows that PV-BG-PHS is better sized and economic. It is observed that using PV-BG-PHS generates energy at 0.279 \$/kW h, whereas the PV-WT-PHS system generates the same energy at 0.375 \$/kW h. This happens due to low wind energy potential which in turn over sizes the PV system and PHS unit which leads



Fig. 7 State of charge of PHS for PV-WT-PHS configuration

Table 4 Cost summary of PV-WT-PHS system

Components	Capital cost (\$)	Replacement cost (\$)	<i>O</i> and <i>M</i> cost (\$)	Fuel cost (\$)	Salvage value (\$)	Total (\$)
WT	6900	2199.7	77.57	0.00	-1239.71	7937.62
PV	1,84,000.00	0.00	4136.81	0.00	0.00	1,88,136.81
Converter	13,003.33	4145.56	361.51	0.00	-2336.29	15,174.10
PHS	1,26,984.00	0.00	1,512.52	0.00	0.00	1,28,496.52
Total	3,30,887.33	6345.33	6,088.40	0.00	-3576.00	3,39,745.05

Table 5 Comparison of simulation results

Configuration	PV size (kW)	WT size (kW)	BG (kW)	Converter size (kW)	PHS string	LCOE (\$/kW h)
PV-WT-PHS	80	3	-	28	39	0.375
PV-BG-PHS	64.4	-	8	21.6	3	0.279

to a high cost of generation. The comparison of the system sizing and LCOE of both the system is presented in Table 5.

6 Conclusion

In this study, two HRES systems, i.e., PV-BG-PHS and PV-WT-PHS, have been compared considering their performance based on technical and economic criteria. It has been observed that for this specific location PV-BG-PHS is more beneficial than the PV-WT-PHS system while optimizing the PV-WT-PHS system higher cost is observed mainly due to the oversizing of the system. Oversizing occurs in this system due to low wind turbine energy production which is due to low wind energy availability at this particular location. Therefore, these results can be very useful while implementing such a renewable energy project in the location. This study presents the feasibility of the HRES project, and thus it will also make the decision-making process easier before investing in such projects in this area.

References

1. Adefarati T, Bansal RC (2019) Reliability, economic and environmental analysis of a microgrid system in the presence of renewable energy resources. *Appl Energy* 236:1089–1114. <https://doi.org/10.1016/j.apenergy.2018.12.050>
2. Nagapurkar P, Smith JD (2019) Techno-economic optimization and social costs assessment of microgrid-conventional grid integration using genetic algorithm and artificial neural networks:

- a case study for two US cities system advisor model supplementary information document. *J Clean Prod* 229:552–569. <https://doi.org/10.1016/j.jclepro.2019.05.005>
3. Janghorban Esfahani I, Ifaei P, Kim J, Yoo CK (2016) Design of hybrid renewable energy systems with battery/hydrogen storage considering practical power losses: a MEPoPA (modified extended-power pinch analysis). *Energy* 100:40–50. <https://doi.org/10.1016/j.energy.2016.01.074>
 4. Connolly D, Lund H, Mathiesen BV, Leahy M (2010) A review of computer tools for analysing the integration of renewable energy into various energy systems. *Appl Energy* 87:1059–1082. <https://doi.org/10.1016/j.apenergy.2009.09.026>
 5. Bahramara S, Moghaddam MP, Haghifam MR (2016) Optimal planning of hybrid renewable energy systems using HOMER: a review. *Renew Sustain Energy Rev* 62:609–620. <https://doi.org/10.1016/j.rser.2016.05.039>
 6. Kumar P, Deokar S (2016) Optimal design configuration using HOMER. *Int Conf Emerg Trends Eng Sci Technol* 24:499–504. https://doi.org/10.1007/978-981-10-4762-6_9
 7. Zahboun H, Zouggar S, Krajacic G, Varbanov PS, Elhafyani M, Ziani E (2016) Optimal hybrid renewable energy design in autonomous system using modified electric system cascade analysis and homer software. *Energy Convers Manage* 126:909–922. <https://doi.org/10.1016/j.enconman.2016.08.061>
 8. Amutha WM, Rajini V (2016) Cost benefit and technical analysis of rural electrification alternatives in southern India using HOMER. *Renew Sustain Energy Rev* 62:236–246. <https://doi.org/10.1016/j.rser.2016.04.042>
 9. Ahmad J, Inran M, Khalid A, Iqbal SW, Rehan S, Adnan M et al (2018) Techno economic analysis of a wind-photovoltaic-biomass hybrid renewable energy system for rural electrification: a case study of Kallar Kahar. *Energy* 148:208–234. <https://doi.org/10.1016/j.energy.2018.01.133>
 10. Mehrpooya M, Mohammadi M, Ahmadi E (2018) Techno-economic-environmental study of hybrid power supply system: a case study in Iran. *Sustain Energy Technol Assess* 25:1–10. <https://doi.org/10.1016/j.seta.2017.10.007>
 11. Rajbongshi R, Borgohain D, Mahapatra S (2017) Optimization of PV-biomass-diesel and grid base hybrid energy systems for rural electrification by using HOMER. *Energy* 126:461–474. <https://doi.org/10.1016/j.energy.2017.03.056>
 12. Shahzad MK, Zahid A, Rashid T, Rehan MA, Ali M, Ahmad M (2017) Techno-economic feasibility analysis of a solar-biomass off grid system for the electrification of remote rural areas in Pakistan using HOMER software. *Renew Energy* 106:264–273. <https://doi.org/10.1016/j.renene.2017.01.033>
 13. Ali L, Shahnia F (2017) Determination of an economically-suitable and sustainable standalone power system for an off-grid town in Western Australia. *Renew Energy* 106:243–254. <https://doi.org/10.1016/j.renene.2016.12.088>
 14. Singh A, Baredar P (2016) Techno-economic assessment of a solar PV, fuel cell, and biomass gasifier hybrid energy system. *Energy Rep* 2:254–260. <https://doi.org/10.1016/j.egyr.2016.10.001>
 15. Salehin S, Ferdaous MT, Chowdhury RM, Shahid S, Ro MSRB, Asif M (2016) Assessment of renewable energy systems combining techno-economic optimization with energy scenario analysis. *Energy* 112:729–741. <https://doi.org/10.1016/j.energy.2016.06.110>
 16. Bhatt A, Sharma MP, Saini RP (2016) Feasibility and sensitivity analysis of an off-grid micro hydro—photovoltaic—biomass and biogas—diesel—battery hybrid energy system for a remote area in Uttarakhand state. *India Renew Sustain Energy Rev* 61:53–69. <https://doi.org/10.1016/j.rser.2016.03.030>
 17. Canales FA, Beluco A, Canales FA, Beluco A (2014) Modeling pumped hydro storage with the micropower optimization model (HOMER) Modeling pumped hydro storage with the micropower optimization model (HOMER). *J Renew Sustain Energy* 6:043131–043212. <https://doi.org/10.1063/1.4893077>
 18. Haghight A, Alberto S, Escandon A, Naja B, Shirazi A, Rinaldi F (2016) Techno-economic feasibility of photovoltaic, wind, diesel and hybrid electrification systems for off-grid rural

- electrification in Colombia. *Renew Energy* 97:293–305. <https://doi.org/10.1016/j.renene.2016.05.086>
19. Shezan SKA, Julai S, Kibria MA, Ullah KR, Saidur R, Chong WT, et al. (2016) Performance analysis of an off-grid wind-PV-diesel-battery hybrid energy system feasible for remote areas. *J Clean Prod* 125. <https://doi.org/10.1016/j.jclepro.2016.03.014>
 20. Junaid M, Kumar A, Mathew L (2017) Techno economic feasibility analysis of different combinations of PV-wind-diesel-battery hybrid system for telecommunication applications in different cities of Punjab. *India Renew Sustain Energy Rev* 76:577–607. <https://doi.org/10.1016/j.rser.2017.03.076>
 21. Maisanam AKS, Podder B, Biswas A, Sharma KK (2019) Site-specific tailoring of an optimal design of renewable energy system for remote water supply station in Silchar, India. *Sustain Energy Technol Assess* 36:100558. <https://doi.org/10.1016/j.seta.2019.100558>
 22. Singh S, Singh M, Chandra S (2016) Feasibility study of an islanded microgrid in rural area consisting of PV, wind, biomass and battery energy storage system. *Energy Convers Manage* 128:178–190. <https://doi.org/10.1016/j.enconman.2016.09.046>

Impact of Wall Fuel and Air Injections Inside the Parallel Fuel Injection-Based Scramjet Combustor: A Numerical Analysis



Kumari Ambe Verma, Kaushal Kumar Sharma,
and Krishna Murari Pandey

Abstract Air breathing engines (Scramjet) are taking more attention in the current research era because of its weight to thrust ratio. Brayton cycle is used to complete the thermodynamic processes just like other gas turbine engines. The engine consumes atmospheric high speed air as oxidizer. Due to this restriction of the engine, it cannot work beyond the atmosphere. To comprehend the impact of innovative transverse fuel injector on the combustor wall has been introduced. Two distinct models are involved. Parallel fuel injection with wall fuel injection in DLR Scramjet model and one additional wall air injector ahead of the wall fuel injector in the same model have been introduced to compare and understand the greater performance. Moreover, distance between wall fuel and air injector has also been compared. Ansys 14.0 Fluent-based solver has been chosen to perform analysis on all the selected model. Two-dimensional computational combustor model is utilized to complete the analysis. DLR scramjet combustor dimensions are considered for the investigation. The present article analyzed all the cases and found that the mixing behavior of the fuel with incoming free stream air approaches toward 100% in all cases. The improved performance is achieved by introducing only wall air injector just after the wall fuel injector. The maximum combustion efficiency has been reached up to 93.1%.

Keywords Transverse fuel and air injection strategy · Parallel fuel injection · Wedge shaped strut · Combustor performance · DLR scramjet combustor

1 Introduction

High speed aerospace vehicle is more widely used for various applications. Among all the engines, Scramjet [1] taking more attention due to its engine specification that often leads to higher thrust to weight ratio. The process involved while completing the thermodynamic processes of the scramjet engine is Brayton cycle [2], similar

K. A. Verma · K. K. Sharma · K. M. Pandey (✉)

Department of Mechanical Engineering, National Institute of Technology Silchar, Silchar
Assam-788010, India

e-mail: kmpandey2001@yahoo.com

to all other type of gas turbine engines. As the speed and altitude of the vehicle is very high because the engine does not carry extra load of oxygen tank. It consumes atmospheric high speed air for the purpose of oxidizer. Due to this restriction of the engine, it cannot work beyond the atmosphere. The inside geometry of the scramjet engine is very different [3–5] from the other flying engines. The engine does not contain any moving and rotating part to change the properties of the flow field. Hence, the parametric variations in the geometry and the strategy to enter the fuel inside the combustor are two key points to improve the combustor performance [6, 7]. Gerdroodbary et al. [8] examined the transverse fuel injection characteristics by adding additional multi-air jets. Sixteen multi-jets arrangement was identified best suitable for mixing. Gugulothua and Nutakki [9] examined the flow field behavior of transverse fuel injection. Modified strut was introduced to explore the combustion performance by Aravind and Kumar [10] with the help of numerical investigation. The author identified shorter mixing length by changing the geometrical arrangement of parallel fuel injector. Hence, the behavior of the combustor can easily be visualized with the help of contour plots of density and Mach number. To explore the performance part, combustion efficiency and mixing efficiency plots have been summarized at many number of cross-sectional distance from the entrance to create a continuous plot of all performance outcome. 2D compressible Reynolds-Averaged Navier–Stokes (RANS) equation has been chosen to solve all the governing equations. $K-\omega$ two-equation (SST) Turbulence model is used to solve the supersonic behavior of flow field. To diminish the computational time with acceptable outcome, single-step chemical reaction is followed. Before doing computational work for all the selected cases, validation is performed by taking the exact experimental data [11, 12]. The detailed analysis has been performed with the help of wall pressure contours and middle section velocity contour plots. Nonetheless, experimental shadowgraph image has also been compared by using density and pressure plots. All the comparison shows good agreement with the experimental work.

The impact of parametric variation of strut fuel injection [13, 14]-based scramjet combustor in addition with novel wall fuel entry scheme has been explored with the help of computational fluid dynamics by the same author [15] and to comprehend more the effect of location of wall transverse fuel injector has also been discovered [16]. In the present work, two distinct models are involved. Combination of both fuel, i.e. parallel and wall fuel injection strategy has been completed in first model, and one additional wall air injector ahead of the wall fuel injector has been introduced in other model to compare and understand the greater performance. Moreover, distance between wall fuel and air injector has also been compared.

2 Experimental Detail of DLR-Scramjet Combustor

The strut-based scramjet combustor was first reported by Waidmann et al. [11, 12]. The author explained the combustion processes and gas dynamics while performing all the cyclic processes involved. The schematics of combustor are shown in Fig. 1.

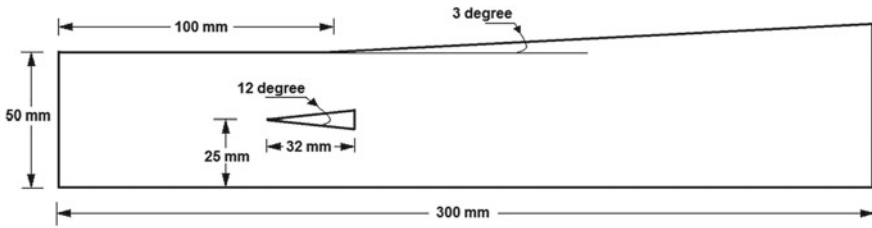


Fig. 1 Schematic of scramjet computational combustor

Two subsequent sections are attached starting with constant cross-sectional area of 50×40 mm and another section is having three degree of divergence at the top wall. Fuel entrainment is done with the help of 1 mm diameter of hole in front of wedge shaped strut face. The exactly same computational model is utilized in the present article.

3 Computational Combustor Model and Mesh Generation

In order to start investigation of the high speed combustion in the selected DLR model. The geometrical parameters are shown in Fig. 1. The influence of the turbulence mixing and their impacts are found near and ahead the fuel injector, i.e. wedge shaped strut. Hence, the refined meshing has been created near to this area. The selection of the final grid is found by improving the element size. The refined grid generation model is shown in Fig. 2. All the computational geometry and mesh generation are executed in the Ansys 14.0 Fluent software [17]. In the present work, the wall fuel injection strategy has been implemented and also wall fuel and air injectors are executed to explore the behavior of both. The diameter of the selected wall fuel and air injector is 1 mm.

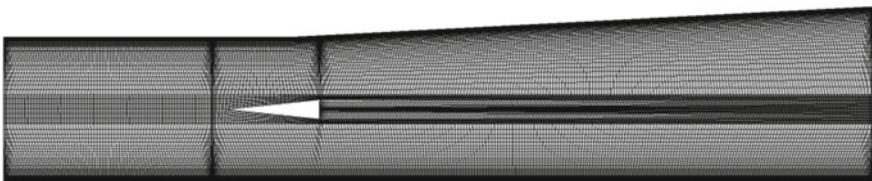
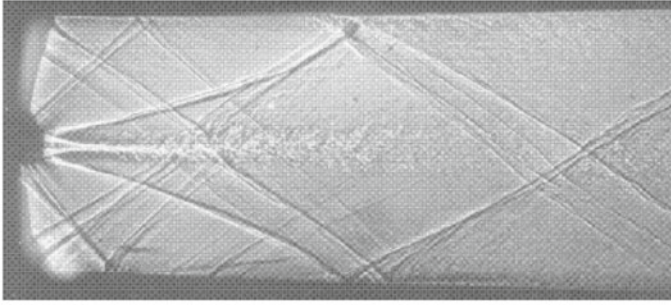
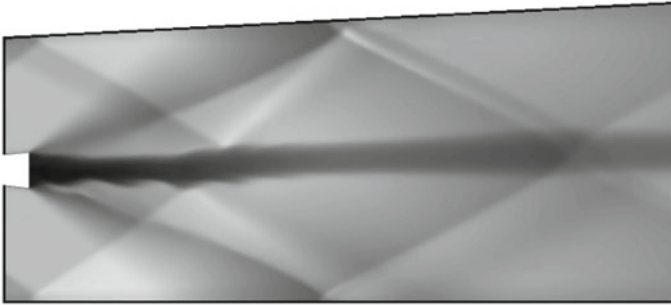


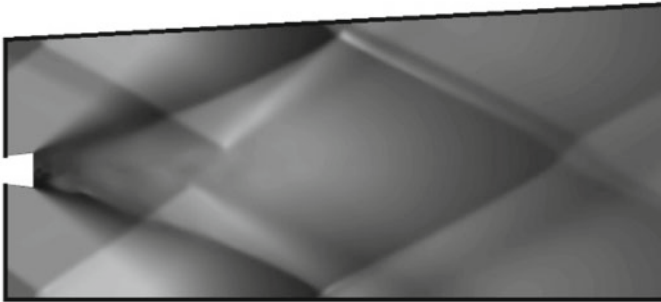
Fig. 2 Meshing of computational model



(a)



(b)



(c)

Fig. 3 a Experimental schlieren image, b computational density contour and c computational pressure contour

4 Computational Simulation Details

The computational examination has been achieved by using computational fluid dynamic approach in Ansys 14.0 [17]. The detailed selection of the numerical and combustion modelling is enlightened in following sections:

4.1 Numerical Modelling

All the investigation in the present work is performed on two-dimensional model. Reynolds-averaged Navier–Stokes equations are used to solve the mathematical model. All the selected governing equation involved in this method are shown in Eqs. (1), (2) and (3). In order to solve turbulence behavior of the flow field, two equation SST $K-\omega$ [18] is opted. Species transport model is selected to include the chemical interaction between fuel and air.

Continuity equation:

$$\frac{\partial \rho}{\partial t} + \frac{\partial}{\partial x_k}(\rho u_k) = 0; \quad k = 1, 2, 3 \quad (1)$$

Momentum equation:

$$\frac{\partial \rho}{\partial t}(\rho u_i) + \frac{\partial}{\partial x_k}(\rho u_i u_k) + \frac{\partial P}{\partial x_i} = \frac{\partial(\tau_{ik})}{\partial x_k} \quad i, k = 1, 2, 3 \quad (2)$$

Energy equation:

$$\frac{\partial}{\partial t}(\rho H) + \frac{\partial}{\partial x_k}(\rho u_k H) = -\frac{\partial}{\partial x_k}(u_j \tau_{jk}) + \frac{\partial q_k}{\partial x_k} \quad j, k = 1, 2, 3 \quad (3)$$

4.2 Supersonic Combustion Modelling

Volumetric reaction (Species transport model) has been chosen to complete the chemical kinetics between fuel and oxidizer. The detailed turbulence chemistry reaction is completed by combining finite rate with eddy dissipation concepts. Single-step chemical reaction mechanism is applied and full detailed chemical reaction is shown in Eq. (4).



4.3 Boundary Condition

The assortment of the boundary condition for the present article is chosen from the Waidmann et al. [11]. The validation has also been completed with the help of same boundary conditions. The detailed value of all the variables is listed in Table 1. Table 2 shows the mass fraction distribution of incoming air and fuel. To simplify the

Table 1 Boundary conditions

Variables	Incoming air	Fuel (Hydrogen)
Mach number	2.0	1.0
Static pressure (Pa)	100,000	100,000 (Parallel) 300,000 (Transverse)
Static temperature (K)	350	250
Density (kg/m ³)	0.9734944	0.09698617
Velocity (m/s)	756.1424	1203.324

Table 2 Species concentration

Mass fractions	O ₂	H ₂ O	N ₂	H ₂
Air	0.232	0.032	0.736	0
Fuel	0	0	0	1

computational convergence, no slip wall conditions are incorporated to avoid single molecular structure effects at the combustor walls. The name selection of the models is free-stream incoming air inlet, outlet, strut fuel inlet, wall transverse fuel inlet and additional wall air inlet. CFL number is taken as 0.5 to get the better convergences.

5 Assumptions for Present Work

The selection of the assumptions is done by reviewing the similar work in the area of supersonic combustion. To eradicate the computational cost of the selected model, few of the listed below assumption have been used to get the appropriate outcome.

- 2D computational combustor model is chosen.
- Single-step chemical reaction is involved.
- Steady-state flow field has been used to suppress large-scale instabilities.

6 Results and Discussion

The computational examination of the current work involves two distinct models. To recognise the impact of innovative wall transverse fuel injector at the lower wall has been introduced. Strut fuel injector by utilizing wall fuel injector in first model and one additional wall air injector ahead of the transverse fuel injector in same model have been introduced to compare and understand the greater performance. Moreover, distance between wall fuel and air injector has also been changed by 0.5, 1, 2, 3 mm. To explore the performance part, combustion efficiency and mixing efficiency plots

have been summarized at many number of cross-sectional distance from the entrance to create a continuous plot of all performance outcome.

7 Validation of the Model

To understand the stages involved while doing computational investigation of the present work, validation is essential to get the precise results. Waidmann et al. [11] and [12] is chosen to compare the experimental data to extracted computational data in Ansys 14.0 Fluent. All the applied boundary condition is same as the experimental details. Both the reacting and non-reacting cases have been equated with the help of middle section velocity plots and experimental shadowgraph image. In this article only reacting case has been explored. Figure 3 shows the association between experimental shadowgraph image and Computational density and pressure contour plots. The visible incident location of the reflected shock waves on the both walls can be seen. The expansion fan created at the edge of the wedge shaped strut face is also common in it.

To explore the more similarity between experimental and computational work, pressure at the lower wall and velocity at the middle section of the combustor have been used. In both Figs. 4 and 5, well-suitable match at the peak and trough can be identified. Figure 5 shows the discrepancy in the downward stream. The obtained discrepancies are under approximation error. Besides, the reasonable agreement between compared data has been seen. Same computational processes are applied in this article.

Fig. 4 Combustor wall pressure

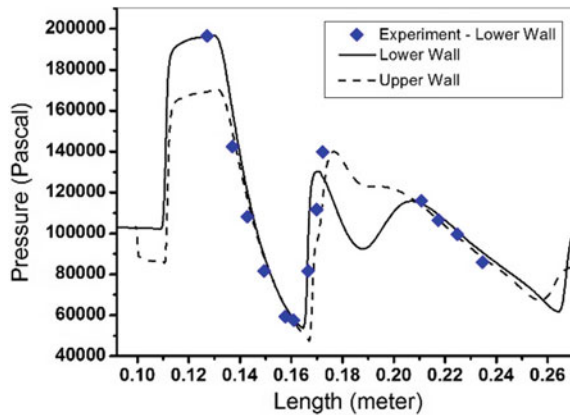
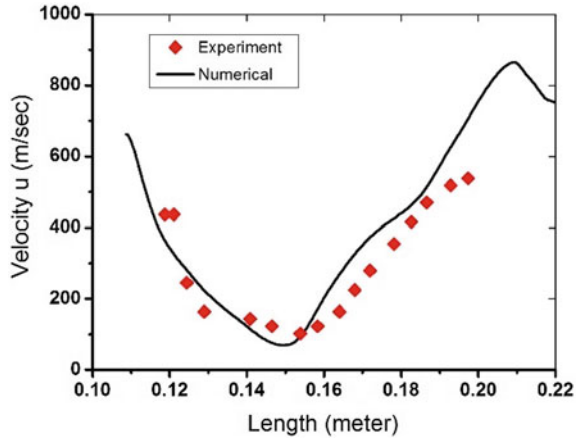


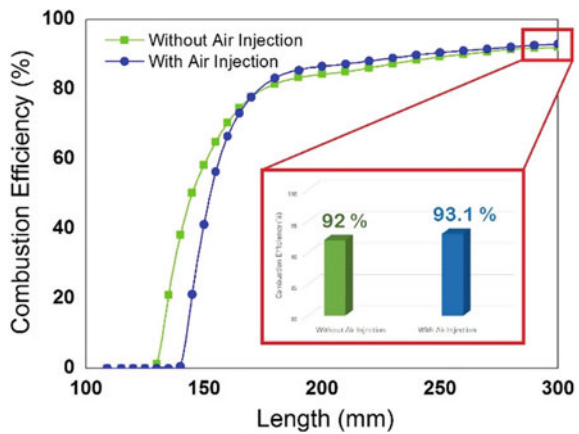
Fig. 5 Velocity profile at middle section ($Y = 25$ mm)



7.1 Combustion Performance

To explore the any type of engines, combustion efficiency [19] is important performance characteristics. The Scramjet engine utilizes the atmospheric air to combust the incoming fuel; however, few regions inside the combustor are not more influenced by the air due to the higher speed separation effects. Hence to improve the combustion performance, additional wall air injector is introduced. Figure 6 shows the plot of combustion efficiency of without and with air injection at the lower wall. The pattern followed by both the models are similar however the maximum performance reach in second model i.e. with air injector. Since the variation of this is not highly appreciated, so the wall air injector does not influence majorly on the combustion efficiency.

Fig. 6 Combustion efficiency of without and with air injection



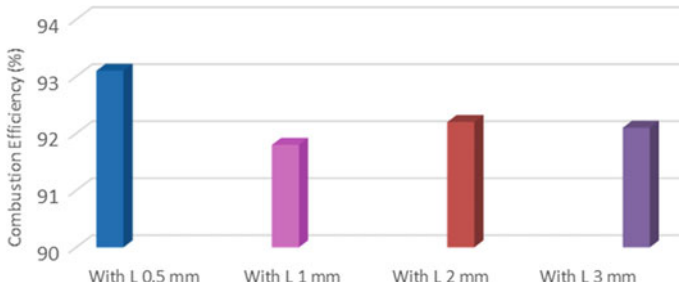


Fig. 7 Combustion efficiency of four sets with air injection at the wall

To explore more about, the distance between wall fuel injector and air injector has also been changed by L 0.5, L 1, L 2 and L 3 mm. Figure 7 shows all four sets of comparison. As the plot suggests that the combustion efficiency gets lesser while increasing the distance between fuel and air injector at the wall except for length 1 mm.

8 Conclusions

The behavioral outcome of all the model is well compared and extracted from the Ansys 14.0 Fluent software. The identified results show the below listed conclusion:

- The improved performance is achieved by introducing only wall air injector just after the wall fuel injector. The maximum combustion efficiency has been reached up to 93.1%.
- 1.1% of increment is observed in modified model which can be monotonic behavior.
- All the sets of model reached its maximum mixing. The earlier 100% mixing is identified in first model with only wall fuel injector.
- Decreasing combustion efficiency plot is observed while increasing the distance between wall fuel and air injector.

References

1. Curran ET (2001) Scramjet engines: the first forty years. *J Propul Power* 17(6):1138–1148
2. Dharavath M, Manna P, Chakraborty D (2013) Thermochemical exploration of hydrogen combustion in generic scramjet combustor. *Aerosp Sci Technol* 24(1):264–274
3. Wang T, Li G, Yang Y, Wang Z, Cai Z, Sun M (2020) Combustion modes periodical transition in a hydrogen-fueled scramjet combustor with rear-wall-expansion cavity flameholder. *Int J Hydrogen Energy* 45(4):3209–3215

4. Shi L, Zhao G, Yang Y, Qin F, Wei X, He G (2020) Experimental study on ejector-to-ramjet mode transition in a divergent kerosene-fueled RBCC combustor with low total temperature inflow. *Aerosp Sci Technol* 99:105734
5. Verma KA, Pandey KM, Sharma KK (2020) Numerical investigation of variation of combustion efficiency of scramjet combustor with change in length of wedge shaped strut blunt end. *Test Eng Manage* 82:7800–7806
6. Seleznev RK, Surzhikov ST, Shang JS (2019) A review of the scramjet experimental data base. *Prog Aerosp Sci* 106:43–70
7. Verma KA, Pandey KM, Sharma KK (2019) Computational investigation on design of scramjet combustor—a review. *Int J Recent Technol Eng* 7(6):544–548
8. Gerdroodbary MB, Fallah K, Pourmirzaagha H (2017) Characteristics of transverse hydrogen jet in presence of multi air jets within scramjet combustor. *Acta Astronaut* 132:25–32
9. Gugulothu SK, Nutakki PK (2019) Dynamic fluid flow characteristics in the hydrogen-fuelled scramjet combustor with transverse fuel injection. *Case Stud Therm Eng* 14:100448
10. Aravind S, Kumar R (2019) Supersonic combustion of hydrogen using an improved strut injection scheme. *Int J Hydrogen Energy* 44(12):6257–6270
11. Waidmann W, Alff F, Bohm M, Brummund U, Clauss W, Oschwald M (1994) Experimental investigation of hydrogen combustion process in a supersonic combustion ramjet (SCRAMJET)” DGLR. *Jahrestag Erlangen, Ger* 1994:629e38.
12. Oevermann M (2000) Numerical investigation of turbulent hydrogen combustion in a SCRAMJET using flamelet modeling. *Aerosp Sci Technol* 4(7):463–480
13. Verma KA, Pandey KM, Sharma KK (2020) Impact of parametric variation on combustion characteristics of hydrogen-fueled strut based scramjet combustor at supersonic speed. *Int J Energy Res* 44(14):11807–11826
14. Verma KA, Pandey KM, Ray M, Sharma KK (2020) The numerical analysis of combustion performance of a wedge shaped strut-based scramjet combustor. *Therm Sci Eng Prog* 20:100714
15. Verma, KA, Pandey KM, Sharma KK (2020). Computational investigation of mixing performance on the effects of innovative transverse fuel injection system in parallel fuel injection based scramjet combustor. *materials today: proceedings*
16. Verma KA, Pandey KM, Ray M, Sharma KK (2020) Effect of transverse fuel injection system on combustion efficiency in scramjet combustor. *Energy*, 119511
17. ANSYS ((2011)) ANSYS fluent 14.0 theory guide. Canonsburg, PA 15317, ANSYS, Inc
18. Wilcox DC (2008) Formulation of the kw turbulence model revisited. *AIAA J* 46(11):2823–2838
19. Gerlinger P, Stoll P, Kindler M, Schneider F, Aigner M (2008) Numerical investigation of mixing and combustion enhancement in supersonic combustors by strut induced streamwise vorticity. *Aerosp Sci Technol* 12(2):159–168

Quality Tools Implementation Practice to Reduce Forging Defects in Crankshaft Manufacturing Industries: An Overview



Amitkumar B. Solanki, Sunilkumar S. Sonigra, and Vivek Vajpayee

Abstract The growing competitiveness in the emerging global market is a challenge that transforms into a vast need for the industry to begin to expand. Each manufacturing industry cares about the quality of its products so as to stay ahead of its rivals and so become their consumers' first choice. It is essential that the finished product meets standard requirements. Since customer satisfaction is derived from quality products and services, it is very important to control quality. In all types of engines, the crankshaft is the significant powerful component. Most crankshafts are made of micro-alloy steel, to acquire the mechanical characteristics necessary. Many designs of the crankshaft are inherently complicated by various defects, e.g. underfilling, overlapping, misalignment, scaling pits, etc. Various types of forging processes die materials for forging and crankshaft production processes are briefly discussed in this paper. The overview of the latest research on forging analysis for single-cylinder crankshafts is presented here by the practice of high-quality tools used to eliminate defects in crankshaft production. This research study explored the use of quality tools, including Pareto graph and chart of cause and effect, to evaluate various forging defects in the crankshaft manufacturing industries to reduce the rejection rate and increase profitability of production yield. Finally, corrective measures are recommended to resolve significant defects in the crankshaft production process. The execution of the remedial plan would diminish the rate of rejection from 4.54 to 0.72%.

Keywords Crankshafts · Quality tools · Forging defects

A. B. Solanki (✉)

Department of Mechanical Engineering, Gujarat Technological University, Ahmedabad, India
e-mail: solankiamit4239@gmail.com

S. S. Sonigra

Department of Mechanical Engineering, Government Polytechnic, Rajkot, India

V. Vajpayee

Forge & Forge Private Limited, Rajkot, India

1 Introduction

The goal in today's industrial landscape is to manufacture best-quality goods with the least investment in capital and to sell them as efficiently as possible. Forging is a very traditional technique for the production of a wide variety of products. The development of the forging industry has risen rapidly over the course of this century. This growth is primarily due to modern and technologically advanced tools, upgraded materials and enormous presses and machines with high quality produced recently. This has intensified rivalry between forging firms and today's key priorities are on the right commodity for the first time. In terms of productivity or durability of the products and services, the outstanding quality of the forged components is crucially important. According to Thomas et al. [1], the Forging Handbook provides a comprehensive overview and discussion of the forging process and applications, forging design, material features and manufacture of forgings. According to Lange [2], forging is the method used by various tools and dies for heating and forming metals through plastic deformation. The process of forging produces components with highly developed mechanical properties with minimal material waste and remains one of the most ancient techniques of metalworking; modern forging is carried out by means of magnetic, compressed air and hydraulic presses or hammers. Examples of forging shapes include engine components (connecting rods, engine valve body parts, crankshafts, etc.), speed gearboxes, cast crane hooks, bolts and disks, hydraulic circuit parts and many more. The forging industry provides products of excellent quality compared to others. There are several drawbacks when the design and development of the forging process are not properly conceived. According to Hawryluk and Jakubik [3], deficiencies that transcend such limitations may be defined as defects. According to Dindore and Badiger [4], the crankshaft can be alluded to as the core of any I.C. Engine is the first source of the power produced by the engine. According to Sharma and Aggarwal [5], the crankshaft is effectively fitted with a dynamic configuration in the engine, converting the linear movement of the piston into a rotational movement under high strength and loads. Zoroufi and Fatemi [6] have published a crankshaft-based literature review on the achievement of quality diesel engine standards, including enhanced fuel engine specifications, robust design, relatively low production costs to maintain durability.

Sang et al. [7] have affirmed that most automotive crankshafts were forged of micro-alloy steel and could substitute alloy steel in order to obtain excellent mechanical properties. By eliminating the conventional heat treatment process by specifying air-cooled steels, micro-alloyed steel has been widely used primarily by providing manufacturers with significant cost savings and weight reduction by optimizing the component design. Mirko et al. [8] provided a model for quality management that included seven strategies for gathering and analyzing data, accumulating expertise, and improving quality.

2 Forging Processes

In order to acquire the intended final configuration, the billet is deformed plastically through the upper and lower dies during forging. In accordance with the metals handbook: forming and forging [9], the billet is heated to the desired temperature, the heating and forging of the billet with impression dies are hammered or squeezed, the forged part is trimmed to eliminate the flash and finishing coining. In addition to ensuring the correct size, the key aim of the forging process is to identify sufficient metal flow in dies. Wang and He [10] have explored new technology and machinery for the precise forging to increase the output capacities of connecting rod in order to fulfill the needs for geometrical accuracy and ongoing improvement. Based on the temperature where the forging is performed, it is categorized as hot forging and cold forging processes, and on the basis of the die design where the process is carried out, it is labeled as open-die forging and closed-die forging (Fig. 1).

2.1 Hot Forging and Cold Forging

- (1) Hot forging: according to metals handbook: forming and forging [9], hot forging is processed at exceedingly high temperatures or at temperatures above re-crystallization temperatures typically $> 0.6 T_M$, eliminating any effect of strain hardening. Where the melting temperature is T_M . For the steel forging, the normal forge temperature is up to $1150\text{ }^\circ\text{C}$. This temperature is required so that the metal does not harden throughout the deformation process.

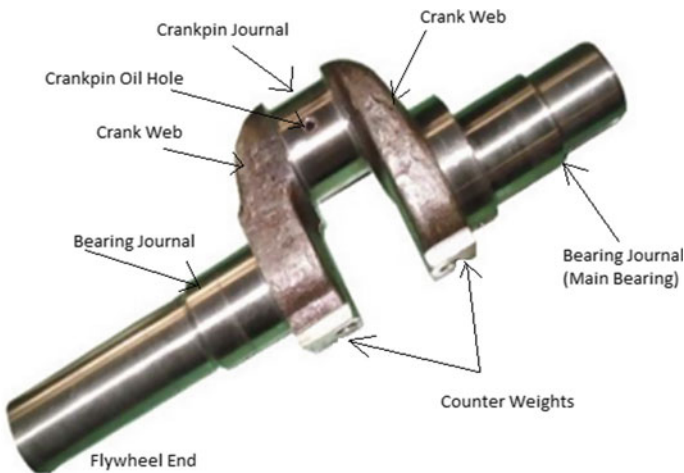


Fig. 1 Forged steel single-cylinder diesel engine crankshaft [9, 11] Source Forge & Forge Pvt. Ltd. Rajkot

- (2) Cold forging: according to metals handbook: forming and forging [9], cold forging is carried out through room temperature ranging from 0.2 to 0.4 TM of the substance, inducing the work hardening effect known as cold forge. Where TM is melting temperature.

2.2 Open- and Closed-Die Forging

- (1) Open-die forging: according to the metals handbook [12], in open-die forging, Fig. 2a, b and c, in which the forming of hot metal components among an upper die linked to the ram and the lower die linked to the hammer. Metal objects are being processed to suitable temperatures from 260 to 1315 °C and are progressively formed by the necessary hammering or forging of the solid workpiece into the required shapes.
- (2) Closed-die forging (impression die forging): In the other side, according to the metals handbook [12], in the closed forging, Fig. 2d where the material remains absolutely restricted by the top and bottom die sections produced throughout the cavity. The material is deformed in a cavity that makes very little evacuation from surplus material, thus imposing increased impact on die design. In this forging, the dies pass into one another and covering the workpiece for the most

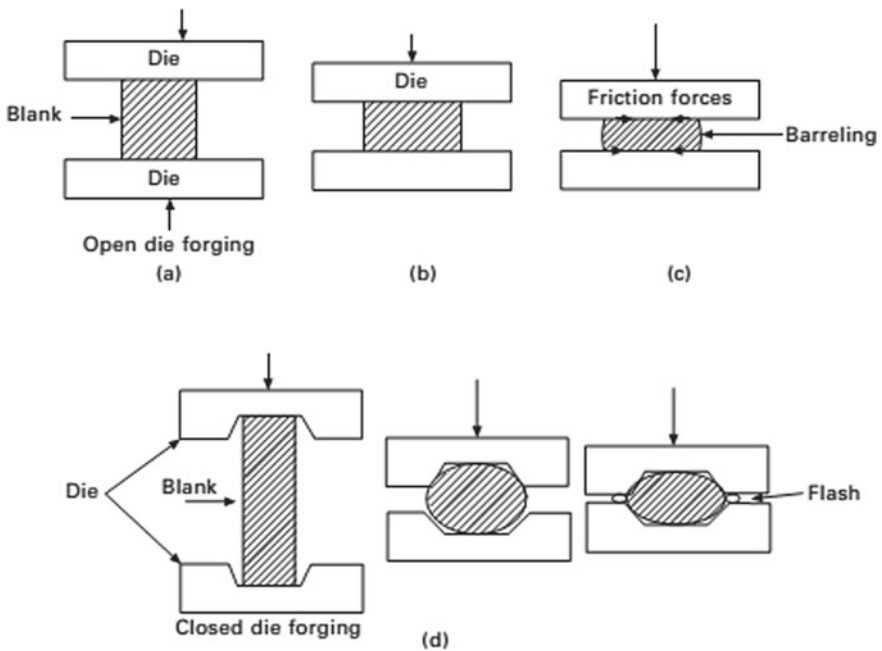


Fig. 2 Open-die (a–c) and closed-die (d) forging processes [12]



Fig. 3 Manufacturing process of forged steel crankshaft [9, 11] *Source* Forge & Forge Pvt. Ltd. Rajkot

part. The preheated raw material is put into the lower die, which is roughly the shape of the actual formed component and the influence of the upper die on a raw material shapes it into the expected forged type.

3 Manufacturing Process of Forged Crankshaft

Montazersadgh [13] has explained that forging crankshafts have been chosen for heavily loaded engines, as forging crankshafts offer, in specific, high power, improved strength and failure resistance than casting shafts. As shown in Fig. 3, hot forging and machining are the main production processes for the forged crankshaft. Each stage of this process is described (see Table 1).

4 Die Materials for Forging of Steel

In Becker's and Shipley's view [14], the key reasons for failure of thermal and mechanical forging dies are surface roughness, and adhesive wear and permanent deformation and loss of fatigue. According to Altan and Deshpande [15], the selection of the right material of die, through its forging to minimize production costs and to establish an enclosed tolerance for the forge component, is an enormously vital task in producing quality components. According to Taylan [16], metal forming: the basics and applications conceded to forge crankshafts being deemed to get a complicated shape which, depending on the forges capability of the metal, requires an appropriate geometry of the related parts and a die configuration. Schmid and Kalpakjian [17] suggested that tool and die steels are quite used for forging dies at temperatures of

Table 1 Manufacturing process with description for forged steel crankshaft [13]

S. No.	Manufacturing process	Description
1	Raw material inspection	The AISI 1055 (EN9) raw material samples are checked for chemical composition
2	Billet cutting	By using band-saw machines or shearing machines, raw material is formed and sliced to the rugged dimensions of the crankshaft
3	Heating	The formed material heated at 950–1150 °C in the furnace
4	Forging process	The content billet is heated up to its forges temperature level and squeezed into the desired form by pressing the billet with high pressure among the upper and the lower dies. Pneumatic forges hammers with a size of 2–10 tons are being used for forging operation
5	Hot trimming	Cut the flash which exists as flattened non-formed material at the edge of the part
6	Heat treatment	The mechanical properties of the substance need to be achieved
7	Shot blast	Cleaning of forges through impelling a rapid velocity metallic shot by the pressure of air or an impact force on forging surface to eradicate the scale from the surface
8	Coining	The accurate form is obtained by the final strikes of the hammer which lead the inventory to fully cover all parts of the print
9	Crack testing	By using the magnaflux crack detection machine
10	Machining and inspection	1. The forged part is machined with a billet during the machining process. The billet technique enables the positioning of counterweights and webs, where the designer needs them to be by using multiple practices such as facing, centering, turning, oil hole boring, internal threading, straightening and grinding 2. Dynamic balancing of counterweights is checked 3. Inspection of cylinder diameters, face distance, crankshaft radius in order to finish the forged steel crankshaft before packing and dispatching

Source Forge & Forge Pvt. Ltd. Rajkot

up to the 700 °C, with adding of vanadium, manganese, chromium, molybdenum, nickel and tungsten, to have the toughness and strengthening properties, abrasion properties and resilience of softening within elevated temperatures.

5 Forging Defects in Crankshaft Manufacturing Industries

There are various issues or defects faced by the manufacturer during production in any forging industry. These defects usually lead to the exclusion of the commodity on the

market. Shamasundar [18] explored the application of the FEM simulation to predict defects such as non-filling, fold and internal residual stresses for thermal heating and to investigate the flow of grain from the forging of the crankshaft. The base of the framework to mitigate the amount of forging deficiencies on the forged part is described by Arentoft and Wanhein [19]. One distinguishes likely defects among six types, including shear defects, cracks (fractures), laps, surface defects, structural and shape defects, and the second classifies possible reasons by applying the defect matrix, that describes the interactions across defects along with their reasons. The defect detection techniques for forged metal pieces through image analysis have been described by Yamazaki and Fukui [20]. These approaches are effective in overcoming fatigue and stress in physical assessment. Hawryluk and Jakubik [3] analyzed forging defects in specified die-forming procedures; the main concern is the creation of unfills because of air packs among the forge and the instrument. Most investigators and experts in forging are eager to agree that the most common forging defects are under-fills and folds are described by Quazi et al. [21]. Barsom [22] researched micro-cracks for 6 cylinder aircraft engine crankshafts in overheated forgings of ultra-low sulfur steels (AISI 4340). On the open surface, the crack grows faster as the central part of the crack is straightened. Incipient melting of grain boundaries caused the micro-crack defects and continued to grow due to temperatures exceeding industry standards that can be caused crankshaft fractures. A concise overview of some of the forging defects, according to Becker and Shipley [14]; and Lange [2]; with possible reasons and their method of correction in the crankshaft manufacturing sector is provided (see Table 2) using the forging defect matrix.

The current research deals with crankshafts produced by hot forging.

Manufactured by Forge & Forge Private Limited, Rajkot, India, [11] fitted to single-cylinder diesel engines numerous defects are found in industry during crankshaft forging (see Figs. 4, 5, 6, 7, 8 and 9) [11] and are mentioned (see Table 3) with both the area of operation and the potential area of occurrence [9, 11].

6 Quality Control Tools and Techniques for Reduce Foremost Defects in Industries

6.1 Introduction

Quality is the power of a product or service, according to Besterfield [23], to meet or exceed consumer standards on a consistent basis. Quality is now involved in all business forms: manufacturing, hospitals, education, the food industry, public utilities, etc. According to Defeo [24], quality can be defined as fitness for use. Corner [25] has alleged a non-conforming good or service. According to Crosby [26], quality conforms to requirements as free from deficiencies- errors requiring rework or resulting in field failures. The value to manufacture goods of excellent quality is cheaper than the value of goods of poor quality, since the value of bad

Table 2 The forging defect matrix

S. No.	Forging defects		
	Defects	Possibility of reasons	Method of correction
1	Overlap	Two metal folding surfaces against each other without fully welding. It is caused by Sharp corner (less fillet) due to poor die design	Accurate billet temperature, die must be preheated, Enhance the radius of the fillet on the die
2	Scale pit	Scale pits are seen on the surface of the forging as irregular depositions, Mainly due to inappropriate cleaning of the inventory required for forging	Adequate cleaning of forged surface
3	Underfilling	Any part of the die cavity is not completely filled by the flowing metal. It is caused by lower volume of stock, poor die design, less raw material, lower billet temperature, insufficient load, improper lubrication	Design of the correct die, suitable raw material, the required heating system, correct lubrication
4	Surface cracking	Excessive surface work, Non-uniform billet temperature distribution, Input material defect, Improper rate of deformation	Properly heat the billet, reject defect raw material
5	Die shift (mismatch)	The die halves are misaligned	Proper alignment of die halves
6	Dent	Unsuitable and careless working	Proper placement of stock in dies and proper handling of hot forging
7	Burnt	Overheating	Proper heating
8	Mislocation	Poor or improper allocation (incorrect location and position) of job in die	Proper die design, Proper usage or control of forging press
9	Oversize and undersize	This is due to the number of parts induced by wear of tools being too wide and too small and the geometry being poor	Proper perform volume, convenient and sufficient geometry of component

scraping, reusing, etc. remains greater than the value of getting things correctly first. In comparison, Mukhopadhyay [27] states that product quality includes related compliance, durability and proper process at the right time and zero defects. As per Basu [28], more than a hundred different resources are available today. The efficiency of the use of tools and technology requires their implementation by the persons involved in the process, and it can only be ensured if the Company promises

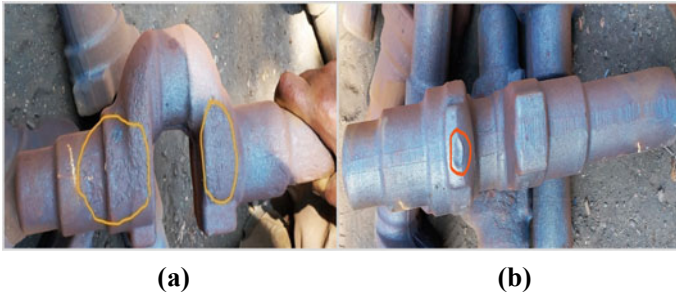


Fig. 4 Pitting at bearing area and on web (a) and dent on bottom die at circular web (b) for single-cylinder crankshaft

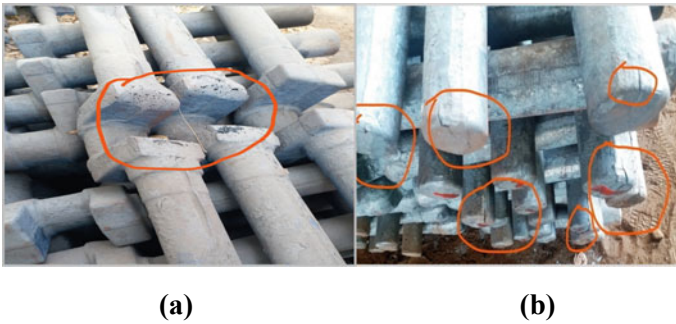


Fig. 5 Burnt at bottom of web (a) and at end Journal and (b) in overheated forgings. *Source* Forge & Forge Pvt. Ltd. Rajkot [11]

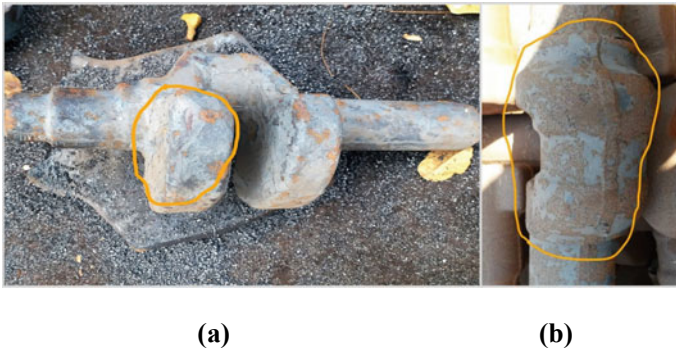


Fig. 6 Underfilling at counter weight portion (a) and mismatch at side of journal (b)

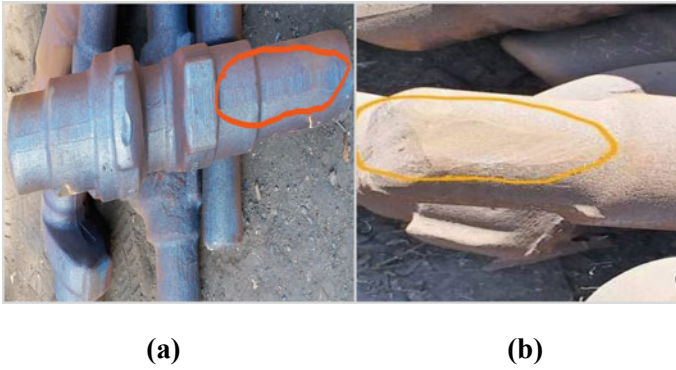


Fig. 7 Seam cracks on main bearing area, journal (a) and on crankpin (b)

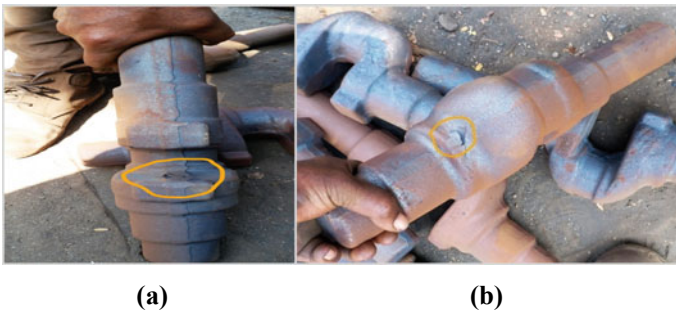


Fig. 8 Overlap at crankpin (a) and at web (b)

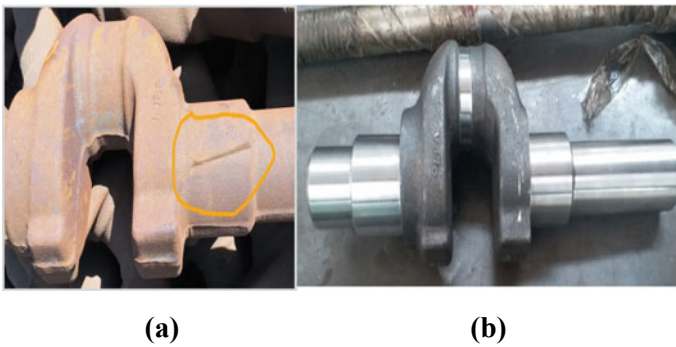


Fig. 9 Mislocation on bearing area (a) and machining error due to oversize (b)

Table 3 Location of important forging defects in crankshaft manufacturing industries

S. No.	Forging defects	Area of operation	Possible occurrence zone
1	Overlap	Die setting, blocker setting-corner radius, raw material, furnace temperature, lubrication, workers conditions	On top die at crankpin and bottom die at near parting line at web (see Fig. 8)
2	Pitting	Scales, environment, die condition, furnace condition	On the main bearing and at circular web, On the top die and bottom die at shank (see Fig. 4a)
3	Underfilling	Die design, die deformation, temperature, lubrication	At counterweight and on side of journal as well as on top and bottom die at flange and at crankpin (see Fig. 6a)
4	Overheating/burnt	Furnace temperature	Micro-cracks in overheated forgings at side of Journal and bottom die of web (see Fig. 5)
5	Cracks	On contact surface/free surface, temperature	On top and bottom die at web and at crankpin (see Fig. 7)
6	Dent	Unwanted material	At bottom die at circular web (see Fig. 4b)
7	Die shift	Die design, Die locks, Blocker Condition, Hammer Alignment, Die halves	Misalignment of upper and lower dies, this will lead to improper dimensions, mismatch at webs portion (see Fig. 6b)
8	Mislocation	Job location and position in die, internal cavities,	At main bearing area and on journal (see Fig. 9a)
9	Oversize	Die design and parameters, too large volume, bad geometry	Oversize at mount and there is machining error due to oversize (see Fig. 9b)

that it will function toward improving productivity, profitability and quality. Nicholas [29] identified all aspects of the modern management of production with a focus on strategic approaches, such as TQM and JIT. He said that the way companies are run and responsive to evolving customer concerns depends upon the way in which they thrive in a world of highly rivalry production.

6.2 Tools for Continuous Process Improvement

According to Chongwatpol [30], continuous production growth and quality control approaches are strategies that can help businesses gain and increase market satisfaction. According to Nur Shafiqah et al. [31], quality tools and strategies are the core elements of an efficient production process. It is essential to recognize key

factors in the successful adoption of the quality tools and strategies by the industries. According to Madu [32], a consistent progression is the strategic management tool that considers enhancement of quality as an endless phase that can lead to progressive changes at any time. According to Summers [33], continuous process improvement involves the implementation of process improvements that result in better customer satisfaction, lower quality failure costs, better productivity, better achievement of goals, long-term strategies, etc. According to Chiarini [34], a fixed set of graphic methods has been reported as helpful in resolving quality problems by means of such seven quality control tools. Ishikawa [35] has implemented seven essential quality control tools, including checklists, bar charts, Pareto analysis, control charts, cause and effect diagrams, flowcharts, scatter plots, etc. to address quality issues in factories and process upgrades. The European organization for quality (EOQ) [36] shows that the data collection phase includes the checklist, the bar chart and the control graph, and the investigation phase includes the Pareto analysis, the fish bone diagram, the flowchart and the scatter chart.

6.3 Literature Review

Various researchers have done remarkable work in introducing tools used to monitor variability in product quality by reducing defects in manufacturing industries, but the imperative contribution of the few researchers is explained below: Bagchi [37] recommended the use of statistical methods such as Pareto analysis as well as cause and effect diagrams to evaluate and enhance quality issues. The assessment of the specifics of such methods concentrates on the continuous improvement of strategies and the identification of acceptable factors for rejection. Sahoo et al. [38] implied a lean manufacturing strategy to eliminate prevalent forge defects, such as un-filling, overlapping and so on in the connecting rod assembly line through the Taguchi experimental design method. Simulation techniques are employed using a finite element approach that would save time and expense and enhance productivity. Root-cause identification methodology was adopted by Mahto and Kumar [39] to eradicate dimensional defects in the cutting process of the CNC Oxy flame cutting machine and to minimize rejection from 11.87 to 1.92% on average. Six cylinder crankshafts evaluated via hot forging and built with TATA motors, Jamshedpur—India reveals that in excess of 80 percent of rejection as well as re-work was related to forging defects described by Chandna and Chandra [40], including certain un-filling, overlap, pitting, foreign objects and store scrap. A variety of consistency approaches like Pareto analysis, worker brainstorming as well as cause and effect diagrams, have been used for evaluation. The forging defects of the optimized 697 counterbalance crankshaft in the forging firm were suggested to solve by corrective steps. At last, the actual rejection level would be dropped from 2.4 to 0.2% and reworked from 6.6 to 2.1%, with very little correction steps and suggestions made for the obtainable crankshaft forging production and the control defects. A versatile method of forging small to medium-sized crankshafts with cost competitiveness

has been developed by Alves and Martins [41]. The buckle of rigid compression rods with compact modular mounting solutions to easily change the final configurations of crankshafts. To minimize Forge defects in integrated hot forging axle-arms, Mathew et al. [42] have developed and implemented quality control tools. A significant defect was identified with the aid of the Pareto diagram, which indicates 83.33% of the cumulative rejection was related to overlapping and un-filling. Using a session to brainstorm, the cause and effect diagram is then used to explain the root causes of those two defects. Corrective steps have been proposed to resolve the forging defects of the integral arms of the axle. Thottungal and Sijo [43] have studied major forging defects, including lapping, misalignment, scales, quench cracks, under filling, etc. which occur in the forging industry with a rejection rate of more than 5% of the total monthly output. Corrective steps were recommended and suggested to minimize the rate of rejection by using an anti-scaling coating, venting to evade under-fills, content flow modeling tools and sufficient lubrication rather than an oil furnace, etc.

6.4 Application of 7QC (Quality Control) Tools

- (1) Check sheet: Check sheet is a systematic, tabled and prepared data collection system for recording the rate of individual incidents over the time of information collection. According to Montgomery [44]; Omachonu and Ross [45]; it allows the user to organize data for later use. Data of rejections due to forging process defects (see Table 4) shows clearly all information contained in the

Table 4 Defects data of single-cylinder forged crankshafts

Forging defects data	Months					
	April 19	May 19	June 19	July 19	Sept. 19	Total
Total production	14,685	11,918	17,479	23,533	7166	74,781
Total accepted quantity	14,038	11,406	16,697	22,398	6826	71,365
Overlap	74	32	252	271	16	645
Burnt	2	1	4	14	7	28
Unfilling	463	371	412	690	283	2219
Mismatch	5	4	0	5	2	16
Crack	3	0	2	0	1	6
Mislocation	69	72	79	106	22	348
Scale Pit	29	31	27	43	8	138
Oversize	0	0	4	2	0	6
Dent	2	1	2	4	1	10
Total rejections	647	512	782	1135	340	3416
% rejections	4.41	4.30	4.47	4.82	4.74	4.54

Source Forge & Forge Pvt. Ltd.-Rajkot

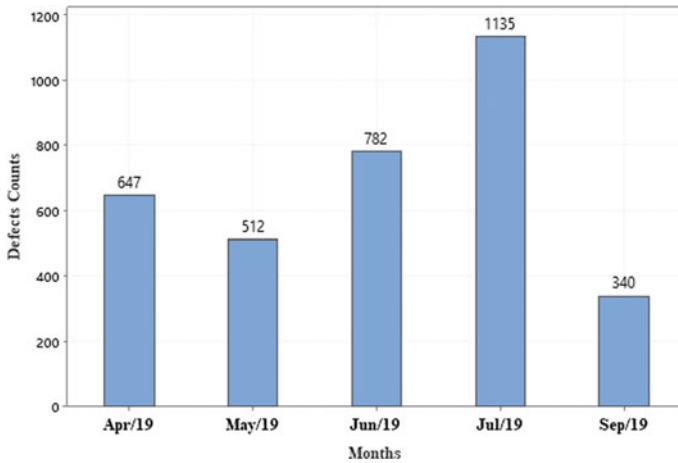


Fig. 10 Histogram: defects over time

monthly rejection survey beginning April 2019–September 2019, including the quantity of forged crankshaft made, accepted, rejected and major forging defects. It is fully evident that the key shareholders of data sets are un-fillings, overlaps, mislocation and scale pits. The crankshaft gross refuse for five months is 4.54% because of forging defects.

- (2) Histogram: Neyestani [46] declared that the histogram is a sort of bar chart in which the collected data is graphically represented and a distribution of variables or causes of problems grouped into categories is displayed. Histogram of defects counts over time throughout April 2019–September 2019 is shown in Fig. 10 for single-cylinder forged crankshafts. Number of rejection contribution of the various forging defects through bar chart is shown in Fig. 11.
- (3) Pareto diagram: Defeo [24] stated that the Pareto diagram is a specific histogram that can be used for categorized and prioritized in organizational efficiency problems, circumstances and triggers. In actual fact, it's a histogram which is graded from the highest to the lowest frequency. It is simple to concentrate on specific defects that occur at high frequency after identifying data in graphical form. According to Grant and Leavenworth [47], the Pareto diagram provides a distinction between the few that are important and the few that are insignificant, so that several can decide which one of the defects to be identified first. Thus, as per the Pareto chart, it will present a major problem which will reduce 80 percent of the quality-related problem so that it is called a data analysis tool. The Pareto 80–20 rule ('Vital Low and Influential Many') notes that 80% of effects are mainly due to 20% of the triggers, and that 80% of the issue can be overcome if 20% of these defects are managed. Defaults of rejecting data are given priority by Pareto rule (80–20), as seen in Fig. 12. Analysis reveals that more than 80% of the rejections are due underfilling and overlap for single cylinder crankshafts.

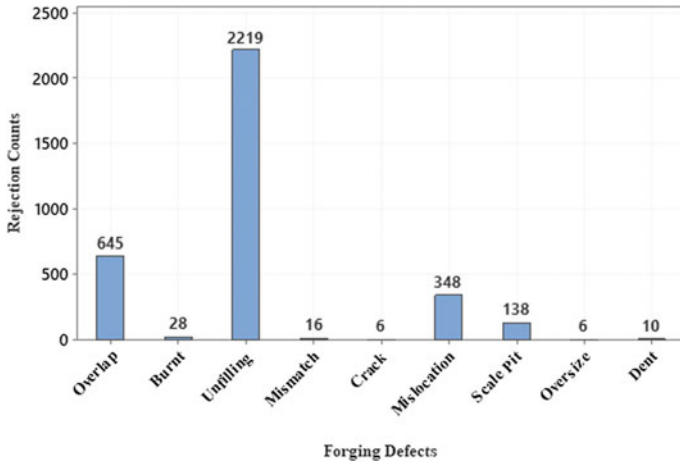


Fig. 11 Forging defects counts

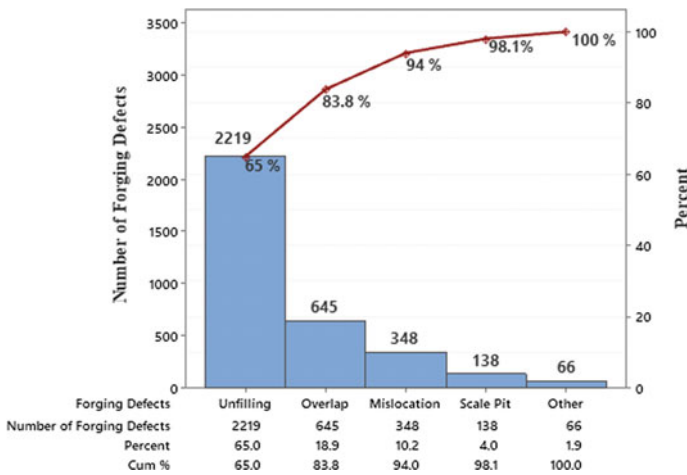


Fig. 12 Defects analysis of rejection through Pareto diagram

- (4) Cause and Effect OR Fish bone Diagram: According to Burke and Silvestrini [48], the cause and effect diagram is a data interpretation style visual method that logically organizes possible causes for a particular problem or effect by graphically showing them in greater detail in root cause analysis. The cause and effect diagram describes several possible causes for an effect or problem. It can be used to organize the brainstorming session. It immediately sorts ideas into useful categories such as personnel, techniques, materials, equipment, setting and measurement. In addition, Neyestani [48] stated that, as a result of its fish skeleton size and shape, a cause and effect diagram is often known as a fish

bone diagram to classify quality problems because of its significance. Data and information analysis is primarily aimed at continuous improvement practices by the use of cause and effect diagram and identifies the most promising rejection factors. Many defects responsible for the rejection of forged crankshafts as shown in Fig. 13 and few critical defects accountable for the rejection of forged crankshafts are overlaps, un-fills, mislocation and pitting as seen in Fig. 14 via the cause and effect diagram (Fish bone diagram).

- (5) Control chart: According to Tague [49], control chart is a vital instrument for predictive process control used to view data graphically that shows how the process changes over time. The main objective of the control chart is to prevent or control process defects. According to Rampersad [50], a center line, a top limit control line or a lower control line will still be available on the control chart to verify if the procedure is unchecked or under supervision. Historical evidence defines these lines. *P* chart is used to evaluate the proportion of defects

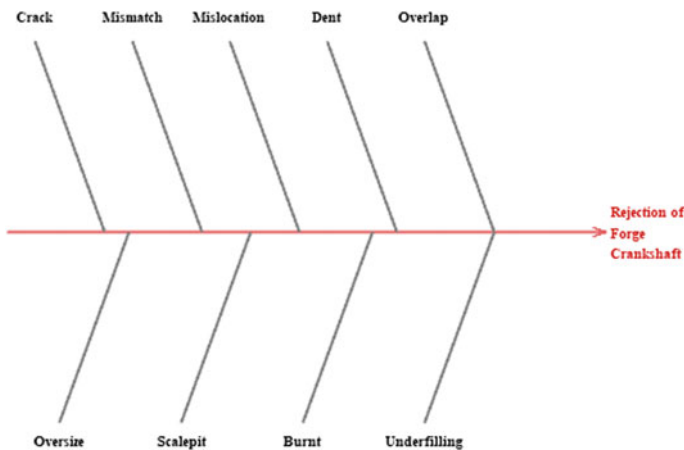


Fig. 13 The cause and effect diagram for rejection of crankshafts due to forging defects

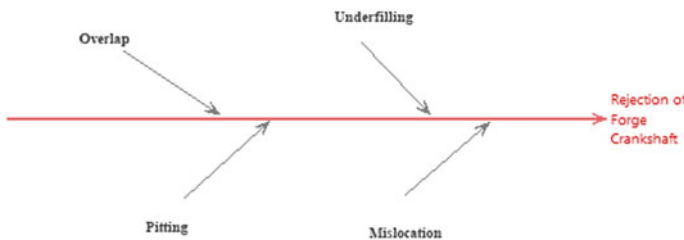


Fig. 14 Key defects responsible for the forge crankshaft rejection

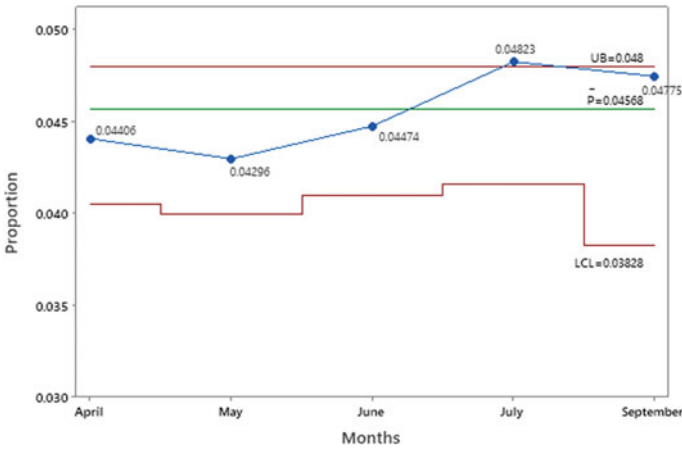


Fig. 15 Control chart (*p* chart) for rejections

shown in Fig. 15. It shows that the production of July 2019 is out of the upper control limit with a proportion of 0.04823 and the production of September 2019 is close to the upper control limit with a proportion of 0.04775. In order to enhance the quality of the product, it is also important to control the rate of rejection.

- (6) Process flowchart: According to Burke and Silvestrini [48], the flowchart is a powerful tool to offer a graphical display that shows a set of symbols representing the set of steps that appear in the procedure to provide an effective platform to any process or entity hierarchy. The flowchart is very helpful for the recognition and enhancement of process quality as a troubleshooting aid, according to Forbes and Ahmed [51]. Mirko et al. [8] proposed the quality management model with seven techniques for monitoring processes, gathering know-how and enhancing quality as seen in Fig. 16.
- (7) It is used to find a correlation between two variables. According to Montgomery [44]; Oakland [52], scatter diagrams are very useful for regression modeling. The 3-dimensional scatter plot of percent Rejection versus. Month versus number of rejections is shown in Fig. 17. This indicates the overall quantity of rejections and the proportion of rejections each one month. The relationship between months and the number of rejections using the scatter diagram as shown in Fig. 18 (Table 5).

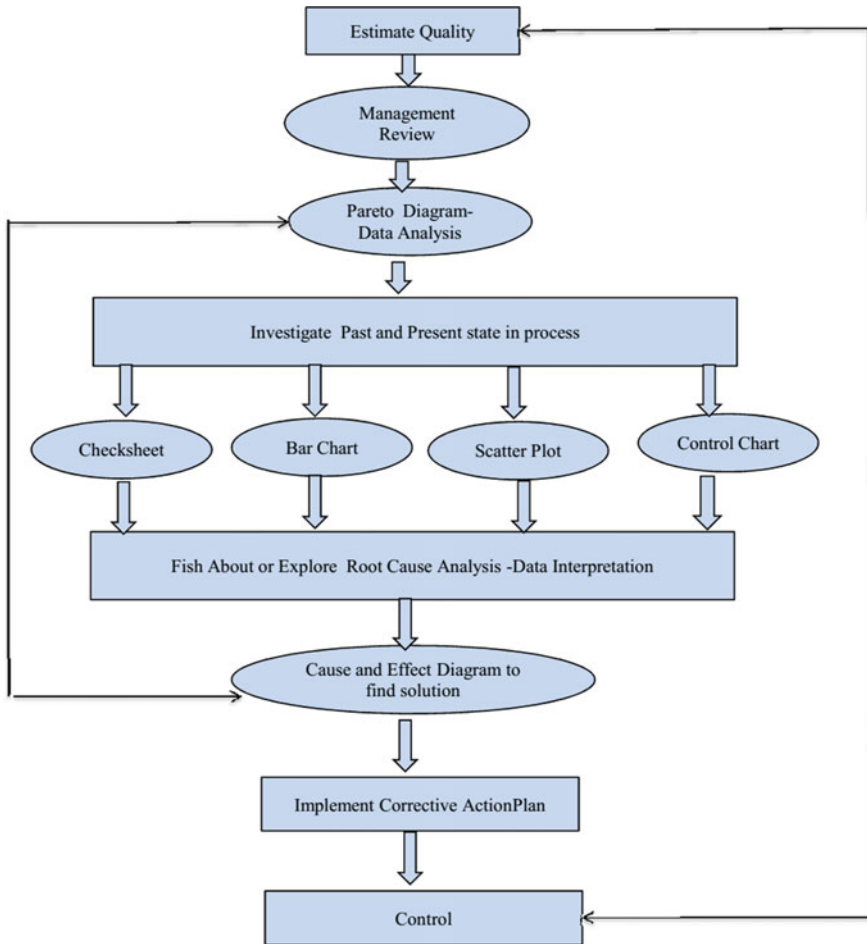


Fig. 16 Flowchart for using seven methods of QC for quality improvement [29]. *Source* Mirko et al. 2009

7 Actions Plan Required to Conquer Major Forging Defects

Also, Standard operating procedure (SOP) implementation, performance, compensation and firm monitoring structures, from time to time equipment maintenance and appropriate training to avoid human mistakes to create a secure working place to minimize production defects in order to increase productivity.

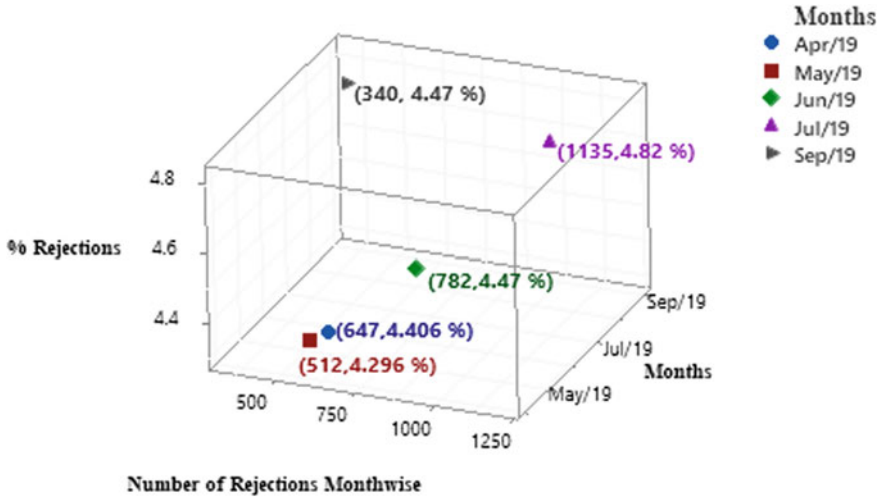


Fig. 17 3-dimensional scatter percent rejections versus months versus number of rejections

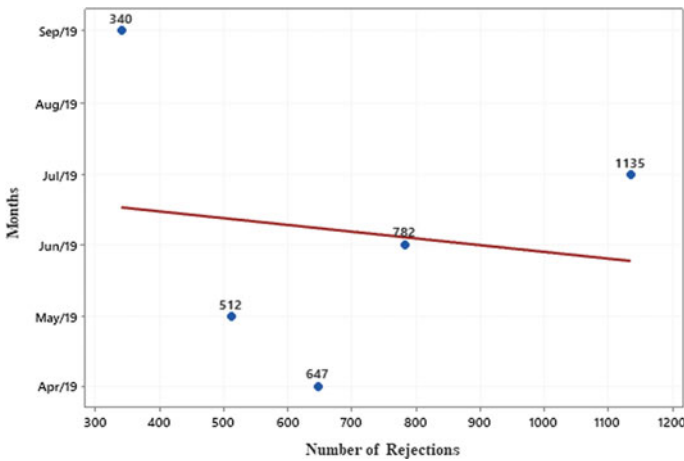


Fig. 18 Scatter plot of months versus number rejections

8 Conclusions

This paper explores and justifies the use of quality tools to mitigate forging defects in the manufacture of crankshafts for continuous improvement. The following are the key considerations in order to counteract the rejection of the crankshaft manufacturing industries.

1. Forging process enhances the quality of the product compared to other production techniques. In order to acquire excellent mechanical properties, cost savings

Table 5 Corrective measure required to overcome major forging defects for forged crankshafts

S. No.	Major forging defects	Corrective steps required
1	Underfilling	<ol style="list-style-type: none"> 1. Customize the design of the blocker by mapping the unfilled portion 2. Set the furnace adequate heating at the required temperature 3. The length of the billet shall be assured by checking more than two times at random at various locations 4. The grinding of the blocker dies as per drawing 5. Modify or remove counterweight from forged part 6. Choose the proper lubricant to die 7. The appropriate standard of raw material must be used 8. Provide adequate training to the worker to prevent error
2	Overlap	<ol style="list-style-type: none"> 1. Remover deformation of the blocker dies as required by drawing 2. By Grinding the die in the curved edges 3. Correct preform geometry with proper corner radius 4. Must use the acceptable quality of the raw material 5. Provide sufficient training to worker to avoid mistakes
3	Mismatch or die shift	Check the die and its location periodically for a recognized defect caused in the die and make a correct alignment of the die halves in order to avoid mismatch
4	Pit marks	The use of ESPON anti-scaling protective coatings on billet during heating for hot forging ensures that scaling is avoided
5	Cracks	<ol style="list-style-type: none"> 1. Using best-quality raw material and reject defective raw material to prevent seam crack 2. Avoid overheating by careful regulation of effective temperature to avoid internal cracking

and weight reduction, most crankshafts are made of micro-alloy steel and technically replacing alloy steel.

2. Fatigue is the dominant mechanism of die failure in hot forging. Preform die design and pre-forming of workpieces are crucial to the achievement of performance and economic (cost-effective) forging.
3. On the open surface the crack grows faster as the central part of the crack is straightened. Incipient melting on grain boundaries caused the micro-crack defects and continued to expand due to temperatures exceeding industry norms that can cause crankshaft fractures.
4. Global manufacturing industries are experiencing un-fills, and overlap is a major defect in their forging operations.
5. Forging analysis is being carried out for single-cylinder crankshafts developed by hot forging with the aid of quality tools. The overall crankshaft rejection for five months due to forging defects is 4.54%. The research reveals that by using

Table 6 Result table designed for % reduce rejection rate for single-cylinder forged crankshafts (April 2019–Sept.2019) [11]

Production		Rejections due to major defects with % rejections			Total rejections	Current rejection rate %	% Reduce rejection rate
Submitted	Accepted	Due to un-fills	Due to overlap	% Rejections			
74,781	71,365	2219	645	3.82%	3416	4.54%	0.72%

Pareto graph and cause and effect diagram, more than 90% of rejections are due to forging defects in the vein of underfilling, overlap and mislocation.

- Few corrective measures and suggestions have been given to the manufacturing industries of crankshafts and regulating major forging defects would reduce the overall rejection rate from 4.54–0.72% (see Table 4) with reference to Table 6 for single-cylinder forged crankshafts.

Acknowledgements The support has been extended by Forge & Forge Pvt. Ltd.-Rajkot and Gujarat Technological University authorities are highly respected and recognized with due regard.

References

- Thomas GB, Semiatin SL, Vollmer DC (1985) Forging handbook. 2nd edn. American Society For Metals
- Lange K (1994) Handbook of metal forming, New edn. Society of Manufacturing Engineers
- Hawryluk M, Jakubik J (2016) Analysis of forging defects in selected industrial die forging processes. *Eng Fail Anal* 59:396–409
- Dindore A, Badiger G (2020) Optimization of crankshaft by modification in design and material. *Int Res J Eng Technol* 7(3):3321–3325
- Sharma PC, Aggarwal DK (2013) A textbook of machine design., Kataria SK & Son, New Delhi
- Zoroufi M, Fatemi A (2005) Literature review on durability evaluation of crankshafts including comparisons of competing manufacturing processes and cost analysis. In: 26th forging industry technical conference, Chicago, USA
- Young SK, Sung HK, Hyounsoo P, Jong DL (2006) Assessment of micro alloying effect to the new automotive forged steel parts. In: Proceeding the 1st international forum on strategic technology e-vehicle technology. IFOST 2006:170–173
- Soković M, Jovanović J, Krivokapić Z, Vujović A (2009) Basic quality tools in continuous improvement process. *Strojniški vestnik-J Mech Eng* 55(5):333–341
- American Society for Metals (1980) Metals handbook: forming and forging. 9th edn. ASM International
- Wang Q, He F (2004) A Review of developments in the forging of connecting rods in China. *J Mater Process Technol* 151:192–195
- Forge & Forge (2011) Available from: <https://www.forgenforge.com/forging.html>
- Davis JR (1998) Metals handbook, 2nd edn. CRC Press, Materials Park, OH, ASM international
- Montazersadgh FH, Fatemi A (2007) Stress analysis and optimization of crankshafts subject to dynamic loading. AISI, USA

14. Becker WT, Shipley RJ (2002) ASM handbook: failure analysis and prevention. ASM International
15. Altan T, Deshpande M (2011) Selection of die materials and surface treatments for increasing die life in hot and warm forging. FIA Technical Conference, USA, pp 1–32
16. Taylan A (1983) Metal forming: fundamentals and applications. American Society for Metals
17. Kalpakjian S, Schmid SR (2020) Manufacturing engineering and technology. 6th edn New Jersey-USA: Pearson Education, Inc., Prentice Hall, pp 145
18. Shamasundar S (2004) Prediction of defects and analysis of grain flow in crank shaft forging by process modeling. SAE Tech Paper 2004(724):1–8
19. Arentoft M, Wanheim T (1997) The Basis for a design support system to prevent defects in forging. J Mater Process Technol 69(1–3):227–232
20. Yamazaki T, Fukui A (2020) Defect detection for forged metal parts by image processing. Int J Future Comput Commun 9:23–26
21. Z. Quazi, Mayuresh M. Naikwade, Review of forging defect and its remedies, trends in mechanical engineering and technology. STM J 10(2):1–3
22. Barsom J (2009) A study of micro-cracks in overheated forgings of ultra-low sulfur steels for aircraft engine crankshafts. Mater Sci Technol Conf Exhibition, ASM Int Mater Park. Ohio, USA, pp 1192–1203
23. Besterfield DH (2018) Total quality management, Prentice Hall
24. Defeo J (2016) Juran's quality handbook: the complete guide to performance excellence. 7th edn. Washington, DC: McGraw-Hill Education
25. Comer G (2002) Six sigma and other continuous improvement tools for the small shop, dearborn. Society of manufacturing engineers, MI
26. Philip BC (1996) Quality is still free: making quality certain in uncertain times. 2nd edn, New York: McGraw-Hill
27. Mukhopadhyay M (2005) Total quality management in education, 2nd edn. SAGE Publications, London, p 225
28. Basu R (2004) Implementing quality—a practical guide to tools and techniques. 1st edn. UK: Thomson learning
29. Nicholas JM (1998) Competitive manufacturing management: continuous improvement, lean production, customer-focused quality. McGraw-Hill Education
30. Chongwatpol N (2006) Implementing continuous process improvement methods in a mid size plastic company, pp 1–60
31. Nur Shafiqah MS, Mohd Amran MD, Khairanum S (2020) A study of the critical success factor of quality tools and techniques implementation: a current review. J Crit Rev, 7(8):1444–1448
32. Madu (2012) Handbook of total quality management 1998th edn. Springer
33. Summers D (2017) Quality. 6th edn Columbus. OH: Pearson
34. Chiarini A (2011) Japanese total quality control, TQM, Deming's system of profound knowledge. BPR lean and six sigma. Int J Lean Six Sigma 2(4):332–355
35. Ishikawa K (1991) What is total quality control? the Japanese way. English and Japanese edn. Prentice Hall Direct
36. Sekhon MS, Brar GS, Singh S (2014) A Six Sigma approach to detect forging defects in a small scale industry: a case study. Int J Eng Tech Res 2(8):33–40
37. Bagchi TP (1997) Total quality management: tools and implements. IE (I) J 78
38. Sahoo AK, Singh NK, Tiwari MK (2007) Implementation of lean initiatives to minimize defects in a forging enterprise. Int J Prod Qual Manage 2(3):322–346
39. Mahto D, Kumar A (2008) Application of root cause analysis in improvement of product quality and productivity. J Ind Eng Manage 1(2):16–53
40. Chandna P, Chandra A (2009) Quality tools to reduce crankshaft forging defects: an industrial case study. J Ind Syst Eng 3(1):27–37
41. Alves LM, Martins PAF (2011) Flexible forming tool concept for producing crankshafts. J Mater Process Technol 211(3):467–474
42. Mathew C, Koshy J, Varma D (2013) Study of forging defects in integral axle arms. Int J Eng Innovative Technol 2(7):322–326

43. Thottungal AP, Sijo MT (2013) Controlling measures to reduce rejection rate due to forging defects. *Int J sci Res Publ* 3(3):238–243
44. Montgomery DC (2019) *Introduction to statistical quality control*. 8th edn John Wiley & Sons, Inc., Danvers, MA
45. Omachonu VK (2004) *Joel E. Ross, Principles of total quality*, 3rd edn, Taylor & Francis, Boca Raton, Florida
46. Neyestani B (2018) Principles and contributions of total quality management (TQM) gurus on business quality improvement. *SSRN J* 1–17
47. Grant EL, Leavenworth RS (2017) *Statistical quality control*. In: 7th edn. McGraw Hill Education
48. Burke SE, Silvestrini RT (2017) *The certified quality engineering handbook*. 4th edn Milwaukee. ASQ Quality Press, WI
49. Tague NR (2005) *The quality toolbox*, 2nd edn. Wisconsin: ASQ quality press
50. Hubert K (2010) Rampersad, *Total quality management: an executive guide to continuous improvement*, 1st edn. Springer, Verlag Berlin and Heidelberg
51. Forbes LH, Ahmed SM (2020) *Lean project delivery and integrated practices in modern construction*. Boca raton, fly: Taylor and Francis Group
52. Oakland JS (2003) *Total quality management: text with cases*. In: 3rd edn. Jordan Hill, Oxford, UK: Butterworth-Heinemann, an imprint of Elsevier

Numerical Simulation of Temperature Distribution for Low Power Laser Clad Coating of Nickel



Dhiraj Raj, Saikat Ranjan Maity, and Bipul Das

Abstract The simulation of temperature field in additive manufacturing process has raised many challenges in the research area. The temperature profile is very necessary to understand the physical aspects of the process. In the current investigation, a three-dimensional model is developed for simulating the temperature profile for low-power-laser-clad coating of nickel on 410 stainless steel substrates. The temperature profile was calculated at six different points. The laser source is considered as a point heat source which is simulated in COMSOL. The parameters chosen as input process parameters for this work are laser power (P), beam spot diameter (D), and laser traverse speed (V) which were fixed at 100 W, 1 mm, and 1.5 mm/s. The time–temperature profile was obtained after the numerical simulation and it was observed that the maximum temperature obtained during the numerical simulation was more than the melting temperature of the preplaced clad layer which results in the formation of molten puddle which later on solidifies to form a clad layer with better metallurgical bonding and low dilution rate.

Keywords Laser cladding · Finite element · Temperature distribution · Heat source

1 Introduction

Laser cladding is an evolving technique that combines material processing technologies, numerical control, sensor, computer, and laser. It is a material deposition technique in which the powder material is melted by laser to form metallurgical bonding and a clad layer on another material [1]. The substrate material is coated by a coating material which is melted along with the substrate by the laser beam energy. The cladding material and the substrate are allowed to harden to form a clad layer having excellent metallurgical bonding and low dilution rate. The cladding process improves the electrical properties and enhances other surface properties of

D. Raj · S. R. Maity · B. Das (✉)

Department of Mechanical Engineering, National Institute of Technology Silchar, Silchar, India
e-mail: bipul@mech.nits.ac.in

the substrate like heat resistance, oxidation resistance, wear resistance, and corrosion resistance. The laser material deposition technique is characterized by better efficiency, good coating and substrate binding, low dilution rate, compact structure, and other excellent properties [2]. The laser cladding technique is widely being used in automobile, aerospace, ocean, chemical, petroleum, and other industrial fields. It is also used in military as well as medical field. The precise control of the cladding process is required for producing a high-quality coating with a minimum amount of porosity and crack. However, it is very hard to control the cladding process because of the isolated essence of the energy of the laser, the high rate of heating and cooling, and the complex connection among the process parameters [3].

In the past decade, various mathematical models were established for simulating the laser cladding process. Li et al. [4] established a 3-D numerical model for investigating the relation between the flow of powder and laser beam energy, the impact of surface tension on the molten puddle, and the geometry of the clad layer. An ellipsoid melt pool was formed and it was observed that in front of the melt pool the change in temperature is more. Khamidullin et al. [5] suggested a numerical model to analyze the effect of powder density on the dimension of clad layer and the heat-affected zone. Zhu et al. [6] proposed a 3-D model for obtaining the temperature profile of laser clad coating of hydroxyapatite bioceramic coating on titanium alloy substrate. In order to investigate the dimension of the clad layer, Tan et al. [7] introduced an analytical model and also studied the consequence of powder feeding rate and scanning speed on the geometry of the clad layer. Kumar and Roy [8] proposed a heat transfer model to investigate the effect of 3-dimensional melt pool convection on the laser cladding process and also studied the effect of molten puddle size and the convection strength on dilution level, the clad geometry, and the microstructure along with the melted temperature pool. Sowdari and Majumdar [9] proposed a model which was based on enthalpy to investigate the location of the solid-liquid interface, height, and width of the molten puddle, and temperature profile. The 3-dimensional finite element model was established by Roberts et al. [10] to compute the temperature distribution for multiple layers formed during laser melting using birth and death techniques. In this paper, to understand the physical aspects of the laser cladding process, a finite element model is developed for simulating the temperature distribution at a different point during the cladding of 410 stainless steel with nickel powder for repairing the defect.

2 Mathematical Modelling

The mathematical model for calculating the temperature profile during the laser deposition technique was performed in COMSOL software. The elementary energy equation is given in Eq. (1) which is used to express the heat transfer phenomena during the cladding process [11].

$$\frac{\partial}{\partial x} \left(k \frac{\partial T}{\partial x} \right) + \frac{\partial}{\partial y} \left(k \frac{\partial T}{\partial y} \right) + \frac{\partial}{\partial z} \left(k \frac{\partial T}{\partial z} \right) + q = \rho c \left(\frac{\partial T}{\partial t} + u \frac{\partial T}{\partial x} + v \frac{\partial T}{\partial y} + w \frac{\partial T}{\partial z} \right) \tag{1}$$

where, T = temperature, q = total internal heat, ρ = density, c = thermal capacity and k = thermal conductivity of the preplaced layer and t = time. The bottom surface of the specimen was thermally insulated and the surfaces besides the bottom surface were having the convective boundary with the surrounding atmosphere. The radiation phenomena have been neglected and the boundary conditions at the surfaces are defined by

$$k_x \frac{\partial T}{\partial x} n_x + k_y \frac{\partial T}{\partial y} n_y + k_z \frac{\partial T}{\partial z} n_z = h(T - T_0) \tag{2}$$

where h = coefficient of convection, n is defined as the normal to the sample, and T_0 = temperature of the surroundings.

The laser cladding method with the correct setup is shown in Fig. 1 with the support of a schematic diagram. When laser beam hits the outermost layer of the cladding material after being reflected from the mirror then, a part of the laser beam gets reflected and the rest is absorbed by the material. The laser energy melts the preplaced cladding material and the substrate material also gets melted to some extent. The preplaced layer of the cladding material formed a coating having a good metallurgical bond with the substrate material.

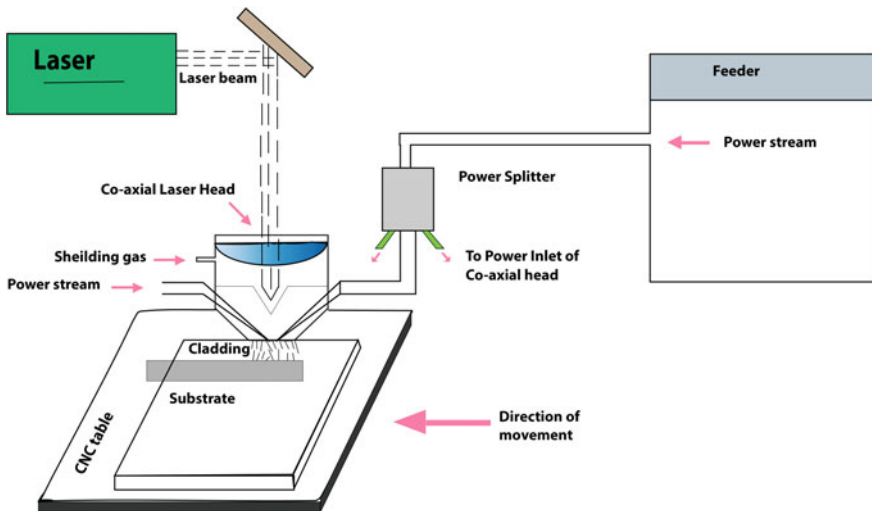


Fig. 1 Laser cladding schematic diagram with proper setup

In this process, loss of heat energy occurs due to convection and radiation should also be considered along with the heat conduction. These complex phenomena of heat transfer increase the complexity of modeling of the process. To reduce the difficulty in proper and effective modeling of the technique the following assumption has been made:

- (1) The initial temperature of the material was assumed to be uniform as 293 K. In this process, a laser beam moving on a circular path having Gaussian profile is used as a point heat source and the Gaussian heat flux Q_{in} is given by Eq. (3):

$$Q_{in} = \frac{2nQ_0}{\pi R_b^2} \exp(-(2R^2)/R_b^2) \quad (3)$$

where Q_0 = total power provided during the process, R_b = beam's focus radius, the coefficient of absorption (n) = 0.25, and R = beam's focus radial co-ordinate given by Eq. (4). The coordinates of the center of the laser beam's concentration are x_1 and y_1 .

$$R = \sqrt{(x - x_1^2)} + \sqrt{(y - y_1^2)} \quad (4)$$

- (2) As the orientation frame is fixed, the system may be regarded as a stationary procedure and a single clad layer is considered to make the issue tractable.
- (3) The loss of laser energy because of the reflection and scattering of the preplaced cladding layer was moped up by considering absorption coefficient Z [12–15]. It is dependent on the nature and characteristics of the surface properties [16]. The absorption coefficient is always presumed as a constant and is in the range of 0.2–0.3 [17]. The Z is taken as 0.25 in this model.
- (4) The point heat source used is moving and highly concentrated and the rate of convection of liquid is very slow and its effect is also small. So, the effect of liquid convection is not considered during the cladding process [18].

The AISI 410 stainless steel plate of $40 \times 40 \times 5$ mm dimension is used as a substrate material. A cavity with a radius of 6.6 mm at the outermost surface and deepness of 2.5 mm is constructed around the crack area on the substrate. The cavity was filled by preplacing nickel powder during the laser cladding process and the temperature distribution at six different points has been calculated which is located on the clad layer as shown in Fig. 2. The process parameter taken during this simulation are Power = 100 W, scanning speed = 1.5 mm/s and laser focus diameter = 1 mm.

The chemical composition and the temperature-dependent properties that is ρ , ζ , and κ of the substrate AISI 410 stainless steel is given in Tables 1 and 2 and for the clad material nickel powder is given in Table 3 respectively [19].

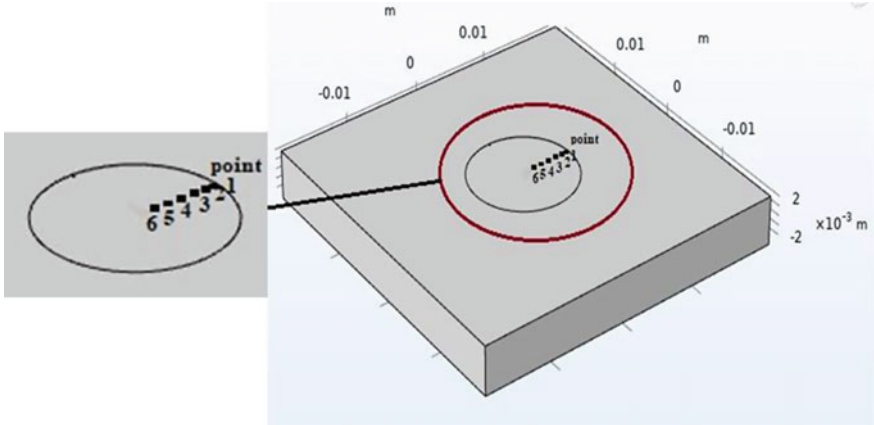


Fig. 2 Geometry of the specimen used for cladding process

Table 1 Chemical composition of the substrate

Material	Carbon	Manganese	Silicon	Phosphorus	Sulphur	Chromium	Nickel
410 stainless steel	0.16	0.9	0.9	0.05	0.04	12–14	0.8

Table 2 Thermal properties of the substrate

Parameters	Minimum value	Maximum value
c (J/Kg K)	450	500
κ (W/m K)	27	34
ρ (Kg/m ³)	7600	7800

Table 3 Thermal properties of clad material nickel powder

Parameters	Minimum value	Maximum value
c (J/Kg K)	452	460
κ (W/m K)	67	91
ρ (Kg/m ³)	8830	8950

3 Result and Discussion

In this model, for achieving computational effectiveness and simulation precision, a dense extremely-fine physics-controlled mesh is used in the preplaced layer and a coarse fine mesh is used in the remaining part of the sample. 47,392 tetrahedrons and 5243 triangular elements are present in the entity of 3-D finite element (Fig. 3).

The temperature distribution is calculated at six different point on the circular path during the movement of laser heat source at six different points as shown in Fig. 4.

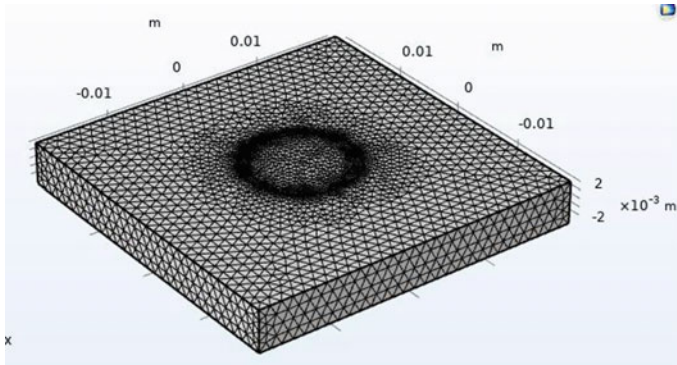


Fig. 3 Finite element mesh model

These points are situated on the path followed by the laser beam traveling on the specimen's coating surface where clad material has been pre-placed. Point 1 is the starting position of the circular path followed by the laser and the other point that is point 2, 3, 4, and 5 are the position of the laser heat source after completion of each rotation and the heat source completes six number of rotations for cladding the total cavity area. From the temperature distribution, it is found that the maximum temperature is obtained when the heat source is near these points and the peak temperature decreases when the laser heat source moves away from these points. The curve obtained in the temperature profile shows that at high temperatures the rate of heating and cooling is also higher which shows that in the high range of temperature the thermal conductivity is very effectual. The maximum simulated temperature (1753 K) obtained at point 6 is higher as compared to the melting temperature (1728 K) of the nickel powder. So, the clad material gets melted along with some part of the base material and a molten puddle is formed during the laser cladding process to form a better-clad layer with excellent surface properties.

4 Conclusion

A 3-D mathematical model is proposed for simulating the temperature distribution at six different points during the laser cladding of 410 stainless steel by using nickel powder as a clad material. A gaussian point heat source is used which is moving on a circular path. The heat losses due to convection and the heat captivated by the substrate and clad layer were considered. The temperature curve shows that a quasi-steady state is obtained by the temperature profile after a certain temperature. The result shows that after completion of the cladding process at $t = 103.5$ s, the temperature of the molten puddle formed (1753 K) is more than the melting temperature of the clad material and just reaches the melting point of the substrate which later on solidifies to give a clad layer with better surface properties.

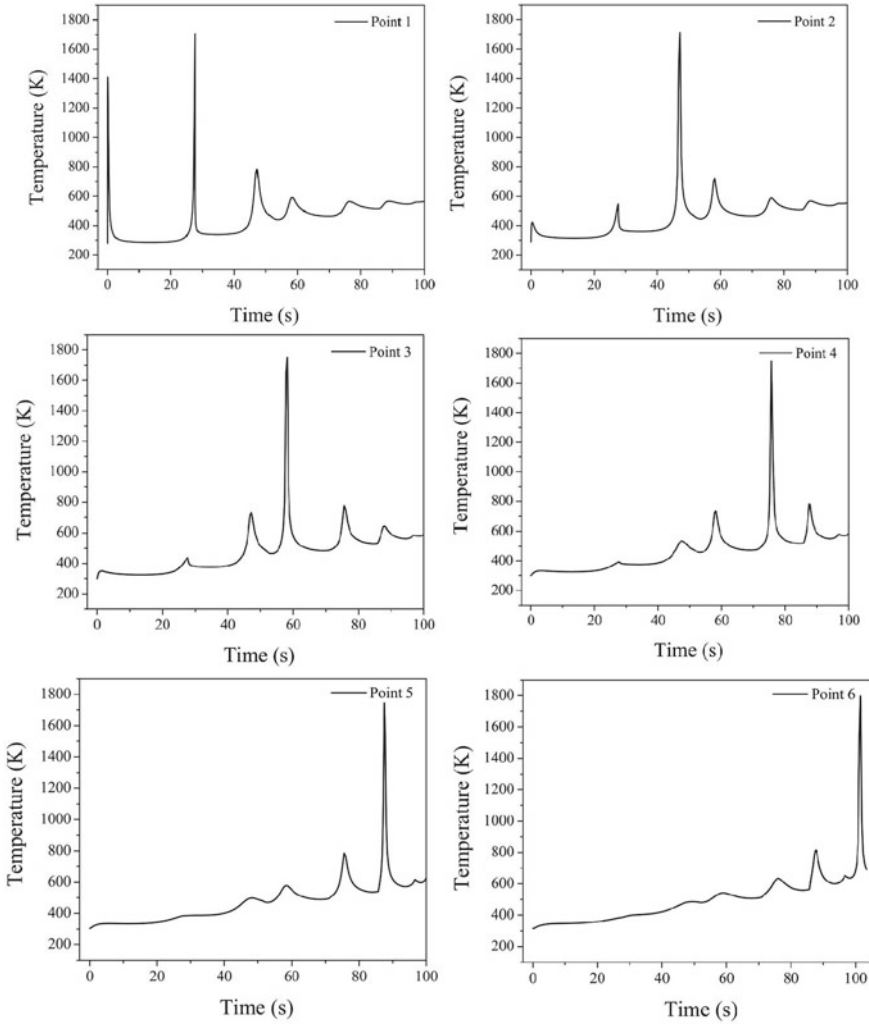


Fig. 4 Temperature distribution at six different points at $t = 103.5$ s

References

1. Lourenço JM, Da Sun S, Sharp K, Luzin V, Klein AN, Wang CH, Brandt M. Fatigue and fracture behavior of laser clad repair of AerMet® 100 ultra-high strength steel. *Int J Fatigue* 85:18–30
2. Meng L, Zhao W, Hou K, Kou D, Yuan Z, Zhang X, Xu J, Hu Q, Wang D, Zeng X (2019) A comparison of microstructure and mechanical properties of laser cladding and laser-induction hybrid cladding coatings on full-scale rail. *Mater Sci Eng A*. 748:1–5
3. Lei Y, Sun R, Tang Y, Niu W (2012) Numerical simulation of temperature distribution and TiC growth kinetics for high power laser clad TiC/NiCrBSiC composite coatings. *Opt Laser Technol* 44(4):1141–1147

4. Li C, Yu Z, Gao J, Zhao J, Han X (2019) Numerical simulation and experimental study of cladding Fe60 on an ASTM 1045 substrate by laser cladding. *Surf Coat Technol* 357:965–77
5. Khamidullin BA, Tsivilskiy IV, Gorunov AI, Kh Gilmutdinov A (2019) Modeling of the effect of powder parameters on laser cladding using coaxial nozzle. *Surf Coat Technol* 364:430–443
6. Zhu W-D, Liu Q-B, Li H-T, Zheng M (2007) A simulation model for the temperature field in bioceramic coating cladded by wide-band laser. *Mater Des* 28(10):2673–2677
7. Tan H, Chen J, Zhang F, Lin X, Huang W (2010) Estimation of laser solid forming process based on temperature measurement. *Opt Laser Technol* 42(1):47–54
8. Kumar A, Roy S (2009) Effect of three-dimensional melt pool convection on process characteristics during laser cladding. *Comput Mater Sci* 46(2):495–506
9. Sowdari D, Majumdar P (2010) Finite element analysis of laser irradiated metal heating and melting processes. *Opt Laser Technol* 42(6):855–865
10. Roberts IA, Wang CJ, Esterlein R, Stanford M, Mynors DJ (2009) A three-dimensional finite element analysis of the temperature field during laser melting of metal powders in additive layer manufacturing. *Int J Machine Tools Manuf* 49(12–13):916–923
11. Du Y, You X, Qiao F, Guo L, Liu Z (2019) A model for predicting the temperature field during selective laser melting. *Results Phys* 12:52–60
12. Pinkerton A, Li L (2004) Modelling the geometry of a moving laser melt pool and deposition track via energy and mass balances. *J Phys D Appl Phys* 37:1885–1895
13. Hofmeister W, Griffith M, Ensz M, Smugeresky J (2001) Solidification in direct metal deposition by LENS processing. *J Manage* 53:30–34
14. Gedda H, Powell J, Wahlstrom G, Li WB (2002) Energy redistribution during CO₂ laser cladding. *J Laser Appl* 14:78–82
15. Pustovalov VK, Bobuchenko DS (1993) Thermal processes in gas–powder laser cladding of metal materials. *Int J Heat Mass Transf* 36:2449–2456
16. Liu Y, Mazumder J, Shibata K (1994) Laser cladding of nickel–aluminum bronze on Al alloy AA333. *Metall and Mater Trans B* 25B:749–759
17. Deng C, Zhang YP, Gao JC (2003) Numerical simulation of temperature field for bioceramic coating cladded by laser. *J Mater Sci Eng* 21:503–506
18. Kim JD, Peng Y (2000) Melt pool shape and dilution of laser cladding with wire feeding. *J Mater Process Technol* 104:284–293
19. George Miller. Azo materials. Oct 23 2001 [Online] Available from: <https://www.azom.com/article.aspx?ArticleID=970>. Accessed 5 Nov 2019

Gear Profile Polishing Using Rotational Magnetorheological Abrasive Flow Finishing Process



Manjesh Kumar, Abhinav Kumar, Hari Narayan Singh Yadav,
and Manas Das

Abstract Tiny gears play a critical role in the transfer of power in smaller machinery used in the aviation, automobile, and biomedical sectors, etc. Nano-finishing tiny gears is a tough job owing to their geometry's intricacy. Precise finishing of small gear increases its life and performance. To impart nano finishing on small gears, it is necessary to remove faults on gear's working surfaces due to manufacturing. The faults include scratch marks, burrs, and pits. Very few finishing processes are applied to small gears due to the narrow spacing between the gear teeth. The rotational magnetorheological abrasive flow finishing process is a magnetorheological polishing fluid-based finishing process which delivers nanometer-level finishing. In the present study, this process is employed to nano finish small steel gear. This problem is addressed by developing gear workpiece fixture and synthesizes optimum polishing fluid in the finishing process. Wire electro discharge machining is used to manufacture the steel gear. After finishing the steel gear, minimum surface roughness of 34.5 nm is achieved. Maximum percentage improvement of surface roughness at involute profile of gear workpiece is obtained as 85.56%. Also, manufacturing defects are removed after the finishing process. After analyzing the finished surface, it is observed that recast layer on the ground surfaces is totally removed after the finishing procedure.

M. Kumar (✉) · A. Kumar · H. N. S. Yadav · M. Das
Mechanical Engineering, Indian Institute of Technology, Guwahati, India
e-mail: manje176103021@iitg.ac.in; manjesh.k@srmmap.edu.in

A. Kumar
e-mail: kumar176103020@iitg.ac.in

H. N. S. Yadav
e-mail: h.narayan@iitg.ac.in

M. Das
e-mail: manasd@iitg.ac.in

M. Kumar
Mechanical Engineering, SRM University AP, Amaravati, India

Keywords Magnetorheological polishing fluid · Nano finishing · Rotational magnetorheological abrasive flow finishing process · Tiny gears

1 Introduction

The need for smaller mechanical devices is steadily rising in the age of nanotechnology. Tiny gears play a critical role in the transfer of power in these miniature devices used in the aviation, automobile, and biomedical sectors. The nanoscale surface polishing on the teeth of the gears will assist in seamless power transfer, noiseless functioning, and extended lifespan. The gear tooth surface suffers a considerable amount of damage due to manufacturing defects and repetitive operations. The hobbing procedure is used to make small gears generally. Some bulged material is detected on the gear surface during the manufacturing process. These extrusions are referred to as rollover burrs. Primary burrs are the name given to this form of rollover burr [1]. Burrs, holes, fractures, pits, and other manufacturing flaws may be found in small gears. Burrs decrease the performance of the gear [2]. The pits are defined as the composition of dents and plastic deformation of the surface [3]. For a tiny gear, finishing the tooth surface is much more complicated than a conventional macro gear. Different types of methods such as hobbing, grinding, honing are available for deburring macro gears but not for tiny gears due to its complex geometry. Small gear is difficult to finish with a conventional method [4, 5]. According to the literature survey, no methods are reported to remove burrs and pits from tiny gears till 2010 [3]. A new method is proposed by researchers to remove pits and burrs from tiny gear tooth edges using a tool shaped like a gear which is made of glass-fiber-reinforced-plastic (GFRP) [3, 4]. This technique is able to extract the microscopic burrs and pits from the surface of tiny gears. Almost all the techniques utilized for the finishing of gears, deal with conventional macro-sized gears which are used for automotive and other purposes.

For resolving the drawbacks of current finishing technologies, an ultra-precision polishing technology, i.e. rotational magnetorheological abrasive flow finishing (*R-MRAFF*) process is employed in the present study to finish tiny gears. In this study, *R-MRAFF* process is used for eliminating burr and pit from the gear teeth profiles and to achieve nano finishing on gear working surfaces. *R-MRAFF* process is a hybrid technique which combines the advantages of abrasive flow machining (AFM), magnetorheological finishing (MRF), and magnetorheological abrasive flow finishing (*MRAFF*) methods [6]. Das et al. [7, 8] used *R-MRAFF* method to finish complex metallic components at the nanometer level. *R-MRAFF* method uses magnetorheological polishing fluid (*MRPF*) [9] which has the capability to increase the viscosity considerably in the occurrence of the applied magnetic field. MR polishing fluid is a combination of magnetic iron powder and non-magnetic abrasive particles in a base media [10, 11]. They used MR polishing fluid (*MRPF*) containing 26.7 vol. % iron particles (IPs) and 13.5 vol. % silicon carbide (SiC) abrasive for polishing stainless steel workpieces and the least achieved *Ra* was 16 nm [7].

In the present experimental investigation, tiny gear is made from SS316L material. The steel gear component is planned and made using wire electro-discharge machining (EDM). The gear is then finished by *R*-MRAFF process. The process variables are first optimized by using the preliminary experimental study. Further, the optimum experimental conditions are used to nano finish the workpiece. The polishing gear surfaces are examined and characterized by utilizing optical profilometer and FESEM image analysis.

2 Experimentation

2.1 Experimental Setup and Methodology

In *R*-MRAFF experimental setup, the desired workpiece is finished by flowing stiffer MR polishing media across the surface in the polishing region underneath the presence of the external magnetic field. Two symmetric hydraulic cylinders are fixed on the top and the bottom of the experimental set up which are filled with oil and provide a vertical to and fro motion on the existing MR polishing fluid. Due to this upward and downward motion, the MRP media is forced through the workpiece fixture from topmost to bottommost polishing cylinder and bottommost to topmost polishing cylinder [7]. The *R*-MRAFF process experimental apparatus is demonstrated in (Fig. 1). A small gear fixture (Fig. 1) is designed and developed to finish small gear in *R*-MRAFF process. The workpiece fixture holds the small gear workpiece during finishing. The workpiece fixture is surrounded by a magnet fixture, as shown in (Fig. 1). This magnet fixture is rotated by an induction motor through the attached belt (Fig. 1). The workpiece fixture is designed in such a manner which is capable of adjusting, holding, and disassembling easily.

A rotating motion is given to the magnet fixture. Due to this vertical and rotational motion, the MR polishing fluid has enough room to retain and flow through the workpiece fixture to finish the gear workpiece. The flow of MRPF during the polishing procedure is demonstrated in (Fig. 2). The MRP media experiences a rotational motion (Fig. 2b) and a reciprocating motion (Fig. 2a) at the finishing zone around the gear workpiece.

The workpiece fixture is fixed in between two polishing media cylinders along with the magnet fixture. Eight holes on the outer side of both the flanges were made for letting the MRPF flow across the workpiece. The retention of more MR polishing fluid helps in better finishing of workpiece. Sufficient area is left in the workpiece fixture to retain enough MR polishing fluid inside the workpiece fixture for finishing gear workpiece.

The material used to manufacture the gear workpiece is SS316L. The radius of the small gear is 7.5 mm. In the present study, steel gear workpieces are manufactured using a wire EDM process. The schematic diagram of the flow of MRP media inside the small gear fixture during the *R*-MRAFF process is shown in (Fig. 2).

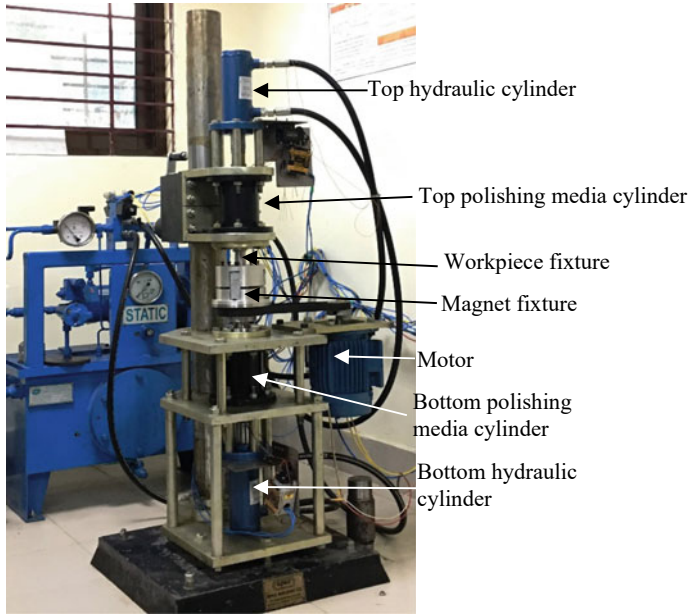


Fig. 1 R-MRAFF process experimental setup

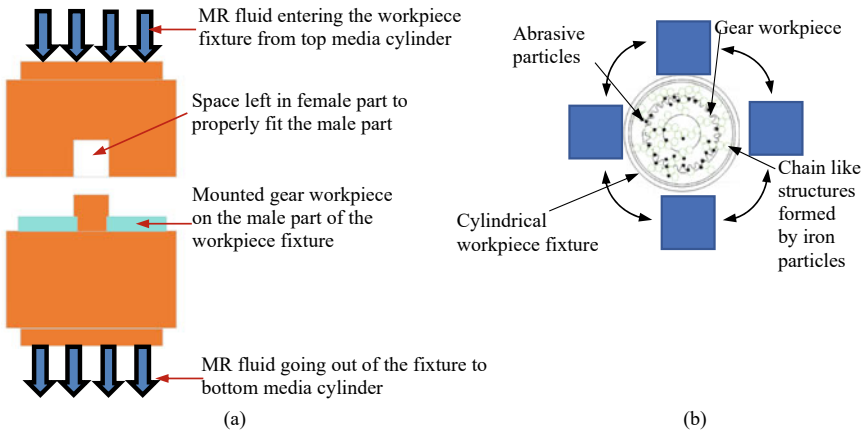


Fig. 2 The flow of MR polishing fluid during the finishing process a side view and b top view

Key process parameters in case of R-MRAFF process are hydraulic pressure, number of finishing cycle, MR polishing fluid composition and concentration, and magnet rpm [8]. Hydraulic pressure, MR polishing fluid concentration, and magnet rpm are maintained constantly throughout the polishing procedure and their value is given in Tables 1 and 2. MR polishing fluid compositions and count of

Table 1 Volume content of MRPF constituents

Constituents	Iron particles	Abrasive particles	Grease	Paraffin oil
Volume concentration (vol. %)	22	8	10	60

Table 2 Experimental condition during preliminary experiment

Experimental conditions	No. of finishing cycle	Pressure (bar)	Magnet fixture rpm
Value	800	30	100

finishing cycles are varying to obtain necessary process parameter values to finish small gear workpiece effectively.

The volume concentration of each constituent of MRPF to polish tiny gear component in R-MRAFF method is listed in Table 1. The base media percentage is increased to allow MRPF to flow more readily within the work fixture.

During the polishing procedure, SiC of 800 mesh size is used as abrasive particles (APs). According to preliminary experiments, an AP of 800 mesh size is adequate to achieve nanoscale scale surface finish on a tiny gear component, 800 mesh size is considered in case of IPs [12]. A preliminary experimental investigation is executed to find out the optimum mesh size of the iron particle. The experimental condition as given in Table 2 for each preliminary experiment is kept same.

After the preliminary experiments, it was observed that polishing small gear with IPs of 800 mesh size is highly appropriate. Better surface quality is obtained after polishing with 800 mesh size IPs. Agglomeration of MRPF is noticed with IPs of 400 mesh size since 400 mesh size is denser and coarser than 800 mesh size. As a consequence, IPs detach from the base media, and IPs have little influence on the gear workpiece’s intricate profiles. Hence, no difference in surface quality is detected between gear teeth profiles using 400 mesh size of IPs.

Following the selection of the MRPF content, the number of finishing cycle is adjusted to determine optimal number of finishing cycles. To begin, the experiment is performed for 200 cycles. It is noted that a little modification in surface roughness takes place on the gear component. Afterward, a finishing cycle of 400 was chosen, and a higher surface smoothness was seen as comparing to while utilizing a finishing cycles of 200, but it was not yet suitable for the gear surface requirement. Once the 800 finishing cycle are completed, the nanoscale level of surface finishing is obtained. With the additional experimentation, certain surfaces with superior surface finish are obtained, but greater cracking and distortion on the gear teeth involute profiles are noticed. The 800 finishing cycles for subsequent experimentation are thus chosen.

After selecting the optimum process parameter conditions, further experiments are carried out to characterize the finished profiles of the steel gear component. The surface roughness and surface topography of the pre and post-polishing gear surfaces at the different positions are analyzed. Also, FESEM image of the involute profile of small steal gear component before and after polishing are analyzed.

3 Result and Discussions

The characterization of the steel gear workpiece is carried out pre and post finishing experiment. An optical profilometer is used for seeing surface roughness and surface topography. FESEM analysis of the workpiece is also carried out to observe any recast layer or loose material is still present on gear involute surfaces. As shown in (Fig. 3), gear tooth face, gear tooth top, gear tooth involute profile, and in between gear teeth surfaces are characterized to analyze the R-MRAFF process capability to deliver nanometer level finished miniature gear with fine surface finish.

3.1 Surface Topography and Surface Roughness Analysis of Steel Gear Component

Figure 4 demonstrates the surface topography and surface roughness profiles at gear tooth face before and after finishing. The deep scratch marks and burrs are removed on final surface (Fig. 4b) from the ground surfaces (Fig. 4a). The R_a of 42 nm (Fig. 4d) is achieved on the face profile of the gear teeth from the ground surface roughness, R_a of 230 nm (Fig. 4c). The percent enhancement of R_a is 81.73%.

Initial gear tooth top surface topography is demonstrated in (Fig. 5a). As demonstrated in (Fig. 5b), pits from the ground surfaces (Fig. 5a) are decreased after the polishing procedure. The high peaks and deep valley of the ground surface roughness profiles (Fig. 5c) is removed in the final surface roughness profiles (Fig. 5d). The final R_a of 34 nm is achieved from the ground R_a of 1090 nm on the tooth top. The percent change in R_a is calculated as 96.88%.

Surface topography and surface roughness of gear teeth involute profiles pre and post-polishing procedure are shown in (Fig. 6). The involute profile before finishing

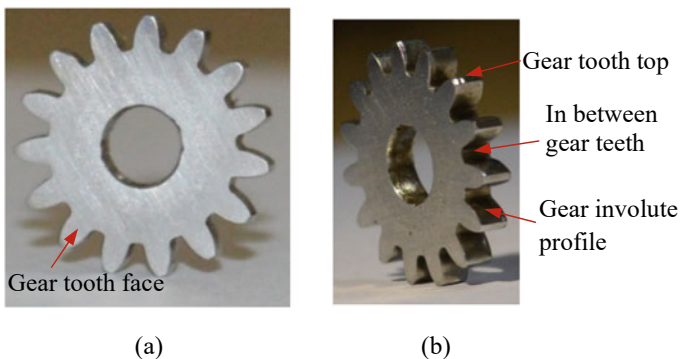


Fig. 3 Gear surfaces taken for characterization **a** teeth face and **b** teeth top, in between teeth, and involute profiles

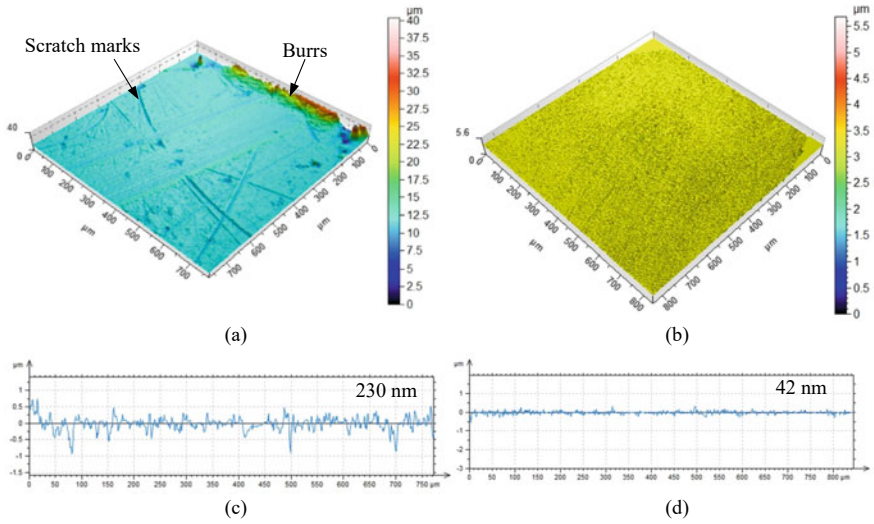


Fig. 4 3D surface topography of gear teeth face profile **a** pre and **b** post finishing; surface roughness profile of gear teeth face profile **c** pre and **d** post finishing

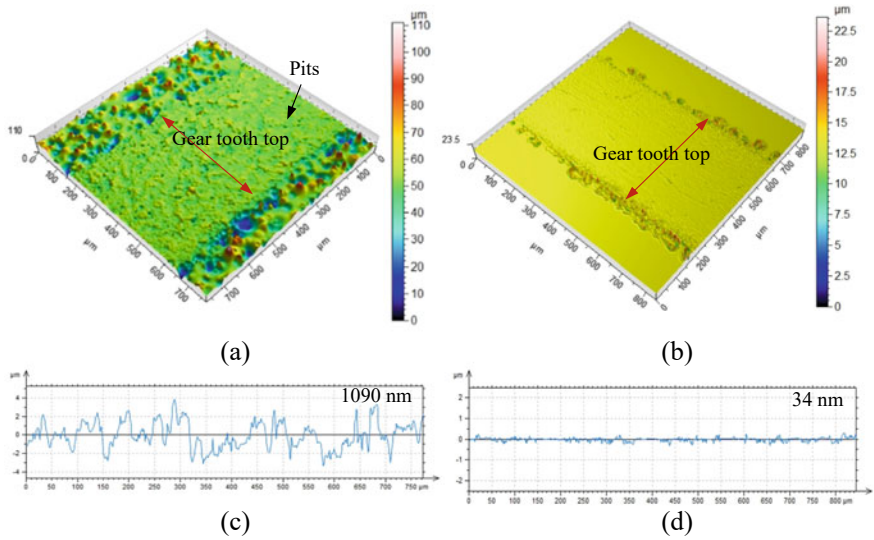


Fig. 5 3D surface topography of gear tooth top profile **a** pre and **b** post finishing; surface roughness profile of gear teeth top profiles **c** pre and **d** post finishing

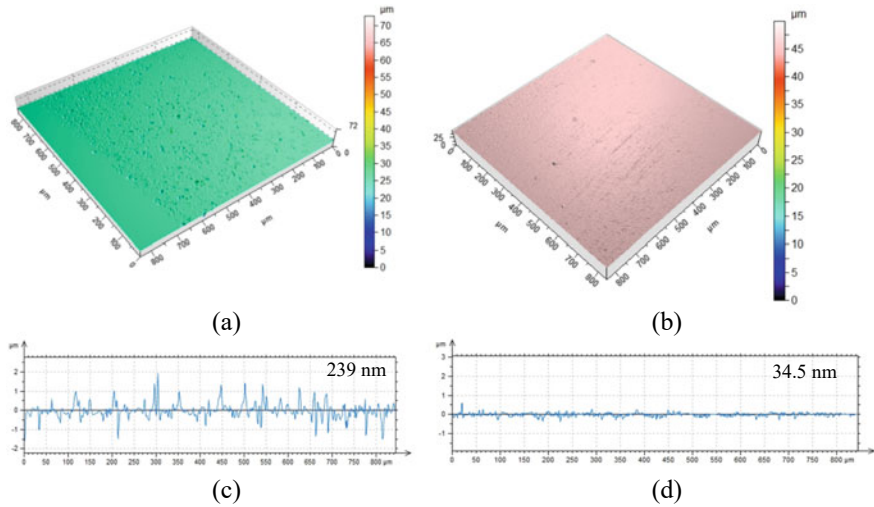


Fig. 6 3D surface topography of gear involute profile **a** pre and **b** post finishing; surface roughness profile of gear involute profile **c** pre and **d** post finishing

is covered with pits as shown in (Fig. 6a). Post polishing with *R*-MRAFF method, pits are removed from the gear teeth profiles, as demonstrated in (Fig. 6b). The final average R_a is achieved as 34.5 nm from the ground R_a of 239 nm, as demonstrated in Figs. 6c and d, respectively. The percent change in R_a in case of involute profile is 85.56%.

The crater-like pits and burrs are present on the initial surface of in between gear teeth profiles (Fig. 7a) are reduced in final surfaces as shown in (Fig. 7b). The surface roughness in between teeth profile is improved from 1630 to 52 nm with 96.80% change as shown in Figs. 7c and d, respectively. The surface roughness achieved for polishing mold by abrasive flow machining (AFM) method, which is utilized for making plastic gear is 70 nm [13]. The traditional abrasive polishing procedures like grinding, honing or their combination does not produce the nano-finishing surfaces of small gear due to complexity in their geometry, narrow spacing between teeth [14]. The glass-fiber-reinforced-plastic (GFRP) tool, which is made exactly like gear shape profiles, is also more useful for removing only the tool marks done by conventional finishing processes [4]. This GFRP tool method is also not able to achieve nano-scale surface finish for small gears.

According to surface roughness study, percentage improvement in surface roughness is higher in in-between profile of gear tooth, tooth top profile, and involute profile surface than gear tooth face surface. In *R*-MRAFF method, the face surfaces of gear component are subjected to more tangential force than shear force due to both MR polishing fluid movements (rotational and reciprocating) and position of the gear workpiece in the workpiece fixture during finishing. On the other hand, involute, tooth top, and in-between profile surface of gear tooth are subjected to more shear force than tangential force. Due to this difference in finishing forces material

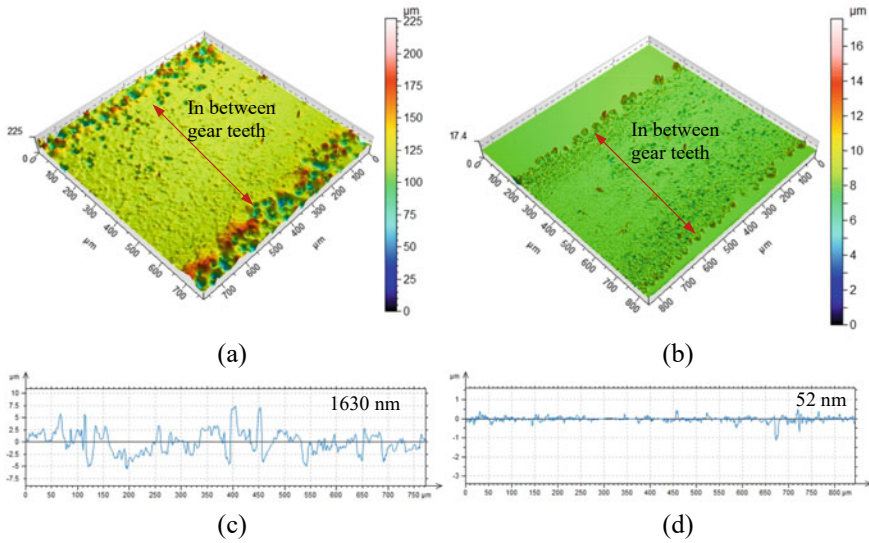


Fig. 7 3D surface topography of in between gear teeth profile **a** pre and **b** post finishing; surface roughness profile of in between gear teeth profile **c** pre and **d** post finishing

removal is higher in involute surface, tooth top and in-between gear tooth profile than face surface of gear tooth. This is acceptable as the gear tooth face is not a working surface.

3.2 FESEM Analysis of Steel Gear Component

FESEM analysis is used to observe the micrographic descriptions of the gear component pre and post finishing. Micrograph analysis helps to observe and analyze a different kind of defects in working areas of gear workpiece. The surface finish on the involute surfaces of the gear teeth is observed, and it is found that the surface finish on the involute tooth profile is better after finishing, as shown in (Fig. 8). The presence of the recast layer is confirmed in the involute profiles of the gear tooth before the finishing process (Fig. 8a). The recast layer and the loose materials from the surface of the involute profile of the gear teeth are completely removed post finishing process, as demonstrated in (Fig. 8b). Also, as shown in (Fig. 8b), final surface is smoother than the initial surface.

The presence of pits with a rough surface is observed at gear tooth involute profile. After the finishing process, fewer dent marks with a smoother surface are observed. The surface texture of the finished surface has negligible scratch mark, dents and pits to initial surfaces as observed from the micrograph analysis.

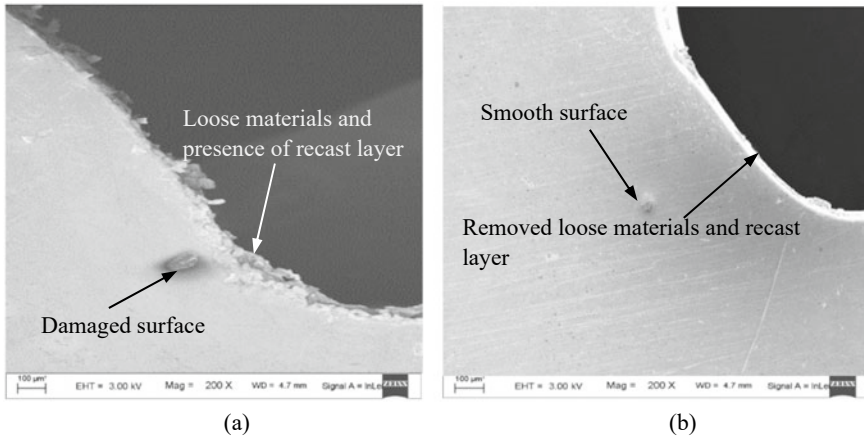


Fig. 8 FESEM image of gear involute profile **a** before and **b** after finishing

The steel gear workpiece is manufactured using a wire EDM process for which it is subjected to recast layers. The presence of the recast layer is found by performing a micrograph and 3D surface topography analysis of the gear. The recast layer is present on gear involute surface before finishing is demonstrated in (Fig. 8a). After finishing process, the recast layer is completely removed from the involute surface of gear (Fig. 8b).

3.3 Material Removal Rate (MRR) of Steel Gear Component

The material removal rate is the amount of materials that are removed per minute. In the present case, the required time to complete the total finishing experiment and volume of the workpiece before and after finishing is measured to calculate the MRR. The MRR is calculated from the following relation Eq. (1) and calculated MRR/min of steel gear workpiece is shown in Table 4.

$$MRR = \frac{\text{Initial weight} - \text{Final weight}}{\text{Finishing time}} \tag{1}$$

Table 4 MRR of steel gear workpiece

Total Finishing time (min)	Initial weight (gm)	Final weight (gm)	MRR/min
210	1.6783	1.5870	0.0004347

4 Conclusion

Small steel (SS316L) gear workpiece is finished using *R-MRAFF* process. The finished surface is analyzed to find out the finishing process capability to remove burrs, pits, and recast layer from the working surface of gear workpiece. The finished surfaces are compared with the initial surfaces of gear profiles by using surface topography, surface roughness, and micrographic image analysis. A preliminary experimental study is conducted on the steel gear workpiece to determine required process parameter conditions for finishing of gear workpiece. Based on the current investigation, following conclusions can be drawn:

- Iron and abrasive particles of 800 mesh sizes used in the MR polishing fluid have given the best result and also do not cause any kind of sedimentation problem during the finishing process. Nanometer level surface finish on all the surfaces of the steel gear workpiece is achieved.
- The optimum number of finishing cycles is 800, which provides the necessary surface roughness without deteriorating the finished gear working profiles.
- The minimum obtained surface roughness on the involute profile of steel gear teeth is 34.5 nm. Maximum percentage improvement of surface roughness obtained as 85.56%.
- The percentage improvement in MRR and finishing rate (FR) is higher in in-between profile of gear tooth, tooth top profile, and involute profile surface than gear tooth face surface. As in *R-MRAFF* process, involute, tooth top and in-between profile surface of gear tooth are subjected to more shear force than tangential force. Due to this difference in finishing forces material removal is higher in involute surface, tooth top, and in-between gear tooth profile than face surface of gear tooth.
- The maximum material removal rate (MRR) achieved for steel gear using *R-MRAFF* process is 0.0004347 gm/min.
- Recast layer is completely removed from the finished steel gear workpiece. And, also manufacturing defects like scratch marks, pits and burrs are completely removed from the finished tiny steel gear profiles.

Acknowledgements We acknowledge the Science & Engineering Research Board (SERB), New Delhi, India, for their financial support for project No. EEQ/2017/000597 entitled “Fabrication of Prosthetic Im-plants and further Nanofinishing using Magnetic Field Assisted Finishing (MFAF) Process”.

References

1. Miyake T, Yamamoto A, Kishimoto W, Yamanaka K, Takano K (1987) Study of Burr formation in face milling (1st Report). *J Japan Soc Precis Eng.* 53(1):98–104
2. Gillespie LK (1999) Deburring and edge finishing handbook. *Soc Manufact Eng*, 230–245.

3. Fujisawa Y, Komori M (2010) Method for removing burrs and pits from small gears using a gear-shaped tool composed of glass-fiber-reinforced plastic. *J Mater Process Technol* 210(9):1159–1170
4. Fujisawa Y, Komori M (2015) Surface finishing method for tooth flank of heat-treated surface-hardened small gears using a gear-shaped tool composed of alumina-fiber-reinforced plastic. *Precis Eng* 39(5):234–242
5. Yi J, Ding Y, Zhao S, Ji B, Zhou J (2009) A novel technique of polishing gear working surface using PECMP. *Int J Precis Eng Manuf* 10(4):57–62
6. Kumar M, Kumar A, Alok A, Das M (2020) Magnetorheological method applied to optics polishing: a review. *IOP Conf Ser Mater Sci Eng* 804(01):12–13
7. Das M, Jain VK, Ghoshdastidar PS (2010) Nano-finishing of stainless-steel tubes using rotational magnetorheological abrasive flow finishing process. *Mach Sci Technol* 14(3):365–389
8. Das M, Jain VK, Ghoshdastidar PS (2012) Nanofinishing of flat workpieces using rotational-magnetorheological abrasive flow finishing (R-MRAFF) process. *Int J Adv Manufact Technol* 62(7):405–420
9. Alok A, Niranjan MS, Kumar A, Kumar M, Das M (2020) Synthesis and characterization of sintered magnetic abrasive particles having alumina and carbonyl iron powder, *IOP Conf Ser Mater Sci Eng* 804(01):2002
10. Sidpara A, Jain VK (2014) Rheological properties and their correlation with surface finish quality in MR fluid-based finishing process. *Mach Sci Technol* 18(3):367–385
11. Nagdeve L, Jain VK, Ramkumar J, Nano finishing of freeform/sculptured surfaces: state-of-the-art. *J Manufact Rev* 6(3):1–20
12. Kumar M, Kumar V, Kumar A, Yadav HNS, Das M (2021) CFD Analysis of MR fluid applied for finishing of gear in MRAFF process. *Mater Today Proc* 25(3):1–7
13. Kenda J, Duhovnik J, Tavcar J, Kopac J (2014) Abrasive flow machining applied to plastic gear matrix polishing. *Int J Adv Manufact Technol* 71(4):141–151
14. Karpuschewski B, Knoche HJ, Hipke M (2008) Gear finishing by abrasive processes. *CIRP Ann Manufact Technol* 57(2):621–640

Particle Swarm Optimization Based Search for Optimal Operating Condition in WEDM Operation of A286 Superalloy



Subhankar Saha, Saikat Ranjan Maity, and S. Dey

Abstract Attaining improved level of process performance in wire-electro discharge machining (WEDM) at any particular parametric condition is always a complicated task due to the inherent nature of the process. Endeavour to improve one performance measure is always done at the cost of the remaining performance measures. Amongst the performance measures, material removal rate (MRR) and surface roughness (SR) are of interest in this paper and they are contradicting in nature. Thus, the present paper targets to optimize the WEDM performances concurrently using a popular solver. Particle swarm optimization (PSO) solver for an Iron-based superalloy namely A286 superalloy. To pursue the optimization procedure, the two objectives are clubbed together to form a single objective by the addition of weights. The optimum MRR and SR obtained are 19.90 mm²/min and 3.49 μm respectively. Additionally, field emission scanning electron microscopy (FESEM) is employed to throw light on the morphological characteristics of the machined surfaces obtained by machining at low pulse energy (LPE) setting and at high pulse energy (HPE) setting.

Keywords Wire EDM · A286 superalloy · Particle swarm optimization

1 Introduction

Over the last few decades, evaluation of machining performances of a wide variety of superalloys has become a potential area of research. The growing urge among researchers to explore this particular domain is mainly due to the tremendous demand for these materials in critical technological applications such as turbosuperchargers, jet/rocket engines, nuclear reactors, etc. Superalloys are highly reliable materials as they defend their mechanical strength at elevated temperature. Besides, exhibiting appreciable resistance to creep at prolonged exposure to elevated temperature is another interesting feature of such alloys. Furthermore, they showcase outstanding

S. Saha (✉) · S. R. Maity · S. Dey
Mechanical Engineering Department, National Institute of Technology, Silchar, India
e-mail: sahamech90@gmail.com

© The Author(s), under exclusive license to Springer Nature Singapore Pte Ltd. 2023
T. S. Sudarshan et al. (eds.), *Recent Advancements in Mechanical Engineering*,
Lecture Notes in Mechanical Engineering,
https://doi.org/10.1007/978-981-19-3266-3_45

577

resistance to corrosion and oxidation which is an essential prerequisite for any components in hazardous environments.

A286 superalloy is an iron-based superalloy which is generally used in gas turbine industry. A286 superalloy is copiously used in the gas turbine wheels (disks) exposed to ranges of medium elevated temperatures [1]. Besides, it is also deployed in frames, after-burner parts, fasteners, casings, rotors, and a few other applications owing to its superior mechanical properties and good thermal resistivity [2]. However, it is worth mentioning that a major limitation of such superalloys is that they pose an ample number of difficulties when machined by conventional machining processes [3]. Thus, it is always a good choice to machine these superalloys with the advanced machining processes like electrochemical machining (ECM), laser beam machining (LBM), Abrasive water jet machining (AWJM), sinking electrical discharge machining (SEDM), and WEDM. Amongst them, wire EDM shows higher pliancy in terms of machining complex shapes, and in fact high levels of accuracy and precision can be achieved [4]. Moreover, surface integrity characteristics are good enough to be considered for safety-critical components.

WEDM has gained lot of attention from the researchers due to its unique way of removing the material from the workpiece. The material gets detached in small quantity repeatedly from the workpiece by fusion or vaporization due to the energy imparted by the repeated occurrence of controlled spark between the wire electrode and the workpiece material. During the spark-off time, the flushing of the debris is taken care of by the dielectric fluid which flows amid the wire electrode and the workpiece.

WEDM has been widely used in the aerospace, automotive, medical and electronic industries for machining difficult-to-cut materials and also capable of generating intricate shapes. The selection of optimum parametric setting in WEDM is a critical step. Proper selection of machine parameters may eliminate the chances of detrimental sequel such as short-circuiting of wire and wire rupture. Moreover, machining at optimal parametric setting helps to attain the required cutting performance. Therefore, various optimization procedures are incorporated by researchers for determining the optimal combination of parameters in WEDM of a variety of materials. In a study, it is intended to evaluate the machining outputs of Monel 400, RSM has been used to map the machining rate (MR) and surface roughness (SR) with the four input WEDM parameters and desirability function has been adopted for optimization [5]. In another study, RSM has been used to optimize the process parameter for cutting speed and dimensional deviation [6]. Majumder and Maity-incorporated GRNN to estimate WEDM responses for nitinol. Besides, the authors also applied a hybrid MCDM approach such as MOORA-Fuzzy to determine the optimum combination of parameters for surface roughness and microhardness [7]. Researchers have explored non-dominated sorting algorithm-II for optimization of MRR and mean roughness depth produced by wire EDM of shape memory alloy recently [8]. Tonday and Tigga [9] optimized the machining time and surface roughness exploiting RSM in WEDM of Inconel 718. Looking at the wide applicability of A286 superalloy stated above, and also scarce database on WEDM of A286 superalloy, the present article attempts to evaluate the machining performances such as

Table 1 Levels of control factors

Factors	Levels		
	1	2	3
P_{ON} (μs)	120	125	130
P_{OFF} (μs)	48	52	56
I_{PEAK} (A)	10	11	12
W_F (m/min)	5	7	9
SV (V)	30	35	40

MRR and surface roughness (SR) of this material. FESEM images are portrayed to demonstrate the impact of pulse energy on features developed on the machined surfaces. Furthermore, it is intended to search for the optimal machining condition for simultaneous optimization of the two responses by exploiting Particle Swarm Optimization (PSO) solver.

2 Experimental Methodology

The machining runs have been conducted on Ultra cut *F-1* model of wire EDM machine tool. In this work, it is envisaged to control five important process parameters which are pulse on time (P_{ON}), pulse off time (P_{OFF}), peak current (I_{PEAK}), wire feed rate (W_F), and servo voltage (SV). The levels considered for the five control parameters are displayed in Table 1. 27 experiments have been performed based on L_{27} orthogonal array and the experimental responses are reported in Table 2. The material removal rate, $MRR = Cs \times L$, is evaluated using the cutting speed (Cs) acquired from the control panel and the plate thickness (L). The Surtronic *S-128 S-Series* roughness tester (a contact-type surface roughness instrument) is employed for measuring the surface roughness with cut-off length of 0.8 mm.

3 Methods

3.1 Particle Swarm Optimization

Particle swarm optimization (PSO), a stochastic optimizer which was introduced by Kennedy and Eberhart [10]. The algorithm initiates with a population of particles (solutions) and continues quest for the optimal in the search domain by means of updating generations. The basic difference of this algorithm from other evolutionary-based algorithms is its unique way of not using any selection criteria in iterative procedure. Thus, members of the population will exist from the beginning to the

Table 2 Experimental responses

P_{ON}	P_{OFF}	I_{PEAK}	W_F	SV	MRR (mm ² /min)	SR (μ m)
120	48	10	5	30	2.45	0.83
120	48	11	7	35	18.90	3.50
120	48	12	9	40	15.65	3.13
120	52	10	7	35	1.70	0.80
120	52	11	9	40	12.85	2.80
120	52	12	5	30	15.35	2.43
120	56	10	9	40	1.15	0.77
120	56	11	5	30	13.85	2.87
120	56	12	7	35	11.30	2.90
125	48	10	7	40	2.10	1.07
125	48	11	9	30	22.95	3.53
125	48	12	5	35	23.15	3.77
125	52	10	9	30	1.75	1.02
125	52	11	5	35	22.10	3.20
125	52	12	7	40	17.70	3.37
125	56	10	5	35	1.70	0.93
125	56	11	7	40	15.15	3.10
125	56	12	9	30	15.75	3.30
130	48	10	9	35	2.45	1.17
130	48	11	5	40	27.00	3.80
130	48	12	7	30	37.10	3.87
130	52	10	5	40	2.10	1.13
130	52	11	7	30	25.25	3.90
130	52	12	9	35	27.60	3.33
130	56	10	7	30	1.75	0.97
130	56	11	9	35	20.90	3.77
130	56	12	5	40	29.70	3.37

end of optimization process. PSO has been extensively applied to deal with many engineering problems. The flow diagram for PSO algorithm is displayed in Figure 1.

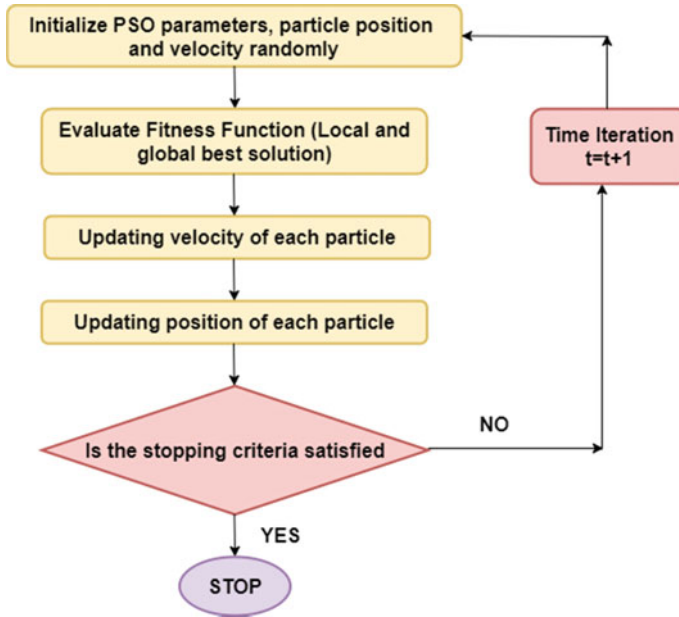


Fig. 1 Flow diagram of PSO algorithm

4 Results and Discussions

4.1 Multi-objective Optimization Exploiting PSO

Multi-objective optimization optimized several objectives concurrently while satisfying the different constraints. A relative preference factor or weight is assigned for all the objectives which serve to club the multiple objectives into single objective (composite fitness function). In other words, the composite fitness function is the weighted summation of the different objectives. Then optimization of the composite fitness function is performed using PSO to achieve a trade-off solution. In the present article, we consider the two objectives i.e.

maximization of MRR and minimization of SR in wire EDM of A286 superalloy. The composite fitness function (CF) thus can be represented by the Eq. 1 shown below:

$$\text{Maximize CF} = w_1\text{MRR} - w_2\text{SR} \quad (1)$$

w_1 is weight allocated to MRR, and w_2 is weight allocated to SR.

$$120 \leq P_{ON} \leq 130$$

$$48 \leq P_{OFF} \leq 56$$

Subjected to:

$$10 \leq I_{PEAK} \leq 12$$

$$5 \leq W_F \leq 9$$

$$30 \leq SV \leq 40$$

To perform the optimization, the objective function for MRR and SR are achieved by regression analysis. For brevity, the regression models are not shown here. In the present article, equal weights ($w_1 = 0.5$, $w_2 = 0.5$) are allotted for both objectives. The composite fitness function as shown in Eq. 1 is then maximized using PSO algorithm programmed in MATLAB R2018a. The search space for optimization is within the specified parameter bounds. Number of parameters considered in the present investigation is 5. To run the optimization, the parameters are tuned as follows:

Population size = 100;

Maximum iteration = 1000;

Maximum run = 20;

It is observed that the convergence of the algorithm is achieved at 100 iterations. Figure 2 furnishes the PSO convergence characteristic wherein it is noticed that for iterations less than 100, the value of composite fitness function remains unsteady but after 100 iterations, it ceases at a steady value of 157.6. Finally, the optimal value of MRR and SR obtained are 19.90 mm²/min and 3.49 μm respectively and the optimal parametric condition are ($P_{ON} = 130$ μs, $P_{OFF} = 52$ μs, $I_{PEAK} = 12$ A, $W_F = 5$ m/min and $SV = 30$ v).

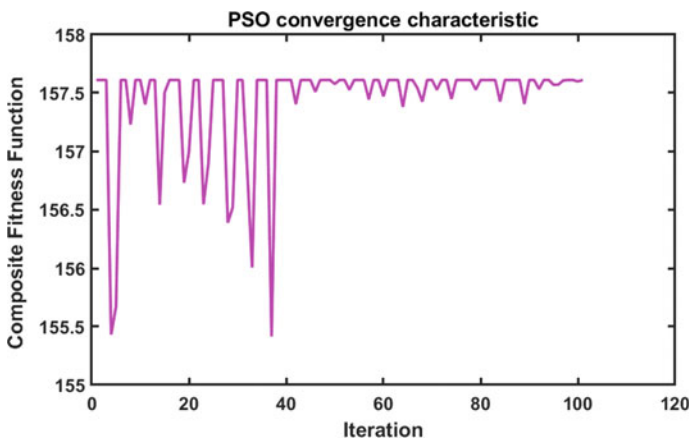


Fig. 2 Convergence plot of PSO algorithm

4.2 Analysis of Surface Morphology

The morphological structure of the machined surfaces is enlightened for WEDM of A286 superalloy by undergoing surface analysis for two samples at low and high discharge energy settings. The analysis has been carried out at random positions of the samples using field emission scanning electron microscopy (FESEM) at a magnification of (i) 2000 × (ii) 5000 × and (iii) 7000 × respectively. Figure 3 reveals the microstructure developed on the machined surfaces for high energy discharge setting ($P_{ON} = 130 \mu\text{m}$ and $I_{PEAK} = 12 \text{ A}$) and low energy discharge setting ($P_{ON} = 120 \text{ m.u}$ and $I_{PEAK} = 10 \text{ A}$).

Craters are cavities that are generated on the surfaces during WEDM machining. Figure 3a reveals the formation of shallow craters at a parametric combination of $P_{ON} = 120 \mu\text{m}$ and $I_{PEAK} = 10 \text{ A}$ which may be ascribed to the lower thermal energy supplied to the work material by the generated spark. On the contrary, deep craters are observed on the machined surface produced at a parametric combination of $P_{ON} = 130 \mu\text{m}$ and $I_{PEAK} = 12 \text{ A}$ as shown in Fig. 3b. This is ascribed to a vigorous amount of fusion and vaporization of the work material as a higher amount of heat

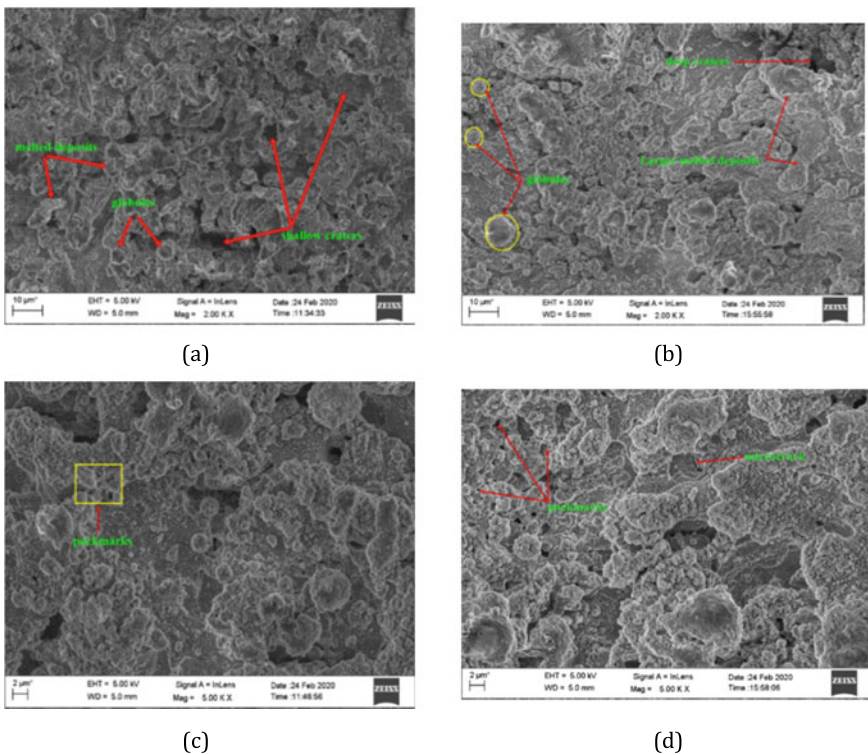


Fig. 3 FESEM micrographs of machined surfaces a and c LPE setting, b and d HPE setting

flow to the workpiece material because of the interplay between the higher discharge current (higher heat generation) and longer pulse on time (spark sustains for longer duration).

Pockmarks are surface defects triggered by the entrapment of gas bubbles within the re-solidified metal. From Fig. 3c, it is evident that there are very few pockmarks which may be attributed to the lesser amount of gases induced in the plasma channel because of small scale vaporization of molten metal due to the reduced spark energy which connotes lower thermal energy impingement on the work material. On the other hand, microstructure reveals evidence of considerable pockmarks disseminated over the machined surface for high energy discharge settings as shown in Fig. 3d which corroborates a large number of gases envelop over the plasma channel on account of higher thermal-induced vaporization of molten metal because of the higher thermal energy absorbed by the work material. Thus, in this process, there is considerable entrapment of vapor bubbles on the molten pool which leads to the possibility of a larger quantity of pockmarks on the re-solidified molten metal.

Globules are spherical agglomerates formed by rapid cooling (vapor–solid phase transformation) of the vaporized work material emanating from the discharge spot. From the micrographs obtained for low and high pulse energy as shown in Fig. 3a and b respectively, it can be depicted clearly that the density and size of globules are higher for higher energy pulse as compared to lower energy pulse, which is indicative of the larger amount of vapor phase cooling that has possibly occurred at higher pulse energy as a higher mass of workpiece material get vaporized on account of higher thermal energy.

Melted deposits as evidenced in micrographs for higher pulse energy settings are larger as compared to melted deposits for lower pulse energy settings as shown in Figs. 3a and b respectively. This indicates that higher thermal energy due to intense spark created at higher pulse energy settings possibly propelled the melting of the large quantity of work material. However, due to the inadequate amount of flushing by the dielectric fluid, a substantial amount of molten metal gets re-solidified on the machined surface as larger melted deposits and the remaining amount gets wiped off by the dielectric fluid.

Micro cracks are another primary feature on wire EDM machined surfaces. The FESEM image for higher pulse energy settings exhibited micro-cracks (see Fig. 3d) whereas the FESEM image for lower pulse energy settings does not exhibit such micro-cracks at all (see Fig. 3c). The difference in the concentration of micro-cracks hinted that there is severe thermal quenching and contraction experienced by the molten pool and re-solidified layer respectively at higher pulse energy input due to the higher thermal energy and thermal gradients during the process. On the contrary, there is comparatively minimum thermal energy and thermal gradients experienced by the molten pool and re-solidified layer at low pulse energy setting which leads to the absence of microcracks.

5 Conclusions

It can be concluded from the present article that PSO detected optimal MRR as $19.90 \text{ mm}^2/\text{min}$ and detected optimal SR as $3.49 \text{ }\mu\text{m}$. The optimum machine parameters as recommended by PSO are $P_{\text{ON}} = 130 \text{ }\mu\text{s}$, $P_{\text{OFF}} = 52 \text{ }\mu\text{s}$, $I_{\text{PEAK}} = 12 \text{ A}$, $W_{\text{F}} = 5 \text{ m/min}$ and $\text{SV} = 30 \text{ V}$. Furthermore, it is witnessed from the FESEM images that the machined surfaces created at HPE settings are prone to formation of large-sized craters, large globules, large melted deposits, large number of pockmarks, and microcracks. However, the formation of such features is not that intense for machined surfaces created by LPE settings.

References

1. Seifollahi M, Razavi SH, Kheirandish S, Abbasi SM (2014) The mechanism of η phase precipitation in A286 superalloy during heat treatment. *J Mater Eng Perform* 22(10):3063–3069
2. Alphonsa J, Raja VS, Mukherjee S (2015) Development of highly hard and corrosion resistant A286 stainless steel through plasma nitrocarburizing process. *Surf Coat Technol* 280:268–276
3. Ezugwu EO, Wang ZM, Machado AR (1999) The machinability of nickel-based alloys: a review. *J Mater Process Technol* 86(1–3):1–16
4. Sharma P, Chakradhar D, Narendranath S (2015) Evaluation of WEDM performance characteristics of Inconel 706 for turbine disk application. *Mater Des* 88:558–566
5. Kumar, V Kumar V, Jangra KK (2015) An experimental analysis and optimization of machining rate and surface characteristics in WEDM of Monel-400 using RSM and desirability approach. *J Ind Eng Int* 11(3):297–307
6. Sharma N, Khanna R, Gupta RD, Sharma R (2013) Modeling and multiresponse optimization on WEDM for HSLA by RSM. *Int J Adv Manufact Technol* 67(9–12):2269–2281
7. Majumder H, Maity K (2018) Prediction and optimization of surface roughness and micro-hardness using GRNN and MOORA-fuzzy-a MCDM approach for nitinol in WEDM Measure 118:1–13
8. Magabe R, Sharma N, Gupta K, Davim JP (2019) Modeling and optimization of Wire-EDM parameters for machining of Ni 55.8 Ti shape memory alloy using hybrid approach of Taguchi and NSGA-II. *Int J Adv Manufact Technol* 102(5–8):1703–1717
9. Tonday HR, Tigga AM (2019) An empirical evaluation and optimization of performance parameters of wire electrical discharge machining in cutting of Inconel 718. *Measurement* 140:185–196
10. Eberhart R, and Kennedy J (1995) A new optimizer using particle swarm theory. In: *MHS'95 proceedings of the sixth international symposium on micro machine and human science*, pp 39–43

Parametric Analysis of Machining of Titanium Grade-2 Alloy in EDM Under Tap Water



Binoy Kumar Baroi, Tapas Debnath, Jagadish, and Promod Kumar Patowari

Abstract The present work aims to explore the consequence of control parameters in machining characteristics of titanium grade 2 alloy in tap water-assisted electrical discharge machining (EDM). In the experimental study, copper and tap water have been used as electrode and dielectric, respectively. Tap water has been used as a substitute for hydrocarbon oil for reducing toxic emissions and contribute towards process sustainability. The machining properties such as rate of surface roughness, material removal rate and tool wear rate have been explored for distinct changes in pulse-on time and current. A Taguchi L_{16} orthogonal array has been incorporated for the experimentation. ANOVA has been executed to determine the distribution of each variable parameters for machining outputs. Material removal rate and tool wear rate have been observed to increase with the current. For an increase in pulse-on time, tool wear rate has been decreased and material removal rate increased. Surface roughness has been found to increase for both current and pulse-on time. Additionally, micrographs have been investigated to obtain the texture of the workpiece surface.

Keywords Copper · EDM · Tap water · Titanium grade-2

1 Introduction

Electric discharge machining (EDM) is a substantial technique which has been predominantly used for reducing any electrically conductive material [1]. The process has been used for fabrication of various designed tools and dies. Insignificant distortion has been imparted on the machined components as there is no physical interaction

B. K. Baroi (✉) · P. K. Patowari
Department of Mechanical Engineering, NIT Silchar, Silchar, Assam, India
e-mail: baroibinoy@gmail.com

T. Debnath
Department of Mechanical Engineering, KITS, Coimbatore, Tamil Nadu, India

Jagadish
Department of Mechanical Engineering, NIT Raipur, Raipur, Chhattisgarh, India

between the tool and workpiece [2]. The dielectric medium between electrode and work surface facilitates the machining process. There is heat affected zone present on the work surface is due to the heat supplied from electrode. The top surface comprises of the recast material settled on the work surface [3]. The tool senses the gap between the tool and workpiece with the help of a servomechanism. A DC servo motor performs this operation. Erosion occurred at a place where the gap between the tool and workpiece is least [4]. When electric voltage is applied between the tool electrodes, breakdown of the dielectric fluid occurs due the electric field intensity. As a result, arc occurs in the tool electrode gap [5]. Temperature of the machining zone is about 8000–12,000 °C that melts and evaporates the electrode materials [6]. Input parameters like voltage, current, polarity, pulse-on time, pulse-off time, dielectric type, flushing pressure and tool workpiece combination perform an important character in the performance of the machining process [7]. Material removal rate, tool wear rate, surface roughness, surface hardness are the most common performance measures of EDM [8]. Die-sinking EDM and wire EDM (WEDM) are the two variants of EDM are available. Die-sinking EDM is used for making die and tool, drilling operation, making complex shapes and also for surface modification of the substrate [9]. WDEM is used for cutting materials into pieces and producing complex geometries [10, 11]. One variant of die dinking EDM is micro-EDM that is used for fabricating micro holes and slots on the work surface by controlling the input parameter [12–14]. Jeswani [15] proposed the utilization of distilled water in EDM. Erden and Temel [16] studied the correlation of distilled water on the measures such as tool wear rate (TWR), surface roughness (SR) and material removal rate (MRR) while machining of steel. It has been observed that removal rate of work material and SR increased for tap water but decreased for hydrocarbon oil. Chen et al. [17] further investigated the work surface removal rate and rate of electrode wear in kerosene and de-ionized water in EDM. MRR had been observed to increase for distilled water whereas EWR decreased. The lower MRR for kerosene has been inferred due to the immense melting temperature of titanium carbide layer onto the surface requiring high energy for work removal. Also, the SR has been found to increase for distilled water. Lin et al. [18] used a hybrid of electric discharge and ultrasonic machining for Ti–6Al–4 V with dielectric fluids as kerosene and water. MRR has been observed to increase and relative tool wear rate (REWR) has been decreased for de-ionized water in comparison with kerosene. Moreover, the recast layer thickness has been found to be lesser for de-ionized water. SR and MRR has been observed to be superior for hybrid EDM-ultrasonic machining in comparison with the conventional EDM. ED machining of Ti–6Al–4 V has been performed using copperas tool electrode in distilled water and kerosene resulting in increased MRR in comparison with kerosene whereas, SR and TWR decreased for clean water. Furthermore, carbon layer deposition has not been identified on the work surface when machined in clean water [19]. Baroi et al. [20] successfully machined titanium grade 2 material using deionized water. Debnath et al. [21] obtained desirable results while machining of SS 430 with brass tool in tap water. For reducing harmful emissions of hydrocarbon oil, Medellin et al. [22] replaced hydrocarbon oil by water as dielectric. The effect of dielectric fluids such as deionized water, mineral water

and blend of mineral and de-ionized water has been studied. It has been concluded that mixture of mineral and deionized water resulted in superior rate of material and tool removal compared to that of hydrocarbon oil. On contrary, water has been found to be environment friendly. Tang and Du [23] utilized gray analysis (GRA) for the enhancement in rate of material and tool removal as well as SR. After optimization, EWR improved to $0.10 \text{ mm}^3/\text{min}$ from $0.14 \text{ mm}^3/\text{min}$, MRR improved to $2.38 \text{ mm}^3/\text{min}$ from $1.28 \text{ mm}^3/\text{min}$ and SR decreased to $1.93 \text{ }\mu\text{m}$ from $2.37 \text{ }\mu\text{m}$. Multi-objective optimization has been utilized for optimizing input parameters in machining of titanium for tap water as conducting medium. For optimized parameters, MRR has been observed to improve to $6.02 \text{ mm}^3/\text{min}$ from $5.90 \text{ mm}^3/\text{min}$, TWR decreased to $0.17 \text{ mm}^3/\text{min}$ from $0.41 \text{ mm}^3/\text{min}$ and SR improved to $2.07 \text{ }\mu\text{m}$ from $2.15 \text{ }\mu\text{m}$ [24]. In addition to the conducting medium, its electrical conductivity in ED machining has been investigated by Guo et al. [25]. The generation of gas bubbles in machining has been observed to be significant in the reduction of the work material. The role of dielectric in machining has also been exercised for milling. Kou and Han [26] machined titanium alloy using moving arc technique by green EDM milling in water as dielectric medium. The MRR has been observed to increase astronomically in comparison with traditional EDM. This has been further investigated by Muthuramalingam [27] on machining titanium by intermixing mineral and deionized water as dielectric. In the experimentation, MRR has been observed to be significantly regulated by the dielectric's electrical conductivity. Optimization is useful tool to optimize the variable parameters for an optimum output response [28, 29]. Different types of optimization techniques are employed to obtain the best combination of input parameters to have a better performance measures [30, 31]. Kar et al. [32] optimize the variable parameters and confirmation test result shows the variation among the predicted and actual result. Ranjan et al. [33] employed overall evaluation criteria (OEC) to get optimum values of MRR, TWR and overcut in EDM.

Literature study reveals that titanium has sound machinability for EDM and, tap water assists in realizing superior results. But limited study has been carried out for tap water assisted electric discharge machining of titanium grade 2 alloy. This paper attempts to present a machinability investigation of titanium grade 2 alloy with tap water as dielectric medium. The influence of parameters like pulse-on time and current has been investigated on the output characteristics such as SR, TWR and MRR. Entire experiments have been conducted in accordance with Taguchi L_{16} orthogonal array (OA). Variance analysis has been executed to show the distribution of control variables on the machining responses.

2 Materials and Methods

The experiments have been conducted in a die-sinking EDM (Make: Sparkonix, Model: S25). In the experimentation, copper has been used as the electrode and titanium grade 2 has been used as workpiece. The workpiece has been shaped and sized into required dimensions using WEDM which has been best suited for hard

Table 1 Experimental details

Input parameters and their levels		
Parameter	Level	Values
Current (A)	4	6, 9, 12, 15
Pulse-on time (μ s)	4	25, 106, 463, 1010
Constant parameters		
Parameter	Values	
Workpiece	Titanium grade 2	
Tool electrode	Copper	
Dielectric fluid	Tap water	
Gap voltage	25 V	
Duty cycle	0.58–0.72	
Time	15 min	

and conducting materials [34, 35]. Facing operation has been done on the surface of the tool and polished for straightening and improving the surface finish. The workpiece has been dimensioned to $25 \times 25 \times 2$ mm and tool is a square tool having 10 mm side. A precise weighing balance (Make: Ishida Co. Ltd., Model-DXR220) has been utilized for weighing of the tool and workpieces, before and after each experimentation for the calculation of MRR and TWR. Trial experimentation has been performed to determine the levels of process parameters as shown in Table 1. SR has been determined by calculating arithmetic average of surface heights on the machined face using a surface profilometer (Make: Tokyo Seimitsu Co. Ltd., Japan; Model: E-35B) consisting of a diamond type stylus having tip of 5μ m. For computing SR, average of five roughness values has been considered for each sample.

Taguchi L_{16} orthogonal array has been chosen for this study and after each experimentation the performance measures have been calculated for every combination of the control variables. Overall evaluation criterion (OEC) has also been applied to understand the process. As the performance measures are of beneficial and non-beneficial criteria, OEC makes non-dimensional values for different combination of the control variables. Table 2 represents the calculated performance measures along with the OEC values.

A separate machining tank has been structured for performing the machining of titanium as shown in Fig. 1. A small vice is placed on the table made inside the tank to hold the workpiece. Distilled water has been filled in the tank and a vice has been kept to support the workpiece. A submersible pump has been incorporated in the tank system for flushing of slug. Flushing action removes the debris particles from the surface of workpiece and cools the surface of both the electrodes. Tool is attached to the tool holder of the actual EDM and the workpiece is attached to vice fitted in the tank.

Table 2 Taguchi L₁₆OA and experimental results

Exp. No.	Current (A)	Pulse-on time (μs)	Pulse-off time (μs)	MRR (mg/min)	TWR (mg/min)	SR (μm)
1	6	25	17	0.893	2.087	3.1
2	6	106	76	1.200	1.767	3.5
3	6	463	222	1.247	1.100	3.8
4	6	1010	392	2.287	1.267	4.2
5	9	25	17	2.407	3.833	4.5
6	9	106	76	2.867	2.927	4.9
7	9	463	222	3.487	2.540	5.2
8	9	1010	392	3.967	2.053	5.4
9	12	25	17	4.187	4.680	5.6
10	12	106	76	4.520	2.500	5.8
11	12	463	222	4.833	1.987	6.4
12	12	1010	392	5.460	2.067	6.5
13	15	25	17	5.840	4.533	6.8
14	15	106	76	5.967	2.853	7.5
15	15	463	222	7.013	2.160	8.2
16	15	1010	392	7.567	2.253	8.6

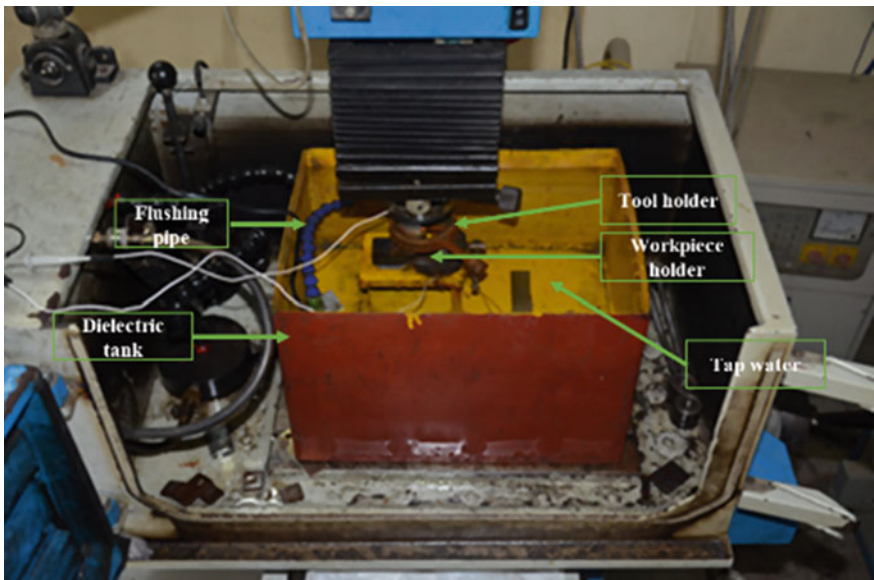


Fig. 1 EDM setup at advanced manufacturing lab

3 Results and Discussion

In the experimentation, EDM of titanium grade 2 has been performed using copper as electrode and dielectric medium is tap water. The pictorial representation of the work material and electrode have been displayed in Fig. 2a,b, respectively.

Experimental results have been displayed in Table 2 along with DOE. A total of 16 number of experiments has been carried out using tap water. A varied range of MRR (0.893–7.567 mg/min), TWR (1.10–4.68 mg/min) and SR (3.1–8.6 μm) has been realized in accordance with input parameters as depicted in Table 2. The variation of output parameters with the change in variable parameters has been mentioned in Table 2.

3.1 MRR Analysis

The alteration in MRR along with control parameters has been depicted in Fig. 3. MRR has been observed to increase with current. Such phenomenon can be attributed

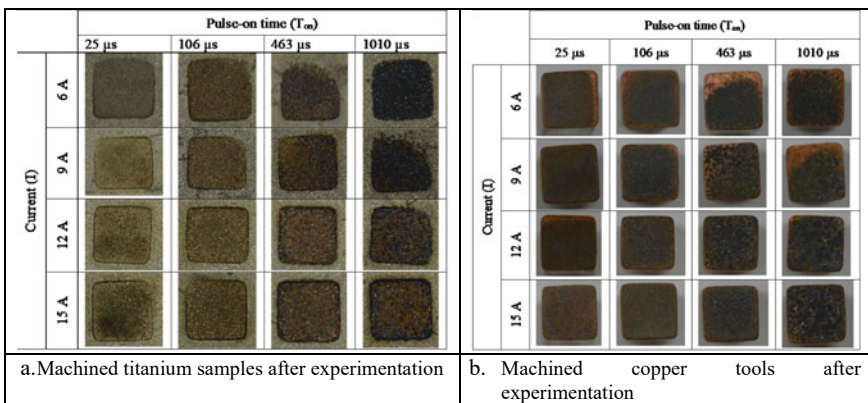


Fig. 2 Microscopic images of titanium and copper

Fig. 3 Variation of MRR

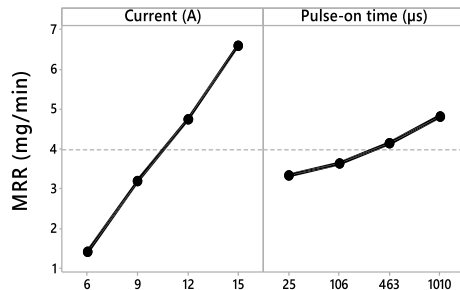
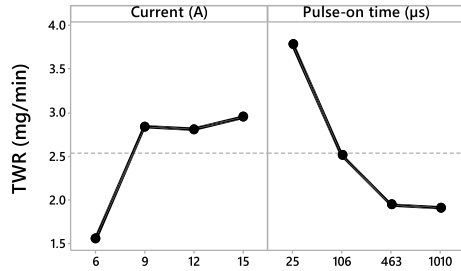


Fig. 4 Variation of TWR



to generation of intense heat energy in the recess between the electrode and workpiece due to high current. For the increased heat energy, greater volume of work material gets eroded from the top surface, thereby increasing material removal [36]. The increased pulse-on time has caused increased MRR resulting from increasing energy supply to the work surface. As a consequence, more removal of material occurs from the titanium causing increased MRR [37].

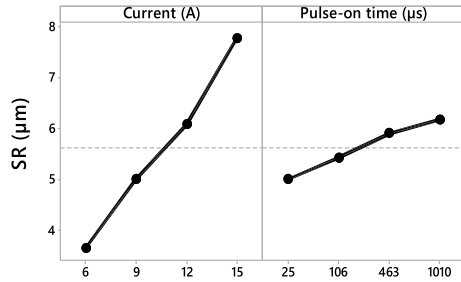
3.2 TWR Analysis

The outcome of variable parameters on tool wear has been displayed in Fig. 4. Similar to MRR, rate of tool wear has been observed to increase with current due to the excessive supply of heat in the intermediate region of tool and work, thus, resulting in extensive removal of material from the surface of the tool causing increased TWR [36]. TWR has been observed to decrease with the greater pulse-on time. This occurs because the ionized channel gets enlarged, thus resulting in decreased heat density supply to the tool and work material. Hence, material removal rate of the surface of tool reduces resulting in favorable TWR [37].

3.3 SR Analysis

The variation in variable parameters for SR has been shown in Fig. 5. SR has been observed to increase with the increment in both pulse-on time and current. The increased pulse-on time and current cause intense generation of heat energy in the recess of tool and workpiece. Hence, vigorous explosions occur in the gap between electrode and work material causing structuring of deep craters on the outer layer of the work resulting in increased SR [25].

Fig. 5 Variation of surface roughness



3.4 ANOVA Analysis

ANOVA is a statistical technique to determine the significant controlling parameters. The outcome of ANOVA has been mentioned in Table 3. ANOVA reveals that the current (91.47%) is the largest contributing parameter for MRR succeeded by pulse-on time (7.91%). For wear rate of tool, pulse-on time (57.51%) has been observed as the prominent factor followed by current (32.55%). In the case of SR, ANOVA attributes current (91.05%) as the significant factor followed by pulse-on time (8.08%). The coefficient of correlation (R^2) and adjusted coefficient of correlation [R^2 (adjusted)]

Table 3 Variance analysis of output measures

Soure	DF	Seq SS	Adj SS	Adj MS	F-Value	P-Value	Contribution (%)
<i>a. Material removal rate (MRR)</i>							
Current	3	58.797	58.797	19.599	439.65	0.000	91.47
T_{on}	3	5.079	5.079	1.693	37.98	0.000	7.91
Error	9	0.401	0.401	0.045			0.62
Total	15	64.277					100.00
$R^2 = 99.38\%$, R^2 (adj) = 98.96%							
<i>b. Tool wear rate (TWR)</i>							
Current	3	5.197	5.197	1.7324	9.82	0.003	32.55
T_{on}	3	9.182	9.182	3.0608	17.35	0.000	57.51
Error	9	1.587	1.587	0.1764			9.94
Total	15	15.967					100.00
$R^2 = 90.06\%$, R^2 (adj) = 83.43%							
<i>c. Surface roughness (SR)</i>							
Current	3	36.4650	36.4650	12.1550	312.56	0.000	91.05
T_{on}	3	3.2350	3.2350	1.0783	27.73	0.000	8.08
Error	9	0.3500	0.3500	0.0389			0.87
Total	15	40.0500					100.00
$R^2 = 99.13\%$, R^2 (adj) = 98.54%							

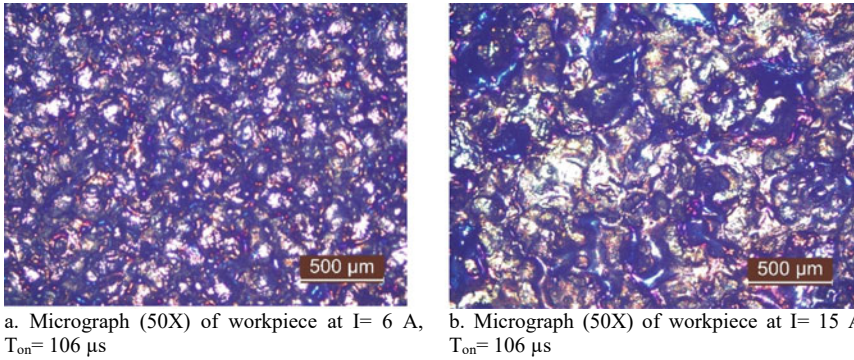


Fig. 6 Surface texture of titanium after experimentation

for MRR (99.38% and 98.96%), TWR (90.06% and 83.43%) and SR (99.13% and 98.54%) are greatly high indicating strong relationship between control variables and performance measures. The smaller contribution of error in MRR (0.62%), TWR (9.94%) and SR (0.87%) than that of process parameters indicate less interaction effect of the control variables.

The microscopic images of the surface texture at minimum and maximum current settings have been depicted in Fig. 6a, b respectively. At lower current, surface texture has been examined as fairly good but at higher current, surface irregularities are more prominent and the craters are deeper. The sludge from the erosion of electrode and work material has been examined to be solidified on the surface of the workpiece. The decomposition of dielectric may also form alloying constituent of re-formed layer [38].

To get the optimum condition of the control variables OEC have been done. The influence of control variables on OEC is shown in Fig. 7. Based on the figure it can be seen that current at level 1 and pulse-on-time at level 2 is best for optimum (maximum) OEC.

OEC have been calculated using the best and worst values of the performance measures as shown in Table 4. The quality characteristics of those response variables have also been mentioned in the Table 4. MRR is a beneficial criterion and TWR and SR are the non-beneficial criteria, hence MRR is larger is the better and TWR and SR are lower the better. Equal weightage has been given to all the responses while calculating OEC.

Fig. 7 Effect of parameters at different levels on mean of OEC

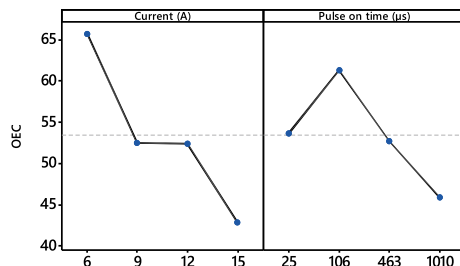


Table 4 OEC table with assigned weightage and QC

Response	Best	Worst	Quality characteristics	Relative weightage (%)
MRR (mg/min)	7.567	0.893	L	33.34
TWR (mg/min)	1.10	4.680	S	33.33
SR (μm)	3.1	8.6	S	33.33

Table 5 Parametric values at optimum condition

Parameter	Value
Current (A)	6
T_{on} (μs)	106
MRR (mg/min)	2.867
TWR (mg/min)	1.767
SR (μm)	3.5

Table 6 Confirmation test and its deviation with actual response value

Predicted OEC	Confirmation OEC	Deviation (%)
73.69	67.89	8.54

At the optimum parametric combination obtained from the mean effect plot of OEC (shown in Fig. 7) the performance measured have been calculated as mentioned in Table 5. Depending on the calculated results from the generated model, optimum OEC has been calculated. Finally, the deviation of the predicted OEC with the actual/experimental OEC have been observed as shown in Table 6.

4 Conclusion

Titanium grade 2 has been machined using die sinking EDM process for a set of control variables. Alteration in rate of material and tool removal, and SR have been examined with respect to the changes in pulse-on time and current. The results have been outlined below.

1. MRR and TWR has been found to increase with current owing to supply of intense heat between the workpiece and electrode gap.
2. MRR has been observed to increase with pulse-on time while TWR decreased because larger pulse-on time removes more work surface material and reduces the energy density to tool thereby decreasing tool wear.
3. Increased current and pulse-on time has resulted in greater SR due to the frequent formation of shallow craters in the inter electrode gap.

4. For MRR and SR, current has been observed as the significant parameter succeeded by pulse-on time but for TWR, pulse-on time has been observed as most influential parameter followed by current.
5. The optimum value of MRR is 7.567 mg/min at 15 A current and 1010 μ s pulse-on time. Optimum value of TWR is observed as 1.10 mg/min at 6 A current and 463 μ s pulse-on time. Whereas, optimum value for SR is found to be 3.10 μ m at 6 A current and 25 μ s pulse-on time.
6. Based on the overall evaluation criteria (OEC) the optimum parametric condition has been identified as current as 6 A and pulse-on-time as 106 μ s. The values of MRR, TWR and SR at this optimum condition are 2.867 mg/min, 1.767 mg/min and 3.5 μ m, respectively.

References

1. Lazarenko BR, Lazarenko NI (1964) Technological characteristics of electrospark machining of current conducting materials. *Electrospark Machining Met* 2:13–14
2. Baroi BK, Kar S, Patowari PK (2018) Electric discharge machining of titanium grade 2 alloy and its parametric study. *Mater Today: Proc* 5004–5011
3. Patowari PK, Mishra UK, Saha P, Mishra PK (2010) Surface modification of C40 steel using WC-Cu P/M green compact electrodes in EDM. *Int J Manufact Technol Manage* 21(1–2):83–98
4. Olubiwe M, Uzoечи LO, Uchegbu VC (2016) Improved electrical discharge machine (EDM) servomechanism controller for machining micro pits. *Int J Eng Res Technol* 5(04):316–320
5. Ho KH, Newman ST (2003) State of the art electrical discharge machining (EDM). *Int J Machine Tools Manufact* 43(13):1287–1300
6. Abdulkareem S, Khan AA, Konneh M (2010) Cooling effect on electrode and process parameters in EDM cooling effect on electrode and process parameters in EDM. *Mater Manufact Process* 25:462–466
7. Shabgard M, Ahmadi R, Seyedzavvar M, Oliaei SNB (2013) Mathematical and numerical modeling of the effect of input-parameters on the flushing efficiency of plasma channel in EDM process. *Int J Machine Tools Manufact* 65:79–87
8. Krishnaand ME, Patowari PK (2014) Parametric study of electric discharge coating using powder metallurgical green compact electrodes. *Mater Manufact Process* 29(9):1131–1138
9. Sarmah A, Kar S, Patowari PK (2020) Surface modification of aluminum with green compact powder metallurgy inconel-aluminum tool in EDM. *Mater Manufact Process* 35(10):1104–1112
10. Debnath T, Patowari PK (2019) Fabrication of an array of micro-fins using wire-EDM and its parametric analysis. *Mater Manufact Process* 34(5):580–589
11. Debnathand T, Patowari PK (2019) Concept development for fabricating threaded micro-pin using wire-EDM. *J Braz Soc Mech Sci Eng* 41(10):402
12. Karand S, Patowari PK (2018) Electrode wear phenomenon and its compensation in micro electrical discharge milling: a review. *Mater Manufact Proc* 33(14):1491–1517
13. Karand S, Patowari PK (2019) Experimental investigation of machinability and surface characteristics in microelectrical discharge milling of titanium, stainless steel and copper. *Arabian J Sci Eng* 44(9):7843–7858
14. Karand S, Patowari PK (2019) Effect of non-electrical parameters in fabrication of micro rod using BEDG. *Mater Manufact Proc* 34(11):1262–1273
15. Jeswani ML (1981) Electrical discharge machining in distilled water. *Wear* 72:81–88

16. Erden A, Temel D (1982) Investigation on the use of water as a dielectric liquid in E.D.M. In: Proceedings of the twenty-second international machine tool design and research conference. Macmillan Education UK, London, pp 437–440
17. Chen SL, Yan BH, Huang FY (1999) Influence of kerosene and distilled water as dielectrics on the electric discharge machining characteristics of Ti–6Al–4V. *J Mater Process Technol* 87:107–111
18. Lin YC, Yan BH, Chang YS (2000) Machining characteristics of titanium alloy (Ti–6Al–4V) using a combination process of EDM with USM. *J Mater Proc Technol* 104:171–177
19. Lin CT, Chow HM, Yang LD, Chen YF (2007) Feasibility study of micro-slit EDM machining using pure water. *Int J Adv Manuf Technol* 34:104–110
20. Baroi BK, Debnath T, Jagadish, Patowari PK (2020) Machinability assessment of titanium grade 2 alloy using deionized water in EDM. *Mater Today: Proc*
21. Debnath T, Baroi BK, Jagadish, Patowari PK (2020) Machinability study of 430 stainless steel using tap water in EDM. *Mater Today: Proc*
22. Medellin HI, de Lange DF, Morales J, Flores A (2009) Experimental study on electrodischarge machining in water of D2 tool steel using two different electrode materials. In: Proceedings of the Institution of Mechanical Engineers, Part B. *J Eng Manuf* 1423–1430
23. Tang L, Du YT (2014) Experimental study on green electrical discharge machining in tap water of Ti-6Al-4V and parameters optimization. *Int J Adv Manuf Technol* 70:469–475
24. Tang L, Du YT (2014) Multi-objective optimization of green electrical discharge machining Ti–6Al–4V in tap water via grey-taguchi method, *Mater Manuf Process* 29:507–513
25. Guo C, Di S, Wei D (2016) Study of electrical discharge machining performance in water-based working fluid. *Mater Manuf Process* 31:1865–1871
26. Kou Z, Han F (2018) On sustainable manufacturing titanium alloy by high-speed EDM milling with moving electric arcs while using water-based dielectric. *J Clean Prod* 189:78–87
27. Muthuramalingam T (2019) Effect of diluted dielectric medium on spark energy in green EDM process using TGRA approach. *J Clean Prod* 238
28. Jagadish, Ray A (2014) Optimization of green electrical discharge machining using an integrated approach. In: IEEE international conference on industrial engineering and engineering management. IEEE, pp 943–947
29. Bhowmik S, Jagadish, Gupta K (2019) Modeling and optimization of electrical discharge machining. In: Springer briefs in applied sciences and technology. Springer, Cham, pp 15–28
30. Jagadish, Ray A (2015) A fuzzy multi-criteria decision-making model for green electrical discharge machining. In: Proceedings of fourth international conference on soft computing for problem solving. Springer, pp 33–43
31. Jagadish, Bhowmik S, Ray A, Rajakumaran M (2018) Optimization of process parameters using fuzzy-grey relational analysis (F-GRA) for green EDM. In: AIP conference proceedings, vol 1998, (1), pp 020011 AIP Publishing LLC
32. Kar S, Sarmah P, Baroiand BK, Patowari PK (2020) Drilling of micro-holes in titanium using micro-EDM: a parametric investigation. In: Lecture notes in mechanical engineering. Springer, pp 589–600
33. Ranjan R, Kar S, Patowari PK (2020) Parametric optimization of drilling on Titanium grade-2 in die-sinking electrical discharge machining. In: Techno-Societal 2018. Springer, Cham, pp 551–559
34. Chakraborty N, Debnath T (2016) Optimization and the effect of controlled parameters for cutting inconel 800 in WEDM. *Int J Recent Technol Mech Electr Eng* 3:44–51
35. Naik TP, Debnath T, Patowari PK (2018) Machinability study on German silver using wire-EDM. In: AIP conference proceedings, vol 1998, p 020004 American Institute of Physics Inc
36. Senthilkumar V, Omprakash BU (2011) Effect of titanium carbide particle addition in the aluminium composite on EDM process parameters. *J Manuf Process* 13:60–66

37. Lin YC, Wang AC, Wang DA, Chen CC (2009) machining performance and optimizing machining parameters of Al₂O₃-TiC ceramics using EDM based on the taguchi method. *Mater Manuf Proc* 24:667-674
38. Keskin Y, Halkac HS, Kizil M (2006) An experimental study for determination of the effects of machining parameters on surface roughness in electrical discharge machining (EDM). *Int J Adv Manuf Technol* 28:1118-1121

Effect of Tool Rotation on Electrochemical Milling of Stainless Steel 316L



Abhinav Kumar, Hari Narayan Singh Yadav, Manjesh Kumar, and Manas Das

Abstract Milling of stainless steel workpiece by conventional process is very challenging as the tool wear and design of tool for complex shapes are very critical and also machine at low rate. The surface finish and the machining accuracy obtained during conventional milling are not good. To overcome these limitations, electrochemical milling is very good alternative. It is a non-conventional process which removes material atom by atom from the layer of the workpiece same as electrochemical machining. As it is non-contact process, the accuracy of the tool surface replicates on the workpiece. Various process parameters enhance the accuracy of milling. In this paper, 'L' shape profile has been milled over the stainless steel 316L of thickness 3 mm with copper rod of diameter 5 mm. An electrochemical milling setup is indigenously developed to perform the experiments. The effect of tool rotation over the machining depth, surface roughness and overcut has been studied. The result shows that the rotary tool enhances the machining depth and surface finish and decreases the overcut of the electrochemical milled surface. The surface roughness value for the milling layer depth of 0.15 mm and tool feed of 8 mm/min with tool having the 500 rpm is 0.072 μm .

Keywords Electrochemical milling · Tool rotation · Surface finish · Machining accuracy

A. Kumar (✉) · H. N. S. Yadav · M. Kumar · M. Das
Department of Mechanical Engineering, Indian Institute of Technology Guwahati, Assam, India
e-mail: kumar176103020@iitg.ac.in

H. N. S. Yadav
e-mail: h.narayan@iitg.ac.in

M. Kumar
e-mail: manje176103021@iitg.ac.in

M. Das
e-mail: manasdas@iitg.ac.in

1 Introduction

Milling of hard material like titanium, stainless steel, high carbon steel, nickel alloys, etc., by conventional machining process leads to frequent tool wear and induces residual stress on the surface. In the recent times, electrochemical machining (ECM) is widely applied in industrial because to its several advantages over several traditional and non-traditional processes such as no residual stresses, no tool wear, and no burrs with high removal of material rate, low surface roughness and can fabricate complex shapes with no dependency on the property of material like strength and hardness [1]. The traditional machining processes are tool-based processes, e.g., drilling, turning, milling, etc. are not practically viable to mill high-strength materials as it leads to higher tool wear. ECM has certain limitations and avoids its commercial use like proper tool design, every material requires new research before machining [2]. Fabrication and design of complex shaped tool require proper design and time which reflects in the final product's cost. Researchers have also utilized mask for the fabrication of complex pattern using through-mask electrochemical micromachining [3]. The larger machining area for the tool requires large power consumption. Current at high magnitude, i.e., pulsed DC requires costly equipment. Direct current, i.e., of constant magnitude is inefficient in sludge removal from the inter electrode gap (IEG) which makes inaccurate machined profile [4].

To counter the above-mentioned problems in conventional machining, electrochemical milling (EC milling), a non-conventional method is introduced. EC milling process is similar to ECM process in principle, and the milling strategy is similar as the traditional end milling process. Milling of large area using simple tool with controlled job as well as the tool movement, thus, avoids designing a 3D-shaped complex tool as in conventional sinking ECM. With the integration of rotary motion to tool as well as internal flushing through tool, debris particles can be removed efficiently from the IEG, thus enhancing the machining accuracy and also avoiding the use of the DC pulse power supply.

Mishra et al. [5] had briefly explained the problem and their solutions associated with milling of high-strength temperature-resistant (HSTR) alloys for example nickel, titanium and cobalt alloys. The problems related to milling strategies (sinking and milling, scanning layer by layer, sinking and scanning and strategy for high-aspect-ratio), flushing techniques (vertical flushing, side flushing, internal flushing and flushing through tool rotation), inaccuracy-related problems (types and concentration of electrolyte, tool insulation, rotation of micro-tool) and milling parameters (Voltage, pulse frequency and duty ratio, tool feed and milling layer depth, IEG) were explained. Handling of electrodes, tool preparation and online monitoring systems were also explained.

Niu et al. [6] has electrochemically milled Inconel 718 with the help of a dead end tube tool along with rotation and inner jet. The tool has six uniformly distributed outlets slit for the flow the electrolyte. The input parameters include tool feed of 2.1 mm/min, 25 V applied voltage, 35 °C and 0.5 MPa of electrolyte temperature and pressure, respectively, helps to achieve a depth of 3 mm in one pass.

Mishra and Sarkar [7] had fabricated an L-shaped feature on Nimonic-263 alloy utilizing electrochemical milling. The tool is allowed to rotate with inner spraying feature. Three different tool features were utilized and their effect on removal rate of material and width overcut was discussed. With 500 rpm of tool rotation and 8 mm/min of tool feed rate, 0.23207 gm/min of MRR and 0.62128 mm of overcut was achieved. An excellent surface finish of 0.07–0.08 μm was achieved.

Rathod et al. [8] had experimentally investigated the various parametric effects on groove profiles generated of stainless steel SS304 by electrochemical micromachining. Various parameters studied were pulse frequency, voltage, duty ratio, micro-tool scanning speed and concentration of electrolyte on surface finish and machine accuracy.

Ghoshal and Bhattacharyya [9] had reported two different methods to provide milling depth during electrochemical milling namely scanning machining i.e. layer-by-layer method and sinking and milling method i.e. total depth at one time and then mill the surface. Single pass with higher milling depth leads to deviation at end from the initial point. So, layer-by-layer technique is considered to be the best choice for electrochemical milling.

In the present experiment, stainless steel 316L of thickness 3 mm is considered as workpiece. It is switched to the power supply's positive terminal. The copper rod of diameter 5 mm is considered as tool and it is switched to the power supply's negative terminal. Both the electrodes are placed in a container filled with electrolyte. For the present investigation, sodium nitrate (NaNO_3) is taken as electrolyte in the concentration of 20 gm/L. Milling of 'L' profile has been used for the experiment [10]. This shape is selected so that the flat and curve edges of milling process can be simultaneously examined.

2 Experimental Setup and Procedure

For electrochemical milling, an indigenous setup is prepared and its schematic is presented in Fig. 1. The setup is similar to the conventional electrochemical machining. The workpiece over which the milling has to perform is made as anode and the milling cutter acts as tool, i.e., cathode. Both the electrodes are dipped into the electrolytes and form an electrolytic cell. In ECM, the removal of material is atom by atom and thus provides a better surface finish compared to conventional milling process. The tool life is very high, as it does not touch with the workpiece. After machining, the tool surface is same as before and available for further milling process. The surface finish of the tool is also critical parameter for the finish of the workpiece.

The L-shaped profile is selected for milling over the workpiece surface. Figure 2 shows the tool path for the milling profile. This profile has a corner which provides the sharp edge. It will help to find the shape accuracy of the process. For the tool to move in this profile, a G-code is written and the same is executed in CNC (computer numerical control) machine via the Mach3 software. This software reads the G-code

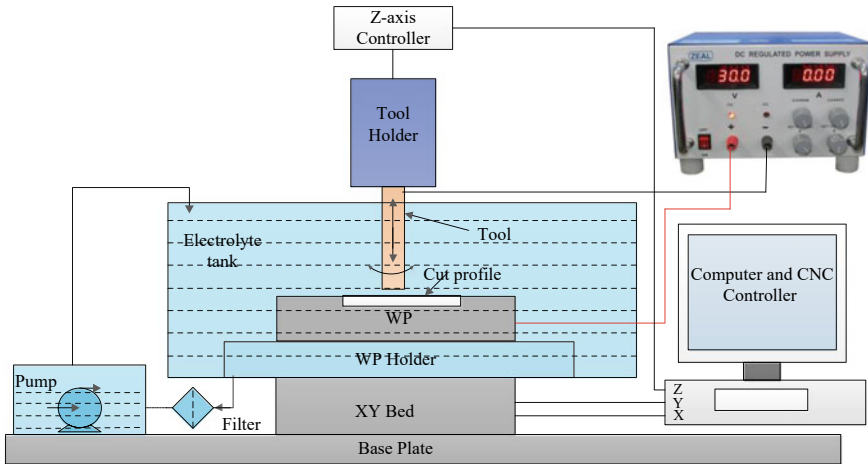
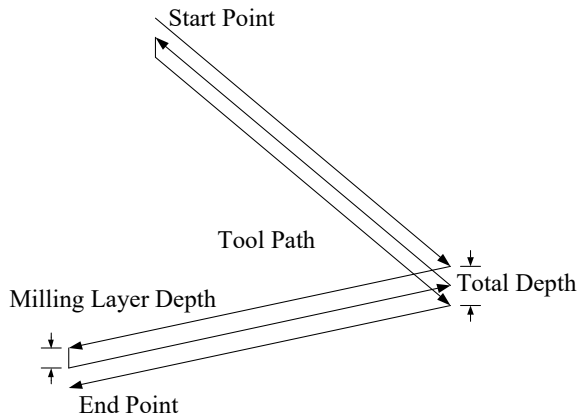


Fig. 1 Schematic of electrochemical milling setup

Fig. 2 Schematic of L-shape tool path



and gives signal to the controller for the precise movement in the all three X - Y - Z axes. For the tool rotation at different rpm, a spindle is attached to the z -axis such that it will rotate and move with respect to z -axis. The workpiece is held in the fixture during milling and both the electrodes are completely dipped into the electrolyte. The electrolyte is continuously flown in between the IEG to remove the debris particles. The tool starts from one corner and takes the milling layer depth after reaching at other end.

Table 1 shows the parameters selected for the electrochemical milling process. For the preliminary experiments, the literature survey helps in selecting the parameters and availability of the resources. The milling is done by scanning methods with different milling layer depth, i.e., layer-by-layer milling as presented in Fig. 2. The

Table 1 Parameters used for milling process [11]

Machining condition	Range
Voltage	20 V
Inter electrode gap	50 μm
Tool feed	5–8 mm/min
Tool rotation	500 rpm
Milling depth	0.15–0.3 mm
Electrolyte concentration	20 gm/L

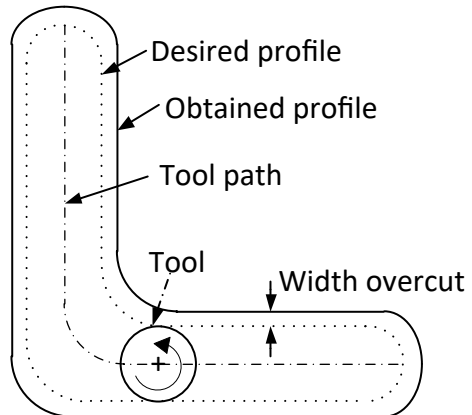
tool feed rate, i.e., the linear motion of the tool is also varied from 5 to 8 mm/min, keeping other parameters constant. The total machining depth is 1.2 mm.

Figure 3 shows the machined profile of the L-shape. All the line sketch were made by MS Visio. The dotted line shows the desired profile. Due to side machining, the final machined profile is larger than the tool diameter (ϕ5 mm), which leads to width overcut, as presented between dotted line and the outer thick line and defined by Eq. 1.

$$\text{Width overcut} = ((\text{Final width} - \text{diameter of tool})/2) \tag{1}$$

Suitable parameters must be optimized to reduce the overcut. The tool is rotated about the z-axis such that it also moves along the defined path. It helps in the removal of the debris particles from the IEG such that fresh electrolyte is available for further milling process.

Fig. 3 Schematic of machined profile



3 Results and Discussion

The parameters that influence the milling process are given in Table 1. A constant DC power source is connected to the two electrodes. Some of the parameters are held constant such as inter electrode gap (IEG), milling depth and the electrolyte concentration. From various literature works, the major influencing parameters which affect the machining conditions of milling are voltage, tool feed and tool rotation. For each experiment, three set of experiments were performed and the average value is taken. The profile measurement is carried out using an optical zoom microscope (Olympus DSX-100) and Image J software. For surface roughness, Non-Contact Talysurf Profiler System and analysis of the data were analyzed with the help of TalyMap software made by Mitutoyo, Japan.

3.1 Influence of Feed Rate on Machining Depth

Figure 4 shows the impact of tool feed on machining depth. The tool feed is in the range of 5–8 mm/min for the machining depth of 1.2 mm with milling layer depth as 0.3 mm. The variation in machining depth with respect to tool rotation and without rotation has been observed. With the increase in tool rate, the time available for milling decreases. For low value of feed rate, material removal will be more which leads to higher machining depth. Rotation of tool avoids the accumulation of debris particles in the IEG. The debris particles stick to the surface and cause stray machining for tool without rotation. This provides higher machining depth and least accuracy.

Fig. 4 Effect of feed rate on machining depth

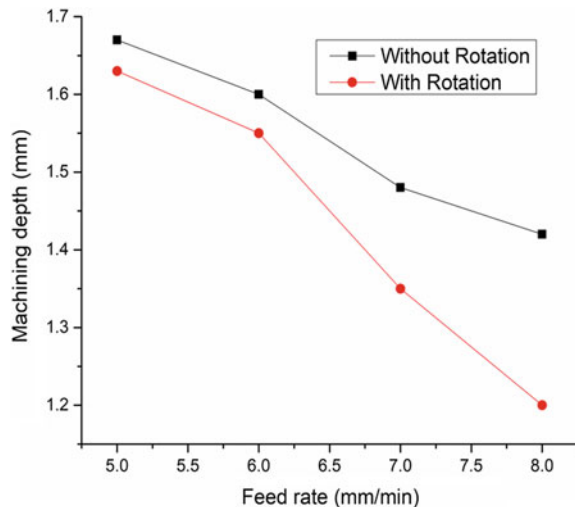
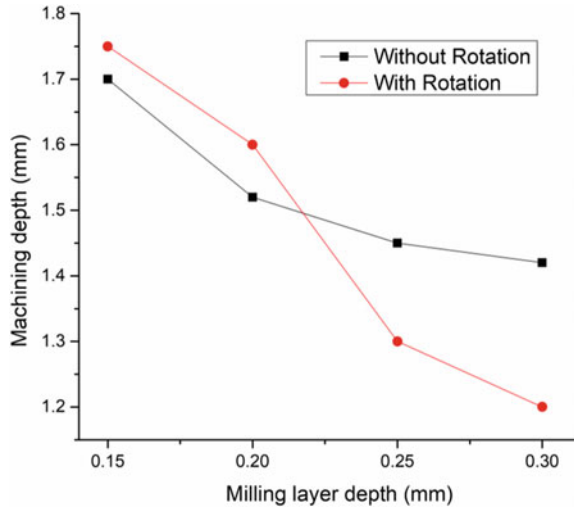


Fig. 5 Influence of milling layer depth on machining depth



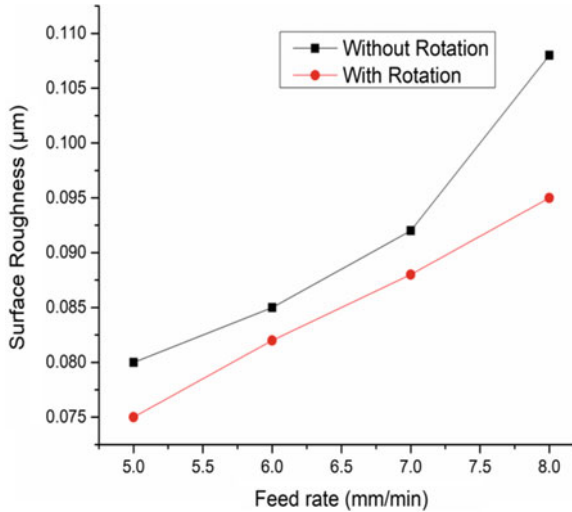
3.2 Influence of Milling Layer Depth on Machining Depth

Figure 5 shows the impact of milling layer depth on machining depth. The milling layer depth is varied in the range of 0.15–0.3 mm for the machining depth of 1.2 mm with milling feed rate as 8 mm/min (constant). The variation in machining depth with respect to tool rotation and without rotation has been observed. For lower value of milling layer depth, time required to reach milling depth of 1.2 mm will be more. It leads to increase in material removal and higher machining depth. For higher value of milling layer depth, time required to reach milling depth of 1.2 mm will be less. The debris particles accumulate near the surface and cause stray machining for tool without rotation. This leads to higher machining depth and least accuracy as current density increases. Rotation of tool avoids the accumulation of debris particles in between the electrodes. This gives higher accuracy of milling depth.

3.3 Influence of Feed Rate on Surface Roughness

Figure 6 shows the impact of tool feed on surface roughness with and without tool rotation. It can be inferred that surface roughness increases on increasing the tool feed. At high feed rate, machining time is less, thus non-uniform milling takes place. This increases the surface roughness of the milled surface. Rotation of tool helps in removal of debris particles thus produces better surface finish than the tool without rotation.

Fig. 6 Influence of tool feed on surface roughness



3.4 Influence of Milling Layer Depth on Surface Roughness

Figure 7 shows the impact of milling layer depth on surface roughness with and without tool rotation. It can be inferred that surface roughness increases on increasing the milling layer depth. For lower milling layer depth, the amount of debris particles is low, which leads to lower surface roughness. At higher milling layer depth, the amount of debris particles is high, which leads to higher surface roughness. As the debris particle does not accumulate on application of tool rotation, it produces lesser overcut than the tool without rotation.

Fig. 7 Influence of milling layer depth on surface roughness

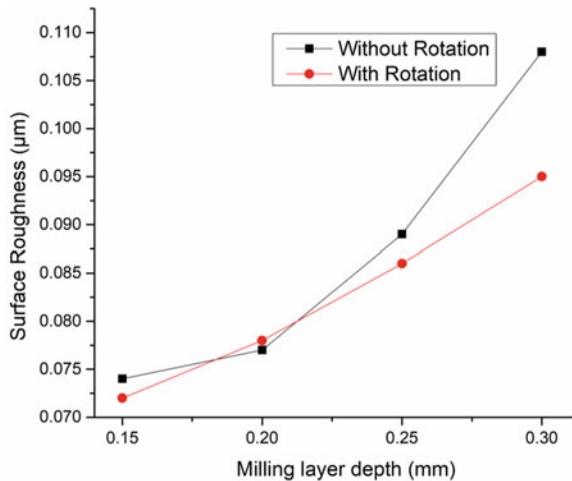
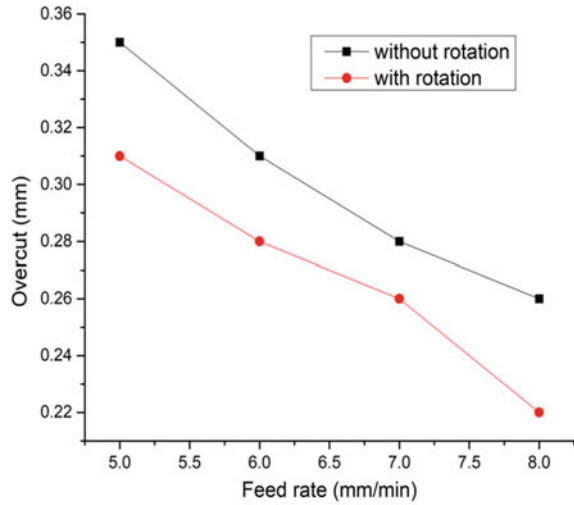


Fig. 8 Effect of tool feed on overcut



3.5 Influence of Tool Feed on Overcut

Figure 8 shows the impact of feed rate on overcut keeping milling layer depth of 0.3 mm. At lower feed rate, time for milling will be higher compared to the higher feed rate. It leads to stray machining and produces higher overcut. It can also be concluded that tool with rotation decreases the overcut. Due to tool rotation, current density is concentrated as it avoids increase in debris particles in the IEG with the help of fresh electrolyte, thus reducing the overcut.

3.6 Influence of Milling Layer Depth on Overcut

Figure 9 shows the impact of milling layer depth on overcut keeping tool feed of 8 mm/min. At lower milling layer depth, time for milling will be higher compared to higher milling layer depth. It leads to stray machining and produces higher overcut as debris particles stick to the surface. It can also be concluded that tool with rotation decreases the overcut. Due to tool rotation, debris particles are removed from the IEG with the help of fresh electrolyte and current density is concentrated, thus reducing the overcut.

The surface roughness value and milled surface for the milling layer depth of 0.15 mm and tool feed of 8 mm/min with tool having a 500 rpm rotation are shown in Fig. 10a, b. The surface roughness value of the milling surface with tool rotation is 0.072 μm . Figure 10c shows that tool without rotation produces stray machining at the corner due to the accumulation of the debris particles.

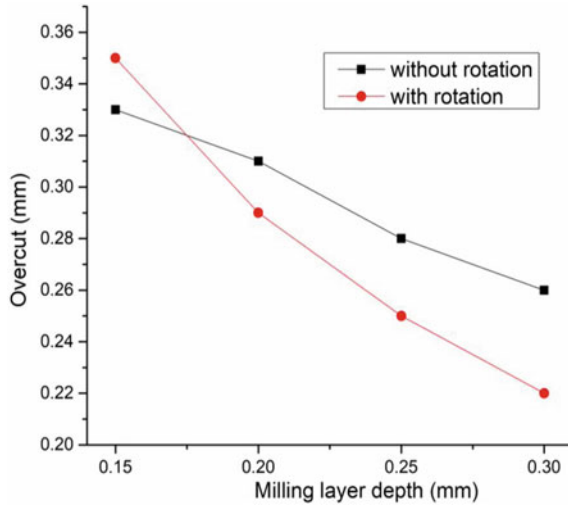
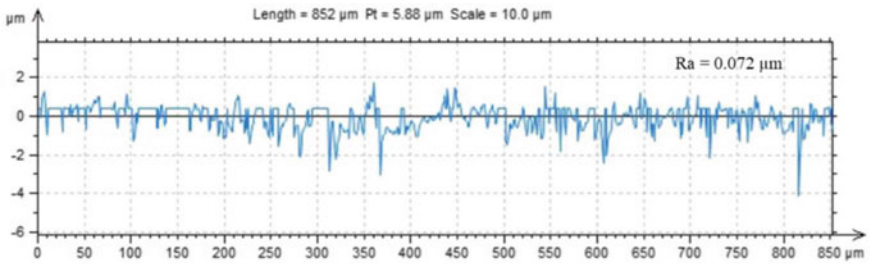
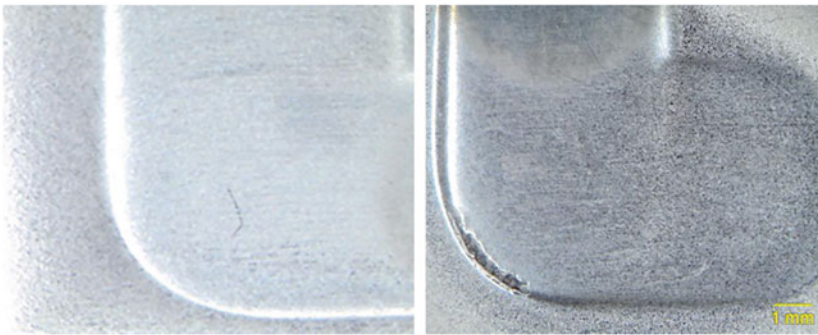


Fig. 9 Influence of milling layer depth on overcut



(a)



(b)

(c)

Fig. 10 a Surface roughness value, b milled profile, c corner stray machining

4 Conclusions

The electrochemical milling of stainless steel SS316L using copper rod of dia. 5 mm has been performed. The profile of the milling is selected as 'L-shape,' and tool follows the shape profile. Several milling parameters were selected, and their effects on output parameters like machining depth, surface roughness and overcut have been analyzed. The effect of tool with and without rotation for these parameters was also analyzed. Following conclusions can be derived.

1. On increasing the feed rate, required machining depth of 1.2 mm is achieved with the aid of tool rotation. For lower feed rate, reaction time is more, and thus, the machining depth increases.
2. On increasing the milling layer depth keeping feed rate 8 mm/min, higher machining depth is obtained for lower milling layer depth. Higher milling layer depth reaches required depth of 1.2 mm in minimum steps.
3. On increasing the feed rate, uniform distribution of current takes place. Thus, surface quality increases. Tool rotation avoids the accumulation of debris particles in the IEG, thus providing better surface finish.
4. On increasing the milling layer depth, surface finish decreases as more debris particles are formed.
5. On increasing the feed rate, overcut decreases as time available for reaction decreases.
6. On increasing the milling layer depth, overcut decreases as milling time reduces.

For future prospective, the effect of electrolyte and its concentration with effective flow of electrolyte on the output parameters like machining depth, surface roughness and overcut can be analyzed. The simulation of electrochemical milling can be performed which helps to visualize different profile and tool path to increase the accuracy.

References

1. Dutta P, Barman A, Kumar A, Das M (2020) Design and fabrication of electrochemical micro-machining (ECMM) experimental setup for micro-hole drilling. In: *Advances in mechanical engineering*, Springer, pp 561–573
2. Jain VK, Balasubramaniam R, Mote RG, Das M, Sharma A, Kumar A, Garg V, Kamaliya B (2020) Micromachining: an overview (Part I). *J Micromanufact No. Part I*
3. Kumar A, Kumar M, Alok A, Das M (2020) Surface texturing by electrochemical micromachining: a review. In: *IOP conference series: materials science and engineering*, 804
4. Kozak J, Rajurkar KP, Wei B (1994) Modelling and analysis of pulse electrochemical machining (PECM). *J Eng Ind* 116(3):316
5. Mishra K, Gupta S, Bhattacharyya, B (2020) Problematic areas in micro-electrochemical milling of HSTR alloys. *Int J Adv Manuf Technol* 111(3):1015–1036
6. Niu S, Qu N, Fu S, Fang X, Li H (2017) Investigation of inner-jet electrochemical milling of nickel-based alloy GH4169/Inconel 718. *Int J Adv Manuf Technol* 93(5–8):2123–2132

7. Mishra K, Sarkar BR (2019) Influence of different featured tools on machining accuracy in electrochemical milling. *Proc Inst Mech Eng Part B: J Eng Manuf*
8. Rathod V, Doloi B, Bhattacharyya B (2015) Experimental investigations into machining accuracy and surface roughness of microgrooves fabricated by electrochemical micromachining. *Proc Inst Mech Eng Part B: J Eng Manuf* 229(10):1781–1802
9. Ghoshal B, Bhattacharyya B (2013) Micro electrochemical sinking and milling method for generation of micro features. *Proc Inst Mech Eng Part B: J Eng Manuf* 227(11):1651–1663
10. Mishra K, Dey D, Sarkar BR, Bhattacharyya B (2017) Experimental investigation into electrochemical milling of Ti6Al4V. *J Manuf Process* 29:113–123
11. Mishra K, Sarkar BR, Bhattacharyya B (2019) Influence of inner-spraying rotating tool during electrochemical milling of nimonic-263 alloy. *Mater Manuf Process* 34(7):807–813

Development of Finite Elemental Analysis Model for Numerical Simulation of TIG Welding of Thin Aluminium Sheet



Rahul Kumar Mahato, Mohd Aslam, Lokavarapu Rama Krishna, and Chinmaya Kumar Sahoo

Abstract Aluminium and aluminium alloy are one of the preferable materials for manufacturing aircraft and automobile components, due to their adequate strength and lightweight. However, it is challenging to weld the aluminium using a conventional arc welding process, due to the formation of aluminium oxide on the surface of the aluminium. TIG welding process is one of the suitable welding processes for welding aluminium alloy. However, TIG welding of aluminium alloy depends on multiple parameters such as voltage, current, and scan speed. The experimental analysis of the welding process is time-consuming and costly. Finite element analysis (FEA) is one of the preferable methods of predicting the welding process and parameters. In this study, the effect of various welding parameters, i.e. voltage, current, and scan speed, on the weld pool formation is analysed using the FEA process. The weld pool thermal behaviours concerning time have been predicted by considering Gaussian heat source utilizing FEA software (ANSYS). The FEA analysis of the welding process showed that melt pool size increases with an increase in welding current and decreases with the increase in scan speed.

Keywords Arc welding · Numerical investigation · Thermal modelling · ANSYS

1 Introduction

Aluminium (Al) and its alloys are one of the widely used industrial materials. Al is one of the primer materials used for the manufacturing of aircraft and automobile components, due to its lightweight and adequate strength. Recent studies showed that civilian aircraft and cars are made up of nearly 80% and 40% aluminium (by weight), respectively [1–3]. The vast application of Al is due to its properties like good electrical, thermal conductivity, and high strength-to-weight ratio, better mechanical properties, corrosion resistance, and better forming capability. Aluminium alloys of

R. K. Mahato · M. Aslam · L. R. Krishna · C. K. Sahoo (✉)

Department of Mechanical Engineering, National Institute of Technology Silchar, Silchar, Assam 788010, India

e-mail: chinmaya.cks@gmail.com

the following series 2xxx, 3xxx, 4xxx, 5xxx, 6xxx, and 7xxx are widely utilized in industrial activity [1, 2]. 6xxx series aluminium alloys (Al–Mg–Si) are heat-treatable and precipitation-hardened materials. The Al alloy of the 6xxx series has been applied in marine, architectural applications, automotive sector, rolling stock, and high-strength structural members. These alloy series encompass product forms such as rolled plate and sheets extrusions, forging, piping and tubing, pressure vessels due to their better formability, corrosion resistance, and high-strength properties [3]. However, it is very challenging to use conventional arc welding (CAW) methods like gas metal arc welding (GMAW), gas tungsten arc welding (GTAW), and manual metal arc welding (MMAW) to weld aluminium and its alloys, due to its high thermal conductivity. Gas tungsten arc welding (GTAW/TIG) is an economical fusion-based welding method, in which heat energy is obtained from the development of an electric arc between the non-consumable tungsten electrode and the base metal. GTAW has also been named tungsten inert gas welding (TIG) due to the use of inert shielding gases (argon, helium, etc.) during welding. The inert gas protects the weld pool from the reaction of atmospheric oxygen. The major challenge in TIG welding of structural elements is to select proper welding parameters like current (A), voltage (V), and scan speed (v) [4]. The improper welding parameters may lead to welding defects like the development of residual stress, distortion, and low penetration of the weld pool [5]. Apart from the process parameters, the mode of welding, i.e. AC, DC, and pulsed current, has also influenced the quality of welding of structural elements [2, 6, 7].

TIG welding is generally preferred for aluminium welding due to reverse polarity welding capability [2, 8]. Yeni et al. [9] successfully welded a thick aluminium plate (of 6 mm) using GTAW, GMAW, and friction stir welding process (FSW). The arc-welded (GMAW and GTAW) samples showed a larger grain size in the welding zone and heat-affected zone (HAZ) compared to the FSW-welded samples. Durgutlu [6] had examined the microstructure, hardness, and notch impact results of 3 mm-thickness 6063 aluminium alloys welded joint using GTAW process. The author had used both pulsed and alternating current to weld the aluminium alloys. It has been reported that the developed microstructure and mechanical properties depend on the heat input during the welding process; the welded joint produced using pulsed current showed finer microstructure with a low hardness value. Bajpei et al. [5] utilized a volumetric moving heat source to simulate the GMAW process to study the developed residual stress and distortion during welding of thin Al sheets; Goldak's double-ellipsoid heat flux distribution was found to be suitable for welding simulation. Kumar et al. [7] showed that the welding quality of AA 6061 alloy depends on the TIG welding process parameter. The study showed that the pulsed type current was found to be suitable as compared to the conventional welding. The microstructural and mechanical analysis of TIG-welded samples is time-consuming and uneconomical. Therefore, the welding simulation using finite elemental analysis helps to analyse the welding process concerning input welding parameters. In the current study, an attempt has been made to FEA simulation of TIG welding of aluminium alloy.

2 Numerical Analysis

Experimental analysis of the TIG welding process is costly and time taking. Therefore, numerical study of the welding process could help to understand the effect of energy input on the weld melt pool characteristics. The total heat input (H) during the TIG welding process is represented in equation (1).

$$H = \eta VI \tag{1}$$

where V and I represent the voltage and current, respectively, and the efficiency (η) is considered as 48%; the efficiency (η) of the welding process considers the heat loss due to convection and radiation. An earlier literature review showed that in the TIG welding process the heat source could be assumed as Gaussian in nature (surface heat flux). The experimental investigation of earlier research also showed that the melt pool shape is similar to Gaussian in nature [4]. Therefore, the Gaussian heat source is used for the analysis. For the numerical analysis of the welding of aluminium substrate, the finite element method (FEM) was selected due to its effectiveness in thermal analysis. Equation (2) represents a mathematical equation to represent the Gaussian heat flux [10].

$$Q = \frac{3}{\pi r^2} \text{He}^{-3 \left[\frac{(x-x_i)^2 + (y-y_i-vt)^2}{r_p^2} \right]} \tag{2}$$

where Q = heat flux on the surface, r_p = radius of the periphery up to which 95% of heat flux is confined, and instantaneous centre of the heat flux can be pressed as (x_i, y_i) , the flux is moving at a distance of x, y .

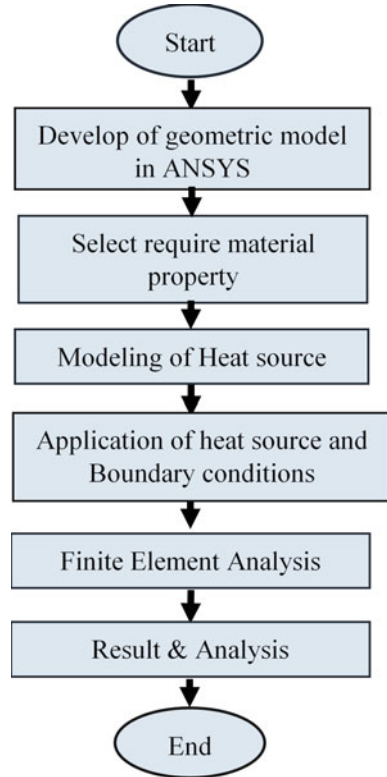
A finite element model (FEM) was constructed using ANSYS (R 18.2). For the FEM simulation, aluminium sheet of 3 mm thickness and $60 \times 100 \text{ mm}^2$ cross-sectional area. The developed model was meshed into the finer and coarse region for saving computational time. The size of the element (edge length) for the finer mesh region was fixed as 0.6 mm and the average size of 4 mm for the coarse region with a biasing factor of 1.2 for a smooth transition. The total model contains 85,188 numbers of nodes and 18,040 elements. The Gaussian heat flux of radius 2 mm was considered for the numerical analysis of the model. The properties of the aluminium 6061 were selected from the FEM analysis software library. Table 1 shows the welding parameters used for the numerical study. Transient thermal analysis was done to calculate the effect of heat input on the temperature distribution of the aluminium substrate.

The following assumptions are considered for the numerical analysis process.

Table 1 TIG welding parameters utilized for FEA of Al 6061

Sl. No.	Current (A)	Welding speed (mm/s)
1	40/60/80	2/4/6

Fig. 1 Flow chart of finite element analysis of welding process using ANSYS



1. The materials are considered isotropic in nature.
2. The fluid flow, arc force, the effect of gravity, and Marangoni flow are neglected.
3. The effect of conduction and convection is considered, and the effect of radiation in the arcing process is neglected.
4. Surface heat flux is considered.

Convection heat transfer is not considered for the bottom surface of the workpiece (Fig. 1).

3 Result and Discussion

Figure 2a, b, c shows the effect of scan speed on the developed temperature profile concerning the time. Temperature is measured at the midpoint of the substrate (50 mm from the edge along the length) and a depth of 1 mm from the surface. The temperature profile shows that at the centre of the workpiece temperature rises slowly with the movement of the TIG heat source (heat flux). It has been observed that the average temperature rise of the substrate is high for the welding processed with low scan

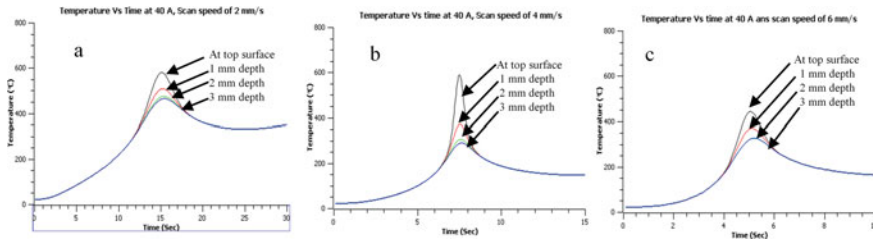
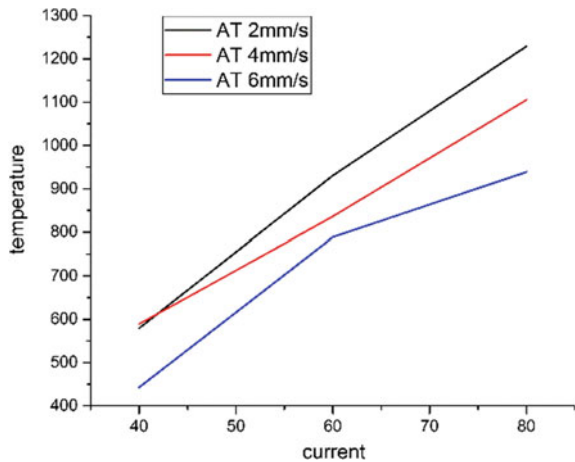


Fig. 2 Effect of welding speed **a** 2 mm/s, **b** 4 mm/s, **c** 6 mm/s for 40 A welding current on the developed temperature concerning time measured using numerical simulation on the centre of the workpiece on the welding path

speed. The peak temperature developed at 40 A welding current with 2 and 4 mm/s scan speed is about 600 °C. However, the weld simulation at 40 A current and scan speed of 6 mm/s showed a reduction in peak temperature (about 500 °C). Figure 2a, b, c shows that at the lower scan speed the average temperature of the workpiece is higher than the weld simulation at a higher scan speed (6 mm/s). It should also be noticed that the after-heat source travels over the workpiece for a significant period of time at a high temperature. A similar observation regarding the effect of welding scan speed has been observed for welding simulation at 60 and 80 A current. However, a maximum temperature of about 440 °C was obtained for welding analysis at 40 A and 6 mm/s, which makes the parameter unsuitable for the welding process (Fig. 3). Similar results regarding the development of maximum temperature for higher current (80 A) and low can speed, i.e. 2 mm/s, can also be observed in Fig. 3. The maximum and minimum temperatures of the aluminium substrate are high in case of low scan speed (2 mm/s), i.e. the substrate remains at for a significant period of time at a high temperature.

Fig. 3 Development of maximum temperature on the weld pool geometry with the variation of welding parameters



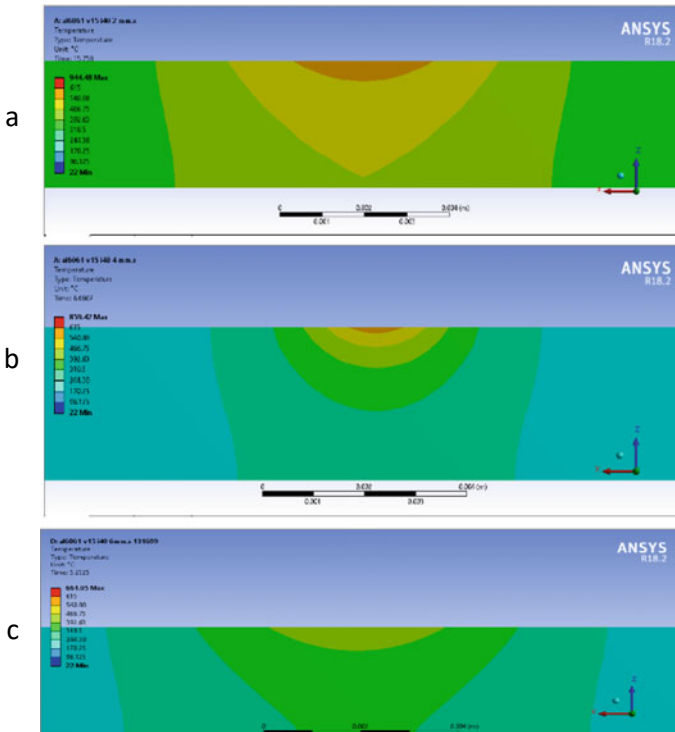


Fig. 4 Temperature distribution at the cross-section of the numerical model processed at 40 A welding current and scan speed of **a** 2 mm/s, **b** 4 mm/s, **c** 6 mm/s

Figures 4, 5 and 6 show the heat distribution across the weld cross-section using isotherm lines during the welding process, i.e. the images of the cross-section have obtained when the heat source at the centre of the substrate. Figure 4 a shows that at low scan speed the temperature of the workpiece is high; however, the melting temperature of the 6061 aluminium alloy is about (582–652 °C) and the maximum temperature varies between 540 and 615 °C. The welding parameters (40 A, 2 mm/s) could melt the surface, and a shallow depth of melt pool can be observed. Figure 4b, c shows low-temperature penetration with the increase in scan speed, and the maximum temperature has not been reached close to melting temperature at 40 A and 6 mm/s (Fig. 4c). Figure 5 shows the temperature distribution of the weld pool processed at 60 A current and different scan speeds. An increasing current (from 40 to 60 A) shows an increase in the melt pool temperature. The maximum temperature at the weld pool simulation model has increased from 615 to 1402 °C. The weld pool temperature distribution (Fig. 5a) produced 60 A and scan speed of 2 mm/s showed a temperature above the melting temperature of the Al alloy, which indicates the possibility of the complete penetration heat across the substrate thickness and melt the substrate. However, the analysis of the numerical model shows (Fig. 5a, b, c) the

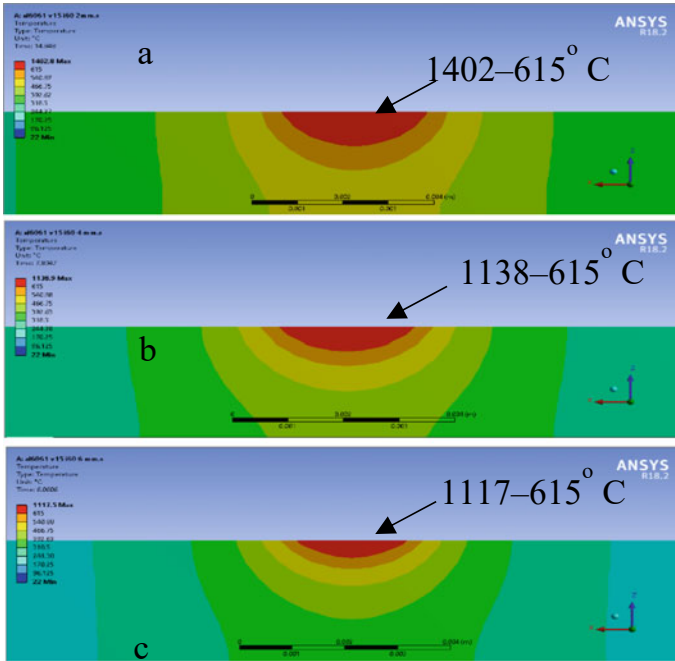


Fig. 5 Temperature distribution at the cross-section of the numerical model processed at 60 A welding current and scan speed of **a** 2 mm/s, **b** 4 mm/s, **c** 6 mm/s

formation of shallow melt pool with an increase in scan speed to 4 mm/s and 6 mm/s, respectively. Therefore, it could be predicted that the welding at a higher scan speed may not be able to create complete melting of the Al workpiece. Similarly, Fig. 6a, b, c shows the temperature profile of the cross-sectional image of the numerical model produced at 80 A current and scan speed of 2–6 mm/s. The cross-sectional image of the FEA simulation shows the development of high temperature at 80 A and 2 mm/s scan speed. The high temperature (> 1600 °C) in the weld area may cause complete melting of the welding zone. With the increase in scan speed, the average temperature of the workpiece decreases, and the high-temperature zone is limited to the top surface of the workpiece. Figure 7 shows the effect of current on melt pool geometry. At high current (80 A), the melt pool size (Weld zone > temperature > melting temperature) is larger than the FEA model processed with a lower current (40, 60 A) with constant scan speed.

The temperature distribution profile (Figs. 4, 5, 6 and 7) developed using the FEA model depends on the applied heat flux. The temperature of the heat flux depends on the heat input, i.e. $H = VI$, where V = voltage and I = current.

The average voltage used for the analysis is constant (15 V), whereas the current is changed to analyse the effect of the heat input on the Al sheet. The welding zone can be represented by the isotherm lines above the melting temperature of the aluminium

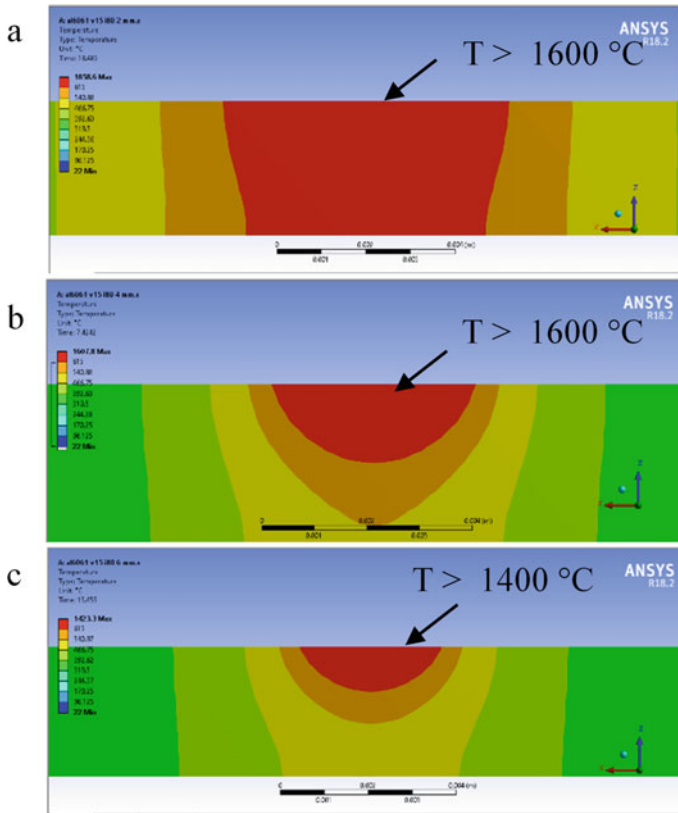


Fig. 6 Temperature distribution at the cross-section of the numerical model processed at 80 A welding current and scan speed of **a** 2 mm/s, **b** 4 mm/s, **c** 6 mm/s

alloy. The effect of the current can be observed, i.e. in Fig. 3, with an increase in the welding current the peak temperature produced in the weld pool increases, whereas the image (Fig. 3) also showed that with an increase in scan speed the peak temperature in the weld zone also decreases. At low welding torch scan speed, the heat source remains on the workpiece for more time compared to higher scan speed. The high input at the lower scan speed enhances the peak temperature and melting area.

4 Conclusion

The numerical models have been successfully developed, and the following conclusion would be drawn from the study.

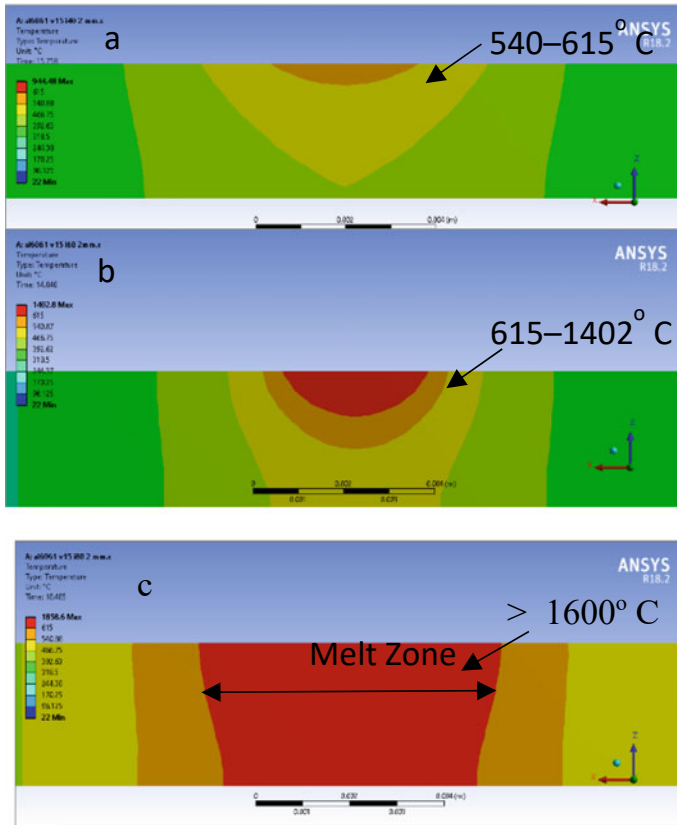


Fig. 7 Temperature distribution at the cross-section of the numerical model processed at 2 mm/s scan speed and welding current of **a** 40 A, **b** 60 A, and **c** 80 A

- The scan speed is observed to be one of the important parameters in the welding process. The welding simulation performed at lower scan speed (2 mm/s) of 40, 60, 80 A showed melting of Al substrate.
- The TIG welding of Al at low current (40 A, 6 mm/s) is not recommended due to the development of low temperature.
- The FEA welding analysis at higher current, i.e. 60, 80 A with 2 mm/s scan speed showed the complete melting at the welding zone. Moreover, the FEA welding model at 80 A and 2 mm/s showed the development of high temperature (> 1600 °C) at the heating zone; the temperature in the weld area may cause complete melting of the welding zone. Welding with higher scan speed (i.e. 4 and 6 mm/s) decreases the weld pool size.

References

1. Kim JS, Watanabe T, Yoshida Y (1995) Ultrasonic vibration aided laser welding of Al alloys: improvement of laser welding-quality. *J Laser Appl* 7(1):38–46
2. Cevik B (2018) Gas tungsten arc welding of 7075 aluminum alloy: microstructure properties, impact strength, and weld defects. *Mater Res Express* 5(6):066540
3. Mathers G (2002) *The welding of aluminium and its alloys*. Elsevier
4. Yue J, Dong X, Guo R, Liu W, Li L (2019) “Numerical simulation of equivalent heat source temperature field of asymmetrical fillet root welds.” *Int J Heat Mass Transf* 130:42–49
5. Bajpei T, Chelladurai H, Ansari MZ (2016) Numerical investigation of transient temperature and residual stresses in thin dissimilar aluminium alloy plates. *Proc Manufact* 5:558–567
6. Durgutlu A (2009) The effect of current type on welded metal microstructure and impact strength in tig welding of aluminum. *Mater Test* 24(1):155–160
7. Kumar, Senthil T, Balasubramanian V, Sanavullah MY (2007) Influences of pulsed current tungsten inert gas welding parameters on the tensile properties of AA 6061 aluminium alloy. *Mater Des* 28.7:2080–2092
8. Kou S (2003) Fusion welding processes. In *Weld Metall* John Wiley & Sons, Ltd, pp 1–36
9. Yeni Ç, Sayer S, Pakdil M (2009) Comparison of mechanical and microstructural behaviour of TIG, MIG and friction stir welded 7075 aluminium alloy. *Kov Mater* 47(5):341–347
10. Farias RM, Teixeira PRF, Vilarinho LO (2021) An efficient computational approach for heat source optimization in numerical simulations of arc welding processes. *J Constr Steel Res* 176:106382

Experimental Analysis on the Influence of Biofuel Amalgamated Al₂O₃ Nano Particles on the Performance and Emission Attributes of a C.I. Engine



Amarendra Deka, Debarup Borah, and Rahul Dev Misra

Abstract With the growing energy demands and the usage of fossil fuels in various energy sectors contributing heavily towards the global warming scenario is of greater concern. With high consumption of the fossil fuels leading to its depletion, alternative and clean energy sources currently play an important role in establishing a cleaner environment while fulfilling the energy demands without affecting the economic growth. Biofuels have emerged as one of the potential alternate energy suitors in today's time and is starting to find its usability in various sectors including transportation and industries. This paper showcases the production of biofuel from the Madhuca Indica seed oils through the transesterification technique. The paper focusses on the addition of Al₂O₃ nanoadditive on the prepared Madhuca Indica biodiesel blends. Various physiochemical properties were investigated for the prepared biodiesel blends. Experiments were conducted at engine loadings of 0, 25, 50, 75 and 100% to analyse the performance and emission attributes of a C.I. engine accompanied by the utilization of Madhuca Indica biodiesel along with the incorporation of Al₂O₃ nanoadditives to the same. The Al₂O₃ nanoparticle blend B30 MIBD 30 Al₂O₃ and B30MIBD 60 Al₂O₃ were seen to exhibit higher BTE than the primary biodiesel B30 MIBD blend. Lower NO_x emissions were recorded with the 60 ppm Al₂O₃ nanoparticle addition in the test fuels for the entire range of engine load conditions. The inclusion of nanoparticles was seen to illustrate boosted engine performance and curtail emissions.

Keywords Transesterification · Al₂O₃ nanoparticles · Madhuca Indica biodiesel · Performance · Emission

1 Introduction

The uncontrolled employment of the fossil fuels has led to acute environmental issues along with a lookout for substitute energy origins to meet the escalating energy urge.

A. Deka (✉) · D. Borah · R. D. Misra
Mechanical Engineering Department, NIT Silchar, Silchar, India
e-mail: amarendra_rs@mech.nits.ac.in

© The Author(s), under exclusive license to Springer Nature Singapore Pte Ltd. 2023
T. S. Sudarshan et al. (eds.), *Recent Advancements in Mechanical Engineering*,
Lecture Notes in Mechanical Engineering,
https://doi.org/10.1007/978-981-19-3266-3_49

623

Also, the issues of greenhouse effect arising due to the high exploitation of the fossils have become a critical concern for the environment and need immediate attention. Biodiesel has come out as an effective alternative and one of the best available energy sources to the conventional fuels [1]. Biofuel is fabricated from transesterification of various vegetable and animal fats, which involves reaction of ethyl alcohol or methyl alcohol with respective vegetable oils in the existence of catalyst to yield alcohol esters along with the formation of glycerine [2]. It is one of the cleanest forms of energy as it can be derived from various organic compounds. These biofuels find its usage in almost all the energy sectors and are also considered as a potential sustainable fuel for being used in C.I. engines. Biodiesel possesses very indistinguishable and alike properties to conventional diesel along with a pristine and clean substitute while burning when it is compared with mineral diesel [3]. Biodiesel usage in automobile and other common energy sectors could be a possible substitute in lessening the harmful emissions from the fossil fuel usage, thus resulting in a cleaner environment. The lower HC and CO emissions from C.I. engines powered with biofuels has made its usage more prominent with the involvement of higher biofuel concentration. The NO_x emissions on the other hand increase drastically with the higher concentrations of the biofuels in the fuel blends. Diesel comparatively has lower NO_x emissions in comparison to the biofuels, as biofuels comprises of higher oxygenates in itself [4]. Though the performance characteristics of biofuels are more likely comparable to the mineral diesel, the emission characteristics of the biofuels need more attention. Due to major environmental threat and climatic transformation, more stress is laid on reducing the NO_x and CO emissions from C.I. engines, as these are responsible for increasing the prevailing emissions. Many of the past research studies reveal that the use of various nanoparticle or nanoadditives are capable in improving the emission characteristics of the fuel [5]. These particles are more effectual in the form of nanoparticles due to their amplification in the volume to surface area ratio. In this paper, the effect of addition of Al_2O_3 nanoadditive on the Madhuca Indica biodiesel has been studied. The physical and chemical properties of the nanoparticle blended along with the Madhuca Indica biodiesel has been deliberated in this paper along with the engine performance and emission parameters of amalgamates of Madhuca Indica biodiesel accompanied by different concentration of Al_2O_3 nanoparticles.

1.1 Novelty of the Work

Numerous works have been investigated in the past on Madhuca Indica biofuel on its application in C.I. engines. Various performance and emission attributes were analysed for different nanoparticles blended with Madhuca Indica biofuel. But there have been no recorded writings on the analysis and study of the Madhuca Indica biofuel with different aggregation of Al_2O_3 nanoparticles on the performance and emission traits when applied to C.I. engines. Keeping this novelty in mind, the following experimental analysis has been conducted.

Table 1 Details of the materials used for preparation of test fuel blends

Particulars	Materials used				
	Crude Madhuca Indica oil	Methanol	Conc. sulphuric acid	Sodium hydroxide	Aluminium nitrate
Manufacturer	P.L. extraction	Blulux	Dhanlaxmi chemicals	Antares chem. pvt. ltd	Powder pack chem.
Purity (%)	88	99.8	98	99	98.9
Density (kg/m ³)		792	1830	2130	1720
Grade	Industrial	Industrial	Industrial	Industrial	Industrial

2 Materials and Methodology

Biodiesel provides one of the promising future aspects in the alternative fuel sector, with the fossil fuels running out at a high depletion rate. The use of crude bio-oils is limited to be used directly due to its high viscosity, low volatility and various compositions of free fatty acids [6]. These oils need to be converted into diesel like fuels before being able to use in various applications. Transesterification technique is one of the common and viable processes used in the conversion from bio-oil into biodiesel. The process first involves conversion of the oil from the seeds and further processing of this crude oil into biofuel through transesterification [7].

2.1 Materials Used

- A. Crude Madhuca Indica oil extracted from the seeds were obtained from P.L. Extraction Firm West Bengal, were used in production of Biodiesel.
- B. Methanol, concentrated sulphuric acid and sodium hydroxide obtained from the local chemist.
- C. Mechanical stirrer fitted with a condenser for the transesterification technique.
- D. Aluminium nitrate, urea and Ph paper obtained from the chemist for preparation of nanoparticles.

The details of the substances employed for the transesterification technique are itemized in Table 1.

2.2 Synthesis of the Madhuca Indica Biodiesel

Transesterification is a technique for conversion of the vegetable oil into esters (diesel like properties) and glycerol with the help of an alcohol in the residence of an acidic

and base catalyst. The catalyst is applied to magnify the yield and the rate of the reaction and also aiding in the breaking of the free fatty acids present in the vegetable oils. Methanol and ethanol are the regularly utilized alcohols in the transesterification process due to its high solubility, faster reaction rate, good physical and effective cost. The extracted crude *Madhuca Indica* oil procured from P.L. extraction is extracted from the *Madhuca Indica* tree seeds collected from puruliya District, West Bengal, using mechanical and pressure expellers. The first step in the selection of the transesterification process is the determination of the free fatty acid (FFA) value. For FFA value less than 4, the oil sample is processed for single-stage esterification and for FFA more than 4, and double-stage (transesterification) is carried out for the production of biodiesel.

$$\text{Acid value} = \frac{MXT \times 56.1}{\text{Weight of oil}} \quad (1)$$

and

$$\% \text{FFA} = \frac{\text{Acid value}}{2} \times 100 \quad (2)$$

Upon determination, due to the higher FFA value of the crude oil, double-stage transesterification is carried out to obtain the *Madhuca Indica* biodiesel.

Initially, the *Madhuca Indica* oil is preheated to a temperature of 100 °C for removing any present moisture. The first step involves the acid catalytic transesterification, where 500 ml of crude *Madhuca Indica* oil is taken in a round bottomed flask. 5% of concentrated sulphuric acid and methanol (3:1 oil to methanol ratio) is added to it. The reaction temperature is maintained at 60 °C for 90 min at a speed of 400 rpm. The blend is supplied with heat and continuous stirring aided by a magnetic stirrer to maintain a stable temperature position in the mixture. At temperatures 60 °C and above, methanol tends to vaporize, so a condenser is fitted with water inlet and outlet provision which aids in condensing the methanol vapours back into the mixture for occurrence of proper and complete reactions. After the reactions are complete, the esterified oil is left to settle in a separating funnel for a day as shown in Fig. 1. The products, *Madhuca Indica* Esters and the glycerol are separated out for the base catalytic transesterification reactions. In this second step, the obtained *Madhuca Indica* esters from the first step is mixed with 1.5% (w/w) sodium hydroxide solution and methanol (3:1 oil to methanol ratio). This mix is maintained at reaction temperature of 60 °C and stirred rapidly for another 120 min. The reactants are kept for resolving in a separating funnel overnight. Upon separation, the top layer comprehends the 100% *Madhuca Indica* esters (biodiesel) and the bottom layer comprising the glycerin compounds. Fig. 2 shows the 100% *Madhuca Indica* Biodiesel (MIBD).

Fig. 1 Settling of Madhuca Indica biodiesel



Fig. 2 Madhuca Indica biodiesel



2.3 Preparation of Al_2O_3 NanoParticles

Nanoadditives of Al_2O_3 are prepared using the solution gel technique [8]. Here, 0.3 mol of aluminium nitrate is mixed with 100 millilitre H_2O with maintained temperature of 20 °C. The aluminium nitrate solution is stirred using a magnetic stirrer. The next step involves blending of 0.05 M urea with the solution, which is further treated for 15 min unless a solution with pH 2 is obtained. The same solution is titrated with another 25 ml of H_2O blended with 0.1 M of NaOH. And it is treated until a solution with pH 6 is obtained. This results in a formation of a gel with pH 7

Table 2 Properties of the prepared Al₂O₃ nanoparticles

Properties	Al ₂ O ₃ nanoparticle
Size of the particle (nm)	18–21
Surface area (m ² /g)	368
Purity (%)	95.32
Bulk density (g/cc)	0.162
Colour	White

on NaOH addition, further the resultant is dehydrated in temperature range of 100–130 °C for 8 h followed by collection of the nanoparticles and allowed to dry at 200 °C for another 1 h in the furnace. The properties of the fabricated nanoparticles are elaborated in Table 2.

2.4 Preparation of the Madhuca Indica Biodiesel and Al₂O₃ Nanoparticle Blend

Now, the prepared Al₂O₃ nanoparticles in amount of 30 and 60 ppm concentration are blended with the transesterified 100% Madhuca Indica biodiesel (B100) to obtain MIBD 30 Al₂O₃ and MIBD 60 Al₂O₃ with the assistance of a magnetic stirrer for 30 min. The nanoparticle-blended biofuel is further checked for stability in its properties before being used for the test. The nanoparticle-blended Madhuca Indica biodiesel is now blended in ratio of 30% with conventional diesel to obtain B30 MIBD 30 Al₂O₃ (30% MIBD and 30 ppm Al₂O₃ nanoparticle) and B30 MIBD 60 Al₂O₃ (30% MIBD and 60 ppm Al₂O₃ nanoparticle) test fuels. The different proportions to obtain the Al₂O₃ nanoparticle and Madhuca Indica biodiesel blend test fuel are tabulated in Table 3.

Various thermophysical and chemical properties such as kinematic viscosity, density, flash and fire point, cetane number and calorific value of the prepared test fuels calculated as per ASTM standards are tabulated in Table 4.

Table 3 Composition of the Madhuca Indica test fuels

Test fuel	Proportion of the elements		
	Crude Madhuca Indica biodiesel (%)	Diesel (%)	Al ₂ O ₃ Nanoparticle (ppm)
B100MIBD	100	–	–
B30MIBD	30	70	–
B30MIBD 30 Al ₂ O ₃	30	70	30
B30MIBD 60 Al ₂ O ₃	30	70	60

Table 4 Physical and chemical properties of the prepared biodiesel and nanoparticle blends

Properties	Unit	ASTM Standard	Proportion of the elements					
			Diesel	Crude Madhuca Indica oil	B100 MIBD	B30 MIBD	B30MIBD 30 Al ₂ O ₃	B30MIBD 60 Al ₂ O ₃
Density	g/cm ³	D4052	0.824	0.920	0.882	0.848	0.842	0.844
Kinematic viscosity	mm ² /s @40°C	D445	2.4	22.58	4.1	3.16	3.38	3.42
Cetane number	–	D613	48	–	53	50	55	57
Flash point	°C	D976	51	210	124	76	82	84
Calorific value	kJ/kg	D240	42,956	–	38,384	39,475	40,325	40,762

3 Experimental Setup

The test engine setup comprises of a four stroke and single-cylinder C.I engine with water cooling facility, an electrical dynamometer for adjusting various loads and a delivery unit for the fuel for performing the required experiments. The setup also comprises of the AVL gas analyser 1000 for measuring the CO, CO₂ and NO_X emissions along with a data acquisition system, which is connected to a computer through the control unit capable of acquiring various data aided by the sensors fitted in several parts of the engine. Figure 3 depicts the test engine setup. The experiments were performed at five load interims in percentage of 0, 25, 50, 75, and 100 with engine speed of 2000 rotations per minute. With a manually aided hand lever, the test engine is started and is made to run at no load conditions for 10–15 min to stabilize it. Gradually the data are measured at the required load conditions for the prepared test fuels from the IC EngineSoft software for the analysis of the engine performance and emission parameters. The test engine specifications are tabulated in Table 5.

4 Results and Discussion

4.1 Performance Characteristics

4.1.1 Brake Power

It is basically the amount of power which is accessible at the crankshaft. A substantial increment in the brake power is noticed with the use of the Al₂O₃ nanoparticle when blended with Madhuca Indica biodiesel. Figure 4 exhibits the discrepancy of the brake power for the engine test load conditions for various test fuel blends used. At



Fig. 3 Test engine setup

Table 5 Specifications of the test engine

Particulars	Units	Specifications
Maker	–	M/s Apex Innovations Pvt. Ltd
Genre	–	Four-stroke
Cooling type	–	Water-cooled
Number of cylinders	–	1
Bore diameter × stroke length	mm	87.5 × 110
Compression ratio	–	17.5:1
Cubic capacity	l	0.661
Combustion principle	–	Compression ignition
Induction type	–	Non-turbocharger
Maximum speed	rpm	2000
Connecting rod length	mm	234
Min. operating speed	rpm	1200
Fuel injection timing	–	23° before TDC
Lubricating system	–	Forced feed system
Lubricating oil pump delivery	l/min	6.50
Dynamometer arm length	mm	185

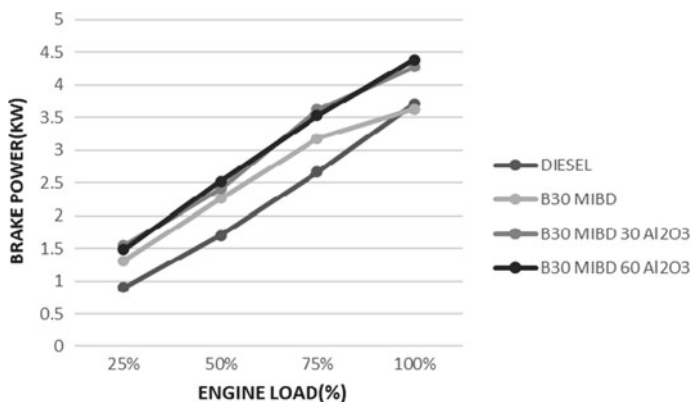


Fig. 4 Test results of the brake power with respect to the engine load

full engine loading conditions, the Al_2O_3 nanoparticle when blended with Madhuca Indica biodiesel was seen to illustrate superior influence on the brake power than at the partial test load conditions. As there is a remarkable increment in the brake power with the use of the nanoparticle blends, which ensures effective combustion and proper transformation of the available energy of the fuel into beneficial work.

Also, the rise in brake power with the inclusion of the nanoadditives is due to the reduction in the carbon and iron deposits, thus lesser frictional contact in various parts, thus enhancing the engine power. The presence of the integral oxygen compounds in the Al_2O_3 nanoparticle along with the inbuilt oxygenates present in the Madhuca Indica biodiesel enhances the oxidation process resulting in lower fuel consumption. The combustion processes are made more efficient and accelerated with the addition of nanoadditives than with primary Madhuca Indica biodiesel blend. Lower ignition delay facilitated by the nanoadditives leads to improved heat release rate and elevated cylinder pressures, resulting in increase in the brake power.

4.1.2 Brake Thermal Efficiency

The efficient translation of the heat energy available from the charge into mechanical energy is defined by the brake thermal efficiency (BTE). Figure 5 shows the outcome for the test fuel Diesel, B30 MIBD, B30 MIBD 30 Al_2O_3 , and B30MIBD 60 Al_2O_3 at various engine loading conditions. From the figure it was perceived that the BTE of mineral diesel was inflated compared to other prepared blends due to the increase in gross calorific value and lower kinematic viscosity of the fuel with respect to the other oxygenated biofuel blend samples. At 100% loading of the engine, BTE for diesel was observed as the highest at 33.24%, while for B30 MIBD 30 Al_2O_3 and B30MIBD 60 Al_2O_3 it was 30.10% and 31.22%, respectively. The least BTE was recorded for B30 MIBD blend at 28.83%. At 100% engine load conditions, B30 MIBD 30 Al_2O_3 and B30MIBD 60 Al_2O_3 were seen to exhibit 4.40 and 8.28%

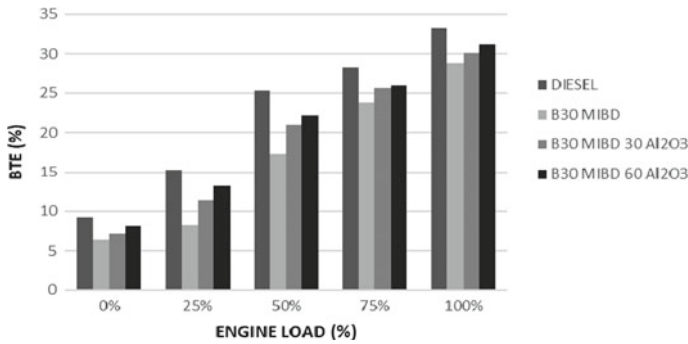


Fig. 5 Test results of the brake thermal efficiency with respect to the engine load

higher BTE than the primary B30 MIBD blend. This is due to the addition of the Al₂O₃ nanoparticle blended Madhuca Indica biodiesel blend, which increases the fuel droplet atomization, thus enhancing the combustion effectiveness.

The B30 MIBD 60 Al₂O₃ blend is seen to portray higher BTE for the entire range of engine load conditions compared to the other test fuel blends. The Al₂O₃ nanoparticle can be considered a potential catalyst and provides oxygen cushioning as the concentration of the nanoadditives are increased, thus effecting the engine performance.

4.2 Emission Characteristics

4.2.1 Exhaust Gas Temperature

The exhaust gas temperatures of various prepared test fuels to the different engine load conditions are encapsulated in Fig. 6. From the figure it can be observed that the EGT for both the Al₂O₃ nanoparticle B30 MIBD 30 Al₂O₃ and B30MIBD 60 Al₂O₃ fuel blends increases with respect to the B30 MIBD blend and mineral diesel with increasing engine load conditions.

The reason being, as the nanoparticle aggregation in the blend escalates, the combustion efficiency of the fuel is revamped aided by the oxygen surge of the biofuel blends, resulting in production of excessive heat which finally affects the exhaust gas temperatures. Also, higher calorific value of the fuel results in inflated exhaust gas temperatures owing to better combustion; however, the blended fuels have lower calorific value than mineral diesel.

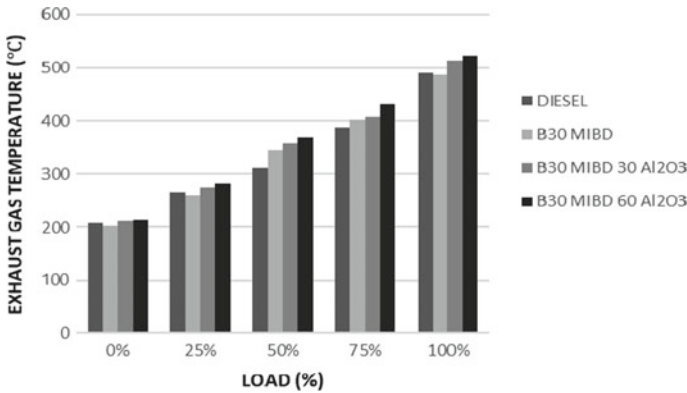


Fig. 6 Results of exhaust gas temperatures at different engine loading conditions

4.2.2 NO_x Emissions

NO_x formation occurs mostly during the end of the combustion at elevated temperatures (above 1400 °C) owing to the consequence of nitrogen and oxygen reactivity. Existence of oxygen plays a vital character in the evolution of NO_x. Though the occupancy of the oxygenated compounds in the biofuel blends revamps the combustion process, it facilitates higher NO_x formation than mineral diesel. Figure 7 exhibits the NO_x emission results for various test fuel blends at varied engine loading conditions. The NO_x emission for all the blends of test fuels is noticed to escalate with increase in various engine loading circumstances due to the improved cylinder temperature at higher loads.

The NO_x formation mostly relies on the engine cylinder temperature during the fuel combustion and can be related with the engine exhaust gas temperature at various

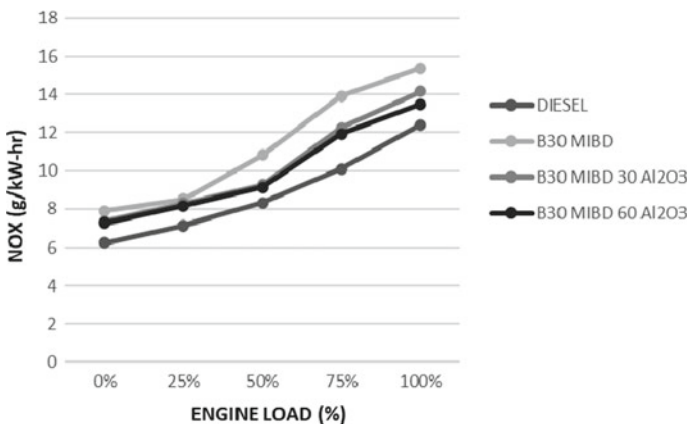


Fig. 7 Variation of NO_x emissions at different engine load conditions

engine loadings. From Fig. 7, it is evident that mineral diesel shows the least NO_x emissions, while B30 MIBD were seen to exhibit higher NO_x emissions compared to the blends of B30 MIBD 30 Al_2O_3 and B30MIBD 60 Al_2O_3 , which is due to the oxygen contents in the biofuel blends.

At full loading conditions, B30 MIBD 30 Al_2O_3 and B30MIBD 60 Al_2O_3 fuel blends exhibited lower NO_x emissions than the B30 MIBD by 7.93% and 12.35%, respectively, which is mostly accredited due to the enhanced cetane index because of the presence of higher Al_2O_3 aggregation. The Al_2O_3 molecule reacts with the NO available from the combustion due to enhanced cylinder temperature, lessens the propensity of formation of NO_x particles. Reduced NO_x emissions with the use of Al_2O_3 nanoadditives blended with biofuels was also observed in a few studies [9–11].

5 Conclusion

The present investigational analysis puts forward the performance and emission attributes of a C.I. engine powered with dissimilar samples of *Madhuca Indica* biofuel blended with Al_2O_3 nanoparticles at concentrations of 30 and 60 parts per million. The outcomes of the conducted experiments for the prepared test fuel blends show that minute improvements in the brake power were noticed for the blends with Al_2O_3 nanoparticles, which resulted in effective combustion and proper transformation of the available energy into beneficial work. The oxygen molecule present in the Al_2O_3 nanoparticles influences the combustion activity upon amalgamating with the fuel. The discharged oxygen molecule from the Al_2O_3 nanoparticle acts with the available unburned hydrocarbons from combustion along with elevated heating rates to revamp the combustion rates. Also, enhanced thermal conductivity of nanoparticles aggregates to boost in ignition span and elevated cylinder pressures. At full engine load conditions, nanoparticle blends B30 MIBD 30 Al_2O_3 and B30MIBD 60 Al_2O_3 were seen to exhibit 4.40 and 8.28% higher brake thermal efficiency than the primary B30 MIBD blend, which accelerates the fuel atomization resulting in higher combustion efficiency. Reduced NO_x emissions were observed with the use Al_2O_3 nanoparticles with respect to B30 MIBD. At full loading conditions, B30 MIBD 30 Al_2O_3 and B30MIBD 60 Al_2O_3 fuel blends exhibited lower NO_x emissions than the B30 MIBD by 7.93% and 12.35%, respectively. The central idea of the conducted experiments indicates that the *Madhuca Indica* biodiesel blended along with the Al_2O_3 nanoparticles can be contemplated as a positive and potential alternative to mineral diesel to be used as a commercial fuel in C.I. engines and other energy sectors.

References

1. Lin L, Cunshan Z, Vittayapadung S, Xiangqian S, Mingdong D (2011) Opportunities and challenges for biodiesel fuel. *Appl Energy* 88:1020–1027
2. Rashid U, Anwar F (2008) Production of biodiesel through optimized alkaline-catalyzed transesterification of rapeseed oil. *Fuel* 87:265–273
3. Saka S, Kusdiana D (2001) Biodiesel fuel from rapeseed oil as prepared in supercritical methanol. *Fuel* 80:225–231
4. Monyem A, Van Gerpen JH (2001) The effect of biodiesel oxidation on engine performance and emissions. *Biomass Bioenergy* 20:317–325
5. Soudagar MEM, Nik-Ghazali NN, Akram N (2020) The potential of nanoparticle additives in biodiesel: a fundamental outset. In: AIP conference proceedings of the advances in mechanical design, materials and manufacture, vol 2247(1), pp 148–153 AIP Publishing
6. Wang JX, Chen KT, Wu JS, Wang PH, Huang ST, Chen CC (2012) Production of biodiesel through transesterification of soybean oil using lithium orthosilicate solid catalyst. *Fuel Process Technol* 107:167–173
7. Vyas AP, Subrahmanyam N, Patel PA (2009) Production of biodiesel through transesterification of *Jatropha* oil using KNO_3 solid catalyst. *Fuel* 88:625–628
8. Tabesh S, Davar F, Loghman-Estarki MR (2017) Preparation of $\gamma\text{-Al}_2\text{O}_3$ nanoparticles using modified sol-gel method and its use for the adsorption of lead and cadmium ions. *J Alloys Comp* 730:441–449
9. Karthikeyan S, Prathima A, Periyasamy M, Mahendran G (2020) Emission analysis of the diesel engine using *Stoechospermum marginatum*, brown marine algae with Al_2O_3 nano fluid. *Mater Today: Proc Int Conf Nanotechnol: Ideas Innov Ind* 33:4047–4053 (part 7)
10. Krupakaran RL, Hariprasas T, Gopalakrishna A, Babu P (2016) The performance and exhaust emissions investigation of a diesel engine using $\gamma\text{-Al}_2\text{O}_3$ nanoparticle additives to biodiesel. *Carbon Manage* 7(3–4):233–241
11. Channappagoudra M (2019) Influence of the aluminium oxide (Al_2O_3) nano particle additive with biodiesel on modified diesel engine performance. *Int J Ambient Energy* 6:231–239

Bearing Fault Identification of Augmented Grayscaled Textured Images Using K-Nearest Neighbor



Jaimin Panchal  and Vinay Vakharia 

Abstract Bearings are the most commonly used components in rotating machinery, and hence, bearing faults may result in significant breakdowns and even casualties. For this, fault diagnosis is usually done with the help of vibration signals. The current paper uses a publicly available dataset from Case Western Reserve University. The two-dimensional grayscaled textured image is extracted from the vibration signals. Solving the problem of an imbalanced dataset is done by applying geometrical augmentation techniques on these images. A set of statistical features are calculated to form a feature vector. This feature vector is then fed to various machine learning algorithms like decision tree, K-nearest neighbor, support vector machine and ensemble bagged tree to get the classification results.

Keywords Bearing fault diagnosis · Geometrical augmentation · Imbalanced dataset · Case Western University dataset · Machine learning algorithms · Fault classification

1 Introduction

There are three major parts in rotary machines, namely a rotor, bearings and a foundation. As we know that rotary machines work in an extremely harsh environment. Hence, those machines are at risk of having faults inside bearings. The failure in loss can be major and can not only decrease productivity but can also endanger human life. Therefore, fault diagnosis and classification are necessary. These can be easily done with the help of vibration signals extracted from bearings using an instrument like an accelerometer.

Vakharia et al. presented a method called minimum permutation entropy which can be used to select the best wavelet for feature selection and fault classification. The

J. Panchal · V. Vakharia (✉)

Department of Mechanical Engineering, School of Technology, Pandit Deendayal Petroleum University, Gandhinagar, Gujarat, India
e-mail: vinayvakharia4343@gmail.com

statistical features were calculated, and the vector was fed to machine learning algorithms called support vector machine (SVM) and artificial neural network (ANN). The method was validated by comparing it with previous works [1]. Gaci presented a new denoising technique called ensemble empirical mode decomposition (EEMD). As most paper uses discrete wavelet transform (DWT) for denoising the signal, the new technique and DWT were compared by implementing on same synthetic and diverse waveforms from real seismic traces recorded in the Algerian Sahara. The fault classification was done using the support vector machine (SVM) [2]. Vakharia et al. proposed a study for fault diagnosis of bearings using ReliefF and random forest classifier. Statistical features like kurtosis, skewness, etc., and complexity measures like Shannon entropy were calculated from time-domain data from discrete wavelet transform (DWT). Finally, feature ranking methods like ReliefF and information gain were used to rank important features based on weight gain, and fault diagnosis was done using support vector machine (SVM) and random forest classifier (RFC) [3]. Uddin et al. formed a two-dimensional gray textured image from vibration signal of induction motor which was then fed to Gabor filter at different frequencies and orientation to extract filtered images with unique texture information. They are passed to singular value decomposition (SVD) to extract discriminative features for performing fault diagnosis using one against all multi-class support vector machines (OAA-MCSVMs) [4]. Li et al. proposed the usage of fast Fourier transform (FFT) to extract spectrum images from vibration signals. These images are processed in the two-dimensional principal component analysis (2DPCA) to reduce dimensions of images. For the classification of faults, the minimum distance method is applied after which validation is done with experimental data [5]. Khan and Kim proposed an automated approach for bearing fault diagnosis by performing two-dimensional analysis of vibration acceleration signals under variable speed conditions. Grayscale images are extracted from the signals which exhibit fault-wise unique textures. A micro-textured analysis is done to generate unique signatures to classify fault using the K-nearest neighbor algorithm [6]. Azad et al. proposed a novel approach to transform a one-dimensional signal to two-dimensional grayscale textured images as in previous works working in one-dimensional signals results in losing a lot of information of time and frequency coefficient. Features are extracted from the images after denoising them using empirical mode decomposition (EMD) which are freed using segmentation-based fractal texture investigation (SFTA) algorithm. These features are then fed to a multi-class support vector machine (SVM) [7]. Boudiaf et al. studied and reviewed various vibration analysis techniques, their capabilities, advantages and limitations for condition monitoring of rolling bearings. Four main techniques are reviewed in this work, namely fast Fourier transform, cepstrum analysis, envelope analysis and wavelet transform. The conclusion was made by studying all these with the Case Western University dataset [8]. Amar et al. presented a novel vibration spectrum imaging feature (VSI) for enhancing the low signal-to-noise (SNR) ratio vibration signals. Spectral images were formed using normalized amplitudes of quasi-stationary time vibrations signals. Techniques like a two-dimensional averaging filter, binary image conversion and thresholding were using to enhance the images for the training and testing using artificial neural networks (ANN) [9]. Khodja

et al. proposed the classification of bearing faults using the images generated by VSI for training and testing of convolution neural network (CNN) classifier. The results were then validated from the experimental test bench by collecting vibration signals at different operating conditions and variable speeds [10]. Uddin et al. proposed a method for fault diagnosis and classification of induction motors. The proposed method converts time-domain vibration data to two-dimensional grayscale images with unique texture patterns and extracting features from them using dominant neighborhood structure (DNS). Principal component analysis (PCA) is used to reduce the dimension of features to improve the performance of classification using OAA-MCSVMs to find failures of induction motor [11]. Ruberto and Fodde presented a complete system to classify medical images for detecting diseases. The system consisted of two parts, and in the first part, complete set of thirty-three statistical features were calculated to form a vector. In the second part, SVM, K-nearest neighbor (KNN), RFC, etc., are used to classify images by using the feature vector generated in the first part [12].

In this paper, images are extracted from vibration signals using the method proposed by Uddin et al. [4], and the data augmentation is done on these images. A feature vector consisting of statistical features (calculated from images) and labels of faults is fed to machine learning models for fault classification.

2 Experimental Setup

Dataset used in this paper is provided by the Bearing Data Center of Case Western Reserve University (CWRU) [13]. Dataset consists of healthy bearings and bearings with faults at the inner race ball, and outer race. An electric discharge machine is used to insert a single-point fault of diameter 0.1778, 0.3556, 0.5334 and 0.7112 mm inside the bearing. Signals are collected at the end of both drives using an accelerometer. The motor is rotated at rpm ranging from 1730 to 1797 at a sampling frequency of 12 kHz (Fig. 1). The number of samples recorded during that time can be seen in Table 1.

Fig. 1 CWRU experimental setup

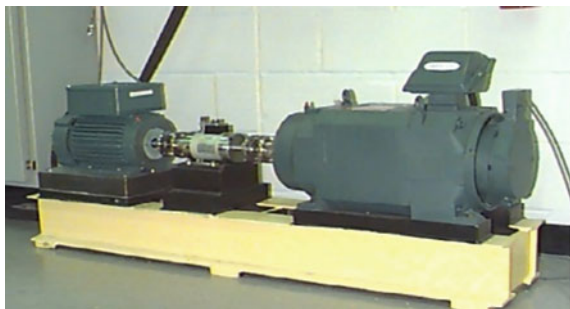


Table 1 CWRU dataset samples

Condition	Number of samples	Fault diameter (mm)
Healthy bearing	4	0.18, 0.36, 0.54, 0.72
Inner race fault	16	0.18, 0.36, 0.54, 0.72
Outer race fault	28	0.18, 0.54
Ball defect	16	None

3 Preprocessing

3.1 Image Formation

The vibration signals obtained from the CWRU dataset are only of one dimension. The process of working with only one-dimensional vibration signals can leave a significant impact on bearing fault diagnosis and classification as proposed by Azad et al. [7] as it can lead to loss of time coefficients. So, the method proposed by Uddin et al. [4] helps in transforming the one-dimensional signal to a two-dimensional grayscale textured image.

The methodology (shown in Fig. 2) used for the conversion is that the vibration signal is divided into M number of sub-parts; then, the two-dimensional matrix is made where the amplitudes of the N signals are placed in the column which generates images of high-resolution $M \times N$. To ease the computational efficiency, image is

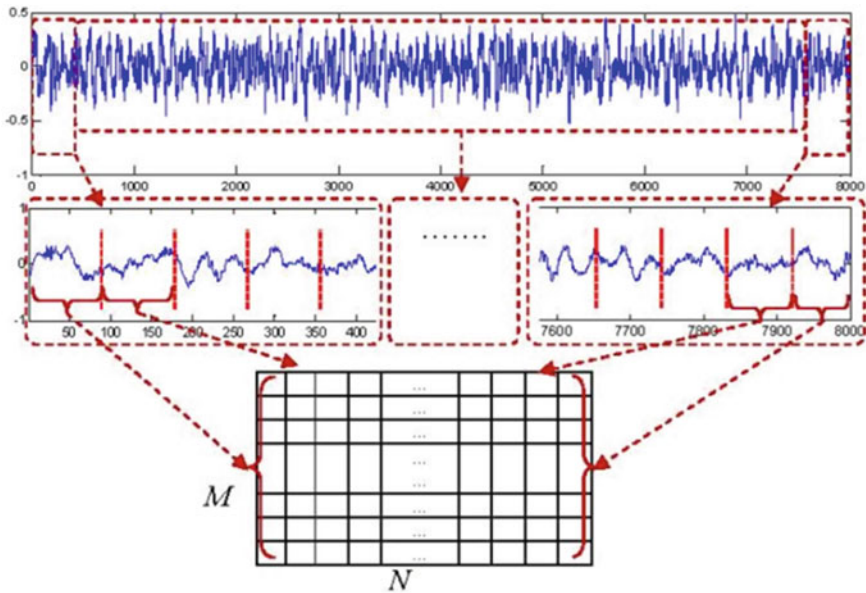


Fig. 2 One-dimensional signal conversion to two-dimensional image [4]

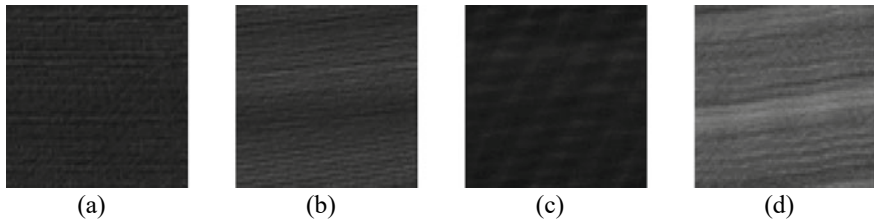


Fig. 3 Two-dimensional grayscaled images generated and rescaled to 64×64

normalized to a grayscaled image of 64×64 pixels as shown in Fig. 3. The total number of images generated for each fault sample is as per Table 1.

3.2 Geometrical Transformation

Working with the imbalanced dataset leads to an inefficient prediction of classes as the total number of samples are different for each class as explained by Galar et al. [14]. For solving this problem, geometrical transformation, a type of data augmentation technique, is used for generating new images by doing various transformations on images such as rotation, translation, shear mapping and flipping. The transformations used on the images are horizontal and vertical flipping and rotation to make the dataset balanced.

4 Feature Extraction

A set of statistical time-domain features like standard deviation, mean, energy and homogeneity (from gray-level co-occurrence matrix (GLCM) as explained by Guha et al. [15]) are extracted from these textured images for constructing the feature vector and labeling the faults.

1. Mean: The average value of the image matrix

$$p_m = \frac{1}{N} * \sum_{i,j=1}^N p_{(i,j)} \quad (1)$$

2. Standard deviation (std): Deviation from the mean value of the image matrix

$$p_{std} = \sqrt{\frac{\sum_{(i,j)=1}^N (p_{(i,j)} - p_m)^2}{(N - 1)}} \quad (2)$$

3. Variance: Square of standard deviation

$$p_{\text{var}} = \frac{\sum_{(i,j)=1}^N (p_{(i,j)} - p_m)^2}{(N - 1)} \quad (3)$$

4. Energy: Returns the sum of squared elements in the GLCM

$$p_{\text{Energy}} = \sum_{(i,j)=1}^N p_{(i,j)}^2 \quad (4)$$

5. Skewness: A measure of lack of symmetry in image matrix

$$p_{\text{skew}} = \frac{\sum_{(i,j)=1}^N (p_{(i,j)} - p_m)^3}{(N - 1) * p_{\text{std}}^3} \quad (5)$$

6. Kurtosis: A measure of the spikiness of the signal relative to a normal distribution

$$p_{\text{kurt}} = \frac{\sum_{(i,j)=1}^N (p_{(i,j)} - p_m)^4}{(N - 1) * p_{\text{std}}^4} \quad (6)$$

7. Root mean square (RMS): The square root of the mean of squares of an image matrix

$$p_{\text{rms}} = \sum_{(i,j)=1}^N \frac{(p_{(i,j)})^2}{N} \quad (7)$$

8. Homogeneity: Measures the closeness of the distribution of elements in GLCM to GLCM diagonal

$$\sum_{(i,j)}^N = \frac{p_{(i,j)}}{1 + (i - j)^2} \quad (8)$$

9. Peak-to-peak value: Difference between maximum and minimum peak values

$$p_{\text{ppv}} = p_{\text{max}} - p_{\text{min}} \quad (9)$$

10. Crest factor: It is the ratio of peak value to RMS value

$$p_{\text{CF}} = \frac{p_{\text{max}}}{p_{\text{rms}}} \quad (10)$$

11. Shape factor: It is the ratio of RMS value and mean value

$$p_{SF} = \frac{p_{rms}}{p_m} \quad (11)$$

12. Impulse factor: It is the ratio of max value and mean value

$$p_{IF} = \frac{p_{max}}{p_m} \quad (12)$$

13. Margin factor: It is the ratio of max value and mean value of a square of the image matrix

$$p_{MF} = \frac{p_{max}}{\frac{1}{N} * \sum_{i,j=1}^N (p_{(i,j)})^2} \quad (13)$$

5 Machine Learning Algorithms

Decision Tree (DT)

One of the most popular supervised training algorithms is a decision tree as it can be used for regression as well as classification. The main goal here is to predict the class which can be easily learned by simple decision rules obtained from training data. For predicting a class for a dataset, it starts from the root of a tree. Then, the comparison of root feature and record's feature is done. Based on a similar record, the branch equivalent to that record is followed and jumped to the next decision point.

K-Nearest Neighbor (KNN)

It is one of the simplest machine learning algorithms as it uses supervised machine learning techniques. The algorithm puts the new data into the most similar category as the old data as it assumes the similarity between those two cases. All the data fed to the algorithm is stored; then at the time of testing, the data is used and easily classified into a suitable category. This algorithm is mostly used for classification problems but can also be used for regression.

Support Vector Machine (SVM)

Support vector machine (SVM) is the most popular machine learning algorithm used for classification as it is a supervised learning technique. Here, each data point is plotted in n -dimensional space (n = number of features). The main goal of SVM here is to select a hyperplane that can differentiate two classes very well.

Ensemble Bagging Tree (EBT)

To produce a better predictive performance, several decision trees are assembled rather than using a single decision tree. To reduce the variance of the decision tree algorithm, bagging is used. Here, several samples of training data are taken randomly with replacement. These small samples are used to train small decision trees to create several models. The average of all these models makes more robust predictions than a single decision tree.

6 Results and Discussions

Extraction of an image, geometrical transformations and feature vector formation has been done in Anaconda Python, and the training and testing of the machine learning models have been done in MATLAB. 800 samples are developed via geometrical transformations to balance the dataset, after which the feature vector consists of a set of 13 features is calculated (Table 2) that is then fed to four different machine learning models shown in the previous section.

The results (Table 3) show that for simple training, KNN and EBT algorithms achieve 100% accuracy without validation. But when that dataset is divided into training and testing, it is seen that KNN achieves the highest accuracy of 100% for

Table 2 Feature vector

SD	Mean	Var	Energy	Homo	Kurt	Skew
0.1467	0.6623	0.0215	1884.7082	126.9868	2.5852	0.1402
0.2145	0.4278	0.0460	938.1570	78.4378	2.9591	0.5792
0.1951	0.5775	0.0381	1521.8166	110.3423	2.5134	0.0877
0.1510	0.6153	0.0228	1644.0397	117.3282	2.8896	0.3977
0.1680	0.7088	0.0282	2173.0984	139.2470	2.9209	0.6353
0.1342	0.7331	0.0180	2274.9918	138.3705	2.7576	0.3280
0.2124	0.5929	0.0451	1624.6722	122.7459	2.1939	0.1266
0.2259	0.5138	0.0510	1290.3038	79.2973	2.1181	0.3041
RMS	Peak2Peak	CF	SF	IF	MF	Label
5.2980	0.7692	0.1887	7.9996	1.5099	0.0356	BF
3.4186	1.0000	0.2925	7.9912	2.3375	0.0856	BF
4.6193	0.9524	0.2165	7.9993	1.7317	0.0469	HB
4.9212	0.7857	0.2032	7.9983	1.6253	0.0413	HB
5.6689	0.8605	0.1764	7.9985	1.4109	0.0311	IF
5.8653	0.7407	0.1705	8.0009	1.3641	0.0291	IF
4.7404	0.9722	0.2110	7.9949	1.6866	0.0445	OF
4.1097	0.9574	0.2433	7.9987	1.9463	0.0592	OF

Table 3 Comparison of different machine learning algorithms

Machine learning algorithms	Training accuracy	Holding accuracy (25%)	Cross-validation accuracy	
			5-fold	10-fold
DT	99.8	99.5	98.9	98.9
SVM	99.9	99.0	99.0	99.1
EBT	100	99.5	98.9	98.8
KNN	100	100	99.3	99.6

25% holding and 99.6% at tenfold cross-validation. From confusion matrices (Fig. 4) of tenfold cross-validation, it is seen that KNN correctly predicts inner race faults but mis-predicts one sample for the other three classes. While SVM mis-predicts four samples for healthy bearing and one sample for the other three faults.

Ensemble bagged tree classified four samples of outer race fault as healthy bearing and classified three samples of healthy bearing as outer race fault. While the decision tree classified six samples of healthy bearing as other faults. It is clear from the above discussion that the KNN model performed best for classification of faults in training and validation.

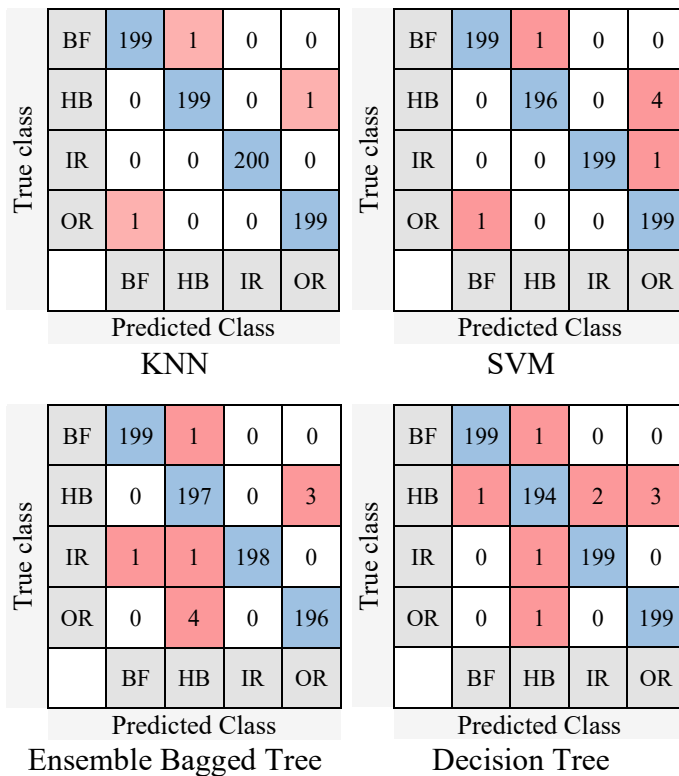


Fig. 4 Confusion matrix of tenfold cross-validation accuracy

7 Conclusion

Image processing applications for fault classification using machine learning techniques have seen rapid development in recent years. The present work utilizes recently developed technique for extracting a two-dimensional grayscale textured image from the vibration. Geometrical transformation, a data augmentation technique, is used for balancing the dataset. A set of time-domain features have been extracted from these images using the GLCM and other techniques that are then fed to four different machine learning models. From these results, it is concluded that K-nearest neighbor (99.6%) performed best for cross-validation.

Acknowledgements The authors would like to express gratitude toward Professor Loparo and Case Western Reserve University, Cleveland, Ohio, for providing a bearing dataset.

References

1. Vakharia V, Gupta V, Kankar P (2015) A multiscale permutation entropy based approach to select wavelet for fault diagnosis of ball bearings. *J Vib Control* 21(16):3123–3131. <https://doi.org/10.1177/1077546314520830>
2. Gaci S (2016) A new ensemble empirical mode decomposition (EEMD) denoising method for seismic signals. *Energy Procedia* 97:84–91. <https://doi.org/10.1016/j.egypro.2016.10.026>
3. Vakharia V, Gupta VK, Kankar PK (2017) Efficient fault diagnosis of ball bearing using ReliefF and random forest classifier. *J Braz Soc Mech Sci Eng* 39(8):2969–2982. <https://doi.org/10.1007/s40430-017-0717-9>
4. Uddin J, Kim JM, Islam R (2018) Texture analysis based feature extraction using Gabor filter and SVD for reliable fault diagnosis of an induction motor. *Int J Inf Technol Manag* 17(1/2):20. <https://doi.org/10.1504/IJITM.2018.10010489>
5. Li W, Qiu M, Zhu Z, Wu B, Zhou G (2016) Bearing fault diagnosis based on spectrum images of vibration signals. *Meas Sci Technol* 27(3):035005. <https://doi.org/10.1088/0957-0233/27/3/035005>
6. Khan SA, Kim J-M (2016) Automated bearing fault diagnosis using 2D analysis of vibration acceleration signals under variable speed conditions. *Shock Vib* 2016:1–11. <https://doi.org/10.1155/2016/8729572>
7. Azad M, Khaled F, Pavel M (2019) A novel approach to classify and convert 1D signal to 2D grayscale image implementing support vector machine and empirical mode decomposition algorithm. *Int J Adv Res* 7(1):328–335. <https://doi.org/10.21474/IJAR01/8331>
8. Boudiaf A, Moussaoui A, Dahane A, Atoui I (2016) A comparative study of various methods of bearing faults diagnosis using the Case Western Reserve University data. *J Fail Anal Prev* 16(2):271–284. <https://doi.org/10.1007/s11668-016-0080-7>
9. Amar M, Gondal I, Wilson C (2015) Vibration spectrum imaging: a novel bearing fault classification approach. *IEEE Trans Ind Electron* 62(1):494–502. <https://doi.org/10.1109/TIE.2014.2327555>
10. Khodja AY, Guersi N, Saadi MN, Boutasseta N (2020) Rolling element bearing fault diagnosis for rotating machinery using vibration spectrum imaging and convolutional neural networks. *Int J Adv Manuf Technol* 106(5–6):1737–1751. <https://doi.org/10.1007/s00170-019-04726-7>
11. Uddin J, Kang M, Nguyen DV, Kim J-M (2014) Reliable fault classification of induction motors using texture feature extraction and a multiclass support vector machine. *Math Probl Eng* 2014:1–9. <https://doi.org/10.1155/2014/814593>

12. Ruberto CD, Fodde G (2013) Evaluation of statistical features for medical image retrieval, p 10
13. Case Western Reserve University dataset. Bearing Data Center. <https://csegroups.case.edu/bearingdatacenter/home>
14. Galar M, Fernandez A, Barrenechea E, Bustince H, Herrera F (2012) A review on ensembles for the class imbalance problem: bagging-, boosting-, and hybrid-based approaches. *IEEE Trans Syst Man Cybern Part C Appl Rev* 42(4):463–484. <https://doi.org/10.1109/TSMCC.2011.2161285>
15. Guha R, Khan AH, Singh PK, Sarkar R, Bhattacharjee D (2020) CGA: a new feature selection model for visual human action recognition. *Neural Comput Appl*. <https://doi.org/10.1007/s00521-020-05297-5>